FAILURE ANALYSIS CASE STUDIES II

Edited by
D.R.H. Jones

Pergamon

Failure Analysis
Case Studies II

FAILURE ANALYSIS CASE STUDIES II

A sourcebook of case studies selected from the pages of
Engineering Failure Analysis 1997-1999

Edited by

D.R.H. JONES

Department of Engineering
University of Cambridge, UK

PREFACE

It is now three years since Elsevier Science published the first book of Failure Analysis Case Studies selected from volumes 1, 2 and 3 of the journal *Engineering Failure Analysis*. The book has proved to be a sought-after and widely used source of reference material to help people avoid or analyse engineering failures, design and manufacture for greater safety and economy, and assess operating, maintenance and fitness-for-purpose procedures. In the last three years, *Engineering Failure Analysis* has continued to build on its early success as an essential medium for the publication of failure analysis cases studies and papers on the structure, properties and behaviour of engineering materials as applied to real problems in structures, components and design.

Failure Analysis Case Studies II comprises 40 case studies describing the analysis of real engineering failures which have been selected from volumes 4, 5 and 6 of *Engineering Failure Analysis*. The case studies have been arranged in sections according to the specific type of failure mechanism involved. The failure mechanisms covered are overload, creep, brittle fracture, fatigue, environmental attack, environmentally assisted cracking and bearing failures. The book constitutes a reference set of real failure investigations which should be useful to professionals and students in most branches of engineering. My sincere thanks go to the authors of the case studies for finding the time to communicate their experiences to the wider world for the benefit of us all.

D.R.H. Jones
May 2001

CONTENTS

Fatigue

Environmental attack

Environmentally assisted cracking

Bearing failures

Overload failures

BURSTING OF A SILO

R. KIESELBACH

Failure Analysis of Metals, Swiss Federal Laboratories for Materials Testing and Research,
Überlandstrasse 129, CH-8600 Dübendorf, Switzerland

Abstract—This paper describes the bursting of a large silo on a farm, which caused considerable environmental damage and cost. The cause was misuse of the silo for vegetable slurry instead of for feed for livestock, and overfilling the silo. © 1997 Elsevier Science Ltd. All rights reserved.

Key words: silo, failure, rupture, hydrostatic pressure

1. INTRODUCTION

Most of the accidents in connection with silos are due to suffocation or gas poisoning of the farmers entering a silo. Some are also caused by the explosion of methane, which is produced by fermentation of the forage. Cases of bursting or explosion are, nevertheless, rather rare.

In the present case, three identical silos had been built on a farm, each with a diameter of 6 m (20 ft) and a height of nearly 25 m (80 ft). The hull of the vessels was made of steel plates measuring 1.4×2.68 m, and the thickness of the sheets varied from 5.7 mm at the bottom to 2.4 mm at the top. All in all, the silo consisted of 16 rings and one base ring. The individual sheets had been protected against corrosion by enamelling, and were joined by bolts and nuts. The joints were protected against corrosion by a special kind of mastic. The total capacity of a silo was approximately 630 m³.

Since the farm no longer had any use for the silos, they were rented to a feed company for the storage of feed for pigs. The slurry was delivered in tank cars and pumped into the silo. The silo was filled up repeatedly in the following months. Finally, a few minutes after a delivery, when the tank car had just left the site, the silo burst and spilled its contents, a slightly sour slurry. The collapse of the top of the silo also damaged the next, still empty silo, which buckled and also collapsed partially. The spilled slurry caused considerable environmental damage in addition to the cost of the silos and the cost of the interruption to service. According to the lorry driver, the silo had been, at that time, approximately three-quarters full, and the manhole lid had not been fastened, but only laid loosely on its flange.

2. INVESTIGATIONS AND TESTS PERFORMED

2.1. *Visual inspection*

The site of the accident was visited and the following observations could be made (see Figs 1–3). Silo 3 had failed and was severed above the seventh ring (counted from the bottom), where a reinforcement ring was attached. A zone, four rings high, had been separated, and hung partially on the silo, partially on the ground. The contents of the silo had spilled for approximately 30 m in a semicircle uphill and 200 m downhill. The pasture had been destroyed, the slurry being slightly sour after lactic acid fermentation.

The detached rings were separated into several pieces, and were in some places still immersed in a pool of slurry, such that it was difficult to make out where the pieces had belonged. Failure had

Fig. 1. Damaged silos: view of the site.

Fig. 2. Bolted joints of the sheets used for the silo. In the lower part, a reinforcement ring was attached.

occurred by rupture of the boltholes of the vessel in circumferential and longitudinal directions (Fig. 4).

After the search had been carried out, specimens were taken, as detailed in Table 1.

After the accident, the silo was still full up to the seventh ring (counted from the bottom), as can be seen from Fig. 5.
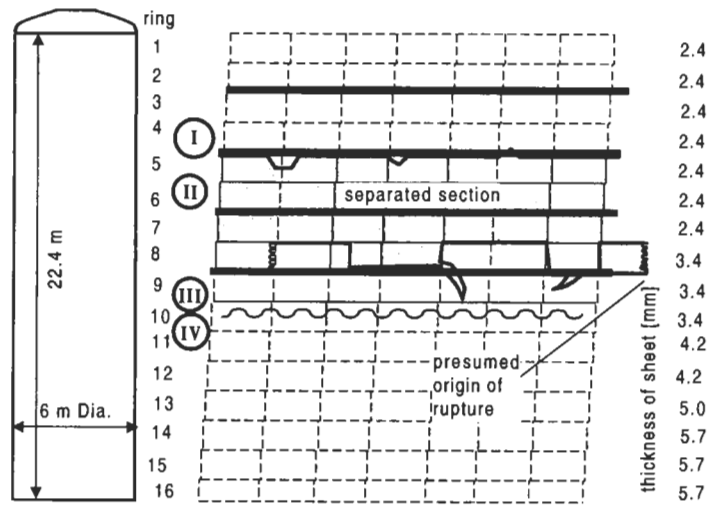
Fig. 3. Schematic drawing of the silo, showing the location of the rupture: (I) level theoretically necessary for bursting by hydrostatic pressure; (II) level for filling with 407 t; (III) permissible filling for density of 1.05 kg l^{-1}; (IV) level after bursting.
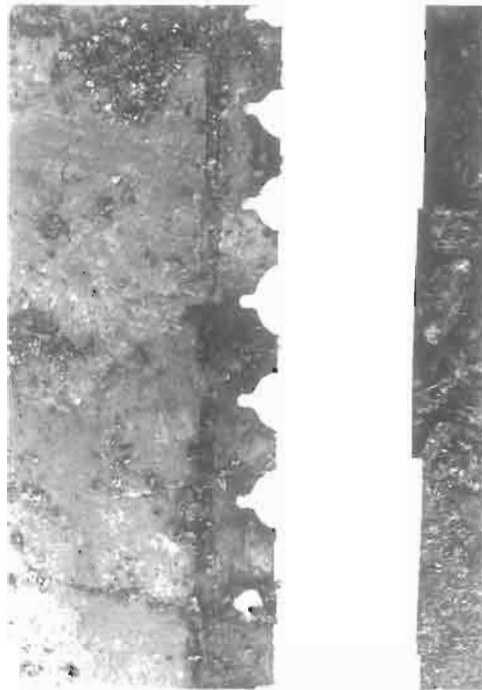
Fig. 4. Longitudinal bolted joint, presumably at location of start of rupture.

Table 1. Specimens and samples taken

A	One sheet/plate with a failed circumferential bolted connection
B	One plate containing an intact circumferential joint
C	One plate containing an intact longitudinal joint
D	Samples of slurry on site
E	Samples of slurry retained at the manufacturer of the slurry
F	Textile fibres from an airbag at the top of the silo
G	Two safety valves from the top of the silo

Fig. 5. Top view of failed silo, showing remaining filling level.

2.2. Tests for traces of an explosion

Specimens F were subjected to laboratory tests to detect possible traces of heat influence by fire or explosion. No such traces could be found. Thus, one can conclude that failure was not caused by the explosion of methane or any other gas produced in the silo by fermentation.

2.3. Tensile tests

The sheet metal was tested using specimens BR, CR, BP and CP, as shown in Fig. 6 and Table 2.
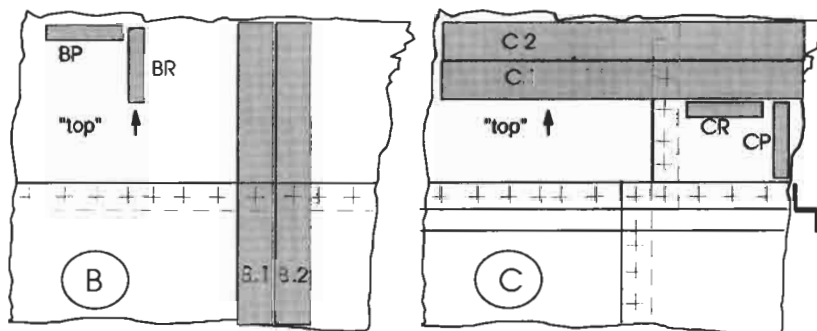
Fig. 6. Specimens for mechanical tests.

Table 2. Results of tensile tests on sheet material from silo

Specimen	Orientation	Yield strength (N mm^{-2})	Tensile strength (N mm^{-2})	Reduction of area (%)	Elongation (5 diameters) (%)	Uniform elongation (%)
BR	⊥ to joint	288	347	78	44.5	25
CR	⊥ to joint	267	316	77	47.5	24
BP	∥ to joint	300	345	75	43	24
CP	∥ to joint	278	313	70	46.3	29
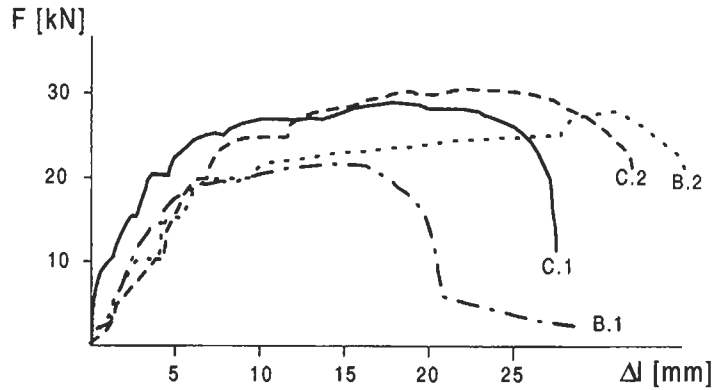
Fig. 7. Behaviour of bolted joints in tension tests.

Specimens B.1, B.2, C.1 and C.2 were tested for the strength of the bolted joints. From Fig. 7, it can be seen that they started to yield between loads of 15 and 25 kN, and that the deformation before fracture was in most cases more than 25 mm.

2.4. *Determination of the density of the slurry*

Four samples E gave an average density of $1.035\,\mathrm{kg\,l^{-1}}$. Sample D taken from the site had a density of $1.05\,\mathrm{kg\,l^{-1}}$.

3. NUMERICAL EVALUATIONS

3.1. *Determination of filling level from records of the user*

After the accident, the user of the silo supplied notes of deliveries, from which the theoretical filling level at the time of the accident could be calculated (Table 3).

This height corresponds to filling up to the upper edge of ring 7 (counted from the top).

3.2. *Stress analysis of bolted joint*

The average values for yield and ultimate strength are provided by the tensile tests on the sheet material, with $R_{p0.2} = 283\,\mathrm{MPa}$ and $R_m = 330\,\mathrm{MPa}$. This gives for shear:

$$\tau_{0.2,\mathrm{perm}} = \frac{R_m}{\sqrt{3}} = 163\,\mathrm{MPa}, \tag{1}$$

$$\tau_{m,\mathrm{perm}} = \frac{R_m}{\sqrt{3}} = 191\,\mathrm{MPa}. \tag{2}$$

For one bolt, at a distance of 25.4 mm from the edge of the sheet, one obtains

$$F_{0.2} = \tau_{0.2,\mathrm{perm}} \times 2.4 \times 25.4 \times 2 = 19.9\,\mathrm{kN}, \tag{3}$$

Table 3. Calculation of filling level from records

Contents according to bookkeeping notes	407,790 kg
Density according to tests, maximum	1.05 kg l⁻¹
Base area of silo (inside)	27.98 m²
Theoretical level	13.9 m

$$F_m = \tau_{m,perm} \times 2.4 \times 25.4 \times 2 = 23.3 \text{ kN}. \tag{4}$$

3.3. Assessment of the theoretical bursting pressure

In the test, the lower bound for the strength of the bolted joint was measured as $F_{Fracture} = 22 \text{ kN}$. This also corresponds to the mean value of the forces calculated from Eqns (3) and (4).

From the spacing of the bolts (108 mm), one obtains the force at fracture per unit length:

$$T = \frac{22 \times 10^3}{108} = 204 \text{ N mm}^{-1}. \tag{5}$$

The burst pressure can be calculated from this, using the diameter of the silo (6 m), as

$$p_{burst} = \frac{2 \times 204}{6000} = 0.068 \text{ N mm}^{-2}. \tag{6}$$

The corresponding level over the ruptured ring is

$$\Delta H = \frac{p_{burst}}{g\rho} = \frac{0.068}{1.05 \times 9.81} \times 10^3 = 6.6 \text{ m}. \tag{7}$$

This is equivalent to the height of 4.7 rings of the silo, and would mean that the level of the slurry was approximately in the middle of the third ring (counted from the top).

3.4. Spurting distance

From the visual inspection at the site of the accident, the approximate spurting distance of the slurry of 30 m is known. Since this was not a simple parabolical throw, but the jet was dispersed further after hitting the ground, the process can only be calculated approximately. The intention of such an assessment is, of course, to determine the filling height of the silo.

The horizontal velocity of the jet is given by $v = \varphi\sqrt{2g\Delta H}$, and from the distance the jet travelled one obtains

$$v = D\sqrt{\frac{g}{2(H_L - \Delta h)}}. \tag{8}$$

Thus, the height of the liquid above the leak is

$$\Delta H = \frac{D^2}{\left(H_L - \dfrac{7}{\Delta h}\right)4\varphi^2} = \frac{30^2}{\{H_L(1+d^*)^2 - 7(1+d^*)\}4\varphi^2}. \tag{9}$$

$d^* = \delta/D$ is the portion of the distance that the jet travels after hitting the ground, φ is the factor of constriction of the jet (normally $\varphi \le 1$), and the other symbols are explained by Fig. 8. If different
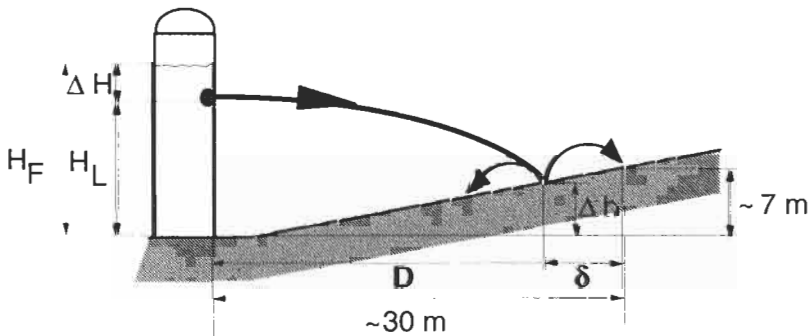
Fig. 8. Schematic view of the spurting of the slurry from the silo.
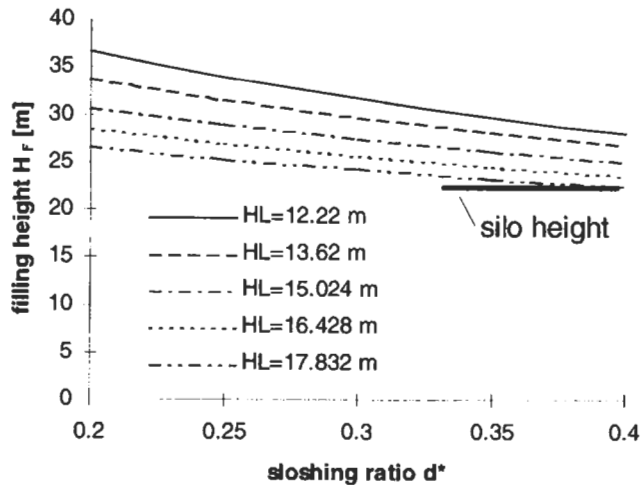
Fig. 9. Filling height of the silo necessary to produce the observed spurting distance, assuming different sloshing ratios d^* and different levels H_L for the initial leakage.

levels H_L for the first leak and different ratios of sloshing ($d^* = \delta/D$) are assumed, it can be seen from Fig. 9 that the silo must have been filled to the top, and the liquid must have sloshed relatively far after hitting the ground to have produced the observed pattern on the site.

4. CONCLUSIONS

(a) The visual inspection at the site of the accident showed the typical picture of failure by overpressure. Indications of an explosion or a chemical reaction, which could have produced the overpressure, were not found. A pressure above atmospheric pressure can also be excluded because the necessary safety devices were installed and operative.

(b) According to the manufacturer of the silo, it was permissible to fill the silo with liquid up to the seventh ring (counted from the bottom), i.e. *ca* 10 m high.

(c) The amount of 407 t, admitted by the user, corresponds to a filling height of *ca* 14 m.

(d) The assessment of the filling height from the observed spurting distance also points to a filling level practically at the top of the silo.

(e) The design, manufacture and assembly of the silo can be judged as proper, suitable and according to normal engineering practice.

(f) Tests on the material also indicate a higher level than the seventh ring (counted from the bottom). This is supported by the observed deformations in the failed bolted joint of the silo.

(g) An additional argument against the statement of the user related to the filling level is the fact that the silo was still filled to the middle of the tenth ring (counted from the top), although the whole neighbourhood was covered with slurry from the silo.

(h) Based on these findings it can be said that failure of this silo was caused by filling it to too high a level with liquid instead of forage.

(i) It cannot be completely excluded that a mix-up in the way of counting the rings has contributed to the failure. Whereas one would normally count the rings starting from bottom, as for buildings, the manufacturer of the silo counts the rings starting from top, because the silo is erected that way, assembling first the top, then putting rings under the top ring until the intended height of the silo is reached.

SHEAR FAILURE OF A ROAD-VEHICLE STEERING SHAFT

J. H. CLELAND

Cambcor Ltd, 30 Windsor Road, Cambridge CB4 3JW, U.K.

and

D. R. H. JONES*

Department of Engineering, University of Cambridge, Trumpington Street, Cambridge CB2 1PZ, U.K.

1. BACKGROUND

This case study describes the failure analysis of a fractured steering shaft from a heavy road vehicle which had been involved in a collision. The investigation was carried out in order to establish whether the failure was the cause or a consequence of the accident.

Figures 1 and 2 are scale drawings of the steering shaft. The shaft was supported by two needle
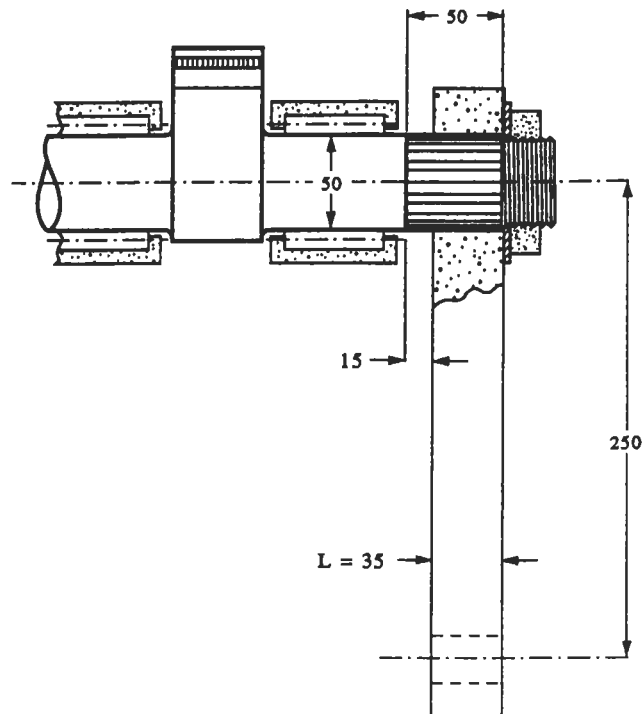
Fig. 1. Side view of the steering shaft. Dimensions in mm.

---

*Author to whom correspondence should be addressed.
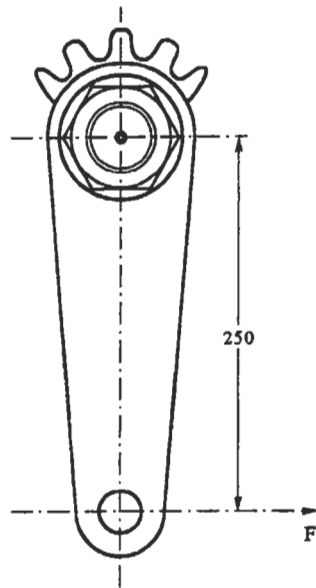
Fig. 2. End view of the steering shaft. Dimensions in mm.

roller bearings. Between the bearings was a toothed sector, which was driven by a worm connected to the steering wheel. The steering arm, which transmitted movement to the track rods, was attached to the end of the shaft by a splined connection. As shown in Fig. 3, the steering shaft had been subjected to a torsional overload. As a consequence of the overload, the splined section of the shaft had been twisted permanently (the ends of the splines were offset by 1.3 mm), and the shaft had fractured where it met the toothed sector. The twisted splines are shown in Fig. 4, and the matching fracture surfaces are shown in Fig. 5. Most of the fracture surface was relatively flat and smooth, but there was a region near the centre which was comparatively rough. Figure 6 is a view taken in the scanning electron microscope of the flat part of the fracture surface, which shows the classic features of shear failure. Figure 7 is a scanning electron micrograph taken from the rough part of the fracture surface, which shows the classic features of fibrous tensile failure. There were no indications of prior defects on the fracture surface.
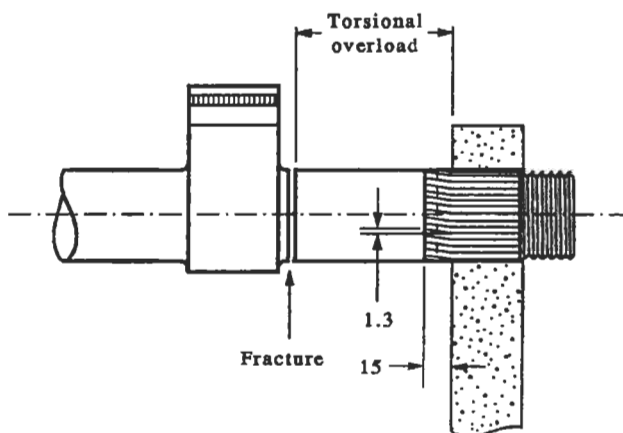
Fig. 3. Side view of the shaft, showing the plane of the fracture and the region of torsional overload. Dimensions in mm.
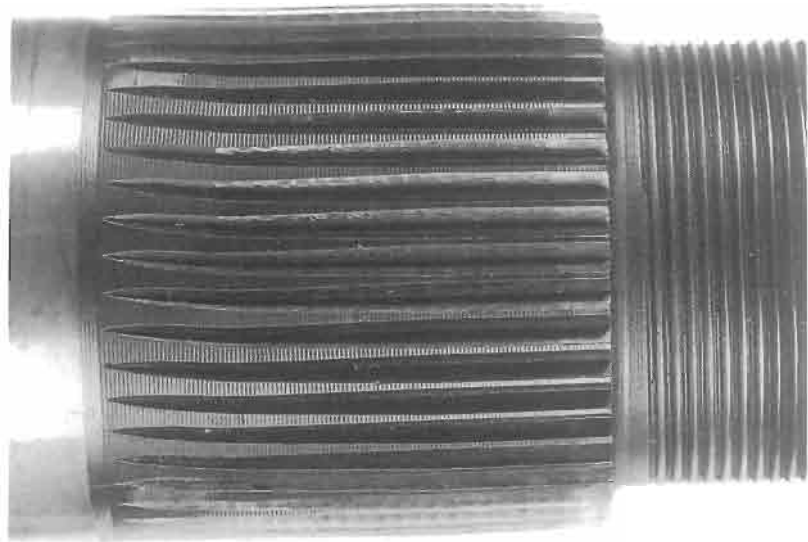
Fig. 4. Photograph of the splined section of the steering shaft, showing the twisted splines.

Fig. 5. Photograph of the matching fracture surfaces.

2. METALLURGY OF THE SHAFT

The shaft was manufactured from a nickel–chromium–molybdenum steel, and was subsequently case hardened. The specified composition is given in Table 1. The specified properties of the core in the quenched condition were as follows: yield stress, 736 MPa minimum; tensile strength, 1079–1324 MPa; elongation, 8% minimum; impact energy, 59 J cm^{-2} minimum. The case was required to have a Rockwell C-scale hardness of 59–63, equivalent to a Vickers hardness (HV) of 680–780 [1].

A thin slice was cut out of the shaft using a high-speed abrasive disc and a copious supply of coolant. One side of the slice was ground and polished for metallographic examination and hardness testing. Figure 8 is a macrograph of the polished cross-section after etching in 2% nital. The case-

Fig. 6. Scanning electron micrograph taken from the shear part of the failure. Magnification: 153 times.
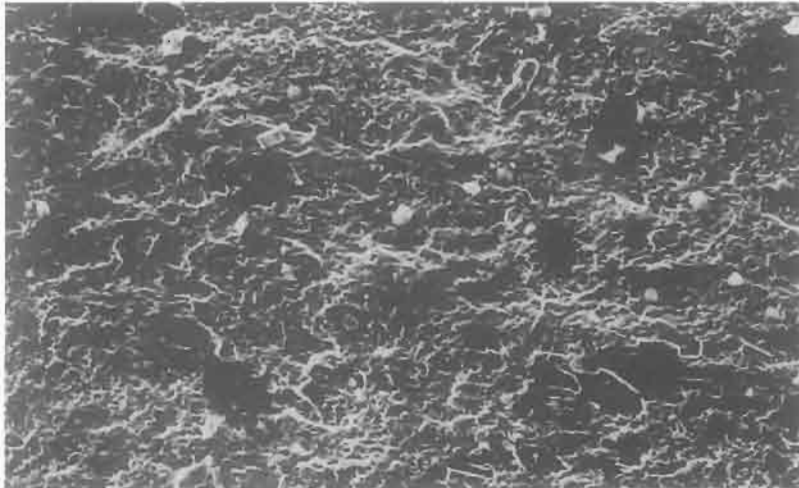
Fig. 7. Scanning electron micrograph taken from the fibrous part of the failure. Magnification: 292 times.

Table 1. Composition specification for shaft

Element	Weight %	Element	Weight %
Carbon	0.17	Phosphorus	0.035 maximum
Silicon	0.25	Chromium	1.6
Manganese	0.5	Molybdenum	0.3
Sulphur	0.035 maximum	Nickel	1.55

hardened layer shows up clearly as a dark etching skin (about 1.5 mm thick) on the outside of the shaft.

The Vickers hardness was measured on the polished surface as a function of the radial distance r from the centre of the shaft (see Table 2). Each result in Table 2 is the average of eight separate readings taken from sites that were spaced uniformly around a concentric circle.

Figure 9 shows the continuous cooling transformation (CCT) diagram for the steel of the shaft. Assuming that the shaft was oil-quenched, the diagram indicates that the structure at the centre should be 10% martensite + 90% bainite with a hardness of HV 340. As shown in Table 2, the

Fig. 8. Polished cross-section through the shaft, showing the case-hardened layer.

Table 2. Hardness measurements on shaft cross-section as a function of radial distance from the centre

r (mm)	HV	σ_{TS} (MPa)	k_u (MPa)
0	350	1120	700
10	360	1152	720
17.5	375	1200	750
22.5	400	1280	800
Case	880	2816	1760

measured hardness at the centre is HV 350, which agrees well with the predictions of the CCT diagram. It is normal practice to temper case-hardened components in the range 150–180 °C in order to improve the toughness [3]. Only if tempering had been carried out above 300 °C would there have been any significant decrease in the hardness of the core. Accordingly, the close correspondence between the measured hardness and the predicted as-quenched hardness does not necessarily indicate that the shaft had been inadequately tempered.

Table 2 shows that the hardness of the case (HV 880) is significantly higher than that specified (HV 680–780). However, there was no indication that this contributed to the failure. As shown in Figs 3 and 4, the splines were able to withstand a considerable shear strain even though they were case-hardened. The maximum engineering shear strain suffered by the splines was

$$\gamma = 1.3 \, \text{mm}/15 \, \text{mm} = 0.087 = 8.7\%, \tag{1}$$

equivalent to a plastic strain in uniaxial tension [4] of

$$\gamma/\sqrt{3} = 0.050 = 5.0\%. \tag{2}$$

3. ESTIMATING THE FAILURE TORQUE

Referring to Fig. 10, it can be seen that the torque required to cause the shear fracture of a narrow concentric band of the cross-section is
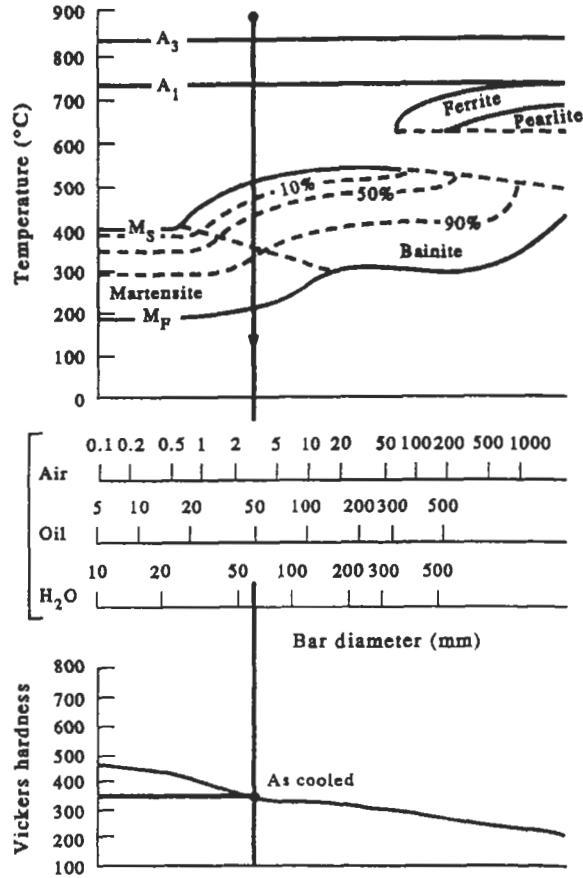
Fig. 9. Continuous cooling transformation diagram for the steel of the shaft [2]. Before quenching, the samples were first heated at 900 °C for 4 h.
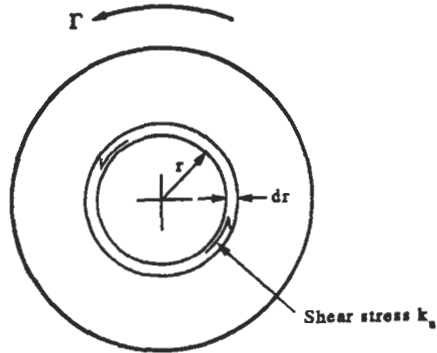
Fig. 10. Calculation of torsional moment.

$$d\Gamma = 2\pi k_u r^2 \, dr, \tag{3}$$

where k_u is the ultimate shear stress. The ultimate shear stress can be estimated from the empirical expression [4]

$$k_u = \sigma_{TS}/1.6, \tag{4}$$
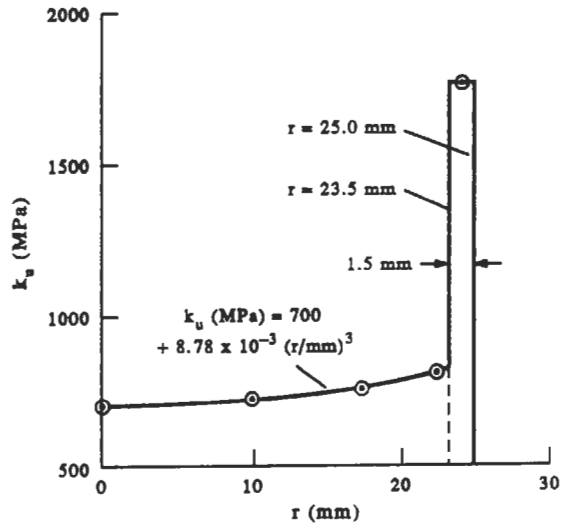
Fig. 11. Plot of ultimate shear stress against radial distance from the centre of the shaft.

where σ_{TS} is the tensile strength. The tensile strength can in turn be estimated from the hardness data using the empirical expression [4]

$$\sigma_{TS}(\text{MPa}) = 3.2 \times \text{HV}. \tag{5}$$

Values of tensile strength and ultimate shear stress were estimated from the hardness measurements using Eqns (4) and (5), and are listed in Table 2. The ultimate shear stress is plotted against radial distance from the centre of the shaft in Fig. 11. As Fig. 11 shows, the ultimate shear stress can be described by the empirical expression

$$k_u(\text{MPa}) = 700 + 8.78 \times 10^{-3}(r/\text{mm})^3 \tag{6}$$

over the core of the shaft (the region from the centre of the shaft to the inner edge of the case). The torque required to cause shear fracture of the core is then given by

$$\Gamma = 2\pi \int_0^{23.5\,\text{mm}} (700 + 8.78 \times 10^{-3}r^3)r^2 \, dr \, \text{N mm} = 2.06 \times 10^7 \, \text{N mm}. \tag{7}$$

The torque required to cause shear fracture of the case can be found from the standard expression [4]

$$\Gamma = \frac{2\pi k_u(r_1^3 - r_2^3)}{3}, \tag{8}$$

where r_1 ($= 25$ mm) is the outer radius of the case, and r_2 ($= 23.5$ mm) is the inner radius of the case. Since $k_u \approx 1760$ MPa for the case, the failure torque is 0.98×10^7 N mm.

The total torque is therefore $(2.06 + 0.98) = 3.04 \times 10^7$ N mm. It is interesting to notice that, even though the case is only 1.5 mm thick, it is responsible for nearly one-third of the total torsional strength. This is partly because the case is more than twice as strong as the core, and partly because the torsional strength depends on the cube of the radius.

It should be stressed that the present analysis provides an upper-bound estimate for the failure torque since it assumes that all parts of the cross-section reach the failure strain at the same instant. In practical terms, this is unlikely unless the failure strains of the core and the case are similar.

4. ESTIMATING THE APPLIED FORCE

We assume that the torque on the shaft was produced by applying a lateral force F to the end of the steering arm as shown in Fig. 2. Taking moments about the axis of the steering shaft, we have

$$F \times 250\,\text{mm} = 3.04 \times 10^7\,\text{N mm}, \tag{9}$$

giving $F = 12.4$ tf. A force of this magnitude can readily be generated in a major collision. If we assume a vehicle weight of 20 t and a modest deceleration of $5g$, then the collision force is 100 tf. This is 8 times the force required to shear the shaft, so the steering arm need only be subjected to one-eighth of the collision force to cause the failure.

5. CONCLUSIONS

The steering shaft had been subjected to a large axial torque, sufficient to cause gross yielding of the cross-section and fracture by a ductile mechanism. There were no indications that failure was promoted by prior defects or inadequate mechanical properties. If a small fraction of the likely collision force had been applied to the end of the steering arm, this would have been sufficient to cause failure. We therefore conclude that the failure was a consequence of the accident, and not its cause.

REFERENCES

1. *Smithells' Metals Reference Book*, 7th edn. Butterworth–Heinemann, Oxford, 1992.
2. Atkins, M., *Atlas of Continuous Cooling Transformation Diagrams for Engineering Steels*. British Steel Corporation, Swinden, 1980.
3. Parrish, G. and Harper, G. S., *Production Gas Carburising*. Pergamon Press, Oxford, 1985.
4. Jones, D. R. H., *Engineering Materials* 3. Pergamon Press, Oxford, 1986.

BREAKUP OF THE FIREWALL BETWEEN THE B AND C MODULES OF THE PIPER ALPHA PLATFORM—I. ANALYSIS BY HAND CALCULATION

A. C. PALMER

Department of Engineering, University of Cambridge, Trumpington Street, Cambridge CB2 1PZ, U.K.

Abstract—In the Piper Alpha disaster, the initial explosion in module C destroyed the firewall between modules C and B, and fragments caused secondary damage which lead to a fire. This paper describes the dynamic analysis of the explosion response of the firewall which was not intended to resist blast and was relatively lightly constructed. The analysis is based on hand calculation of idealised elastic and elastic–plastic models. © 1998 Elsevier Science Ltd. All rights reserved.

1. INTRODUCTION

An explosion occurred on the Piper Alpha production platform in the North Sea on 6 July 1988. In the subsequent fire 167 lives were lost, and the platform was destroyed. The incident was the subject of a major public inquiry and extensive investigations and litigation. The inquiry concluded that the initial explosion occurred in module C, and resulted from a flammable cloud created from a hydrocarbon release, at a blind flange fitted where a pressure safety valve had been removed for maintenance.

Observers saw a fireball emanate from module B at the west face of the platform some 10 s after the initial explosion. The appearance of the fireball was consistent with a condensate release. The inquiry concluded that the B/C firewall, between the C module and the B module, had been at least partially destroyed by the explosion, and that fragments from the firewall had been projected into module B and had ruptured a 4 in. pipeline carrying condensate.

The accident had unusual features. No wreckage could be examined, because most of the platform collapsed into the sea during the fire, and only the two accommodation modules were recovered. It was decided that any attempt to recover additional wreckage would not have a forensic value that would justify the risks and costs that would be incurred, since it would no longer be practicable to distinguish damage that had occurred during the original explosion from damage during the fire, collapse and subsequent recovery. On the other hand, some revealing photographs were taken less than half a minute after the explosion.

This paper describes additional research into possible explosion damage to the firewall, carried out as part of subsequent legal proceedings. The analysis is complicated by the fact that the firewall was not intended to resist pressure, and that it contains elements of widely different strengths, with a limited capability to redistribute loads.

Complex structures of this kind are nowadays almost invariably analysed by finite-element methods. However, for legal reasons that regrettably cannot be examined here, there were two independent analyses, one by hand calculations alone and the other by the finite-element method. The structure is too complicated for analysis by hand calculation to give a complete picture, but a hand calculation does give useful results which will answer the key questions that are important to an understanding of what happened. In particular, it can tell us:

1. whether or not the wall would break up;
2. when it would break up, in relation to the timing of the explosion;
3. if it broke up, how fast the fragments would be moving.

This paper is concerned with the first and second questions, and describes the hand calculations. A second paper will describe the finite-element calculations and compare the results of the two analyses.

2. STRUCTURE OF THE B/C FIREWALL

The platform topsides between the 87 ft and 107 ft levels had four modules, identified by letters A to D from south to north. The firewalls between the modules were intended as fire barriers, and were not designed to resist blast. The B/C and A/B firewalls were similar in construction, but the C/D firewall was thicker and more massive: the significance of this point is discussed below.

The B/C firewall was 6.35 m high, and extended across the whole 46.63 m breadth of the platform. Its construction is illustrated in Fig. 1, which shows part of the wall, and details of the cross-section and clamping.

The wall was composed of rectangular and square panels within rectangular frames, some 2438 by 1524 mm (8 by 5 ft "large frames"), others 1524 by 1457 mm ("small frames"), and a few smaller. Each panel was bounded by a rectangular frame made of $50.8 \times 50.8 \times 6.35$ mm ($2 \times 2 \times 1/4$ in.) steel angle, welded at mitre joints at the corners. The frame held a sheet of fire resistant composite, an 8.5 mm asbestos–cement core faced on both sides by 0.5 mm galvanised steel sheets, pierced by 6.35 mm tined holes on a 17.5 mm square grid. The composite sheet was bolted into the frames by 9.53 mm (3/8 in.) Whitworth bolts ("panel bolts").

The frames were bolted together by 9.53 mm bolts ("frame bolts"). There is conflicting evidence about the spacing of the frame bolts, which gave values between 15 and 24 in., and the subsequent analysis is based on an intermediate spacing of 18 in. (457.2 mm). Generally, but not always, the lowest panel was large, the next panel small, and the top panel large.

At the foot of the wall the frames were welded to the deck plate. At the top the frames were bolted to 76×51 mm angle cleats, which were bolted to 102×63 mm cleats, which were welded to the ceiling plate.

The firewall lay on the south side of the heavy trusswork which formed part of the module structural framing. The truss was a sequence of N-shaped panels. The wall was clamped to the truss by two lines of clamps, one just over 2438 mm from the floor (just above the lower bolted join between frames), and the other just over 3962 mm from the floor. Each clamp held the wall against the truss by two lengths of 9.53 mm studding. An explosion in module C would push the wall to the south, away from the trusswork, and would put the studding in tension.

There were minor variations in construction along the length of the wall, which included a door, pipe penetrations of a few composite panels, and some smaller frames.

3. OVERPRESSURE LOADING OF B/C FIREWALL BY AN EXPLOSION IN MODULE C

The inquiry report [1] examined the evidence for the size of the flammable cloud before the first explosion. It concluded that the fuel involved was condensate, and that the mass of fuel within the flammable part of the cloud was probably in the range 30–80 kg [1], Section 5.

Computational fluid dynamics (CFD) calculations were carried out by CMI [2]. The calculations are based on a gas cloud containing 45 kg of condensate, homogeneous and at stoichiometric concentration, and ignited close to the south wall. Figure 2 gives the calculated pressure history at point P1, which is in module C, on the B/C wall near the west end. The maximum pressure reached at P1 was 19.5 kN/m² (0.195 bar). The maximum pressures at other points within module C were higher. The CFD calculation assumed that the wall broke up when the instantaneous pressure reached 10 kN/m².

In the subsequent dynamic analysis the pressure history is idealised as an asymmetric triangular pulse with peak 19.5 kN/m², rise time 81 ms and fall time 46 ms. Figure 2 compares this idealisation with the calculated history.

36"×12"×194 UB

133 229 6C

FLANGE
EXTENSIONS

SITE WELD
TO TRUSS

4"×2.5" L CLEAT WITH
BOLTED HOLE FOR 3/8"
WHITWORTH BOLTS

32

DETAIL 1
(SCALE 1:10)

2"×2"×1/4" L FRAMES
3/8" WHITWORTH
FRAME BOLTS

PANEL BOLTS

3/8" 3DF2 COMPOSITE
SHEETING

DETAIL 2
(SCALE 1:10)

SITE WELD TO 3/8" THK
DECK PLATE

DETAIL 3
(SCALE 1:10)

1524

A

2445

1457

2445

PANELLING ELEVATION VIEWING FROM SOUTH
(SCALE 1:75)

A

DETAIL 1

NORTH
(C MODULE)

SOUTH
(B MODULE)

DETAIL 2

DETAIL 3

SECTION A-A

Fig. 1. B/C firewall: elevation and details.

21
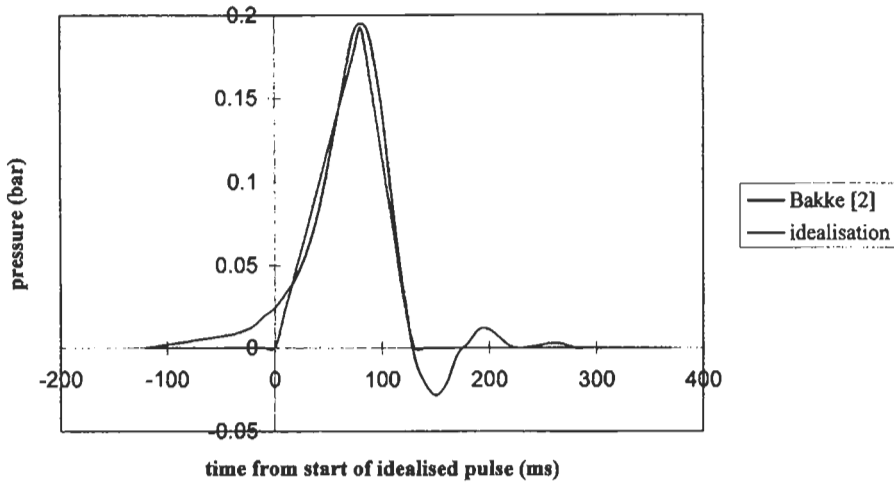
Fig. 2. Pressure pulse at point P1.

4. APPROACH TO STRUCTURAL ANALYSIS

There are several possible modes of failure of such a firewall under lateral pressure loading by an explosion. The panels can come apart by fracture of the frame bolts between them, the composite sheets can fail in bending or in tension, the panel bolts can fracture in tension or tear through the fixing holes, the angle section can fail in flexure or in torsion, and so on.

If an increasing pressure is applied to the wall, then the wall will fail in bending. Other modes of failure are possible in principle, but simple calculations show that they do not govern: in other words the wall fails in bending at a lower pressure than it would fail in other modes. For example, elementary calculations show that failure by a panel bolt hole mode, in which the panel bolts tear through the holes in the composite panels, requires a significantly higher load than several bending modes do. That is confirmed by the results of a pressure test on a small 900 mm square section of Durasteel panel, which withstood $70 \, kN/m^2$.

Supplementary comparative calculations were carried out to check the resistance of the wall to other modes of failure, and this aspect is examined in Section 10.

5. LOCAL STRENGTH OF FIREWALL

If the dominant mode of failure is bending, the stress parameter that determines the local structural response is the bending moment stress resultant, denoted m. The limiting maximum value that m can take depends on how the panel fails locally. It can be calculated by routine methods of structural mechanics. Table 1 lists the different possible modes, gives the limited value of the moment stress resultant for each mode, and includes a simple sketch of each mode.

The local strength against frame bolt failure in tension depends on the direction of bending. If the angles connected by the bolts are loaded so that they put the bolts in tension by relative rotation around the angle toes, the maximum tension, T, in each bolt has the lever arm g_2 between the bolt axis and the toe. The bending moment per bolt is then Tg_2, and if the frame bolt spacing is s the moment stress resultant is Tg_2/s. If the direction of bending induces relative rotation about the angle heels, the lever arm is g_1 and the maximum moment stress resultant is Tg_1/s.

The calculations used to arrive at the numbers were carried out algebraically, so that each calculation leads to a formula and the influence of uncertainties and variations in material parameters can readily be assessed. Some modes apply to small areas: flexural collapse within a composite panel is an example, since it must occur within the compass of a frame if it is not to involve frame bending

Table 1

mode	sketch	m (N)	note
1		829	frame bolts yield; rotation about toes
2		945	hinge in panel
3		1244	frame bolts yield; rotation about heels
4		2571	hinge in angle leg
5		3344	frame and panel

too. Other modes only apply to large areas: for instance, failure by fracture of frame bolts obviously does not apply to areas which do not include the connection between adjacent frames.

The table shows that the bolted connections between the frames are weak by comparison with the frames themselves, whereas the bending moment capacity of the composite panels is about the same as the capacity of the bolted connections. This suggests that the capacity of the wall to resist pressure is limited *either* by the frame bolts *or* by the strength of the composite panels between the frames.

6. GLOBAL STRENGTH OF SEGMENTS OF FIREWALL

The wall can be thought of as a sequence of right-angled triangular segments, alternately base up and base down, each segment corresponding to one of the triangles of the N-form truss. The base of each triangle is bolted or welded to the ceiling or the floor, and the other two sides are clamped to a vertical or a diagonal of the truss.

The triangles are almost identical, although not precisely so, because the relation between the layout of the frames and the layout of the truss varies between segments. If we neglect that variation, each triangular segment can be treated as part of an infinite plate between parallel abutments, supported to form the infinite sequence of right-angled triangular segments sketched in Fig. 3. Under a uniform pressure loading extended over the whole plate, each segment will deform identically, and symmetry then imposes some conditions of the deformation. If $w(x, y)$ is the deflection of triangular segment 1 in Fig. 3, $w(-x, b-y)$ is the deflection of segment 0, $w(a-x, b-y)$ is the deflection of segment 2, and so on. Symmetry and continuity impose additional conditions on the derivatives on the boundaries: for instance, on the vertical boundary between segment 2 and segment 3

$$w_x(0, y) = -w_x(0, b-y) \tag{1}$$

and therefore the rotation is zero at midheight, and the mean rotation is zero on the boundary between segments 2 and 3. The same condition applies on the inclined boundaries between 1 and 2, between 3 and 4, and so on. Each triangular segment has no rotation on its horizontal side, and no
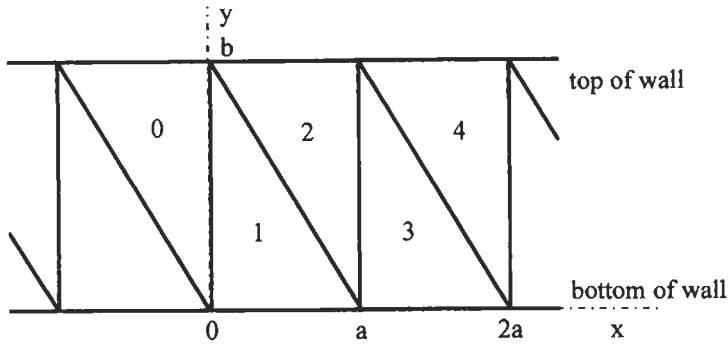
Fig. 3. Elevation and reference axes.

mean rotation on its inclined and vertical sides, and it is a good approximation to treat it as clamped on all three sides.

The next step is to relate the maximum moment stress resultant to the loading. Consider first a series of geometrically-similar plates, each characterized by an area A and loaded by a uniform pressure p, and made of the same material. It can then be shown by dimensional analysis that the maximum value of m must be proportional to pA. The form of the relationship is therefore:

$$m = pA/k \qquad (2)$$

The value of k depends on the material properties, on the shape of the plate, and on how the edges are fixed.

We can calibrate this relationship by using analytic solutions for simple shapes. Values derived in this way are listed in Table 2. Each solution takes the plate edges as clamped. The table could be based on elastic solutions, for which the stress in the plate does not anywhere, reach the yield point, or it could be based on plastic solutions, which correspond to a condition in which the plate yields and a collapse mechanism develops. Since we wish to focus on the conditions that are present when the plate fails, the second plastic option is chosen. The values of k are derived from solutions to the problem of plastic collapse of a thin plate, within the well-established theoretical framework of plastic analysis of plates.

The analytic solution for a circular plate is exact. The other solutions are based on lower and upper bounds on collapse pressure, which can be derived from the lower and upper bound theorems of plasticity theory.

The table shows that the value of k does not depend strongly on the shape of the plate. This suggests that we can adopt a single value of k, and can use it to derive an approximate general relationship between pressure, area and maximum value of the moment stress resultant. The relationship ought to be applicable under the following conditions:

1. the plate is only supported at its edges, and not by internal supports;
2. the breadth and width of the plate are comparable, so that the plate is not long in one direction and narrow in the transverse direction: Table 2 suggests a maximum length/breadth ratio of 2;
3. the shape is convex.

Table 2

shape	$k = pA/m$	source	yield condition	notes
square	42.8	[6, 7]	Johansen	refined upper bound
square	32.0	[7, 8]	Johansen	lower bound
circle	35.4	[9]	Tresca	exact
2:1 rectangle	56.6	[8, 10]	Johansen	upper bound
hexagon	40.0	[11]	Johansen	lower bound
equilateral triangle	41.6	[6]	Johansen	upper bound

An approximate relationship between the area of a section of firewall and the maximum pressure it can sustain can be derived by bringing these results together. Taking the smallest value of 829 N from Table 1, and taking k as 50 from Table 2, the relationship is

$$p = 41450/A, \tag{3}$$

where p is in N/m² and A is in m². Most of the triangular segments have an area of aboout 14.55 m², the precise value depending on the detailed layout. The corresponding breakup pressure is therefore approximately 2.8 kN/m² (0.028 bars), much smaller than the calculated maximum pressure at point P1. This indicates that the firewall cannot withstand the pressure of the explosion in module C. A small number of triangular segments are slightly larger at 16.2 m², and have a correspondingly smaller breakup pressure.

7. DYNAMIC RESPONSE: ELASTIC MODEL

Section 6 gives us an estimate of breakup pressure under slow loading, in which the loading time is long by comparison with the lowest natural period of flexural oscillations. The next step is to consider the dynamic response of the firewall to the actual pressure pulse, which is quite short (between 100 and 200 ms), so that the dynamic response may be quite different from the response to the same maximum pressure applied slowly.

Two idealisations were used. The first idealisation treats the deflection of the firewall as elastic, but treats the critical deflection at which breakup begins as having both elastic and plastic components, since the bolts have some capacity to extend plastically before they break. The second more complete idealisation treats the wall as elastic-plastic, and is examined in Section 8.

The first step is to determine the natural frequency for a firewall segment, so that the loading time can be compared with the period corresponding to the lowest natural frequency. Appendix A is a summary of this calculation, which was carried out using the Rayleigh method.

The calculation idealises each firewall segment as a uniform plate with clamped edges. The mass is taken as uniformly distributed and equal to the average mass per unit area. A comparison "exact" calculation based on the actual distribution of mass in a typical segment confirms that this is an excellent approximation: the difference between the "exact" and "averaged" natural frequencies is 0.8%. The equivalent stiffness is more difficult to estimate, because the absence of structural continuity between adjacent frames leads to a significant contribution to the firewall flexibility from torsion in the angle sections between the frame corners and the nearest frame bolts. The equivalent plate flexural rigidity D was estimated as 10 000 N m. This was taken as the base case, but the study examined the sensitivity of the conclusions to the assumed value of D: this point is returned to later.

The estimated lowest frequency is 73 rad/s, which corresponds to a natural period of 86 ms. Looking back to Fig. 2, we can see that the loading time is of the same order as the natural period, neither much longer (so that the response would be quasi-static) nor much shorter (so that the response would correspond to impulsive loading).

The next step is to calculate the dynamic response. Pressure loading which is nearly uniform over a firewall segment primarily excites the lowest mode (corresponding to the lowest frequency). The lowest-mode response for central deflection can be written down as a formula which is a multiple of two terms. The first term is the deflection that would occur if the loading were applied slowly. The second term multiplies the first, and accounts for dynamic effects: it is a function of the natural frequency, the time that has elapsed since the pressure pulse began, and the duration and shape of the pulse. The multiplying second term is identical to the corresponding formula for a simple one-degree-of-freedom mass-on-spring system.

The results are shown in Fig. 4, which plots deflection at the centroid of a triangular segment against time; time is measured from the start of the triangular pulse in Fig. 2.

The deflection when the wall begins to break up can be estimated as the sum of two components:

1. the elastic deflection of a segment under the estimated collapse pressure under quasi-static loading, represented by x_Y in Fig. 5;
2. the additional deflection associated with plastic elongation of the frame bolts until they reach their specified minimum elongation, represented as $x_F - x_Y$ in Fig. 5.
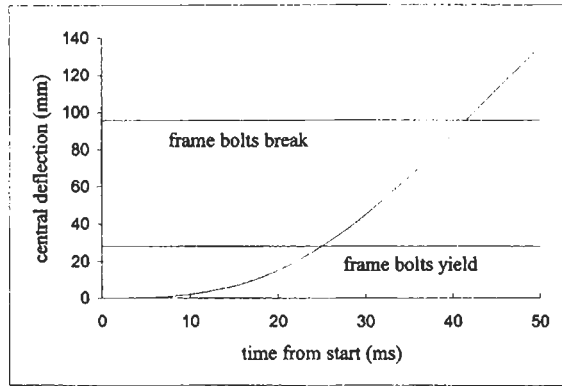
Fig. 4. Response calculated by elastic analysis.
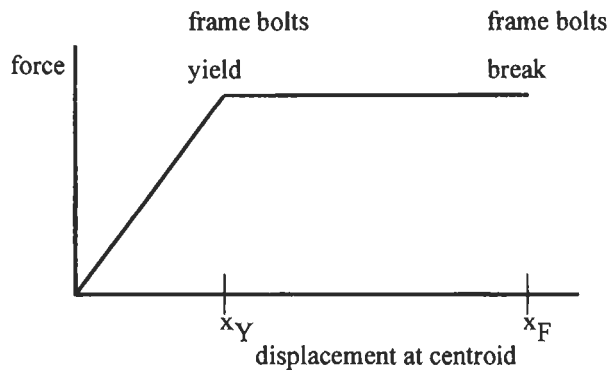
Fig. 5. Idealised relationship between applied force and displacement at centroid.

Taking D as 10 000 N m, the corresponding x_Y is 28 mm and $x_F - x_Y$ is 68 mm, so that the estimated deflection when frame bolts begin to break is 96 mm. This deflection is reached after 42 ms. The instantaneous pressure at that time is just below 0.1 bars, which is consistent with the value adopted for the onset of venting in the CFD calculation described in Section 2.

8. DYNAMIC RESPONSE: ELASTIC–PLASTIC MODEL

The analysis described in Section 7 treats the dynamic response as elastic, but determines the critical deflection at which the wall begins to break up as having both an elastic component (the general deflection of the firewall) and a plastic component (the additional deflection corresponding to plastic extension of the frame bolts). It can be improved by treating the dynamic response as elastic–plastic, explicitly taking into account the second phase of the motion, in which the wall is deflecting plastically by the plastic extension of frame bolts, but the frame bolts have not yet reached the extension at which they break.

The elastic–plastic analysis idealised the wall as a single degree-of-freedom mass-spring system. The function that relates the force applied to the firewall and the deflection x at the centroid of a triangular firewall segment is idealised in Fig. 5. The initial response is linear and elastic, up to the pressure at which the frame bolts yield: the corresponding deflection is denoted x_Y. The wall then deflects at constant force, until at a larger deflection x_F the most heavily-loaded frame bolts break. The pseudo-plastic deflection $x_F - x_Y$ corresponds to the extension of the frame bolts between yield

and fracture. An equivalent mass factor takes account of the lower velocity of the edges than the sides.

The first part of the response is elastic up to first yield in the frame bolts: the solution is a relationship between displacement and time, and the initial conditions are zero displacement and zero velocity at the start of the pulse. The second part of the response is plastic: the solution is another relationship between displacement and time, with two integration constants determined by matching the solutions for the first and second parts of the response.

Figure 6 is the calculated relationship between wall segment centroid displacement and time, for the elastic-plastic model, and for five values of D.

Taking D as 10 000 N m, the breakup displacement is reached after 42 ms, which is close to the value calculated from the elastic analysis in Section 7. The physical reason for this is that the initial phase wall response is dominated by the effect of the pressure pulse on the mass of the wall, and the stiffness of the wall has only a secondary effect, at least in the first 50 ms or so. This can be confirmed by expanding the analytic solution as a power series in t, and noticing that the wall stiffness appears only in the smaller second term.

The time at which the frame bolts begin to break is insensitive to the assumed value of D, whose calculated value depends on how close the frame bolts are to the frame corners. Calculations in which D ranges from 10 000 Nm to 39 000 Nm show that the breakup time changes only from 42 s to 44 s after the start of the pulse, and so the assumed value of D has a negligible effect on the calculated pressure at breakup.

Once the first bolt has broken, the forces in neighbouring bolts rapidly increase, and they break soon afterwards. This adverse redistribution of internal forces leads to rapid separation of the firewall into panels. The pressure has still not reached its peak when the wall disintegrates into its component panels, and the remainder of the pressure pulse further accelerates the panels and projects them into module C.

9. ALTERNATIVE FAILURE MECHANISMS

The analysis described above takes the governing factor as tension failure of the frame bolts. Other modes of failure are possible. The composite panels could collapse as plates within the frames, but a calcuiation based on plate theory and a test on a 900 mm square panel shows that this requires a much higher pressure than does failure of frame bolts.

Another possible mode is tension failure of the clamps that hold the frames to the truss. Each clamp consists of two lengths of 3/8 in. studding, and can carry 37.9 kN. There are 42 clamps, and
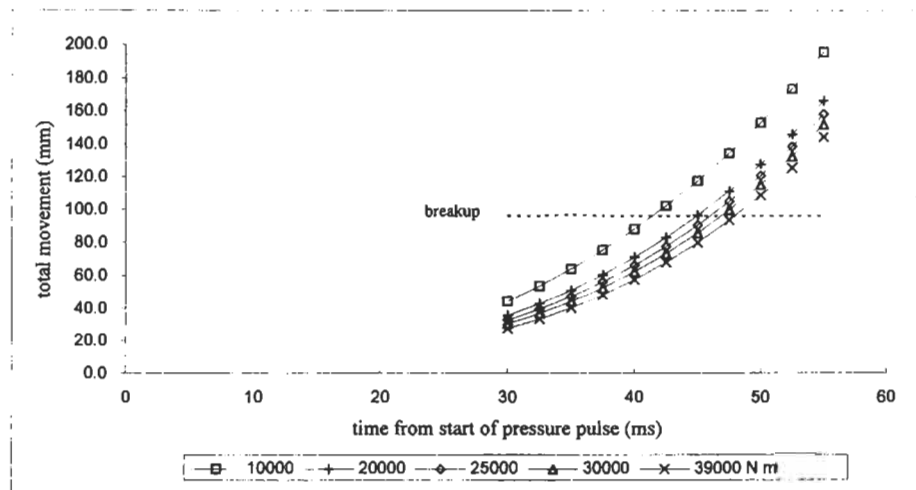
Fig. 6. Elastic–plastic analysis: movement at centroid as function of D.

together they can carry 1.59 MN. The total load that corresponds to the 19.5 kN/m² maximum pressure applied simultaneously across the whole firewall is 5.77 MN. The clamps are at midheight, and can be expected to carry at least half the total load. It follows that the clamps are not strong enough to carry the total load on the wall, and that the clamps would break if the the wall had not already broken up by failure of the frame bolts.

The analysis is based on plate theory, which is approximate because the deflection is not necessarily small by comparison with the effective thickness of the firewall. The effective thickness of the wall was estimated by finding the thickness which gives the same ratio between the fully-plastic membrane stress resultant at collapse in pure tension and the fully-plastic membrane stress resultant at collapse in pure bending [3], both calculated for the governing mode of frame-bolt failure in tension. The effective thickness turns out to be 80 mm for one direction of bending and 120 mm for the other. Moreover, the sides of the wall segments are not rigidly fixed at the top and bottom. It is known [4] that small inward movements at the edges of transversely-loaded plates much reduce the stiffening effect of membrane action, and an approximate calculation showed that in this instance an inward edge movement of the order of 1 mm would be enough to eliminate a significant increase in strength because of membrane effects. It was concluded that these effects could be neglected.

10. RESPONSE OF C/D AND A/B FIREWALLS

The wall between modules C and D was much stiffer and stronger than the wall between modules B and C. The estimated collapse pressure of one of its triangular panels under quasi-static slow loading is about 12 kN/m² (0.12 bars), compared to the peak pressure of 19.5 kN/m² at P1 in module C. The lowest natural frequency of one of its triangular segments is about 410 rad/s, corresponding to a period of 15 ms, and its response is not far from quasi-static.

The control room was in D module to the north of the C/D firewall, and had an additional wall of steel plate. Two survivors were in the control room at the time of the explosion. They were blown across the room, and saw that equipment near the wall had been damaged and that smoke was apparently entering at the top part of the wall. Accordingly, since the C/D wall is stronger than the B/C wall, it can be concluded independently that the B/C wall would have been more severely damaged by an explosion in C module than the C/D wall was.

The A/B wall was similar to the B/C wall in construction and arrangement. There is evidence from survivors that the A/B wall was not damaged. This supports the conclusion that the initial explosion was in C module. If the initial explosion had been in B module, it cannot be explained how the explosion leaves A/B intact but breaks down the stronger C/D wall. This is a particularly robust conclusion, and is of course independent of the calculations.

11. CONCLUSIONS

The analysis of the B/C firewall is consistent with the conclusion of the public inquiry, that an initial explosion in C module was followed by breakup of the firewall and projection of panel fragments into B module.

REFERENCES

1. The Honourable Lord Cullen, *The Public Inquiry into the Piper Alpha Disaster*, HMSO, 1990, Command 1310.
2. Bakke, J. R., *Gas Explosion Simulation in Piper Alpha Module C Using FLACS*. Christian Michelsen Institute, 1989, Report CMI no. 25230-1.
3. Jones, N., *Structural Dynamics*, Cambridge University Press, 1989.
4. Jones, N., *International Journal of Mechanical Sciences*, 1973, **15**, 547–561.
5. Gradshteyn, I. S. and Ryzhik, I. M., *Table of Integrals, Series, and Products*. Academic Press, 1979.
6. Mansfield, E. H., *Proceedings of the Royal Society A*, 1957, **241**, 311–338.

7. Wood, R. H., *Engineering Plasticity*, Cambridge University Press, 1968.
8. Jones, N., Report 71-20, contract GK-20189X, 1971.
9. Hodge, P. G., *Limit Analysis of Rotationally Symmetric Plates and Shells*. Prentice-Hall, 1963.
10. Wood, R. H., *Plastic and Elastic Design of Slabs and Plates*. Ronald Press, 1961.
11. Johnson, R. P., *Structural Concrete*. McGraw-Hill, 1967.

APPENDIX

Estimate of lowest natural frequency of firewall segment

An upper bound to the lowest natural frequency w of a plate with all edges clamped, uniform mass per unit area m and uniform plate flexural rigidity D, can be estimated by Rayleigh's method from

$$\omega^2 = \frac{D}{\mu} \frac{\int_A \left(\frac{\partial^2 w}{\partial x^2} + \frac{\partial^2 w}{\partial y^2}\right)^2 \, dA}{\int_A w^2 \, dA}$$

where $w(x, y)$ is a arbitrary deflection function which satisfies the kinematic boundary conditions, and both integrals are over the area of the plate. We consider a triangular plate whose vertices are $(0, 0)$ $(a, 0)$ and $(0, b)$, and take

$$w(x, y) = \left(\frac{x}{a}\right)^2 \left(\frac{y}{b}\right)^2 \left(1 - \frac{x}{a} - \frac{y}{b}\right)^2 3^6 w_0$$

which satisfies the boundary conditions for a clamped plate. The calculation is assisted by the integral

$$\int_0^b dy \int_0^{a(1-y/b)} \left(\frac{x}{a}\right)^l \left(\frac{y}{b}\right)^m \left(1 - \frac{x}{a} - \frac{y}{b}\right)^n \, dx = \frac{l!m!n!}{(l+m+n+2)!} ab$$

which is a special case of a standard integral quoted by Gradshteyn and Ryzhik [5]. After some algebra:

$$\omega^2 = 4004 \frac{D}{\mu a^2 b^2} \left(\left(\frac{a}{b}\right)^2 + 1 + \left(\frac{b}{a}\right)^2\right).$$

FAILURE OF A FLEXIBLE PIPE WITH A CONCRETE LINER

MARK TALESNICK* and RAFAEL BAKER

Department of Civil Engineering, Technion, Israel Institute of Technology, Haifa 32000, Israel

Abstract—This study documents the functional failure of a concrete lined steel sewage pipe. Symptoms of the pipe failure are presented. Failure of the pipe system can be attributed to incompatibility between the mechanical behavior of the pipe and the methodology employed in its design. The underlying cause of the failure may be traced to a lack of sufficient backfill stiffness. *In situ* testing was used to evaluate the stiffness of the side backfill. The existing pipe–trench system condition was analysed numerically and a criterion developed for the consideration of the structural integrity of the pipeline. © 1998 Elsevier Science Ltd. All rights reserved.

1. INTRODUCTION

The present paper documents a failure of a large diameter concrete lined steel sewage pipe, buried in a clay soil profile. The project consisted of a 3.5 km long gravity pipe in central Israel which failed before being placed in service. The present contribution documents the failure of this pipe–trench system. Field and laboratory testing provided significant insight into the probable cause(s) of failure. The case study accentuates some basic design principles, as well as the use of simple field tests as an effective diagnostic tool to evaluate site conditions.

2. DESIGN, CONSTRUCTION AND SITE CONDITIONS

The sewage pipeline was designed and constructed in central Israel during 1992–1994. The design called for a steel pipe with an inner diameter of 120 cm and a wall thickness of 0.64 cm. The inner surface of the pipe was lined with an aluminum based cement of between 1.8 and 2.2 cm thickness. The primary purpose of the inner liner was to provide protection of the steel pipe from the affects of the corrosive sewage flowing inside. The outer surface of the pipe was covered by a 2.5 cm thick concrete layer.

The design of the pipe–trench system was based on a flexible pipe criterion. This implies that the pipe maintains structural and functional integrity by mobilizing lateral resistance from the surrounding soil. The pipe was designed to withstand static soil loads alone.

A design section of the pipe–trench system is shown schematically in Fig. 1. The pipe invert was founded at a depth of between 4.5 and 5.5 m below the ground surface, depending on the natural topography. The natural soil consists of a highly plastic clay (CH, liquid limit: $\omega_l = 62\%$, plasticity index: $I_p = 36\%$). A perched water table (depths of as little as 2–3 m) exists in part of the project area. The design specified the excavation of a 2.5 m wide trench (twice the pipe diameter), placement of a 20 cm thick layer of poorly graded gravel (GP) with a particle size between 16 and 20 mm. The pipe was placed directly on the gravel layer. Following placement of the pipe section the design specified that (a) dune sand (SP) with calcareous concretions ($D_{60} = 0.17$ mm and $D_{10} = 0.12$ mm) be placed around the pipe to a height of 30 cm above the pipe crown elevation; (b) above that

---

*Author to whom correspondence should be addressed.
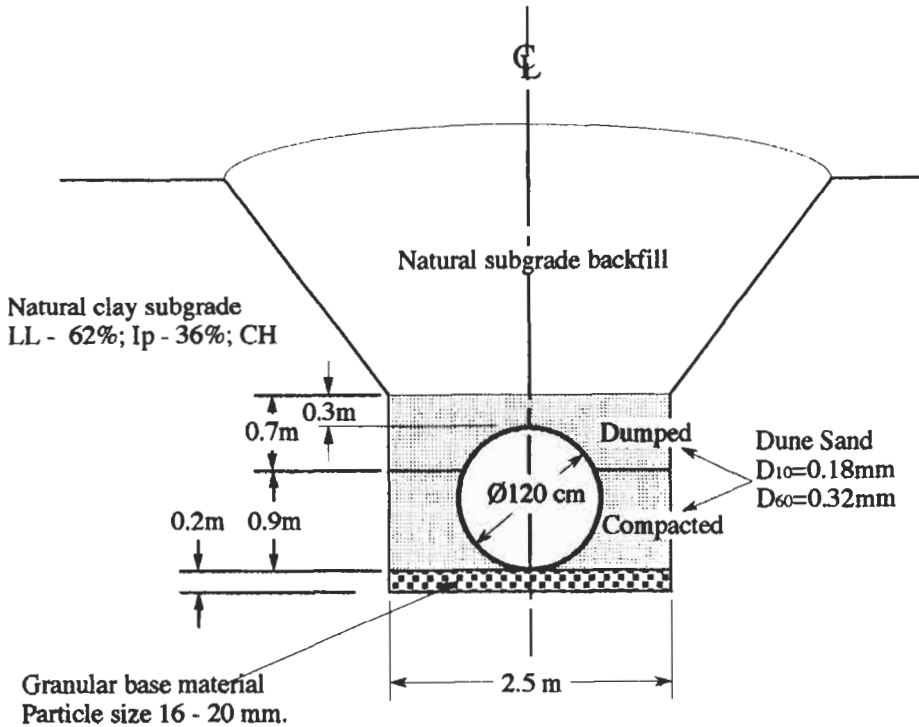
Fig. 1. Typical design section of the trench–pipe system.

height, natural clay material should be returned to the excavation to the original ground elevation; (c) the lower 90 cm of the sand backfill be compacted in layers to a design dry density of 95% of the maximum density according to ASTM standard D1557 ($\gamma_{d\,max} = 17.1$ kN/m^3); and (d) all materials placed above the compacted sand layers be dumped in without compaction. Construction of the pipeline was completed in mid 1994. The pipeline was abandoned (before any sewage flowed along its length) in mid 1995 because of severe cracking of the inner concrete liner.

3. OBSERVATION OF PIPE FAILURE

Upon observation of the internal liner cracks, a survey of the pipe condition was initiated. The survey included measurement of vertical and horizontal pipe deflections, visual description of the inner pipe surface and elevation of the pipe invert. The survey was performed along most of the 3.5 km length. The survey was carried out by the Technion Foundation for Research and Development—Building Materials Testing Laboratory.

Results of the survey indicated that vertical pipe deflections greater than 3% (of the pipe diameter) were common over significant sections of the pipeline length. In places the deflections reached more than 8%. Severe cracking of the inner pipe liner was noted over substantial sections of the pipeline. Open cracks and peeling of the liner was observed at many locations. Longitudinal cracks with apertures greater than 0.35 mm were found in pipe sections which had undergone vertical deflections of 2.0% and less. Cracking of the internal pipe liner resulted in a substantial reduction in the protective capability of the concrete liner against corrosion of the steel pipe. Typical results pertaining to one 120 m pipe segment are shown in Fig. 2. The survey indicated significant deviations of the measured pipe invert level from the design elevation. Over significant portions of the pipeline length, the measured invert elevation was found to be as high as 25 cm below the design level. However, it must be noted that over several other segments along the pipeline length the surveyed invert level was found to be above the design elevation.
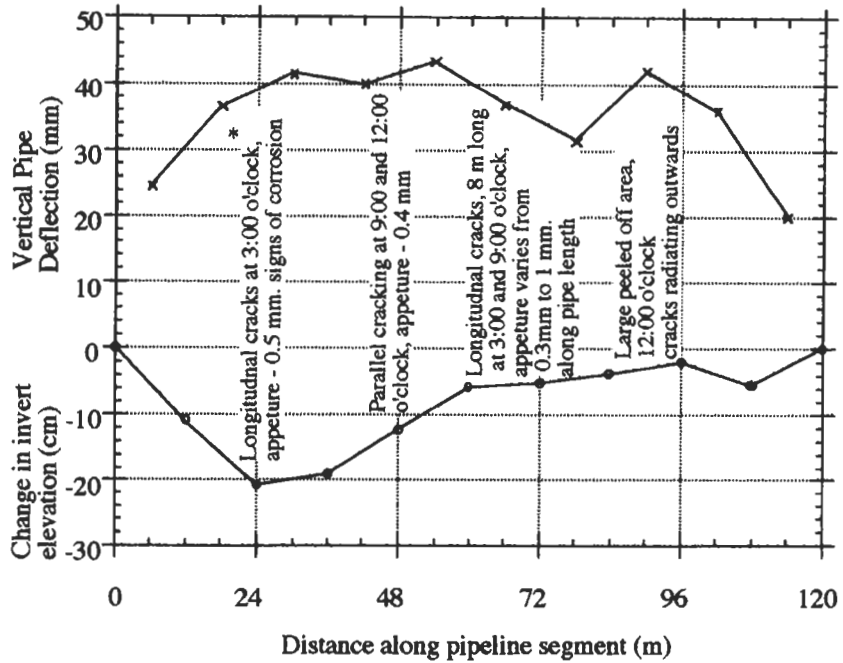
* examples of damage description from along pipe segment AA11-AA12

Fig. 2. Typical data obtained from damage survey.

4. GENERAL DESIGN PERSPECTIVE AND PURPOSE OF INVESTIGATION

It is common to define two major categories of soil-pipe systems:

Flexible pipes. In this case the pipe is prevented from collapsing through the mobilization of soil reaction. In order to mobilize the soil reaction the pipe must deform. A successful design in this case depends on the ability of the pipe to retain its functional and structural integrity under the deformation required to mobilize soil resistance. This case represents a typical soil structure inter-action problem.

Rigid pipes. The common design assumption for this category of pipe is that their load carrying capacity is independent of the reaction of the surrounding soil, and pipe deformation is neglected.

It is not obvious to which of the above categories the present pipe belongs. On one hand, being basically a thin-walled steel pipe its unrestrained load carrying capacity is rather low, making it a natural member of the flexible pipe category. On the other hand, the brittle inner concrete liner may be damaged (cracked) at deformations below those required to mobilize sufficient soil reaction.

It appears, therefore, that the pipe under consideration represents a borderline case which does not obviously belong to either one of the common design categories. Proper pipe design requires analysis of the soil pipe system, rather than use of standard design methodologies.

The objective of the present investigation was to determine the cause(s) of damage and the areas responsible. For this purpose it was necessary to determine mechanical properties of the pipe section, and soil conditions in the field. A secondary objective of the investigation was to study the suitability of the pipe as a structural shell for a more flexible insert which would act as a barrier between the flowing corrosive sewage and the steel pipe. For this purpose it was necessary to evaluate the structural integrity of the pipe in its present, damaged, condition.

5. EXPERIMENTAL PROGRAM

The experimental program consisted of two components. The first was laboratory testing of pipe sections in order to determine their stiffness (stiffness factor $= EI$), vertical deflection or strain, which induces cracking in the inner pipe liner and collapse loads. The second was a field investigation which included opening of test pits at several sections along the pipeline. Excavation of the test pits allowed for visual description of the soil-trench cross section, and performance of dynamic cone penetration (DCP) tests within the sand backfill alongside the pipe. The field investigation was limited to a 330 m pipeline segment.

5.1. *Results of tests on pipe sections*

Ring compression (bending) tests were carried out on three sections of pipe. Each section was placed in a hydraulic press and loaded across its vertical diameter by a line load along the full segment length. Throughout loading of each test section, vertical and horizontal deflections were monitored. Visual physical damage to the inner pipe lining (cracking) was also recorded. Figure 3(a) presents the experimental load deformation curve of one of the pipe sections together with observations with respect to crack development throughout the test. Figure 3(b) shows that the results for the three sections are fairly similar.

Based on the data presented in Fig. 3 it is possible to obtain the following information:

(1) The collapse load of the pipe section is between 50 and 55 kN/m. Collapse occurred at vertical deflections of 63–87 mm which correspond to diametrical strains of 5–7%. It is noted that these values characterize the unsupported behavior of pipe sections.
(2) The maximum moment acting in the pipe section at the collapse load may be determined by eqn (1), after Timoshenko and Gere [1]. For the pipes tested the maximum moments at collapse varied between 5.6–6.0 kN m/m,

$$M_{max} = \frac{P \cdot R}{2} \cdot \left[\frac{\pi}{2} - 1 \right], \tag{1}$$

where P is the collapse load per unit length as noted above, and R is the pipe radius.
(3) The stiffness factor of the pipe (EI) can be determined based on the linear section of the force deflection curve using eqn (2) [1].

$$EI = \frac{PR^3}{4 \cdot \Delta y} \left(\pi - \frac{8}{\pi} \right), \tag{2}$$

where Δy is the vertical pipe deflection under load per unit length P.
The calculated stiffness of the three pipe sections was found to be approximately 13.5 kN m. It is noted that the EI is an inherent property of the pipe section which is independent of lateral support conditions. This experimentally determined pipe stiffness is representative of the composite pipe cross section, which includes both concrete layers and the steel core.
(4) Severe cracking of the inner liner wall (defined as a crack opening of 0.3 mm [2]) occurred at a vertical diametric strain of approximately 1.2%. The working assumption used throughout the investigation has been that cracking occurs at the same strain value irrespective of the support conditions. Obviously the load required to impose this strain level is dependent upon lateral support conditions.

5.2. *Results of field investigation*

Dynamic cone penetration testing was performed at several stations along the investigated portion of the pipeline. Technical details of the testing procedure and interpretation of results may be found in [3]. The testing was performed following excavation of the fill material down to the pipe crown. Two or three DCP soundings were performed within each excavation to a depth of approximately 1.6–1.8 m. The end point of the sounding was located at a depth of approximately 0.5 m below the pipe invert. The plots shown in Fig. 4 are typical results found at six stations. It is noted that, in
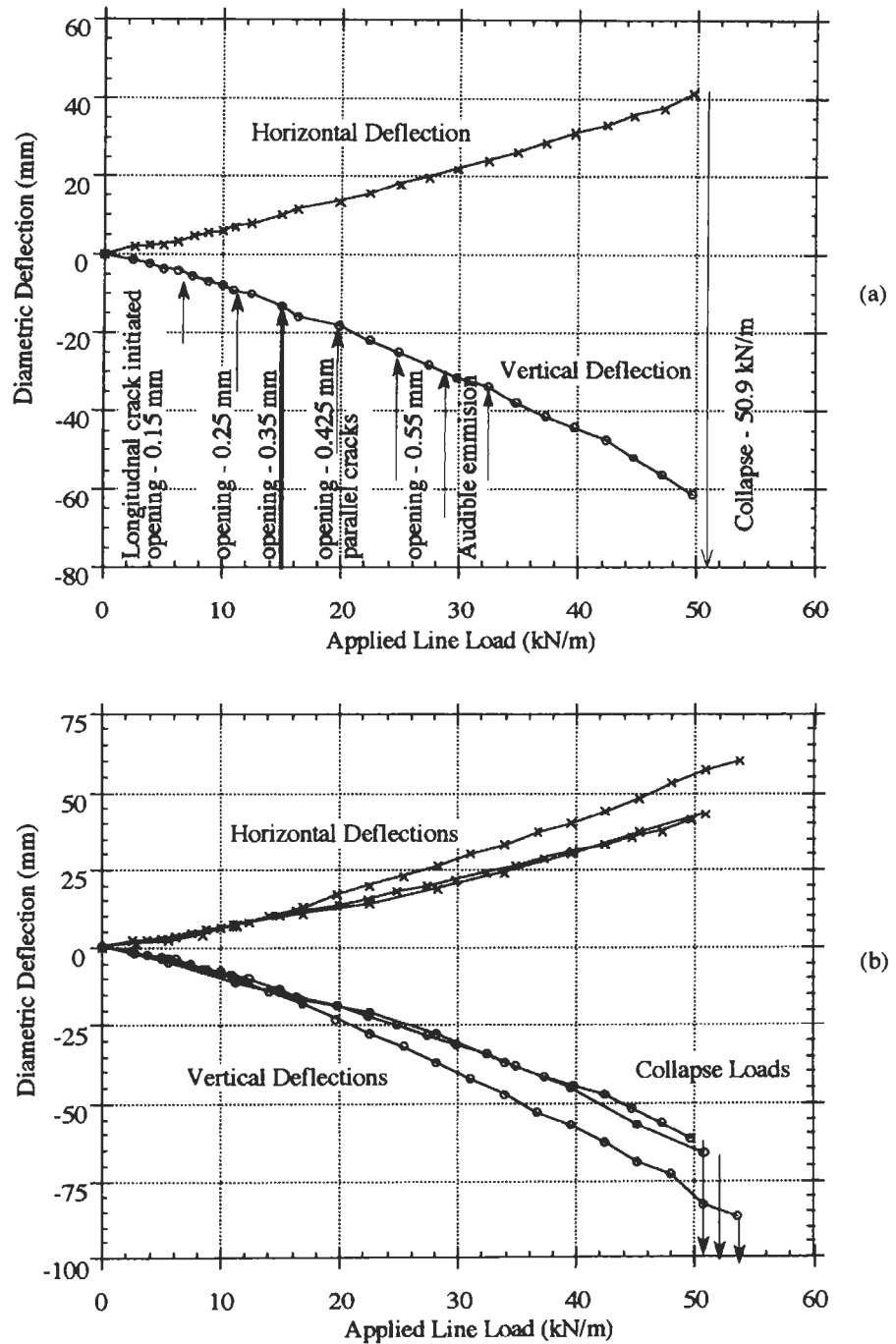
Fig. 3. Pipe load–deformation tests: (a) including damage observations, (b) comparison of results for three sections tested.

general, flatter portions of depth–blow count curves represent material more resistant to penetration. The slope of the depth–blow count curve is called the DCP number (mm/blow) which characterizes the stiffness of the material at a particular depth. In general a lower DCP number would indicate
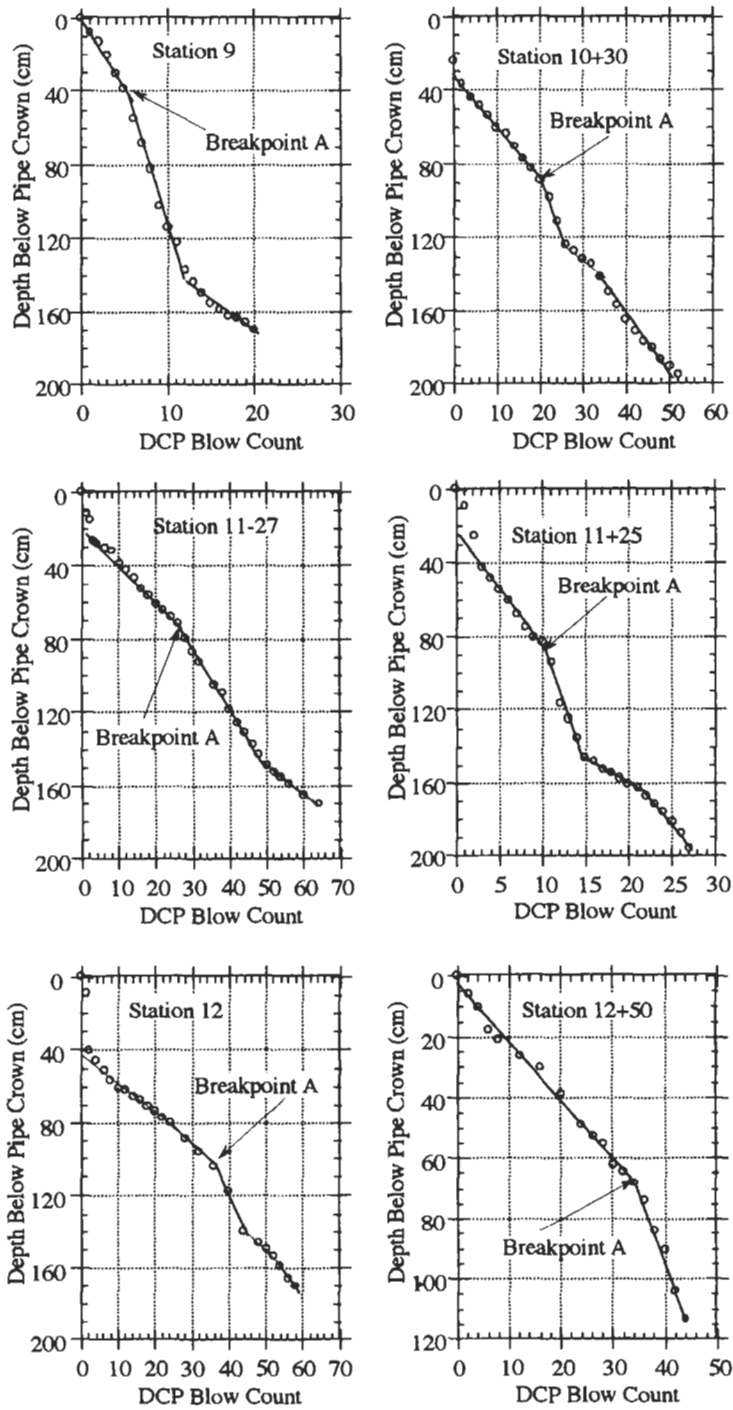
Fig. 4. DCP sounding data.

stiffer material. In homogeneous soils low DCP numbers infer dense materials. Figure 5 shows the distribution with depth of the DCP numbers as inferred from the results shown in Fig. 4.

At three locations along the pipeline segment considered, test excavations were opened to depths of 0.5–0.6 m below the pipe invert. The excavations were made at locations where DCP soundings had been performed. Groundwater was encountered in each of the excavations. In order to enable visual examination, water in the excavations was pumped out. The examination revealed the following qualitative features in each of the test pits (see Fig. 6).

(1) Sand backfill of thickness between 10–35 cm was found below the pipe invert. It is noted that the design called for the pipe to be placed directly on the gravel layer. The best available information indicates that the pipe was laid out according to the design specifications.
(2) Below the sand backfill a layer of natural clay subgrade approximately 5–25 cm in thickness was found. The thickness of this intermediate layer increases from the invert of the pipe towards the trench wall (see Fig. 6(a)).
(3) Below the intermediate clay layer the gravel base was found, and below it, the natural clay subgrade.

The sand backfill in the zone of the pipe haunches was found to be very loose, significantly less dense than the sand fill in the upper part of the trench. The gravel layer was seen to be completely impregnated by a mixture of the natural clay subgrade and the sand backfill.

Figure 7 shows very good correlation between the actual soil profile revealed by the visual examination (Fig. 6) and the results of the corresponding DCP sounding shown in Fig 4. The location of the discontinuities in the distribution of DCP numbers shown in Fig. 5 are generally consistent with the layer boundaries in the lower portion of the trench profile. Breakpoint A shown in Fig. 7 implies that the sand below mid pipe elevation (haunch zone) is considerably looser than the sand above this level. Breakpoint A is a common feature of all the plots shown in Fig. 4 and Fig. 5.

Despite variations in the absolute value of the DCP numbers, each of the sounding profiles shown in Fig. 5 have the following common features:

(1) There is a marked increase in DCP number at depths between 75–145 cm below the pipe crown which corresponds to the bottom part (haunches) of the pipe section.
(2) There is a marked decrease in DCP number at elevations corresponding to the visually observed gravel layer below the pipe invert, followed by an increase in DCP numbers as the sounding entered the natural clay subgrade.

6. INTERPRETATION AND ANALYSIS OF FAILURE

The vast majority of field measured pipe deflections (as shown for example in Fig. 2) exceed the 1.2% limit found to induce severe liner cracking of pipe sections in the laboratory. As a result the extensive damage observed in the internal pipe liner in the field this is not surprising.

Steel pipes are usually considered to be flexible and they are designed in accordance with "flexible design methodologies". However, in the present case the deformations associated with such a design far exceed the limiting capability of the inner pipe liner to withstand cracking. As a result, although the pipe section may remain structurally sound, it loses its functionality due to cracking of the liner.

Although it is impossible to specify a sharp criterion defining a flexible pipe, the value of 2% vertical deflection is often noted in the literature as the boundary between flexible and rigid pipes [4, 5]; i.e. a flexible pipe should be capable to withstand 2% deflection without damage. According to this criterion the present pipe does not belong to the flexible pipe category and should not have been design based on this methodology.

It is worthwhile to note that design standards of flexible pipes allow vertical pipe deflections to be as high as 5.0–7.5% [6, 7].

The large vertical deformation of the pipe and cracking of the pipe liner appear to be related to insufficient backfill stiffness as observed in the field investigation. The existing stiffness of the sand backfill may be inferred on the basis of the DCP tests performed alongside the pipe. Using empirical
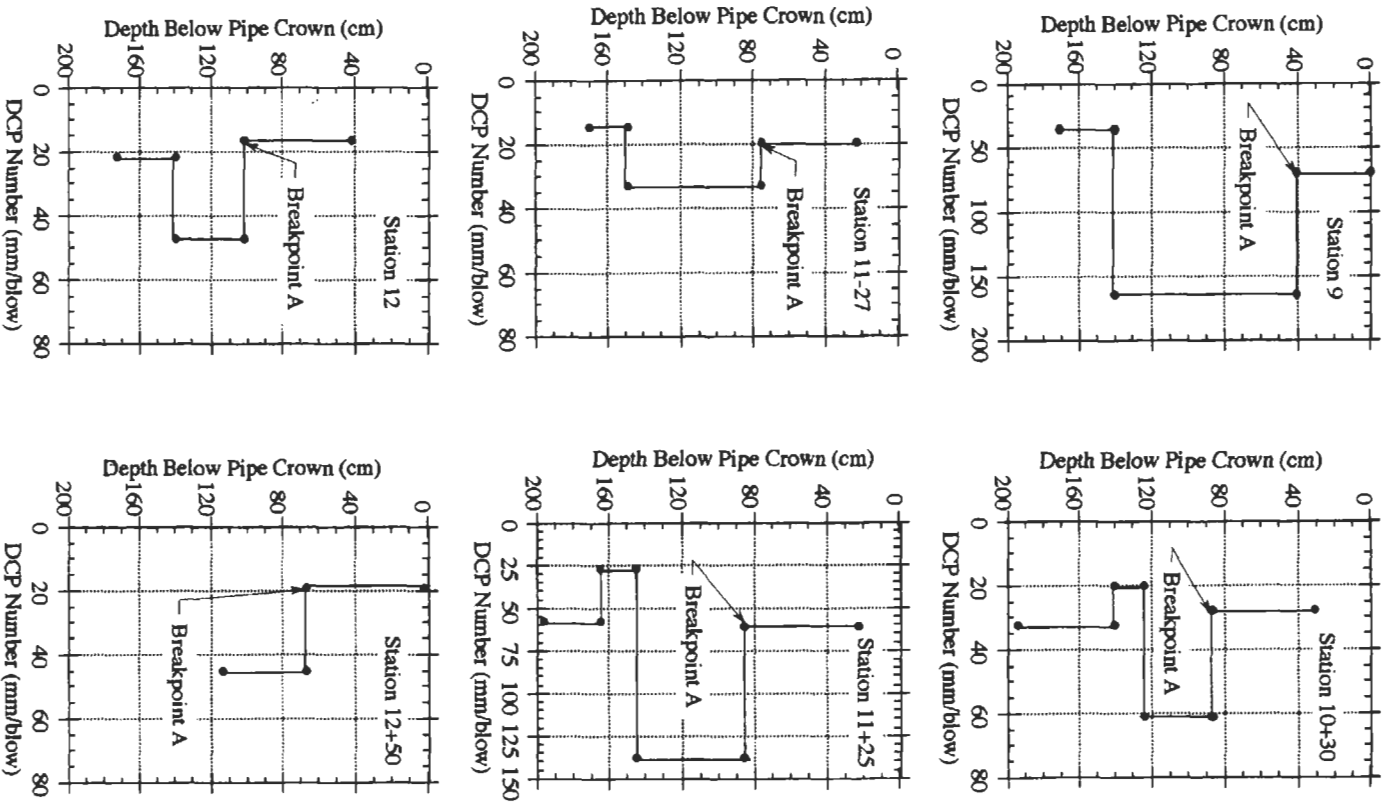
Fig. 5. DCP number versus depth profiles.
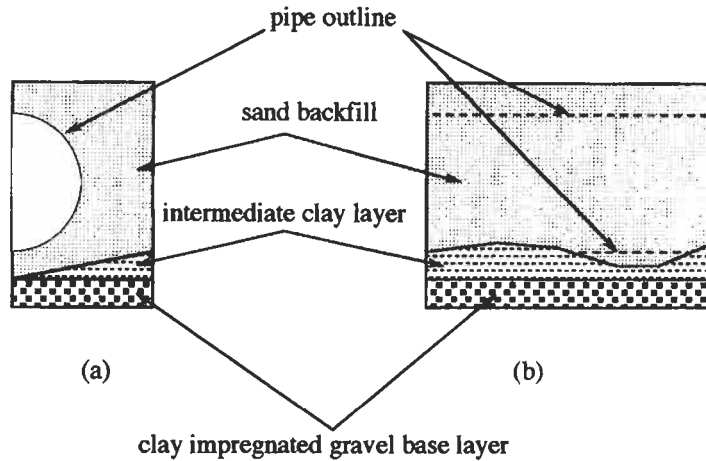
Fig. 6. Schematic of visual observations in test excavation: (a) cross-section, (b) longitudinal section.
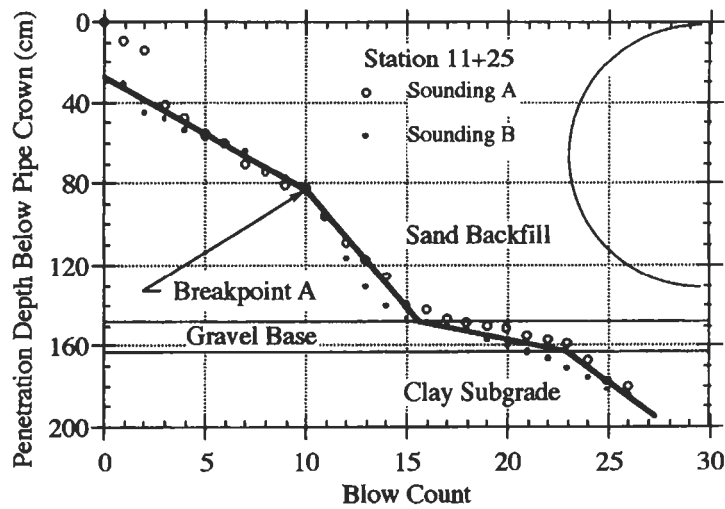
Fig. 7. DCP sounding profile, excavation profile composite.

relations between DCP numbers, laboratory CBR values (California Bearing Ratio) and elastic moduli it is possible to establish the following relation [3, 8]:

$$E = \frac{126,400}{DCP^{0.71\sqrt{\log DCP}}}, \tag{3}$$

where E is the elastic modulus (in kPa) and the DCP number is in mm/blow.

Applying eqn (3) to the DCP numbers established below breakpoint A (Fig. 5) the elastic moduli shown in Table 1 were inferred.

The data in Table 1 show good inverse correlation between moduli inferred on the basis of DCP results and measured pipe deflection in the field, that is, lower moduli result in larger pipe deflections. Such a relation should be expected on the basis of the Spangler equation [9] (eqn (4)) which forms the basis of standard design procedures for flexible pipe [6, 10].

$$\Delta y = \frac{K \cdot W \cdot D_l \cdot R^3}{EI + 0.061 \cdot E' \cdot R^3}, \tag{4}$$

Table 1. Field measured pipe deflection, DCP, moduli values

Station no.	Depth (cm)	DCP no. (mm/blow)	Elastic modulus E (kPa)	Pipe deflection δ (cm)
9	40–140	165	575	6.9
10+30	90–130	62	2500	3.8
11+27	75–150	35	5500	1.4
11+25	85–145	135	785	3.9
12	95–140	46	3800	2.5
12+50	> 65	50	3400	3.0

where Δy = pipe deflection (m), W = soil cover loads, taken as average prism load (kN/m), K = bedding constant (non-dimensional), D_l = deflection lag factor (non-dimensional), R = pipe radius (m), EI = pipe stiffness factor (kN m), E' = soil reaction modulus (kPa).

Equation (4) was utilized with $W = 80$ kN/m (corresponding to a depth of 4–5 m of soil cover) and a bedding constant K of 0.11. The choice of the bedding constant was based on the visual examination and it corresponds to poor bedding conditions below the pipe invert. The deflection lag factor D_l, which accounts for pipe creep and dynamic loading, was taken as unity. The pipe stiffness factor, EI, was taken to be 13.5 kN m based on the results from laboratory tests.

Figure 8 shows a comparison between the predicted deflections based on Spangler's equation and the data shown in Table 1. The open symbols shown in the plot will be referred to at a later stage. The figure shows good correspondence between the predicted and measured results, thus supporting the assumption that the large field deflections were due to insufficient stiffness of the soil backfill. More significant however is the fact that use of a very simple and cost effective field tool (DCP) coupled with empirical correlations ($DCP–E$ relation and the Spangler formula) make it possible to predict reasonably well, the expected deflections of the pipe. In the particular case under consideration such an approach provides an excellent diagnostic tool to assess the pipe condition (cracking) along the length of the pipeline.

7. STRUCTURAL STABILITY OF PIPELINE

The secondary objective of the present work was to investigate the possibility of using the existing pipeline as a structural shell to an extremely flexible insert which would provide protection from
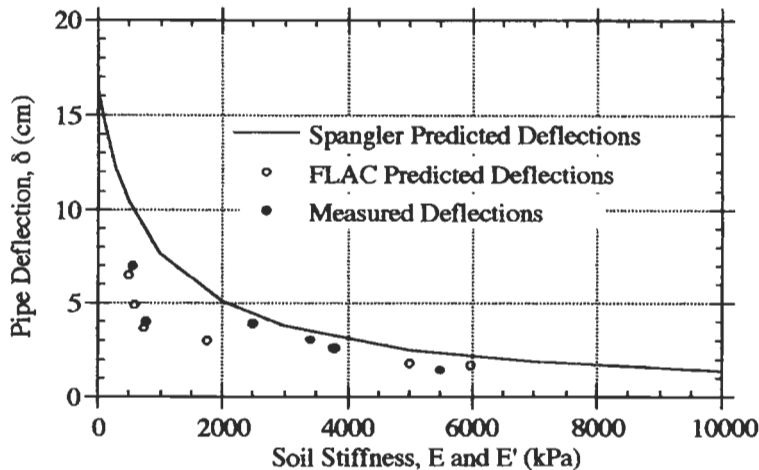
Fig. 8. Pipe deflection vs side backfill stiffness.

the corrosive effect of the sewage. The insert would in effect functionally replace the damaged internal concrete liner.

Design of engineering structures is frequently based on the notion of safety factors with respect to strength. In the case of a pipe section it is reasonable to define a safety factor as:

$$FS_{\text{Mom}} = \frac{M_{\text{ult}}}{M_{\text{max}}},$$ (5)

where FS_{Mom} is a safety factor with respect to moments, M_{ult} is the yield moment of the pipe cross section, as determined on the basis of the laboratory testing and, M_{max} is the maximum moment existing in a pipe section as loaded in the field. Essentially the basic engineering question to be answered is whether the pipe in its existing deformed state, has a sufficiently high safety factor allowing it to be utilized as structural element protecting the flexible insert.

In general the load distribution acting on a pipe section in the field is unknown, therefore, there is no straightforward approach to estimate the moments (M_{max}). To overcome this difficulty it was decided to analyze the pipe–trench system numerically using the commercially available software called FLAC (Fast Lagrangian Analysis of Continua [11]). FLAC is a two-dimensional explicit finite difference program for the computation of engineering mechanics. The program simulates the behavior of structures built of soil, rock and other materials which may undergo plastic flow when their yield limits are reached. It allows for the presence of structural members which may be modeled as beams or cables. The pipe was represented as a series of beam elements having a total thickness equal to the composite pipe section thickness. An equivalent section modulus (EI) as determined in the laboratory tests was used (i.e. no attempt was made to model the internal composite structure of the pipe section). The different soil layers were modeled as elasto-plastic Mohr–Coulomb media each assigned representative soil deformation and strength parameters. The discretization scheme and chosen material properties are shown in Fig. 9. A plane strain problem with a single axis of symmetry (AA′) was considered. One half of the soil–trench system was represented by 984 two-dimensional solid elements, and the other by 13 one-dimensional beam elements.

Since soil behavior is stress history dependent, we found it important to follow, in a numerical sense, the field construction sequence. Toward this end the following three numerical steps were taken:

(1) Establishment of the initial, at rest, state of stress in an homogeneous half space of the clay profile.
(2) Establishment of stresses and strains in each element resulting from "excavation" of the trench profile (ABCD—Fig. 9).
(3) Establishment of the stresses and strains resulting from placement of the pipe and backfilling of the trench. It is noted that the initial conditions for this step are the stresses and strains established in the previous stage.

In order to test the suitability of the numerical system as a predictive tool a parametric study relating vertical pipe deflection to the stiffness of the sand backfill was performed. The results of these calculations are shown as the open symbols in Fig. 8. The numerical results compare very well with the field values. Both the numerical computations and the field values fall below the curve representing the Spangler model. Such an outcome is reasonable considering the fact that the Spangler formula is a design tool rather than a predicitive one. It should be noted that the data shown in Fig. 8 involves three different "types" of elastic moduli, namely: modulus of soil reaction labeled as E' in the Spangler equation; conventional modulus of elasticity E as used in FLAC; and a stiffness modulus based on the DCP results.

Despite these differences in definition of the sand backfill stiffness, the correspondence of the data is quite remarkable. It is not clear whether this is a general phenomenon; or true only in this particular case.

For each assumed value of soil modulus the numerical scheme yields not only the vertical shortening of the pipe diameter (used in Fig. 8), but also the distribution of the beam moments around the pipe circumference. It is possible therefore to plot the maximum moment developed in the pipe section as a function of the vertical shortening of the pipe diameter as shown in Fig. 10. The dashed line in the figure represents the maximum moment deflection relation for an unrestrained
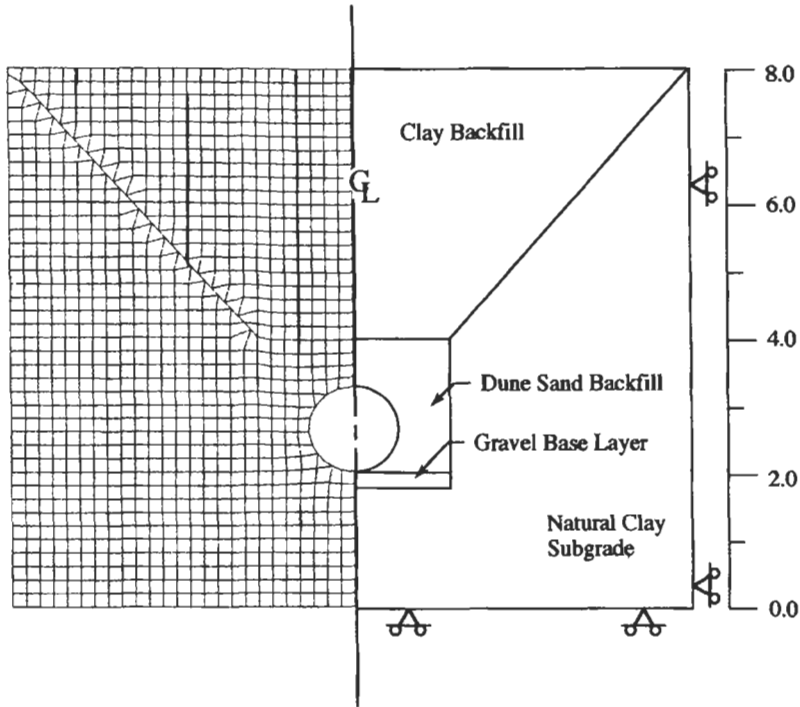
	unit weight kN/m^3	Modulus Deformation kN/m^2	friction angle (deg)	cohesion kN/m^2
Natural Clay	18.5	25,000	25	10
Sand Back Fill	16.0	500-6,500	35	
Gravel Base	20.0	25,000	45	
Clay Back Fill	17.5	12,500	20	

Fig. 9. FLAC input: (a) grid, (b) system profile and parameters.

pipe section (laboratory conditions). The plot illustrates that for any given pipe deflection the maximum moment in an unrestrained pipe is greater than the maximum moment in a buried one. Including within Fig. 10 the definition of the safety factor (eqn (5)), it is possible to construct a safety factor-deflection relation, shown as the curve through the triangular points in the figure. This curve can be used to assess which pipe segments are sufficiently safe to be used as a structural shell. For example, assuming a required safety factor of 2, all pipe segments which have undergone deflections greater than approximately 5 cm would be considered unsuitable. The advantage of this approach is its simplicity. Pipe deflection is a simple parameter to measure, whereas moments in the pipe section are not.

8. CONCLUSIONS

The following conclusions can be drawn from the present investigation into the failure of this pipeline:

(1) "Flexible" pipes with rigid liners must be designed with care. Flexible pipe design methodologies may be applicable, however, the deformation limitations of the liner must be carefully
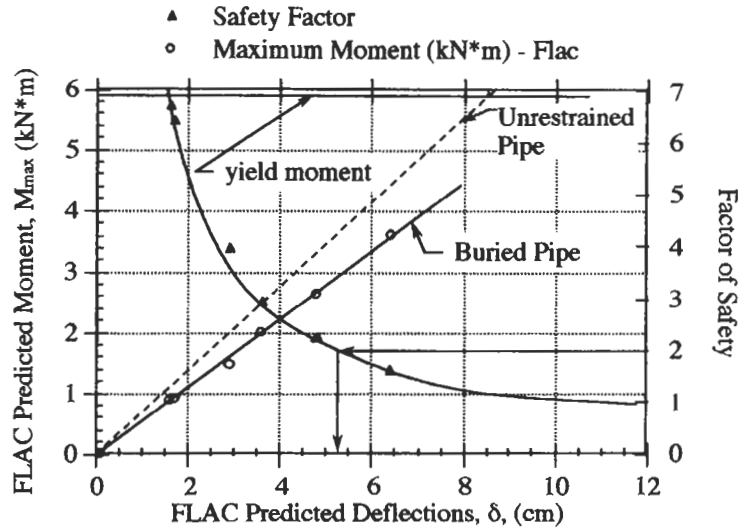
Fig. 10. Maximum moment, safety factor, deflection plot.

considered. Careful control over the stiffness of the trench backfill material is of the utmost importance. In the particular case considered, deflection of the pipe was in places 6–7 times the deformation initiating severe damage.

(2) DCP sounding has proven to be a simple field tool capable of estimating soil stiffness moduli of the trench backfill materials. Field measured deflections, predicted deflections based on standard design procedures and deflections predicted by use of a sophisticated numerical technique, correspond remarkably well.

(3) A criterion for the structural stability of the pipeline in terms of moments has been presented. This criterion makes it possible to utilize the measured deflections in a decision process aimed at establishing which parts of the pipeline are suitable for use as a protective structural shell. The advantage of the criterion is due to the fact that it directly relates safety factor to the measurable quantity of deflection.

REFERENCES

1. Timoshenko, S. and Gere, J. M., *Theory of Elastic Stability*, 2nd edn. McGraw-Hill, New York, 1961.
2. AASHTO Designation T280: Standard practice for concrete pipe, sections or tile.
3. Livneh, M. and Ishai, I., Pavement and material evaluation by a dynamic cone penetrometer. *Proceedings of the 6th International Conference on Structural Design of Asphalt Pavements.* Ann Arbor, MI, 1987.
4. Moser, A. P., *Buried Pipe Design.* McGraw-Hill, 1990.
5. Howard, A. K., Pipe bedding and backfill. Geotechnical Branch, Division of Research, Bureau of Reclamation, United States Department of the Interior, Engineering Research Center, Denver, Colorado, 1981.
6. AWWA (American Water Works Association), Steel pipe—a guide for design and installation, AWWA Manual M11, 2nd edn.
7. ASTM Standard F679: Standard practice for Poly(Vinyl Chloride) (PVC) large-diameter plastic gravity sewer pipe and fittings. ASTM Standards, Vol. 08.04 Plastic pipe and building products.
8. Yoder, E. J., *Principles of Pavement Design.* Chapman and Hall, 1959.
9. Spangler, M. G., The structural design of flexible pipe culverts. Bulletin 153, Engineering Experiment Station, Iowa State University, 1941.
10. ASTM Standard D3839: Standard practice for the underground installation of "Fiberglass" (glass-fiber reinforced thermosetting resin) pipe. ASTM, Vol. 08.04 Plastic pipe and building products.
11. Itasca, FLAC (Fast Lagrangian Analysis of Continua), Itasca Consulting Engineers, Minneapolis, Minnessota, 1992.

Torsional failure of a wire rope mooring line during installation in deep water

C.R. Chaplin

Department of Engineering, University of Reading, Reading RG6 6AY, U.K.

Abstract

During the deployment of mooring components for an FPSO in deep water excessive torsional distortion was induced which led to failure of all six spiral strand mooring ropes. A mechanism has been investigated which accounts for the failures. The following issues are fundamental to the incident being considered:

- the different torque/tension characteristics of chain and wire rope
- the sensitivity of different components to twist
- the interactions between chain and a work wire.

1. Introduction

Beneath the South Atlantic waters off the coast of Brazil there are several large reservoirs of oil. Much of this oil is located in water depths of between 500 and 2000 m. This makes the Brazilian offshore oilfields the deepest in the world, in terms of water depth, and it is inevitable therefore that floating production systems installed by Petrobrás are continually breaking new ground. This is especially true of the mooring and anchoring systems employed, and the methods used to install them. This paper analyses a particular problem encountered during the installation of compound chain and spiral strand mooring lines on the FPSO (floating production, storage and offloading system) P34 in the Barracuda field of the Campos Basin [1].

2. Background

Wire ropes are used in combination with chain, anchors and now fibre ropes, not only as component parts of mooring systems, but also as the principal tension element for raising or lowering mooring components: the work wire. Whether installed as components in a mooring line,

or used for raising and lowering, wire rope commonly acts in series with other components. These different components operate in static and dynamic equilibrium with each other, transmitting mechanical loading along the line between surface and seabed. The different classes and sizes of components inevitably have different mechanical characteristics, and while such properties as strength, stiffness, mass, and even differences in fatigue are well understood, the responses to twist and applied torsion, though widely appreciated as a potential source of problems, are generally not well understood. And it is in the torsional response of the different components that some of the most significant differences in behaviour can be observed. The interplay between these differences is important in determining the overall behaviour of a system, but not only as regards the behaviour of the system which has been conceived by the mooring designer. The historical sequence of operations, starting from the installation of the first component, can effectively alter the configuration, and thus the response, of the final system.

Because of the relative sizes and weights of the different components used, water depth becomes especially important when considering torsional behaviour during deployment operations. These problems have parallels in the field of mine hoisting where the torsional response of wire rope has long been recognised as an important consideration [2–4]. The considerations given to the mine hoisting problem, especially in the context of developments for ultra deep shafts (3000–4000 m) in South African gold mines [5–7], has been a valuable source of information for understanding the mooring system and work wire handling problems.

3. The selection of rope construction

There is a significant range of different wire rope constructions supplied by rope manufacturers for offshore mooring use, each with different combinations of attributes. When selecting wire rope for different applications a number of different considerations will apply and the final selection will inevitably represent a compromise. The essential characteristic of a rope is that it has high axial strength and stiffness, in relation to its weight, combined with low flexural stiffness. This combination is achieved in a wire rope by using a large number of steel wires, each of which is continuous throughout the rope length, which when loaded axially in parallel provide the tensile strength and stiffness, but when deformed in bending have low combined bending stiffness provided their bending deformation is decoupled.

To facilitate handling it is necessary to ensure that the rope has some integrity as a structure, rather than being merely a set of parallel wires; this is achieved by twisting the wires together. Whilst this gives the rope coherence, it also creates lateral forces within the rope which increase with the axial tension. Consequently, each wire is gripped between its immediate neighbours so that when there is a local fracture of an individual wire, the clamping forces generate frictional shears. As a result within a short distance of the break, the broken wire is carrying its full share of the rope load. This clamping can also increase bending stiffness raising wire stresses associated with operation over pulleys and drums. To minimise this effect and so maintain bending flexibility, every wire in the rope must have some freedom to slide along its path within the rope construction, effectively to cancel out the differences in bending strain implied by simple beam bending considerations (this is the essential difference between a rope and a solid bar).

The above bending requirements would be satisfied by a simple twisted bundle of wires; however,

(a) spiral strand   (b) six strand   (c) multi-strand
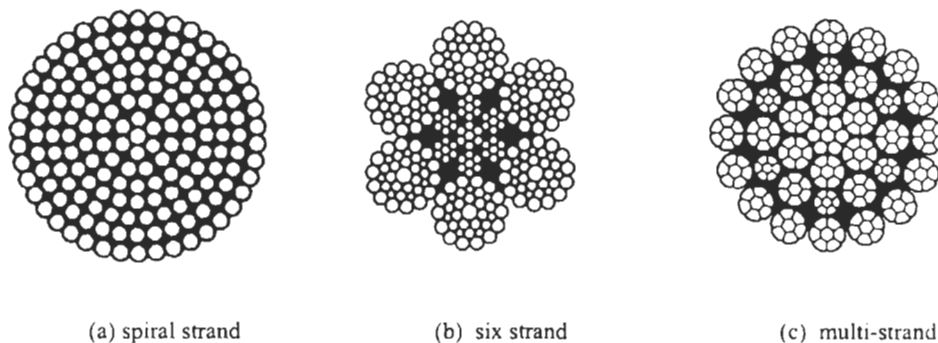
Fig. 1. Typical rope constructions.

such a structure would, if freely suspended, simply untwist. It would also be very vulnerable to damage of the outer wires, which if broken at one location, would just fall away and serve no further contribution to the load bearing function of the rope. The resolution of these problems provides the basic motivation for the design of different rope constructions. Wire rope can be constructed to be more or less 'torque balanced' (or non-spin, or spin resistant) to minimise any axial torque generated by tensile load, and any tendency to rotate when suspended. However such constructions tend to have other disadvantages, so before proceeding to a detailed consideration of torsional behaviour of wire ropes, it is relevant to consider the relative merits of the three generic classes of rope construction.

3.1. Spiral strand

Geometrically, perhaps the simplest of rope constructions, spiral strand consists of concentric helical layers of wire (Fig. 1(a)). The outer layers of a spiral strand, which constitute the bulk of the cross section, generally have wires of the same diameter, opposite helical senses, and the same, or similar, helix angle (but consequently different helical pitch, or lay length) with a core often geometrically similar to that of conventional stranded ropes (of mixed wire sizes but common pitch and sense). The characteristics of spiral strand, as relevant to offshore mooring applications, can be summarised as follows:

- spiral strands offer high strength and stiffness for a given diameter and wire grade;
- spiral strands can provide a high degree of torque balance;
- wires tend to be of larger diameter than in *stranded* ropes of comparable diameter—this benefits corrosion resistance but can limit the tensile strength of the wire employed (especially if shaped wires are used as in mining or ropeway applications);
- the outer rope surface is essentially cylindrical which facilitates sheathing in polymer to provide long term corrosion protection;
- exposed outer wires are vulnerable to damage and this construction is unsuitable for operation on and off multi-layer winch drums at more than low tension (unless having 'full lock' outer wires, and especially if sheathed);

- the construction is considered generally unsuitable for operation at pulley and winch diameter ratios less than about 35 : 1;
- the construction is inherently expensive to manufacture because of the number of separate operations needed to build up the layers, and the high capital cost of the large scale equipment needed;
- this construction is *not* tolerant to imposed twist, which is quite different to being torque balanced, as discussed below.

3.2. Six strand

This is the wire rope construction that is most widely used for general engineering purposes. Six (or eight strand) ropes (Fig. 1(b)) are manufactured in essentially two stages: wires are twisted together to form the strands (which have an equal lay length to allow different wire diameters to nest together), then six (or eight) strands are twisted together over a core to make the rope. Two main categories of core can be used: a fibre core, as in general engineering rope (easier to splice and cheaper to make), and wire rope core which provides higher strength, and higher axial, as well as transverse, stiffness, the latter being especially important in resisting crushing when wound at high load onto multi-layer winches. Another major feature of the construction of six strand ropes is the helical sense of the strands in the rope relative to the wires in the strand: where these are different the outer wires appear to align with the rope axis and the construction is termed ordinary (or regular) lay; where the helical sense is opposite, along the strand crowns the wires are at a greater angle to the rope axis and the construction is termed Lang's lay. For offshore use in connection with moorings, when a stranded rope is used, ordinary lay constructions are used almost exclusively. The relevant characteristics of such ropes are as follows:

- the rope has a high degree of damage tolerance and can be used at high loads on multi-layer winches;
- for any given ultimate breaking load this construction tends to be the cheapest of all;
- because of the problems of sheathing, and thinner wires, these ropes are not generally selected for very long term exposure to seawater;
- six strand ropes are not torque balanced (though that is possible—three strand ropes are manufactured for oceanographic use at very high tensions in very deep water where a high degree of torque balance is essential);
- ordinary lay ropes have better torque balance than Lang's lay ropes;
- this construction is tolerant to torsion, though perhaps not to the same degree as Lang's lay ropes.

3.3. Multi-strand

Multi-strand ropes (Fig. 1(c)) have two or more layers of strands, the sense and lay of which are selected to achieve a maximum degree of torque balance. The strands of these ropes are sometimes compacted (either by drawing or rolling) to improve the outer profile of the rope, and the strand to strand contact stresses. These ropes are used offshore for applications requiring flexibility and torque balance, such as single fall crane ropes or diving bell hoist ropes. The characteristics of multi-strand ropes are as follows:

- multi-strand constructions can combine sufficient bending flexibility and crushing resistance to operate on multi-layer winches, and possess good torque balance;
- these ropes have smaller outer wires than other ropes of comparable strength, so tend to have inferior corrosion resistance;
- because of the high contact stresses at the crossed contacts between the strands in different layers, fatigue damage in these ropes tends to develop internally rendering them prone to high levels of strength loss without externally visible signs;
- these ropes are significantly more expensive than conventional six strand ropes of similar strength.

Multi-strand ropes have been used for mooring a floating offshore production platform, but with limited success.

4. The torsional response of wire rope

Under conditions of rotational restraint, conventional six strand ropes develop a torque which is approximately proportional to the tensile load, however this torsional response is modified by twisting or untwisting the rope. This characteristic is illustrated in Fig. 2 in which axial rope torque (M) is plotted as a function of axial tension (F) for different levels of twist ($d\phi/dz$), where a positive twist implies a reduction in lay length. As would be expected, a reduction in lay length increases the torque generated by applied tension. The offsets on the torque axis show the torque at zero tension: this is a function of the torsional stiffness. A typical characteristic for a torque balanced rope is also shown for comparison: note that torque balance is never perfect due to the various geometrical changes associated with tensile deformation (both radial and axial).

Simplifying these torque characteristics for six strand rope to a set of parallel lines makes it possible to describe the relationships by an equation of the form:
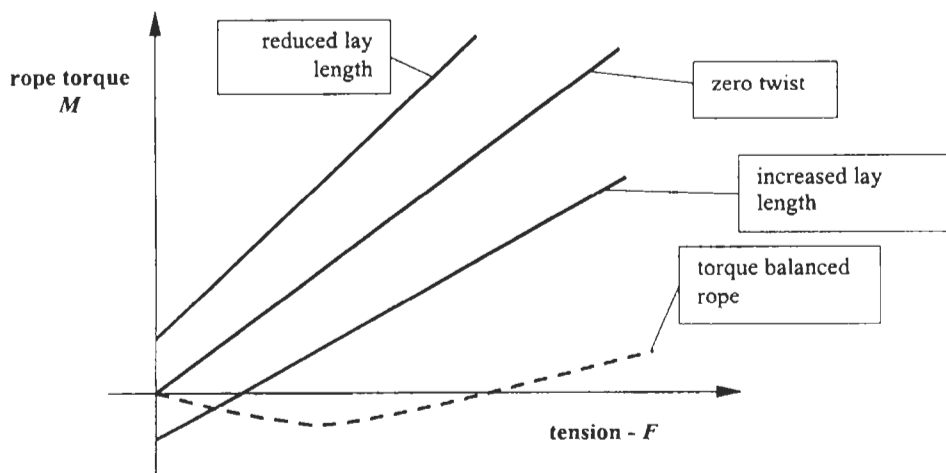
Fig. 2. A schematic representation of axial torque as a function of rope tension showing the characteristics typical of six strand rope (as manufactured, twisted up, and untwisted), and a nominally torque balanced rope for comparison (the dashed line).

$$M = C \cdot F + T \frac{\mathrm{d}\phi}{\mathrm{d}z}$$

where C (the torque factor) and T (the torsional stiffness) are constants (in practice these are not constants and the relationships are much more complex being highly non-linear as well as having different slopes and significant hysteresis, consequently being affected by the amplitude of any deformation). In this simplified form, both 'constants' are a function of rope diameter and construction, C begin directly proportional to diameter and T increasing with the fourth power of diameter for any given construction.

One example of the consequences of this type of behaviour is seen in the rotational deformation of a rope in a very deep mine shaft where the maximum tension in the rope, at the shaft headframe, derives from two components of similar magnitude: attached mass and rope mass. The result is a linear fall in tension down the rope. With a rope that is not torque balanced, this would suggest a similar gradient in torque, but that cannot be sustained so there is a counter rotation of the upper part with respect to the bottom to provide a constant torque throughout the rope. In offshore applications there is a need to understand such behaviour in order to anticipate when torsional problems can arise.

A simple knowledge of torque factor (constant C in the expression above), which may be supplied for different rope constructions by the rope manufacturer, only gives the torque generated as a function of tension when the rope is in its manufactured state of twist and constrained from rotation, and does not indicate torsional stiffness. A more informative way of looking at the torsional characteristics of rope is to review the torsional stiffness as a function of tensile load, state of rotation, and torsion amplitude. This kind of response has been modelled by Rebel [7] who has measured torsional response in this way, as illustrated in Fig. 3, for fibre cored ropes with six triangular strands, as used for mine hoisting in South Africa.

An alternative to Rebel's highly complex model is another linear expression to characterise torque/tension behaviour of six stranded rope, which has been developed by Feyrer and Schiffner [4]. This is somewhat more sophisticated than the two term expression above, reflecting the changes in torsional stiffness associated with changes in tension. In the expression:

$$M = c_1 Fd + c_2 Fd^2 \frac{\mathrm{d}\phi}{\mathrm{d}z} + c_3 Gd^4 \frac{\mathrm{d}\phi}{\mathrm{d}z}$$

where c_1, c_2 and c_3 are constants, which have been determined for different rope constructions; d is rope diameter; G is wire shear modulus; F and M are tension and torque respectively, as before.

5. Sensitivity of wire rope to torsional distortion

Whether a rope is torque balanced or not the manner of use can result in the imposition of torsional distortion. Of course this is more likely for ropes that are not torque balanced, than those which are, but torque balance is not a safeguard. In practice the feature common to most torque balanced constructions of having concentric layers, whether of wires or strands, renders such ropes very vulnerable to twist.

There are two classes of distortion damage that can result from twist being imposed on a rope:
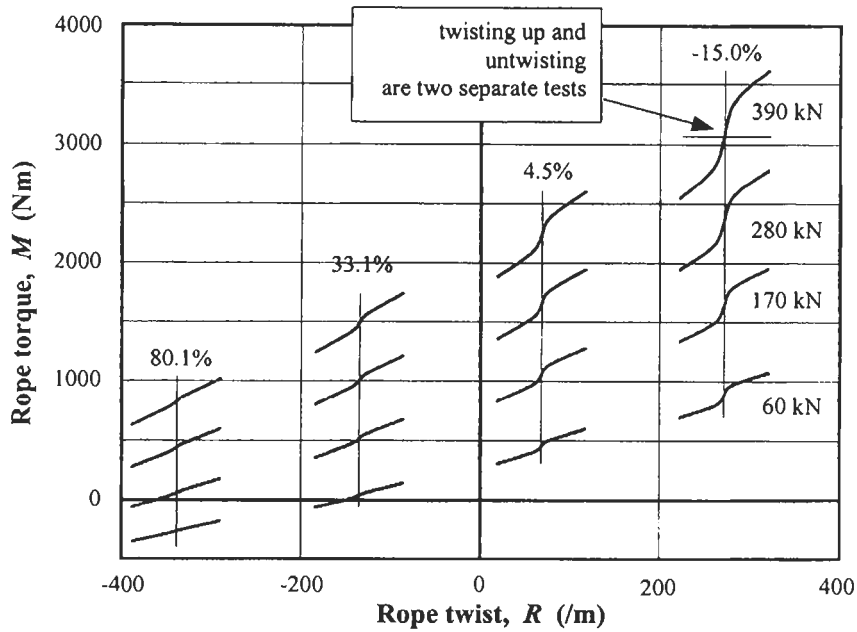
Fig. 3. Results of series of torsional tests at constant tensile loads on 46 mm triangular strand Lang's lay rope, from Rebel [7].

a loop (or kink, but also termed a hockle) formed in the rope as a whole; and constructional deformation involving hockling of individual strands or wires, or strands forming a 'birdcage' caused by local buckling. In either case, the instability can be prevented by maintaining adequate tension. The most serious deformations occur at very low tension. Uncontrolled reloading of a rope once it has developed a torsional instability is likely to lead to severe permanent deformation which can reduce strength dramatically, and damage fatigue resistance catastrophically.

The overall, 'whole rope', hockle can be removed by skilled handling if spotted before reloading, but the smaller scale, strand hockling cannot generally be removed without serious permanent degradation. The tendency to overall or constructional deformation is a function of the bending stiffness of the rope components, and the loading caused by imposed twist.

In a six stranded rope, untwisting whilst maintaining tensile load will eventually lead to local de-stranding of the rope (Fig. 4) which, when tension is relaxed, will allow the torque carried by the individual strands to cause local strand hockles (Fig. 5). If torque is imposed at low tension, whether untwisting or twisting up, then the whole rope will hockle. However, six strand ropes can sustain very severe torsional deformation, provided a minimum tension is maintained. Six strand Lang's lay mine hoist ropes have been reported [7] operating with lay length changes from -30% to $+70\%$ without any major compromise to service life.

Torque balanced spiral strand and multi-strand ropes both tend to have outer elements with diameters, and consequently bending stiffness, which are a much smaller proportion of rope diameter than the six strand equivalent. These outer elements also have a helical sense that opposes the layer underneath. Consequently, as already indicated, these ropes are more susceptible to

52
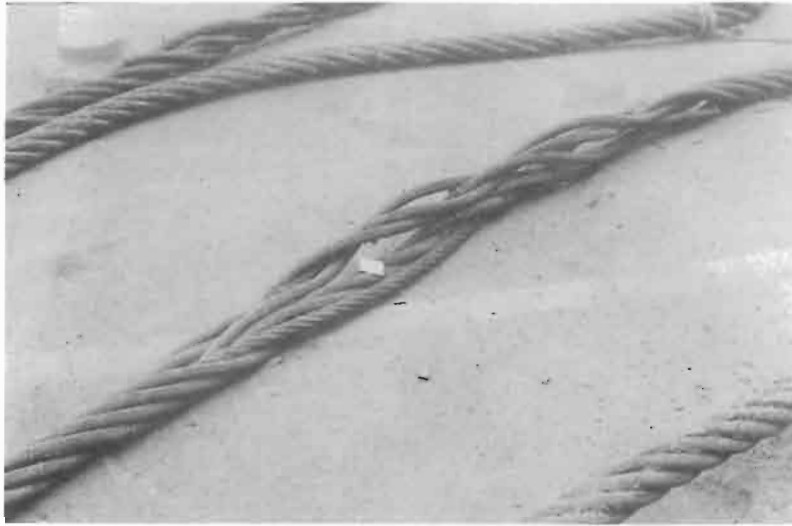
Fig. 4. Destranding of a six strand mooring rope.

Fig. 5. Hockles formed in the individual strands of an eight strand work wire.

'birdcage' damage through imposed twisting. But twisting, even without instabilities, is damaging to these ropes because of the effect of unbalancing the load distribution between wires or strands in different layers. This can reduce fatigue endurance significantly. By contrast, the wires in six strand ropes retain a better load balance under twisting, so their fatigue performance is maintained.
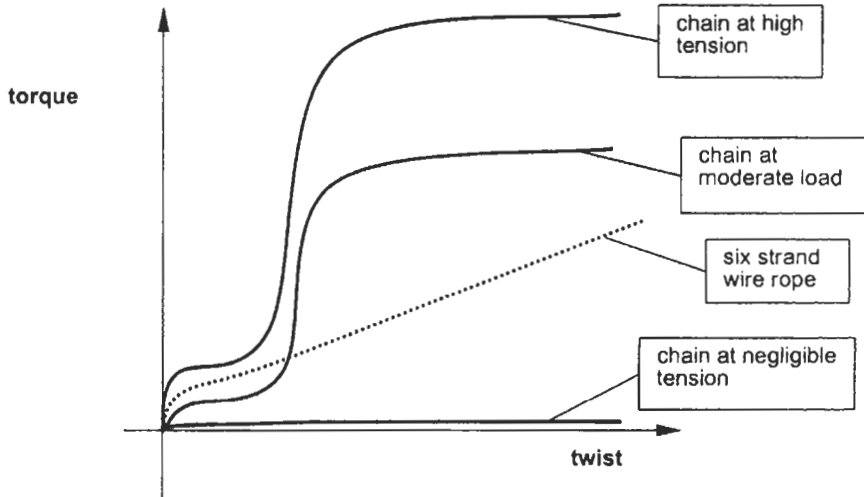
Fig. 6. Schematic representation of the proposed torsional behaviour of chain as a function of tensile load, compared with a six strand wire rope.

6. Torsional characteristics of chain

A common practice is the use of mooring systems which combine wire rope and chain in series. The torsional properties of chain are somewhat of a mystery other than a general acceptance that relative rotation of the order of 3° per link is possible with only nominal torque resulting. Because of the torque reaction which can be generated in rope, unless there is perfect torque isolation between components, the response of chain is significant. However, because of the dearth of specific information it is necessary to speculate, and approximate the behaviour of chain.

Under a given constant tensile loading chain can be expected to have a limited range of rotation (the accumulated 3° per link) at more or less constant torque. This essentially frictional torque will increase with tensile load. Once the limit of this rotation has been reached the chain will rapidly become very stiff, but eventually a limit will be reached at which the chain will start to knot up, and if the tensile load is constant this process might be expected to continue at a more or less constant torque. At zero tension there is effectively no resistance to rotation and chain can absorb rotation almost indefinitely. These characteristics are illustrated diagrammatically in Fig. 6.

7. Interactions in installed mooring systems

With six strand rope and chain in series, and assuming both ends are prevented from rotating as tension increases, the rope will generate a torque which will be transmitted through the whole line. Initially, the chain will take up its 3° per link, allowing some corresponding unlaying of the rope, but as the chain stiffens, further transfer of rotation will meet increasing resistance and the torque will increase more rapidly. In a quasi-static situation this should not cause any problems, but the dynamic response may well be different. Most experienced engineers have a natural feel

for potential dynamic resonances, but with very large structures and large masses these intuitions can be misleading. The torsional stiffness of wire rope mooring lines, as compared with equivalent solid bars, is so low that the period of natural torsion oscillation can be quite high, and there is reason to believe from observed mooring line failures, that such motions can sometimes be excited by the environmentally induced motions of floating structures. If the torsional amplitudes are large enough, and vessel motions such as to allow very low tensions to occur, then the kind of torsional instability described above can develop. Indeed, the destranding in the mooring rope illustrated in Fig. 4 is thought to have been induced by just such behaviour.

This kind of dynamic torsional problem is initiated by the torque developed in the rope which then causes rotation because of the different characteristics of the adjoining component. The use of a torque balanced rope will effectively remove the rotational response and so overcome the problem, but operating procedures that always maintain a minimum tension would also avoid the rope being damaged.

It is also worth noting that the components in series which excite this kind of counter rotation need not be rope and chain. Any torsionally mismatched pair will be susceptible, be they six strand and torque balanced ropes, unbalanced ropes of different construction, or even two ropes of the same construction but different diameter.

8. Problems encountered during installation

Mooring installation operations provide numerous opportunities for torsion related problems. Apart from the tendency for a stranded rope to rotate under tension, one common mechanism for inducing twist is dragging the rope along the seabed [8]. This can happen when installing a wire rope mooring line deployed from a mobile unit. The problem only becomes apparent when the tension in the rope is relaxed, and distortion is induced between fairlead and a deck mounted winch. Reeling back onto the winch then causes miscoiling which can subsequently lead to severe crushing damage.

The mechanisms which are the principal interest in this paper are those associated with raising and lowering components, and specifically, operations involving six strand 'work wires'. Numerous operations which involve wire rope coupled to a chain that is lying on the seabed can induce twist in the chain, which can, at a later time, be transferred into yet another component. If that component is sensitive to imposed twist then the consequences can be very serious. An example of such a deployment, based on the problems encountered during deployment of the P34 mooring system [1], will be considered in detail and a hypothetical mechanism for the torsional damage to the P34 spiral strand mooring lines analysed.

The operation to be analysed involves the installation of a mooring lined in 1000 m water depth. The original intent was that the completed line should consist of a conventional drag embedment anchor attached to somewhat in excess of 1000 m of chain, attached in turn to a spiral strand and thus to a floating production, storage and offloading vessel (FPSO). The anchor and chain were to be pre-installed with the free end of the chain lying on the seabed attached to a six strand wire rope supported by a surface buoy. The particular stage of the operation being considered is the
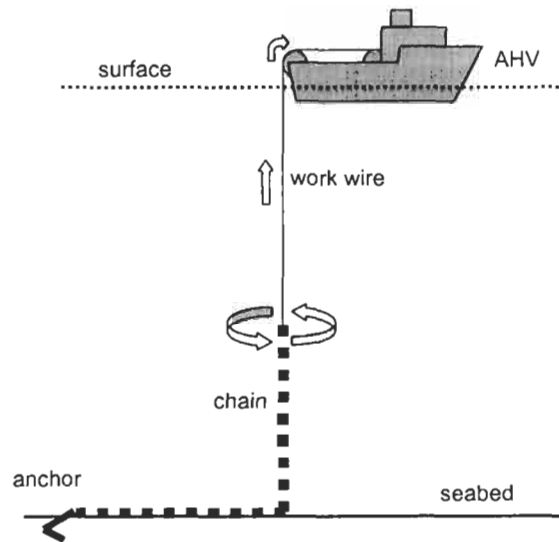
Fig. 7. Schematic representation of anchor handling vessel (AHV) lifting the anchor chain with six strand wire rope 'work wire'. The increasing tension as more chain is lifted causes rotation at the point of connection between rope and chain, the turns accumulating in the chain at zero tension on the seabed.

recovery of the end of the chain for the purpose of attaching the spiral strand. This is achieved by hauling the rope pendant onto the anchor handling vessel (AHV) winch.

The chain is sized for the mooring application, but the rope is a work wire, and for this use has to support only the weight of the chain. At the start of this process all the chain is on the seabed and the rope is just supporting its own weight. As the rope is wound onto the winch the tension, which is always greatest at the surface, gradually increases as the heavy chain is raised. This increase in tension causes the rope to untwist since there is no torsional restraint from the slack chain on the seabed (see Fig. 7). As the chain is progressively lifted, the untwisted rope is wound onto the drum and the opposing twist transferred along the chain, accumulating in the final grounded section adjacent to the anchor. Once the end of the chain is on the deck of the AHV, the spiral strand is attached from a second AHV and the combination lowered back to the seabed as the spiral strand is paid out. The arrangement with the three components and two AHVs prevents further rotation. Finally the work wire is disconnected and the spiral strand tensioned. The increase in tension in the chain transforms its torsional stiffness, causing the accumulated twist to be transferred to the lower stiffness spiral strand. When the system is again relaxed to await hook up to the FPSO, the spiral strand can no longer sustain the imposed twist and forms kinks or hockles. When these hockles are pulled straight for final connection to the FPSO the rope is effectively destroyed, deforming as shown in Fig. 8.

To try to quantify the turns transformed from the work wire to the chain, the torsion model defined by Feyrer and Schiffner [4] has been used with values the authors obtained for a rope of appropriate construction but, at 20 mm, of rather smaller diameter. Other quantities for the base case are as given below, and relate to the incident referred to by Komura [1] in so far as details are known.

Fig. 8. Characteristic damage induced in spiral strand by pulling out a hockle or kink.

Rope:

construction	6×36 with IWRC	
diameter	64 mm	
mass in seawater	10 kg/m	
c_1	0.085	from [4]
c_2	0.187	from [4]
c_3	0.000531	from [4]

(Note: in the expression for torque/twist units of N and mm have been used throughout and twist $(d\phi/dz)$ is defined in radians/mm.)

Chain:

diameter	89 mm
mass in seawater	150 kg/m
water depth	1000 m.

The calculation has been made on an incremental basis for each 50 m of chain raised, calculating the degree of twist in the corresponding 50 m of rope wound onto the AHV winch. This twist is based on the mean calculated for the start and finish of each increment, and is determined by considering the twist at each tension associated with torque value of zero, the boundary condition determined from an assumption of zero tension where the chain touches the seabed. The calculation indicates that a total of 94 turns will have accumulated in the chain on the seabed by the time the end of the chain reaches the surface. On the assumption that the chain can accommodate 3° of rotation per link, then, the number of turns subsequently transferred to the spiral strand will be reduced by 19, to 75. In practice the chain may develop some resistance to the progressive transfer of so many turns, possibly lifting knotted clumps above the seabed, which would further increase
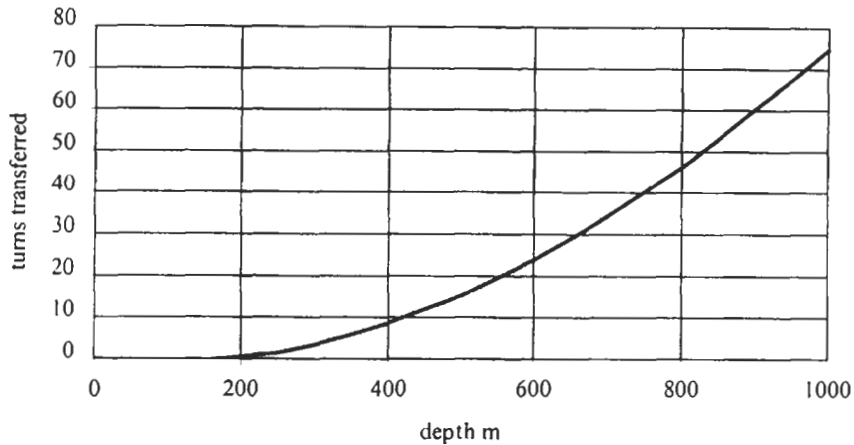
Fig. 9. Number of turns transferred from the chain when tensioned as a function of water depth.

the suspended weight but still not change the minimal torsional stiffness where the chain tension is zero.

Figure 9 shows how reduction in water depth reduces the number of turns transferred from the chain when tensioned, with the other parameters as specified initially. Figure 10 shows how using ropes of different diameter can influence the turns transferred, with results shown for two different water depths, 1000 and 700 m. In both figures, allowance has been made for an assumed capacity for the chain to accommodate 3° of rotation per link before adopting a high torsional stiffness. This capacity of chain to absorb induced turns can overcome the problem completely in shallower water (as seen by the effective cut-off in Fig. 9). It is evident from Fig. 10 that significant reductions in turns can be achieved from the use of rope with greater diameter and hence higher torsional
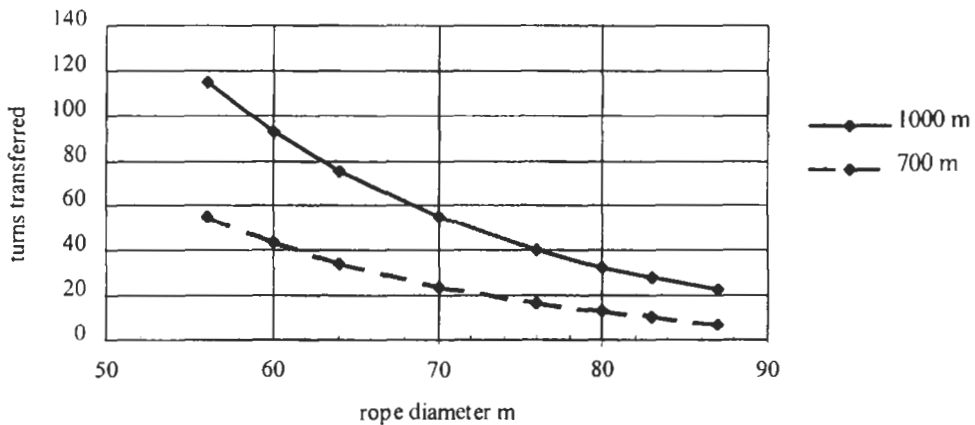
Fig. 10. Number of turns transferred from the chain when tensioned as a function of rope diameter, the upper line for 1000 m water depth and the lower for 700 m water depth.

stiffness. Obviously comparable reductions in chain diameter to reduce the rope tension would have equivalent effects.

The operation analysed here is only one example of a process which can induce rotation, though this is perhaps the category of operation most likely to induce the higher amounts of twist. Inevitably when working in even greater water depth much higher twists will be involved.

It must also be pointed out that the torque/tension model used for these calculations is fairly simple and has not been validated for ropes of the size used offshore. The analysis reported here has also been performed using the even simpler two-term model of rope response [9] predicting a 35% lower rotation in the pendant rope, but otherwise a very similar pattern of behaviour.

The reported facts relating to the P34 mooring line losses are that the deployment procedure was as described above, and that the spiral strand was found to be torsionally damaged beyond recovery when connected to the FPSO. The mechanism described here has been deduced from an analysis of the operation. There are no observations that can confirm, or otherwise, the relative states of twisting in different components at each stage, but no other explanation has been advanced.

9. Steps to avoid induced torsion

Apart from expensive solutions such as using two lines to different AHVs, or other devices attached to the connection between components to prevent the transfer of turns, what else might be done to avoid this kind of problem? There are essentially three categories of solution: one involving rotating connectors (swivels), the second involving the use of torque balanced ropes, and the third involving the selection of twist tolerant components. The merits of each are considered below:

9.1. Rotating connectors

- Conventional swivels are of little use here because they have high friction and therefore really only operate at very low tension. This is ideal to release torque to facilitate handling of a rope adjacent to a connector when restrained on the deck of an AHV.
- The use of special 'low friction' swivels in the case study above may have little benefit when coupled between chain and pendant work wire. This is because of the combination of significant tensile load and very low torque (associated with the low torsional stiffness of the unloaded chain). Furthermore there is no validated quantitative data available for the relationship between load transmitted and 'break-out' torque for these devices, which makes any analysis impossible.
- Permanent installation of a 'low friction' swivel between the chain and spiral strand should have the benefit of limiting the transmission of accumulated turns from chain to rope as the mooring system is tensioned. However, such a policy would still run the risk of residual turns in the chain forming knotted clumps with serious loss of strength and fatigue performance (this risk is of course present with any option that does not prevent twisting of the chain in the first place, and in fact one of the mooring chains in the P34 operation described above was broken at just such a knot during retrieval).
- The use of a 'low friction' swivel as a permanent connection in a mooring line which combines

components having different torque/tension characteristics (e.g. chain and six strand ropes) is likely to result in torsional oscillations as the tension fluctuates. This will introduce additional fretting between the wires of the rope to compound fatigue. There is no reliable published fatigue data to indicate how seriously this might affect endurance.

9.2. Torque balanced ropes

- The choice of ropes with constructions having better torque balance characteristics, for pendant ropes and work wires, would have undoubted success in reducing the introduction of turns into chain, and subsequently spiral strand. However, these ropes are significantly more expensive than the six strand constructions currently employed.
- Ropes of such constructions are currently used routinely for diving bell hoisting and as single fall 'whiplines' for cranes.
- There is some precedent for using torque balanced ropes as work wires during installation, for example in lowering the clump weights for the Lena guyed tower in the early 1980s.
- Torsionally balanced ropes tend to have smaller outer wires than their six strand equivalents. This makes them less robust and more vulnerable in aggressive mooring deployment operations.

9.3. Use of twist tolerant ropes

- If installation procedures are likely to induce turns that can ultimately be transferred to components with a low tolerance to twist, especially torque balanced wire rope, then one remedy is the avoidance of such twist sensitive constructions for a mooring line.
- Current developments in moorings for deep water include the use of polyester fibre ropes. Most of the constructions selected to date for this application comprise a braided outer cover for a set of essentially parallel sub-ropes which form the load bearing members. At present there is no information available as to the torque/tension characteristics of these ropes, but given the low level of twist in the sub-ropes, a reasonable level of tolerance to imposed rotation might be expected. It is of interest to note that, necessity being the mother of invention and as a result of good fortune, Petrobrás were able to replace the damaged spiral strand by available polyester fibre ropes.

10. Conclusions and recommendations

- Wire ropes used as either mooring components or as work wires during installation can have a tendency to twist under tension. This twist can be transferred from one component to another (especially during installation operations) with potentially serious consequences as regards twist sensitive components such as torque balanced wire rope, and even chain in extreme cases.
- These mechanisms whereby turns can be generated are exacerbated by water depth, indeed the capacity of chain to absorb some twist can overcome the problem completely in shallower water.
- Quantitative models of the torque/tension characteristics of *all* components employed are necessary to facilitate prediction of their torsional interactions. However, the first step in any such prediction is to appreciate that such mechanisms occur at all.

- Possible steps to mitigate against this problem include:

  (1) the use of torque balanced ropes as pendants and work wires;
  (2) the use of low friction swivels (although there is a dearth of data on such devices and furthermore the effect of cyclic rotation in permanent moorings has not been investigated); and
  (3) the avoidance of twist sensitive rope constructions as permanent mooring components.
- More information is needed to facilitate accurate prediction of these interactions. This is especially the case of chain and swivels. There is an understanding of the problem in the rope fraternity (both wire and fibre) where it has long been recognised particularly in the context of deep mine shafts, but experimental data for realistic rope sizes is not currently available.

Acknowledgement

References

[1] Komura AT. Experiences in some installations of mooring lines with polyester rope in Campos Basin Brazil. Proceedings of the Third International Conference on Continuous Advances in Mooring and Anchoring. IBC, Aberdeen, June 1998.

[2] Layland CL, Rao BE, Ramsdale HA. Experimental investigation of torsion in stranded mining wire ropes. Transactions of the Institution of Mechanical Engineers 1951:323–36.

[3] Kollros W. The relationship between torque, tensile force and twist in ropes. Wire 1976;19–24.

[4] Feyrer K, Schiffner G. Torque and torsional stiffness of wire rope parts I and II. Wire 1986;36(8):318–20 and 1987;37:23–7.

[5] Wainwright EJ. The manufacture and current development of wire rope for the South African mining industry. Proceedings of the International Conference on Hoisting of Men, Materials and Minerals. Canadian Institute of Mining and Metallurgy Toronto, Canada, June 1988.

[6] McKenzie ID. Steel wire hoisting ropes for deep shafts. Proceedings of the International Deep Mining Conference: Technical Challenges in Deep Level Mining vol. 2. Johannesburg SAIMM, 1990, p. 839–44.

[7] Rebel G. Torsional behaviour of triangular strand ropes for drum winders. Proceedings of the Application of Endurance Prediction for Wire Ropes, OIPEEC, Reading, September 1997, p. 135–60.

[8] Chaplin CR. The inspection & discard of wire mooring lines. London: Noble Denton, 1993.

[9] Chaplin CR. Torsion problems caused by wire rope during mooring installation operations in deep water. Proceedings of the Mooring and Anchoring. IBC Aberdeen, June 1998.

Creep failures

63

TYPE III CREEP CRACKING AT MAIN STEAM LINE WELDS

K. G. SEDMAN and J. C. THORNLEY

RPC, 921 College Hill Road, Fredericton, NB, Canada E3B 6Z9

and

R. M. GRIFFIN

NB Power, 515 King Street, Fredericton, NB, Canada E3B 4X4

Abstract—After 204,000 h of operation, some welds in the main steam line of a thermal generating station were examined ultrasonically. This examination found a major reflector close to a butt weld in the line. That reflector proved to be cracking that was 90% through-wall. The cracking was not visible on the outside surface of the pipe. The cracking was type III creep cracking, and had initiated in the mid-wall region within bands of coarse-grained material. From that mid-wall position, cracking had propagated outwards towards the OD surface, and inwards to reach the ID surface. There was no evidence of the involvement of any weld flaws in the initiation or the growth of the cracking. Stress analysis of the piping system, using commercially available software, indicated that the stress in the major area of cracking exceeded that allowed by the ASME B31.1 design code. © 1997 Elsevier Science Ltd.

1. INTRODUCTION

The #8 unit of the Grand Lake generating station of New Brunswick Power has an output of 60 MW. The boiler is coal-fired, and its design pressure and temperature are 1475 psi (10.17 MPa) and 1005 °F (541 °C). During normal operation, the boiler produces steam at a pressure of 1450 psi (10.00 MPa) and 1000 °F (538 °C). The path of the main steam line is shown in Fig. 1. The steam leaves the superheater outlet header in a single 12 in. (300 mm) diameter line. After making several turns, this 12 in. line enters a forged tee (Fig. 1). Here, the steam flow branches into two 8 in. (200 mm) lines. A sketch of the tee is shown in Fig. 2. The branches from the tee are labeled X and Y. The tee achieves the diameter reduction, not within the forged body of the tee itself, but via a pair of eccentric reducers, one welded to each side of the tee. All of the materials are of the 1.25Cr–0.5Mo type, conforming to ASME standards appropriate to piping, forgings or castings. In the fall of 1994, cracking was discovered in the unit's main steam line. At this time, the unit had accumulated 204,000 h of operation.

2. INITIAL DISCOVERY OF CRACKING

The welds along this steam line had been previously inspected in some detail in 1987, 1990 and 1991. These inspections had used fluorescent magnetic particle examination (MT), and metallographic (replica) examinations. Only shallow cracking had been found using these two inspection methods, and, at many sites, the most that was found was a few creep cavities at grain boundaries in the weld heat-affected zones (HAZs).

In 1994, the decision was made to augment the inspection with ultrasonics. A large reflector was recognized almost immediately in the X-side 8 in. pipe to reducer weld. The inspector responsible placed the reflector in the neighbourhood of the HAZ on the pipe side of the weld, and believed that, at its extremities, the reflector might consist of a number of smaller reflectors. A substantial boat sample was removed to help determine the nature of the reflector. The boat sample was centred
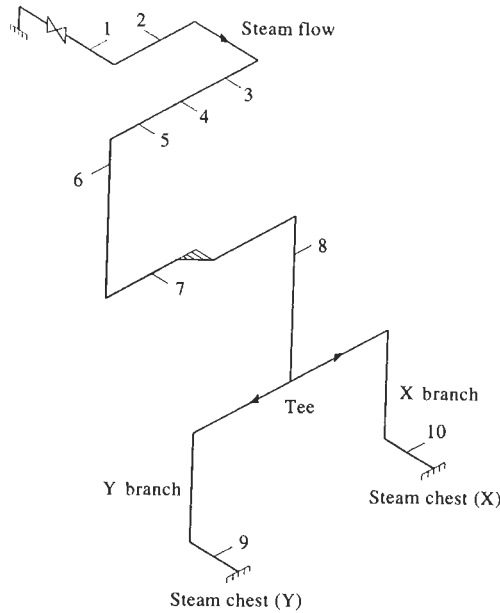
Fig. 1. Path of the pipe from the secondary superheater outlet header to the two steam chests. The numbers 1, 2, 3 etc. refer to hanger sites.

on the HAZ on the pipe side of the weld. The boat sample was not large enough to simultaneously sample the HAZ on the reducer side of this weld.

The metallographic examination of a section through the centre of the boat sample revealed a crack that extended from the weld root to within 2 mm of the outside surface of the pipe (Fig. 3). That is, cracking, unseen at the outside surface, was 90% through-wall. This cracking was entirely within the HAZ. It lay in the inner part of the HAZ, that is, in that part of the HAZ closest to the weld metal. The cracking sometimes came to within one or two grains of the fusion line, but it was never seen to touch the fusion line: also, it never strayed into the outer (intercritical) part of the HAZ. All of the cracking was intergranular. Grain boundary cavitation, varying in density, was associated with the cracking throughout. Both of these latter features are typical of long-time (low strain rate) creep cracking. Using the classification introduced by Schüler *et al.* [1], this cracking, in the inner HAZ, is termed type III creep cracking.

For most of its length, the crack had grown along the almost vertical wall formed by the fusion line. In the outer 1 or 2 mm, however, the last weld bead overhung the remainder of the fusion line, and the crack had not managed to grow around that overhanging bead (Fig. 3). The density of the
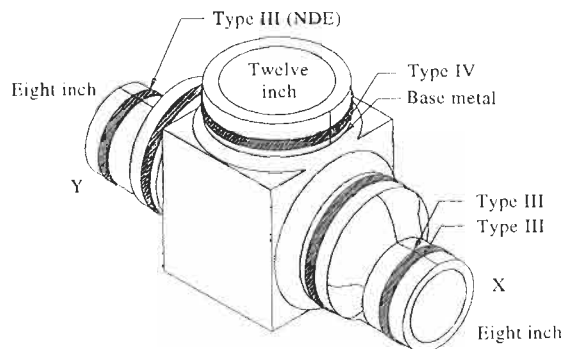
Fig. 2. At the forged tee, steam enters through the 12 in. line, and divides into two streams, along the 8 in. lines. Sites where creep cracking was found are labelled type III, base metal, or type IV, according to the sort of cracking found there.
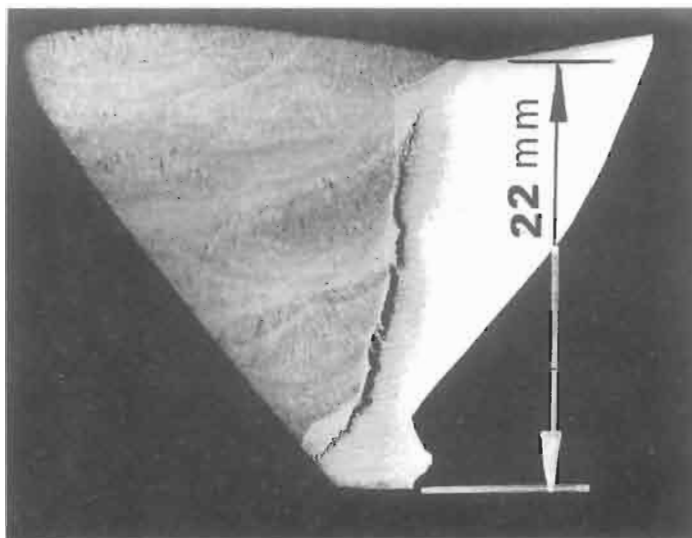
Fig. 3. Section through the cracking whose discovery prompted this investigation. It is in the 8 in. line on the X side of the tee. The cracking extended from the bore to a spot 90% through-wall. The cracking ran through the inner part of the HAZ. (Nital etch, bright field.)

grain boundary cavitation suggested that, if the crack had reached the outer surface, it would have done so along the outer parts of the HAZ, i.e. as type IV cracking.

The cracking did not consist of a single crack from the root to near the crown. There were many short overlapping cracks, in a band in the inner HAZ, and these had joined together. The widest cracks were in the mid-wall region. For this reason, it was believed that the cracking had probably initiated there, and had grown inwards to reach the pipe bore, and outwards towards the pipe's OD surface. The larger crack segments had faces coated with about 60 μm of oxide.

This crack site was one of those where the MT examination had found no indications whatever in the years from 1987 to 1994. The replica metallographic examination had found the creep damage to be more advanced here than at any other site sampled along the steam line, but, even here, on the outside surface, at its maximum, the damage was only to the stage of aligned voids being present (Fig. 4). These external examinations had not indicated the extent of the damage that lay underneath.

3. EXAMINATIONS AT OTHER SITES

When this major cracking was recognized, several other steam line welds and their HAZs were examined. These examinations used ultrasonics and *in situ* metallography, and two further boat samples were taken. The examination of one of these, removed at an ultrasonic reflector, revealed subsurface cracking in the pipe side HAZ of the weld joining the Y branch to its steam chest. This cracking was not as severe as it was at the X-side reducer. However, like that cracking, it was always seen to be in the HAZ close to, but never on, the fusion line (Fig. 5). Some minor lack-of-fusion and slag entrapment flaws were also found. These weld flaws had often been extended by grain boundary cavitation, and by microcracks a few grain boundaries in length. They were sometimes adjacent to the creep cracking in the HAZ. However, no interaction was seen between the cracking or creep damage in the HAZ, and the creep damage associated with the weld flaws.

Creep damage in the 8 in. line, was recognized, to some degree, at every site examined. This creep damage was either seen directly by metallographic examination or inferred by finding ultrasonic reflectors in the appropriate HAZ sites. In contrast, very little damage was found in the 12 in. line. One reflector located in the weld metal in the 12 in. line was interpreted as coming from a creep crack, and a boat sample was taken there. However, when the boat sample was sectioned, only relatively small weld defects were found. At another spot in the 12 in. line, there was a 2.5 mm long intergranular crack in the weld metal. There were cavities at the tip of this crack, so that it was

66
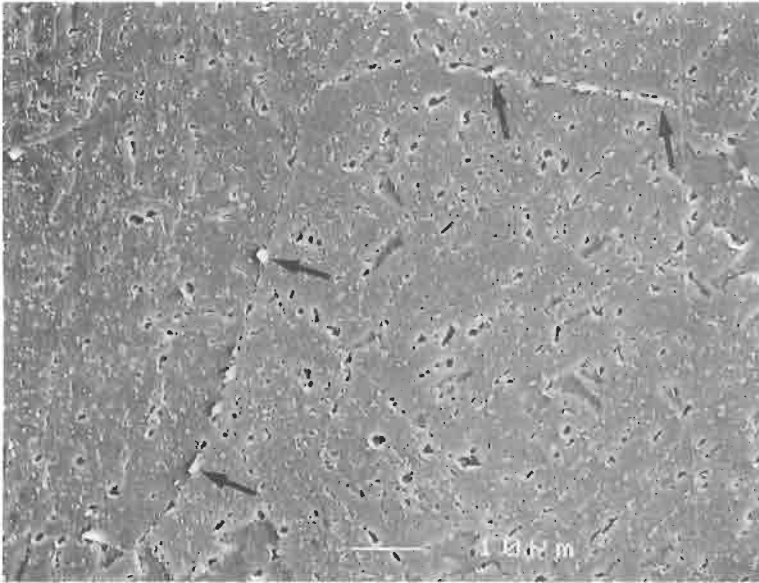
Fig. 4. Photomicrograph from a replica taken on the outside surface of the reducer to 8 in. pipe weld on the X side of the tee. It shows aligned voids along grain boundaries in the pipe side HAZ of the weld. This is the most advanced stage of creep damage that was seen on the outside surface of the 8 in. pipe. It is the stage that would immediately precede microcrcking. (Nital etch, cellulose acetate replica, scanning electron micrograph.)

Fig. 5. Cracking on the 8 in. line side of the Y-side connection to the steam chest. The darker band to the right is weld metal. (Photomicrograph taken from a replica made in the cavity produced by removing a boat sample.) (Nital etch, bright field, cellulose acetate replica.)

probably a type I [1] creep crack. However, no other cracking, and very little deterioration, was seen in the 12 in. line.

Examination of the tee forging by MT and *in situ* metallography revealed what appeared to be creep cracking in the forging at two separate sites. (These cracks were open to the surface, rather than buried.) The decision was made to remove and replace the tee and its reducers.

4. EXAMINATIONS OF THE SCRAPPED TEE, AND OF THE REDUCERS AND THEIR WELDS

When the retired tee became available, parts of it were examined by conventional, as opposed to replica, or boat sample, metallographic examination. The reducer side HAZ of the reducer-to-pipe weld on the X side of the tee was one site that was examined. (The major cracking that started this investigation had been in the pipe HAZ of this same weld.) There were cracks at three different depths through this reducer side HAZ. Two were "mid-wall" sites, and the third was at the root (Fig. 6). These cracks were relatively small. The mid-wall cracks had a radial extent of about 3 mm, while that at the root had a radial extent of about 1.2 mm. All of these cracks were in coarse-grained bainitic HAZ (Figs 7–8) (ASTM grain size 5). In the nine different sections that were taken through this particular weld, only one weld flaw was found (Fig. 9). This flaw lay partly on the fusion line. It had extended by creep cracking into the weld metal, and into the X-side reducer HAZ. The extension was into fine-grained HAZ (ASTM grain size 10 or 11 in the HAZ), but the extension was by no more than 0.5 mm. There was intense, but local, grain boundary cavitation associated with the growth from this flaw.

In addition to discovering this cracking in the X-side reducer's HAZ, other cracking, that had been diagnosed previously only by replica metallography, was confirmed by the examination of solid sections. There was type IV cracking to 0.6 mm deep (2% through-wall) in the tee side HAZ at the 12 in. pipe connection. A zone of intense cavitation extended from the type IV cracking to a depth of 6 times that of the cracking itself. There was also base metal creep cracking in the tee. These cracks were 2 mm deep at the section site (6% through-wall). The cracking of the base metal was associated with far less cavitation than was the type IV cracking in the HAZ.

The sectioning of the tee also allowed the thickness of the oxide in the bore of the 8 in. pipe to be measured. This oxide was between 120 and 200 μm thick.
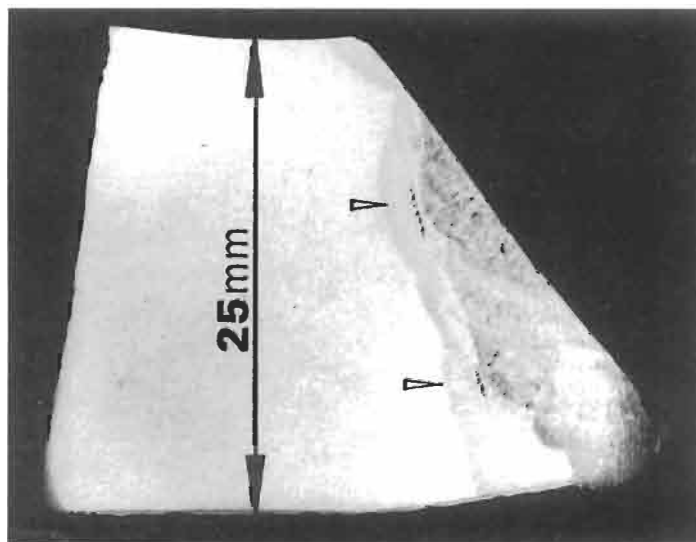
Fig. 6. Section through the X side of the reducer to pipe weld. The two arrows indicate small clusters of creep cracks. They are in coarse-grained parts of the HAZ. (In this case, the HAZ is the reducer HAZ. In Figs 3 and 5, the cracked HAZ was the 8 in. pipe HAZ.) (Nital etch, bright field.)

Fig. 7. One of the clusters of cracks in the HAZ on the reducer side of the weld joining the X-side reducer to the 8 in. pipe HAZ. The whole cluster is about 3.8 mm top to bottom.
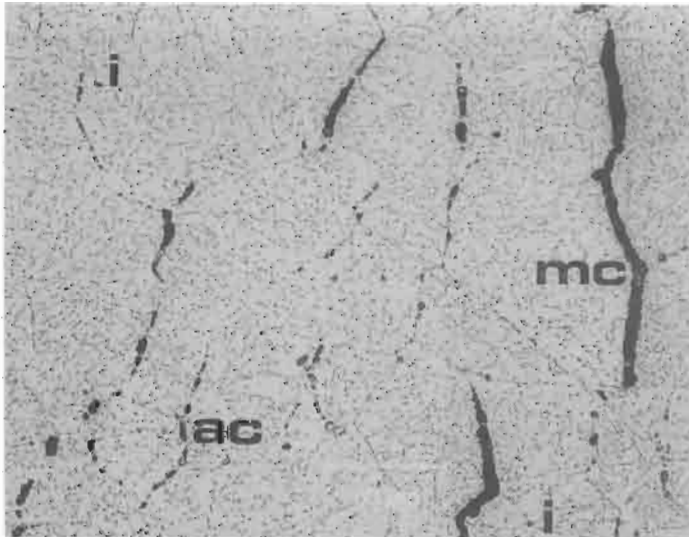
Fig. 8. This is close to one of the clusters of cracks in the reducer's HAZ. There are isolated grain boundary cavities, i, aligned groups of cavities, ac, and microcracks produced by the coalescence of aligned groups, mc. These are three stages in the progressive generation of creep cracks. (As in Figs 5–7, this is a coarse-grained region of the HAZ.) (Nital etch, bright field.)

Fig. 9. This lack-of-fusion/slag flaw on the fusion line had extended about 500 μm by creep. Where it grew into the HAZ, it grew into fine-grained material, and there was a very high density of creep rupture voids. (The darker material on the right is weld metal.) (Nital etch, bright field.)

5. DISCUSSION

5.1. *Age of the X-side tee crack*

The oxide on the faces of the crack in Fig. 3 is about 60 μm thick. This oxide thickness can be compared with that in the bore, and can be used to estimate the time during which this cracking has been open to the bore of the pipe. A model of hyperbolic growth of the oxide gives the oxide thickness, x, at time t as

$$x = Kt^{1/2}. \tag{1}$$

For the pipe bore, x, on average, is 160 μm, and t is 204,000 h. Therefore, we have

$$K = x/t^{1/2} = 160/(204{,}000)^{1/2} \, \mu\text{m h}^{-1/2}. \tag{2}$$

The time taken to grow a 60 μm thick oxide layer, as inside the crack, is then

$$t_{60} = (60/K)^2 = (60/160)^2 204{,}000 = 26{,}690 \, \text{h}. \tag{3}$$

It seems, therefore, that the almost through-wall crack on the X side of the tee, having been initiated in mid-wall coarse-grained zones in the HAZ, only broke through to the bore surface about 20,000 or 30,000 h before that cracking was discovered.

5.2. *Piping support and stress analysis*

In conjunction with the material examinations, the pipe support structure was reviewed in detail. The analysis of the pipe supports, hanger settings, and stresses for the in-service piping systems was complicated by hangers that were not functioning, and by a lack of information on the original cold

spring in the line. A complete stress analysis using computer software (Autopipe) [2] was completed using both the original design parameters and the actual pipe configurations based on field inspections.

The results of these analyses suggested that the piping at the tee was overstressed, and that two factors contributed to that overstressing:

(1) Improper hanger selection at location 6 in the original construction.
(2) Bottoming out of the hangers at locations 5 and 6, and topping out of the hanger at 3.

In-service piping systems do not creep uniformly through time or throughout their length. Axial stresses due to bending and dead-weight vary along the length of any system, and other factors concentrate stresses and, thus, creep strain. At the tee block and steam chest connection, the stresses (strains) are also concentrated due to the local geometry. When analyzed using the original design parameters, the stresses at the location of the major flaws were found to be greater than the design stress allowable based on the 1993 ASME B31.1 Code [3].

In addition to this, the allowable stresses used in the early 1960s for the design of piping systems using ASTM A335 P11 materials, such as the 1.25Cr–0.5Mo steels used here, have been recognized as being too high. At the design temperature of 1005 °F, the allowable stresses have been reduced from 7600 psi (52.4 MPa), prior to 1965, to the current level of 6090 psi (42.0 MPa).

5.3. *Mid-wall cracking initiation*

The stress analysis shows that the maximum stress occurs at the pipe's outer surface. Given a homogeneous material, the cracking would therefore be expected to start at that outer surface. The evidence is that the cracking did not start there, but started within the pipe wall. To understand why cracks would be initiated at sites other than the apparently, most highly stressed sites, it must be remembered that the material around a weld is not homogeneous, either compositionally or structurally. The HAZs of these particular welds, close to the fusion line, consisted of alternating bands of grain-coarsened and grain-refined steel. These bands have very different high-temperature mechanical properties to each other. In general, coarse-grained materials, including coarse-grained ferritic steels, have a higher creep strength, or a lower creep rate, but less creep ductility than finer grained steels of otherwise identical composition [4, 5]. There is a tendency, therefore, for a load to be shed from the finer grained and creep soft, but ductile zones, to their coarser grained and creep harder neighbours. These coarse-grained areas can withstand this extra load shed from their finer grained neighbouring zones, in the sense that their creep extension is relatively slow. However, these regions tend to be "creep brittle". They exhaust their creep ductility, giving rise to the cracking that is seen here.

5.4. *Importance of weld defects*

It should be emphasized that this cracking occurred without the involvement of weld flaws. Whenever cracking is found in an operating plant, and that cracking is associated with a weld, there seems to be a natural tendency, for many of the personnel involved, to lay the blame on some sort of "weld defect" or "bad welding". This is true when creep cracking is involved, as here. It is also true when the cracking mechanism is fatigue cracking or stress corrosion cracking. The belief that cracking in, or at, a weld is a result of the weld having been originally faulty can be very difficult to displace. That belief can adversely affect the scope and type of both present and future inspections, and can influence repair decisions. Often, however, it is not "weld flaws" or "bad welds" that are responsible for in-service cracking at welds. The problems that occur at welds are usually more a product of the intrinsic properties of most fusion welds: because the residual stresses tend to be high and tensile at the surfaces of a weld that has not received post-weld heat treatment, stress corrosion cracking may occur there. Because stress (strain) concentrations are generally associated with fusion welds, welds tend to be potent sites for the initiation of fatigue cracks. In the present specific case, because of the microstructural changes generated by the thermal cycle of fusion welding, some weld zones have an increased susceptibility to creep cracking.

It is important, however, in any particular case, to try to find out whether specific weld flaws are involved. If a weld flaw is involved, the cracking may be localized to a specific site, or to an

identifiable number of sites. If the cracking is dependent only upon material composition, service and microstructure, that cracking can be general throughout those parts of a system utilizing common materials, design and methods of fabrication. In the present case, the evidence was that weld flaws were not involved in the initiation or growth of the cracks. The observation that weld defects tend not to be involved in creep cracking in high-temperature piping has been made elsewhere, based on a much larger database [6].

5.5. *Significance with respect to life extension inspections*

The incident emphasizes the need for a volumetric inspection of weld zones of high-temperature pipework as part of either periodic inspection or life extension studies. Creep cracking can be initiated at any position within a weld HAZ, or within the weld metal itself [6–9]. Hence, inspections of piping systems, for which there is not an established history of cracking, must take into consideration the possibility of cracks growing from any position through the pipe wall. It also needs to be emphasized that the volumetric inspection needs to be accompanied by a metallographic examination, probably by replication, of the pipe's outer surface.

The probable location of final failure can be predicted with a reasonable degree of reliability for some particular combinations of materials, fabrication procedures, and design. Thus, in main steam lines longitudinally welded using the submerged arc process, the critical zone appears to be the weld metal itself [8], and the greatest attention has to be paid to flaws found within the weld deposit. For butt welds, in most cases [6, 8], it seems to be the outer part of the HAZ, i.e. the type IV region, that seems to be where creep cracks are most likely to be found. In the present case, based on the experience in many other boilers, the outer part of the HAZ would also have been expected to have been the most critical area. The experience at the Grand Lake station shows, however, that, until cracks have been found for some specific combination of circumstances, or even in some particular boiler, all weld zones must be considered candidates for creep cracking.

6. CONCLUSIONS

(1) The main steam piping at this generating station had cracked 90% through-wall with only the outer 10% of the pipe wall remaining uncracked.
(2) The cracking had grown in the inner part of a weld HAZ (type III cracking).
(3) Fluorescent magnetic particle inspection on the OD surface at the site of the 90% through-wall crack did not reveal any indications.
(4) Replica metallographic examination at the same OD surface site revealed creep rupture cavities, but did not reveal cracking even to the stage of a single microcrack one grain boundary long.
(5) The cracking was discovered by using an ultrasonic examination.
(6) The cracking had started in coarse-grained weld metal close to the fusion line, and within the body of the pipe.
(7) The piping which cracked was overstressed with respect to current allowable stresses for P11 material under ASME rules.

REFERENCES

1. Schüler, H. J.., Hagn, L., Woitscheck, A., *Der Maschinen Schaden*, 1974, **47**, 1–13.
2. Autopipe (Pipe Stress Analysis and Design Program) Version 4.60.03, Rebis, Walnut Creek, CA, 1995.
3. American Society of Mechanical Engineering, B31.1 1993 edition.
4. Price, A. T. and Williams, J. A., in *Recent Advances in Creep and Fracture of Engineering Materials and Structures*, ed. B. Wilshire and D. R. J. Owen. Pineridge Press, Swansea, 1982, pp. 265–353.
5. Alberry, J. T. and Jones, W. K. C., *Metals Technology*, 1977, **14**, 45–51.

6. Brett, S. J., VGB Conference on Materials and Welding Technology in Power Plants, Essen, 1994.
7. Buchheim, G. M., Osage, D. A., Brown, R. G. and Dobis, J. D., *Journal of Pressure Vessel Technology*, 1995, **117**, 227.
8. Chan, W., McQueen, R. L., Prince, J. and Sidey, D., in *Service Experience in Operating Plants*, PVP Conference, Vol. 221, ed. W. H. Bamford, R. C. Cipolla and C. E. Jaske. ASME, 1991.
9. Henry, J. F., Ellis, F. V. and Lundin, C. D., *Welding Research Council Bulletin* 354, 1990.

CREEP FAILURE OF A SPRAY DRIER

P. CARTER

Advanced Engineering and Testing Services, CSIR, Private Bag X28, Auckland Park 2006,
Republic of South Africa

Abstract—NDT, design calculations and metallurgical analysis were performed on specimens from a collapsed spray drier. Failure modes initially regarded as possible were: corrosion leading to reduced sections and loss of strength, fatigue and fracture, and creep. The calculations pointed to creep, and no positive metallurgical or physical evidence was discovered to support any of the hypotheses. However, the compression stresses implied that creep deformation could have occurred without inducing discernible creep damage. It was concluded that buckling and collapse of the structure was due to excessive creep deformation. © 1998 Elsevier Science Ltd. All rights reserved.

Keywords: Creep, buckling, overheating, process-plant failure, stress concentrations.

1. BACKGROUND

A spray drier which had been in service for nearly 20 years at the Western Platinum Mine metallurgical plant, collapsed on a quiet day while operating normally. The spray drier consisted of a cylindrical shell some 15 m in height and 5.5 m in diameter, supported vertically on four 5 m steel columns. Combustion gas controlled at 550°C from a chain-grate stoker entered an annular chamber encircling the base of the shell. The gas entered the cylinder from a number of ports on the inside of the annulus; it then travelled up the cylinder, drawn by an induced draught fan, in order to dry a slurry falling from the top of the drier in a counterflow arrangement. The dry product was collected from a cone at the bottom of the cylinder. The drier was lagged and clad from top to bottom to conserve energy.

Figures 1–3 show views of the collapsed drier. Braced columns, the lagged and clad annulus and shell, and the bottom cone, are all visible.

These figures show the remarkable nature of the collapse, with the column and cone moving down axisymmetrically until the weight was supported by the cone on the ground.

The aim of the investigation was to explain the failure and to make recommendations to ensure that it was not repeated on the two remaining driers, which had seen some 7 years' service.

2. INSPECTION

Ultrasonic NDT was performed on columns and some areas of the annulus and shell on the remaining two driers. Attempts to measure the temperature of the insulated skin of the annulus of these driers were made with limited success. A probe inserted into the lagging against the outer annulus shell indicated temperatures in the range 330°C–360°C. This was felt to be unrealistic, due to the fact that the plate had gas at 550°C on one side and 250 mm of fibre glass lagging on the other side. Where possible, thickness checks were made on the failed drier, and sections of shells and columns were removed for metallurgical analysis.

These investigations all gave negative results, that is, no significant corrosion was observed, and both columns and shell material were consistent with Grade 430 mild steel without any deterioration in properties. No evidence of fatigue and fracture was found and in particular, no physical evidence of creep damage was found.
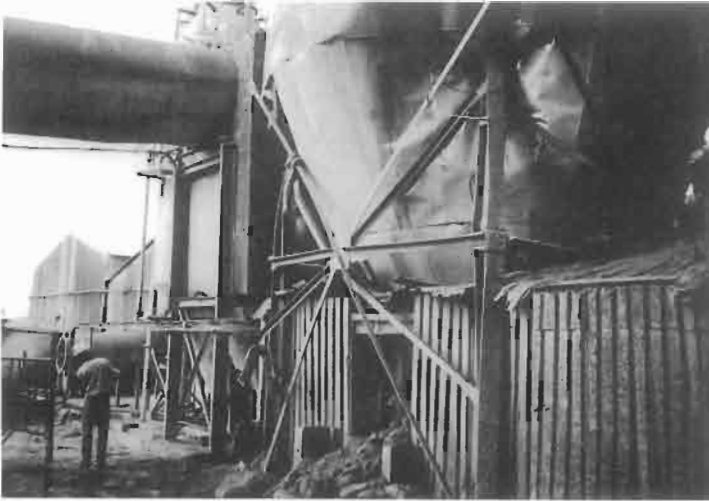
Fig. 1. View of base of collapsed drier.
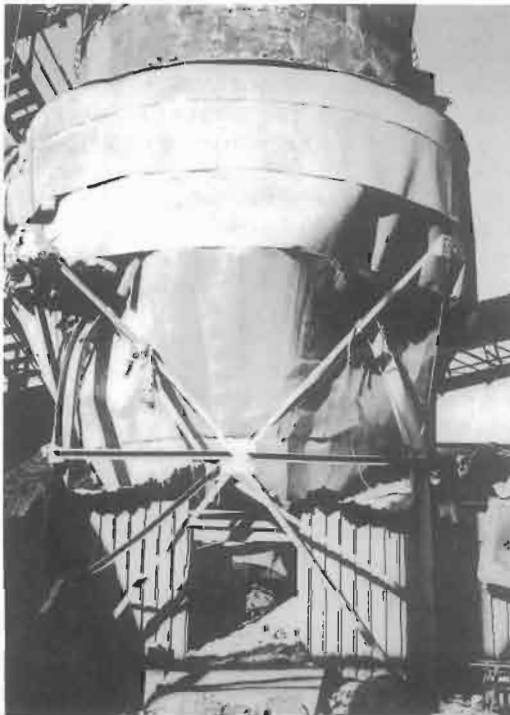
Fig. 2. View of base of collapsed drier.

There was clear evidence of a localised buckling deformation in columns and shells in the region of the welded column-shell joint. This was distinguishable from the damage associated with a collapse event itself.

Fig. 3. View of buckled column.

3. STRESS ANALYSIS AND ASSESSMENT

The approach in this section is to compare stresses at critical points in the structure with allowable and failure stresses, inferred from BS 5500 [1], the design code for pressure vessels, which has high temperature materials data.

Figure 4 is a summary of design and failure data for Grade 43 steel, based on a service life of 150,000 hours or 17 years. Failure data for creep rupture is inferred from design data using the quoted safety factor of 1.3.

Further, extrapolation for temperatures >480°C is necessary. There is a justification for using
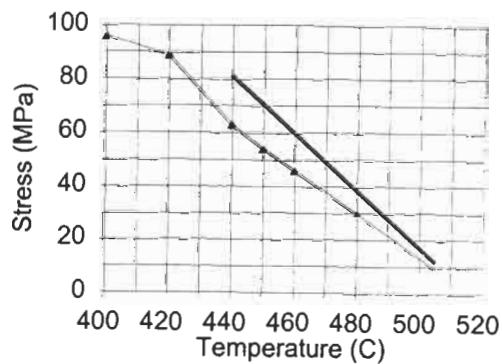
▲ Design — Failure

Fig. 4. BS 5500 stress-rupture data for Grade 430 steel.

tensile creep rupture design and failure data for this case. Although creep-rupture does not occur in compression, it is expected that strain rates will be similar for tension and compression.

Strain limits associated with allowable stresses are in the region of 1%. Significantly more strain will accumulate if stresses approach the rupture limit, so using design failure stresses in compression to assure strain limits is justifiable.

Stress analyses were performed on two details of the drier:

(i) Axisymmetric gas annular duct and main shell connection (Fig. 5, SCF1).
(ii) Shell-column connection (Fig. 6, SCF2).

The results in each case are expressed as a stress concentration factor (SCF) based on the average loading on the shell, estimated as 45 tonnes. The results are summarised in Table 1.

These calculations are based on a linear elastic material model. The effect of creep is to redistribute stresses. A beam in bending can redistribute elastic stresses so that for a high creep exponent (≥ 6) the maximum stress is about 67% of the maximum elastic stress. The gas duct SCF of 8.9 is associated with bending, so under creep conditions, a value of 6 is appropriate.

The elastic stress distribution for the geometry in Fig. 6 would have the characteristics of a notch, since the idealised structure is supported at a point.

An estimate of the creep stress concentration factor can be obtained using a Neuber calculation described in the ASME III Code Case N47 [2]. Here, the product of stress and strain using the inelastic isochronous stress–strain curve must be the same as the product of elastic stress and strain, including stress concentration.

The BS 5500 [1] data may be used to infer a stress–strain curve such that a stress of 18 MPa at 500°C causes a strain of 1% in 1.5×10^5 h. Assuming a high exponent (6, say), this approach produces a creep stress concentration of 3, compared with the elastic value of 5.4. Thus for creep conditions, the maximum stress in the structure is 22 MPa, compared with 32 MPa for elastic conditions.

Examining the BS 5500 [1] data in Fig. 4, it is clear that for design purposes a maximum metal temperature of 480°C would be allowed for the above stresses. To explain the failure, a temperature between 490°C and 500°C is required.
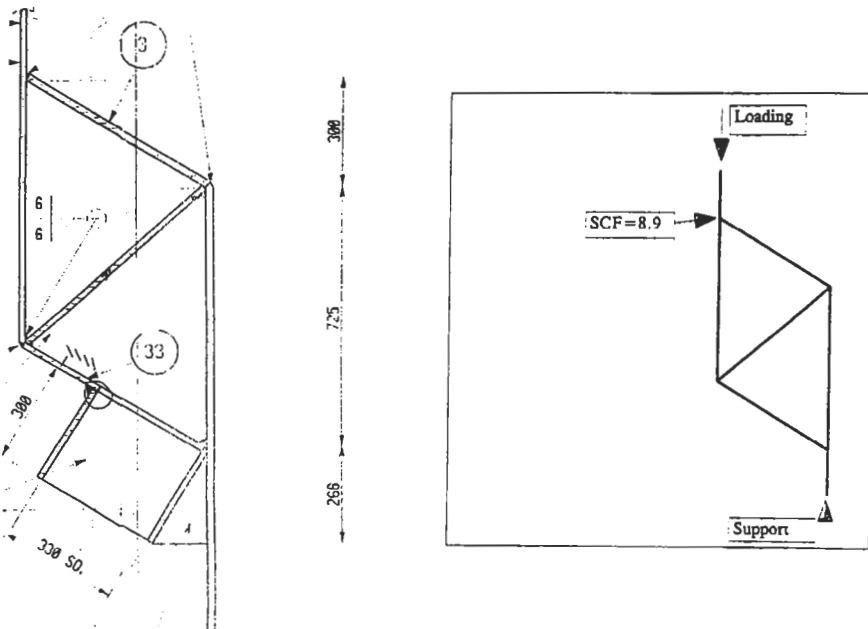
Fig. 5. Gas duct cross-section.
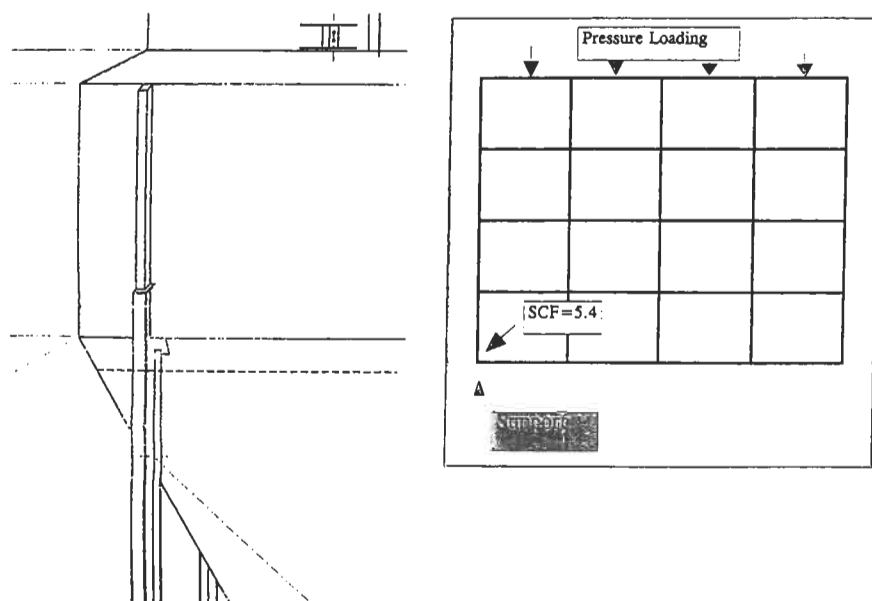
Fig. 6. Column-shell detail.

Table 1. Stresses and allowable stresses (500°C)

Region	Nominal stress (MPa)	SCF (elastic)	SCF (creep)	Stress (MPa)	Allowable (MPa)	Failure (MPa)
Gas duct	3.6	8.9	6.0	22	13	17
Column-shell	3.6	5.4	3.0	11	13	17

The values of stress and allowable stress in this paper should not be regarded as anything other than estimates. However, they do clearly indicate the nature of this failure.

4. CONCLUSIONS

The collapse of the spray drier after 20 years in service is an unusual example of a low stress, high temperature compression creep failure.

To avoid a similar fate on other more recent (and stronger) spray driers, it was recommended that the lagging and cladding in the region of the annular gas duct and the column-shell joints, be removed.

REFERENCES

1. BS 5500 Specification for Unfired Fusion Welded Pressure Vessels, British Standards Institution, London.
2. ASME Boiler and Pressure Vessel Code, Code Case N47-12, ASME, New York.

Catastrophic failure of a polypropylene tank Part I: primary investigation

P.R. Lewis*, G.W. Weidmann

Department of Materials Engineering, Faculty of Technology, The Open University, Walton Hall, Milton Keynes MK7 6AA, U.K.

Abstract

The creep rupture of a new polypropylene tank used for holding caustic soda solution is described from the primary evidence. The immediate cause of fracture was a pinhole in the centre of a weld, which initiated a brittle crack. The crack grew slowly during each loading until it penetrated the wall shortly after the fourth filling. The design of the structure fell short of the required dam- rather than barrel-like form needed for resisting hydrostatic pressure. © 1999 Elsevier Science Ltd. All rights reserved.

Keywords: Tank; Creep rupture; Weld; Polypropylene

1. Introduction

Polypropylene is a popular material for applications where toughness, low density and environmental resistance are needed. It has been used for many years for constructing storage tanks (e.g. silos for storing bulk powders) and as a lining for large GRP tanks (e.g. for storage of corrosive fluids) [1]. However, good design demands that allowance must be made for the maximum stresses to which such products can be exposed in service. The example described in this case history offers some apposite lessons in using polymeric materials for highly stressed products, especially where failure can threaten life and property. The failure bears distant similarity with the failure of a steel silo reported earlier [2].

On 23 August 1994, a large storage tank containing concentrated caustic soda (NaOH) fractured suddenly along one of its welded seams, a jet of liquid shooting across the factory. The incident occurred without any prior warning of failure, and in a tank which had only recently been installed (6 March 1994) at a factory used to manufacture dairy detergent. The last full loading was only the fourth since installation. The tank was made of polypropylene (PP) panels welded together.

---

* Corresponding author. Tel.: 01908 653271; fax: 01908 653858.
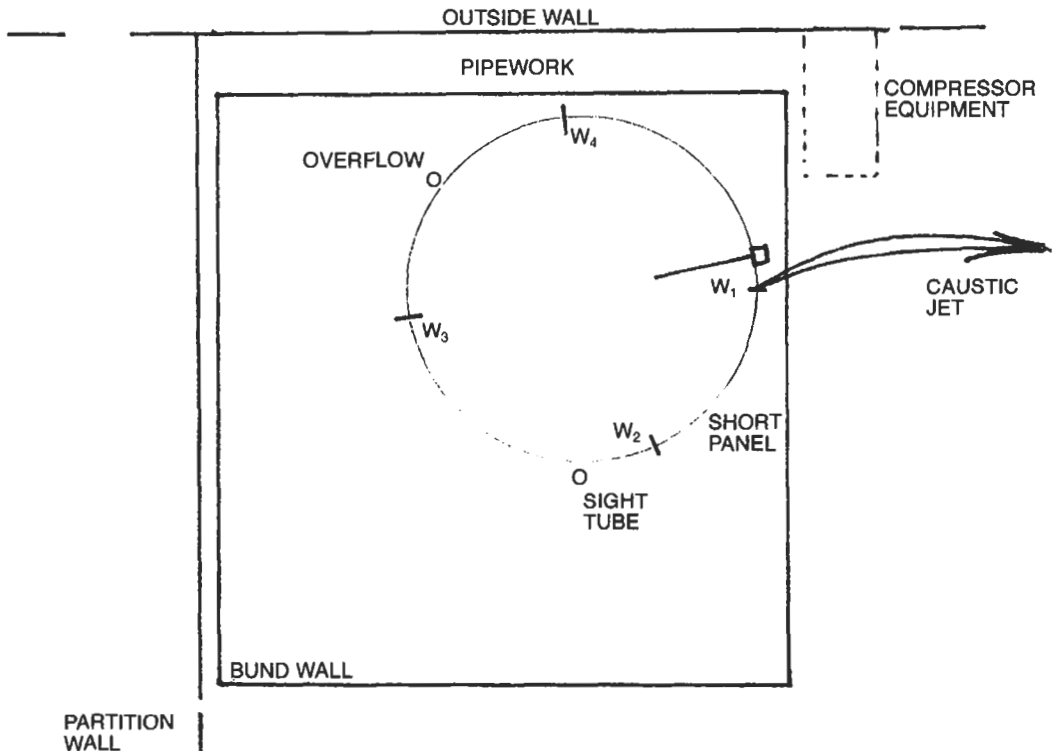
Fig. 1. Sketch plan of the caustic soda tank (diameter ca 2.7 m), showing four vertical welds (W1–4) and their position relative to the bund wall. Three of the four plastic panels had a contour length of ca 2.5 m, the fourth being shorter, at about 1.2 m. An internal heating element lay below the critical crack, but had apparently never been used. The sight and overflow tubes led to the top of the tank.

The jet of caustic soda could not be contained safely, since the fracture had occurred about 1.5 m from the floor of the tank (which itself was free standing on the factory floor), the jet projecting the liquid stream over the adjacent bund wall (Fig. 1). Since the initial fracture was only relatively small, the jet stream continued for several hours under hydrostatic pressure from the tank (which had only been filled that same morning by tanker) before the bund wall contained the liquid. The unconfined fluid spilled out over nearby equipment, and subsequently flowed into adjacent premises, which used specialised printing equipment. Severe damage ensued owing to the highly corrosive nature of the concentrated caustic soda, a fluid which degrades much organic and inorganic material very rapidly. Escape into local water streams could also have created a further hazard to animal and plant life as well as a potential danger to water supplies in the area, but was collected and safely disposed by the Fire Brigade and others. The tank apparently met the stringent conditions imposed by the only public standard available, the German Code of Practice DVS 2205 [3]. An English translation of the document only became available some time after onset of the investigation, and is discussed fully in Part II of this paper.

Preliminary analysis of the failure indicated that the critical fracture might have been caused by weld defects (blow holes), so that a programme of tests was undertaken on the weld material as

Fig. 2. Failed plastic tank, showing the bund wall in section (the front part was removed by the Fire Brigade). The jet of caustic soda flew from the tank wall near the right-hand edge in the figure, just above the top of the bund wall. It rose upward from a small crack in the weld, and landed some 4–5 m away from the exit point.

well as the panel plastic. They included DSC and FTIR to check material constitution, and simple tensile tests to measure directly the strength of the welds. The experimental part of the investigation was carried out by P.R. Lewis, the translation of the key standard (DVS 2205) covering such tanks being carried out by G.W. Weidmann.

2. The accident

Failure of the tank occurred at about 18:45 h, and was discovered by the Production Director at the factory. He was in the upstairs office at the factory, and was about to leave the premises at the end of his working day, when he heard a bang or 'popping' sound coming from the factory floor. It was followed by the sound of 'rain', and looking down through an internal window, he saw a jet spray of fluid issuing from the lower part of the recently filled black storage tank, situated in a further corner of the factory (Fig. 2). He observed that the jet was issuing in the form of an "...8 or 9 inch wide stream..." from the side of the tank facing a storage bay. The jet curved upwards, so easily clearing the top of the adjacent bund wall, and was about 4–5 m long. The end of the jet was hitting storage containers, and flowing down onto the factory floor.

The broken tank was simply a static storage container with a sight tube on one side, and pumping facilities (Fig. 2). By 22:00 h that evening, the level of liquid in the tank had fallen substantially, so lowering the hydrostatic pressure, decreasing the length of the jet stream, and causing it to fall within the bund wall. The load of caustic soda which escaped freely into the factory represented

almost half the total capacity of some 30 t, and had only been delivered to the premises that day. Pumping of the fluid from the tanker into the tank had been completed by about 09:15 h, and nothing untoward had apparently been observed by operators working in the factory, either at that time or later during the day before catastrophic fracture. It is worth observing that the corner of the factory where the tank stood was poorly illuminated (Fig. 2). Sub-critical cracks would have been difficult to spot, since they would simply have been fine hairline features against a black matte background of the polypropylene material of the panel walls. There was no evidence of any leakage of fluid before the accident near the critical crack—such leakage would have been relatively easy to see, owing to the contrast between the white deposit and the black surface of the tank.

2.1. Site inspection

A visit to the site showed that failure had occurred by a single crack apparently running the complete length of one of the four vertical welds directly visible on the exterior wall of the tank (Fig. 3). The crack was brittle and it was whitish in appearance in one large region near the centre of the panel. There was also extensive surface contamination from caustic soda crystals and sodium carbonate. The results of measurement of the tank are shown in Figs 1 and 4. Its circumference was also measured at two points. One was at a height about 1.5 m above the ground, approximately level with the centre of the crack, and the other at a location well away from the crack, at the top of the second buttress. The results were: circumference at crack level = 8.57 m; circumference at top of second buttress = 8.55 m.

The difference of 2 cm thus represented creep of the wall, plus any crack opening that may have occurred as a result of the fracture. Since the crack had only opened by about 1 mm, it was concluded that creep of the material accounted for most of the increase in circumference, of about 0.23%. Some bulging of the failed panel was in fact detectable by eye, as shown in Fig. 3 (the effect can be seen clearly by tilting the figure and looking along the edge of the tank). The tank had been created at crack level by welding four 12 mm thick panels together, three being of roughly equal contour length (2.43, 2.48 and 2.45 m clockwise from the cracked panel, Fig. 4) the panel adjacent to the crack having 1.21 m contour length. The visible tank structure at first buttress level (i.e. below the crack) had been created in a similar way by welding three panels of about the same contour length (2.47, 2.49 and 2.48 m clockwise, offset by 0.71 m from the cracked panel weld). The final panel comprised a panel of contour length 1.31 m.

The surface of the tank was examined closely for any trace of surface damage, whether from impact or abrasion, which might have accounted for the catastrophe. None of any kind was found, the patterned exterior surface appearing pristine in condition, especially near the crack itself. If impact had initiated failure, then it was here that might show surface damage (Fig. 3). Even small impacts could damage the plastic, owing to its relative softness. It was decided to cut out several areas of the tank with a circular saw for further analysis of the fracture surface.

3. Fractography

The fracture surface was revealed by estimating where the ends were situated, and then carefully cutting through the double panels so as to leave a few mm of material holding the crack together

Fig. 3. Face view of the failed weld in the plastic panels of the tank. The large white arrow indicates the position of the crack initiation point in the centre of the weld, the crack eventually widening to the points shown by the two smaller arrows. The surface surrounding the failed weld is pristine and totally undamaged, with no abrasive wear or traces of impact damage.

at each end of the specimen. It was then broken apart by a sharp bending movement, oriented so that the wide wings of the panel formed the arms of the beam. The material behaved in a totally brittle fashion, owing to the sharp ends of the crack.

The fracture surface proved to be relatively simple, with a central whitened zone at the outer weld edge on which were situated several small voids. One of these features appeared more prominent than the others, being surrounded by several concentric zones of slightly different greyish hue. Examination of the centre of this origin showed there to be a small hollow pit oriented at right angles to the major axis of the weld, and meeting the outermost surface at one end (O_1 on Fig. 5). The inner surface appeared highly reflective, almost polished, very similar to that produced by melting a free surface. There was also a thin flap of polymer partly concealing the outer part of the hole from external view. Measurement of the pit showed it to be 1.0 mm in length from the
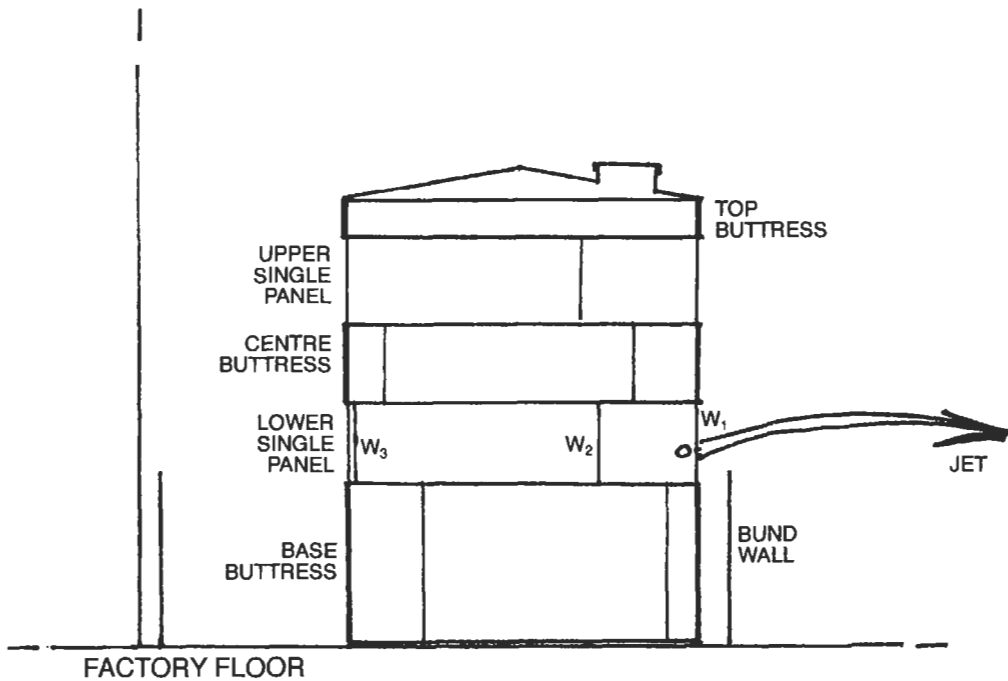
Fig. 4. Sketch section of the failed caustic soda tank, from the office side of the factory floor. It consisted of rectangular thermoplastic panels welded together, and reinforced with three extra horizontal buttresses (shown by the bold lines). The critical crack started (point O) in a vertical weld (W1) in the lower of the two unreinforced parts of the tank, and the jet rose in a gently curving arc above the bund wall.

surface, 0.6 mm wide at the outer surface of the weld and about 0.15 mm deep. Matching the two halves of the fracture showed that the critical crack had bisected the pit along its longer cross-sectional dimension. Thus the cross-section was roughly elliptical, of minor axis 0.3 mm, and major axis 0.6 mm. The were similar, but sub-critical pits discovered elsewhere on the fracture surface (Fig. 6).

Since the fracture surface had been washed with water to remove the white crystals of caustic soda and sodium carbonate, the white zone at the centre of the failed panel cannot be contaminant, so what does it represent? Almost certainly, it is crazed material present ahead of a slowly growing crack, polymer material which has been dilated by stress, and thus contains minute voids which scatter light and hence appear white. The four main zones present around the largest defect (Fig. 5) on this hypothesis, thus represent four periods of slow crack growth, corresponding to the four full loadings of the tank with caustic soda. It may be noted that each region shows progressively greater size, due to the greater stress concentration exerted after each full loading. The smaller surface defects also initiated slowly growing cracks, which never reached critical size for catastrophic propagation, but were instead intercepted by that of the critical crack (Fig. 6).

What then, of the roughly vertical lines seen on the matte black portion of the fracture surface (not shown in the figures here)? Each was clearly visible against the black surrounding by a faint trace of whitening. Such lines probably represent crack arrest points, which either occurred after
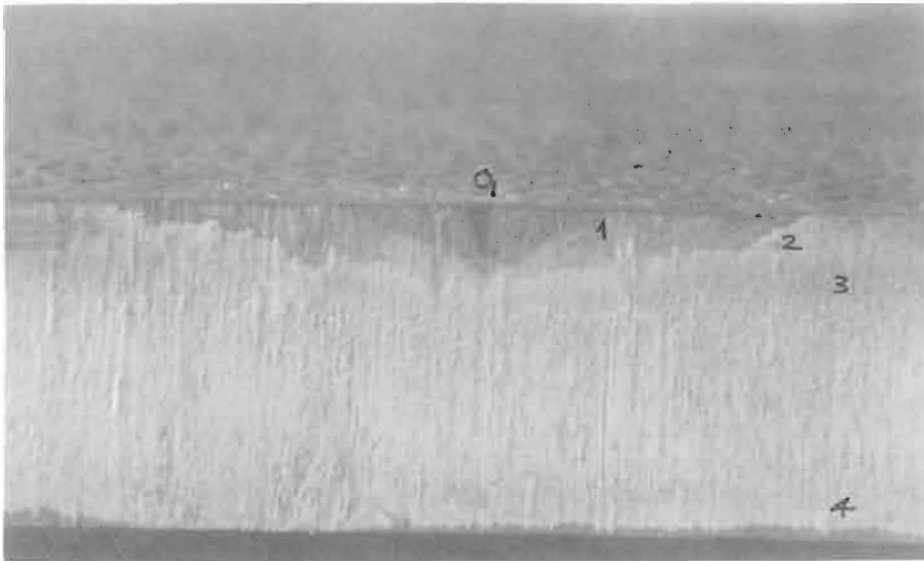
Fig. 5. Close-up of the origin of the critical crack in the main fracture surface, taken using oblique lighting to highlight surface features. There are four propagation zones (1–4) visible around the large pit (O_1) which opens to the outer surface of the 12 mm thick section through the skin of the tank.
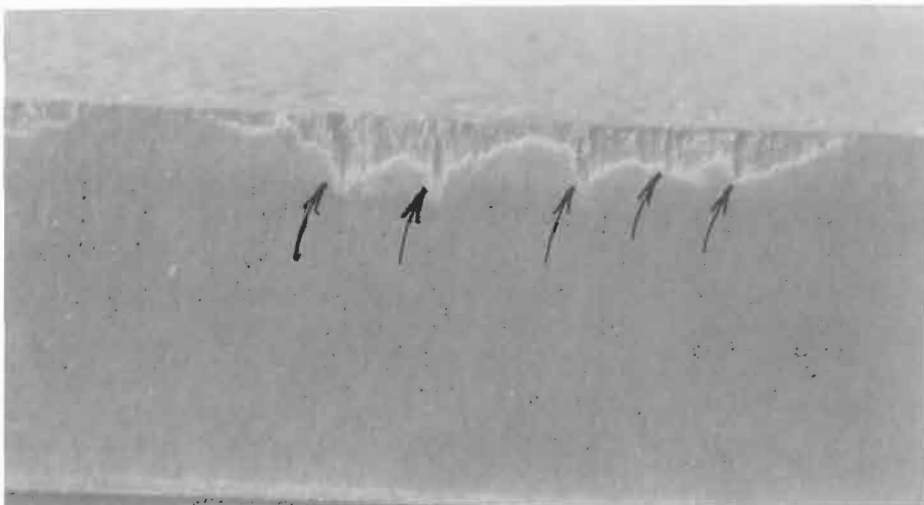
Fig. 6. Close-up of set of pits (arrows) on the outer surface of the critical weld, with brittle crack zone connecting the set, created during one of the early loadings. The pits are pin-holes created by thermal welding and not detected by subsequent spark testing. The sub-critical crack zone was intersected by the critical crack during the final catastrophic failure.

the first penetration of the crack to the interior of the tank, or some time afterwards, when the crack was examined by firemen, inspectors and workmen. The in situ crack could be opened by hand pressure against one of the adjacent panels, and it is likely that inspections simply extended the size of the brittle crack. It is important to note that this hypothesis would explain why the initial size of the jet was only "...8 or 9 inches..." wide. This visual estimate corresponds not unreasonably with the actual 134 mm (5.25 in) length of the central white zone. Alternatively, other crack arrest lines in the proximity of the white zone give measurements of 7.25 in (184 mm) and 8.75 in (222 mm), which may indicate that the critical crack had grown somewhat after the first penetration of the tank. The crack would have then been wetted by the caustic soda, and further crack growth enhanced through the lowering of surface energy.

4. Re-examination of the failed tank

Since the mechanism of failure of the panel had now been identified as brittle fracture through slow crack growth from pre-existing flaws (pits) within the weld zone, it was now thought essential to determine why only one of the four vertical welds had failed in this way. The problem could be tackled in two ways. Firstly, was it true that the other panels were completely unaffected by the high loading stresses? Examination on site had been necessarily made under poor lighting conditions, and some of the welds were physically difficult to access. The analysis of fracture clearly indicated that catastrophic failure must have been preceded by the slow growth of hairline cracks from defects on the outer surface of the weld, so that close examination of the other welds should reveal similar, but sub-critical features either if they had been welded under the same conditions, or if there was a more general problem with the basic design of this tank. It was therefore decided to re-visit the site before the tank was destroyed totally, and inspect the other welds directly.

Secondly, the behaviour of good versus poor weld material had been roughly tested by comparing the behaviour of sections cut from the two large panels. Both specimens fractured in a brittle manner along the weld, the fracture surface from the poor weld showing a distinctly greater number of internal defects than the good weld material. So it was natural to place such a result on a more systematic basis by cutting tensile specimens for rigorous analysis. Further, tests of each weld and surrounding panel would be required to ascertain whether or not there were any material differences between 'good' and 'poor' welds which could explain the differences between them.

The prime objective of a second visit to the site was to inspect the final two vertical welds which had not been examined earlier, for hairline cracks. The first weld examined was that one lying partly under the HazChem warning notice (Fig. 2), and it showed an irregular bead smoothing mark, but otherwise no hairline cracks were detected. Fine grade talcum powder was smeared over the weld to highlight any cracks. The second weld proved more difficult to access, since it lay on the side of the tank nearest the outside wall of the factory, and was therefore in almost complete darkness. The bund wall was also very close to it, so making access extremely difficult. There appeared to be numerous linear features along the weld zone, so the whole weld was taken away for closer examination.

4.1. Confirmatory microscopy

Inspection of the two welds extracted with a small part of the adjacent panels confirmed the results obtained in the factory. The whole weld sections showed numerous hairline cracks in the
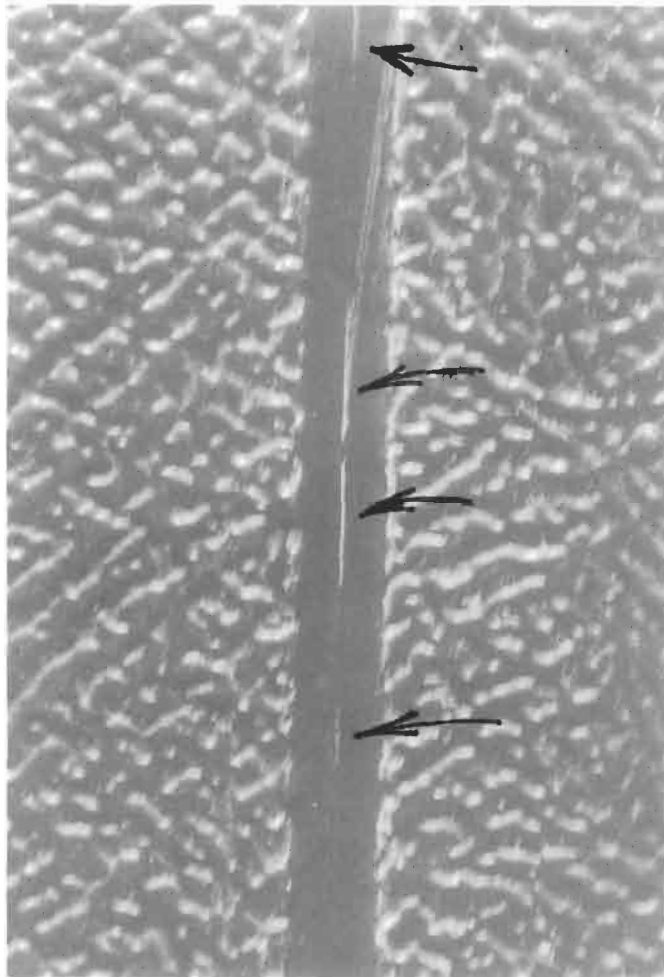
Fig. 7. Close-up of hairline subcritical cracks (arrows) in another vertical weld of the failed tank. The weld was adjacent to that which failed, occurring about the same height, towards the centre of the panel. The cracks were found during re-inspection of the tank, by dusting the welds with fine talcum powder, and represent sub-critical cracks formed during loading the tank with caustic soda. The weld itself is about 2.5 mm wide.

second weld, where they were seen to bisect the complete weld, being almost perfectly aligned with the major weld axis (Fig. 7). This crucial piece of evidence allowed the cracks to be identified and distinguished from the striations caused by bead smoothing. The latter marks tended to wander slightly in direction, while the hairline cracks were perfectly straight in their alignment.

Low power examination in an optical microscope showed that the weld possessed no less than about 10 hairline cracks, varying in length from about 3 mm to more than 40 mm, the longest one being situated at the approximate centre of the panel. Direct measurement of crack width from these plates show the cracks to be about 0.3 mm wide at the top surface. Many of the cracks also had small parts which appeared to be slightly wider than the rest of the crack, especially towards their centres.

The appearance of sub-critical cracks on the outer surface of an intact weld confirmed the picture which had emerged from the study of the fracture surface, namely that cracks had been initiated at pre-existing defects in the welds (small pits at the outer surface), and had grown slowly as a result of superimposed pressure from the full tank. As the tank was emptied, the pressure fell, and slow crack growth stopped. With time, as the cracks grew in size, the stress concentration at their ends became more severe, and when crack growth resumed on refilling the tank, the speed of crack growth increased. This would account for the increasing area under each of the zones shown in Fig. 5. Sub-critical cracks were found elsewhere on the main fracture surface (Fig. 6), and represent cracks which had grown but not propagated catastrophically. It remained to investigate what extra information could be gleaned from closer examination of the welds themselves, particularly comparison of welds which showed no cracks whatsoever (despite being exposed to similar pressures to those which failed) and the intact welds.

5. Mechanical testing of welds and panels

An initial test made on large lengths of panel material cut across the welds had indicated that the fracture surface of the intact weld possessed fewer defects in the weld than that from the critical weld. The samples were simply cut using a circular saw, and bent over with the textured, external surface subjected to the greatest tensile stress, to cause failure in the weakest part. In both cases, one bend was insufficient to break the samples. Both samples broke essentially in the same way, by brittle fracture along the centreline of the weld. The resultant fracture surfaces were very different, however, with a greater density of visible defects from the failed weld. Tensile tests on two dumbbells from each of the two types of weld was conducted to confirm the hypothesis.

5.1. Etching of weld zones

It was of interest to see if the weld zone could be revealed by an appropriate etching method applied to the cross-section produced by polishing. Several reagents were evaluated on a separate sample, including hot chromic acid of various strengths, nitric acid and, finally, organic fluids known to swell or partially dissolve polypropylene. When xylene was used as a polishing medium for the final stage of the polishing process, it was found to show the weld zone very clearly. The method was applied to standard samples of the weld taken from the failed and unbroken panels (Fig. 8).

The etching revealed the internal structure of the form of the welds, both macrographs showing the weld to be wider at the external surfaces, and narrowing down to a reasonably uniform band of material within the bulk of the weld. Both samples also showed a centreline extending from bead to bead, which presumably represents the direct contact surface between the original panels when they were brought together during the thermal welding process. It also represents the zone along which fracture occurred during failure of the tank. There seemed to be a significant difference between the two weld regions, however. That from the failed weld appears to be thinner in width in the narrow, middle portion than that from the intact panel. Direct measurement from the samples with a lupe and graticule gave the width of the failed weld as about 0.6 mm, while the width of the intact weld is about 0.8 mm. It was concluded that the welding process was such as
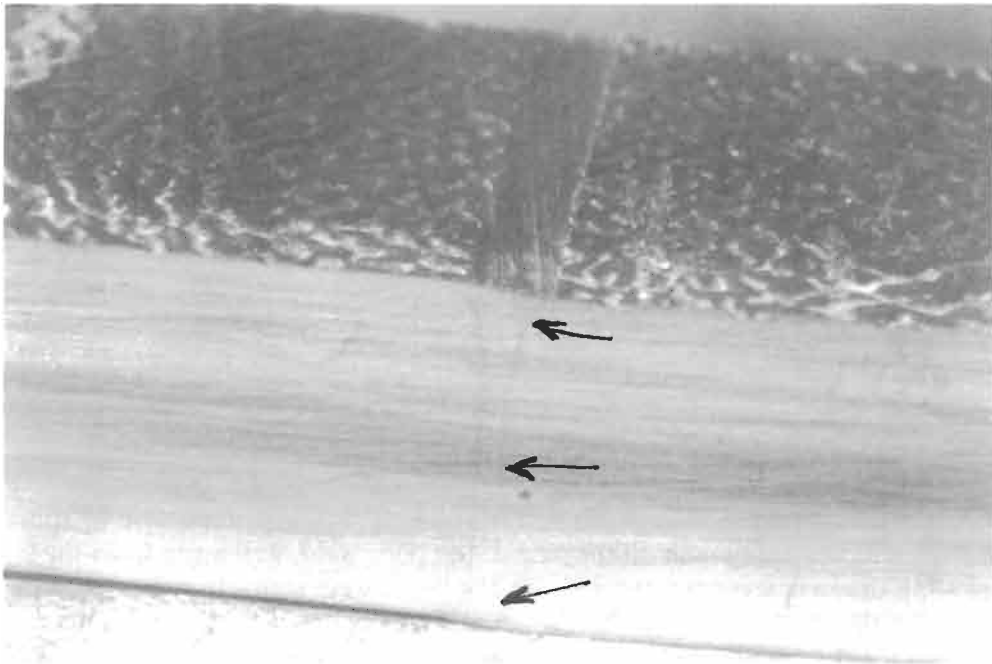
Fig. 8. Close-up of weld section from an intact panel. The section has been finally polished with 1600 grade emery paper and exposed to boiling xylene vapour. The weld appears wider at the outer and inner surfaces of the panel (arrows), and the darker central line represents the original join of the sheets. The weld section from the failed panel showed a slightly thinner central zone.

to give some variability in the size of the heat-affected zone (HAZ), and that there was probably a direct connection between size of the HAZ and the liability of the weld to fail.

5.2. Tensile tests

Specimens were tested in tension at a crosshead movement rate of 10 mm min^{-1}. Failure of all the weld specimens occurred in a completely brittle fashion at the centre of the welds, clean and sharp fracture surfaces being obtained. By contrast, the panel specimens could not be broken within the limited elongations available with the machine used in the tests. In the bulk panel samples, the material showed cold drawing after a yield point, normal behaviour for polypropylene material. The weld samples, however, broke during initial straining, before or near the yield point, when the load/elongation curve turns. The results of detailed analysis of the load/elongation curves are shown in Table 1. The panel materials exhibited no sign of brittleness (so they are not included in the table), but both kinds of weld material failed by brittle cracking at relatively low strains.

When it comes to comparing the numerical data large differences emerged. Thus although the 'poor' weld material was only 4% weaker than 'good' weld material (when evaluated in terms of tensile strength), it showed a mean failure strain nearly 32% lower than that of good weld material. Thus the total work of fracture (the area under the load/elongation curve) is significantly less. The experiment demonstrated rather clearly that the poor welds comprised material weaker than one

Table 1
Tensile properties of welds from failed tank

Sample	Section dimensions (mm)	Strain at break (%)	Tensile strength (MN m^{-2})	Mean strain at break (%)	Mean tensile strength (MN m^{-2})
Good weld, Sample 1	11.75 × 10.2	0.28	21.7		
				0.30	21.3
Good weld, Sample 2	11.8 × 10.4	0.32	20.8		
Poor weld, Sample 1	11.6 × 9.8	0.20	20.7		
				0.21	20.4
Poor weld, Sample 2	11.6 × 10.5	0.21	20.1		

of the alternate welds which had shown no sign of cracking. It is also important to appreciate that the whole weld samples were taken, in the case of the poor weld, well away from the failure zone itself, suggesting that whatever was wrong with the failed weld seems to have been a property of the whole weld rather than, for example, a small restricted zone of the feature. One key property of the PP sheet, tensile strength at yield, was consistent with the values measured directly on weld material from the failed tank. The figure from the manufacturer's technical literature is 20 MPa, compared with slightly greater values shown in Table 1 (20.1–21.7 MN m^{-2}).

6. Inspection of the welding method

It was now reasonably clear that defects present in the outer surface were the direct and immediate cause of fracture of the tank. Analysis of the four welds on the unbuttressed lower portion of the tank had also indicated that the welds varied in defect density, and hence intrinsic strength. It was therefore relevant to examine the welding process used in tank manufacture.

The welding apparatus itself comprised two tables separated by a central gap, where welding would be effected. The surfaces to be joined were first clamped on each side of the table, aligned together in the way intended for the butt weld. The two tables then slid out under hydraulic control, and the hot blade rose from beneath the central gap. The panel edges moved up against either side of the hot blade to start the fusion process, for a time of contact and pressure determined by the operator. He stated that he controlled the heating time by simply observing the state of the two edges: when a bead started to form by melting of the contact surfaces, it was judged that the panels were ready for the next step in the process. The exact time would depend mainly on panel thickness.

The blade withdrew beneath the table, and the tops then slid together, carrying the hot edges together under controlled hydraulic pressure. Fusion between the two panels occurred, the time of contact under pressure again being determined by the operator. A spark test was conducted on welds, the method involving holding a small spark generator immediately above the weld and observing the behaviour of the spark as it was moved along the weld. The joint was supported on a metal, conducting table, so that should a pinhole void connecting upper and lower surfaces be
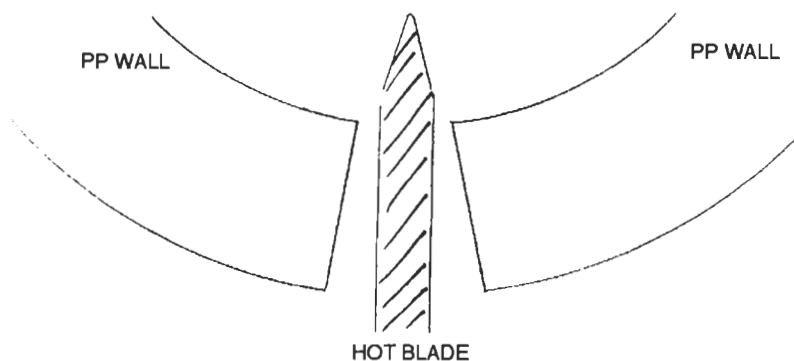
Fig. 9. Weld formation in final closure of plastic panels to form large diameter hoop. The panels are bent round to meet a hot knife, the knife is withdrawn, and the two ends pressed together to form the final joint. One problem is that the panels are still in a state of strain, which is not relieved. Stress relaxation will occur with time, but residual stresses may contribute to early failures if the design itself is faulty.

present, the spark would travel through the gap and the defect be discovered. The method was relatively crude, and could not detect pinholes which did not connect the two opposite surfaces of the weld, for example.

The large circumferential hoops are created first, in the following way. Flat sheets previously cut to the appropriate length with the table saw are welded up until the last joint is ready to be made. The ca 8.55 m length (in the case of the failed tank) is then bent round by hand to form a complete circle, and the ends thermally welded by the machine to make the hoop (Fig. 9). The hoop is therefore under a continuous bending stress, with a large tensile component in the outer surface, and a compressive component on the inner. This is discussed further, especially the effect on the gross stress to which the welds are exposed as a result, in Part II of this investigation.

Similar hoops made in the same way are then stacked and welded to create the tower. The operator thought that the horizontal welds thus made were somewhat weaker than the butt welds made initially, but certainly much stronger than hand made welds.

7. Materials analysis programme

Material from both panels and welds was also tested for its chemical integrity. The tests employed included infra-red spectroscopy (using a Fourier Transform or FTIR spectrometer) and melting behaviour (using a Differential Scanning Calorimeter or DSC). The objective in these tests was to see if there were any perceptible differences in chemical behaviour between 'good' and 'poor' weld material, between weld and panel material and between independent samples of polypropylene and material taken from the tank.

FTIR spectroscopy showed that the tank material was an ethylene–propylene copolymer. Little variation in chemical composition could be detected from several weld sample and normal tank material. Moreover, there was no evidence of oxidation, especially in the welds. The results of various DSC experiments conducted on the various tank materials are shown in Table 2.

The thermograms showed that both sets of samples had very similar endotherms, with melting

Table 2
Melting behaviour of tank materials

Sample	Crystalline melting temperature (°C)	Heat of fusion (mJ mg^{-1})
Intact weld	164.8	53.48
Panel to left	162.2	54.85
Panel to right	163.74	53.18
Failed weld	165.13	50.11
Panel to left	162.24	49.21
Panel to right	164.10	50.96
Ref polymer ICI GWM 101	166.73	48.69

maxima at about 165°C. However, there are differences between the two samples, that from the cracked weld showing a slightly higher melting point just above 165°C, while the uncracked weld has a melting point just below. The cracked weld also possesses a slightly lower level of crystallinity, judging by the computed areas under each curve. It was reasonably clear that, overall, the melting behaviour of the different panels and welds were very similar to one another and to that of a reference material, and that the material does not appear to be sub-standard.

8. Discussion

The material appeared to be normal, although the welds did show differences, so what could be inferred about the cause or causes of failure?

8.1. Tank failure

Examination of the cracked panel which caused the leak of caustic soda showed that leakage occurred from a single 12 mm thick panel of polypropylene about 1.5 m from the base of the tank. The open crack initially was about 200–230 mm in length and was vertically oriented along the mid-centre of one of the four welds used to fabricate the circumference of the tank at this point above the base. Detailed examination of the fracture surface showed that the crack had been initiated during one of the four previous full loadings of the tank since its installation on 6 March 1994. Initiation had occurred from a pinhole defect on the outer surface of the weld near the centre of the panel, and at least three regions of growth had occurred since installation. The periods of growth appeared to correlate reasonably well with the four full loadings, the extent of each area increasing with each successive loading owing to the increasing size of the sub-critical crack. It is also clear that several other cracks were also initiated following installation from similar surface defects on the outer surface of the weld. Although the cracked panel as extracted from the tank appeared to span the entire length (about 0.62 m) of the single thickness panel from lower to upper

reinforcing buttresses, the occurrence of several crack arrest lines on the fracture surface indicated that the crack extended after the initial fracture, either while fluid was still issuing from the tank, or at a later stage when the crack was investigated by the firemen and others at the scene of the accident. Simple hand pressure on the side panel revealed the fracture surface, the act of doing so putting extra stress on the long crack which already existed.

8.2. Pressure conditions in the failure tank

The exact stress on the lower tank panel where fracture occurred can be calculated relatively easily, since the volume of the contents is known and the height of the top level of the contents is also known within reasonably close limits. Together with a knowledge of the density of the caustic soda, the hydrostatic pressure acting on the panel at the failure locus can be determined from the simple formula

$$\text{pressure } P = h\rho g \tag{1}$$

where h is the height from the origin of the fracture to the top level of the liquid when fully loaded just prior to the accident, ρ is the density of caustic soda at ambient temperature and g is the gravitational constant ($= 9.81 \text{ m s}^{-2}$).

The thickness of the panel at the origin of fracture is about 12 mm, and the ratio to the radius of the tank (of about 1.35 m) is 112.5, a figure well in excess of the figure of about 10 normally regarded as the threshold ratio between thick and thin walled pressure vessels [4]. The failed tank can therefore be regarded as a thin-walled vessel, subjected to simple hydrostatic pressure. Neglecting for the moment the self weight of the vessel and any creep in the plastic wall, the situation is that described by Roark [4] in his Table 28 (case 1d). There is only one important stress acting in the wall, the hoop stress, σ_H acting around the circumference of the wall. There is no stress acting in a vertical direction. It is therefore a force tending to extend the circumference in tension, and hence acting on the vertical welds. This hoop stress can be calculated at the origin of the fracture using the simple formula

$$\sigma_H = \frac{PR}{t} \tag{2}$$

where P is the pressure as determined above, R is the radius of the tank, and t the wall thickness.

Taking the design height of the failed tank as 3.5 m and the measured height of the crack origin from the base of the tank as 1.486 m, then the height, h of fluid lying above the origin of the critical crack is 2.014 m. This assumes that the last load delivered of 22.32 t came up to the top of the vertical section of the tank. In fact, there is an overflow valve fitted just below this junction, so the estimate of 2.014 m is probably slightly exaggerated. A round figure of $h = 2$ m will be taken as a reasonable estimate of the total height of caustic soda above the origin. The specific gravity of aqueous caustic soda of 47% concentration lies between 1.4873 and 1.5065 [5], so that a mean value of 1.4969 may be rounded to a density value of about 1.5 g cm^{-3} (or 1500 kg m^{-3}) at about 20°C. The pressure at the origin of fracture is therefore

$$P = 1500 \times 2.0 \times 9.81 = 29.4 \text{ kPa}$$

hence, from eqn (2),

$$\sigma_H = \frac{29400 \times 1.35}{0.0117} = 3.4\,\text{MN m}^{-2}$$

Knowing the mean failure stress of weld sample under the controlled conditions of a simple mechanical test (Table 1), it was now possible to determine the stress concentration factor, K_t, which was present at the side of the critical pinhole. Thus,

$$K_t = \frac{\text{failure stress under test conditions of weld}}{\text{actual stress at origin}} \tag{3}$$

Hence,

$$K_t = \frac{20.4}{3.4} = 6$$

It is possible to test this conclusion in a very simple way by evaluating the stress concentration factor for the specific dimensions measured on the pinhole directly. The cross-section of the pinhole was ellipsoidal in shape with axes roughly 0.6×0.3 mm. Using Inglis's evaluation of this configuration, as given by Peterson [6], then the parameter $b/a = 0.6/0.3 = 2$. Interpolation on Peterson's figure gives a value of

$$K_t = 5$$

The agreement between theory and practice is good, bearing in mind the errors of measurement from the fracture surface as well as the errors associated with experimental tensile analysis, sampling error, and so on.

The above analysis is the simplest possible for this situation, and there are some known deviations from the simple assumptions underlying the various calculations given above. For example, creep had occurred in the exposed lower single panel where the fracture happened. Figure 3 shows the bulging caused by the pressure from the caustic soda contents, a fact confirmed by direct measurement of the circumference at two points on the tank, when a creep strain of about 0.2% was recorded. It may also be borne in mind that the tank by the time of investigation and measurement had been empty for about a month, so that some considerable strain recovery will have occurred. Such bulging will of course have added a small but not insignificant bending moment to the critical weld, adding an extra tensile component to the stress system acting on the pinhole.

A more serious deviation is that posed by the bending stress imposed by the need to form the final weld. Although the details of analysis of the problem are reserved for Part II, it is very evident that a tensile stress in the outer surface of the panels will enhance the possibility of failure from weak zones such as welds. Although there will be some stress relaxation after welding, there will be a substantial contribution to the gross stress acting on the weld defects. In addition, panels cut from the tank will tend to relax back to flatness. This was confirmed by re-measuring the dimensions of the portions of cut panel still retained after sampling. Three substantial samples (chord length ca 76 cm) were measured for their radii of curvature:

sample 1 (single sheet from buttress near good weld), $R = 2.0$ m
sample 2 (double sheet near good weld), $R = 1.6$ m
sample 3 (double sheet near poor weld), $R = 1.64$ m

The image shows two tank designs.
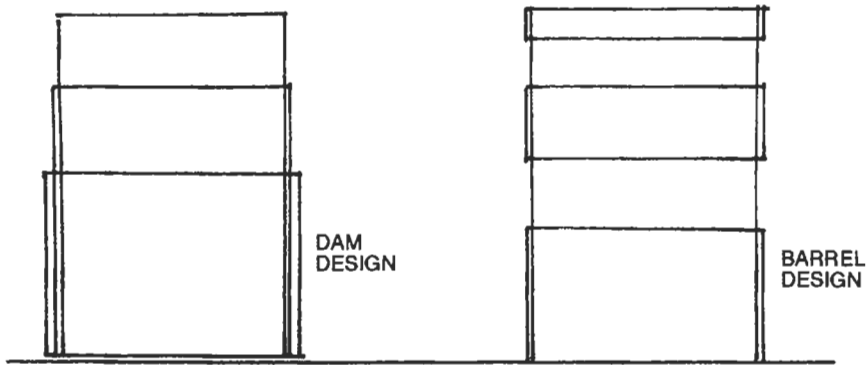
Fig. 10. Contrasting designs for large storage tanks, with dam design at left and barrel design at right. The dam design has concentric walls to resist a steadily increasing hydrostatic pressure, while the barrel design has buttresses to protect the horizontal welds thought to be most at risk.

These values may be compared with an original radius of the tank of 1.35 m, showing that these sections had relaxed substantially over the ca 4 month period since extraction from the failed tank.

8.3. Cause of failure

A particularly important design point was evident early in the investigation, broadly confirmed by the classical analysis already presented. In vessels subject to simple hydrostatic pressure, the pressure increases in a linear way with height, so that the safest way to build supporting walls to resist the pressure from the contents is to increase the wall thickness in a correspondingly linear way. This well-known engineering principle is of course applied in dam walls for example, where the walls increase in thickness approaching the base (Fig. 10). That same principle had not been applied to the design of the failed tank, where the wall thickness was intermittently uniform, the three buttresses increasing the wall thickness, but only within three specific zones. They seem to have been designed to protect horizontal welds, rather than the vertical welds, which are in tension. The horizontal welds hidden below the buttresses are probably in a state of compression, from the superimposed load of the tank above, and less likely to fail since the compressive strength of most materials, polymers included, is almost always greater than their tensile strength. This is despite the perception that such extrusion-welded joints are weaker than butt-welded joints. So the design of this tank leaves the lower panel circumference exposed to very high hoop stresses, which will naturally tend to be felt most severely at the weakest points, viz, the four welds connecting the panel sections together. The design issue is discussed further in Part II of this joint investigation.

8.4. Other installations

Other tanks holding corrosive fluids had been installed at a similar time to the failed tank, using essentially the same design philosophy, materials and method of welding. They were therefore examined for weldline cracks. Some small hairline cracks were found, but were far from criticality, largely because few of the tanks had been fully used to their maximum capacity. In one alarming

case, an installation with a concentrated caustic soda tank adjacent to a concentrated ferric chloride tank, an access bridge could not support the supply vehicles, so the tanks were always kept well below capacity! It is understood that the tanks concerned have now been brought up to an acceptable standard.

Despite an extensive literature search for other examples of failure in such tanks, only one relevant example was found. References to earlier tank failures are exclusively concerned with GRP rather than thermoplastic vessels [7], or are theoretical exercises for comparison of different plastic tanks for fatigue resistance [8]. There is a report of a test tank which failed during a second fill of water to test the particular design calculations used [9]. The tank was under-designed with a barrel-like structure of the kind already discussed here. Unfortunately, details of how exactly the tank failed remains unclear, although the paper remains a good basis for the estimation of design stresses. Designing the wall to resist the creep strain developed by hydrostatic pressure is discussed, but without explicit mention of the need to increase the wall thickness towards the base, a point which receives greater emphasis in DVS 2205. It is also discussed in detail, with tables of recommended wall thickness, in a publication from Forbes Plastics Ltd [10]. The publication presents a good basis for design of plastic tanks, and should help to prevent future failures of the kind discussed in this article, especially in the more stringent regulatory environment for bulk storage of materials [11].

Acknowledgements

References

[1] Forbes L. Plastics now set the standards for tanks. Process Industry Journal Nov/Dec 1989.
[2] Kieselbach R. Bursting of a silo. Engineering Failure Analysis 1997;4:49.
[3] DVS 2205 is published by the publishing arm of the German Welding Institute (Deutscher Verlag für Schweiß-technik, or DVS).
[4] Roark's Formulas for stress and strain. 6th ed. 1989. p. 516.
[5] Lange's Handbook of chemistry. 10th ed. p. 1150.
[6] Peterson RE. Stress concentration factors. 1974. Figure 128. p. 195; also in Pilkey WD Peterson's stress concentration factors. 2nd ed. Chart 4.50 1997.
[7] Ezrin M. Plastics failure guide: cause and prevention. Hanser, 1996. section 10.5.2, p. 345 ff.
[8] Hertzberg RW, Manson JA. Fatigue testing. Plastics World May (1977);50–53.
[9] Forbes K, McGregor A, Turner S. Design of fluid storage tanks from polypropylene. Brit Chem Engng October 1970.
[10] Forbes Plastics Ltd. A Guide to DVS 2205. Denver, Downham, Norfolk PE38 0DR, 1993.
[11] Forbes L. Risk assessment of tanks. Water and Waste Treatment March (1993).

Catastrophic failure of a polypropylene tank Part II: comparison of the DVS 2205 code of practice and the design of the failed tank

G.W. Weidmann*, P.R. Lewis

Department of Materials Engineering, Faculty of Technology, The Open University, Milton Keynes MK7 6AA, U.K.

Abstract

The design of a failed, large (20 m³) polypropylene storage tank is compared with the recommendations of the German Code of Practice, DVS 2205, to which it allegedly conformed. It is shown that the tank was seriously under-designed, and that the situation was exacerbated by the introduction of residual tensile stresses in its walls during its manufacture. © 1999 Elsevier Science Ltd. All rights reserved.

Keywords: Code of practice; Design; Failure; Polypropylene; Standard; Tank; Weld

1. Introduction

The problem of designing load-bearing structures in plastics differs from that of designing comparable structures in metals such as steels in several important ways, particularly if the design life of the structure is intended to be a long one (20 or 30 years, say). These differences arise because the behaviour of plastics under load is not only time-dependent but also non-linear, because their range of recoverable strains is typically some ten times larger than in metals, because plastics can often be more sensitive to stress concentrations than metals, and because plastics react in a different way to environmental agents than metals. Failure to appreciate these differences has led (and unfortunately still does lead) to premature failure of plastics products, and to their acquiring an early reputation for being 'cheap and nasty'.

The basis of much rational design with plastics is the so-called 'pseudo-elastic design method' proposed initially by Baer et al. [1]. In this, the appropriate time- and temperature-dependent values of modulus and Poisson's ratio are substituted for the elastic ones in the standard stress–strain solutions for a given loading configuration and part geometry. Initially, before sufficiently

---

comprehensive data on the creep and creep rupture behaviour of specific plastics became available, this approach was limited to strains small enough that an assumption of linear viscoelastic behaviour was a good approximation. Nowadays, this restriction does not apply since copious data are available on all the commoner thermoplastics largely generated from investigations into the long-term behaviour of materials for pressurised pipes.

One of the few, perhaps the only, report of a combined theoretical and experimental investigation into the design against failure of large plastics tanks is that of Forbes et al. [2]. They applied the pseudo-elastic design method to polypropylene tanks with capacities up to 9100 gallons (41 m³). The design was based on a stress analysis solution of a fourth order linear differential equation as given by Timoshenko and Woinowsky-Kreiger [3] which takes into account the effects of the transition from horizontal base to vertical wall and of transitions in wall thickness. These effects are manifested as increases in the radial expansion of the tank walls just above the transition points, but they can also be thought of as kinds of stress concentrating features. Using a limiting hoop strain of 1%, the results of this analysis produced a design chart for the wall thickness of tanks of increasing capacity up to 10,000 gallons (45 m³). Their results were validated by full-scale tests on two large tanks.

The failure of a 20 m³ polypropylene storage tank and the ensuing investigation were described in Part I of this work [4]. The tank was constructed to a design which was verified by the calculations of a consultant engineer and allegedly conformed to the design code DVS 2205 [5], the German Code of Practice for the design of free-standing thermoplastics containers (there is no corresponding British Standard, although there is one for GRP tanks, BS4994: 1987). This code of practice provides a guide to the determination of the maximum permissible stresses that will avoid different modes of failure in thermoplastics containers over specified lifetimes. It takes into account, interalia, the type of thermoplastic, its chemical interaction, if any, with the contents of the container, the operating temperature, and effects arising from changes of wall section and method of manufacture. This paper reviews the design methodology of DVS 2205, and compares the design of the failed tank with the detailed recommendations that result from DVS 2205. Figure 1 shows the dimensions of the tank as designed (taken from the design sketch), together with the wall thicknesses, in mm, at different heights.

2. Design methodology of DVS 2205

The following translated extract from DVS 2205, Part 1 [5] outlines the essentials of the design methodology.

3. Strength parameters
3.1. General
The fundamental bases of the design calculations are the long-term values of materials parameters. In general, depending on the type of loading, three limiting criteria are possible:

(1) stress or strain
(2) deformation (e.g. excessive bending)
(3) stability (e.g. kinking or buckling)
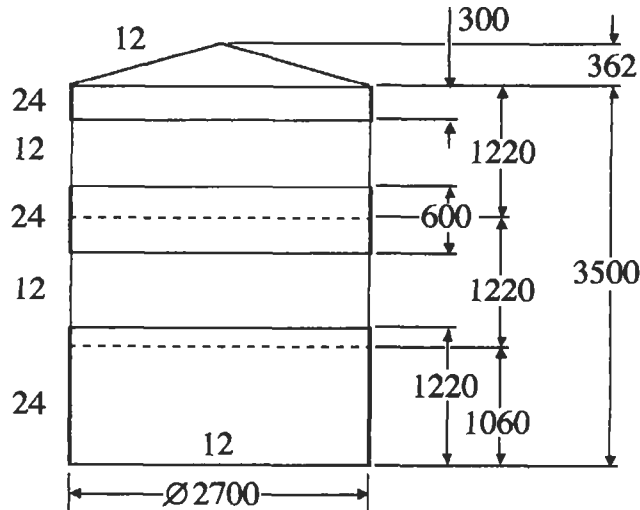
Fig. 1. Sketch showing wall thicknesses and dimensions (in mm) of the failed tank.

For (1). The calculation can be based either on the creep rupture strength or on a limiting value of creep strain. In most cases there will be multiaxial stress states. Here it is the largest stresses or the largest strains in the principal stress directions that are to be compared with the permissible stress and permissible strain respectively.

The permissible values are obtained by modifying the materials parameters through reduction factors (Section 4), a joint factor (Section 5) and safety factors (Section 6). The factors given in Sections 4 and 5 should only be applied to the stresses. The same applies to the safety factors in Table 4 of Section 6.

For (2) and (3). The determining strength parameter here is the creep modulus. This can be obtained from the creep modulus diagrams, which show its dependence on time, temperature and stress. For criteria based on stability, there is a corresponding safety factor (Section 6) to be taken into account.

The tank failed at a welded joint under the action of a hoop stress (i.e. a stress acting circumferentially). Therefore excessive deformation and stability can be discounted, and the appropriate limiting criteria to explore are those of stress or strain. DVS 2205, Part 1, Section 3.3. provides a way of deciding on which of these criteria the design calculations should be based.

Where not all the strains are known (for example, strains associated with residual or internal stresses in weld beads . . . or notches), which would necessitate extra safety factors to compensate for this uncertainty, the design calculations should follow the stress-based route (see Section 3.2.1.).

Since the failed tank was of welded construction and, indeed, failed at a welded joint, the above suggests that the limiting stress criterion should be the one adopted, as offering the more conservative approach.

2.1. Calculation of the limiting stress, σ_{zul}

Graphical creep rupture data provided for different thermoplastics materials (Figs 5–10 in DVS 2205, Part 1) allow the corresponding creep rupture stress, K, to be evaluated at the design lifetime and the intended service temperature. A maximum permissible stress, σ_{zul} ('zul' is the abbreviation of 'zulässig', the German for 'permissible') is then calculated by multiplying K by a series of factors which take into account the effects of type of welded joint, any chemical interaction between the container and its contents, the specific strength of the container material, any fluctuating loading and the degree of hazard of the contents.

Details of the calculation of the limiting stress for the failed tank are set out in Appendix 1. From this we get that the maximum permissible stress level, σ_{zul}, for a 25-year life of polypropylene copolymer similar to that used in the failed tank at 20°C is

$$\sigma_{zul} = 2.54 \, \text{N mm}^{-2} \tag{1}$$

2.2. Calculation of wall thickness

The required wall thickness, s, of the container at different depths, h, from the surface of the contents in the full container can now be determined from the standard equation for hoop stress, σ_θ, as a function of the static head pressure, p, exerted by the contents at those depths. The basic equation for the wall thickness, s, is derived in Appendix 2 and is

$$s = \frac{dh\rho g}{2\sigma_\theta} \tag{2}$$

where d is the container diameter and g is the acceleration due to gravity. In DVS 2205, Part 2 [5], by putting $\sigma_{zul} = \sigma_\theta$ in eqn (2), three cases are considered. These are:

(i) for containers with constant wall thickness

$$s = C\frac{dh\rho g}{2\sigma_{zul}} \tag{2a}$$

(ii) for containers with graded wall thickness, s_n at depth h_n (e.g. Fig. 2, which approximates to the dam wall type of structure referred to in Part I of this work [4])

$$s_n = C\frac{dh_n\rho g}{2\sigma_{zul}} \tag{2b}$$

where $(h_n - h_{n+1}) \geqslant 500$ mm.

The factor C in (i) and (ii) takes into account the constraining effect of the joint with the base of the container in case (i) and the similar effect of change of wall thickness in case (ii). The value of C varies between $C = 1$ and $C = 1.82$. For a flexible base and/or a gradual change in wall thickness, $C = 1$ can be used. For a rigid base and/or large and abrupt changes in wall thickness, the value of $C = 1.82$ should be applied (this is the equivalent of the corrections to the radial expansion arising from the solution of Timoshenko and Woinowsky-Kreiger [3] discussed earlier).
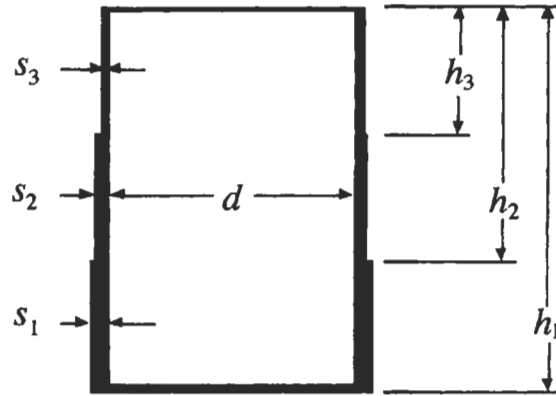
Fig. 2. Tank with graded wall thickness.

(iii) for containers with vertical welds, the increase in wall thickness has already been taken into account in the joint factor, f_s, so that

$$s = \frac{dh\rho g}{2\sigma_{zul}} \tag{2c}$$

The largest value of wall thickness obtained from eqns 2(a)–(c) is the definitive value to be used.

3. Application to the failed tank

3.1. Equation for the wall thickness of the failed tank

The failed tank had four abrupt and large changes in wall thickness (a factor of two) between its base and its top (see Fig. 1). Taken together with the constraining effect of the base, this suggests that a value of $C = 1.82$ should be used in eqns 2(a) and (b) to calculate the wall thickness. Then, with

$$d = 2700\,mm = 2.7\,m$$

$$\rho = 1540\,kg\,m^{-3}$$

$$g = 9.81\,m\,s^{-2}$$

$$\sigma_{zul} = 2.54\,N\,mm^{-2} = 2.54 \times 10^6\,N\,m^{-2}$$

The equation for s becomes

$$s = 1.82 \times \frac{2.7 \times 1540 \times 9.81 \times h}{2 \times 2.54 \times 106}$$

$$= 1.46 \times 10^{-2}h \tag{3}$$

If h is expressed in mm, eqn (3) gives s also in mm. This eqn allows the minimum wall thickness at any vertical position on the container to be calculated.

The failed tank had a design capacity of 20 m³, so that its fill level, corresponding to the maximum of the hydrostatic head h_{max}, was

$$h_{max} = \frac{\text{volume}}{\text{base area}}$$

$$= \frac{20 \times 4}{\pi d^2} \, \text{m}$$

$$= \frac{20 \times 4}{\pi \times 2.72} \, \text{m}$$

$$= 3.5 \, \text{m or } 3500 \, \text{mm}$$

Then, from eqn (3), the minimum wall thickness just above the base should have been 51.1 mm. In fact it was 24 mm—just over a factor of 2 less.

3.2. Comparison between the failed tank and DVS 2205

The line marked DVS 2205 in Fig. 3 shows eqn (3) plotted in terms of height from the base (i.e. $(h_{max} - h)$, rather than hydrostatic head h. Also shown is the outline of the wall thickness variation as shown in Fig. 1 for the failed tank. The shading indicates the regions of the tank wall where the thickness is less than that obtained from the DVS 2205 design code. It is clear that there are serious discrepancies between the thicknesses of the failed tank wall and those derived from the design code.

The extent of the discrepancy between the design of the failed tank and the DVS 2205 require-
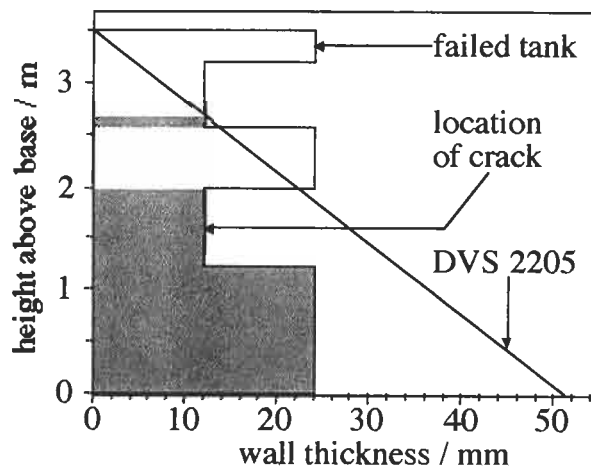
Fig. 3. Variation of wall thickness, s, of failed tank with height, $h_{max} - h$, from its base compared with that specified by DVS 2205 design code (shaded areas are less than the code's thicknesses).
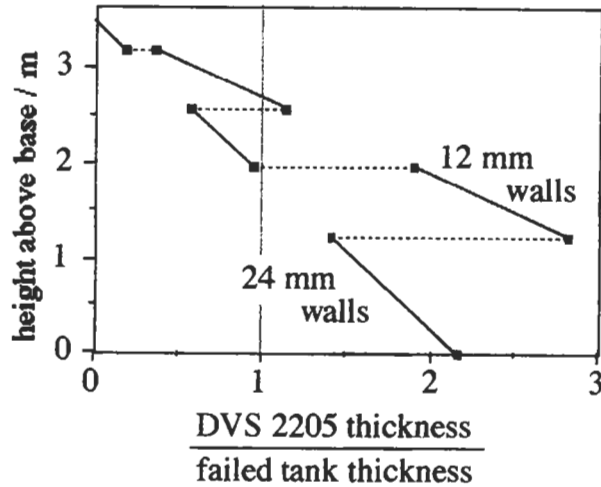
Fig. 4. Ratio of DVS 2205 wall thickness to that used in the failed tank and its variation with height above the base of the tank.

ments is highlighted in Fig. 4. This plots the ratio of the wall thickness from eqn (3) to that of the failed tank as a function of height from the base. The largest discrepancy is found in the lower 12 mm thick section—just the section where the failure originated.

4. DVS 2205 and consultant engineer's calculations

From the consultant engineer's calculations that were made available to us, it is apparent that he worked with a limiting strain criterion—a creep strain of 2% after 25 years. From this he obtained a value of the corresponding stress as 3.95 N mm^{-2} by iteration and interpolation on the appropriate creep modulus vs time curve (Fig. 26 of DVS 2205, Part 1—Appendix 3). For some reason he did not use the recommended procedure of obtaining the value directly from the appropriate isochronous stress-strain curve (Fig. 15 of DVS 2205, Part 1—Appendix 3), though this would not have affected his result significantly. His value of 3.95 N mm^{-2} was used as σ_{zul} in his design calculations. What was ignored was that a similar safety factor to that used for the stress-based calculation should have been applied to the limiting strain *before* determining the corresponding stress level (see eqn (11) in DVS 2205, Part 1). This is important because, as mentioned earlier, plastics exhibit non-linear stress–strain behaviour, so that stress cannot be assumed to be proportional to strain in a thermoplastic such as the polypropylene copolymer in this case. Had he applied a value of $S = 2.0$, he would have obtained a stress level of about 2.4 N mm^{-2}—a value much closer to the one derived here. Also ignored was the factor C (see eqns 2(a) and (b) above), which takes into account the constraints due to the base joint and the changes in wall thickness. The net result is the discrepancies in thickness shown in Figs 3 and 4, which translate into a maximum hoop stress in the tank walls which is almost a factor of *three times greater* than would have arisen under the recommendations of DVS 2205.

The consultant engineer later claimed that he used the joint factor, f_s, despite its non-appearance

in his original calculations, and its non-applicability to a calculation based on a limiting strain. Even then, he took a value of f_s of 0.8, corresponding to that for heated-tool, butt-welding in DVS 2205. The design code is quite clear that where hot-gas, extrusion is used, as it was for the horizontal welds in the failed tank, the lower value of $f_s = 0.6$ should have been used.

5. Extra bending strains

In Part I of this work, it was noted that extra strains were introduced in one of the stages of fabricating the tank. The tank was built up of rectangular, flat, polypropylene panels, the edge of which were butt welded together in a machine to produce a flat strip whose length equalled the circumference of the tank. This strip was then bent round into a circular hoop and its ends welded together to form a section of the tank. The bending was done mechanically with no assistance from elevated temperatures such as would have been used in thermoforming, and with no subsequent annealing. Thus the strains associated with the bending were permanent and contributed to the overall strain in the tank walls.

5.1. Determining the extra strains and resulting stresses

The magnitude of these extra strains can be estimated from simple bending theory. The elastic strain ε in a member bent to a radius R is given by

$$\varepsilon = \frac{y}{R} \tag{4}$$

where y is the distance from the central plane of the member's thickness (the neutral axis, Fig. 5). Applying eqn (4) to the failed tank gives

$$\varepsilon = \frac{6}{1350} = 0.44\% \text{ for 12 mm thick material}$$

Since the 24 mm material was fabricated by adding an extra 12 mm thickness band to the tank after the horizontal welds had been formed, the bending strains in the thicker section would have been virtually the same as in the 12 mm material.

In polymeric materials subjected to a constant strain, the associated stress falls with time due to viscoelastic stress relaxation (this is analogous to the creep that occurs under constant stress
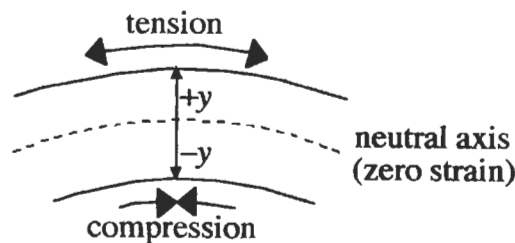
Fig. 5. Schematic of bending.
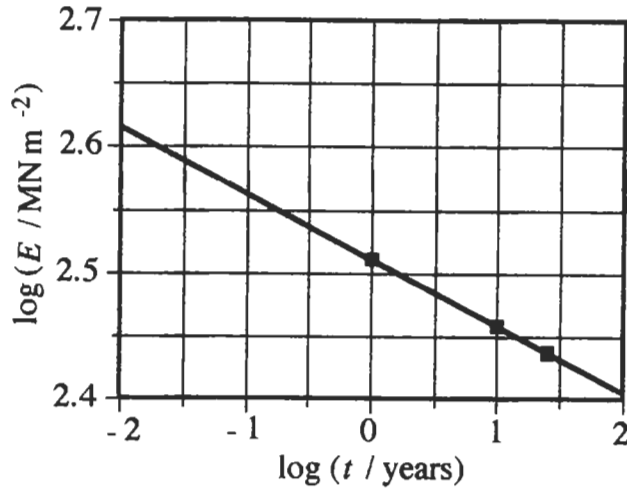
Fig. 6. Creep modulus vs time for polypropylene copolymer (data from Figs 24–26 of DVS 2205 Part 1).

conditions). Strictly speaking, the appropriate values of the stress relaxation modulus should be used to determine the levels of stress at different times. However, in the absence of data on the stress relaxation modulus, the creep modulus can be used as a reasonable approximation. Figure 6 shows the variation of creep modulus with time (logarithmic plot) for polypropylene copolymer using data from Figs 24–26 of DVS 2205 Part 1 (see Appendix 3) at a stress level of 2 MN m^{-2}. From this, between 0.01 years (4 days) and 0.5 years (6 months), corresponding to the life of the failed tank, the creep modulus, E, varies from about 410 MN m^{-2} to about 335 MN m^{-2}. At three months, corresponding to the mean lifetime of the tank, E is about 350 MN m^{-2} (all these values of E are approximate because of the assumed validity of a linear extrapolation on a log–log plot). From the relation that stress = modulus × strain, these values of modulus suggest a maximum tensile bending stress (at the outer surface of the tank) varying between about 1.8 MN m^{-2} at short times and about 1.5 MN m^{-2} at six months ('about' because of the use of creep modulus instead of stress relaxation modulus).

5.2. Effect of the additional bending stresses

The additional bending stresses add to the hoop stress resulting from the hydrostatic pressure exerted by the contents of the tank. The addition of the two stress distributions is shown schematically in Fig. 7, with a hoop stress value of 3.2 MN m^{-2}, corresponding to that acting at the level of the crack with a full tank, and a bending stress of 1.6 MN m^{-2} corresponding to three months' stress relaxation (i.e. an approximate mean time between fabrication and failure). It can be seen that the resultant stress distribution ranges from a maximum tensile stress on the outer surface of the tank of 4.8 MN m^{-2} to a minimum, but still tensile, stress of 1.6 MN m^{-2} on the inner surface. In other words, the maximum tensile stress has been increased by about 50% by the presence of the residual bending stresses. However, the mean stress remains at 3.2 MN m^{-2} at the mid-plane position.

Given that it has been established that the hoop stresses in the tank were almost three times
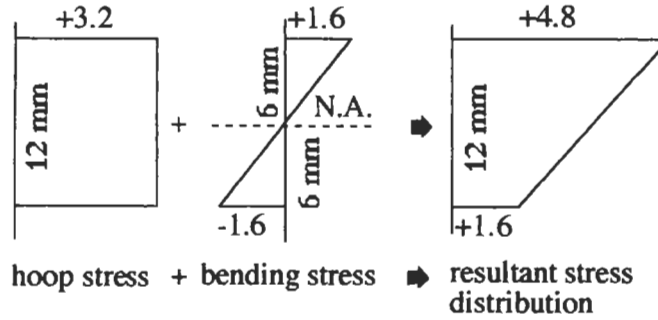
Fig. 7. Schematic addition of stress distributions through the thickness of the tank wall (stresses are shown in MN m^{-2}; tensile stresses are taken to be positive).
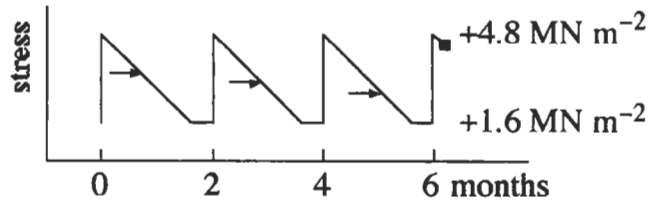
Fig. 8. Schematic of stress variation at outer surface in response to filling cycles of the tank: the arrows indicate schematically the critical stress for slow crack growth.

greater than those derived from DVS 2205 (see Section 4), the effect of an extra 50% stress cannot be anything but serious. Cracks tend to start at surface flaws, which is just where the tensile stresses are highest, and in Part 1 of this work it was found that this was indeed how the crack in the failed tank started (see Figs 3 and 6 in Part I). Two mitigating features, that delayed the failure of the failed tank, were, firstly, that there was a stress gradient through the thickness of wall material, so that any crack starting at the outer surface would propagate into a decreasing stress field, and, secondly, the loading of the tank was periodic. This meant that the maximum surface tensile stress at the site of failure varied between about 4.8 MN m^{-2} when the tank was full, to about 1.6 MN m^{-2} when the liquid level had sunk below the failure height. This is sketched schematically in Fig. 8 for the four loadings of the tank in its six or so months of service. (Bear in mind that this is a simplified schematic—the maximum stress should fall off slightly as the bending stresses relax. In addition, there is no information on the exact form of the loading cycle.) Also indicated (by the arrows) is the schematic behaviour of the critical stress for slow crack growth, showing how this stress would have fallen at each loading cycle, reflecting the crack growth in the preceding cycle.

6. Conclusions

In our opinion, the under-dimensioning of the wall thickness of the failed tank, leading to hoop stresses in the tank walls up to nearly three times higher (about two and a half times higher at the site of the failure) than the maximum values permitted by the DVS 2205 design code was the most

significant factor in causing the failure. The fact that one, or perhaps two, of the vertical welds, in particular, were of poorer quality than the others (see Part 1) would have been accommodated by the reduction and safety factors enshrined in the code. Reinforcing the horizontal welds in the tank walls, but not the vertical ones, reflects a basic lack of comprehension of the stresses involved. The largest stresses are those acting horizontally (i.e. circumferentially) and are tensile, whilst the vertical stresses are much smaller and, in the absence of local deformation, are more likely to be compressive. Finally, the stage of manufacture that involved inducing permanent bending strains into the tank walls made what was already a high risk of failure even higher by adding up to 50% to the maximum stress arising from the hydrostatic pressure exerted by the tank's contents. Taken together, these factors made the premature failure of the tank inevitable.

Acknowledgements

Appendix 1

Calculation of the limiting stress, σ_{zul}

Equation (1) of DVS 2205, Part 1 [5] gives σ_{zul} as

$$\sigma_{zul} = \frac{K_{(A_1,A_3)} f_s}{A_2 A_4 S} \, \text{N mm}^{-2} \tag{A1}$$

where

$K_{(A_1,A_3)}$ is the creep rupture stress in N mm^{-2} at the appropriate time and temperature,

A_1–A_4 are the reduction factors,

f_s is the joint factor (if joints have to be taken into account), and

S is the safety factor.

The reduction factors are material-specific, and take the following into account:

A_1 dependence of the strength on the duration of loading

A_2 effect of the surrounding medium (reciprocal resistance factor)

A_3 dependence of the strength on temperature over the load duration

A_4 effect of specific toughness.

The values of A_1 and A_3 are implicit in the accompanying creep rupture curves. The value of the strength parameter $K_{(A_1,A_3)}$ required for the calculation is obtained from the diagrams in Section 10 for a specified service life and service temperature.

The failed tank was made from a polypropylene copolymer, and was to have a design life of 25 years at 20°C when containing caustic soda with a specific gravity of 1.54. Although the vertical

seams were machine welded, the horizontal ones were formed by hot gas extrusion welding. From DVS 2205, Part 1 we get the following values for the above factors for the copolymer:

$K = 9.3$ N mm^{-2} (from Fig. 7 for 2.2×10^5 h at $20°$; see Appendix 3)
$f_s = 0.6$ (for hot gas extrusion welding)
$A_2 = 1.0$ (i.e. no chemical interaction)
$A_4 = 1.1$ for polypropylene copolymer
$S = 2.0$ (caustic soda *is* hazardous).

Then

$$\sigma_{zul} = \frac{9.3 \times 0.6}{1.0 \times 1.1 \times 2.0} \text{N mm}^{-2}$$

$$= 2.54 \text{ N mm}^{-2}. \tag{A2}$$

Appendix 2

Equation for wall thickness

The standard expression for the hydrostatic head pressure, p at a depth h in a liquid of density ρ is

$$p = h\rho g \tag{A3}$$

where g is the acceleration due to gravity.
The hoop stress, σ_θ, in a circular vessel of diameter d and wall thickness s due to an internal pressure p is

$$\sigma_\theta = \frac{pd}{2s}. \tag{A4}$$

so that the wall thickness is

$$s = \frac{pd}{2\sigma_\theta.} \tag{A5}$$

Combining eqns (A3) and (A5) gives the equation for the wall thickness, s

$$s = \frac{dh\rho g}{2\sigma_\theta} \tag{A6}$$
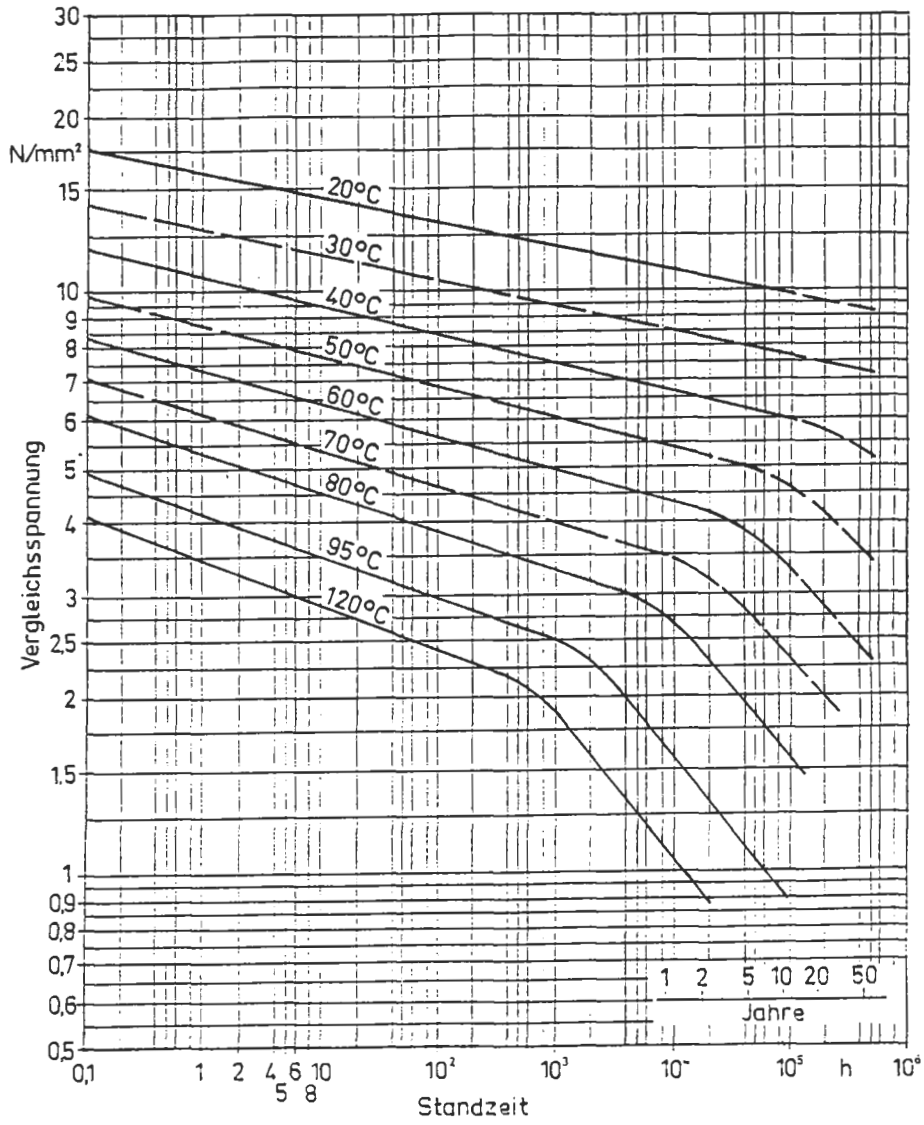
Fig. A1. Creep rupture curves for polypropylene (PP) Type 2 pipes conforming to DIN 8078 (Fig. 7 from DVS 2205 Part 1).
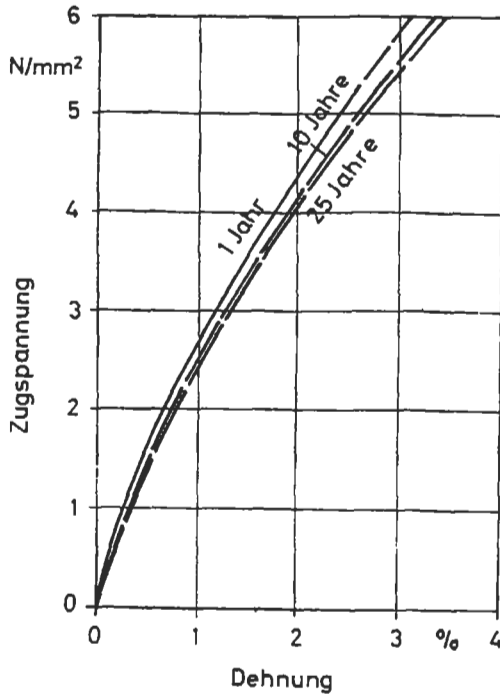
Bild 15. Isochrones Spannung-Dehnung-Diagramm von Polypropylen (PP), Typ 2, für 20°C.

Fig. A2. Isochronous stress–strain curves for polypropylene (PP) Type 2 at 20°C (Fig. 15 from DVS 2205 Part 1).
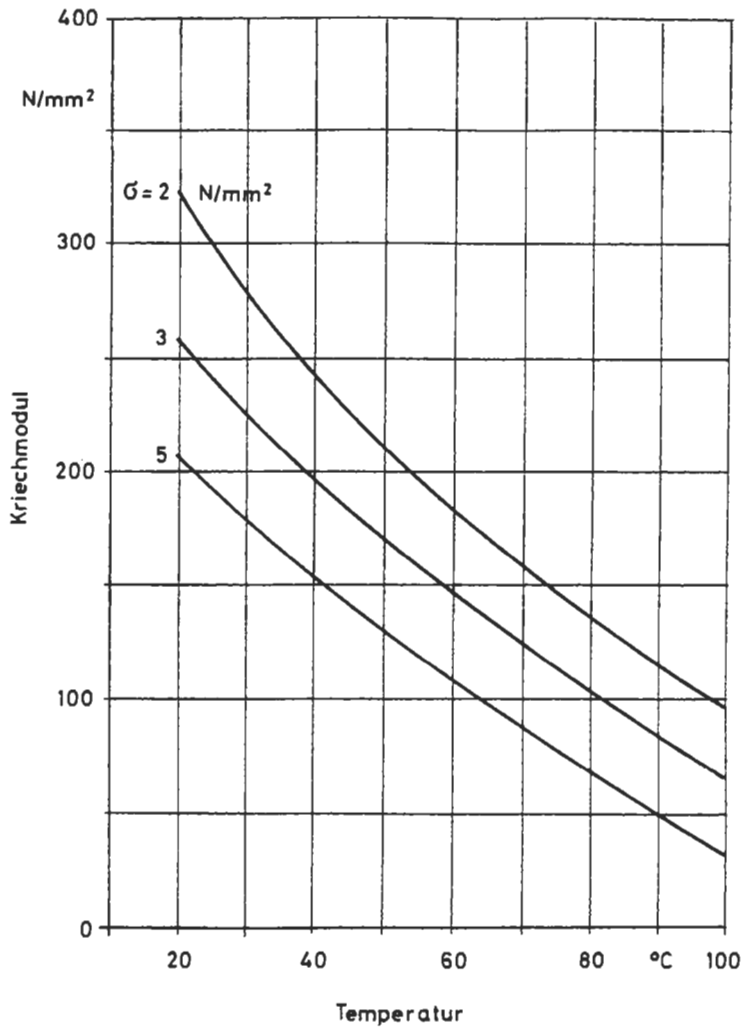
Fig. A3. Creep modulus of polypropylene (PP) Type 2 at 1 year (Fig. 24 from DVS 2205 Part 1).
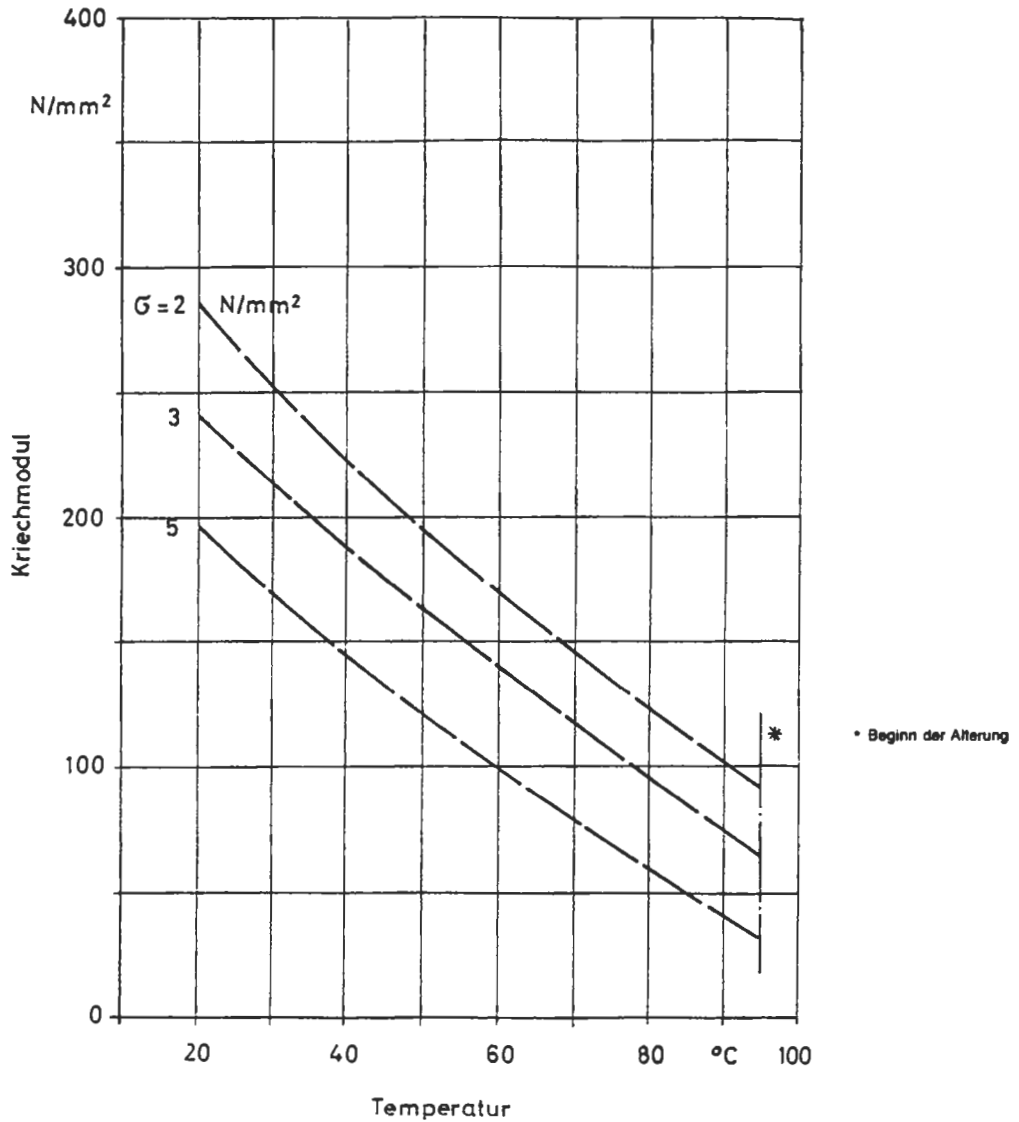
Fig. A4. Creep modulus of polypropylene (PP) Type 2 at 10 years (Fig. 25 from DVS 2205 Part 1).
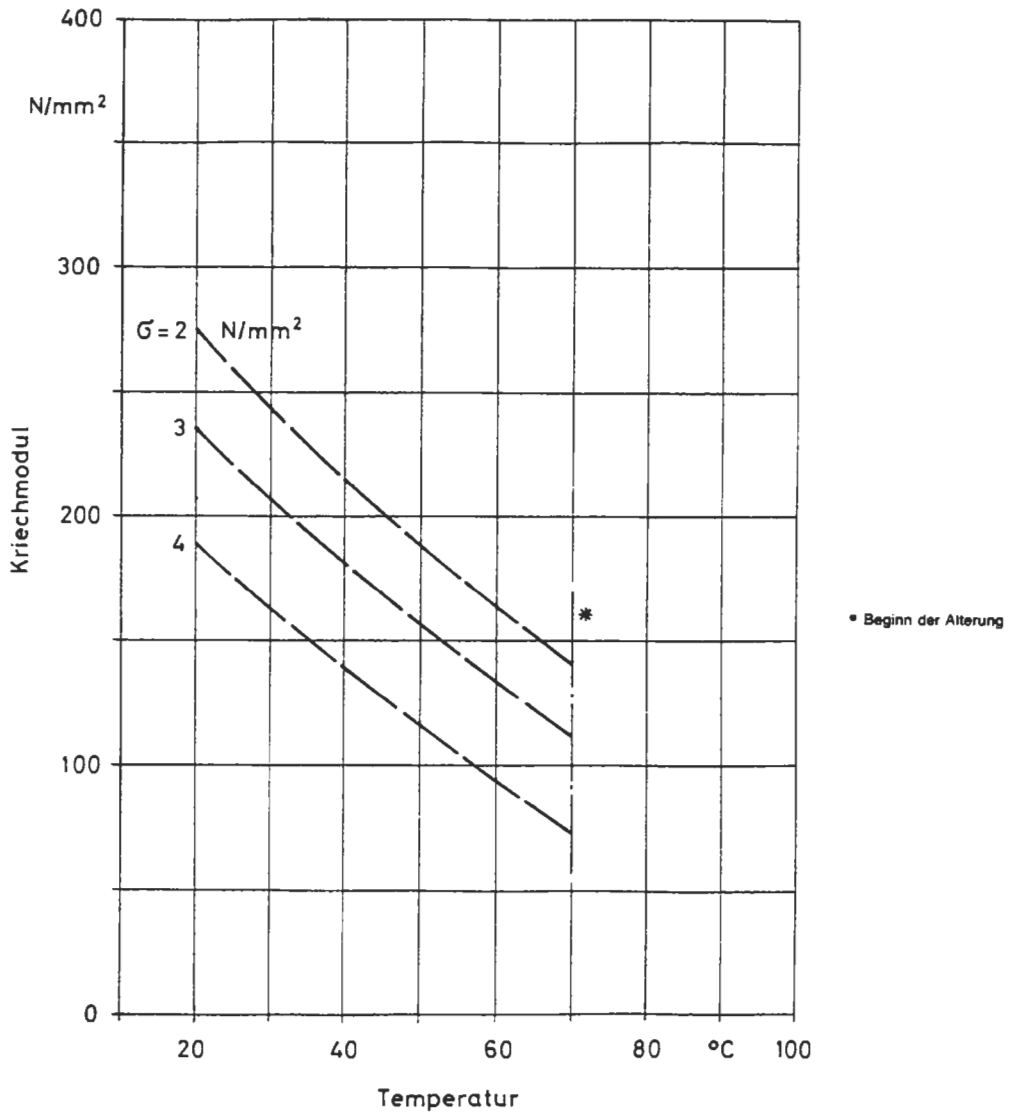
Fig. A5. Creep modulus of polypropylene (PP) Type 2 at 25 years (Fig. 26 from DVS 2205 Part 1).

114

Appendix 3

Figures 7, 15 and 24–26 from DVS 2205 Part 1

References

[1] Baer E, Knox JR, Linton TJ, Maier RE. SPEJ 1960;16:396.
[2] Forbes K, McGregor A, Turner S. Design of fluid storage tanks from polypropylene. Br Chem Engng, October, 1970.
[3] Timoshenko S, Woinowsky-Kreiger S. Theory of plates and shells. McGraw-Hill, 1959.
[4] Lewis PR, Weidmann GW. Catastrophic failure of a polypropylene tank Part I: primary investigation. Engng Failure Analysis 1999;6:197.
[5] Code of Practice DVS 2205; Design calculations for containers etc. made of thermoplastics. Part 1 (June 1987): Characteristic parameters; Part 2 (May 1984): Stationary, circular, unpressurised vessels; Part 3 (April 1975): Welded joints. Düsseldorf: DVS-Verlag GmbH.

Brittle fracture

INVESTIGATION OF THE MV *KURDISTAN* CASUALTY

S. J. GARWOOD

Rolls Royce and Associates, PO Box 31, Derby DE24 8BJ, U.K.

Abstract—The failure of the MV *Kurdistan* demonstrates the classic combination of high stress, low toughness and defect which are required to cause initiation of a brittle failure. This paper describes the failure investigation. The casualty illustrates the importance that secondary stresses and thermal stresses can have on the conditions which lead to failure. The formal investigation into the *Kurdistan* involved the use of elastic–plastic fracture mechanics (for the first time in a U.K. court) to help ascertain the circumstances leading to the failure. © 1997 Elsevier Science Ltd. All rights reserved.

1. BACKGROUND

The "MV *Kurdistan*" (originally named "*Frank D Moores*") was completed in June 1973 by Swan Hunter (Shipbuilders) Ltd at the Hebburn Shipyard, Tyne and Wear. In common with her three sister ships, the *Kurdistan* was designed with a dead-weight of $\sim 32,000$ t, and was strengthened for ice over the front third of the ship using Grade A steel plate ~ 22 mm (0.86 in.) thick rather than the normal 15 mm (0.57 in.). The ship was classed with Lloyds, as +100A1 Oil Tanker Ice class 1 + LMC. The owners were Common Bros of Newcastle.

On 15 March 1979, the *Kurdistan* was carrying 30,000 tons of bunker C6 fuel oil, which was heated to 140 °F (~ 60 °C). This was the first occasion this ship had carried this cargo, although its sister ships had apparently been carrying similar cargoes for a number of years with no problems. The ship had only recently (October 1978) come out of dock, where the heater coils required for the transportation of the bunker fuel had been fitted.

The ship was steaming off the east coast of Canada in deep water, a voyage from Point Tupper, Nova Scotia to Baie des Sept-Iles, Quebec. There was a south-south-easterly gale to storm passing over the area, causing rough seas and a heavy swell when, in circumstances fully described in [1, 2], the vessel encountered a field of pack ice (Fig. 1). The ice field was apparently entered at full speed (~ 15 kn) at 12.35 Atlantic Standard Time on 15 March 1979, and, due to the combination of wind and swell, the ice pressure was sufficient to halt the progress of the ship completely within 1.5 miles. At 12.53, the captain ordered the ship to reverse out of the ice field. This manoeuvre was completed at 13.05, and the ship turned to proceed to steam (at ~ 7–8 kn) into the swell along the edge of the ice field, the wind conditions causing the loose ice to close into the ice edge.

The vessel had apparently travelled just two ship's lengths after leaving the ice field (1305.5 h) when, heading into the swell, the bow lifted, and the ship was felt to "shudder". This "shuddering" was also described by various members of the ship's complement as pounding and vibration.

Following this incident, two cracks were reported in the side shell in the vicinity of the No. 3 tank (Fig. 2). On the starboard side, a 6 in. (150 mm) crack was visible approximately 12 ft (~ 4 m) below the level of the deck, and 23 ft abaft of the bulkhead. On the port side, a vertical crack, starting ~ 12 ft, and ending ~ 18 ft (~ 5 m), below deck level, 37 ft (~ 11 m) abaft of the bulkhead, was apparent. Oil was seen to leak from both cracks, particularly the port side, which appeared to have opened up by ~ 0.5 in. (12 mm) in the centre. At this time, ullages (measurements of the tank levels) were taken of the No. 3 wing tanks, indicating a large drop in oil level. At 14.30, air was reported to be heard entering the No. 3 centre tank, and an ullage of 8 ft was recorded (the ullage should have been 4 ft). At this time, the wing tanks had an ullage of 10 ft. It was assumed that a longitudinal bulkhead had also cracked, and that oil was entering the wing tanks from the centre tank. To prevent further spillage, oil was pumped from the No. 3 to the No. 4 wing tank.
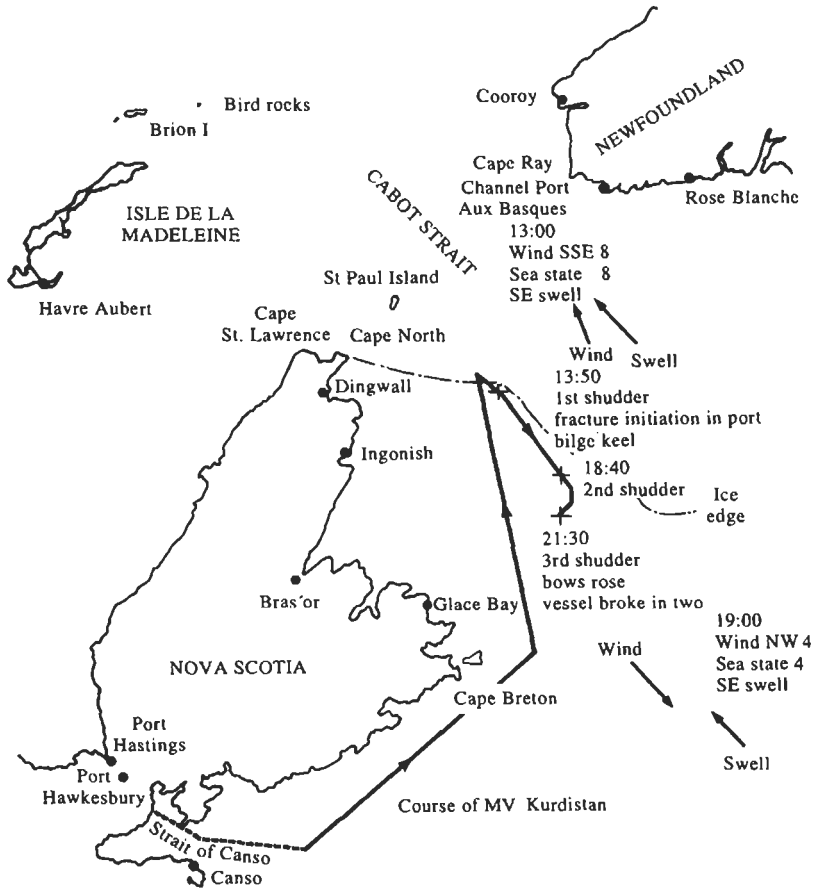
Fig. 1. Course of the MV *Kurdistan*; 15 March 1979.

When the shuddering occurred, the ship was in a rough swell in open sea at 200 fathoms depth. The sea-water temperature was reported as $-0.7\,°C$, with an air temperature of $\sim 0\,°C$.

Approximately 5 hr after the observance of the initial cracks, a further vibration and shuddering
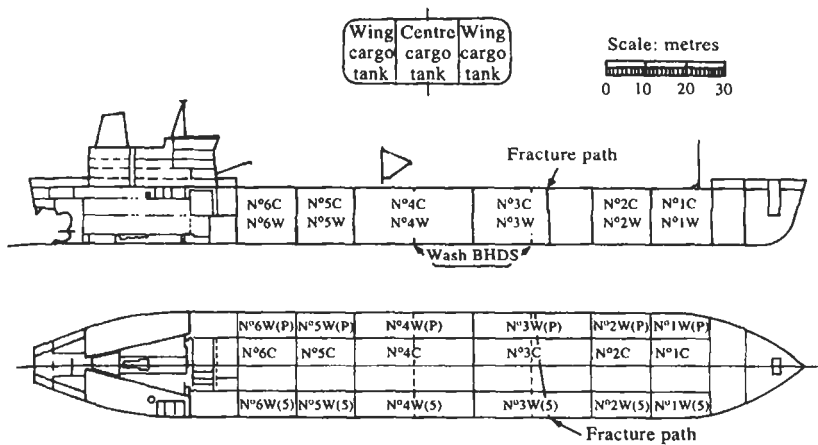
Fig. 2. General details of the MV *Kurdistan*.

Fig. 3. Bow section of MV *Kurdistan* after breaking in two.

was reported. At 21.40, a third shudder was experienced, and ~150 ft (~46 m) of the bow section lifted up, severely distorting the deck plates, and the bow broke away from the aft section of the ship (which was approximately two-thirds of the ship's length).

The ship would have been in a sagging condition in a calm sea, meaning that the keel would be in tension under these conditions. Hence, on breaking in two, the fractured ends of the two sections of the ship dipped into the sea, with the bow and stern rearing out of the water (Figs 3 and 4). At this point, the ship was abandoned. The 41 persons on board *Kurdistan* were all in the aft section of the vessel. With the exception of the chief officer, who remained on the vessel, the crew and their

Fig. 4. Stern section of MV *Kurdistan* after breaking in two.
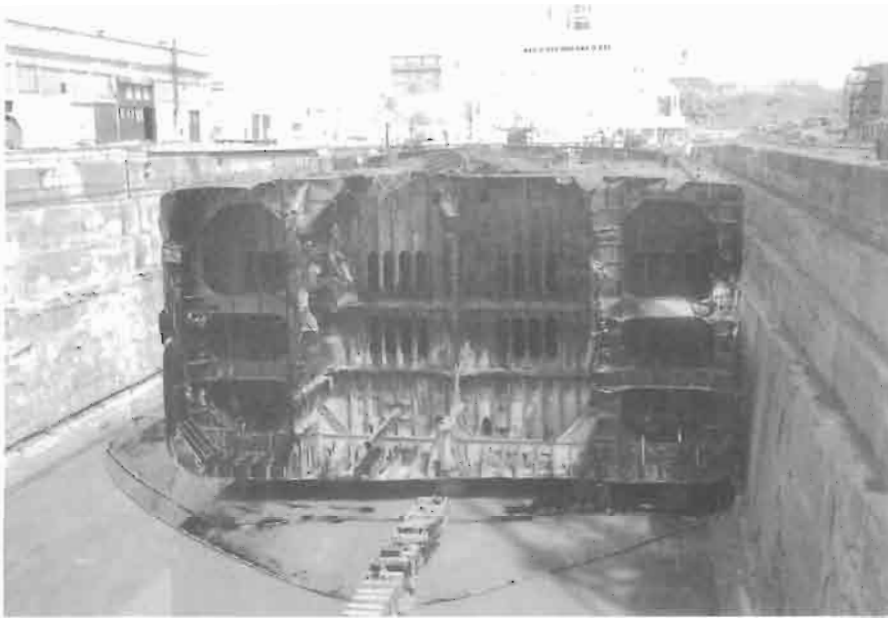
Fig. 5. General view of the stern section of the MV *Kurdistan*.

families were picked up from the two lifeboats launched. The chief officer was rescued by helicopter on 16 March. The stern section of the ship was subsequently salvaged and towed to dry dock at St John, New Brunswick, docking on 15 April, after the oil had been pumped out of the remaining tanks (Fig. 5). The bow section was sunk on 1 April to prevent further pollution. Over 5000 tons of bunker oil had been lost from the rupture of the No. 3 centre tank alone.

On 11 April, the Welding Institute (TWI) was called in by Mr T. Chorley, Chief Ship Surveyor of the U.K. Department of Trade (DoT), Sunley House, Holborn, London, to assist one of their senior ship inspectors in surveying the ship on docking. Dr Garwood of TWI accompanied Mr Hume of the DoT to Canada on 15 April to make the inspection. The inspection was carried out employing a platform controlled by a crane to inspect the ship's sides and check fracture surfaces, and, by wading along the dock floor, to inspect the fracture faces of the longitudinals, centre keel and bottom plate (Fig. 6).

As a result of this visit, TWI was commissioned to undertake a detailed technical investigation into the causes of the fracture. Six samples were extracted from the vessel for the investigation, which was completed and reported in April 1980 by TWI. The *Kurdistan* was subsequently towed to Amsterdam, where it received a new front and returned to sea.

Although no lives were lost, because of the serious environmental problems caused by the oil pollution resulting from the breaking in two of a well-found vessel less than 6 years old, the U.K. and Canadian authorities agreed to the holding of a formal investigation. This public enquiry was held in London before Mr R. F. Stone QC, starting on 12 January 1981 and lasting 51 days. The report of the investigation [2] was published in 1982. Subsequently, a paper on the casualty was presented to RINA in 1987 [3], and a description of the fracture mechanics methods used was given in [4].

This paper outlines the conclusions of the investigations and subsequent publications, and compares the predictions used in the original study with those obtained from the latest revisions to the fracture mechanics assessment procedures [5].

2. PRELIMINARY INSPECTION OF THE VESSEL AT St JOHN DRY DOCK— 16 & 17 APRIL 1979

(To provide historical accuracy, the text of the preliminary inspection from [1] is repeated here with no editorial changes apart from the removal and renumbering of figure references.)
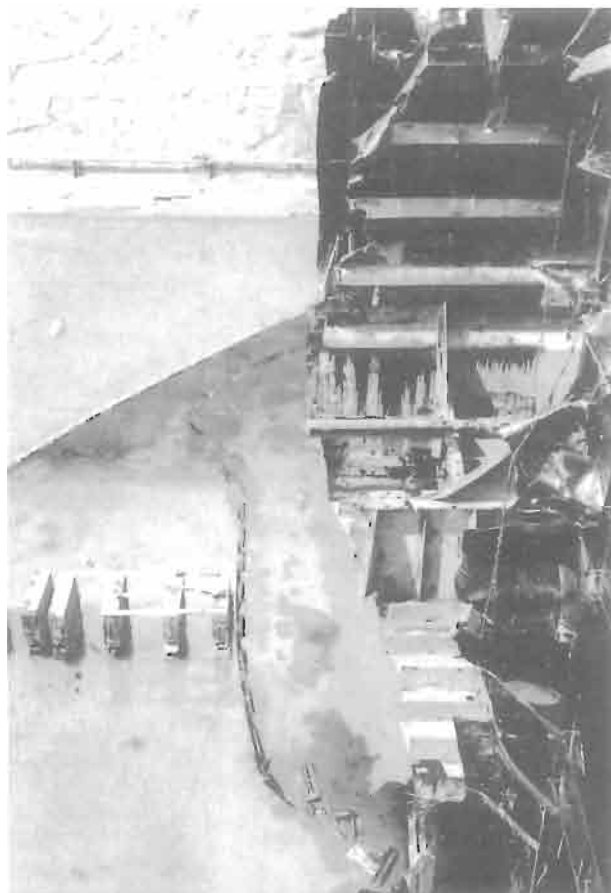
Fig. 6. View of longitudinals, centre girder and bottom shell from port side of vessel.

The dock had been pumped dry to within about 20 in. (~ 0.5 m) of water. A fair amount of thick bunker oil was still present on the sides of the ruptured tanks, and this oil was running over the fracture face at the bottom of the shell, and was dripping down from the upper parts of the longitudinal bulkheads. The fracture face of the side shells and gunwales was inspected from a skip suspended from a crane. Unfortunately, due to the tortuous nature of the deck plate fracture, it was impossible to inspect this area in great detail. Similarly, it was impossible to view the longitudinal bulkheads from close at hand. However, it was possible to assess the amount of deformation which had been experienced by these members. Visual examination of the bottom shell fracture faces, longitudinals and the bilge keel of the aft section of the ship as a whole was made by walking along the bottom of the dock. Much of the fracture face of the sheer strake, side shell, bottom shell and flat plate keel were covered in oil, and had to be cleaned to allow close inspection of the fracture surface. The fracture occurred forward of the wash bulkheads in No. 3 tank (Fig. 2).

As can be seen from the general view in Fig. 5, a clean break of the bottom shell plate occurred with little or no deformation (see also Fig. 6). Deformation did occur to the ship's plate on both sides in the region 20–30 ft (6–9 m) below the deck plate. Severe deformation also occurred to the deck plates, and to the upper sections of the longitudinal bulkheads (Fig. 7). Apart from these regions, the failure for the most part was accompanied by little or no ductility, being macroscopically brittle.

From a detailed examination of the fracture surfaces, three possible initiation sites were detected. All three sites were clear of oil, and had experienced some corrosion of the fracture faces. The site which appeared to cause the most significant damage, at least during the initial incident described by the crew, appeared to be located in the port bilge keel (Figs 8 and 9). The chevron or herring-

122

Fig. 7. Side view from port showing fractures to bulkheads, port gunwhale and deck plating.

bone markings which usually characterize brittle fractures could be traced from at least 10 ft (~ 3 m) above the bilge keel detail on both the starboard and port sides, and along the length of the bottom shell to the port bilge keel. There was no evidence of the crack having arrested at any point along the bottom shell once the crack had begun running in the shell plate. However, this conclusion must be conditional since the quantity of oil spilling out of the fractured stern section, and the degree of corrosion on the parts of the shell free from oil, prevented a detailed examination of the entire shell. Periodic checks of the crack morphology could only be made by local cleaning. Checks were made particularly at weld details.

Figures 10 and 11 show close-ups of the bilge keel detail. The major initiation site appears to be contained in the port bilge keel detail. The bilge keel was formed by two plates joined by intermittent welding, the longitudinal bilge plate (or ground bar) then being continuously welded to the shell. There is a lack of penetration defect in the weld connecting the longitudinal bilge plates. At this particular site, there is an intermittent weld on the upper surface of the ground bar. The chevron marks on the bilge bar or bulb plate would appear to emanate from this site. The longitudinal bilge plate or ground bar weld has a lack of penetration defect, and also has a notch sited in a weld detail (Figs 10 and 11). The chevron markings on the shell plate clearly indicate that fracture emanated from the region of the ground bar to shell plate weld.

The crack morphology of the bilge keel and shell material indicate that the crack propagated with virtually no ductility, i.e. there was little evidence of shear lips on the crack surface. On areas which had been protected from corrosion by oil, the crystalline appearance characteristic of brittle fracture was evident.

Figures 8 and 9 show the bilge keel and shell on the port side. The bilge bracket detail is also
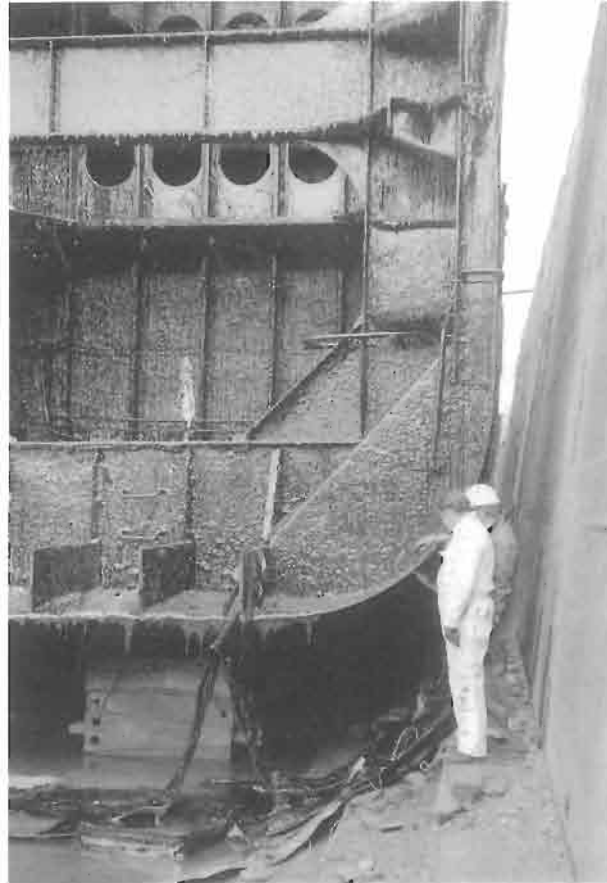
Fig. 8. Port bilge keel and keel showing three longitudinals, bilge bracket and fracture face of hull plating.

clearly visible. The fracture in the shell occurred just aft of the forward bilge bracket, but there was no evidence that the crack was connected in any way with the bracket as the fracture of the shell appeared to be entirely in the plate material. After propagating from the bilge keel, the crack ran in a brittle manner up the port side shell plate (as shown in Fig. 8). Unfortunately, the exact point at which the crack arrested could not be ascertained as the brittle fracture continued into the heavily buckled and deformed region of the hull where all fracture characteristics had been completely destroyed. Due to the deformation incurred in this region, however, it would appear reasonable to assume that this was one of the last parts of the hull to fracture, and thus the initially brittle crack did arrest in this region.

Figure 12 shows the deck plates. From the crew's evidence, this was the last region to fracture, the two halves of the ship hinging on the deck. This would seem to be substantiated by the deformation of the plate. However, the brittle behaviour of the gunwale plate, sheer strake and port deck section is also evident. A discontinuity of the fracture was apparent on closer examination of the port gunwale. The chevron markings above and below this discontinuity point towards an initiation site in the shell plate port side.

These markings were followed down the port sheer strake until the web–sheer strake detail. At this joint, there appeared to be an initiation point, since the chevrons below this detail indicated fracture emanating from this weld, where there appeared to be a lack of penetration defect. However, as the fracture face was almost horizontal at this point, close inspection was difficult. The fracture appeared to have propagated down the ship's hull from this detail for approximately 6–8 ft (2–2.5 m) before running into the heavily deformed region described above, as seen in Fig. 13. As this possible initiation site is ∼12 ft (∼4 m) below the level of the deck, it would appear that the crew's

Fig. 9. Port bilge keel showing bilge bracket: also showing longitudinal.

evidence is consistent with the fracture features, and that a crack of ~6 ft (~2 m) opened up, propagating downwards from the sheer strake–web detail, and arrested during the first incident. Subsequent propagation upwards to the gunwale probably occurred during the second incident, and the final separation of the two sections of the ship involved the joining of the arrested 6 ft crack and the crack propagated from the bilge keel. This process was accompanied by the deformation shown in Fig. 13.

After the first reported noises, two cracks 6 ft (~2 m) long on the port side, and 6 in. (150 mm) on the starboard side, had been visible ~12 ft (~4 m) below the deck in No. 3 tank. The bottom ends of these cracks could apparently be seen at times during the swell. At the time, the existence of a crack along the bottom shell plate had not been contemplated by the ship's crew. However, the magnitude of the loss of oil indicated from the ullages taken suggested that the centre tank was also leaking. Together with the fact that water was reported to have been pumped from the No. 3 tanks before the occurrence of the second reported incident, this would point to the likelihood that the bottom plate fracture had occurred at, before, or just after, the reported cracks in the side plates. It is interesting to note that the No. 3 centre tank appeared much cleaner (of oil) than the wing tanks (Fig. 5). The loss of oil from the bottom shell fracture may well have been missed due to the presence of loose ice driven around the ship by the swell and the prevailing wind.

It is difficult to determine the exact extent of the initial bottom shell fracture with regard to the longitudinals and centre girder, these will be described in detail later. As well as propagating up the port side the crack would appear to have run completely along the bottom plate and through the starboard bilge keel (parent plate material) as shown in Fig. 14, without stopping. Figure 14 also shows a region of crystalline appearance of the fracture on a small section where the residual oil

Fig. 10. Port bilge keel-to-keel detail.

Fig. 11. Port bilge keel plate to bilge keel detail.

Fig. 12. View of the deck plate fracture: part of the deck and longitudinal ripped out during final fracture is also shown.

has been removed: the remainder of the fracture surface has corroded. Figure 6 indicates that the fracture entered the starboard bilge keel forward of the initiation point on the port. The equivalent bilge keel detail to the port side fracture was thus intact on the starboard side.

The crack appeared to continue propagating upwards through the starboard shell plate for at least 10 ft (~3 m). As on the port side, a region of deformed plate was then evident where the fracture face had been destroyed by mechanical damage. There was also evidence of some damage occurring to the starboard side after the complete failure of the ship, involving a rip in the ship's plate just above the starboard bilge keel.

Inspection of the stringer and starboard shell plate detail revealed another possible initiation site, and a possible arrest and reinitiation site nearby. The fracture initiation site was situated about 12 ft (~4 m) below the deck level in a stringer–shell plate detail just below the sheer strake. The stringer itself suffered severe deformation. It was impossible to inspect the fracture surface above this site as it had been badly damaged. The starboard fracture site was evident at the point just to the right of the deformed stringer at the bottom of the sheer strake.

As described above, the bottom shell fracture appeared to occur either as one event or at least as a series of very close events emanating from the port bilge keel detail, and the likelihood is that the bottom shell was fractured during the first reported incident. As mentioned above, it is difficult to determine the exact extent of the fracture to the centre girder, longitudinals and longitudinal bulkheads caused during the initial incident.

The centre keel girder is shown in Figs 5 and 6. As the bottom shell plate fractured, so the crack ran up the girder in a brittle manner for approximately 1–2 in. (25–50 mm), after which full 45° shear fracture occurred. This fracture ran up to the cope hole, the ductile fracture continuing thereafter. The other longitudinals failed, as given below. A general view of the longitudinals can be seen in Figs 5 and 6.

Longitudinals starboard of centre girder (*numbering from centre girder*)
1 Brittle fracture
2 Brittle fracture
3 Brittle fracture
4 Brittle fracture
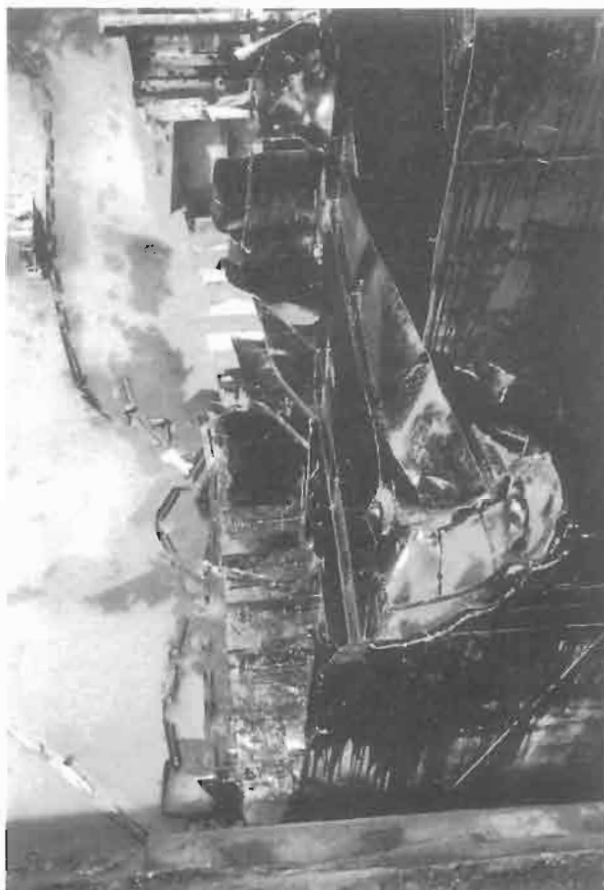
Fig. 13. Port hull plates and longitudinal bulkhead fractures: deformation to the web frame on the port side is also visible.

5   Brittle fracture
6   Brittle fracture
7   Brittle fracture

LB = longitudinal bulkhead—3 in. (75 mm) brittle fracture; 1 ft (300 mm) ductile (then heavily deformed).

8   1 in. (25 mm) brittle crack ran into drainhole; ductile above
9   1 in. (25 mm) brittle crack ran into drainhole; 6 in. (150 mm) brittle fracture before ductile
10   Brittle fracture
11   Brittle fracture
12   1 in. (25 mm) brittle fracture, drainhole; 4 in. (100 mm) ductile, brittle above
13   1 in. (25 mm) brittle fracture, drainhole, ductile above

Longitudinals port of centre girder (numbering from centre girder)
1   1 in. (25 mm) brittle fracture, drainhole, brittle above
2   2 in. (50 mm) brittle fracture, drainhole, brittle above
3   Brittle fracture
4   Shear fracture along weld (lack of penetration) into drainhole, plate 4 in. (100 mm) proud of main fracture, ductile for 4 in. (100 mm), brittle fracture above
5   Brittle fracture
6   Brittle fracture
7   Brittle fracture

LB = longitudinal bulkhead—ductile and heavily deformed.
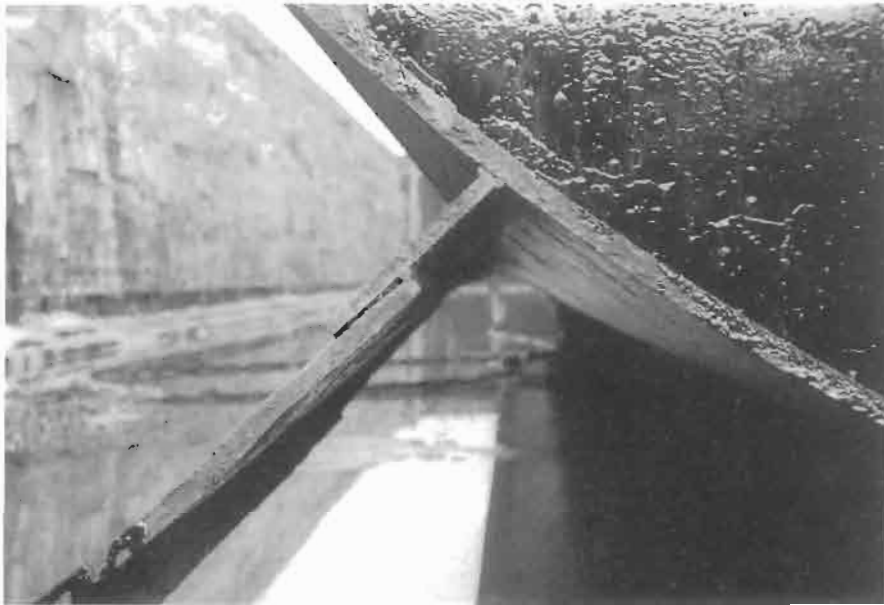
Fig. 14. Starboard bilge keel.

8 Brittle fracture
9 Brittle fracture [1 in. (25 mm) in centre ductile]
10 Brittle fracture [into drainhole 1 in. (25 mm) ductile, then brittle]
11 Brittle fracture
12 Brittle fracture
13 Ductile

Generally, even where full 45° shear fracture was evident, the reduction of area accompanying the fracture was small. An inspection of the port bilge keel remaining on the aft section of the ship revealed cracks in two weld details similar to the bilge keel initiation site on the port side. Extraction of these samples was requested. The heating coils used to keep the oil in the tanks at 140 °F (60 °C), are evident in many of the figures. It must be pointed out, however, that the initiation site in the port bilge keel would have been surrounded by sea-water, and, as such, could be considered to be at the water temperature of -0.7 °C.

Two meetings were held between the interested parties on 16 and 17 April 1979, respectively. At the first it was agreed by all concerned that TWI should carry out any tests required to ascertain the reasons behind the failure. At the second meeting, the five test samples required for this investigation selected by the DoT and TWI representatives during their inspections were described to the interested parties, who agreed to the extraction of these samples and their shipment to the TWI. Details of the samples required were left with the ship owners, and a Lloyds' representative was appointed to supervise the extraction of the samples. The positions of the required test samples were then marked on the vessel by the DoT and TWI representatives.

3. DISCUSSION OF THE RESULTS OF THE FAILURE INVESTIGATION

3.1. *Introduction*

Three of the samples identified during the dry dock inspection of the vessel described above contained initiation sites. At the start of the mechanical and metallurgical test programme described in [1], each of these samples were treated with equal importance. However, as the test programme developed, various aspects became clearer, and the port bilge keel sample was identified as the primary sample. To keep this section of the paper reasonably concise, rather than outline the gradual progression of the failure investigation, the sequence of events leading to the failure of the MV

Kurdistan, deduced from the investigations of [1] are presented in chronological order below, drawing on the test data where necessary to justify the conclusions reached. A summary of the mechanical test results is given in Table 1.

3.2. *The initiation of fracture*

The port bilge keel detail extracted in the principal test sample was the primary initiation site. Crack initiation by a cleavage mechanism occurred from a defect situated in the ground bar butt weld contained in this sample. This defect was formed by incomplete penetration due, in part, to the lack of an edge preparation on the ground bar plate (Fig. 15). In addition, during assembly of this detail the bulb bar plate was almost certainly attached by intermittent welds (Fig. 16) prior to the completion of the ground bar weld. This procedure resulted in an area of no weld on the outer lower edge of the ground bar joint, which, together with the lack of penetration defects present in the double-sided section of the weld, formed the defect shown in Fig. 17. This defect constituted an effective stress raiser, which was extended in service by fatigue, as illustrated in Figs 18 and 19. Three separate areas along the length of the defect showed evidence of fatigue damage, as shown in Fig. 20. This fatigue crack growth had the separate effects of increasing the overall defect size and enhancing the acuity at the notch tip. The initiation toughness of the weld metal in this region was believed to be low at the sea temperature at the time of the incident ($-1\,°C$) at low strain rates, and very low under medium and high rates. This conclusion was reached from toughness tests carried out on the corresponding weld detail from the starboard side of the vessel (Table 1). Metallurgical examination showed that this detail had similar microstructure, composition and hardness to the ground bar weld metal in which the initiation site was located, and is thus considered to have very similar toughness properties. The weld detail of the ground bar weld of the starboard sample differed from the port sample in that it was double-sided over its entire length, although, due to the lack of edge preparation, it contained a comparable lack of penetration defect. No evidence of any fatigue crack propagation comparable to that found in the port sample was observed.

Table 1. Summary of mechanical test results

Plate tensile properties (primary sample) at $+20\,°C$
$\sigma_y = 243\text{--}258\,\text{N mm}^2$
$\sigma_u = 417\text{--}448\,\text{N mm}^2$
Elongation $= 32\text{--}34.5\%$

Pellini NDT temperatures

Plate No.	NDT
1A	$>0\,°C$
1C	$-5\,°C$
2A	$+5\,°C$
3A	$0\,°C$

Weld metal Charpy results (starboard bilge keel sample)

Test temperature ($°C$)	C_V energy (J)	Crystallinity (%)
-10	8	95
-1	5, 8, 48, 80	95, 90, 50, 35
$+5$	6, 10	95, 85
$+10$	14, 30	60, 60
$+20$	28	70

Weld metal CTOD results (BS 5762) at $-1\,°C$

Test rate (mm s^{-1})	CTOD (mm)	Type of result
0.01	0.10	δu
	0.11	δm
1.0	0.04	δc
	0.16	δc
	0.07	δc
4.50	0.03	δc
	0.04	δc

Fig. 15. Ground bar butt weld in double-sided region. Note incomplete penetration. ×7.

Fig. 16. Intermittent lap fillet weld in sample 1 between ground bar and bulb bar, seen from above.

Although the lack of penetration defect of the starboard sample must have seen comparable loading to that experienced by the detail which initiated in the port sample, this was not a critical defect. The presence of a complete double-sided weld was obviously sufficient to reduce the overall stress and local stress concentration effects experienced by this weld to levels below that at which any significant fatigue crack propagation had occurred. Because of the lower overall stress and local stress concentration levels, and the presence of a smaller and blunter defect in the starboard detail, fracture initiation from this site was much less likely. As noted in [1], if the ground bar weld detail
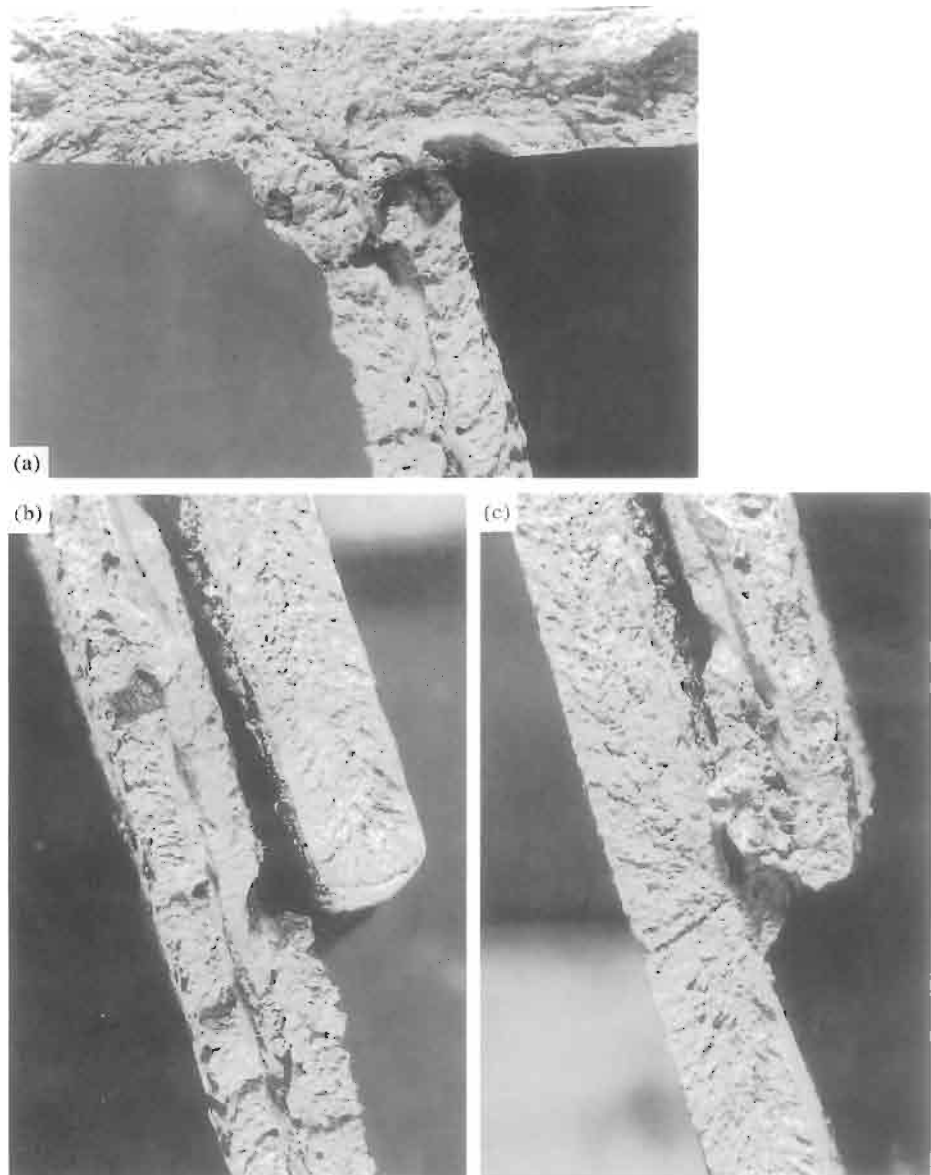
Fig. 17. Close-ups of port bilge keel.

in the port sample had been two-sided, stress levels approaching ultimate tensile strength of the plate material would have had to have been experienced under static conditions to cause failure. The defect that actually existed in the ground bar detail in the port sample was greater than the maximum defect size, which it is believed could have been tolerated safely at stresses likely to be experienced under normal operating conditions at low strain rates ($\dot{K} = 60 \, \text{N mm}^{-3/2} \text{s}^{-1}$).

From visual inspection of the fracture surface, it was deduced that initiation occurred from the fatigue cracked areas situated in the ground bar weld metal (Fig. 19). The intermittent weld and ground bar to shell plate weld details in this area were not considered to be prime initiation sites since:

(a) crack tip opening displacement (CTOD) tests have shown that these regions were likely to have had a significantly higher initiation toughness than the partial penetration butt weld detail;
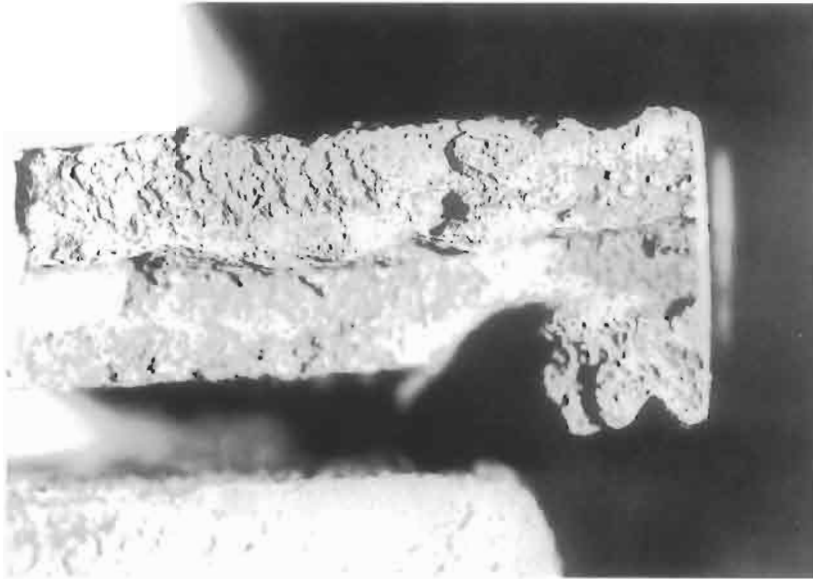
Fig. 18. Fracture surface of ground bar butt weld in sample 1 in single-sided region, close to inboard edge of bulb bar. Note smooth, featureless region in root of weld. ×4.

Fig. 19. Fracture surface of ground bar butt weld in sample 1 in single-sided region, close to outboard edge of ground bar. Note smoother fracture surface in weld root, from which some chevron patterns (arrowed) emerge. ×4.

(b) evidence from chevron patterns showed that the crack ran through the bilge bar to shell plate weld into the shell bilge plate;

(c) the notch acuity of the defect was lower in these areas due to the absence of a fatigue crack.

The directions of propagation from the initiation sites in the port sample are believed to have been as shown in Fig. 20.
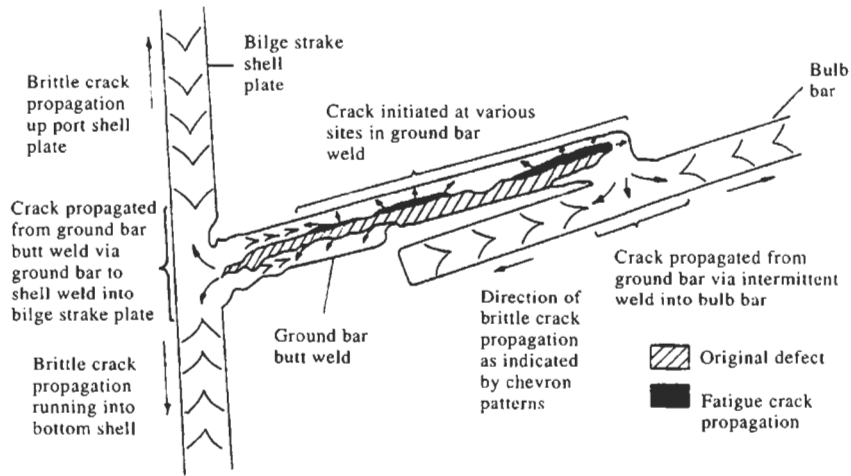
Fig. 20. Crack initiation in ground bar weld and subsequent propagation into shell—port bilge keel detail.

3.3. *Propagation*

Once the crack had initiated in the ground bar weld, it was able to propagate into both the bulb bar and the shell, since the dynamic toughness of the shell to ground bar fillet weld, and the bulb bar to ground bar intermittent lap weld were insufficient to arrest a running crack at the sea-water temperature ($-1\,^{\circ}$C), as evidenced by the Charpy data obtained on representative samples (Fig. 21). In addition, there was no crack arrest hole in the ground bar butt weld, the presence of which may have prevented the crack from propagating into the hull. Furthermore, the dynamic toughness of the Grade A plate used in the hull and the bulb bar was also inadequate to arrest a running crack, as discussed in [1].

Although the oil cargo was believed to be heated to around $60\,^{\circ}$C, it is surmised that the shell plate below the water-line was close to the sea temperature of $-1\,^{\circ}$C, since the results of the Pellini drop weight tests indicate that the nil ductility transition (NDT) temperature was around $0\,^{\circ}$C (Table 1). Had the shell plate been at a higher temperature, it is likely that shear lips would have been observed on the shell plate fracture surface, and no such evidence for ductile fracture was observed.

Once the crack had entered the shell, it propagated in two directions:

(a) Up the port side until it arrested at an indeterminate point at least 3 m above the bilge keel. Due to extensive mechanical damage to the fracture surface, the precise point of arrest was not evident.

(b) The crack also ran across the entire breadth of the bottom shell plate and up the starboard side
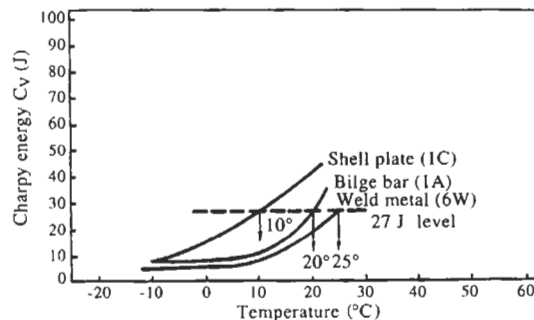
Fig. 21. Lower bound Charpy curves—port bilge keel.
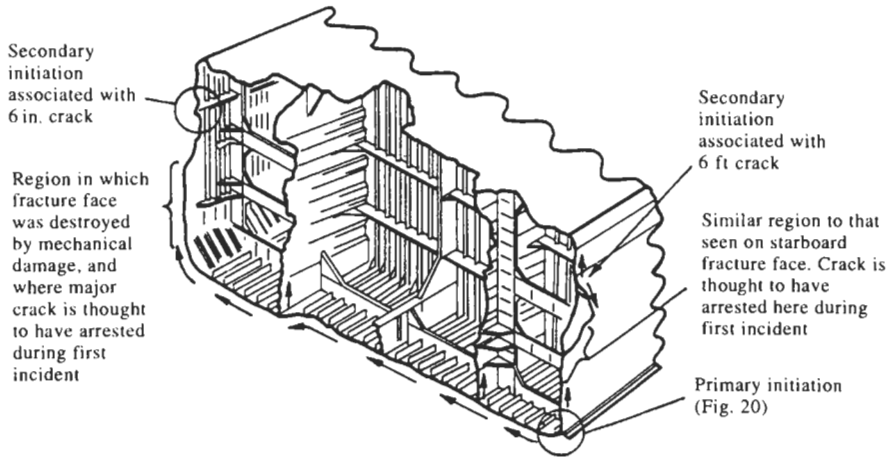
Fig. 22. Extent of crack propagation after the first reported incident. General view.

with no visible interruption, until it arrested at least 3 m above the bilge keel, in another area which had suffered extensive mechanical damage.

The path of the fracture initiating from the primary sample is shown in Fig. 20.

As the crack propagated along the bottom shell, it entered the longitudinal girders and bulkheads to the degree shown in Figs 22–25. In several of these, especially the bulkheads, the crack was arrested, due to higher temperatures of the shell caused by the heated cargo, and to the thinner plate in the bulkhead material.

As discussed in [1], it was believed that the initiation sites found in two of the other samples removed at St John could not have occurred except as a consequence of the extensive bottom and side shell fracture described above, and fracture would have initiated at the sites during, or immediately following, the major shell fracture. This conclusion is reached due to there being no weld defects present, the high toughness of the weld metal, and the fact that these sites would normally be

After the first incident:
Port longitudinals 8, 11 and 12 are thought to have fractured completely,
No. 9 is likely to have been partially intact. The brittle fracture ran into a drain hole in No. 10 and arrested.
The longitudinal bulkhead and No. 13 are considered to remain intact.
No. 13 in fact failed in a fully ductile manner in a vertical plane forward of the bottom shell fracture path.
Brittle fracture appeared continuous along the length of the bottom shell fracture.
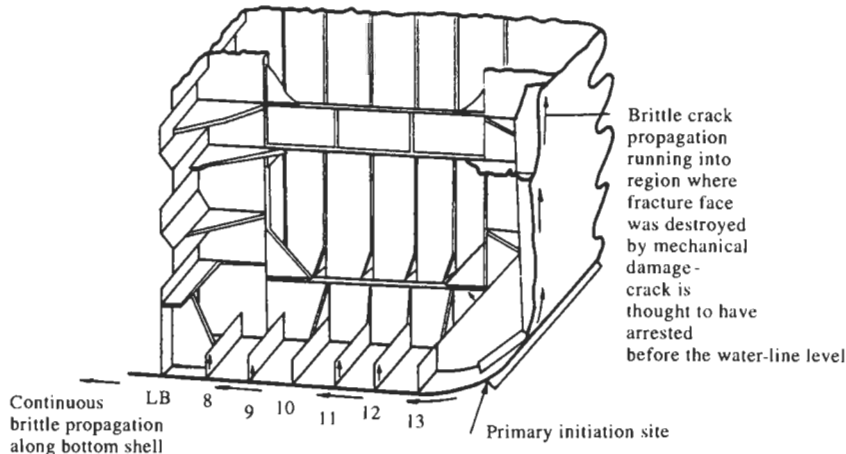
Fig. 23. Crack propagation—port bilge keel region during the first incident.

After the first incident:
The centre girder is likely to have experienced 1-2 in. brittle fracture
which arrested leaving the girder essentially intact.
The starboard bulkhead experienced 3 in. brittle fracture which then arrested.
Longitudinals 1-7 starboard of the centre girder are thought to have fractured.
Longitudinals 1 and 2 (port) may have seen crack arrest in the drain holes.
Port longitudinals 3, 5, 6 and 7 fractured. No. 4 remained intact.
Brittle fracture was apparently continuous along the length of the bottom shell.
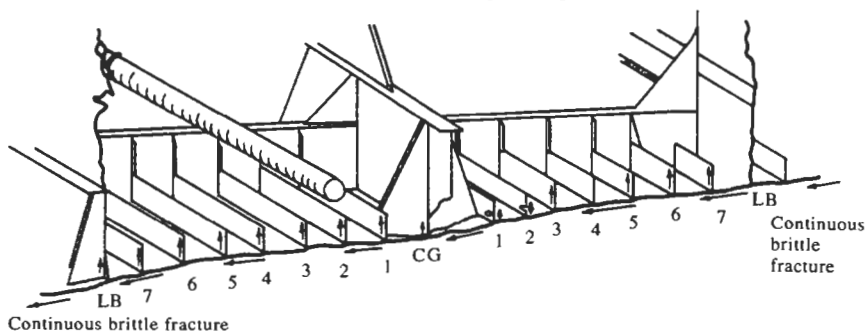
Fig. 24. Crack propagation during the first incident—bottom shell fracture.

Brittle crack propagation
running into region where
fracture face was destroyed
by mechanical damage -
crack is thought to have
arrested before water-
line level

After the first incident:
apart from a 3 in. brittle crack
extending from the bottom shell
the longitudinal bulkhead
remained intact.
Longitudinals 10 and 11 are
thought to have fractured but 8,
9, 12 and 13 probably experienced
arrest of the brittle crack
as it entered the drain holes and
thus remained partially intact.
Brittle fracture was apparently
continuous along the bottom
shell and through the starboard
bilge keel.

Brittle crack
propagated through
starboard bilge keel

Fig. 25. Crack propagation during the first incident—starboard bilge keel region.

situated in a low-stress region. Thus, it is considered that these were secondary, and not primary initiation sites. The extent of propagation from these cracks could not be determined, but cracks initiating from these sites were thought at the time of the investigation likely to correspond with the location of oil leaks witnessed by the crew.

After the first incident, it would appear that the vessel was held intact by partially fractured longitudinal bulkheads and bottom longitudinals, the upper regions of the hull sides, and the deck plate and its associated longitudinals. The bottom shell plate crack could have arrested either due to a rise in temperature, and hence toughness of the steel, or to its running out of driving stress.

3.4. *Events leading to final fracture of vessel*

Due to the extensive damage to the shell structure which existed after the initial incident, separation of the two sections of the vessel is considered to have been inevitable, and thus the events leading to the final fracture of the vessel must be considered to be of secondary importance. Due to

the extent of the bottom shell fracture, the remaining intact and partially fractured structures would have experienced higher than designed stresses. This situation would have been aggravated by the entry of sea-water into the shell, which would, of course, have cooled the internal members. These factors, together with the presence of sharp crack tips, resulted in the progressive failure of these members by both ductile and brittle fracture mechanisms. It was unclear whether the side shell fractures emanating from the port bilge keel connected with those from sites in the secondary samples, or whether the cracks from these latter two sites were bypassed by subsequent fracture events. This would seem to be most likely, due to the complex interaction of cracks observed in these regions. Final separation of the vessel occurred when the deck plates and their associated longitudinals failed.

3.5. *Possible causes of fracture*

The fracture mechanics calculations performed using PD6493 (1980) procedures as described in [1] (Table 2) showed that the defect situated in the port bilge keel detail of the primary sample exceeded the tolerable defect size at $-1\,°C$ for normal operating conditions. These calculations showed that the combination of (a) the position of the bilge keel defect under the still water bending moment loading; (b) the influence of the thermal stresses caused by carrying a hot cargo in cold waters; (c) the effect of high tensile residual stresses, and (d) the wave loading on exiting the ice field, would have subjected the bilge keel defect to a high applied crack opening displacement. Hence, there existed some risk of fracture from this defect under normal operation at a sea-water temperature of $-1\,°C$ or lower.

It was believed that, under rough sea conditions, the strain rate in the defect region could have been elevated, by wave loading, to levels exceeding $\dot{K} = 10^3\,\mathrm{N\,mm^{3/2}\,s^{-1}}$. Under these circumstances, there would be a decrease in the toughness of the weld in which the defect was situated, which, when accompanied by relatively high local stresses, would have meant that the defect in the primary sample exceeded the critical defect size at $-1\,°C$, and thus fracture would have been highly probable. Table 1 shows the decrease in CTOD toughness with applied strain rate. The medium test rate was roughly equated to the likely loading rates under rough sea conditions to predict the critical flaw sizes shown in Table 2. It was not considered likely that high strain rates ($\dot{K} > 10^5\,\mathrm{N\,mm^{-3/2}\,s^{-1}}$) would have been experienced under normal operating conditions.

There was evidence that cleavage fracture occurred directly from the tips of the fatigue cracks in the weld metal of the defect region in the port bilge keel (Fig. 19). As some ductile extension was experienced in a comparable weld metal at low strain rates (δu value in Table 1), this, combined with the defect assessment calculations, led to the conclusion that local strain rates above the lowest rate employed in the toughness evaluations were experienced by the port bilge keel region at the time of the incident.

3.6. *Report of the public enquiry and further discussion*

The results of the failure investigation reported in April 1980 were considered in the light of detailed reports from the crew, and evidence from a range of experts at the public enquiry held over 51 days in London during 1981. The report of the court was presented on 12 November 1981 ([2]). This report fully describes the circumstances leading to the casualty, and, with assembled evidence, was able to adjudicate on the most likely timing of events for the failure, which had been the major area of disagreement between the parties represented at the enquiry. The court found that the weight

Table 2. Critical defect assessment—half length of critical through thickness flaw size [2]*

Test rate (mm s⁻¹)	CTOD (mm)	Applied load (N mm⁻²)					
		100	150	200	250	300	450
0.01	0.10	27.3	22.8	19.8	17.3	15.5	11.5
1.0	0.04	10.8	9.1	7.8	7.0	6.3	4.8
450	0.03	8.3	6.8	6.0	5.3	4.5	3.5

*Equivalent defect size of actual flaw assessed as buried defect $\bar{a} = 8.6\,\mathrm{mm}$.

of evidence pointed to the brittle fracture initiation occurring as the vessel encountered head seas near the ice edge subsequent to the manoeuvring in the ice field, the failure initiation in the port bilge keel having been triggered by wave impact on the bow.

As described in the paper by Corlett *et al.* [3], the period spent in the ice almost certainly led to the general cooling down of the longitudinals and the shell beneath the water-line, as the bunker oil solidified on the inner surface of the vessel in the calm conditions in the ice field. Without this general lowering of the temperature of the ship plate to its NDT (nil ductility temperature) value, the primary initiation induced in the port bilge keel would not have propagated with such disastrous consequences. As noted in the failure investigation [1], there was evidence of other bilge keel details which had cracked at some earlier occasion, but had not propagated into the ship's structure.

The fracture mechanics calculations performed in the failure investigation and referred to by the report of the court [2] were performed using the BSI PD6493 1980 procedures with an adjustment to remove the inherent factors of safety in the analysis to facilitate critical predictions as described in [4]. Subsequently, this analysis method was updated in 1991, and the *Kurdistan* casualty was re-examined as part of the validation exercise along with many large-scale laboratory tests and other well-documented failures [5].

The reanalysis is illustrated in Fig. 26 using the level 2 procedure of BSI PD6493: 1991 with weld metal CTOD values relating to the low and medium strain rates. Assessment points are drawn for stress inputs of 100, 150 and 200 N mm^{-2}, assuming a yield strength of 227 and 300 N mm^{-2}, relating to plate and weld metal, respectively. The reanalysis indicates that failure (indicated by points outside the failure locus) would, in fact, have been possible at low strain rates as the higher load level is approached. For the intermediate rate, CTOD toughness failure is predicted for the still-water condition of 100 N mm^{-2}. This reanalysis confirms the criticality of the combination of high applied stresses (due to the combination of cargo loads, wave loads and hot cargo in cold seas), high residual stresses, the presence of a significant weld defect, and low toughness.

The toughness of the weld was, of course, prejudiced by the incorrect weld procedure, but also
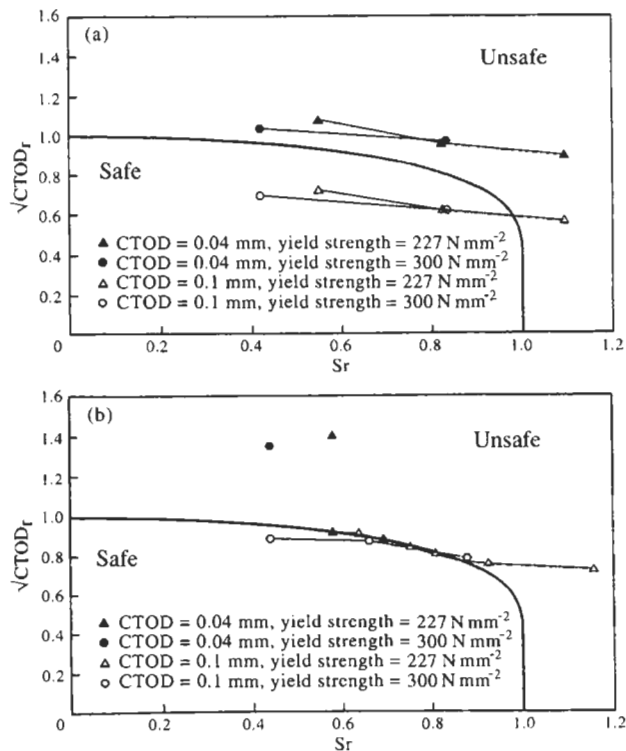

Fig. 26. (a) MV *Kurdistan* level 2 assessments—embedded defect assumption. (b) MV *Kurdistan* level 2 assessments surface defect assumption.

138

by the strain rate induced by the wave loading as the vessel exited the ice field. The reanalysis indicates that a marginally higher rate than the low strain rate would have been just sufficient to reduce the toughness below a CTOD of 0.1 mm, and would have caused a brittle initiation under the prevailing loading conditions.

Like many other brittle failures, however, the *Kurdistan* illustrates that catastrophic failure occurs only when the circumstances for brittle fracture propagation occur. In this case, if the vessel had not cooled down due to its passage through the ice, the port bilge keel initiation event may not have propagated beyond the ground bar. This failure illustrates, as do many other cases, the influence welded attachments can have on the integrity of structures.

4. CONCLUSIONS

(1) The MV *Kurdistan* suffered a catastrophic brittle fracture initiating in the port bilge keel weld, which propagated into the ship's structure, causing the vessel to break in two just forward of the wash bulkhead in the No. 3 tanks.

(2) All materials tested met the required standards. However, the weld in the ground bar of the port bilge keel was incorrectly made, inducing a large weld defect, and reducing the local toughness.

(3) The weld defect experienced some fatigue damage, increasing the local notch acuity, and, as the vessel encountered "head on" seas on emerging from an ice field, a brittle fracture was initiated.

(4) The combination of still-water bending moment, thermal stresses, wave loading, residual stresses from welding, defect size, and low toughness meant that brittle fracture initiation was inevitable.

(5) The combination of events leading to the *Kurdistan* encountering the ice field, and the characteristics of its bunker oil cargo, meant that the temperature of the ship's plate was reduced to the external water temperature ($-1\,°C$) despite carrying a hot cargo. This resulted in the catastrophic propagation of the brittle fracture from the bilge keel initiation site as the vessel emerged from the ice field, resulting in the eventual complete fracture of the vessel.

REFERENCES

1. Garwood, S. J., Threadgill, P. L. and Wood, A. M., Failure investigation concerning the "M V Kurdistan" casualty—final report. Welding Institute Contract Report 3642/1/80, April 1980.
2. *M V Kurdistan—Formal Investigation Report of Court No.* 8069. HMSO, London, 1982.
3. Corlett, E. C. B., Colman, J. C. and Hendy, N. R., Kurdistan—the anatomy of a marine disaster. Royal Institution of Naval Architects Spring Meetings, Paper No. 8, 1987.
4. Garwood, S. J. and Harrison, J. D., in *Pressure Vessel and Piping Technology—1985. A Decade of Progress.* ASME, pp. 1043–1054.
5. Challenger, N. V., Phaal, R. and Garwood, S. J., Appraisal of PD 6493:1991. Fracture assessment procedures Part III: assessment of actual failures. TWI Research Members Report 512/1995, June 1995.

INVESTIGATION OF FAILED ACTUATOR PISTON RODS

T. F. RÜTTI* and E. J. WENTZEL†

Boart Longyear Research Centre, PO Box 1242, Krugersdorp 1740, Republic of South Africa

(*Received* 3 *February* 1998)

Abstract—Actuator pistons had failed after very short service life by intergranular cracking in a circumferential weld. Analysis of the welds and subsequent heat treatments showed that the austenitic filler material used to weld the carbon steel resulted in carbide precipitation during nitriding. Combined with high residual stresses, these carbides promoted intergranular fracture at normal operational loads.

It is shown how the changes that had been made to the initial design and processing of the actuators were not entirely compatible with each other and reduced the "metallurgical safety factor".

Recommendations for improvements were successfully implemented. © 1998 Elsevier Science Ltd. All rights reserved.

Keywords: Welding, nitriding, heat treatment, preheat.

1. INTRODUCTION

Boart Longyear Research Centre was subcontracted to investigate the failure of actuator piston rods. An adapter was welded to the end of each piston rod and fractures in the welds were resulting in failures of the actuators. The pistons were subjected to two static loads of no more than 50 kg onto which a 30–35 Hz cyclic load was superimposed. Down-time of the machines, and possible injury to the operators, were endangering the manufacturer's position in the market.

This report illustrates how the changes—some of them beyond the manufacturer's control—that had been made over the years to the initially sound materials selection, design and processing of the piston rods, resulted in a gradual erosion of the "metallurgical safety factor". Eventually, the combination of materials and processes resulted in an inadequate product that was unable to withstand operational loading conditions.

2. BACKGROUND

A carburised adapter made of En32 (carbon case-hardening steel) was press fitted into the end of the piston rod made of En9 ("55" carbon steel). The area on the adapter that was to be welded was blanked off during carburising with a refractory compound to prevent an increase in carbon content. The rod and adapter were machined so that after press fitting there was a single-V groove with a 90° included angle that allowed the two components to be circumferentially welded using a single pass GTAW with an AWS A5.4 E312-16 filler rod (29 Cr, 9 Ni—generally recommended for welding steels of low weldability). No preheating was applied. The completed piston rod was then either nitrided or phosphated, depending on customer requirements. It appeared that only the nitrided piston rods were failing.

After reports that the first few components had failed by fracture of the weld, two "rosette welds" (essentially plug welds or tack welds through a hole in the rod onto the adapter) were added where the adapter extended into the rod. These welds were supposed to act as shear pins and prevent the adapter from being pulled out of the piston rod once the circumferential weld had cracked.

---

* Author to whom correspondence should be addressed.
† Present address: Combined Design Engineers, PO Box 754, Rondebosch 7701, Republic of South Africa.

Table 1. Major changes made to the manufacture of the piston rods

	Original design	Final design
Rod steel	En8—0.4%C	En9—0.55%C
Rod heat treatment (before welding)	Quench and temper	None
Rod microstructure	Tempered martensite	Ferrite/pearlite
Welding method	SMAW	GTAW
	Circumferential butt weld	"Rosette weld" added
Surface finish	Chrome plating	Nitriding

Historically, a number of changes were made to the design and manufacture of the piston rods, as outlined in Table 1. The steel grade was changed because a change of suppliers—the latter did not produce En8. The heat treatment of the rods prior to welding was omitted because the as-received En9 met the hardness specification of the quenched and tempered En8.

3. INVESTIGATION

3.1. *Visual inspection*

Figures 1 and 2 show the end of a typical piston rod fracture. The very low degree of wear on the adapter indicated that the actuator had only been in service for a very short period of time.

The cracks appeared to have originated in the centre of the weld and then propagated along the centre of the weld for about half of the circumference. The cracks subsequently branched and propagated axially along the rod, probably due to the bending stresses that arise during operation. The fracture surface appeared brittle with large elongated grains being clearly distinguishable. There were no visible signs of fatigue or plastic deformation.

The "rosette welds" had fractured and had not, as was their intended purpose, held the adapter and the piston rod together once the main weld had failed. A large amount of porosity was evident on the "rosette weld" fracture surface.

3.2. *Chemical analysis and mechanical tests*

Spark emission spectroscopy of various parts of the failed components, as well as raw materials, showed that the chemical compositions of all parts were within the specifications for the respective
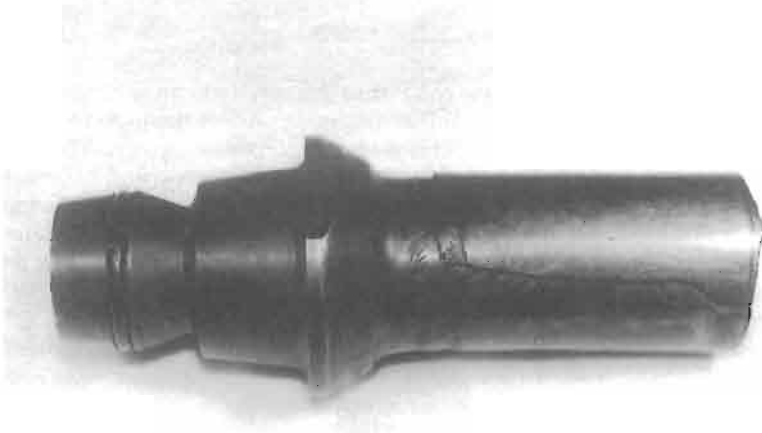
Fig. 1. Typical failed actuator piston rod showing the adapter, the circumferential weld and a large crack.

Fig. 2. Typical fracture through the centre of the weld and along the piston rod. The location of one of the rosette welds can be seen.

nominal steel grades. A 0.2 wt% excess of Mn was noted in one steel, but this was not deemed relevant to the failures.

Vickers microhardness tests showed that the weld metal had a hardness of 350–370 Hv. The region immediately adjacent to the fusion line had a hardness of 220 Hv, which decreased rapidly to 200 Hv. The carburised case of the adapter plug had a hardness in the region of 350 Hv.

3.3. *Metallography and fractography*

Sections of the weld were mounted in resin, polished and etched. The microstructure comprised large, elongated grains of a duplex ferrite/austenite nature (Fig. 3) with large carbides both within
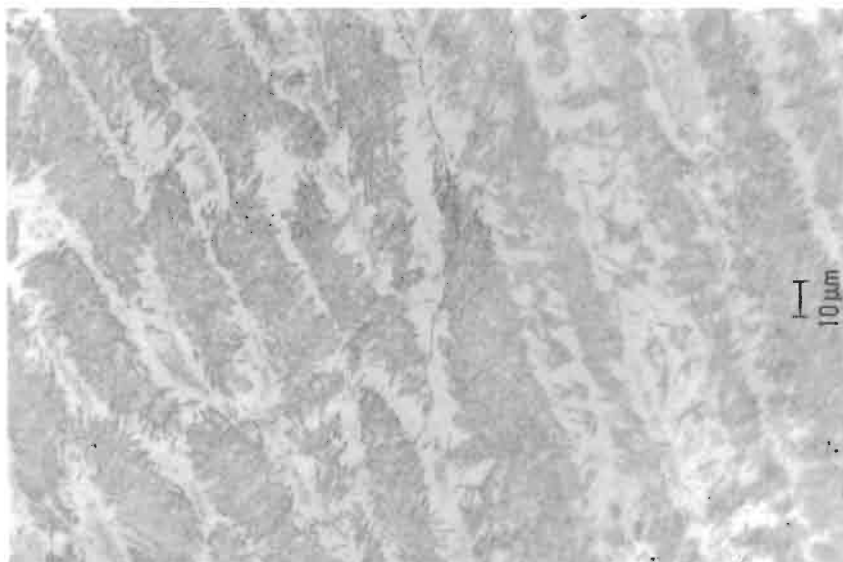
Fig. 3. Optical micrograph of one of the E312 welds showing austenite/ferrite duplex structure and a hairline crack (centre of photograph) (etchant: Vilella's etch).

the grains and at grain boundaries (Fig. 4). Hairline cracks were clearly visible along some of the grain boundaries.

The surface of the weld showed a nitrided layer which was cracked at regular intervals (Fig. 5). Sections of the surface adjacent to the weld bead clearly showed the white layer from the nitriding process. Surface cracks were visible. Since the white layer was not present in the crack (Fig. 6), these cracks probably originated after the nitriding process.

Some of the areas on the adapter that were supposed to have been blanked by the refractory compound were carburised. This showed that the blanking procedure was not adequate and resulted in the low weldability of the adapter.

The fracture surfaces showed no signs of fatigue. Fracture was intergranular and numerous intergranular cracks were visible on the fracture surfaces (Fig. 7).
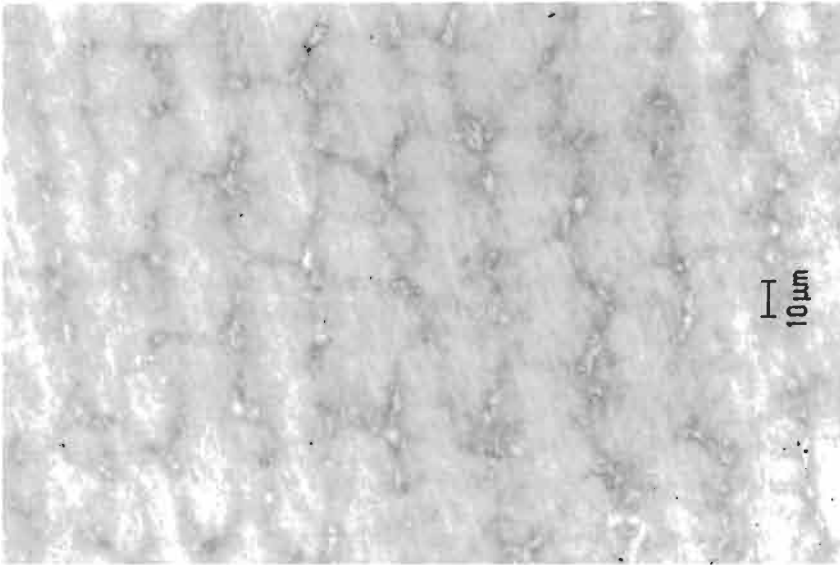
Fig. 4. Optical micrograph of one of the E312 welds showing severe carbide precipitation (etchant: Beraha's tint etch).

Fig. 5. Optical micrograph of the E312 weld showing cracks that originated after the nitriding (etchant: 2% Nital).
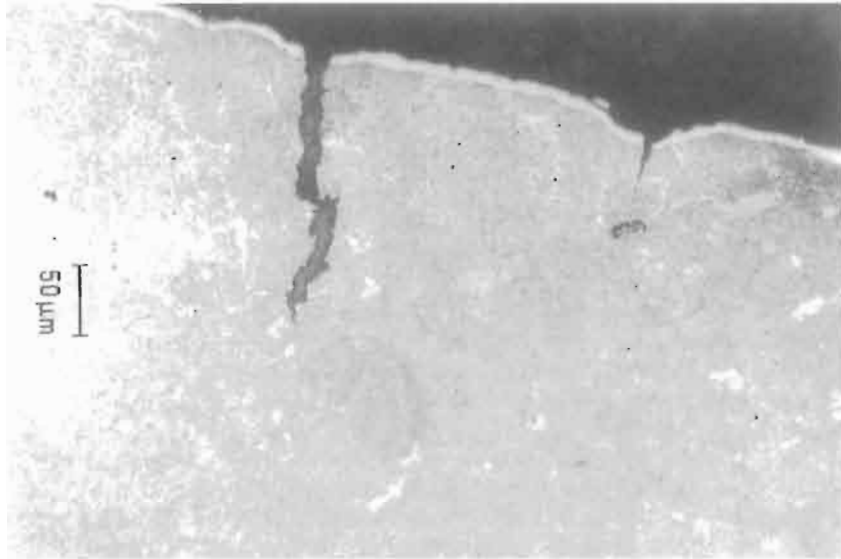
Fig. 6. Optical micrograph of the En32 steel immediately adjacent to the weld showing cracks that originated after the nitriding (etchant: 2% Nital).

Fig. 7. SEM fractograph of the fracture surface as received. The intergranular nature of the fracture and secondary cracks can be seen.

4. DISCUSSION

The absence of evidence of fatigue and the short operational life of the actuators indicated that the components entered service flawed or contained such high residual stresses in the weld that operational loading resulted in cracking and fracture.

Table 2 shows the nickel and chromium equivalents of the various steels used. The exact extent of dilution of the weld metal was not determined, but the combination of the parent metals and E312 filler metal places the resultant weld metal composition into the A + F or A + M + F zone on the Schaeffler diagram. Since the welds were very wide and a large degree of dilution had taken

Table 2. Ni and Cr equivalents calculated on average nominal compositions

Steel grade	Ni equivalent	Cr equivalent
En9	16.8	0.5
En32 (uncarburised)	4.8	0.5
E312	13.8	30.0
ER 70S-6	5.2	1.5

place, the former composition was more likely. Indeed, the microstructure of the E312 weld consisted mainly of austenite and ferrite (Fig. 3), but a large degree of grain boundary and intragranular carbide precipitation, probably chromium carbides, was also observed. The carbide precipitation probably took place during nitriding, resulting in the high hardness of the weld and weakening of the grain boundaries.

The high residual stresses (estimated at 300–500 MPa) due to the different thermal expansion coefficients of the duplex weld metal and the low alloy parent metal (11–13×10^{-6}/K and 16–18×10^{-6}/K for En9 and high Cr/high Ni steels respectively), coupled with the highly constrained joint configuration and the weakened microstructure, probably resulted in cracking of the weld on cooling after nitriding. This conclusion is supported by the fact that the actuator piston rods that were phosphated did not fail—there was no thermal cycle to allow for carbide precipitation. Unfortunately, no phosphated piston rods were available for evaluation, so this could not be confirmed.

The absence of preheat resulted in a very high cooling rate which had a twofold effect. Firstly, the HAZ was very hard and susceptible to cold cracking which was confirmed by the martensitic structure and some small cracks found in the HAZ. Although the nitriding subsequently tempered this microstructure to 200 Hv, the delay between welding and nitriding was often several days which was sufficient for damage to occur. Secondly, the weld microstructure comprised long, narrow grains with no equiaxed grains near the centreline. The result was increased weld centreline segregation and reduced toughness.

The weld bead was very wide and relatively shallow (Fig. 8), and in some cases insufficient penetration resulted in a circumferential stress concentrator in line with the centreline of the weld. Ideally, where two components are only welded along a part of their contact surface, the un-fused plane should be off-centre and not parallel to the weld centreline.
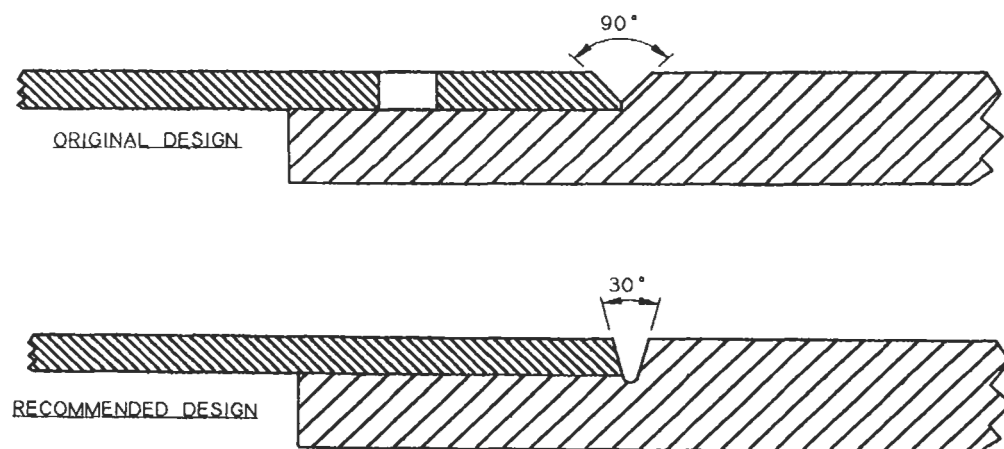

Fig. 8. Schematic drawings of the original and recommended weld preparations.

5. CONCLUSIONS

(1) Available evidence showed that the primary cause of the failure was the combination of the high alloy filler material (E312) used to weld the high carbon steel rods (En9) and the subsequent nitriding.

(2) The welds contained extremely large and elongated grains with hairline grain boundary cracks and carbide precipitation both at grain boundaries and within the grains. The carbides probably originated during nitriding and resulted in a hard, brittle weld.

(3) The piston rods failed by intergranular cracking through the centre of the weld. Once the cracks were sufficiently long to result in bending of the rod away from the adapter, the cracks branched and propagated along the length of the rod. Such cracking was facilitated by the brittle ferrite/pearlite microstructure with the as rolled grain structure.

(4) Other contributory factors included the absence of preheating, differences in thermal expansion coefficients of the weld and parent materials, the highly constrained nature of the weld joint, the width of the weld preparation and the poor penetration of the weld.

(5) The "rosette welds" did not appear to have played any role in the prevention or retardation of the failures.

(6) The blanking during carburising of those sections of the adapters that were to be welded was not satisfactory and randomly varying degrees of carburising occurred in metal that was subsequently welded. This increased the hardenability of the weld and the likelihood of cracking.

6. RECOMMENDATIONS

6.1. *Weld preparation geometry*

The weld preparation had to be changed for two reasons. Firstly, the width of the weld was reduced and the depth of penetration increased, since the strength of a butt weld is only determined by its depth, while excessive width can result in excessive dilution, high heat input and residual stress. Secondly, the weld bead was designed such that the gap between the En9 tube and the En32 adapter is not tangential to the weld interface nor parallel to the weld centreline (Fig. 8).

This was achieved by a double "J preparation" with an included angle of 30° and by grooving the adapter by up to 0.7 mm.

6.2. *Filler material*

This investigation showed that the E312 filler material was not suitable for the welds under consideration. A plain carbon filler material such as AWS A5.18 ER70 S-6 was recommended as a replacement, since this would not be adversely affected by nitriding. Trials with the recommended filler showed that the temperatures at which nitriding takes place resulted in a beneficial tempering/stress relieving heat treatment. In addition, the alloying of this material due to the dilution by the parent materials rendered the thermal expansion properties of the filler somewhere between those of the En9 and the En32 steels. The residual stresses in the plain carbon weld metal should thus be substantially lower than those in the highly alloyed stainless steel weld metal.

Because of significant differences in thermal expansion coefficients between high alloy austenitic steels and low alloy ferritic steels, the use of austenitic filler metals for the welding of steels with low weldability must be approached with extreme caution. This is especially true where the joint is highly constrained.

6.3. *Welding procedure*

Preheating is essential when welding steels that have good hardenability, since this reduces the susceptibility to embrittlement of the heat affected zone and formation of low temperature transformation phases.

The recommended minimum preheat temperature was established at 244°C using a standard formula and a carbon equivalent of 0.71 for the En9 piston rod. If significant carburisation of the adapter had occurred, this temperature would have to be increased.

Since the piston rods were welded semi-automatically with a stationary electrode and a rotating work piece, it was suggested that applying a gas flame for two revolutions would suffice as an intermediate solution. Induction heating was recommended as the long term solution, since the temperature profile will be more even through the thickness of the joint, the temperature of the weld joint is raised to the preheat temperature without overheating and oxidising the surface, and it is faster than flame heating.

Weld penetration was improved by increasing the current by 20% and reversing the polarity to electrode negative (DC current) for maximum depth to width ratio.

6.4. *General*

The above recommendations were intended specifically to remedy the problems with the weld failures. During the investigation a number of other areas that required attention came to light.

- En9 is a hardenable steel but the hardenability properties were not being used—instead, the weldability was reduced. Steels with similar strengths but lower carbon equivalents and thus better welding properties and lower preheat temperatures needed to be considered. Alternatively, by quenching and tempering the rods, higher strengths can be achieved and thus a reduced wall thickness might suffice, resulting in lighter components.
- The refractory compound shielding on the adapter that was intended to prevent carburising of the area that is to be welded was found to be unsatisfactory. Possible alternatives included copper plating and removal of the carburised area by machining. However, if the copper plating is not removed, this could lead to weld contamination.
- Much of the effect of carburising was cancelled by the nitriding process, i.e., the hardness of the case was reduced from the specified 60 HRc after carburising to ± 40 HRc after nitriding. Since nitriding was a major contributor to the failure, the value of this process needed to be critically evaluated.

7. SUMMARY

The problem of the failed actuator piston rods was analysed and solved, the solution tested and successfully implemented into the large scale production of the actuators within two weeks. No further weld fractures were reported.

A large number of metallurgical aspects of the weld was considered in this investigation, most of which were not profound revelations to anyone versed in materials science and did not require exotic testing facilities or specialised expertise. The main point that the authors wish to emphasise, with this investigation serving as an example, is that careful consideration should be given to every stage of a design, processing or material selection change in any product. Too often, metallurgical aspects of such changes are ignored or glossed over, each change eroding the "metallurgical safety factor" until the sum of the changes results in a non-viable component that enters service flawed or has marginal mechanical properties.

Any one of the changes outlined in Table 1 would not in itself have resulted in the failures, but their implementation left fewer options and less room for error for the following changes. For example, changing the surface treatment (based, at the time, on the customer's colour preferences rather than corrosion or wear properties) raised the processing temperature from 70°C (phosphating) to 580°C (nitriding) which had far-reaching effects on tempering, precipitation of carbides and other brittle phases, residual stresses, etc. but may have proved insignificant if the base material had had a lower carbon content or a low carbon/low alloy filler metal had been utilised.

This is where a well managed and frequently examined change management system such an ISO can play a vital role in guaranteeing ongoing unwavering quality in the face of changing suppliers, process capabilities and customer requirements—but not without the watchful guidance of a materials engineer.

PREMATURE FAILURE OF PRESTRESSED STEEL BARS

A. VALIENTE and M. ELICES*

Departamento de Ciencia de Materiales, E.T.S.I. Caminos, Universidad Politécnica de Madrid,
Ciudad Universitaria s/n, 28040—Madrid, Spain

Abstract—The details of two failures of prestressed steel bars are reported and a failure analysis is carried out using Linear Elastic Fracture Mechanics: the fracture toughness was measured using two standardized procedures and the pertinent stress intensity factor computed by numerical methods. The analysis of the failures show that the usual design requirements for prestressing bars fail to warn against brittle failures if damage exists. Some procedures, based on the concept of damage tolerance, are suggested to avoid similar accidents. © 1998 Elsevier Science Ltd. All rights reserved.

1. INTRODUCTION

Prestressing, a powerful technique in Civil Engineering, can be defined as the application of a predetermined internal force to a structural member in such a manner that the combined internal stresses in the member, resulting from this force and from external loading, will be confined within specific limits. Whether prestressing is applied to steel or concrete, its ultimate purpose is twofold: first, to induce desirable strains and stresses in the structure and second, to counterbalance undesirable strains and stresses.

The term *pre-tensioning* is used to describe any method of prestressing in which the tendons are tensioned before the concrete is placed. In contrast, *post-tensioning* is a method of prestressing where the tendon is tensioned after the concrete has hardened or—as in this case-study—the steel structural element is built. Post-tensioning offers a means of prestressing on the job site.

When post-tensioning short members, the elongation of the tendon—during the stressing—is small, and requires very precise measurement by the workmen. This is why *bars* are preferred to *cables* as short tendons for post-tensioning. In this example, some frames of a steel structure were post-tensioned with high-strength alloy steel bars.

The bars, once stressed, remain as such forever. Under these high stresses—about 780 MPa or 0.6 uts (ultimate tensile stress)—they are very susceptible to small damage. Surface scratches, cracks, pits or notches, that will not usually affect the performance of bars of concrete reinforcement may become dangerous when present in prestressed bars. In fact, the fractures reported in this paper happened at loads as low as 0.3 uts and were triggered by very small surface cracks.

The purpose of this paper is to illustrate this fact. Two failures of post-tensioning bars with surface damage are analyzed using the tools of Fracture Mechanics and some procedures, based on the concept of *damage tolerance*, are suggested to avoid similar accidents.

2. CASE STUDY: FAILURE OF PRESTRESSED BARS

2.1. *Background*

The reported failures occurred in a prestressed steel structure. To improve the transversal stiffness in some steel frames, post-tensioning with a couple of bars was applied diagonally, as shown in Fig.

---

* Corresponding author.

Fig. 1. Prestressed steel frame using two bars.

1. The tendons were high strength steel bars, 36 mm diameter, with a rupture load $F_R = 1300$ kN. The chemical composition and mechanical properties of the steel bars are shown in Tables 1 and 2, respectively.

Two fractures happened during building erection when stressing the bars; one at 400 kN (about $0.3F_R$) and another at 600 kN (about $0.46F_R$); both failure loads were well below the scheduled working load of $0.6F_R$.

Examination of the fracture surfaces revealed that in both cases the fracture was triggered by a small surface crack. The morphology of the fracture surfaces was very similar in the two bars; a representative picture is shown in Fig. 2. Observation by scanning electron microscopy revealed a quasi-cleavage morphology.

Table 1. Chemical composition of the steel bars

Element	C	Si	Mn	P	S	V
Weight %	0.65	0.70	1.20	0.014	0.018	0.25

Table 2. Mechanical properties

Elastic modulus	Yield stress	Tensile stress	Elongation under max. load
208 GPa	1143 MPa	1285 MPa	6.7%

Fig. 2. Fracture surface of a broken bar.

2.2. *Failure analysis*

The fact that fracture was triggered by a surface crack, and also the brittle aspect of the fracture surfaces, suggested linear elastic fracture mechanics as the simplest tool to analyze the failures. To this end the fracture toughness of the bars was measured, the stress intensity factors for the surface cracks were computed and all these results were compared with the available information on the failed bars.

2.2.1. *Fracture toughness.*

Fracture toughness was measured following standards ASTM E 399 [1] and ASTM E 1304 [2], and the two results were almost the same. Standard Single Edge Bend Specimens (SEBS), with 16 mm thickness, were used according to ASTM E 399, and short bar specimens, of 19.5 mm thickness, according to ASTM E 1304. Figure 3 shows the geometry of these samples and the position of the bar from which they were extracted; in both samples the crack plane was transversal to the bar axis in order to reproduce the same propagation plane as in the failed bars.

Experimental results are shown in Table 3. No more tests were performed in view of the small scattering in the recorded toughness values. The small values ($K_{IC} = 33–35$ MPa m$^{1/2}$) are indicative of brittle behaviour. Two additional test results—load vs COD (Crack Opening Displacement)—from each type of sample, corroborate this supposition.

Figure 4(a) is a typical example of the load–COD records from notched beams. The unloading branch shows successive failures until the broken sample is split in two halves. This behaviour is characteristic of a quasi-stable brittle fracture, where energy absorption is almost constant. To check this hypothesis the *iso-K* curve—corresponding to $K_{IC} = 35$ MPa m$^{1/2}$—was drawn on Fig. 4(a). It fits extremely well with the unloading branch, adding further support to the use of Linear Elastic Fracture Mechanics. The *iso-K* curve was computed from the stress intensity factor, K_I, and compliance, COD/P, expressions given in Ref. [3], i.e.:

$$K_I = \frac{4P}{B\sqrt{W}} f\left(\frac{a}{W}\right) \tag{1}$$

and

$$\frac{COD}{P} = \frac{24}{BE} g\left(\frac{a}{W}\right), \tag{2}$$
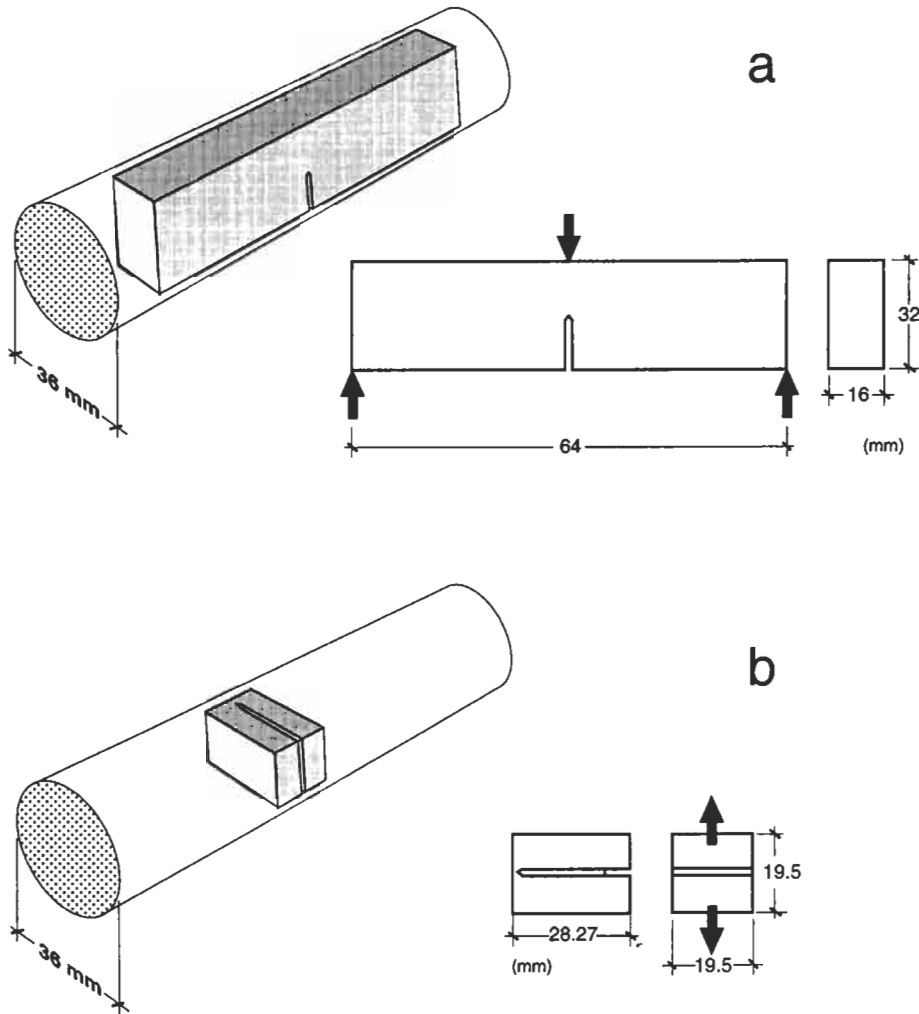
Fig. 3. Test samples for fracture toughness measurement. (a) Notched beams according to ASTM E 399. (b) Short bars according to ASTM E 1304.

Table 3. Fracture toughness K_{IC} (MPa m$^{1/2}$)

Beam	ASTM E 399	32	33	33
Short bar	ASTM E 1304	35	35	36

where P is the applied load, E the elasticity modulus, B, W and a are, respectively, the specimen thickness, width and crack size, and $f(a/W)$ and $g(a/W)$ are non-dimensional functions given in [3]. The *iso-K* curve is the P–COD curve [eqn (2)] after replacing a from eqn (1) with $K_I = K_{IC}$.

Figure 4(b) is also a typical load–COD record obtained from short bar specimens. Crack propagation is stable and proceeds stepwise until reaching the maximum load. Qualitatively, this is the kind of record one should expect for a brittle material with a fracture criterion based on a unique value of fracture toughness rather than a R-curve.

2.2.2. *Stress intensity factor.* The initial surface cracks of the two broken bars were modelled as
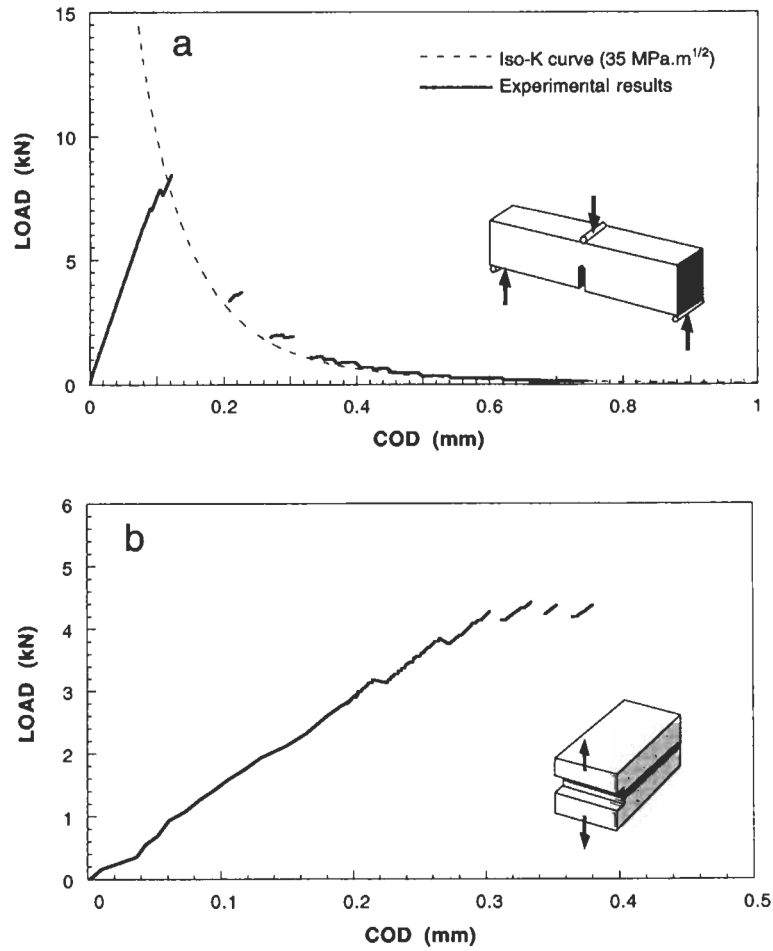
Fig. 4. Load vs crack opening displacement records. (a) Notched beams. (b) Short bars.

elliptical cracks, as sketched in Fig. 5 (a and b are the ellipse semi-axes). The stress intensity factor for this geometry was numerically computed in 1976 by Astiz [4, 5] and also by photoelastic techniques by the authors [6]. When $b > a$ the maximum stress intensity factor is at point A (see Fig. 5) and its value can be expressed as

$$K_1 = \frac{4P}{\pi D^2} \sqrt{\pi a} \sum_{i=0, i \neq j}^{4} \sum_{j=0}^{3} C_{ij} \left(\frac{a}{D}\right)^i \left(\frac{a}{b}\right)^j, \tag{3}$$

where P is the applied load and D is the bar diameter. The coefficients C_{ij} are given in Table 4. A

Table 4. Values of C_{ij}

C_{ij}	$j = 0$	1	2	3
$i = 0$	1.118	−0.179	−0.339	0.130
$i = 2$	1.405	5.902	−9.057	3.032
$i = 3$	3.891	−20.370	23.217	−7.555
$i = 4$	8.328	21.895	−36.992	12.676
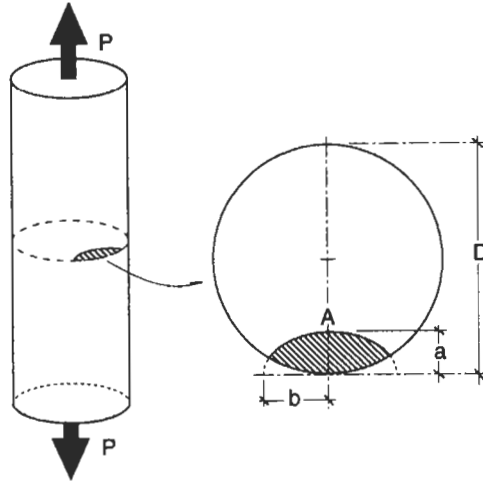
Fig. 5. Geometry and notation of the surface crack.

recent paper on this subject [7] provide more general expressions but the one given above is accurate enough for our purposes.

2.2.3. *Rupture load.* When Linear Elastic Fracture Mechanics is applicable, the rupture load can be deduced from

$$K_{\mathrm{I}}(P, a, \mathrm{geometry}) = K_{\mathrm{IC}}. \tag{4}$$

Taking into account (3), the rupture load is given by:

$$P = \frac{D\sqrt{\pi D}}{4} K_{\mathrm{IC}} \cdot M\left(\frac{a}{D}\right), \tag{5}$$

where the non-dimensional function $M(\xi)$ for small values of a/b (as in the considered examples) can be approximated by

$$M(\xi) = \xi^{-1/2} \cdot (1.0806 + 0.6386\xi - 2.4445\xi^2 + 13.463\xi^3)^{-1}. \tag{6}$$

2.2.4. *Comparison with failure data.* Figure 6 gives the rupture load P as a function of crack depth, a, for $D = 36$ mm and $K_{\mathrm{IC}} = 33$ MPa $\cdot$ m$^{1/2}$. Failure of the two prestressed bars happened at loads of 600 and 400 kN with corresponding crack depths of 0.92 and 1.50 mm. These two rupture data are drawn in Fig. 6. As can be seen there is an excellent agreement with theoretical predictions.

Two more rupture data of bars from the same batch, with small surface cracks similar to the reported ones, are also drawn in Fig. 6 and show the same good agreement. These additional data are experimental results of fracture tests with two precracked bars under axial tension. Precracking was achieved by fatigue using a three point bending assembly and a shallow starter notch with a straight front. Examination, after testing, of the two kinds of cracks—the service and laboratory cracks—showed no difference.

The low values of the bar fracture toughness and the crack-life surface defects allowed a failure analysis based on Linear Elastic Fracture Mechanics. The good agreement with experimental results and theoretical predictions gives further support to this working hypothesis.

3. DESIGN IMPLICATIONS

3.1. *Damage tolerance*

The analyzed failures reveal the importance of small surface cracks and provide a means of improving the performance of the prestressing bars when such damage may appear. The bars will
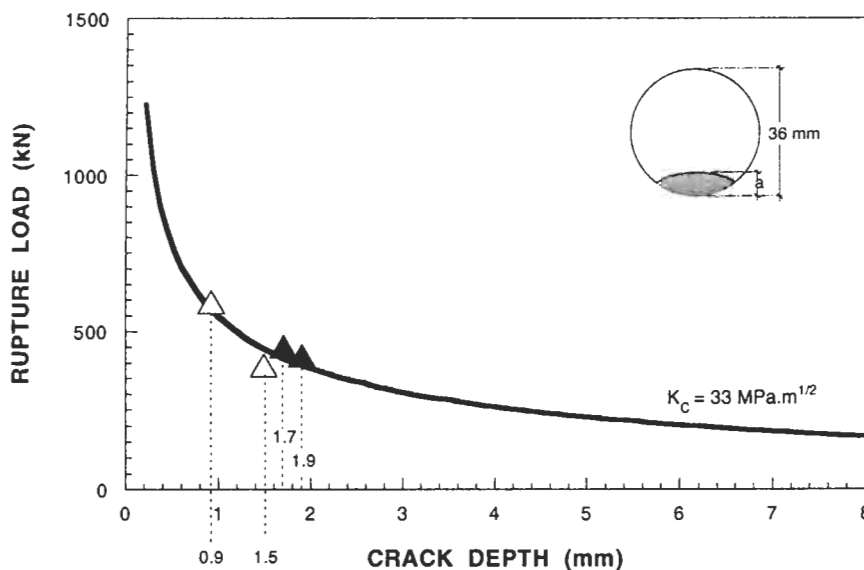
Fig. 6. Rupture load of a cracked bar as a function of crack depth (for $D = 36$ mm and $K_{IC} = 33$ MPa m$^{1/2}$). ($\triangle$), Actual cracks. ($\blacktriangle$), Fatigue cracks (laboratory).

be more damage tolerant if their fracture toughness is increased. A simple example illustrates this statement: consider what would happen if higher toughness bars were to sustain the recorded rupture loads—$0.46F_R = 600$ kN and $0.30F_R = 400$ kN. This situation is depicted in Fig. 7(a): if the fracture toughness were 60 MPa m$^{1/2}$ instead of 33 MPa m$^{1/2}$, the critical depth of a surface crack would be about 2.6 and 5.4 mm for 600 and 400 kN, respectively, while for $K_{IC} = 100$ MPa m$^{1/2}$ these figures rise to 6.4 and 10.6 mm. All these values are quite unrealistic for surface cracks, compared to the figures of about 1 mm measured in the broken bars. Higher toughness improves damage tolerance.

Damage due to cracks is much more dangerous than other kinds of damage, such as pits or notches. This was confirmed by testing several bars with artificial notches (the bars came from the same batch as the two broken bars). The results are shown in Fig. 7(b). Notches are not so sharp as cracks, since the curvature radius at the tip of a notch is finite. Artificial notches used in these tests had tip radii of 0.08 and 0.5 mm (see insert in Fig. 7(b)), giving a local stress increase, but not so high as in cracks. Experimental results depicted in Fig. 7(b) show that, for the same depth, cracks are more dangerous than notches, and notch performance is better the higher the tip radius. A review of brittle fracture of steel bars due to cracks or notches, a low temperatures or under high strain rates, is given in Ref. [8].

Figure 7 shows that brittle fracture prediction, the curve for $K_{IC} = 33$ MPa m$^{1/2}$, is a lower envelope for the failure load of a surface damaged bar. A higher envelope corresponding to plastic collapse can be easily derived when a perfect plastic behaviour is assumed. The final result for a straight front surface crack ($a/b \approx 0$) is:

$$P = \sigma_y D^2 N(a/D), \qquad (7)$$

where σ_y is a suitable yield stress, and the non-dimensional function $N(\xi)$ is given by

$$N(\xi) = \frac{\pi}{4} - \frac{1}{4}\arccos(1 - 2\xi) - \frac{1}{2}\arcsin[2^{2/3}(\xi - \xi^2)]$$

$$+ \frac{1}{2}(1 - 2\xi)(\xi - \xi^2)^{1/2} + 2^{-1/3}(\xi - \xi^2)^{1/2}[1 - 2^{4/3}(\xi - \xi^2)]^{1/2}. \quad (8)$$

Both curves are drawn in Fig. 7(b). Damage in the form of notches lay in between. Quantifying damage due to pits or notches is difficult on account of the many variables involved. Nevertheless,
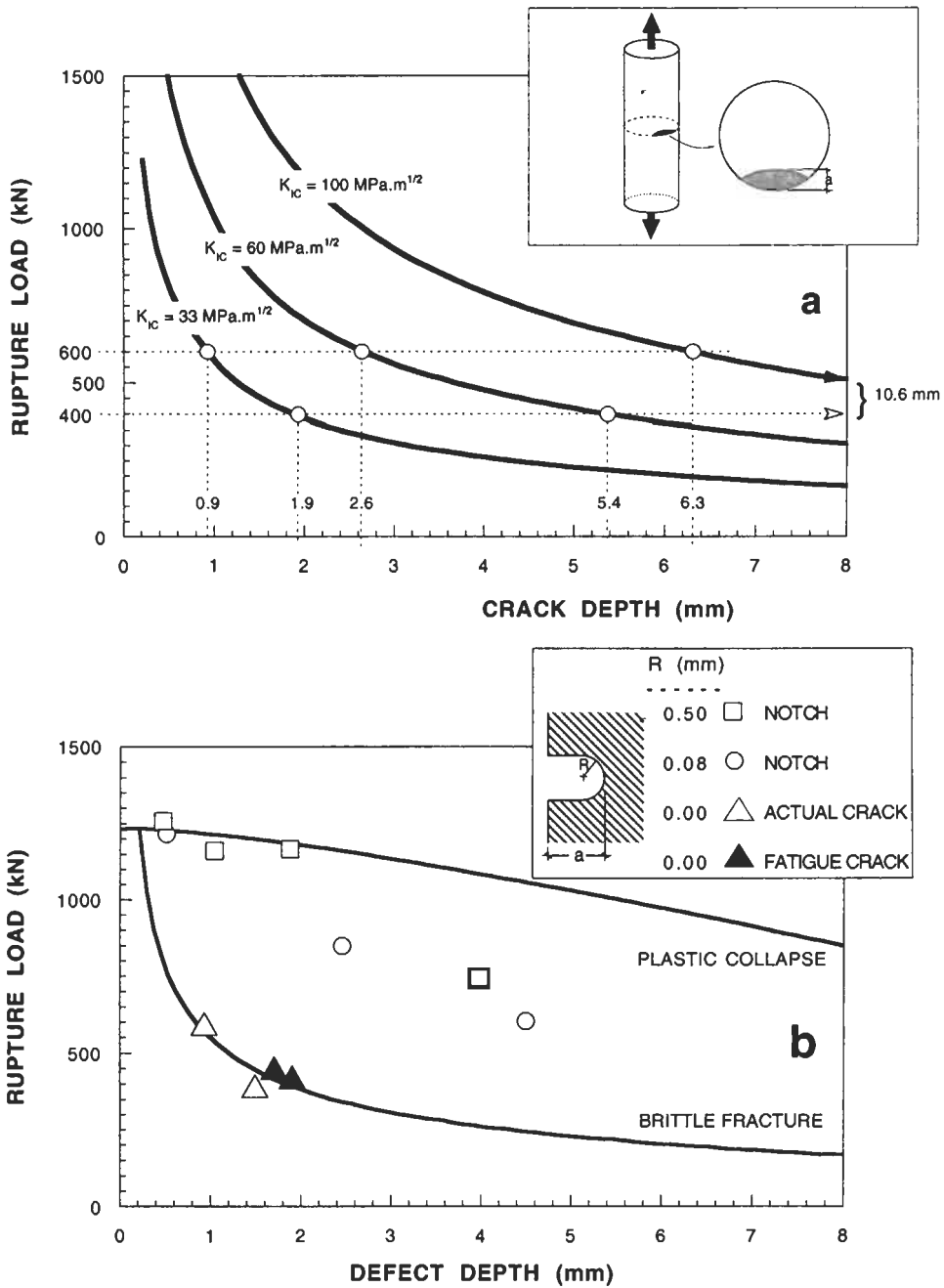
154

Fig. 7. Damage tolerance diagrams. (a) Cracks: influence of fracture toughness. (b) Notches: influence of tip radius.

Table 5. Critical surface crack depth

Fracture toughness (MPa m$^{1/2}$)	33	60	100
Critical crack depth (mm)	0.5	1.6	4.1

what appears clearly from the above results is that damage tolerance improves with increased fracture toughness.

3.2. *Final recommendations*

The analyzed failures show clearly that the usual requirements for prestressing bars—i.e., yield strength, ultimate tensile strength and ductility—are not enough to warn against brittle failures, if the risk of damage has to be considered. In this case study, the mechanical properties (recorded in Table 2) were higher than those required by the standards, and in spite of this, fracture occurred at very low loads—$0.3F_R$ and $0.46F_R$—due to damage in the bars.

The risk of such accidents would be greatly reduced, or even avoided, if the fracture toughness of the bars were measured (or known) and an estimation of the critical crack sizes made, by a simple exercise of damage tolerance as shown in this paper. For the scheduled working load—$0.60F_R = 780$ kN—the critical sizes for different toughness are given in Table 5.

These values are indicative of the defect size the designer can assume in different working scenarios. Clearly, cracks are more dangerous than notches or pits, even though cracks are less frequent. Nevertheless, cracks can develop from notches under repeated loads, by fatigue, or in aggressive environments, due to stress corrosion cracking for example.

Summing up: damage tolerance procedures can be used profitably as a complementary design criterion in prestressing with steel bars. The fracture toughness should be required as an additional mechanical property that can be measured according to well established standards. Knowledge of the toughness of the prestressing bars may be helpful to the designer and builder to compare, select or reject different batches.

REFERENCES

1. ASTM E 399-83, *Standard Test Method for Plane-Strain Fracture Toughness of Metallic Materials*, 1983.
2. ASTM E 1304-89, *Standard Test Method for Plane-Strain (Chevron Notch) Fracture Toughness of Metallic Materials*, 1989.
3. ASTM E 813-88, *Standard Test Method for J$_{IC}$, a Measure of Fracture Toughness*, 1988.
4. Astiz, M. A., PhD thesis, Universidad Politécnica de Madrid, Escuela de Ingenieros de Caminos, 1976.
5. Astiz, M. A., *International Journal of Fracture*, 1986, **31**, 105–123.
6. Astiz, M. A., Elices, M., Morton, J. and Valiente, A., *Society of Experimental Stress Analysis (SESA), Michigan Conference, U.S.A.*, 1981, pp. 277–282.
7. Levan, A. and Royer, J., *International Journal of Fracture*, 1993, **61**, 71–99.
8. Elices, M., in *Fracture Mechanics of Concrete: Structural Application and Numerical Calculation*, ed. G. C. Sih and A. DiTommaso. Martinus Nijhoff, 1985.

Fatigue

CATASTROPHIC FAILURE OF A RAISE BORING MACHINE DURING UNDERGROUND REAMING OPERATIONS

ALAN JAMES

Metallurgical and Corrosion Services Programme, MATTEK, CSIR, Private Bag X28,
Auckland Park 2006, Republic of South Africa

Abstract—This paper describes the investigation of the catastrophic failure of a raise boring machine used for underground reaming operations. The results of the investigation indicate that failure was due to the fracture of the 32 drive head bolts, 30 of which had failed as a result of corrosion-induced fatigue. Metallurgical examination confirmed that the bolts had been manufactured in accordance with the SAE J429 Specification. A number of recommendations have since been implemented by the mine, who have also introduced a quality system specifically for the control of drive head bolt sets. The equipment has now operated without problems for several years. © 1997 Elsevier Science Ltd. All rights reserved.

1. INTRODUCTION

The process of raise boring (or back reaming) has been in use for over 30 years, and has proved to be a very successful technique in underground mining operations. Its primary use is in the production of interconnecting vertical or near vertical channels (raises) between underground levels in mines. However, this method of rock drilling can also be used for producing channels at any angle between the vertical and the horizontal [1].

This technique of underground drilling was developed to overcome some of the problems of personnel safety in the mining industry. Previously, the process of drilling and blasting was used, which required people to enter dangerous areas of mine workings. The development of raise boring techniques also gave the mining industry a new method to construct long ore passes and ventilation raises which is economical in both time and cost.

Current raise boring operations are used to produce raises of up to 6.0 m in diameter and up to 1000 m in length.

2. REAMING PRINCIPLES

2.1. *Rock mechanics*

The process of drilling and boring in rock differs from other similar engineering operations in two respects [2]. Firstly, the diameters and lengths of holes and tunnels in rock are usually much greater than those made in other materials, and the volume of material removed in making them is especially large. Secondly, the mechanical properties of rock differ significantly from those of other engineering materials. The latter usually deform in an elastic–plastic manner, whereas most rocks deform in an elastic–brittle manner. Rock is also a very abrasive material.

Typical stress–strain curves for an elastic–plastic material and an elastic–brittle rock are shown in Fig. 1. A consequence of the brittle or work-softening nature of rock deformation is that it tends to be unstable, and results in the formation of chips when a rock surface is loaded by an indentor of any kind. Virtually all mechanical devices for drilling or boring rock behave like indenters. However, the precise form of these working tools varies considerably in accordance with the strength, brittleness and hardness of the rock which they are designed to work. In general, they do not cut the rock in the usual sense of the word, but cause it to spall away on either side of the area
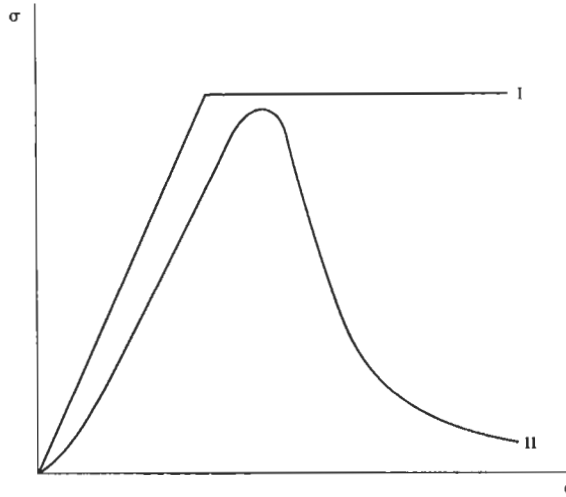
Fig. 1. Stress–strain curves for an ideal elastic–plastic material (I) and an elastic–brittle rock (II).

of contact between the tool and the rock surface. Hence, the volume of rock removed by the passage of the tool is greater than the volume of rock penetrated. Penetration rates can be estimated from factors such as the specific boring energy, the power delivered to the working face, and the uniaxial compressive strength of the rock. The latter, however, is not an accurate guide to boreability, which can vary by a factor of 3 or more for rocks of similar compressive strength.

2.2. *The reaming operation*

The principle of underground raise production involves two basic operations: firstly, the drilling of a pilot hole, and, secondly, back reaming. A diagrammatic representation of a raise borer being used for the slope drilling of a pilot hole is shown in Fig. 2. During the pilot hole drilling cycle, drill rods connect the raise boring machine with a bottom-hole assembly consisting of ribbed stabilizers, roller reamer and pilot bit. The rock debris is flushed to the surface and collected in a settling drain. Any common flushing medium can be used, i.e. air, water or foam.

After the pilot hole has been completed, a raise boring head is used to back ream the required raise between the underground levels. The raise boring head has a number of rock cutters to facilitate the reaming operation (Fig. 3).

3. BACKGROUND

The catastrophic failure of the raise boring machine occurred during the reaming of a 3.66 m diameter by 266 m long hole at a dip angle of 88° to the horizontal (i.e. almost vertical). All 32 bolts on the raise borer drive head failed after 119 m of reaming had been completed. Prior to the failure, no abnormalities had been reported and the operation had been running smoothly.

The raise borer had been subjected to a major overhaul approximately 2 years before the failure. An exploded view of the drive head assembly, with respect to the derrick and base plate, is shown in Fig. 4. To facilitate the overhaul, the equipment was moved from its underground location to the surface. All the drive head bolts were replaced. A cutaway diagram of the drive head installation, showing the relative positions of the cover, drive head bolts and body, is shown in Fig. 5.

Since overhaul, the raise borer had been used to ream a series of smaller diameter (2.44 m) holes 92, 97, 89 and 91 m in length. The medium used for flushing was mains water. After these holes were reamed, the equipment stood underground for a period of 3 weeks. The next hole that was reamed was 97 m long, and was produced using mine service water for flushing. Catastrophic failure of the raise borer occurred during the reaming of the subsequent 3.66 m diameter by 266 m long

BLOOIE ASSY.

AIR WATER INLET →

DISCHARGE ←

SLOPE DRILLING

DRILL PIPE

HEX STABILIZER

BIT REAMER
STABILIZER

TRI-CONE BIT

Fig. 2. Slope drilling of a pilot hole.

RIBBED STABILIZER(S)

SAVER SUB
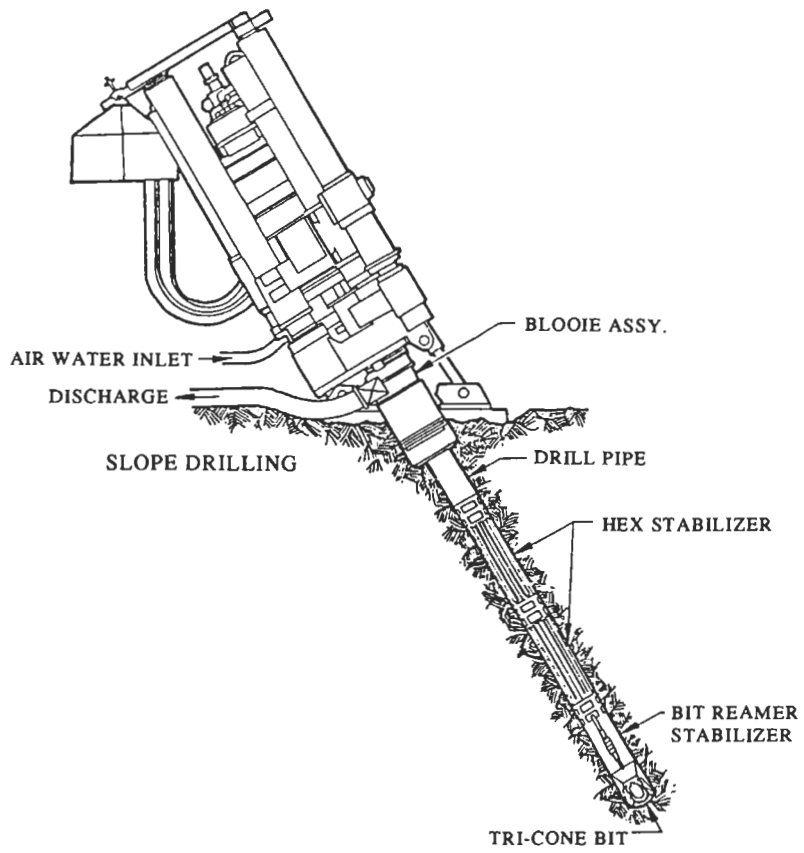
ROCK CUTTERS
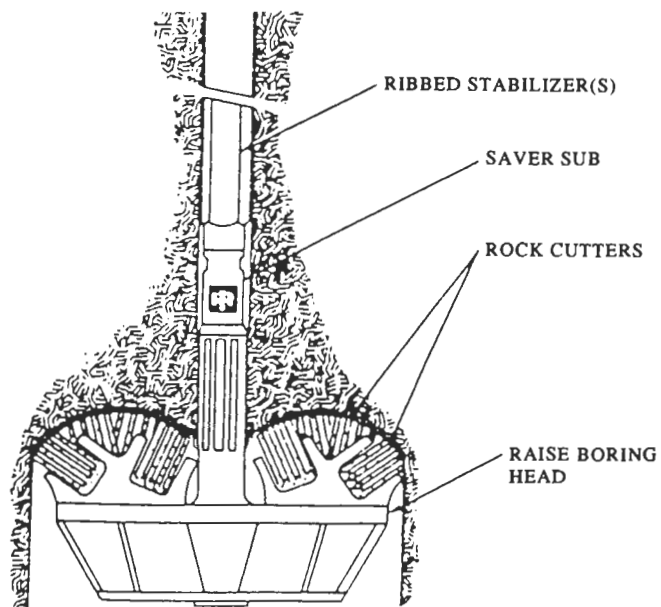
RAISE BORING
HEAD

Fig. 3. Raise boring head and rock cutters.
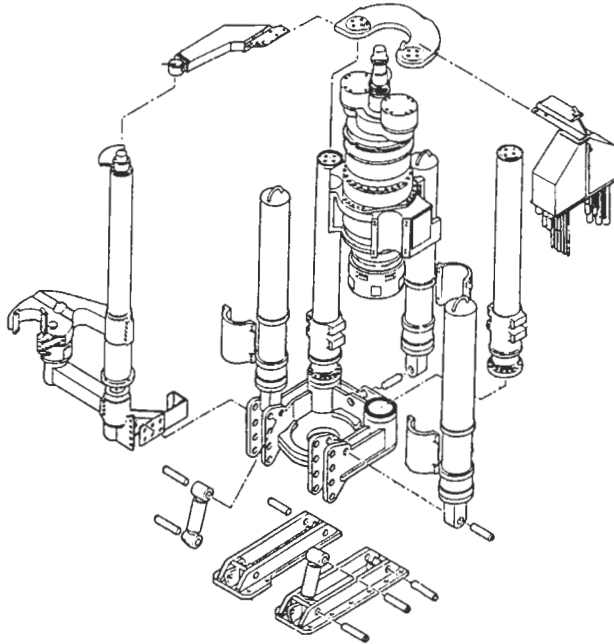
Fig. 4. Exploded view of the drive head assembly.

hole. The 119 m of rock had been reamed over a period of a few months at almost the full working capacity of the equipment. Mains water was used as the flushing medium.

The torque and thrust capabilities of the raise borer are as follows:

- maximum torque capacity: 494,876 N m (365,000 ft lb)
- maximum thrust capacity: 4454 kN (1,000,000 lb)
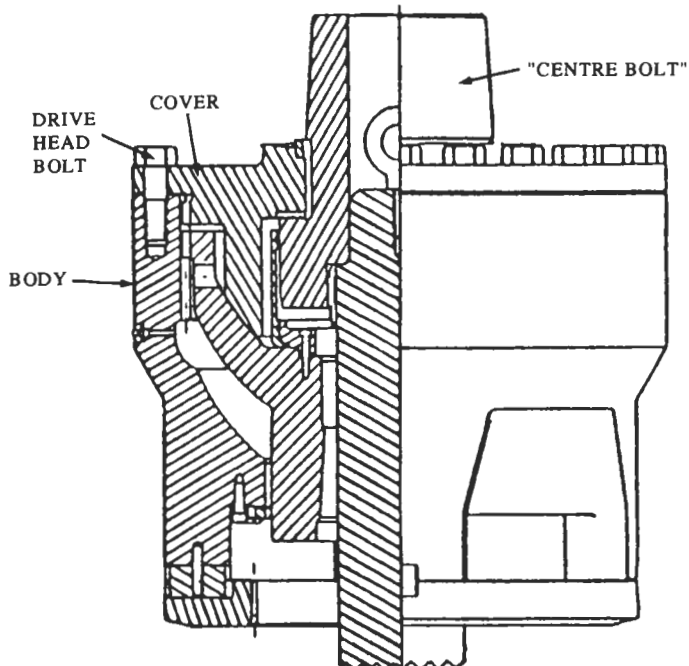
Fig. 5. Cutaway diagram of the drive head installation.

The applied torque and thrust during the reaming of the hole on which failure occurred was as follows:

- torque varied between 358,599 and 466,170 N m.
- the original thrust was thought to be constant at approximately 4454 kN: however, on further checking it was found that the actual thrust was 5033 kN, i.e. 13% above maximum.

By design, the drive torque is transmitted through the connection via splines, and the drive head bolts are intended to carry only the applied thrust.

The bolts are 32 mm (1.25 in.) in diameter by 89 mm (3.50 in.) long SAE Grade 8 hexagonal head cap screws having a torque specification of 1140 N m (840 ft lb). Prior to installation, all the bolts are coated with an anti-seize compound.

4. SITE VISIT

A site visit was made in order to carry out an inspection of the raise boring machine, which had been brought to the surface and had been dismantled in the company workshops. During "breaking-out", it was noticed that the torque of the drive head cap screw or "centre bolt" was well below the normal figure.

The fractured bolt sections in the locating holes had been extracted and clearly identified in clockwise sequence from 1 to 32 (position 1 being at the 6 o'clock position for reference purposes). It was not possible to extract the sections of bolts 21, 25 and 28 due to seizure in the holes. The fractured bolt sections were subsequently "matched" to their corresponding bolt head sections by fracture surface comparison. The original orientation of each bolt in the locating holes had been marked on the bolt heads.

It was clear from the position of fracture of the bolt sections still situated in the body of the machine and the positions of fracture of the other bolts that failure had occurred at or near the joint between the cover and the body.

The underside surface of the cover, including the area containing the locating holes, showed general rusting from the ingress of water.

5. EXAMINATION OF THE FRACTURED BOLTS

The fractured bolts were visually examined on-site, and then examined in the laboratory using a binocular microscope after suitable cleaning. Apart from bolts 7 and 28, which had failed by 100% tensile overload, the failure of the drive head bolts was associated with fatigue. A view of the fracture surfaces of bolts 19 and 20, showing typical areas of fatigue, is shown in Fig. 6.

Each bolt was assessed in order to estimate the amount of fatigue crack propagation with respect to the cross-sectional area. The results are presented in Table 1.

In order to try and understand the nature of the stressing which had produced the fatigue cracking, the orientation of the fatigue crack origin(s) on each bolt, with respect to the original orientation of the bolts in the locating holes, was determined. A diagram showing a plan view of the positions of the fractured bolts and the corresponding fracture origins is shown in Fig. 7.

The general surface condition of the bolts was found to be poor, with extensive surface corrosion and pitting corrosion in the threads (Fig. 8).

6. METALLURGICAL EXAMINATION

6.1. *Chemical analysis*

Three bolts were arbitrarily chosen for chemical analysis, the results of which are presented in Table 2.
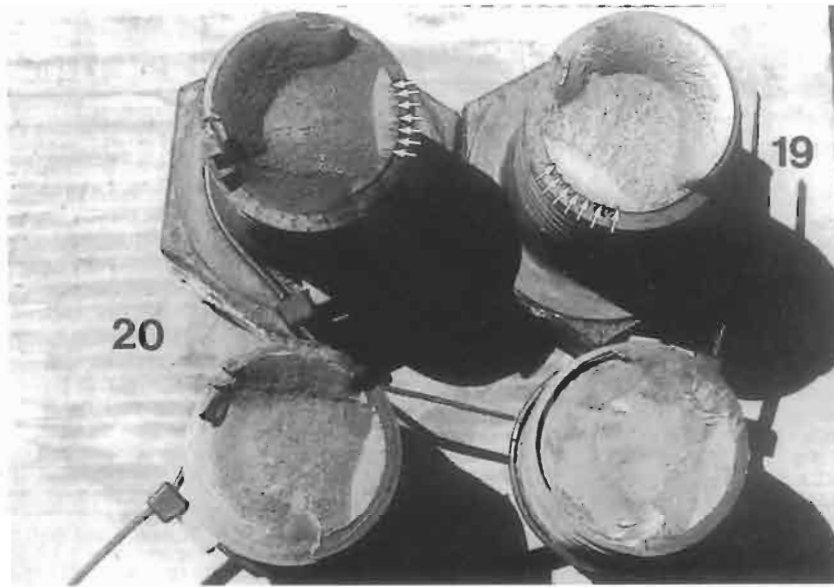
Fig. 6. Fracture surfaces of bolts 19 and 20, showing areas of fatigue from multiple origins (arrowed).

6.2. *Scanning electron microscopy*

The fracture surface of bolt 20, which showed a typical area of fatigue, was examined using scanning electron microscopy. At low magnification, the extent of the corrosion could be clearly observed, with the origins of fatigue crack initiation corresponding to corrosion pitting in the thread root. At high magnification, features typical of fatigue propagation were observed (Fig. 9).

6.3. *Optical microscopy*

Longitudinal sections were cut from bolts 3, 17 and 31, and prepared for optical microscopy using standard metallographic procedures.

In the unetched condition, the steel from which the bolts were manufactured was relatively free from non-metallic inclusions. Etching in 2% nital revealed a fine, tempered martensite micro-structure for each bolt, and no evidence of surface defects such as decarburization (Fig. 10).

Table 1. Area of fatigue crack growth relative to the cross-sectional area of each bolt

Bolt no.	Percentage area of fatigue	Bolt no.	Percentage area of fatigue
1	30	17	20
2	< 10	18	15
3	15	19	10
4	15	20	10
5	20	21	15
6	< 10	22	10–15
7	0	23	20
8	10	24	< 10
9	20	25	< 10
10	15	26	30
11	< 10	27	20
12	10	28	0
13	20	29	10
14	10	30	15
15	20	31	10
16	20	32	20

Fig. 7. Plan view of the cover, showing the positions of the fractured bolts and the corresponding fracture origins.

6.4. *Hardness testing*

Hardness tests were carried out on bolts 3, 17 and 31 using a Vickers-type machine, giving an average figure of 385 HV. (The SAE J429 Specification for Grade 8 bolts has a core hardness requirement of 33–39 HRc, equivalent to 327–382 HV per ASTM A370). The hardness figures achieved on the bolts is equivalent to an ultimate tensile strength of ± 1230 MPa (ASTM A370).

7. DISCUSSION

The examination of the raise boring machine has established that 30 of the 32 drive head bolts have fractured as a result of fatigue cracking. The other two bolts have fractured in a purely tensile overload manner.

The fatigue cracking has originated from multiple positions in the thread roots, indicative of a high stress concentration and/or corrosion fatigue. Fatigue is characteristic of cyclic stressing, and the small ratio of fatigue area to final tensile overload area on the bolt fracture surfaces indicates a high operational stress. All the areas of fatigue on the bolts are associated with corrosion pitting.

Table 2. Chemical analysis of three bolts

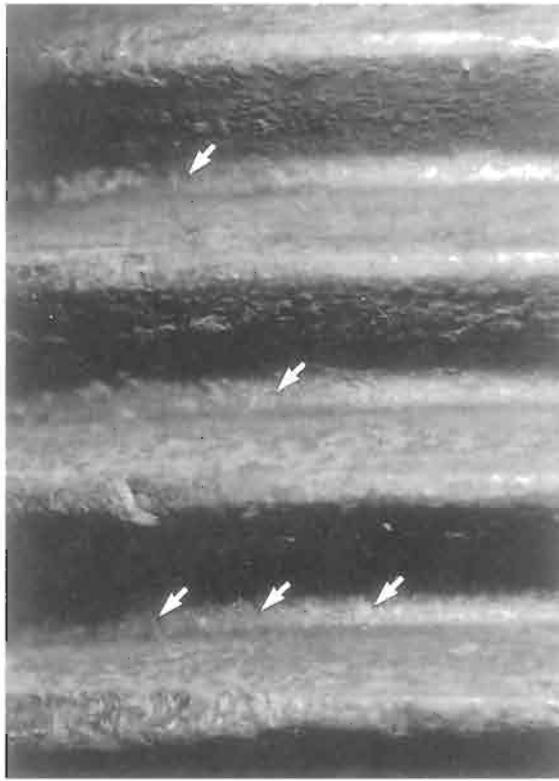| Bolt no.	Mn	S	P	Si	Cr	Mo	Ni	Cu	Al	Fe	
2	0.43	0.89	0.021	0.013	0.22	0.34	0.29	0.01	0.01	0.036	Balance
16	0.50	0.69	0.030	0.013	0.26	0.37	0.26	0.01	0.01	0.039	Balance
23	0.48	0.69	0.031	0.013	0.25	0.36	0.25	0.01	0.01	0.041	Balance
SAE* J429 Grade 8	0.28–0.55		<0.045	<0.040							Balance

166

Fig. 8. General surface condition of the bolt threads, showing evidence of pitting corrosion (arrowed).

The operating system of the raise borer must, therefore, be assessed in order to eliminate the high cyclic stressing and/or the corrosion.

It can be seen from Fig. 7, which indicates the orientation of the various fatigue crack origins relative to the original assembly position of the equipment, that there is no clear crack initiation pattern, and, therefore, no definitive pattern of cyclic stressing. However, the more-or-less random nature of the crack initiation is consistent with fracture by a corrosion fatigue mechanism. If the cover was "dishing" upwards during operation, this would have the effect of transmitting a high cyclic tensile stress on the inner region of the bolts, i.e. where cracking has originated on bolts 3, 4, 6, 8, 15, 16, 26 and 32. Similarly, for the downward "dishing" of the cover, the cyclic tensile stress would be greater where cracking has originated on bolts 12, 13, 18, 21 and 22. Clearly, the stress system in this case is complex. Measurements carried out on the cover indicated that the item was "dished-in" (downwards) by only 0.01 mm. The contact face of the body was also found to be perfectly flat so there was no apparent major permanent deformation of the cover or body.

The "centre-bolt" torque was found to be well below the normal figure during dismantling. This could have had the effect of allowing more vertical movement of the drive head cover. With the equipment working under such severe operating conditions it is essential that all cap screws and bolts are torqued correctly in order to minimise movement.

Based on the 552 mm^2 cross-sectional area of the drive head bolts (26.5 mm from thread root to thread root) and the approximate ultimate tensile strength of 1230 MPa, each bolt could theoretically withstand a tensile load of 679 kN before failure, and, therefore, the set of 32 bolts could withstand a load of 21,728 kN before failure. Considering a total thrust pressure of 5033 kN (the total thrust pressure includes the mass of the drill string) and the 32 bolts correctly assembled, the system is therefore operating at a factor of around 4.3. This will, however, be reduced due to the combined stress concentration effect of the thread root, and, more significantly, by the effect of corrosion pitting.

During assembly, the drive head bolts are liberally coated with a proprietary anti-seize compound,
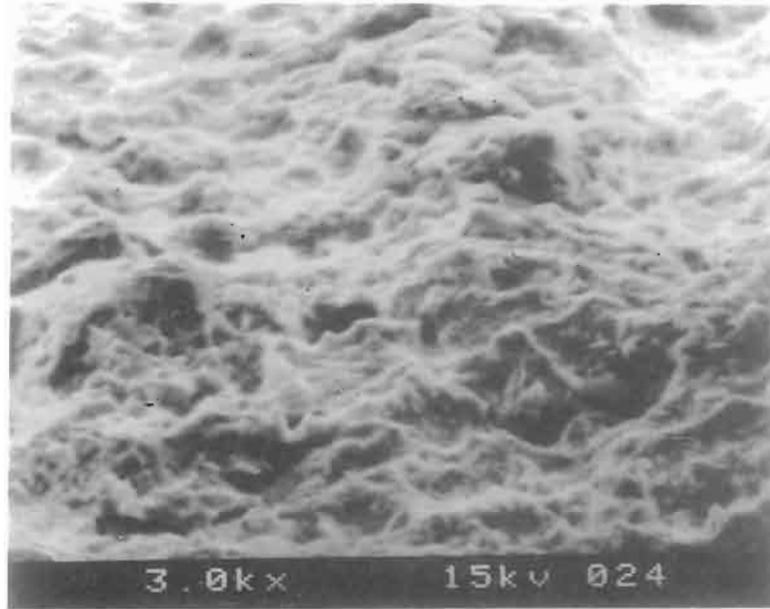
Fig. 9. Scanning electron fractograph showing features characteristic of fatigue. × 3600.

which is described as a high-temperature, extreme-pressure, corrosion-resistant assembly lubricant. This was very difficult to remove prior to the laboratory examination, but, clearly, it does not afford protection to the surface of the bolts. Water seeping across the contact area (joint) of the cover and body to the drive head bolt locating holes can, therefore, penetrate the anti-seize compound.

A water additive is used for its lubricating and hole cleaning properties, but only if the system is a closed loop. In addition, the additive would have no corrosion-inhibiting effect on the water. A medium such as an oil-based red lead primer should be used at the connection joint between the cover and the body in order to prevent water from reaching the drive head bolts. The torque tightening of the 32 bolts will cause the compound to "spread" and allow satisfactory sealing of the mating surfaces.
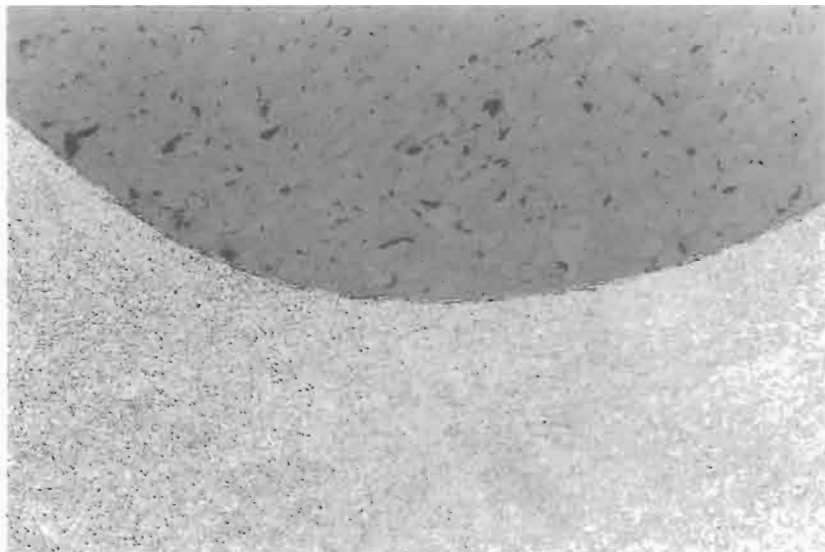

Fig. 10. Longitudinal section of a bolt thread root showing fine tempered martensite, and no material or manufacturing defects. Etched in 2% nital. × 285.

The metallurgical examination of the bolts showed that the failure was not associated with any material or manufacturing defects. The bolts conformed to the specification requirements in all respects.

8. CONCLUSIONS

(1) The catastrophic failure of the raise boring machine is associated with the fracture of the 32 drive head bolts. Thirty of the bolts have failed as a result of corrosion-induced fatigue.
(2) The bolts have failed due to a combination of high cyclic stressing induced by the operation of the equipment at 13% above maximum thrust and corrosion from the water in the flushing system.
(3) Chemical analysis, microscopic examination, and hardness testing have established that the bolts conform to the required SAE J429 Specification.

9. RECOMMENDATIONS

(1) To prevent corrosion of the bolts the following measures are recommended:

   (a) An oil-based red lead primer should be used to create a barrier at the cover–body connection.
   (b) Mains water should be used at all times for flushing.
   (c) Equipment should not be stored underground for any length of time.

(2) Excessive thrust pressures during operation should be avoided, i.e. the equipment should be used within the limits for which it was designed.
(3) All components should be torqued to the correct figure to prevent excessive movement in the drive head.

10. FINAL NOTE

Since the investigation, a strict quality control system has been introduced at the mine for the control of bolt sets used on raise boring machines. In addition, all the report recommendations have been implemented, and the torque settings on the drive head bolts have been increased with the approval of the machine manufacturer. Following subsequent finite element modelling, the thickness of the cover and the length of the drive head bolts have been increased for greater stiffness. The equipment has now operated without problems for several years.

REFERENCES

1. Hammond, I., *Australian Mining*, 1992, **84**(5), 14–18.
2. Cook, N. G. W. and Lancaster, H. F., in *Tunnelling in Rock* (a course of lectures held at CSIR, Pretoria, 22–26 October 1973), ed. Z. T. Bieniawski. Pretoria, 1973.

Premature fracture of a composite nylon radiator

P.R. Lewis*

Department of Materials Engineering, Faculty of Technology, The Open University, Walton Hall, Milton Keynes MK7 6AA, U.K.

Abstract

Fracture of a GF nylon composite radiator occurred in a new car, leading to seizure of the engine. The fracture probably started at a cold slug or void present on an unusually large weld line in the radiator, itself probably created by poor moulding conditions. Rather than being a design fault, the failure was probably caused by lack of quality control during injection moulding. © 1999 Elsevier Science Ltd. All rights reserved.

Keywords: Radiator; Nylon; Composite; Void; Weld line; Fracture

1. Introduction

A new design of radiator tank failed on a new car during test driving. The tank was constructed from glass-filled (GF) nylon, a composite material used in engine compartments for its temperature resistance and strength. Many inlet manifolds, such as that on the new Jaguar XK8 for example, are now made from GF nylon 6,6 using the lost-metal injection moulding process [1].

The car had only travelled about 500 miles before catastrophic failure of the cooling system, which led to seizure of the engine. Some 200 similar prototype tanks had been produced and fitted to similar cars, and the manufacturer was concerned that there might be a design problem. Although they had considerable experience with the material in other radiators, the bodies were moulded by a sub-contractor elsewhere.

They therefore wished to know how the crack had been formed in the radiator, and whether the problem was due to faulty material, poor design or manufacture, or a combination of such causes. A programme of microscopy was undertaken to examine the fracture surface and other features of the moulded tank. A new, unused tank was used for comparison. Mechanical testing was also used to examine the quality of the material.

---

* Tel.: 01908 653278; Fax: 01908 653858

2. Survey of failed whole radiator

The failed part was examined for its surface quality first, and key features then examined with an optical microscope. SEM was used to resolve details of interest.

2.1. Macroscopic inspection

The radiator comprised a single moulding (Figs 1 and 2) with a centre gate, judging by the large sprue remnant in the centre of the underside (Fig. 3). The clean appearance of the sprue suggested operator cut-off, its relatively large diameter of ca 1 cm being necessary to allow the high viscosity
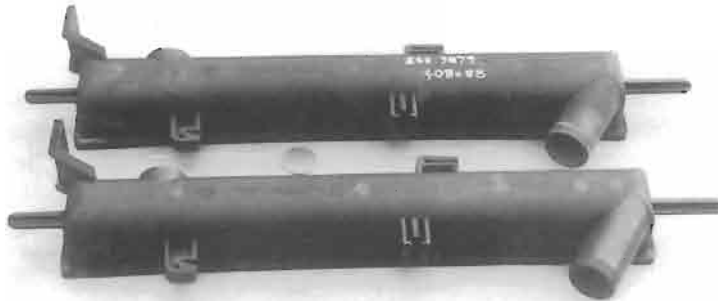

Fig. 1. Failed and new radiator boxes compared. The upper, failed sample cracked after 500 miles in service.
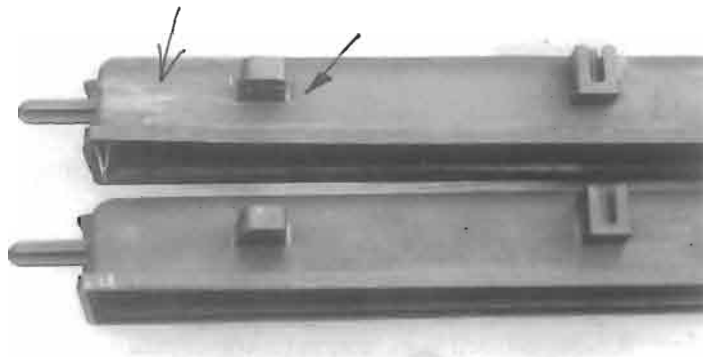

Fig. 2. Comparison of lower ends of upper, failed box and new box below. Closed arrow shows brittle crack which ran along inner corner of adjoining fan buttress. Open arrow shows contamination from leaking cooling water when tank was in situ.
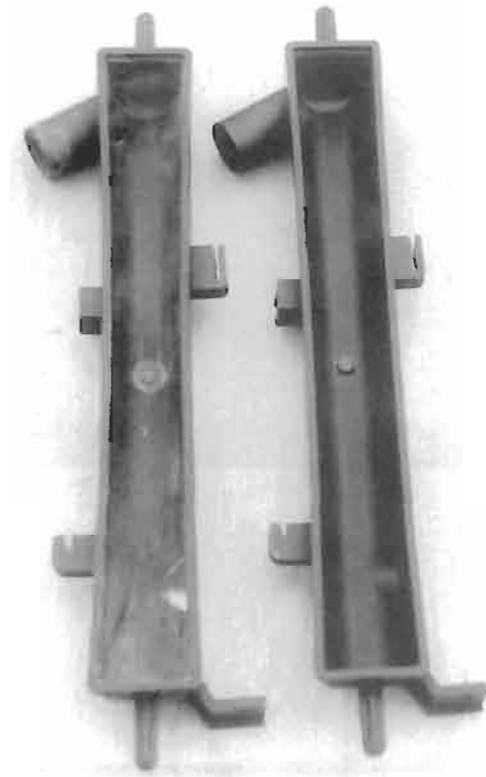
Fig. 3. Comparison of dimensions of failed (LHS) and new radiator boxes. Note longitudinal distortion of failed box.

glass-reinforced nylon 6,6 compound to enter the tool cavity smoothly. The failed tank is compared directly with a new moulding taken from the same batch in the three figures. A small amount of carbon black had been added to the compound to give a matte black colouration. Both tanks were date stamped, indicating that they had been moulded only recently.

Direct comparison of the tanks showed the failed tank to be distorted along its greatest axis, the sidewalls bulging inwards, as shown in Fig. 3. Such distortion can be caused by relaxation of internal frozen-in strain developed during moulding at temperatures below normal, or low melt temperatures in the barrel of the moulding machine. The tank had experienced only a few cycles from ambient temperatures and pressures up to working conditions in excess of 100°C and 25 psi over atmospheric pressure. Such conditions allow internal chain orientation to relax to the equilibrium state owing to the extra thermal energy provided for diffusion.

2.2. The crack and adjacent features

The single crack which had led to loss of water pressure and loss of cooling action for the engine, was situated near an external buttress, used to support a nearby fan. Tidemarks were visible immediately next to one end of the crack, their position showing the tank to be placed in a vertical,
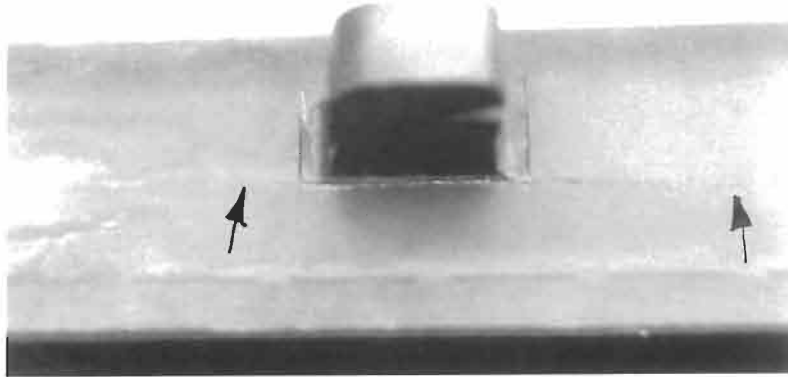
Fig. 4. Macrograph of brittle crack, running along stress concentration of buttress corner, and ending at points shown by closed arrows.
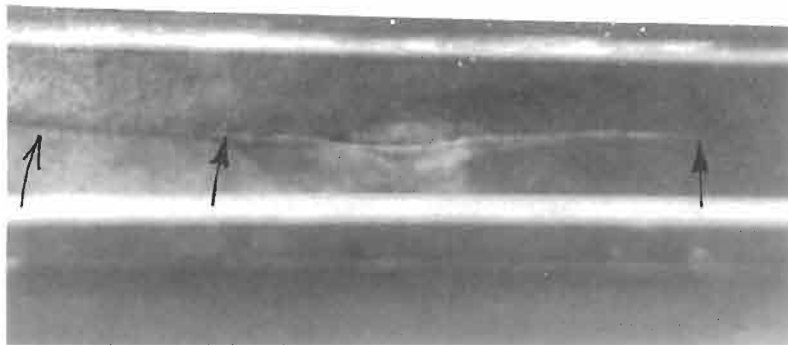

Fig. 5. Macrograph of brittle crack on inner surface, with ends shown by closed arrows. Weld line at left (open arrow) co-linear with crack, and surrounded by extensive flow line pattern.

upright position when in use on the car. The crack was brittle in nature, and extending ca 6.3 cm internally and almost the same distance externally (Figs 4 and 5).

The external surface was clear of any other major defects, and no defects were at first apparent on the inner surface owing to a superficial deposit from the cooling water system. On gentle rubbing, however, very clear traces of flow line patterns could be seen over much of the inner surface. Such patterns were revealed because the ends of the glass fibre reinforcement tend to roughen the otherwise smooth surface, and they also tend to be aligned with the melt flow, so will collect particles and show any major changes in fibre or melt orientation. Figure 5 in particular,
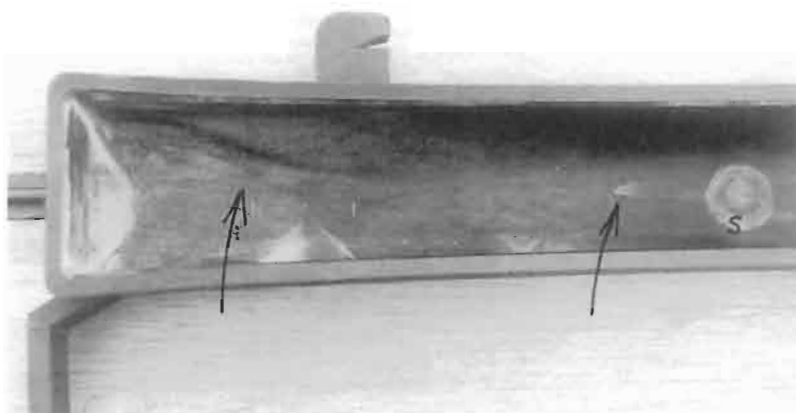
Fig. 6. Close-up of top inner surface of failed box showing complex flow lines (open arrow, left) and sprue (S). Cold slug near sprue at centre (open arrow, right).

shows a serious weld line surrounded by an extensive flow line pattern, the weld line leading directly into the crack.

The flow pattern could also be traced further away from the crack (Fig. 6). It appeared to emanate from the sprue, and was aligned towards one of the far corners of the box. A defect found close to the sprue, comprised a deep, short irregular weld line often known as a 'cold slug'. Such defects are generally caused by incomplete melting of the moulding pellets, whose external shape is thus partly preserved in the melt (Fig. 6).

Whiting gently rubbed into the inner surface of the new box revealed a flow line at a very similar position, under the fan buttress. However, not only was this flow line less severe, it was also clear that the overall flow pattern thus shown was quite different to that in the failed box. In particular, there were no cold slugs, and the flow pattern was absent near the sprue.

2.3. Etching experiment with new tank

New tanks of slightly different design, but made from the same material, were used to measure the intrinsic strength of the material as well as investigate the internal structure of the moulding. A new tank was sectioned and polished for microscopy. The exposed section was etched with chromic acid, a method which reveals internal structure by selectively removing the polymer matrix (Figs 7 and 8). Etching revealed first, voids ranging in size from ca 0.3 mm (or 300 μm) to less than 20 μm in diameter. The largest voids were detected in the centre of the thick edge section (Fig. 7), the smallest visible at this scale tending to occur more widely in the centre of the thinner wall section (Fig. 8). The etchant also revealed changes in fibre orientation, especially evident in the region between thin and thick sections of the edge (Fig. 7), but also present elsewhere in both specimens. The effect is caused by changes in orientation of the polymer melt, since the glass fibres tend to align themselves with the laminations of the melt as injection into the tool cavity occurs during hot moulding. The short fibres tend to align parallel to the surfaces of the tool, where
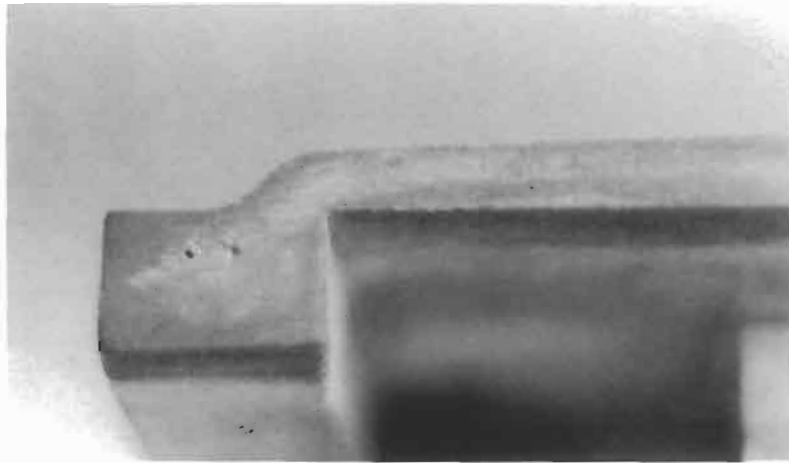
Fig. 7. Macrograph of abraded and polished section through edge of new radiator box, after light etching with chromic acid. Voids are present in the thick edge section, and change in fibre orientation is shown along the thinner section by shading.
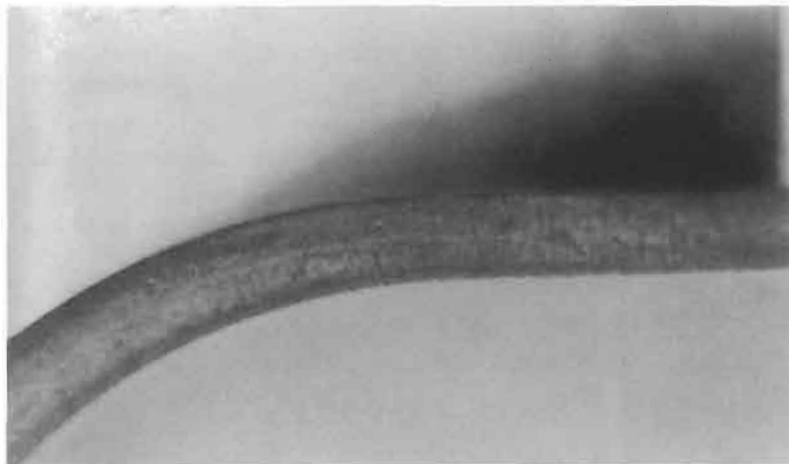

Fig. 8. Macrograph of curved thin section of new radiator box after abrasion, polishing and chromic acid etching. Change in fibre orientation can be clearly seen at the left (arrows), with a skin/core effect, and microvoids are present in the interior.

parallel laminar flow occurs, but tend to tumble towards the interior, where the polymer laminae are folded into a much more complex pattern. Here, the orientation of the fibres is much more random, so the light reflected from the section is lighter in tone. On the other hand, light is absorbed by preferential orientation of the fibres at the surfaces. The effect is generally known as the 'skin/core effect' [2].

Unfortunately, the ideal tends to break down when real moulding sections are examined in detail. The skin/core effect was seen at its best, ideal form at the left-hand part of the thinner section (Fig. 8). Here, there was a clear skin approximately 0.5 mm thick on both inside and outer
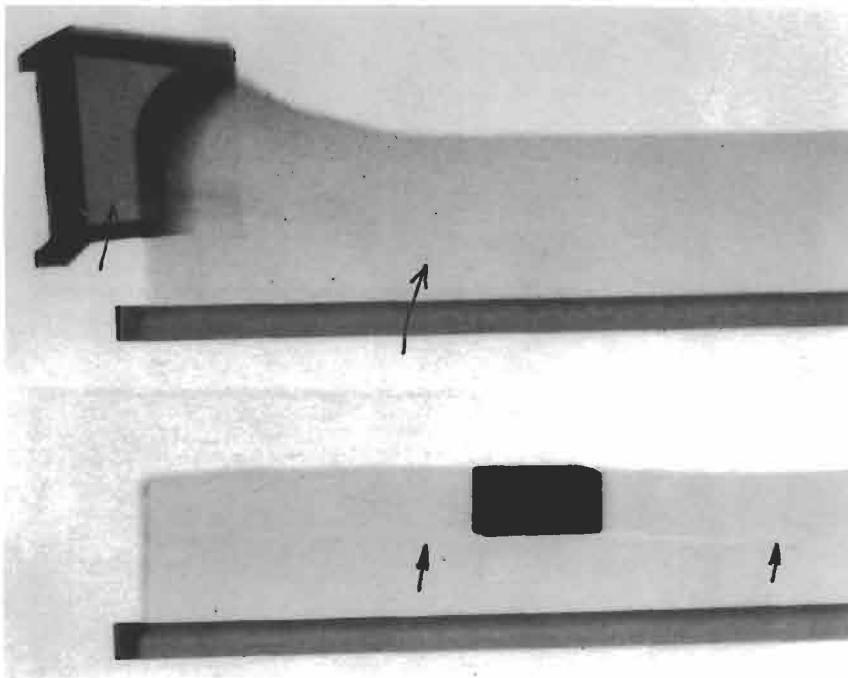
Fig. 9. X-radiograph of side of new tank (top) and part of failed tank (bottom). Trace of flow lines can be seen in the upper radiograph (between the open arrows). The crack is well shown in the lower section (solid arrows). The thick lower edges of both radiographs show variable density along their length due to internal voids.

surfaces, but it increased in size towards the middle part of the section, and finally broke up into a more complex region on the right-hand side of the figure. The oriented skin appeared to be much thicker in the edge section of Fig. 8, and the skin/core effect less clear cut towards the right-hand part of the thinner wall abutting the edge buttress. The voids tended to be more prevalent in the randomly oriented core parts of the sections, especially in thicker parts of the moulding.

2.4. Radiography

Some of the sections were radiographed using soft X-rays provided by a medical source [3, 4]. They showed the critical crack in excellent detail, and also provided evidence of the flow lines and clumping of fibres seen in the etched sections (Fig. 9). One shot from the failed tank, showed the faint trace of a 'cold slug' near the sprue. It reinforced an earlier observation (Fig. 6), giving an important clue to the cause of failure, because it indicates incomplete melting of the granules used to feed the injection moulding machine.

3. Microscopic examination

It was important to examine the fracture surface, for determining the crack morphology. Since the crack was trapped in the solid side of the tank, it was necessary to break the material in a
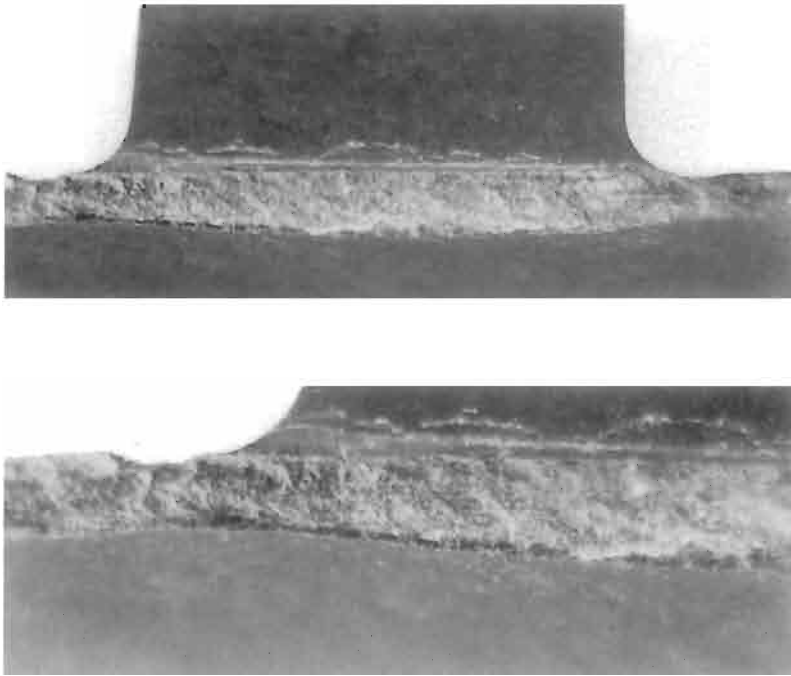
Fig. 10. Close-ups of main crack near buttress corner. Note lower edge shows what appears to be a weld line running into the bulk material.

controlled fashion so as to liberate the crack surface. The process was tackled in two stages, first involving cutting along the main corners in the failed tank, so as to produce a 'lay-flat' set of samples. One interesting result of this procedure was that the outward bulging in the whole tank was reversed, so that the sides bulged inwards (cf. Fig. 3). It was also noticed that the material everywhere in both samples proved rather brittle, as perhaps what one might expect from the high filler content of 30% glass fibre.

3.1. The fracture surface

The second part of the procedure involved liberation of the crack (Fig. 10). The fracture surface was later plated with gold for SEM. This allowed detailed inspection of the 10 μm diameter fibres present (Fig. 11). The gold treatment was also helpful in enhancing the contrast for optical microscopy (Fig. 12).

3.2. Tidemarks from the leak

The side of the external buttress just by the critical crack showed several stains produced by escape of cooling fluid, and comprised a brown tide line underlying a set of white tidemarks (Fig. 10). The white marks indicate a series of small contamination incidents, possibly five or more before final failure. Each may mark a point when the crack or cracks connected the inner reservoir
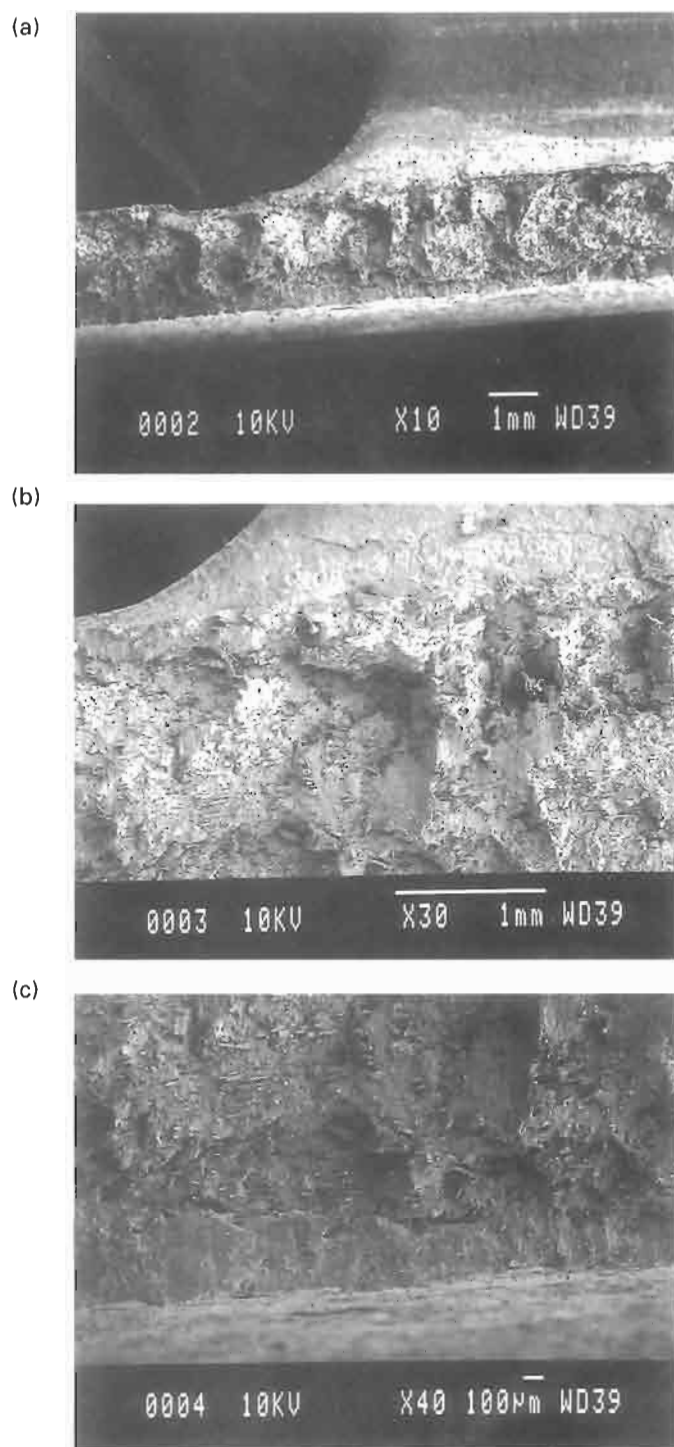
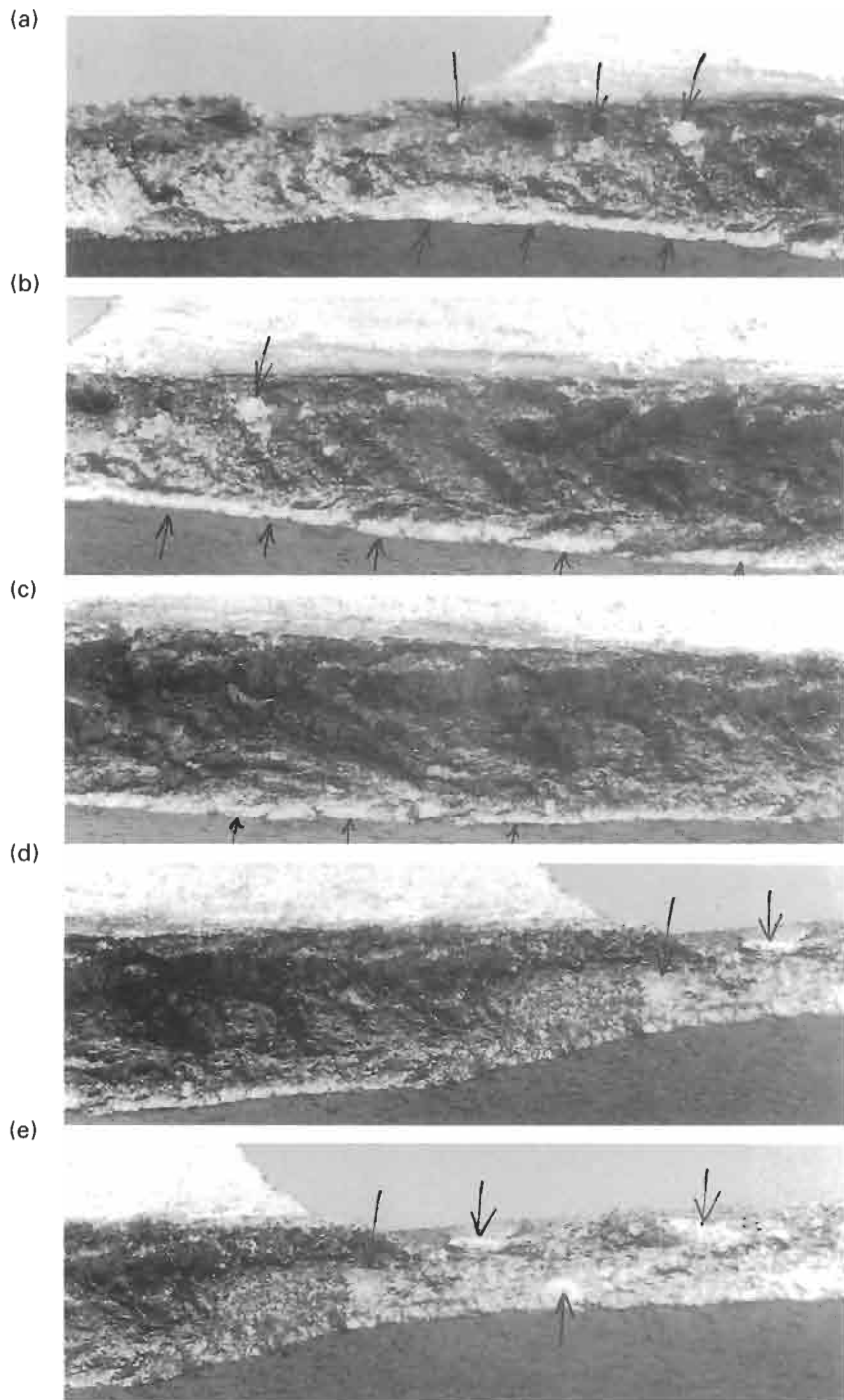Fig. 11. Various SEM shots of fracture surface.

Fig. 12. Panoramic sequence of gold-plated fracture surface, left to right across crack from top to bottom. Remnants of cold slugs and lower weld line shown by open arrows.

to the exterior, so allowing seepage of cooling fluid to the outer surface of the tank. This occurred during use of the car, so pressurising the cooling system, subjecting the outer skin to tension and initiating cracks. It suggests that the several cracks propagated until penetration to the reservoir occurred, leading to small spurts of fluid being ejected onto the adjacent buttress.

It is tempting to suggest, judging by the size of the brown stain, that the initial leak occurred just by the left-hand corner of the buttress (Fig. 11). Not necessarily so. The tank in use is vertical, so if leaks were occurring anywhere above this corner, liquid would tend to collect here as a bead since it would be adhering to the corner created by the buttress and the adjacent tank surface.

So what defects were visible on the fracture surface? One feature was the several smooth, irregular zones, most clearly seen in the optical macrographs of Fig. 12. There were several areas where such features occurred: a smaller cluster under the first buttress corner; a group near the second buttress corner and a linear, shallow zone on the underside of the fracture surface. The irregular form of the first two groups suggested that they may represent fragments of the original pellets used in the moulding process which have not fused together, and thus represent lines of weakness within the solid material. They could thus be most closely related to the cold slug defect found on the inner surface of the moulding, near to the sprue (Fig. 6) and one of the radiographs. The linear zone was the clearest indication of a 'true' weld line, which would be formed when the pellets have lost their original shape due to melting, but then two streams of molten plastic have impinged without fusing. The smooth areas in the interior could also represent internal weld zones.

3.3. SEM examination of fracture surface

High magnification SEM examination of an area near the first buttress showed a widely varying microstructure [Fig. 11(a)]. Some areas appeared free of fibres, while others possessed a dense distribution of broken fibre ends. Fibre orientation in the area below the left-hand corner of the fan buttress appeared to be uniform, and oriented to the buttress and neighbouring external surface. At a slightly higher magnification, Fig. 11(b) shows the virtually fibre-free part at the inner edge of the fracture immediately below the first buttress corner. A crack branching directly into the bulk delineates the internal edge of this feature, which represents the linear weld line mentioned above. The smooth surface of this zone contrasts sharply with the very rough surface immediately above, where numerous fibre ends protrude from the surface. Voids may be present just above this zone. The final plate [Fig. 11(c)] shows the lower weld line next to the inner surface below the buttress.

So where did the cracks start? There are numerous points or zones which could represent origins: the most likely positions are the two zones near to the corners of the fan buttress, which is a fairly severe stress concentration, where extra stress magnification will have been created by latent defects such as voids, cold slugs or weld lines.

4. Mechanical tests on tank material

It was important to conduct some simple tensile tests on bars cut directly from both new tanks and the failed tank to determine the intrinsic strength of the material, in both the failed and new

boxes. The ideal samples to examine would be those cut across suspected weld lines, since then the defects would be subjected to the highest stress when the samples were pulled in tension.

Four samples were cut, two from the new tank in a region showing serious flow lines, and two from the failed tank showing similar flow lines, but well away from the failure crack. One of each pair was cut parallel to the flow lines, the other at right angles to the flow lines. The samples were about 7 cm long, and possessed a ca 1 cm narrow central region about 5 cm long, so giving a dumbell shape. The samples were cut very carefully using a small hacksaw along the pre-marked shape, and polished by hand with a series of finer emery papers to remove any edge imperfections which could cause premature fracture.

All the specimens were tested at room temperature (ca 25°C) and ambient humidity (ca 50%), using a constant strain rate of 0.1 mm s^{-1}. Three of the four samples broke centrally, the fourth (No. 2) on the edge of the shoulder. All the samples broke in a brittle fashion, i.e. the two parts of the fracture surfaces could be fitted back together. The results were as follows:

Sample No. 1 (new, lateral) $\sigma_\beta = 84\,\mathrm{MN\,m}^{-2}$

Sample No. 2 (new, parallel) $\sigma_\beta = 81\,\mathrm{MN\,m}^{-2}$

Sample No. 3 (old, parallel) $\sigma_\beta = 80\,\mathrm{MN\,m}^{-2}$

Sample No. 4 (old, lateral) $\sigma_\beta = 55\,\mathrm{MN\,m}^{-2}$

The elongation to break was very similar for the first three samples, at approximately 9%, and 10% for the final sample.

It may be noted that the best result of 84 MN m^{-2} calculated for sample No. 1 fell somewhat below the ideal value given in the data sheet for this polymer (140 MN m^{-2}). Sample No. 3 appeared to have failed from a surface tool impression mark, present as a sharp corner across part of the dumbell, for example. Inspection of the fracture surfaces, however, showed them to be reasonably free of internal voids and cold slugs of the kind found in the fracture surface (Fig. 12). All the fracture surfaces showed a central 'spine' or cusp indicative of skin-core control of fracture, quite unlike that of the critical fracture. The calculated elongations to break are rather greater than the value of 6% quoted on the same sheet, both strength and elongation to break being given for samples conditioned to ambient temperature and humidity essentially identical to those used here. Comparison of the tensile strengths showed that the material from the new tank is superior to that from the failed tank. Although there were visible flow lines in all the samples, failure did not seem to be related to them in any clear, unambiguous way. In general, the tests reinforced earlier impressions when cutting the tanks for analysis of relatively stiff but brittle mechanical behaviour. The addition of 30% chopped glass fibre improves the stiffness of nylon, but at the expense of strength.

5. Discussion

A reasonably clear picture of the failure emerged as a result of detailed examination of the critical fracture surface, and comparison of the properties of new and unused tanks. The critical crack probably resulted from the coalescence of several smaller cracks below the fan buttress.

There were several types of defect seen in the fracture surface here, including a large weld line, cold slug fragments and voids. The latter are especially likely to form at or near a thickening of the tank wall (e.g. Fig. 7). Judging by the several white stains observed on the buttress surface immediately above the lateral corner, it is likely that there were several very slow leaks before the final, catastrophic failure when the cracks propagated catastrophically. The bead would have formed during this phase of the failure. It was possible to quantify the effect of the several weakening mechanisms at work in the failure. The initiating mechanisms are:

1. the geometric stress concentration at the buttress corner;
2. internal voids;
3. fragments of cold slug adjacent to the corner; and
4. frozen-in strain due to cold tool or cool melt conditions when moulded.

The maximum tensile stress to which the outside of the side wall is exposed can be estimated by simply assuming that the tank can be modelled by a cylindrical pressure vessel. The maximum stress developed in such a vessel is the hoop stress, which acts around the short periphery of the tank, at right angles to the long axis of the tank. It is the most serious stress experienced by a cylindrical pressure vessel or tube, and is twice the longitudinal stress. It is reasonable to use the hoop stress as the critical stress imposed on the tank, since the crack has propagated in a longitudinal direction, i.e. under the influence of a hoop stress. It is given by the equation

$$\text{Hoop stress} = p.D/2t \tag{1}$$

where p is the internal pressure, D the diameter of the cylinder and t the wall thickness. Taking D as ca 45 mm and t as 2.5 mm together with the value of p as 25 psi, then the hoop stress is thus about 225 psi or about 1.55 MN m^{-2}, a relatively benign stress for a material with a measured tensile strength of ca 80 MN m^{-2}.

The stress concentration at the buttress corner can be modelled by a standard figure provided by Peterson [5], which represents a notch in bending for various geometries. Inserting the measured values for the three geometric parameters — r, the radius of curvature at the corner = ca 0.01 mm; d, the thickness of the section = 2.5 mm and D, the thickness of the buttress = 30 mm — then the critical ratios for interpolation on the graph are: $r/d = $ ca 0.004 and $D/d = $ ca 12.

Using the value of r/d of ca 0.004, then interpolation gives the stress concentration factor, K_t (the ratio of real to nominal applied stress) as

$$K_t = 4.2 \tag{2}$$

If the spherical void occurs in this zone, then the K_t value will be about 2, but it is likely to be an underestimate, since they vary greatly both in shape and inner surface. If flatter and elongated, then a more realistic model is that of a penny-shaped crack [6]. The K_t factor varies from about 2 up to greater than 11 on this stress concentration diagram, depending on the ratio t/r, where t is the minimum radius and r the radius of the circular cavity. This was the most difficult parameter to estimate since direct measurement was difficult and impracticable with the available microscopic data. Taking a pessimistic value of say, $t/r = 20$, then the K_t value will be about 6, so the net stress factor could be

$$K_t = (6 \times 4.2) \sim 25 \tag{3}$$

The third factor, the frozen-in strain, produced a visible widening of the original crack of ca 0.5 mm over a diameter of approximately 50 mm. This is equivalent to a strain of approximately 1%, or approximately 0.5 kN load, equivalent to a stress of approximately 20 MN m^{-2} by interpolation on the load–extension curve. So the total resultant (pessimistic) stress is given very approximately by the equation

$$\text{Total stress} \sim (25 \times 1.55) + 20 = 59 \text{ MN m}^{-2} \tag{4}$$

This value may be compared with the best experimental estimate of about 80 MN m^{-2}, and with a lower bound of about 55 MN m^{-2} for the inherent strength of the composite nylon material.

The argument may thus be summarised. The combined effects of a geometric stress concentrator at the corner of the adjacent buttress and cracks (either present as a void or at the surface of a cold slug or weld line just below the corner), effectively magnified the real stress experienced by the material by some 25 times. The material of the tank was also in a state of strain produced by cold moulding, so that an extra component of about 20 MN m^{-2} must be added to the magnified stress, giving a total stress of about 59 MN m^{-2}. This value is comparable with the mean strength measured for the material, and exceeds the lowest value actually obtained. It thus becomes possible to see why cracks were initiated near the buttress corner and grew intermittently with each successive pressurisation of the tank. Crack growth would, of course, have accelerated with each successive exposure, since the length of the crack and hence the magnification at the tip would have grown in step. The last event would probably have been the worst, and the event which directly caused catastrophic leakage of cooling fluid, before the crack re-stabilised, owing to relaxation of the frozen-in strain (Figs 3 and 6).

It is finally important to point out that no allowance has been made in this calculation for the extra stresses imposed on the tank through the buttresses and lugs by fitment of fans, motors, cowls etc. Similar considerations apply to the inlet and outlet pipes, especially as they will be stressed by fitment of connecting tubes. All such add-ons will of course exacerbate the situation.

The possibility that the rogue moulding was produced during the warm-up period of the injection moulding machine, remains the most likely cause of the failure.

6. Conclusions

1. A failed radiator tank has been examined in detail for the origin and causes of its rapid catastrophic fracture on a new car. The crack was brittle in nature and had started at or near a corner buttress. It propagated in several steps, probably corresponding to intermittent use of the car, and exposure of the radiator to a normal, expected hydrostatic internal pressure of 25 psi. This pressure is equivalent to a sidewall stress of only about 1.55 MN m^{-2}, well within the ca 80 MN m^{-2} strength of the material.
2. This benign stress was magnified, however, by a combination of three factors, two of which are related to the moulding conditions under which the product was made, and the third is related to the design geometry of the tank. The first factor was the presence of cold slugs of unmelted or partly melted material in the outer sidewall, probably caused by moulding into a cold tool or using too cool a melt. A larger, similar slug was discovered near the sprue, but had not led to failure since it was not near to the second factor involved, a geometric stress concentrator.

The failure cracks started from cold slugs or voids, because they occurred near the base of an adjacent buttress, which possessed a sharp corner with the sidewall, and represented a stress raising factor of about 4.2. The cold slugs and/or voids were more serious in their stress magnifying effect, possibly having a stress raiser of about 6, so the effective stress concentration in this zone was about 25 times the nominal applied stress of only 1.55 MN m^{-2}.

3. The final factor which made the situation critical was the presence of a substantial level of frozen-in strain, produced by cold moulding the material. This effectively added some 20 MN m^{-2} extra stress to the surface of the cold slug, producing a total stress in the region of about 59 MN m^{-2}, a stress comparable with the mean strength of the material. Brittle cracks were thus initiated at the surface of cold slugs or voids when the system was first pressurised, and grew progressively at each use of the cooling system. The cracks had penetrated through to the interior of the radiator, but only small quantities of water leaked out under pressure, judging by the several traces of contaminant found near the crack. When the cracks reached a critical size, they propagated catastrophically, releasing pressure from the system, and hence resulted in loss of the cooling facility.

4. The failed specimen appears to be a maverick which was probably accidentally included in the batch sent to the car manufacturers. Normal QC procedures usually prevent such mouldings being used, but when this batch of tanks was moulded, they failed to catch the rogue product. Careful visual inspection at the moulding machine would probably have caught the rogue, provided the operator was aware of what to look for in terms of defects such as weld lines and cold slugs. It is a difficult product to examine quickly for such defects owing to its black colouration, which were only revealed by dusting with whiting and by very close visual inspection.

Acknowledgements

References

[1] Lewis PR (Course Chair), Design and manufacture with polymers, T838. Post-graduate OU Course in the Manufacturing Programme, 1998, Block 5.2, section 4:47.

[2] Lee SM, editor. International encyclopaedia of composites. New York: VCH, 1990: for entry on Processing, void formation in melt flow thermoplastic composites, p. 302.

[3] International encyclopaedia of composites. Op cit., for entry on Characterisation, a general review covering X-radiography, OM and SEM.

[4] Folkes MJ, Russell DAM. Orientation effects during the flow of short-fibre reinforced thermoplastics. Polymer 1980;21:1252–1258.

[5] Peterson RE. Stress concentration factors. John Wiley & Sons, Inc., 1974, Fig 39; also in Pilkey WD, Peterson's stress concentration factors 2nd ed. John Wiley & Sons, 1997, Chart 2.29.

[6] Peterson, op cit., Figure 150; Pilkey, op cit., Chart 4.71.

FATIGUE FAILURE OF THE DE HAVILLAND COMET I

P. A. WITHEY*

School of Metallurgy and Materials. The University of Birmingham, Edgbaston, Birmingham B15 2TT,
U.K.

Abstract—The de Havilland Comet I entered service in 1952, and became the first commercial airliner to be powered by jet engines. It was introduced as the flagship aircraft on the routes of the British Overseas Airways Corporation, and was hailed as a triumph of British engineering. However there were a number of accidents involving this aircraft, culminating, in 1954, in the loss of two aircraft in similar circumstances. These were Comet G-ALYP near Elba, and Comet G-ALYY near Naples. A Court of Inquiry was convened, and the task of discovering the cause of these accidents was given to the Royal Aircraft Establishment at Farnborough. The investigation explored a number of avenues, and finally gave structural failure of the pressure cabin brought about by fatigue as the cause of the accidents. The use of fracture mechanics methods not used in 1954 has enabled the analysis of these fatigue cracks to be made, and the initial defect size has been estimated to be approximately 100 μm in the case of G-ALYP. This is not incompatible with the manufacturing techniques of the time, and information regarding cracks in the cabin identified during manufacture. © 1997 Elsevier Science Ltd.

1. HISTORICAL BACKGROUND

In the 1930s and 1940s, there were a number of technological advances in the sphere of military aviation, which took aircraft design from propeller-driven biplanes to jet-powered monoplanes. However, by the end of the 1940s, the world of civil aviation was still dominated by large propeller-driven aircraft.

On 2 May 1952, the de Havilland Comet (Fig. 1) entered service as the first commercial jet

Fig. 1. The de Havilland Comet I. © British Aerospace plc (reproduced with permission).

*Present address: Aerospace Group, Rolls–Royce plc, PO Box 3, Filton, Bristol BS12 7QE, U.K.

airliner, and propelled civil aviation into a new era. The de Havilland DH106 had been conceived in 1943 by Sir Geoffrey de Havilland, and design work had begun in September 1946. The prototype first flew on 27 July 1949, by which time agreements to supply 14 aircraft to the British Overseas Airways Corporation (BOAC) and two to the Ministry of Supply had been signed. On entering service, the aircraft could carry 36 passengers at a cruising speed of 450 mph ($200 \, \text{m s}^{-1}$), with a range of 2500 miles (4000 km).

To enable the payload to be sufficiently large for commercial viability, the weight of the aircraft and fuel had to be kept to a minimum. The construction techniques used were a mix of old and new, rivets being used in certain areas as well as a method of glueing the aircraft skin and stringers, called "Redux". This new technique had been pioneered by de Havilland, in the Hornet and Dove aircraft, to reduce the weight of the structure whilst maintaining the strength. The power for the aircraft was delivered by four Ghost turbofan engines built by the de Havilland Engine Company Limited. To enable these engines to run as efficiently as was practicable, this aircraft was expected to fly at 40,000 ft (10.7 km), or double the cruising altitude of the then commercial airline fleet. At this cruising altitude, the passengers and crew require an artificial oxygen supply, and it was decided to pressurize the cabin at the equivalent to a comfortable 8000 ft (2.4 km), which gave a pressure differential across the aircraft skin of 8.25 psi (56 kPa) at cruising altitude. This was double that which had been previously employed, and de Havilland conducted many tests to ensure the integrity of the cabin.

As well as the four turbofan engines, there were a number of other new features, including high-pressure refuelling, the hydraulic actuation of the control surfaces, and an air-conditioned cabin, which altogether made this a completely new aircraft.

The Comet I was seen as the new hope of the British aircraft industry, but a number of crashes tarnished the image of this graceful airliner. There were a number involving take-off, which culminated, on 3 March 1953, in the death of the crew delivering Comet CF-CUN to Canadian Pacific Airlines. These were ascribed to the unfamiliarity of the pilots with the new aircraft. The mid-air break-up of Comet G-ALYV 50 km north-west of Calcutta, exactly 1 year after the inaugural flight, was found to be due to excessive stresses in the airframe due to a tropical storm in the area.

However, there then followed two accidents under similar conditions in the space of 3 months, which could not be so easily explained. The first of these was on 8 January 1954, and involved Comet G-ALYP (Yoke Peter) approximately half an hour after take-off from Ciampino airport in Rome bound for London on the last leg of a journey from Singapore. Yoke Peter was climbing to 27,000 ft (8.27 km) in good weather conditions when it was seen to crash into the sea near Elba in a number of pieces, some of which were in flames. The Comet fleet was grounded, and the possible causes examined, a process which was not assisted by the inspection of the wreckage, as most of this was on the seabed at the time. A number of recommendations were made, resulting in improvements to the Comet I, and the fleet re-entered service on 23 March 1953.

On 8 April 1954, Comet G-ALYY (Yoke Yoke) took off from Ciampino airport bound for Cairo. After approximately 30 min, when Yoke Yoke would have been reaching the top of its climb to 35,000 ft (10.6 km), all contact was lost, and wreckage was later found in the sea near Naples. The operator of the Comets (BOAC) again withdrew all Comets from service, and on 12 April the Ministry of Transport and Civil Aviation removed the Certificate of Airworthiness from the Comet.

2. THE INVESTIGATION

Following these accidents, the Secretary of State for Civil Aviation requested a full investigation into their causes by the Royal Aircraft Establishment (RAE) at Farnborough, and a Court of Inquiry was established [1]. This investigation encompassed a number of lines of approach, but two aspects of particular interest are the reconstruction work on G-ALYP (Yoke Peter), and the accelerated simulated flight testing of Comet G-ALYU (Yoke Uncle).

Comet Yoke Uncle had been obtained from BOAC after flying for 3539 h and undergoing 1221 cabin pressurizations [2]. The accelerated simulated flight testing took the form of cabin pressurization using water, and wing loading using hydraulic rams (Fig. 2). Water was chosen to pressurize the cabin as it is reasonably incompressible, and any failure would not result in the complete loss of the pressure cabin due to the stored energy. If air had been used, any failure of the

Fig. 2. Aerial view of Comet G-ALYU in testing tank. Crown Copyright. Reproduced with the permission of the Controller of HMSO.

skin would have been equivalent to the explosion of a 500 lb (220 kg) bomb in the cabin [1]. To remove the effects of the weight of the water inside the cabin, Yoke Uncle was placed inside a water tank with the wings protruding through seals in the walls of the tank.

This arrangement enabled the loads associated with a flight to be applied in 5 min. This accelerated testing showed a severe weakness to fatigue crack growth in the aircraft skin around cut-outs such as windows and escape hatches. The skin of Yoke Uncle had undergone 3057 flight cycles [1] (1221 actual and 1836 simulated) before a fatigue crack grew to failure from a rivet hole near the forward port escape hatch (Fig. 3). The crack length before final failure was less than 2 mm in this accelerated test [2]. This failure was then repaired, and the simulated flight testing continued. Cracks were observed around a number of other windows and in the wings, and their growth monitored. This programme of tests was only stopped after 5546 pressurizations, when a fatigue crack grew to failure from the port number 7 window, and removed a 4.5 m section of cabin wall. It was concluded [2] that Comet Yoke Uncle, had it continued to fly, would have suffered cabin failure at around 9000 h. In addition to the cabin pressurization simulation, there were also proving tests conducted every 1000 flights to a pressure of 11 psi (76 kPa) to simulate those conducted by the operators or designers from time to time [2] to test the structural integrity of the cabin.

The reconstruction of Yoke Peter at Farnborough continued until September 1954 as pieces were recovered from the seabed by the Royal Navy. This process used underwater television cameras for the first time, and was assisted by the break-up of scale models of the Comet at Farnborough to ascertain the pattern of the falling pieces. Eventually, about 70% of the aircraft was recovered, and this allowed a scenario for the last moments of the aircraft to be constructed.

Yoke Peter was the first jet aircraft to enter commercial service and, at the time of the accident,
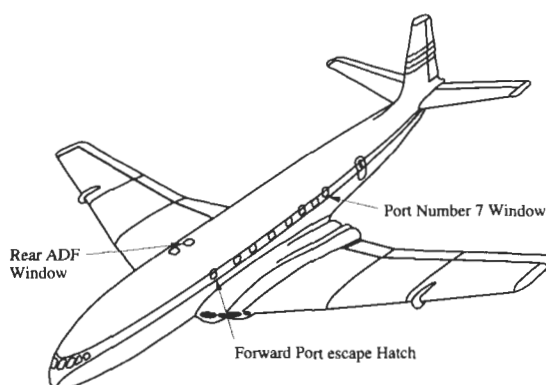

Fig. 3. The main failure sites on Comets G-ALYP and G-ALYU.

was undertaking its 1286th pressurized flight in addition to 255 flights without cabin pressurization. The Court of Inquiry [1] concurred with the findings of the RAE investigation [2] that the cause of the accident was sudden cabin failure due to fatigue crack growth followed by the break-up of the aircraft. The accident which occurred to G-ALYY was attributed to the same cause, as the flight circumstances were similar, although insufficient wreckage was ever recovered to prove the case.

The root of this rapid failure due to metal fatigue was shown to be high stresses around cut-outs, such as windows, in the aircraft skin. The aircraft manufacturer, de Havilland, had made estimates of these stresses averaged over a large area, and ascertained the fatigue life of the aircraft by testing sections of the cabin and the 22 gauge (0.71 mm) pressure cabin skin was thickened to 20 gauge (0.91 mm) around the windows. However, the Court of Inquiry reported that the nature of the sections used meant that they were not representative of a whole aircraft, as bulkheads fitted to these sections to enable pressurization may have affected the stresses around the cut-outs in the locality. This enabled the forward cabin section tested by de Havilland to withstand 18,000 cycles before fatigue failure from a defect in the skin near the corner of a window. In addition, this section was proof tested to 16.5 psi (114 kPa), or twice the operating pressure, before the fatigue testing began, and this may have caused local plastic deformation in the regions of high stress of interest here [1]. Proof testing of the pressure cabin was undertaken on all Comets during manufacture, before acceptance by BOAC, and at predetermined times during service, to 11 psi (76 kPa), but never to 16.5 psi (114 kPa), and a safety valve to prevent overpressurization of the cabin during service was set to 8.5 psi (59 kPa).

Cracks were known to be present in the aircraft upon manufacture, and there was an approved technique for identifying such defects and "locating" them by drilling the end of the crack with a $\frac{1}{16}$ in. (1.6 mm) drill [1]. In most cases, the crack was seen not to extend beyond the location hole, and this was assumed to be adequate security against further crack growth. In fact, there was a "located" crack near the forward port corner of the rear ADF (automatic direction finding) window (Fig. 3) on Yoke Peter, which did not grow beyond the locating hole until the final failure of the cabin.

The failure of Yoke Peter was deduced to be a fatigue crack near the starboard rear corner of the rear ADF window (Fig. 4). This crack emanated from a 10 mm diameter bolthole, and propagated to failure after unexpectedly few pressure cycles of the cabin. This bolthole in such a highly stressed
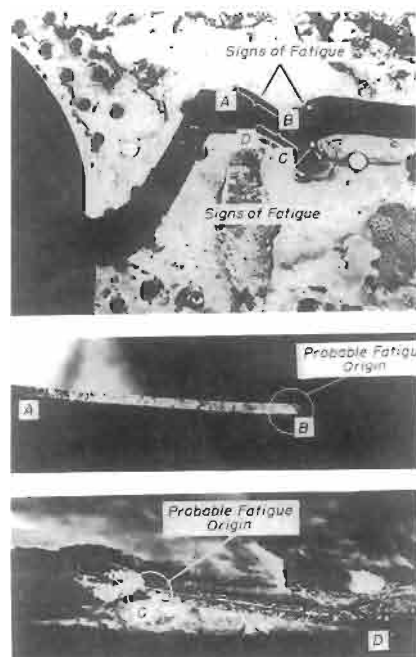

Fig. 4. Close-up views of the failure in the skin of Comet G-ALYP. Crown Copyright. Reproduced with the permission of the Controller of HMSO.

area was recognized as a prime site for fatigue failure initiation, and de Havilland subsequently redesigned the windows and increased the thickness of the skin in these areas to prevent this occurring on later Comet aircraft. The stress around a cut-out was shown to be over 3 times the remote stress due to cabin pressurization both experimentally [2] and theoretically [3]. Using the S–N data available at the time, it was possible to explain the shortened fatigue life.

3. ANALYSIS OF THE FAILURE

It is of interest to use fracture mechanics analyses (not used in 1954) to give an insight into the relative importance of the factors which combined to produce the catastrophic failure.

The bolthole which was the origin of the failure in Yoke Peter was over 50 mm from the ADF window (Fig. 4), and the stress in this area was significantly below the maximum stress at the ADF window itself. In fact, as part of the RAE investigation, strain gauges were placed around areas such as the ADF windows on Yoke Uncle to examine the stresses in this area. The stress in the vicinity of the bolthole was calculated to be around 70 MPa, compared to 315 MPa around the edge of the windows. This stress is reasonably close to that expected as a general level for a pressurized cylinder of 1.6 m radius, and a thickness of 1.42 mm. This thickness is derived from the 0.71 mm (22 gauge) skin and 0.71 mm thick doubler plate around the ADF window. Although the crack grew principally towards the ADF window, the stresses in this area were shown, using strain gauges, not to vary much, and the crack was only 25 mm long when failure occurred [2].

If it is assumed that linear elastic fracture mechanics can be applied, use may be made of the Paris law

$$\frac{\mathrm{d}a}{\mathrm{d}N} = A\Delta K^m. \tag{1}$$

However, to begin such an analysis it is necessary to obtain fatigue crack growth data for this particular alloy. The alloy in question is DTD 546B, an aluminium-coated high tensile strength aluminium alloy for sheet use containing between 3.5 and 4.5% copper [4]. This alloy was developed before fatigue crack growth plots were taken for materials, but data can be obtained from the actual fatigue of Comet I G-ALYR (Yoke Robert) in a water tank at the RAE [5].

A number of cracks were monitored on Yoke Robert propagating from the rivets near corners of the cabin windows, and the data given as plots of number of cycles against crack length.

Yoke Robert underwent 11,313 cycles, and cracks were prevented from further growth at a length of 165 mm, as this was felt to be the length at which cracks would propagate to failure within a few more cycles. This gives a fracture toughness of around 35 MPa m$^{1/2}$. Using the strain gauge measurements made on the same fuselage, it is possible to construct a plot of da/dN against ΔK for the Comet I skin (Fig. 5).

This plot gives a value for A of 9.6×10^{-7} for da/dN measured in mm/cycle, and a Paris exponent,
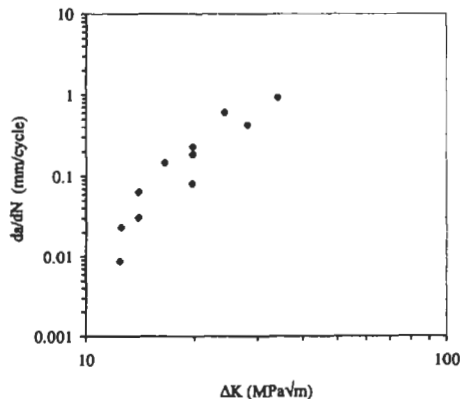

Fig. 5. Fatigue crack growth of the Comet I fuselage.

m, of 4.0. The crack growth rate is much faster than for subsequent aluminium alloys, but it is unclear whether this is due to the alloy itself, the application, or the water environment of the test. The consequences of the water environment of the tank test were addressed by Atkinson *et al.* [5] at the time of the tests, and it was felt that a cabin skin would be cycled through wet and dry periods during service (outside due to the weather and inside due to condensation), and this cycling may be more damaging than the environment of a tank test. The degraded environmental performance in aluminium alloys in aerospace applications has also been noted by Barter *et al.* [6].

The relation between ΔK, the applied stress range, $\Delta\sigma$, and the crack length, a, can be written as

$$\Delta K = F(a)\,\Delta\sigma\sqrt{\pi a}, \tag{2}$$

where $F(a)$ is a term (weight function) modifying the stress field in the presence of the bolthole, and is a function of the crack length. The relationship in Eqn (2) can be substituted into Eqn (1) to obtain

$$\frac{\mathrm{d}a}{[F(a)\sqrt{a}]^m} = A(\Delta\sigma\sqrt{\pi})^m\,\mathrm{d}N. \tag{3}$$

The number of cycles to failure for particular initial and final crack sizes can be calculated by integrating the above equation. The weight function for a crack emanating from a hole is a function of the crack length, and hence makes the analytical evaluation of the integral more difficult. However, there are tabular and graphical forms of these weight functions [7] which can be incorporated into the calculations. It may be assumed that there was only one crack emanating from the bolthole. There was a second fatigue crack at the opposite side of the hole, but it had not grown to any great extent before failure occurred. The value of $\Delta\sigma$ to be placed into Eqn (3) can be assumed to be the maximum value of the stress for the appropriate crack length, as one pressure cycle of the aircraft cabin always began at and returned to a pressure difference of zero, and hence the stresses in the skin approached zero. The weight function used here is the case for a uniaxial tensile stress perpendicular to the crack growth direction. This may not have been the case for the Comet skin, and a biaxial tensile stress field may be closer to reality: however, the effect on the calculation of initial crack sizes is small, and serves to increase the initial defect size required to cause failure after 1286 pressurization cycles.

Such a calculation gives an estimated initial defect size of around $100\,\mu$m, corresponding to the total life of 1286 flights for Yoke Peter. As cracks many millimetres in length were seen during construction, and located using a $\frac{1}{16}$ in. (1.6 mm) drill, it is not surprising that a crack of the order of $100\,\mu$m in size was not spotted during manufacture and subsequent inspections. It can also be shown that, due to the accelerating nature of fatigue crack growth, the crack would have been visible emanating from under the bolthead for very few flights. A compressive stress around the bolthole, introduced during formation of the hole, would have reduced the fatigue crack growth rate in the vicinity of the hole [8], and would thus require a larger initial defect size to cause failure after 1286 pressurized flights than has been calculated above.

Using similar calculations for G-ALYU (the accelerated flight simulation Comet), which had only 1.7 mm of fatigue crack growth before failure after 3057 "flights", the size of the initial defect would be predicted to be smaller, at less than $10\,\mu$m.

At the time of the Court of Inquiry, much was made of the difference in the lives of Yoke Peter (1286 pressurizations), Yoke Yoke (903 pressurizations), and Yoke Uncle (3057 pressurizations). The explanation at the time was that the expected spread in fatigue results from shortest to longest was a ratio of 1:9, and the largest ratio here was 1:3.4. These results are not a surprise as the weakest aircraft would always fail earlier than average, and Yoke Uncle, chosen at random from the Comet fleet, was always statistically likely to have a longer fatigue life than those which had failed.

The difficulty in observing cracks during manufacture and subsequent inspection was highlighted by the number of cracks monitored during the fatigue testing of Yoke Robert [5]. In this case, cracks were first observed when they were around 6 mm in length, even though the probable locations of the cracks were known. Using the crack growth data, the approximate initial defect size was less than $10\,\mu$m. This is much less than the $100\,\mu$m estimate for Yoke Peter, and no cracks were observed in Yoke Robert around the ADF windows, even when the doubler plate had been removed for inspection. It is probable that there was a larger than average production crack near the starboard

rear corner of the rear ADF window on Yoke Peter, and that this grew to failure after only 1286 flights.

It has been reported that Mr Ronald Bishop, the Chief Designer at de Havilland during this period, felt that the mistake made was to allow rivets and bolts to be used to assemble the windows and reinforcements onto the aircraft skin. Other parts of the aircraft were glued using "Redux", but the tooling required was thought to be too difficult to achieve, and too expensive for these cut-out areas. Other riveted areas, some wing skin sections for example, were known to be susceptible to fatigue crack growth from the rivet holes, and the use of riveting to fix such thin-section aluminium sheet in the vicinity of cut-outs was probably more damaging than the shape of the windows. In fact, none of the cracks in the body or wings of the test Comet emanated from the cut-outs directly, but came from rivet or boltholes near cut-outs, and the initial failure site on Yoke Peter was from a bolthole rather than the edge of the ADF window.

4. CONCLUSIONS

The de Havilland Comet was a truly novel aircraft. It had a number of new features which are now accepted as part of modern aircraft design, but at the time set a completely new trend. A number of technical advances had to be made to enable the aircraft to fly, and these stretched the scientific knowledge of the time to the limit. However, as with all pioneers, the first to enter a new field are the first to encounter the problems, and this is especially so in commercial aviation, where failure can be spectacular and high-profile.

The failure of the pressure cabin was due to fatigue crack growth from defects which were probably present from the construction of the aircraft and had not been a problem in earlier designs of aircraft, as the required cabin pressure had been lower. That this problem was not detected by the rigorous testing undertaken by de Havilland was probably due to an unfortunate set of circumstances with regard to the order in which the tests were performed, and could not easily be foreseen at the time. The knowledge gained from these unfortunate accidents enabled scientific knowledge to advance, and testing procedures to be instigated which ensured the increased safety of future civil aircraft.

All the observed cracks in the pressure cabin [1, 2] emanated from bolt or rivet holes near the cut-out areas. It was probably not the shape of the cut-outs that was so damaging to the fatigue life of the cabin, rather the method of fixing the windows and doubler plates onto the pressure cabin. Had the windows not been square then the "Redux" glueing method might have been applied to these areas, and the failure avoided.

After the problems of the Comet I, de Havilland produced the Comet IV, which was larger, carried 80 passengers, and had a greater range. This aircraft entered history as the first commercial jet aircraft to cross the Atlantic on 4 October 1958, and inaugurated a route which has carried many millions of passengers since. However, 3 weeks later, a Pan American Boeing 707 flew the same route carrying 120 passengers, and indicated the supremacy of the American airline industry. The Comet continued to be built until 1962, by which time 113 had been made, showing the quality of a design commenced in September 1946, and has entered history as the first commercial jet airliner and the first to operate a scheduled service across the Atlantic.

REFERENCES

1. Cohen, Baron L. of Walmer, Farren, W. S., Duncan, W. J. and Wheeler, A. H., *Report of the Court of Inquiry into the Accidents to Comet G-ALYP on* 10 *January*, 1954 *and Comet G-ALYY on* 8 *April*, 1954. HMSO, London, 1955.
2. Royal Aircraft Establishment, *Report on Comet Accident Investigation*, Accident Report 270. Ministry of Supply, London, 1954.
3. Green, A. E., *Proceedings of the Royal Society A*, 1945, **184**, 231–252.
4. Material Specification, Aluminium-coated high tensile aluminium alloy for sheet and coils. DTD 546B, Ministry of Supply, HMSO, London, 1946.

5. Atkinson, R. J., Winkworth, W. J. and Norris, G. M., Behaviour of skin fatigue cracks at the corners of windows in a comet I fuselage. R&M 3248, HMSO, London, 1962.
6. Barter, S., Sharp, P. K. and Clark, G., *Engineering Failure Analysis*, **1**, 255–266 (1994).
7. Wu, X.-R. and Carlsson, A. J., *Weight Functions and Stress Intensity Factor Solutions*. Pergamon Press, Oxford, 1991.
8. Clark, G., *Fatigue Fracture, Engineering Materials and Structure*, **14**, 579–590 (1991).

LOW-CYCLE FATIGUE OF TITANIUM 6Al–4V SURGICAL TOOLS

H. VELASQUEZ, M. SMITH, J. FOYOS, F. FISHER and O. S. ES-SAID*

Department of Mechanical Engineering, Loyola Marymount University, 7900 Loyola Blvd, Los Angeles,
CA 90045-8145, U.S.A.

and

G. SINES

Department of Materials Science and Engineering, University of California at Los Angeles, Los Angeles,
CA 90095-1595, U.S.A.

Abstract—A handle holder is used in heart valve replacement surgery to insert a mechanical flow valve into the patient's heart. In order to position the valve correctly, a 0.1″ diameter titanium 6Al–4V handle holder shaft is bent until the proper angle is found. This bending of the tool makes it vulnerable to low-cycle fatigue failure. Low cycle fatigue testing of titanium 6Al–4V specimens shows that surface cracks appear approximately 20 cycles before failure occurs. It is recommended that the tool be carefully inspected before each use and replaced when surface cracks appear. The data showed that the life of the tool may be increased by 30% if it is bent in the same direction during its entire use. © 1998 Elsevier Science Ltd. All rights reserved.

1. INTRODUCTION

During heart valve replacement surgery the patient receives a major incision that runs across the chest. All access to the patient's heart is through this opening in the chest. Selection of the optimal replacement valve size follows. Once the valve has been selected it is placed in the patient's heart. A handle holder (Fig. 1) is used by the surgeon to place the valve during the surgical procedure. The handle holder is a screwdriver-like tool made of titanium 6Al–4V equipped with a plastic tip used to hold the prosthetic valve. The valve, held at the tool's tip during positioning, is released upon placement in the heart. To position the valve, it must be inserted through the incision, maneuvered through the chest wall and finally put into place. The surgeon bends the thin shaft of the handle holder until the proper angle is found to insert the valve. The reusable handle holder is often bent several times during each surgical procedure and thus becomes vulnerable to low cycle fatigue [1]. It is therefore essential that the surgeon knows when to replace the tool to avoid a fatigue failure during surgery.

The objective of this study is to determine the fatigue life of the shaft. After conducting tests on titanium 6Al–4V sample rods, use-limit recommendations were made.

2. INVESTIGATION METHOD

To determine whether a testing device to automate the cyclic loading would be required or if manual testing was possible, the number of cycles (N) required for low-cycle fatigue failure of the shaft was approximated by using the Coffin–Manson law [2]:
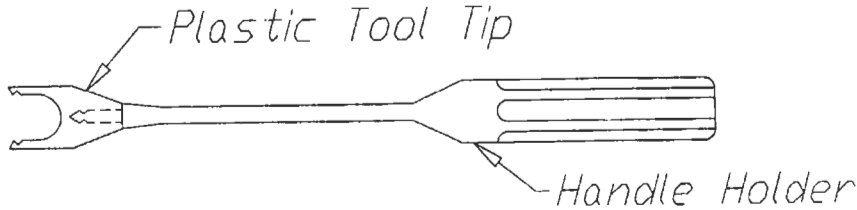
---

* Author to whom correspondence should be addressed.

Fig. 1. Schematic of a handle holder titanium 6Al–4V heart valve surgery tool.

$$N = (C/\Delta\varepsilon_\rho)^2, \tag{1}$$

where the constant $C = \varepsilon_f/2$, ε_f is the true fracture strain and $\Delta\varepsilon_\rho$ is the plastic strain range. The true fracture strain (ε_f) can be calculated from a tensile test according to the relation:

$$\varepsilon_f = \ln 1/(1-q), \tag{2}$$

where q is the fractional reduction in area.

The plastic strain range ($\Delta\varepsilon_\rho$) is equal to the radius of the rod h divided by the radius of curvature ρ (Fig. 2):

$$\Delta\varepsilon_\rho = h/\rho. \tag{3}$$

A tensile test was conducted on a 3/16″ diameter rod. The fractional reduction of area, q, was 0.4 thus giving $\varepsilon_f = 0.51$. The estimated radius of curvature ρ for the worst case was 0.787″; the tool rod section radius was 0.050″, thus giving a plastic strain of $\Delta\varepsilon_\rho$ of 0.0635. The 16 cycle life calculated from eqn (1) was low enough to indicate that manual testing would be feasible.

In the following experiments we define one cycle as follows: (1) the test specimen begins undeformed, (2) the specimen is bent to a predetermined angle in one direction, (3) the specimen is bent back to the original shape, (4) the specimen is bent to the same angle but in the opposite direction, (5) the specimen is bent back to the original shape. Steps 1–5 define one cycle. For the experiments conducted to determine the number of cycles required for low cycle fatigue failure, steps 1–5 were defined as two cycles, i.e. one cycle was counted each time the specimen was bent and returned to the original shape.

To determine the number of cycles required for low cycle fatigue failure of the handle holder shaft, six 3/16″ diameter titanium 6Al–4V rods were divided into two groups of three. Though the handle holder shaft diameter is 1/10″, the more available 3/16″ diameter rods were used for the cyclic load testing. Eqn (4) was used to determine the radius of curvature ρ to be used with 3/16″ material that would cause a bending strain equal to that of a 1/10″ diameter shaft.
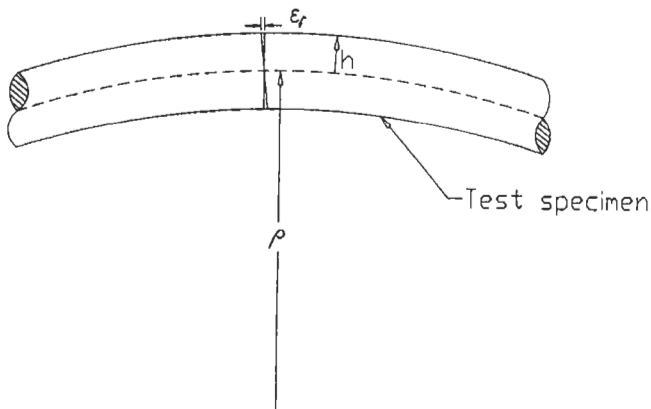

Fig. 2. Bending strain figure.

$$\frac{h_1}{\rho_1} = \frac{h_2}{\rho_2} \qquad (4)$$

where h_1 = the radius of specimen 1, ρ_1 = the radius of curvature for specimen 1, h_2 = the radius of specimen 2, ρ_2 = the radius of curvature for specimen 2. The equivalent radius of curvature for the $3/16''$ diameter specimens was calculated to be $1.5''$.

The handle holder manufacturer supplied several tool samples having typical bends used during surgery (Fig. 3). The tools were bent by hand during testing just as they would be during surgery. The $3/16''$ rods were bent to a predetermined angle ($60°$) to simulate the worst case scenario during normal use (Fig. 4). The first group of specimens (group 1) was tested by bending until failure in
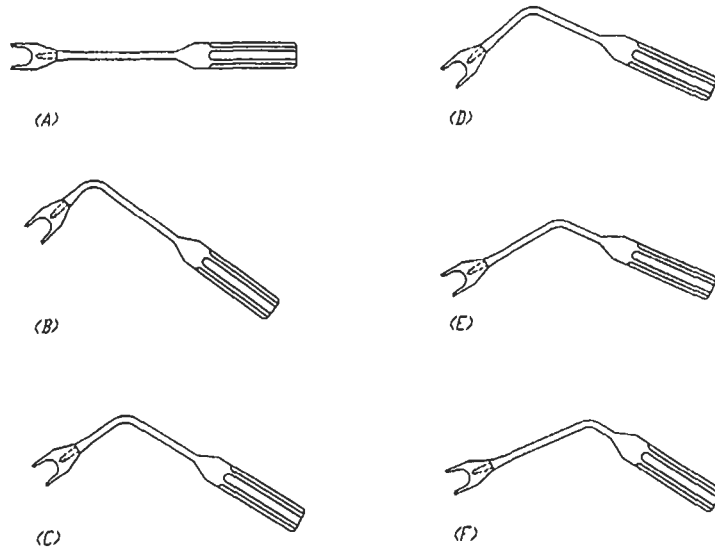
Fig. 3. Handle holder with typical bends used in surgery. (A) Handle holder before bending. (B–F) Handle holder with typical bends.
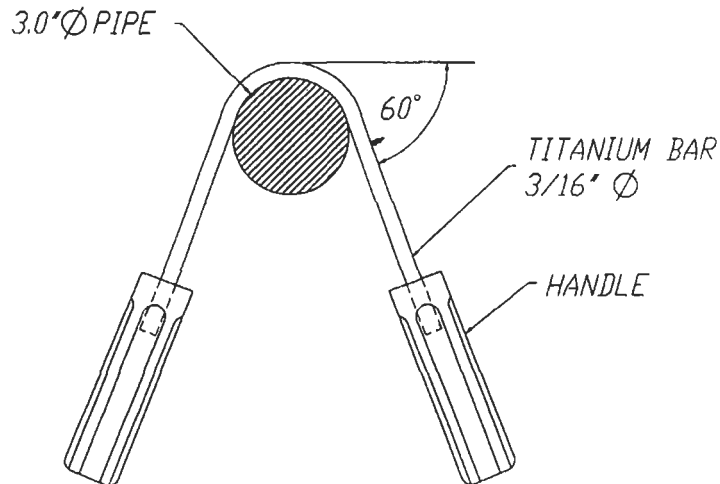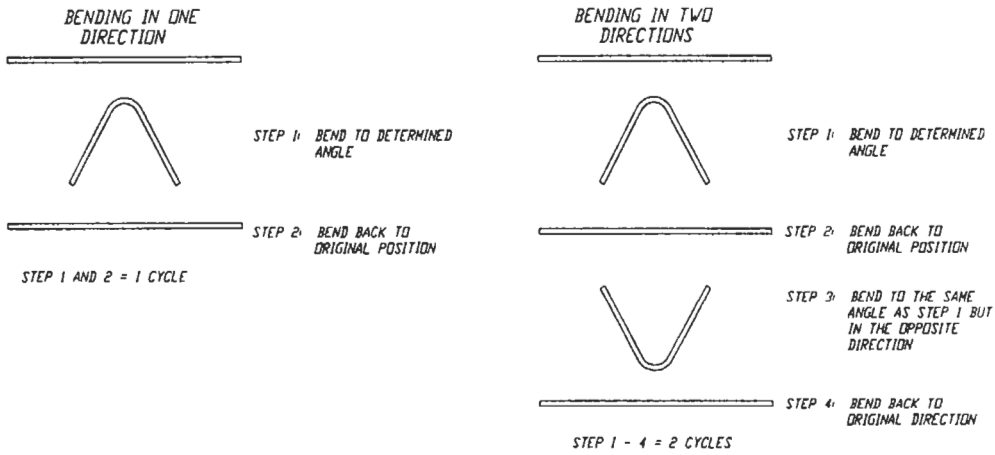

Fig. 4. Experimental setup.

BENDING IN ONE
DIRECTION

STEP 1: BEND TO DETERMINED
ANGLE

STEP 2: BEND BACK TO
ORIGINAL POSITION

STEP 1 AND 2 = 1 CYCLE

BENDING IN TWO
DIRECTIONS

STEP 1: BEND TO DETERMINED
ANGLE

STEP 2: BEND BACK TO
ORIGINAL POSITION

STEP 3: BEND TO THE SAME
ANGLE AS STEP 1 BUT
IN THE OPPOSITE
DIRECTION

STEP 4: BEND BACK TO
ORIGINAL DIRECTION

STEP 1 - 4 = 2 CYCLES

Fig. 5. Description of testing conducted.

one direction only and the second group (group 2) was tested by reverse bending (Fig. 5). Two handles with setscrews were used to hold the rods during testing (Fig. 4). The specimens were bent over a 1.5″ radius mandrel secured by a vise. It was noted that surface cracks appeared prior to failure. The number of cycles required for surface cracks to appear as well as the number of cycles to failure were counted and recorded.

3. RESULTS

From Table 1, the average number of cycles to failure for a group 1 shaft is 85, and for group 2 is 58. The sample to sample variation within each group was less than 15%. Group 2 cycle life was found to be 32% less than that of group 1. Group 1 specimens were bent an average of 29 times between the onset of cracking and failure while group 2 specimens lasted an average of 22 cycles after crack onset.

4. DISCUSSION

During heart valve replacement, the surgeon may bend the handle holder tool several times to correctly position the valve. Though confident life predictions are possible from the test data, it may pose an undue burden on a surgeon to suggest counting and recording accumulated bend data.

Fortunately, visible cracks consistently appear on the shaft surface well before failure occurs (Fig.

Table 1. Experimental results

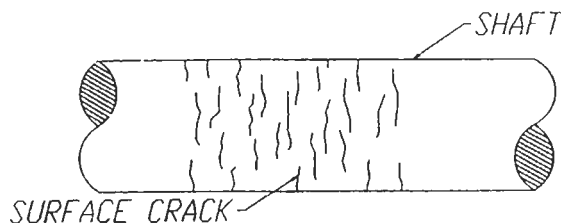| | Group 1 Bending in one direction only | | | Group 2 Reverse bending | |
Sample	Number of cycles N for failure	N, cracks were first noticed	Sample	Number of cycles N for failure	N, cracks were first noticed
1	90	65	4	51	33
2	77	45	5	60	31
3	87	55	6	63	43

Fig. 6. Surface cracks.

6). In fact from the time that cracks become apparent to the time when failure occurs, the data shows that at least 10 more cycles may be safely performed. Clearly, the onset of cracking can be easily used to warn of impending failure. Since the low cycle fatigue testing was conducted on 3/16″ diameter specimens, 1/10″ diameter rods were also tested to ensure that the surface cracks would be visible under normal visual inspection. This testing showed that the cracks are visible on the 1/10″ diameter handle holder shafts.

The data also showed that the life of the specimens in group 1 which were bent in one direction only was about 30% longer than that of the specimens in group 2 which were tested in reverse bending. It is recommended that the tool be bent in the same direction throughout its life whenever possible.

5. CONCLUSION

Cyclic loading test on titanium 6Al–4V specimens showed that appearance of surface cracks can act as a low cycle fatigue warning system in the 1/10″ diameter tool shaft. It is recommended that the tool receive a careful visual inspection before each surgery and be replaced whenever surface cracks become visible. To extend tool life it is also recommended that the tool be bent in one direction only whenever possible. The Coffin–Manson equation was useful in deciding testing procedure, but should not be used for service life prediction in this critical application.

REFERENCES

1. http://www.heartlab.rri.uwo.ca/valve.surgery.html.
2. Dieter, G. E., *Mechanical Metallurgy*, McGraw-Hill, New York, 1976, pp. 412–413.

FAILURE ANALYSIS AND EXPERIMENTAL STRESS ANALYSIS OF A THREADED ROTATING SHAFT

R. B. TAIT*

Department of Mechanical Engineering, University of Cape Town, Private Bag, Rondebosch 7700,
Republic of South Africa

Abstract—The occurrence of a fracture of an actuator wormshaft, used for opening and closing a valve in Koeberg's Nuclear Power Station cooling water system, during routine testing, was cause for concern. Two such fractures occurred in a particular type of actuator shaft and another 40% of such shafts exhibited fatigue cracking. Conventional fractographic failure analysis indicated that there was a signifcant bending stress component in the fatigue failure, the origin of which was unclear. The actuator had two torque limiting devices once the valve had seated, the last of which was a disc brake system, and it was suspected that inappropriate setting of the disc brake contributed to the high cyclic bending stresses and hence the fatigue failure.

In this paper, an experimental stress analysis was undertaken by strain gauging the actual shaft of an actuator *in situ* and measuring the bending, tension and torsional stresses in operation during rotation, and valve closure. It transpired that the brake disc location and setting was not the prime cause of the high bending stresses, but rather that a single, "thin" lock nut was canting over slightly against some Belvel spring washers and applying significant bending stress, via the actuator housing, to the shaft. The conventional tolerances on this ordinary nut, together with the design, and variable setting up were sufficient to cause substantial bending, and ultimately fatigue, of the shaft, under straight-forward, low, nominally tensile loading. This simple nut on a threaded shaft fatigue failure scenario has wide application in a variety of similar bolted shaft applications. A substantially longer recessed nut was used and reduced the offset bending stresses significantly (from 180 to 25 MPa), vindicating the interpretation. The final design incorporated a system not unlike this long nut solution, in that the recessed nut did not exhibit any canting over. This, together with improved shaft processing, effectively solved the problem. © 1998 Published by Elsevier Science Ltd. All rights reserved.

Keywords: Fatigue, mechanical connections, power-plant failures, strain gauging, stress analysis.

1. INTRODUCTION

The premature development of cracks, apparently through fatigue, in the first couple of threads of some Rotork 30 NBAT actuator wormshafts of Koeberg Nuclear Power Station (KNPS), near Cape Town, had focused attention on what could have been a potentially serious problem. Indeed, on two occasions complete fracture occurred from these fatigue cracks under test bench loading conditions at Koeberg, and over half of the shafts of this type had developed (fatigue) cracks.

The actuator that failed at Koeberg, together with others that developed fatigue cracks, was very similar to a type shown in Fig. 1. In this figure, the worm gears, torque switch and the wormshaft with the end locking nuts are clearly visible. Because it was considered that it must be possible to operate the actuator under emergency conditions, for example in the event of a depressurisation leak in the containment area, the valve was required to be operable even if the electrical supply was below that at which the actuator motor was rated.

For this reason, the actuator armature was rewound for use at Koeberg in order to make it capable of providing enough torque to close the valve even when the voltage had dropped from the rated 380 V. This created the problem that the maximum output torque of the motor under normal operating conditions (approximately 950 Nm on the valve) was now sufficient to cause damage to the valve seat and/or actuator itself.

When the motor is energised, it rotates the wormshaft causing the valve to turn via the wormgear arrangement. Once the valve has seated, the wormshaft begins to translate axially, compressing a set of Belvel washers (Fig. 2) which resist the axial movement. As the shaft translates. at a certain
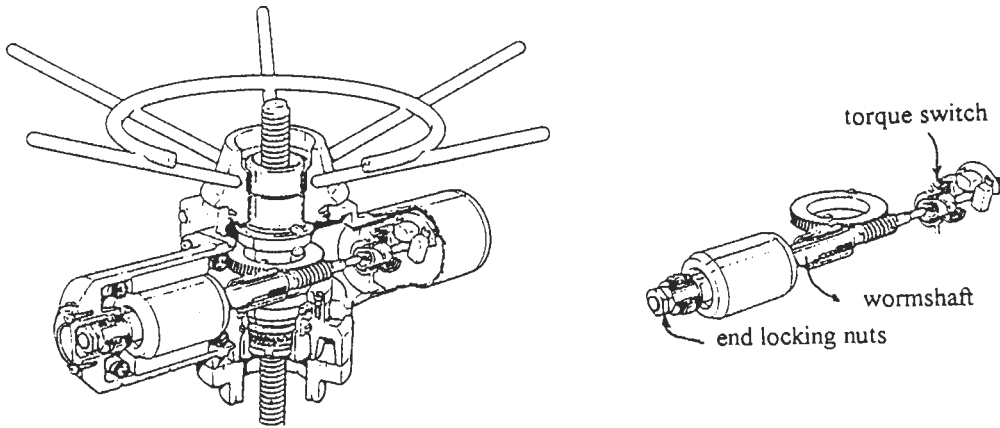

Fig. 1. Schematic diagram of a conventional Rotork actuator. The recessed locking nut (failure site) and wormshaft are clearly visible.

point it trips the torque limit control selector which is preset to trip at a specified torque (approximately 136 Nm valve torque). The load at which the switch trips is set to be high enough to close the valve, but not great enough to cause valve seat damage. In the event of failure of the trip switch, however, the full torque of the motor may be exerted on the actuator shaft and the valve seat.

It was thus decided, for the KNPS application, that in addition to the torque switch, a further device would be added to prevent the motor from being able to damage the valve in the unlikely event of failure of the torque switch. This took the form of a disc brake assembly, the axial position of which could be adjusted on the shaft in order to limit the axial movement of the shaft and hence prevent excessive valve torque (Fig. 2). Thus if the torque switch failed or was overridden, the shaft would move axially (and horizontally as shown) once the valve was seated, until the disc brake engaged, causing the motor to stall and thus preventing further torque being developed on the valve. The valve torque at which this happened, was usually set to approximately 366 Nm, while the torque
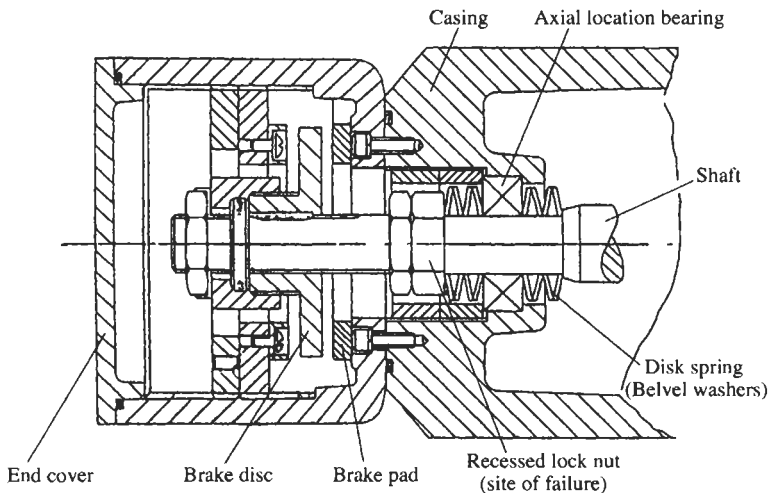

Fig. 2. Diagram of the modification made to the Rotork NABT 4 valve actuator, incorporating in particular the brake disc. The Belvel washer disc spring, locking nuts and axial location bearing are clearly apparent.

switch tripped at approximately 110–130 Nm and the maximum torque capacity was approximately 950 Nm.

In view of the concern about the shaft cracking problem, arising only from test bench loading, extensive analysis of the wormshaft, both overseas [1] and locally [2–4] had been undertaken. The overseas analyses, involving Rotork (Bath) and Nuclear Electric (Bristol), were quite extensive and considered *inter alia* analytical stress analysis, metallurgical analysis, physical component fatigue testing, theoretical fatigue crack growth calculations, finite element stress analysis modelling, production methods and surface hardening treatment, and finally experimental life tests. The summary of these overseas tests effectively concluded [1] that the combined effect of the French requirement for motor categories and the British Rotork shaft sizing requirement, was that the motors were slightly too powerful for the shaft, at least for the 30 NATB series. The option of changing to completely new motors (or shafts) was, however, unacceptable to the electricity power utility, ESKOM.

Subsequently microscopic analysis [3] revealed that pre-existing defects and micro cracks could exist as the result of manufacture, at the root of the threads, which would facilitate fatigue crack growth and, ultimately, fracture, if the cyclic loading conditions were sufficiently high. It was initially believed [1, 2] that the manufacturing technique of heat treating first, followed by finish grinding of the threads, led to the inherent thread root defects. Thus, by reversal of this process, i.e. heat treatment after thread grinding, it was hoped to solve or at least alleviate the problem. Despite this change in manufacturing route the cracking problem still continued. The fractographic analysis also indicated that there was a significant bending stress component in the fatigue fracture surface. Despite this clear evidence of bending fatigue on the local shafts, the Rotork report [1] indicated from their analyses and tests, that there should not be a fatigue cracking problem, within the projected life of the plant, yet they did not consider any vibration or "judder" effects, which can and do occur on the *local* test bench—up to 20% of the time, according to the principal operator [4]. In addition *local* test bench setting up details and test bench loading could conceivably have been different from the Rotork U.K. conditions, even though the test bench was built by Rotork to their own specifications. In addition operational procedures may have differed. For example, Rotork [1] refer to only 10–12 stall conditions per year, whereas the author observed and counted over 15 in one single actuator test bench run on a single day! In view of the discrepancies between analysis and testing overseas, and the local performance, the inference was that there might have been some *local* phenomenon which led to the fatigue cracking.

In addition, for any meaningful life evaluation of the shafts, an essential critical set of data that is required are the cyclic stresses and load spectrum that the shaft experiences, both in calibration and torque setting tests as well as in service. Under high levels of cyclic stress, such as 390 MPa [1], fatigue is bound to occur, except in cases where the surface finish is completely free of defects, i.e. a highly polished surface finish. Even then fatigue crack initiation could still form by persistent slip band formation, but admittedly this would only occur after large numbers of initiating fatigue cycles, beyond the normal life of the plant.

An additional key unknown in the stress evaluation was the degree of *bending* stress applied, presumably due to, for example, uneven loading on the brake disc from run out or uneven disc brake contact or brake pad wear. If the bending component was minimal the stress levels would be significantly reduced [1]. Hence a key feature in the wormshaft component fatigue life may well be setting up details to avoid any bending (as opposed to merely axial or torque loads).

Hence there was a move to measure, physically—rather than estimate, theoretically—the stresses in the actuator wormshaft in operation *in situ*, initially on (i) the Koeberg test bench and subsequently, (ii) the plant, to assess the likelihood of fatigue cracking. If the combination of inherent defect size, from manufacture, and cycle stress amplitude, in bench testing (and service), were sufficiently high, i.e. greater than threshold, then fatigue would be inevitable [4].

This paper, therefore, attempts to answer some of these questions by using strain gauge measurements of the shaft in operation on the test bench, to evaluate these stresses and the consequent potential for fatigue. Such physical stress measurements were needed to establish what the peak stresses and range of stresses were, as well as their origins. In particular, was the critical evaluation of the presumption that the high stresses in the threaded portion of the shaft arose from the disc brake loading and that these were more severe from bending rather than axial or torsional loading.

2. EXPERIMENTAL DETAILS

2.1. *Shaft system and strain gauging*

The requirement of measuring the strains in the vicinity of the first one or two threads, where the cracking occurred, was not without constraints. If there were to be a bending stress component, presumably from the disc brake loading unsymmetrically, then a strain gauge located here would need to be at the same distance from the brake as are the first one or two threads.

To place the strain gauge rosette on the unthreaded portion of the shaft close to this first thread was not acceptable because the Belvel washers are located here and they need to slide freely on the shaft. Similarly the thread root itself cannot be readily straingauged because it is too small an area and would be susceptible to stress concentration effects (SCF). Consequently the first three threads were ground off an actuator shaft with the corners radiused, yielding a total smooth shaft length of 9.5 mm. The shaft diameter was reduced in this region to 15.50 mm since the only wormshaft actuator available was one that had already exhibited some limited fatigue cracking at the first thread. It was thus necessary to grind the diameter down to below the fatigue crack depth (effectively removing it) and for this it was necessary to go to a diameter of 15.50 mm. After grinding, the shaft was non destructively inspected rigorously, using magnetic particle inspection (MPI) techniques which confirmed that this reduced section, and indeed the rest of the threads, were free of any detectable crack like defects. The reduced section is shown diagrammatically in Fig. 3(a).

In order to convey the strain gauge bridge leads to the end of the shaft, a 4.0 mm diameter hole was bored along the centre line axis of the shaft to the reduced section and a connecting hole drilled between the two (Fig. 3(a)). The reduced shaft section was then polished and two strain gauge rosettes, with a so called 0°, 45°, 90° configuration, attached on opposite sides of the shaft, remote from the drilled lead access hole, and located where the first thread had been. The strain gauges of the rosette were aligned so that they had one purely axial and one completely transverse gauge.
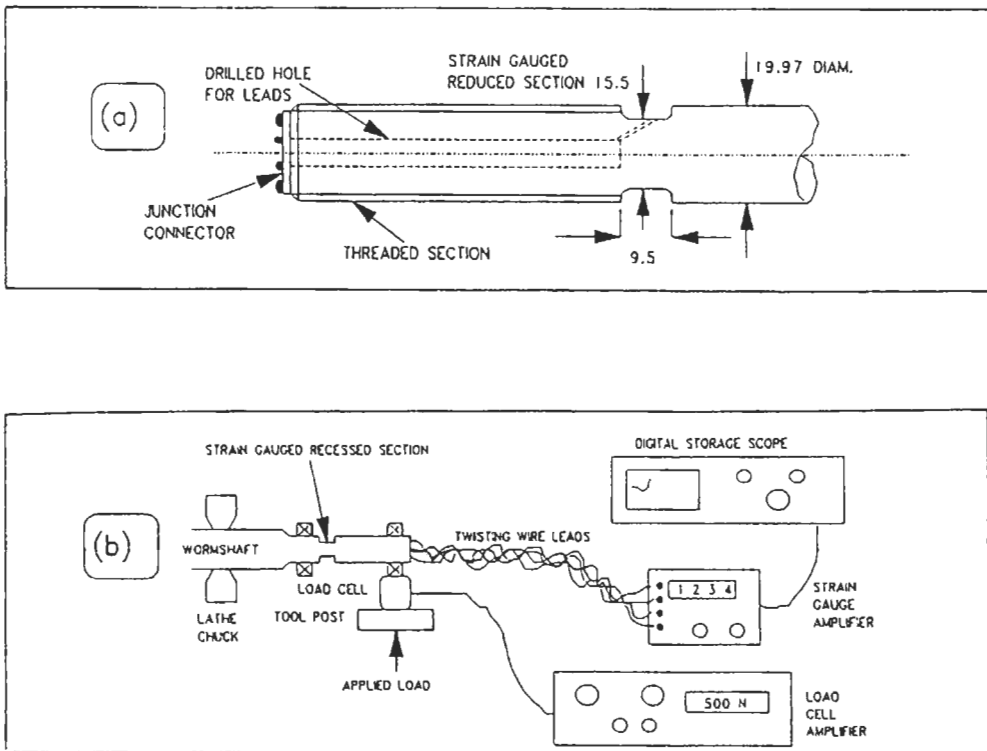

Fig. 3. Schematic diagram of (a) the modification made to the shaft to facilitate strain gauging, together with (b) the layout for calibration of the strain gauged shaft on a lathe.

The lead wires and bridge energising wires were all led through the middle of the shaft to the end and permanently attached to a custom built junction connector glued to the end of the shaft. In this way the straingauged shaft could be conveniently handled and other attachments or machine elements such as nuts, disc brake, lock nut assembly, etc, easily fixed to the shaft in the usual manner.

After assembly the strain gauge signals under load conditions could be monitored by simply soldering fine wires of up to 2 m in length to the junction connector and in turn connecting these to the strain gauge amplifier and digital storage scope facility. Thus it was not necessary to have a slip ring system or small transmitter telemetry device which would have altered the balance and stress conditions at 1400 rpm. The shaft was seldom running for more than 15–20 s at a time, and in any case the rotation direction could be readily reversed to avoid excessive twisting of the wire leads. Under test conditions the twisting of the wires, even at 1400 rpm, was quite acceptable and the concept worked elegantly. When the wires became too twisted they were discarded and readily replaced.

The recessed diameter section was protected with an epoxy glue which was machined smooth after drying so that the Belvel washers readily slipped over onto the full shaft diameter without causing any damage, or spurious strain reading, to the strain gauges themselves. The integrity of the gauges and wiring was checked at all stages of development. Since the strain gauge lead wires were permanently fixed to the junction connector at the end of the shaft, any stress condition of the shaft (e.g. bending or tension) could be selected simply by wiring up the appropriate long twisting wire (i.e. TW) leads to the strain gauge amplifier.

It should be borne in mind that the raw strains recorded would be appropriate for the reduced section actually measured (diameter 15.5 mm, and including the central bored hole) and the resultant stresses determined required modification by a factor (0.825, i.e. reduced) if the stresses were to refer to the original shaft diameter at the thread roots (diameter 16.5 mm). It should also be borne in mind that no allowance has been made for the stress concentration effect of the threads which would increase the localised stress by a factor of typically between 2 [5] and 4 [6].

2.2. *Lathe calibration*

To assess the performance of the strain gauged wormshaft system under rotation conditions, as well as to calibrate the facility, it was mounted on a lathe which could be set to run at 1500 rpm (close to the test bench rotational speed).

Firstly the TW gauge leads were connected to check sequentially for tension, torsion and bending stresses, but at zero angular speed and for each of these configurations performance was satisfactory. It was then necessary to assess performance under rotational conditions. The wormshaft was mounted in a lathe and the main bearing fixed to the shaft at a distance of 75 mm from the strain gauges. Load was applied controllably, through a 5 kN load cell mounted on the tool post, to the bearing, to simulate known bending conditions under rotation. A schematic diagram of the lathe calibration system is shown in Fig. 3(b).

With this system the strain gauges performance in bending can be checked and in effect "calibrated". The effective conversion at the voltage selections used on the digital voltmeter was 2.2 microstrain per millivolt and the behaviour was linear and this was also used for the bench tests at Koeberg.

2.3. *Test bench programme*

The test bench programme at Koeberg needed to measure the stress (inferred from the strains) that might arise from the disc brake loading and to distinguish between bending, tension and torsion components. To facilitate this the trip switch torque limiter device was overridden (i.e. disengaged) so the disc brake torque limiter would indeed be loaded against the brake pads. Typical torque conditions for these tests on the test bench were at a torque of 190 ± 15 Nm. For completeness, tests were also conducted (i) with the trip switch engaged (so that the brake *did not* touch the brake pads); and (ii) with the whole disc brake torque limiter system removed and the actuator simply stopped under so called "stall" test conditions. It was expected that under this latter test condition there would be only low tensile stresses and no bending stresses at the strain gauge, since the disc

brake unit was removed, even though the full stall torque was not insubstantial. The results of this test programme are described in the following section.

3. RESULTS

3.1. *Bending test series*

For the bending test series five tests were initially undertaken with the trip limit switch overridden, so that the shaft rotation was nominally arrested by the action of disc brake against the brake pads. The output from the strain bridge was recorded on the digital storage scope which also had the capability of producing a hard copy of the stored image. The amplitude settings were 0.5 s/cm horizontally and 0.2 V/cm vertically. It was expected that these tests would yield an oscillating signal about the x axis which would gradually increase in stress amplitude, as the brake engaged, until the wormshaft was arrested.

This type of strain trace was indeed obtained, of which test number 3 (Fig. 4(a)) is typical, but with one major variation—the trace exhibited a substantial offset strain and did not oscillate about the *mean* position. These traces may be regarded as composed of 3 regimes which may be characterised as follows (refer to Fig 4(a)). Region I corresponds to the free rotation of the shaft under full speed conditions. Small (noise) oscillations about the mean indicate the gauges were responding but there was no bending in the shaft. As the torque limiter brake was applied (region II) individual oscillations in the trace at the frequency of rotation (period 0.042–0.05 s) were observed. These increased in amplitude as the brake engaged, until the brake effectively arrested the shaft and load was maintained. The curious observation, however, was the large offset strain of approximately 178 $\mu\varepsilon$ (microstrain) in this case (Fig. 4(a)). This will be discussed in greater detail later. Region III is the appropriate constant load condition, once the shaft had been arrested. When the power was dropped completely the strain trace returned to zero and the x axis.

When the limit switch system was engaged (i.e. not overridden) then the disc brake torque limiter was not put under load. The recording of the bending stress for this case indicated minimal stresses (less than 5 MPa) (Fig. 5(a)) as expected.

Although the number of bending tests was limited due to time constraints, it is nonetheless useful to interpret these bending strains in terms of (i) the measured offset; (ii) cyclic amplitude; as well as (iii) peak strain, together with the consequent derived stresses. These stresses, with the torque switch limiter overridden, are effectively equivalent whether derived from a modulus viewpoint or from a calibration curve approach and the data is summarised in Table 1. The data in the table is considered to be accurate to within approximately 8% and from this data it can be inferred that, under nominally "normal" bench test loading conditions it is possible for significant peak bending stresses of approximately 170–200 MPa to occur. Such cyclic stresses are not trivial, especially when one takes into account the stress concentrating effects of the threads, from which it would appear fatigue at the thread roots is highly likely. The inherent cyclic stress is, however, typically less than 50 MPa, which seems reasonable from a design viewpoint.

3.2. *Tension test series*

The strain gauges were now connected to the strain gauge amplifier using the TW leads in a "tension bridge" configuration as opposed to a "bending bridge" configuration. The loading tests against the disc brake torque limiter with the limit switch disconnected, just as in the bending test series, were repeated. A typical strain time trace result is shown in Fig. 4(b) from which, it is clear that the cyclic stresses were very low as the disc brake engaged but the wormshaft, once arrested or stalled, showed a net tensile stress, as might be expected. The magnitude of this tensile stress, however, was not excessive, typically 45 ± 5 MPa.

Again for completeness a tension test was conducted where the limit switch detector was employed (so that the disc brake torque limiter did not come into operation) and the measured tensile stress was low (< 12 MPa) (Fig. 5(b)). Thus under safe operation of the limit switch the wormshaft tensile stresses were low and the performance quite satisfactory.
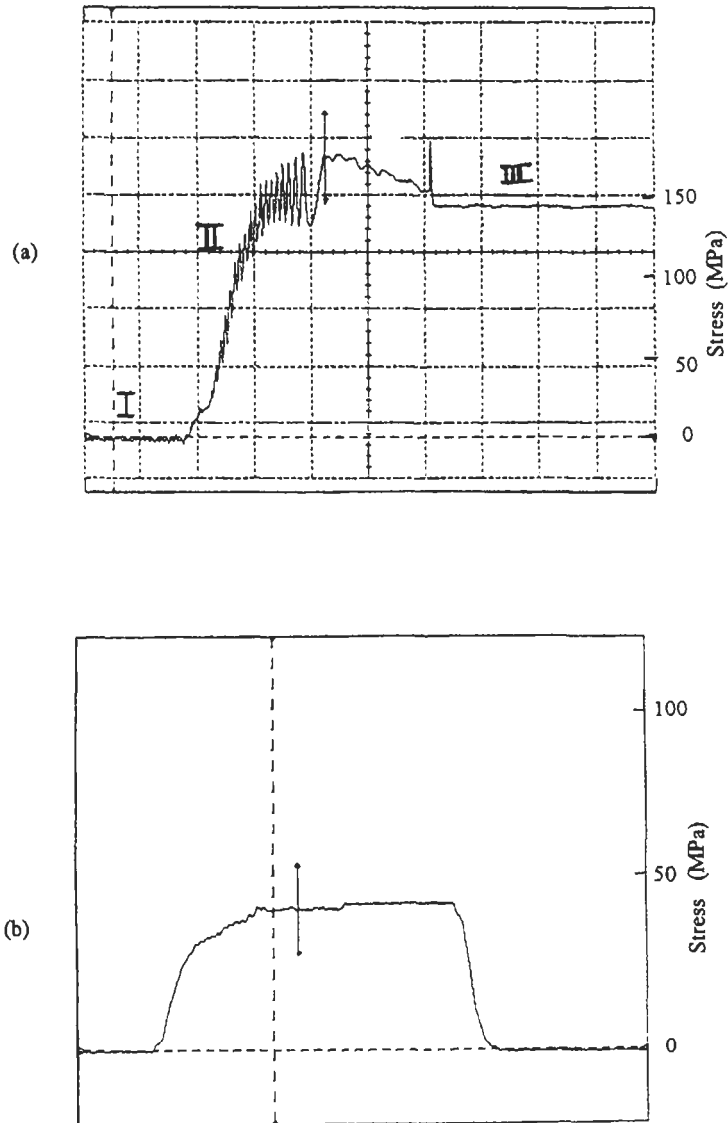
Fig. 4. Strain time traces for the strain gauged shaft on the Koeberg Rotork test bench for (a) bending and arrest against the disc brake, (b) tension and arrest against the disc brake. Note the significant offset.

3.3. Torsion test series

The torsion traces, e.g. Fig. 6, are consistent with the bending traces (e.g. Fig 4(a)) in that the first downward trend appeared to be due to take up of the Belvel washers. This was followed by an oscillation as the disc brake torque limiter engaged leading to arrest of the wormshaft at fixed level before the power was switched off. The levels of stress, however, were low, typically 55 ± 4 MPa on the actual shafts, and were considered as not excessive.

3.4. Stall tests

Mostly for completeness, it was considered worthwhile to undertake some tests under so called "stall" conditions on the test bench, but with the whole disc brake torque limiter assembly removed.
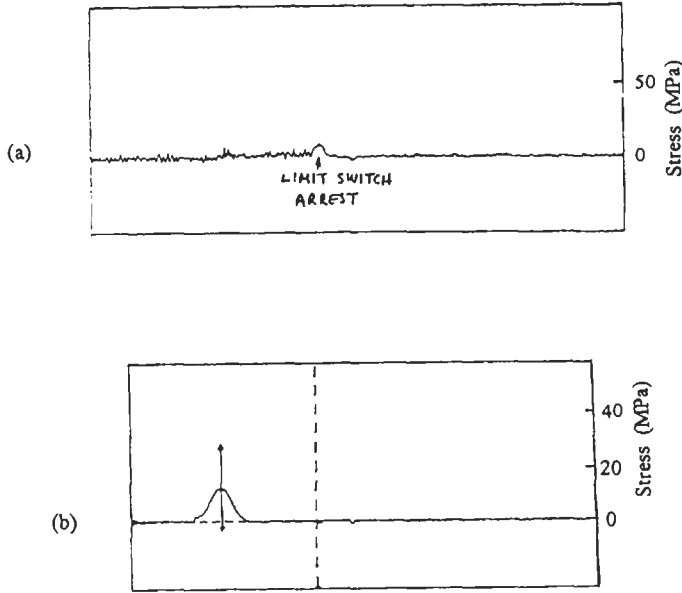
Fig. 5. Strain time traces for limit switch operation and arrest for (a) bending and (b) tension. In both cases the resultant stresses are small.

Table 1. Bending strains and stresses from the bending bridge configuration, including the disc brake torque limiter

Test number	Measured strain offset after stall ($\mu\varepsilon$)	Measured cyclic strain ($\mu\varepsilon$)	Measured peak strain ($\mu\varepsilon$)	Stress offset (MPa)	Cyclic stress (MPa)	Peak stress (MPa)
1	1567	502	2310	130	42	191
2	1732	630	2420	143	52	200
3	1780	583	2169	147	48	180
4	2024	575	2288	168	48	189
5	1970	620	2222	163	51	184
6	1582	625	2156	131	52	179
Mean	1776	589	2261	147	48.8	187
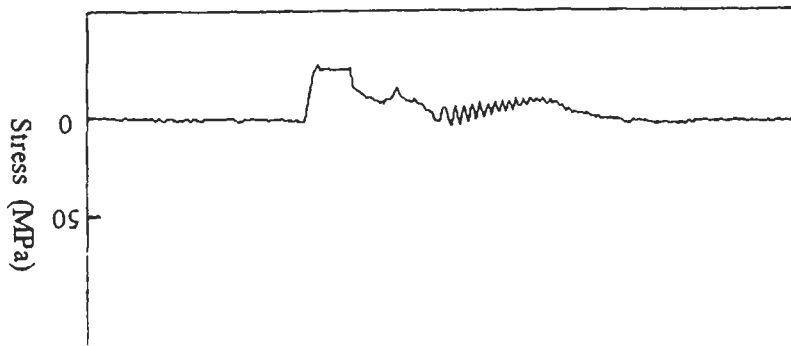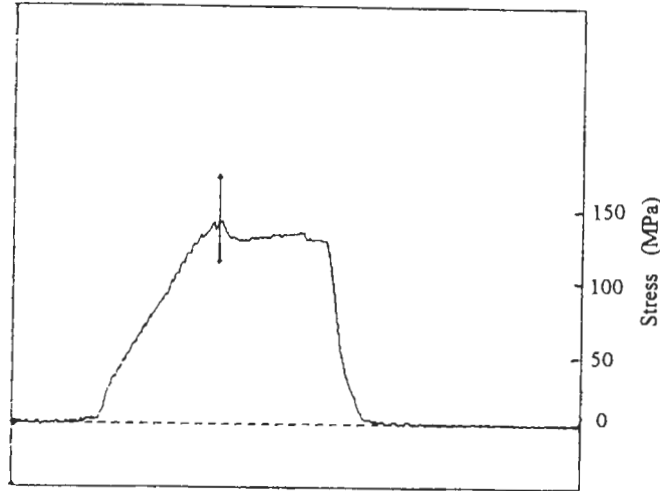
Fig. 7. Strain time trace in the bending configuration under so called "stall" conditions, with the disc brake completely removed. Far from exhibiting minimal stresses the trace shows substantial offset bending strains imposed through the Belvel washers and recessed nut assembly.

Table 2. Bending strains and stresses from the bending bridge configuration under stall conditions using the standard (thin) recessed locking nut

Test	Measured strain after stall ($\mu\varepsilon$)	Peak strain ($\mu\varepsilon$)	Offset stress (MPa)	Peak stress (MPa)
S 1	1328	1685	110	140
S 2	1408	1628	117	135
S 3	1524	1602	126	133
S 4	1452	1597	121	132
S 5	1386	1540	115	128
Trip 1	—	57	—	4.7

The strain gauge system was wired up with the TW leads as a bending bridge as this configuration exhibited the largest strains. The test was simply to stall the actuator on the test bench at a relatively high torque of 700 ± 70 Nm, which is typical for such stall tests. It was expected that there would be negligible *bending* stresses since the disc brake unit was absent.

The strain time traces, were, however, remarkable. Rather than a small ripple about the x axis, a significant offset strain (and hence stress) was observed (Fig. 7). The offset strains were large (Table 2), with typical direct bending peak and offset stresses of approximately 133 and 118 MPa respectively. These are not trivial, and, when considered with SCF effects, would easily cause fatigue cracking.

4. DISCUSSION

The implication of these observations was most revealing. The assumption all along had been that since the cracking had been occurring from bending fatigue in the first couple of threads, the disc brake torque limiter had presumed to have been responsible for the high cyclic stresses. What these latest "stall" tests suggested was that although the disc brake indeed contributed to the stress amplitude, a major part of the high stress value appeared to arise from the recessed "thin" nut and Belvel washer combination. The recessed nut which holds the Belvel washer string in place can

effectively apply a bending stress to the shaft through the motor housing, which carries the load of the Belvel washers through the main bearing (Fig. 2).

If the Belvel washer assembly string or the recessed nut were to apply anything but absolutely symmetric loading, then there could be a significant bending stress developed in the shaft. The question of how well the recessed thin nut located on the thread became important. Since the recessed nut in question for the tests had a relatively loose tolerance, on the one hand, and only engaged less than two threads on the other, it was possible that the nut may have located in a non symmetrical position on the shaft—especially under load and under the influence of imperfect Belvel washers, which themselves exhibit a loose fit. The thin nut could effectively "rattle" on the shaft. Such poor location of the nut could result in a bending stress component to the shaft, especially under high torque, rapid stall conditions.

In view of this somewhat unexpected finding, it was decided to test the concept (i.e. that the high bending stresses in the shaft were caused by the seating of the Belvel washer/thin nut combination), by replacing the thin nut with one very much longer. The tolerance and thread details were still the same, but with a recessed nut of length 28 mm and engaged thread length of 8 threads (as opposed to approximately 4 mm long and nearly 2 engaged threads), the capacity for the long nut not sitting squarely on the shaft was substantially reduced. In addition, a further 28 mm long nut was manufactured, but with a deliberate oblique face (2 degree offset) to simulate the thin nut under non axisymmetric location.

Bending tests for both disc brake arrest and so-called "stall" tests at comparable torques (to Figs 4 and 7) using the square faced long nut are shown in Fig. 8(a) and (b). These strain time traces show substantially reduced offset bending stresses, reduced from typically 124 ± 6 MPa to approximately 24 ± 3 MPa for "normal" stall conditions. With the long nut but $2°$ oblique face under stall conditions high offset stresses of typically 172 ± 3 MPa, were obtained. Tension stresses were less (15.5 ± 3 MPa) and under trip switch arrest conditions the stress levels were even lower. The use of the square longer nut assembly to reduce the offset stress appears vindicated and subsequent to making the manufacturers aware of this finding, they undertook to redesign this "thin" lock nut system. The final design incorporated a system not unlike the above long nut solution in that the recessed nut did not exhibit any canting over. The fatigue cracking problem of these actuator shafts has been overcome, and the problem effectively solved. What is of special interest here is the observation that, as a result of the tolerance of the nut in an ordinary "nut and
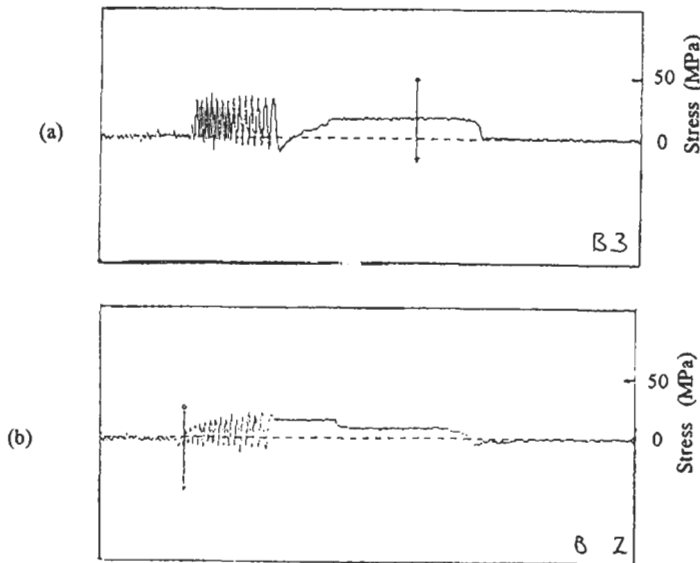

Fig. 8. Strain time traces for the long nut in bending configuration for arrest from (a) the disc brake and (b) under "stall" conditions with the disc brake removed (comparable to Figs 4 and 7). The large offset stress has effectively been removed.

bolt", if tensioned rapidly, and if "thin" so only a few threads engage, substantial bending stresses can occur on the shaft or "bolt", and this is exacerbated if the nut is "thin", as was the case here.

5. CONCLUSIONS

An experimental stress analysis of a Rotork actuator incorporating a disc brake assembly has been undertaken. Use was made of a double rosette strain gauge system and lead through wires to the shaft core with simple, yet elegant twisting wire connections to the monitoring equipment, which obviated the need for telemetry or slip rings and balancing.

On site tests of the actuator arrest under trip, stall and disc brake conditions was undertaken with the strain gauge bridge configured to monitor sequentially either bending, tension or torsional stresses.

High bending offset stresses (187 ± 12 **MPa**), initially attributed to the disc brake,were in fact due to poor setting up and loose tolerance of the thin lock nut–Belvel washer combination, which was canting over and applying significant bending stress, via the actuator housing, to the shaft. Such stresses were easily high enough to have caused the rapid fatigue cracking.

Redesign of the lock nut system effectively incorporating a longer nut system which could not cant over on the shaft, together with improved processing of the shaft, effectively solved the problem.

REFERENCES

1. Burrell, I. J., Rotork Engineering report ER181, June 1991.
2. Blackbeard, P. J., ESKOM Report G911211011, 12 September 1991.
3. Scheffler, O., Scientific Investigation Bureau, Report 920546, *Rotork Actuator Shafts*, 25 May 1992.
4. Tait, R. B., Rotork 30 NABT Actuator Wormshaft—April Report, 21 April 1992.
5. Shigley, J. E., and Mischke, C. R., *Mechanical Engineering Design*, 5th edn, McGraw-Hill, 1989.
6. Ward, K. A., Nuclear Electric Report, No TD/SIP/mem/1190091, Section 3.5 and Appendix C, 1991.

AN INVESTIGATION OF THE FAILURE OF LOW PRESSURE STEAM TURBINE BLADES

N. K. MUKHOPADHYAY, S. GHOSH CHOWDHURY,* G. DAS,
I. CHATTORAJ, S. K. DAS and D. K. BHATTACHARYA

National Metallurgical Laboratory, Jamshedpur 831007, India

Abstract—An analysis of the failure of LP turbine blades of a 210 MW thermal power plant has been presented in this paper. The blade material is of 12% Cr steel with tempered martensitic microstructure. Microstructural analysis as well as hardness and tensile tests did not indicate any degradation in terms of microstructure and mechanical properties. Physical discontinuities were observed in the braze joint which might have been formed due to improper brazing operation. Failure of the brazed joints between the blade and lacing rod was found to be due to improper brazing operations and corrosion effects during service. Fractographic evidence showed that the cracks were initiated from various points on the blade surface, which were at the interface with the lacing rod. Striations and beach marks were also observed which indicated the occurrence of high cyclic loading on the blades. Frequency data obtained from plant indicated the possibility of excessive vibration generated due to fluctuation in grid frequency during operation. Thus, the situation was aggravated due to a resonant condition of vibration, facilitating the propagation of cracks which were initiated earlier. © 1998 Elsevier Science Ltd. All rights reserved.

Keywords: Thermal power plant, turbine blade failure, vibration, fatigue.

1. INTRODUCTION

Steam turbine blades are critical components in power plants which convert the linear motion of high temperature and high pressure steam flowing down a pressure gradient into a rotary motion of the turbine shaft. As the steam enters turbine from the boiler, it passes through different stages such as high pressure (HP), intermediate pressure (IP) and low pressure (LP) zones. Statistics shows that LP turbine blades are generally more susceptible to failure compared to those of the HP and IP. There are various mechanisms by which LP blades fail [1–3]. Almost 50% of the failures are related to fatigue, stress corrosion cracking and corrosion fatigue. The fatigue failure takes place as a result of vibration arising from the fluctuation of bending stress due to the asymmetric flow of steam. Once a crack is initiated, the component is assumed to have failed since crack growth takes place rapidly. Even this fatigue failure can be accentuated by corrosion. Creep damage is not important for the LP blades. It is reported that failure initiates from various locations of the blade and these are 26% from shroud, 20% from lacing hole, 40% in the aerofoil region and 14% in the blade attachment [1]. Therefore, the mechanism of the failure varies along the length of the blades.

In general, LP blades in a steam turbine assembly are designed to run for 30 years, but many cases of premature failure of blades are encountered in practice. A recent survey indicates that causes for about 40% of the failures could not be pinpointed [1]. To reduce the incidence of failure, it is necessary to take into account all the aspects important for the performance of a blade. Thus, it is necessary to understand the metallurgy of the blade material, operating stresses and the operating environment. As the blade's design is complex, the actual state of stress is highly complicated. However, if the design conditions do not deviate in service, the state of the stresses in a blade should not cause any concern. The stresses acting on the blades mainly originate from centrifugal loading and vibratory response of the blades. Vibratory stresses are normally maintained at low

---

level by (a) ensuring blade frequencies within a narrow limit and thus avoiding resonant vibration and (b) limiting steam bending stresses.

The total number of blades at a particular stage is divided into groups. Blades in each group are tied by lacing rods passing through the outer and inner lacing holes. The rigidity of the group is maintained by joining the lacing rods with blades by brazing at the hole edges. In respect of the materials, the inclusions and surface defects are minimised to reduce the tendency for fatigue failure. Regarding the environment, attention is given to steam quality so that corrosion fatigue does not take place. A large amount of investment is made to achieve the best design of a turbine with a clean steel having correct microstructure and mechanical properties. Failures that are still encountered are mainly related to improper maintenance and operating conditions. Knowledge of failures due to such reasons often go a long way in preventing failures and to greatly improve the economy of power generation.

In this paper the results of the analysis of failed LP turbine blades of a 210 MW unit of one thermal power plant are presented [4]. The unit was first overhauled after five years of commissioning. Within nearly two years of operation after overhauling, the unit was forced to shut down because of high level of noise and vibration at the LP zone during operation. On opening the turbine casing, four turbine blades of the 29th stage were found fractured. In the present case, the stage where failure took place, there are in total 120 blades and these were divided into 15 groups having eight blades each. A stage is defined as the position of the wheel containing the blades, which is counted from the position of the HP zone along the shaft towards the turbogenerator. In the present unit, HP and IP zones contain 12 and 11 stages whereas in the LP zone, there are eight stages namely stages 24–31 among which the 25th and 29th stages (also known as Bauman stages) are very much prone to vibration arising from steam flow during operation. The total number of start ups were 325 (i.e., 46 times cold start and 279 times hot start). The turbine was operated mostly at 50 Hz; however, for certain period of time, it was operated above/below this level. The durations for such operations are 1850 h in the frequency range of 51–51.99 Hz and 200 h of 52–52.4 Hz. It was noted that, due to some problems in grid frequency regulation, the unit was operated at 45.5 Hz for 13 s over two days prior to failure.

The objective of the present paper is to analyze the causes of the failure i.e., whether it is due to: (a) material defects in the blade, lacing rod or brazed joints; (b) improper brazing process; (c) improper plant operations in regard of deviations from the stipulated frequency criterion and/or water chemistry.

2. EXPERIMENTAL DETAILS

A portion of the blade containing the fractured surface was collected from the assembly. The virgin and service exposed brazing material and the inner and outer lacing rods were also obtained from the plant. Specimens for microscopy were cut from blade and lacing rods and polished using standard metallographic techniques and etched with nital. Optical microscopes and JEOL JSM 840A scanning electron microscope (SEM) were employed to observe the microstructure in order to ascertain the quality of the material. Energy dispersive analysis by X-rays (EDX) attached to the SEM was carried out to ascertain the composition of blade, lacing rod and braze joint. Fractography was done in the SEM to analyze the fracture features. Portions of blades and rods were mounted for hardness testing with 10 kg loads in a Vickers indentation testing machine. Tensile tests were performed in an INSTRON with a strain rate of 10^{-3}/s. To simulate the effect of stress conditions arising from the steam pressure on the blades, high cycle fatigue tests were carried out with single edge notch (along with the width direction of the blade) test pieces ($36 \times 9.5 \times 2.5$ mm) deformed in 3-point bending on an AMSLER Vibrofore machine operated with a frequency of 50 Hz.

3. RESULTS

3.1. *Visual inspection*

On opening the turbine casing, three blades were found fractured from the location of the inner lacing hole and another one from the outer lacing hole. The assembly of the blades with inner and

Fig. 1. Photograph showing the assembly of the blade without the lacing wire which has been removed by debrazing. Arrows indicate the position of lacing holes from where crack initiation occurred.

outer lacing holes but without lacing rods is shown in Fig. 1. The locations of the fracture i.e., at inner and outer lacing holes are indicated by arrows (Fig. 1). The lacing rods attached to the blades were fractured and some of the fractured portion could not be identified inside the casing. Distortions due to impact from the broken blade and lacing rod piece were found at the leading and trailing edges of many blades. The brazed joints between the lacing rods and the edges of the lacing holes were found disjoined at many places. Holes, cavities and several other physical discontinuities were observed in the brazed material attached to the lacing hole. It was obvious that decohesion of the brazing joint had occurred at many places. It is important to note that many brazed joints were found failed and developed defects which were revealed by nondestructive examination such as dye penetrant testing during the last overhauling period. The broken and damaged braze joints were removed and braze repairing was carried out in those areas. The colour of the blade was black indicating Fe_3O_4 (magnetite) scale of varying thickness.

3.2. *Chemical analysis*

A typical chemical analysis of the materials obtained by standard chemical analysis techniques is given in Table 1. The blade and rod were found to be of the same type containing 0.2% C and 12–14% Cr (AISI 400 series of stainless steel). Other alloying elements are within 1%. The brazing wire was found to contain Ag, Cu, Zn, Cd in the range of 65, 15, 10, 10 (wt%) respectively.

3.3. *Microstructure*

The blade material showed a tempered martensitic microstructure (Fig. 2(a)), whereas a bainitic microstructure (Fig. 2(b)) could be observed from the inner and outer lacing rod. These are

Table 1. Bulk chemical analysis of the blade and lacing rod (wt %)

Material	C	Si	Mn	Cr	Mo	S	P
Blade	0.23	0.83	0.46	12.1	0.25	0.007	0.03
Lacing rod	0.21	0.40	0.50	13.4	0.14	0.01	0.05
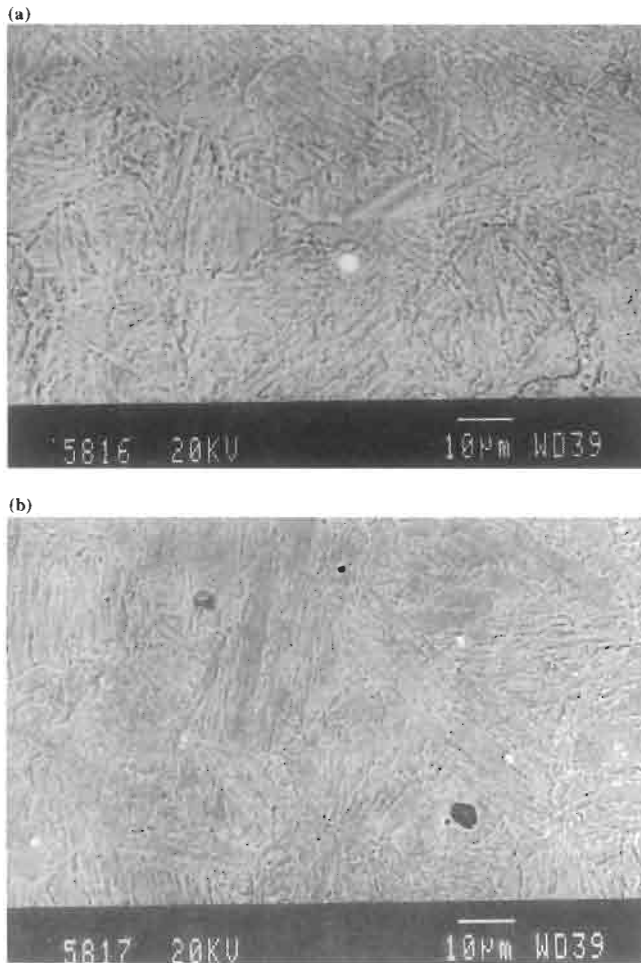
Fig. 2. (a) Tempered martensitic microstructure of the blade material; (b) tempered bainitic microstructure of lacing rod.

the normally expected microstructures. The same reproducible microstructures were observed in randomly selected places, indicating the homogeneous nature of microstructure. No indication of microstructural degradation was thus observed in either blade or lacing rod structures [3].

3.4. Fractography

A low magnification fractograph is shown in Fig. 3. The holes, discontinuities and pores of various sizes were observed in the area associated with the lacing holes/braze interface. These discontinuities marked 'A' in Fig. 3 indicate poor wetting with the blade surface during the brazing operation. The small holes marked 'B' might have been generated due to galvanic corrosion. The EDX was carried out for composition analysis near the microvoids and holes. It was found that the Zn content in the remnant brazing material had decreased whereas Fe, although not present in the original braze material, was detected. The elemental redistribution of the alloying elements, mainly Zn, is indicating galvanic corrosion. Because of high electronegativity compared to Ag, Cu and Fe, the anodic dissolution of Zn from the braze material in wet steam is possible. Ammonia present in wet steam may also enhance corrosion of the brazing material. It was apparent that corrosion had decreased the strength of brazed joint rendering the interface weak, leading to decohesion.

A high magnification fractograph of the fractured surface on the thicker section of the blade is presented in Fig. 4(a). The crack initiation point is identified at 'X'. The enlarged view of region 'X'
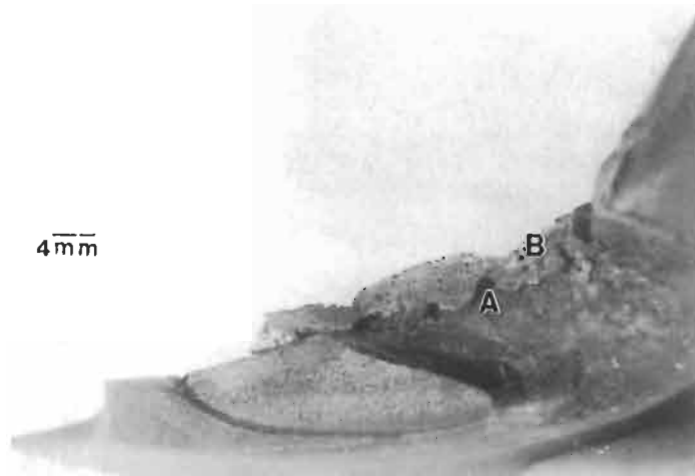
Fig. 3. Low magnification image of the fractured surface of the blade showing physical discontinuities (marked as A) and holes (marked as B) in the braze joint.

is shown in Fig. 4(b). Another initiation point at 'Y' (Fig. 4(c)) indicates multiple crack origin sites along a plane inclined to the radial direction (centrifugal axis) of the blade. The fretting mechanism due to rubbing or low amplitude impact collision between blade and loosened lacing rod appears to be the controlling factor for crack initiation. The stage II of crack growth due to fatigue has been established from the presence of striations and ratchet marks (Fig. 5(a) and (b)). The last stage of the crack propagation associated with overload has been identified from the presence of ductile features. The fracture surface of the thinner side of the blade (the other side of the lacing hole) showed a distinct transition from intergranular/quasicleavage to a ductile fracture mode from the inner surface to the outer surface. The crack initiation point was at the corner which was diagonally opposite point 'X' (marked as 'Z' in Fig. 4(a)). Though there are no striations present in the fracture surfaces, it may be interpreted as fatigue crack growth with high stress intensity range and mean stress. These types of features under fatigue load in thinner sections (i.e., plane stress condition) have been reported in the literature [5]. It can also be surmised that the presence of quasicleavage features was due to superimposed static or steady load (in this case mainly centrifugal load) during fatigue crack growth. Figure 6 shows intergranular features and cracking from point 'Z' in Fig. 4(a)). Figure 7 shows decohesion at the braze–blade interface.

3.5. Mechanical properties

The hardness values of the blade and rod in all the regions were consistently found to be 265 ± 10 VPN (Rc 26) and 225 ± 10 VPN (Rc 20) respectively. The values are found to be within the specified limit [3]. The microhardness of brazed joint which had been collected after removing from the lacing rod was measured to be 150 VPN, whereas the hardness of the brazing wire was found to be 200 VPN. The lowering of hardness indicates the degradation of the brazing joint while in operation.

The stress/strain diagram obtained from a tensile test shows that the steel possesses good yield strength (620 MPa), tensile strength (800 MPa) and elongation (21%) which are as per the recommended values [3]. The material was not brittle as evidenced by the presence of dimples in the fracture surface of the tensile specimen.

3.6. High cycle fatigue test

Specimens of dimensions $36 \times 9.5 \times 2.5$ mm were prepared for testing. The geometry of the notch is as follows: V notch with depth 2 mm and radius of the tip 0.25 mm. In one specimen a static load of 0.7 kN and a dynamic load of 0.5 kN, were applied whereas in another specimen a static load of 0.5 kN and a dynamic load of 0.3 kN were applied. The maximum load (1.2 kN) is equivalent to

216
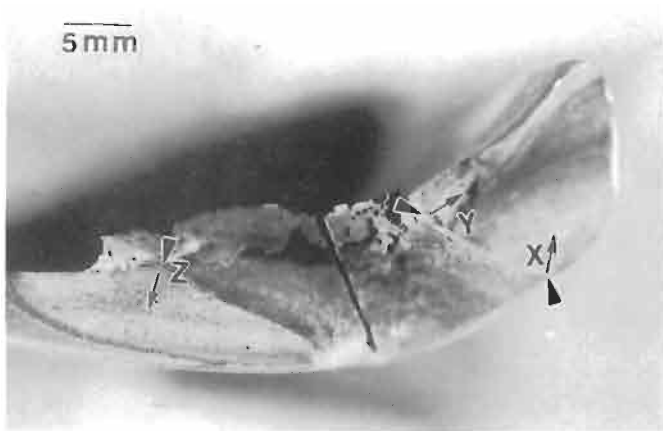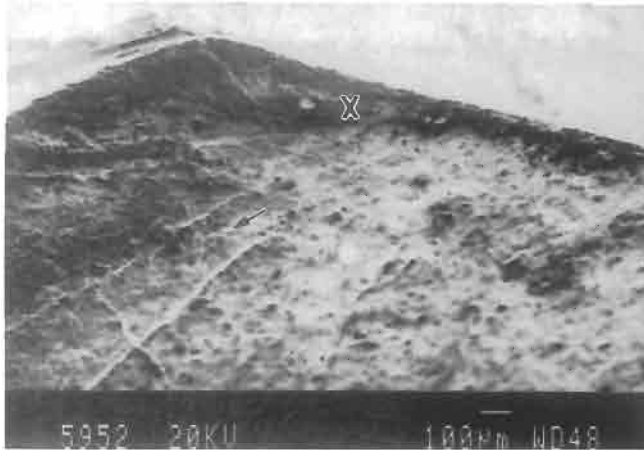
Fig. 4. (a) Crack initiation points marked by arrow head in optical micrograph; (b) SEM fractograph taken from area marked as 'X' in Fig. 4(a); (c) SEM fractograph from area marked as 'Y' in Fig. 4(a). Arrows indicate crack growth directions (dark line at the centre indicates the cut-mark along which fracture surface was cut into two pieces for SEM observation).
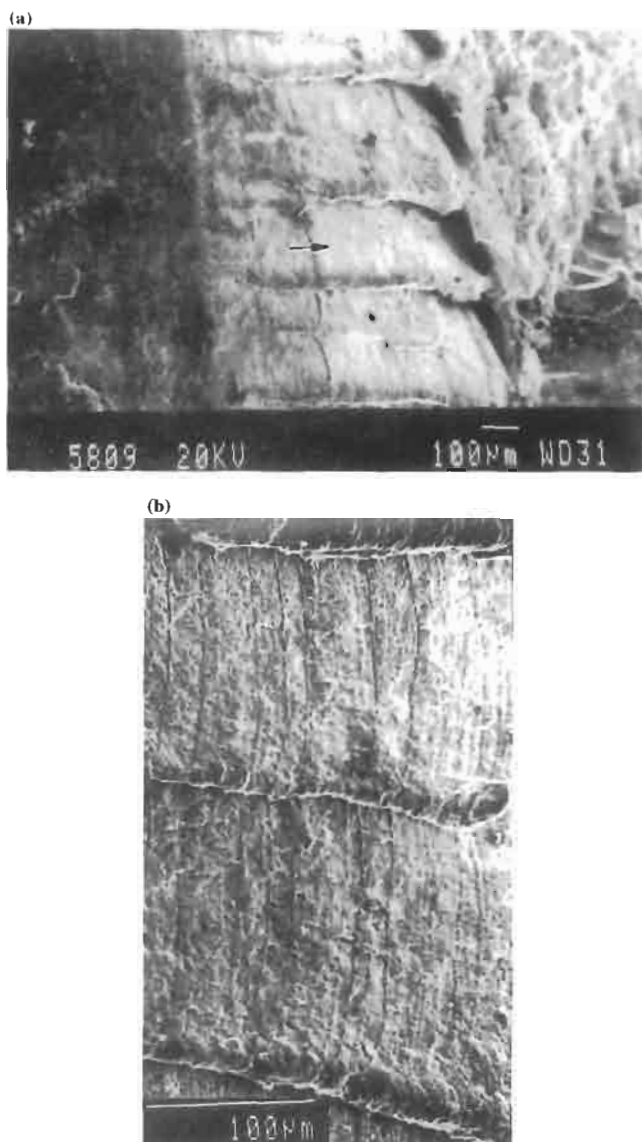
Fig. 5. (a) Enlarged area marked as 'C' in Fig. 4(c); (b) magnified portion of (a) revealing fatigue striations and ratchet markings. Arrow indicates the crack growth direction.

half of the yield stress with this specimen geometry. In the specimen with 0.7 kN static load and 0.5 kN dynamic load a crack was detected after 10^4 cycles followed by rapid failure. The fracture surfaces examined by SEM did not exhibit any striations or beach marks (Fig. 8(a)). The presence of a large number of secondary cracks in the fracture surface indicates a high amount of work hardening during crack propagation which is in conformity with the literature of fatigue failure. In the case of the second specimen no cracks were observed until 13×10^5 cycles. The test was then interrupted and loads were increased to a static load of 0.6 kN and a dynamic load of 0.5 kN. Cracks were observed after 2×10^5 cycles and the specimen failed immediately. Fatigue striations were observed in the fracture surface which was roughly 2 mm away from the notch root (Fig. 8(b)). It is concluded from the second test that the damage accumulation during the initial loading facilitated the crack initiation within a short time at the higher stress level. The simulation, thus, indicates that depending on the level of mean stress and amplitude of the alternating stress, one can
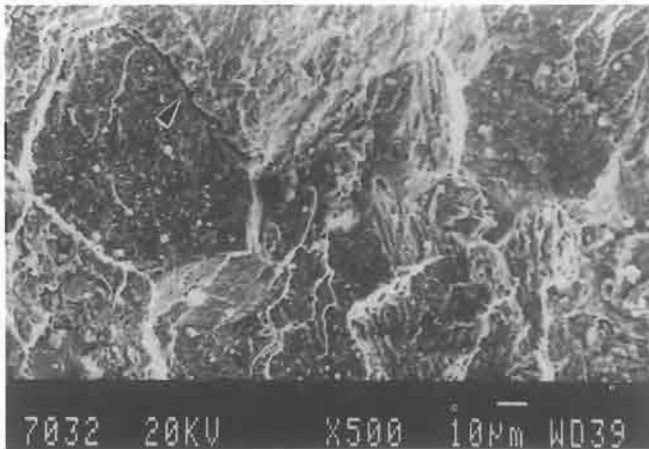
Fig. 6. Fractograph from the site marked as 'Z' in Fig. 4(a) showing the presence of intergranular features. Intergranular crack is indicated by the arrow head.
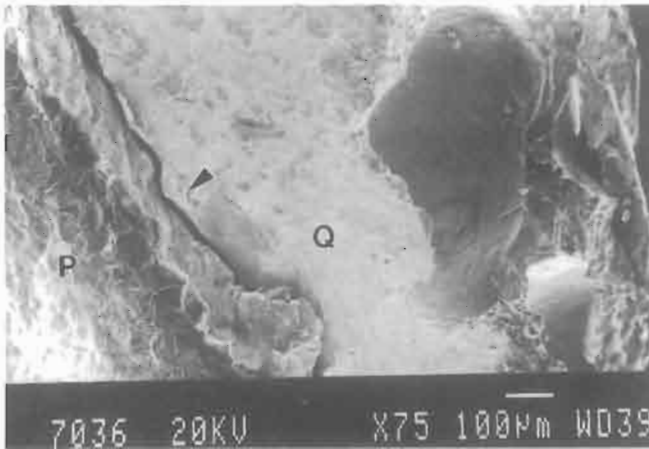
Fig. 7. Decohesion at the braze–blade interface (marked by arrow head). P: blade; Q: corroded portion of the braze.

observe various types of features on fatigue fractured surfaces. This agrees with other investigations on fatigue reported in the literature [5, 6].

4. DISCUSSION

4.1. *Corrosion mechanism of braze material*

Brazed ferritic steels are extremely susceptible to interfacial corrosion when a Ag–Cu–Zn–Cd brazing filler material is used. The conditions conducive to this form of corrosion are that (a) one member of the joint must be stainless steel, (b) the brazing alloy must be susceptible to this attack and (c) the joint must be exposed to wet or damp conditions [7]. It is obvious from the environment of LP zones that all three conditions existed at the lacing wire-blade brazed joint. The brazed material exhibited numerous pits and micropores which are morphologically similar to plug type dealloying. This was confirmed by SEM-EDX observations which revealed significant depletion of Zn from the brazing near to the lacing hole. Cr was detected in the braze material close to the blade–braze interface suggesting depletion of Cr from the blade. It is difficult to pinpoint the exact mechanism leading to this interfacial attack although dealloying of the braze with simultaneous

(a)

(b)
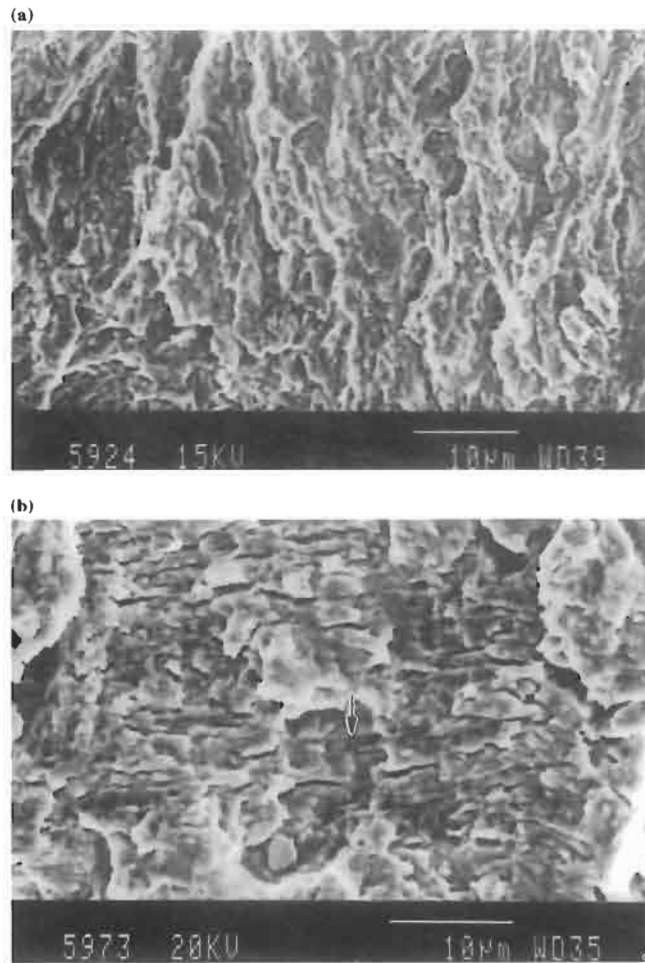
Fig. 8. Fractograph from simulated HCF test 1(a) and test 2(b). Fatigue striations can be noted in (b).

galvanic corrosion of the steel parts is indicated; the latter is accelerated by the loss of chromium, especially of the blade, by the mechanism suggested by Kawakatsu [8]. The loss in chromium is also reflected in the occurrence of some grain boundary cracks as shown in Fig. 6. There is no evidence that stress corrosion cracking was the cause of failure of blades. Interfacial corrosion of the type observed resulted in significant weakening of the braze joint (Fig. 7) and detachment of the lacing wire leading to fretting fatigue for crack initiation.

4.2. Stress patterns in the blade

The stresses acting on the blade in the steady state condition are (i) centrifugal stress and (ii) bending stress. Bending stresses, originating from the steam pressure of a typical 210 MW unit are shown in the literature to be within 8 MPa near to the central portion of the blade and within 4 MPa near the inner and outer lacing hole [1]. The stress (σ_c) due to the centrifugal load can be calculated from the following equation [9]:

$$\sigma_c = \frac{MV^2}{Ar}$$

$$= \frac{4\pi^2 M r N_s^2}{A}, \tag{1}$$

where M = mass, V = surface velocity, r = radius from the rotation axis, A = area of cross section, N_s = turbine speed in rps. Here we have calculated the centrifugal stress at the root point ($r = 0.5$ m), middle point ($r = 0.75$ m), and near the inner ($r = 0.8$ m) and outer lacing hole ($r = 0.95$ m) of the blade. The blade geometry is tapered and the cross-sectional area is a decreasing function from the root point to the tip of the blade. Similarly, M is also decreasing from the root of the blade to the tip whereas the other parameters, V and r are an increasing function from root to tip of blade. M is estimated to be 2.5 kg at the root, 0.8 kg at the middle, and 0.5 kg at the inner and 0.1 kg at the outer lacing hole. The approximate cross-sectional area at those points have been calculated to be 880, 480, 400, 160 and 96 mm^2 respectively. The stresses as calculated are found to vary from 140 MPa to 59 MPa at various points, which are shown in Fig. 9. The stresses at the inner lacing hole and outer lacing hole are estimated to be 100 MPa and 60 MPa respectively. It is important to consider that when the braze joints are broken, the stress concentration at those points could be as high as three times the average values computed at those points, rising to 300 MPa and 180 MPa respectively. These values can be taken as upper bound estimates and implies that the holes can act as strong stress raisers and as potential crack originators.

The stress variation due to a change of frequency of ± 5 Hz from the value of 50 Hz (which can be taken as the maximum variation) near the inner lacing hole during operation, can be calculated from the following equation:

$$\Delta\sigma = \frac{2\sigma\Delta N_s}{N_s}, \tag{2}$$

which gives the value as ± 20 MPa, which can be experienced by the system time to time. Though these stress values have not been calculated by rigorous stress analysis, the values can be taken as upper bound estimates from the simplified calculation which helps to understand the stress patterns in the blades. Thus from the low value of stress, it can be realized that the material will resist fracture in a normal situation unless corrosion or other causes become controlling factors. However, it should be noted that this fluctuation of stresses of 20 MPa makes a cycle within the load cycle generated by the centrifugal load. Thus, the blade will be experiencing an irregular or random stress cycle. Corrosion effects were not observed on the fracture surface of the blades except in the thinner region of the blade. For a high cycle fatigue failure such as the case here, the maximum stress level can be low and far below the yield strength level. In the present case the cyclic loading had a chance to play a role because the brazed joint gave way at many places making the blade act as cantilever
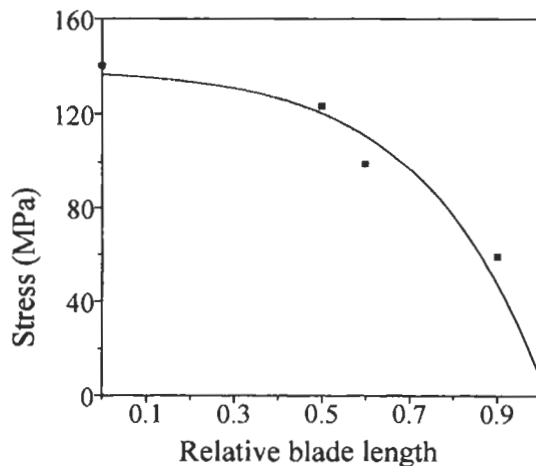

Fig. 9. Pattern of centrifugal stresses in an LP blade during operation at 50 Hz frequency.

beam. The fluctuation of load pattern affecting bending stress and centrifugal stress and the resonance vibration from time to time with varying durations create complex alternating or vibratory stress. This vibratory stress led to fretting between the loosened lacing rod and blade causing fatigue damage. Thus, the crack initiation became easier from the contact points ('X' in Fig. 4(a)) and a crack propagated through a high cycle fatigue mechanism (HCF).

4.2.1. *Fatigue behaviour*. The most widely used fatigue crack growth law describing the crack propagation rate (da/dN) is the Paris equation [10]:

$$\frac{da}{dN} = A(\Delta K)^m, \tag{3}$$

where A and m are material constants and ΔK is the stress intensity range i.e., $K_{max} - K_{min}$ [K_{max} = maximum stress intensity factor corresponding to the maximum load during the cyclic loading, and K_{min} = minimum stress intensity factor]. K is defined from fracture mechanics as approximately $\sigma\sqrt{(\pi a)}$, where σ is applied stress and a is the crack length. Crack growth behaviour is controlled by mean stress and alternating stresses. If the mean stress is high, the stage I and stage III crack propagation rate increases more compared to stage II. In fact, features due to a static mode of fracture, i.e., intergranular, quasicleavage and dimples can also be seen on the fracture surface under fatigue loading.

In the present investigation, striations have been observed in the thicker portion of the blades. In the thinner parts other features such as intergrannular, quasicleavage and dimples have been observed. Laboratory simulated fatigue testing discussed earlier has also shown the presence of striations under various kinds of loading condition. Growth by fatigue was later followed by final failure due to an overload by shear at an angle to the crack growth direction (Fig. 10) [11].

4.3. *Turbine speed and grid frequency*

A turbine assembly is designed for operation under a fixed power line frequency with limited scope for under-frequency or over-frequency operation. If a power plant operates in a load demanding mode, the resulting start and stop cycles impart cyclic thermal stresses on the turbine components (dynamic or static component). This is normally plastic strain controlled fatigue or low cycle fatigue. In contrast, high cycle fatigue loading occurs on the rotating components if there are grid frequency variations within the design limit. In this case, resonance can also occur in certain rows of blades compounding the problem of fatigue. The resonant vibration can be identified by examining the relation between the natural frequency and excitation frequencies of a system. There is a relation between grid frequency and the selection of speed of the turbogenerator, which can be expressed [2] as:
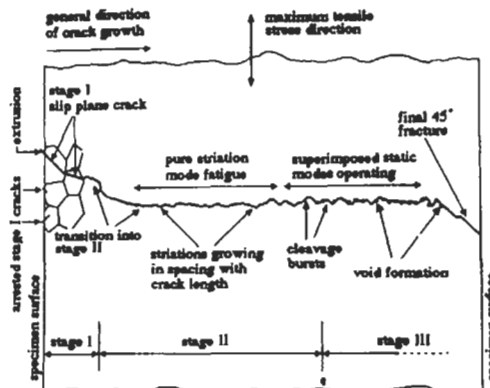

Fig. 10. Schematic diagram showing the nature of crack growth behaviour.

$$f = \frac{PN}{120},\qquad(4)$$

where f = frequency (Hz), P = no. of poles (it is 2 in the present design of turbogenerator) and N = the speed of the turbogenerator and turbine (rpm). It can be understood from eqn (4) that f becomes equal to turbine speed if N is expressed in rpm and P is 2. This relation helps one to realize how the turbine speed is related to the frequency of the grid. Since the number of poles is constant, frequency variation controls the variation of the turbine speed. In the grid system the frequency will remain at 50 Hz when the input power and the output power of the system are in a balanced state. Any variation in the system affects the frequency and thus the speed of the machine.

Using Southwell's theorem we can calculate the natural frequency of the blade for the fundamental mode for a small vibration from the following relation [12]:

$$f_{nd}^2 = f_{ns}^2 + f_{\omega}^2$$
$$= f_{ns}^2 + N_s^2,\qquad(5)$$

where f_{nd} = natural frequency of the blade when it is rotating at N_s (rps), f_{ns} = natural frequency of the blade tested during a static condition (which is obtained from the test data of the plant as 160–170 Hz) and f_{ω} = excited frequency of the blade when it is rotating with speed N_s (rps). The natural and excited frequency can be plotted in Campbell diagram (Fig. 11), in order to understand the possibility of resonance during operation [2]. It is found from the above equation that the natural frequency of the blades in the fundamental mode of vibration lie in the range 170–180 Hz during operation at 50 Hz grid frequency.

When the turbine rotates with ~ 3000 rpm, which is required for 50 Hz line frequency, the third harmonic of the excitation frequency is 150 Hz and the fourth harmonic of the excitation frequency is 200 Hz which will not match with the natural frequency of the blade (170–180 Hz) and, therefore, the possibility of resonance is ruled out during the operation of stipulated frequency. For resonance to occur, it requires a minimum over-frequency of 56.5 Hz as well as maximum under-frequency of 45 Hz.

It is important to note that before the day of failure the operating frequency from the plant data was found to be at 45.5 Hz for 13 s. It is also found that nearly 10% of operating life was above a
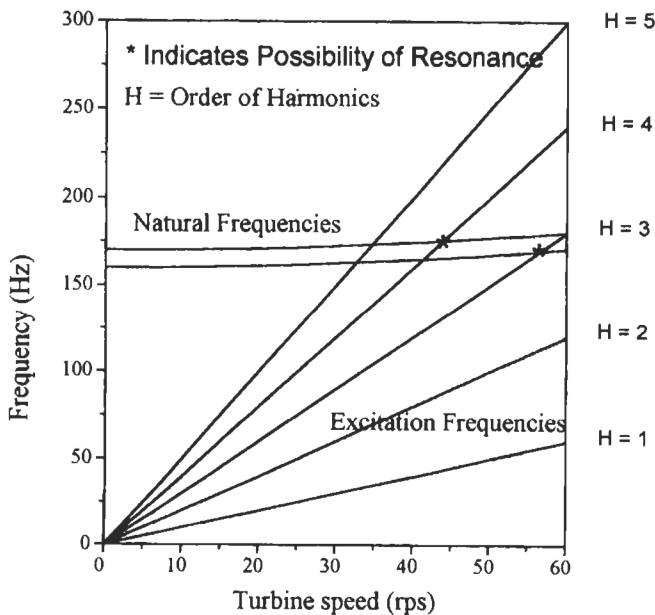
Fig. 11. Campbell diagram for understanding the possibility of resonance.

50 Hz frequency range and 1% was above 51.5 Hz. Thus the resonant vibration was highly probable and could lead to high vibratory stress. In addition to resonant vibration, the fluctuations from under-frequency to over-frequency operation and frequent interruption of the normal operation obviously would have caused excessive vibration which the defective and corroded braze joints were unable to withstand leading to situations conducive to crack initiation and ultimately to failure. From our simulated HCF test it was concluded that damage accumulation at a lower load can lead to crack initiation rapidly even though the mean stress is increased slightly. If the braze joint had been strong enough, the short term effect of resonance or frequency fluctuation demanded from the system of power supply could have been overcome and the blades would have survived. Thus, faulty brazing and improper operating conditions had a combined effect leading to the present failure. It appears that the degradation of the braze joint was the primary cause and the vibrations causing high cycle fatigue was the ultimate cause of failure of the turbine blades.

5. CONCLUSIONS

The work has shown that the LP blades of a steam turbine, whose material conditions were found to be good, failed due to high cycle fatigue. The fatigue loading conditions were brought about primarily by the failure of braze joints which had been used to join the lacing rods to the blades to impart rigidity.

Due to failure of the brazed joints, the natural frequencies of the blades were affected. Fretting between the lacing rod and blade interface was operative and led to the formation of weak points favourable for fatigue crack initiation. The failure of the brazed joint was due to a poor brazing operation carried out during the earlier overhauling period, worsened by corrosion during service. The crack growth was aided by excessive vibration due to frequent fluctuation from under-frequency to over-frequency operation. The effect of resonant vibration, which also seemed to occur, would lead to an increase in ΔK value and mean stress of the cyclic loading and favour the situation of crack initiation and growth.

REFERENCES

1. Atrens, A., Meyer, H., Faber, G. and Schneider, K., in *Corrosion in Power Generating Equipment*, ed. M. O. Speidel and A. Atrens. Plenum Press, 1983, p. 299.
2. *Modern Power Station Practice*, 3rd edn. British Electricity International, Pergamon Press, 1992, p. 73.
3. Viswanathan, R., *Damage Mechanisms and Life Assessment of High Temperature Components*. ASM International, 1989, p. 313.
4. *Failure Analysis of Steam Turbine Blades*. NML Report: NML/MTC/CIEP/1.46, 1997.
5. Beevers, C. J., Cook, R. J., Knott, J. F. and Ritchie, R. O., *Metal Science*, 1975, **9**, 119.
6. Griffiths, J. R., Mogford, I. L. and Richards, C. E., *Metal Science*, 1971, **5**, 150.
7. Mcdonald, M. M., in *Metals Handbook*, Vol. 13, 9th edn. ASM International, p. 876.
8. Kawakatsu, I., *Weld J.*, 1973, **52**, 2335.
9. Kearton, W. J., *Steam Turbine Theory and Practice*. CBS Publishers, 1988.
10. Dieter, G. E., *Mechanical Metallurgy*. McGraw-Hill Publication, 1988, p. 375.
11. Tarafder, S., in *Failure Analysis*, ed. S. R. Singh *et al.* NML, 1997, p. 147.
12. Thornton, D. L., *Mechanics Applied to Vibration and Balance*. Chapman & Hall Ltd, 1951, p. 560.

VIBRATION-INDUCED FATIGUE FAILURE OF AN IMPULSE LINE

K. R. AL-ASMI and A. C. SEIBI*

Department of Mechanical Engineering, Sultan Qaboos University, PO Box 33, Al-Khod, Muscat 123, Sultanate of Oman

Abstract—This paper presents a case study dealing with the operational failure of an impulse line used to connect a tapping in a crude oil pipeline header to a pressure transmitter in an oil field booster station. The 3/8 in diameter stainless steel tubing failed where it entered a Swagelok connection to the pressure transmitter. The investigation was complicated due to the non-availability of information pertinent to the field conditions and the operational urgency to isolate the case of failure. A combination of scanning electron fractography and finite element structural analysis showed that the failure was caused by high-cycle fatigue resulting from the transverse vibration of the tubing. Remedial measures were suggested to reduce the amplitude of the vibration. © 1998 Elsevier Science Ltd. All rights reserved.

Keywords: Fatigue, fatigue markings, finite element analysis, mechanical connections, vibration.

1. BACKGROUND

This paper presents a case study dealing with the failure analysis of an impulse line used to connect a tapping in a crude oil pipeline header, at 70 bars, to a pressure transmitter. The 3/8 in. diameter stainless steel tubing (type 316) failed during operation at an oil field Booster Station consisting of eight turbine driven pumps, not all operating at once. The investigation was complicated due to the nonavailability of information pertinent to the field conditions and the operational urgency to isolate the cause of failure. The situation was of particular concern as the failed tubing was newly installed, as part of ongoing revamp programme, and several similar connections were installed and in service in at least two other pumping stations. The investigation proceeded on X-ray element analysis and microscopic examination of the failed line, site measurements, structural analysis of the line using a general purpose finite element programme, and an evaluation of the mechanical properties of the tubing using tensile and hardness testing.

To understand the sources of this failure, relevant information related to the operating conditions of the booster station was gathered during a site visit. It was noticeable that vibration was present in all pipe work, walk ways, and support structures, irrespective of whether the pump was operating or not and that all pumps are coupled through the discharge pipe network. Figure 1 shows a general view in the vicinity of typical pressure taps, depicting the connection from the discharge header to pressure transmitters. Note the large overhanging mass of the valve body and flange, mounted on the pressure taps (Fig. 1a). The additional support, seen in Fig. 1b, was installed after failure occurred, to reduce excessive movement of the tubing due to vibration. The tubing was connected to the pipe and the pressure transmitter using standard 'Swagelok' connectors (Fig. 2), where two wedges are driven inward by the action of the nut. In this type of connection, the inner faces of the wedges apply a radial pressure on the outer surface of the pipe and deforms it permanently. The extent of deformation depends on the degree of tightening. This type of connection will, therefore, cause a defect in the outer wall of the pipe and a possible hardening of the material where the plastic deformation has occurred.

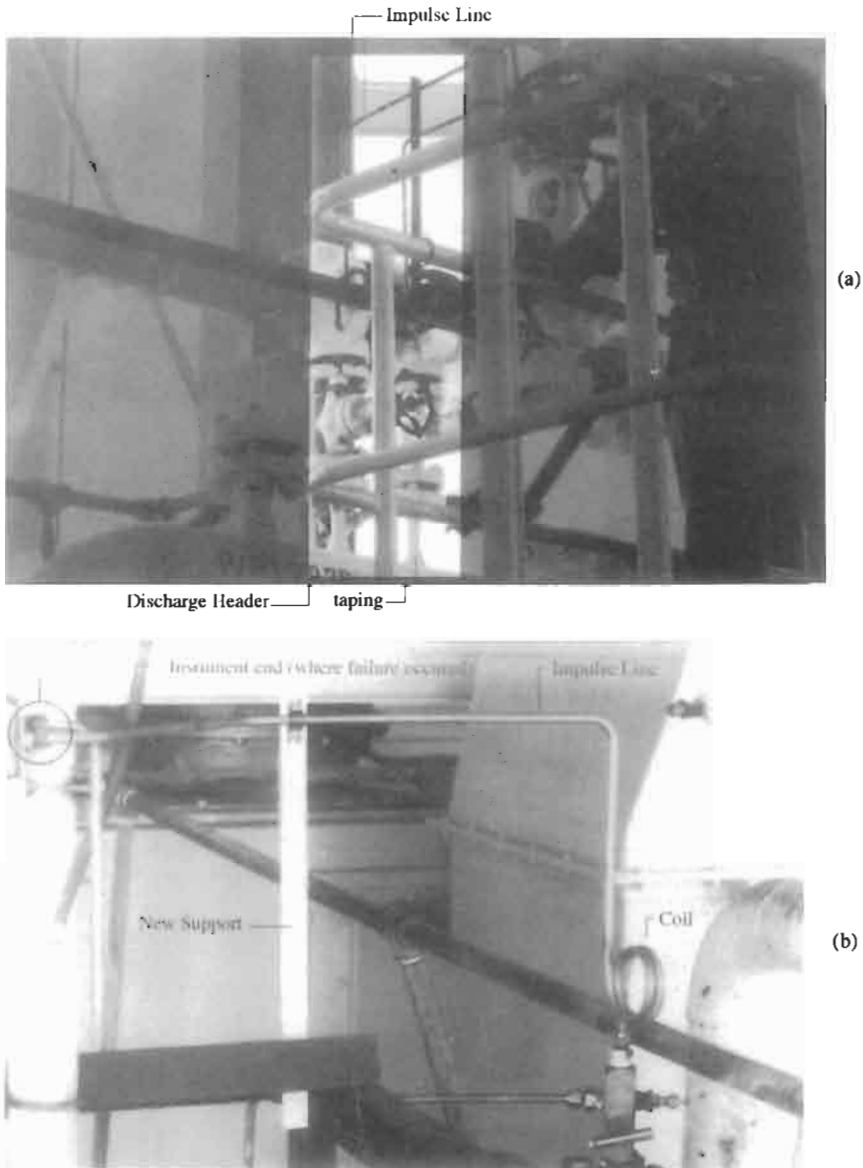* Author to whom correspondence should be addressed.

Fig. 1. A general view of the discharge header: (a) shows three pressure taps, two are connected, one is flanged-off. (b) shows a close-up of the impulse line, depicting the connection-type, coil, and support.

2. FAILURE ANALYSIS

The failed line fractured at the root of the mounting collar, at the instrument side (see Fig. 1). Visual examination showed that the fractured piece was jammed inside the nut (Fig. 3). It was noted that the broken piece was excessively off centred, indicating possible misalignment of the tubing during original mounting. A sample cut from the failed line was subjected to chemical analysis which confirmed that the tubing material was stainless steel type 316, as originally specified.

Samples of the fracture piece were examined using SEM (Scanning Electron Microscopy). The examination showed that the mode of failure was predominantly fatigue. Figures 4–7 show SEM photographs. Figure 4 shows the fracture surface, taken close to the outer layers of the tubing. A
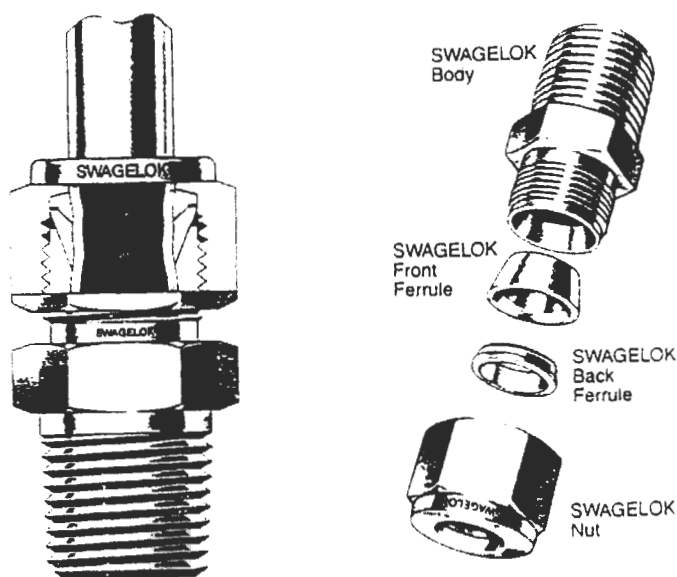
Fig. 2. 'Swagelok' connection type.

close-up view of REGION A is shown at a higher magnification in Fig. 5. The surface exhibits slip traces and slip steps but no fatigue striations are visible within the area. Figure 6 shows the fracture surface away from the outer edges. Here we see a typical high-cycle fatigue fracture with regular (or near regular) striations but at different slip planes. A close-up view of the highlighted area at higher magnification is shown in Fig. 7.

3. FINITE ELEMENT ANALYSIS

3.1. *Finite element model*

A qualitative study of the impulse line using finite element analysis was conducted in order to gain more insight on the system characteristics. the models included pipe-end connection flange, supports, coil configuration and took account of the fluid pressure; a schematic of the model arrangement is shown in Fig. 8. The figure also illustrates the two types of coil configurations (axial and transverse) and gives dimensions of the impulse line. Both modal analysis and harmonic response were studied to determine the effects of controlling parameters such as pipe-end connection size, flange size, and impulse line height/length and coil geometry. The boundary conditions used in the model were calibrated to site measurements.

3.2. *Modal analysis*

The only parameters that were found to influence the frequency response significantly are the flange connection size, flange size and the vertical height of the impulse line. Table 1 shows the first ten natural frequencies of the failed (transverse-coil) configuration with 1/2 in. flange connection. The table also includes the natural frequencies for the 1 in. connection. It is noted that the natural frequencies for the 1 in. connection are much higher than those with 1/2 in. connection. Similar effects on the natural frequencies were observed by changes in the flange size and impulse line height; smaller flange and shorter height of impulse line gave rise to higher values of natural frequencies. Table 2 shows the combined effect of small flange and short height. The intermediate support (which was added after failure took place) was found to have limited effect on the natural frequencies.

Figure 9 shows the mode shapes for the first four frequencies for the 1/2 in. flange connection

(a)

(b)
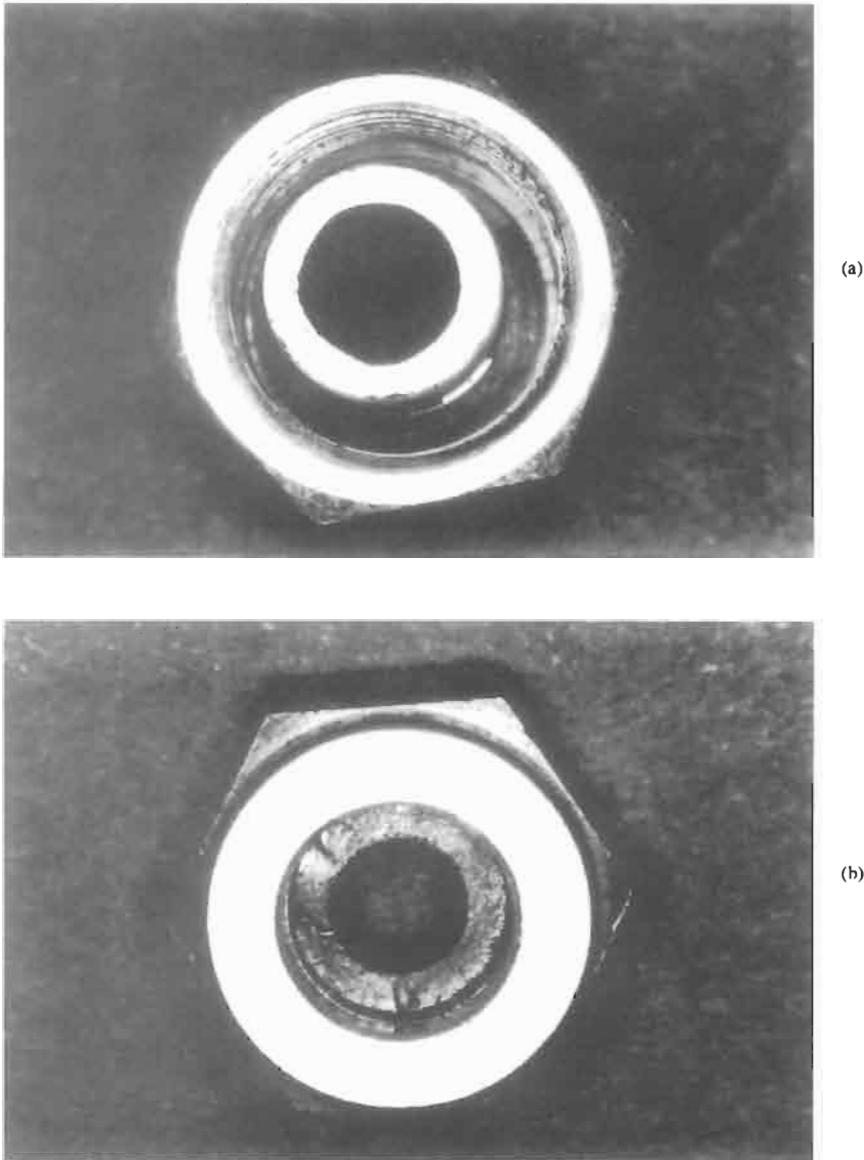
Fig. 3. End connector with the factured piece jammed inside the nut.

with transverse-coil configuration (similar to the failed line). It is interesting to note that in this configuration significant movement of the flange assembly can also occur (mode 4), implying stress concentration is also possible at the root of flange connection.

3.3. *Harmonic response*

Harmonic analysis performed on the impulse line showed that peak displacements occur at node 33 (see Fig. 8), for both axial and transverse coils. The excitation of the system was simulated by introducing base motion in the FE model along the header axis, representing the effects of flow disturbances in the discharge pipe.

Figure 10 shows the harmonic responses (at node 33) for the transverse and axial coil con-

Fig. 4. Fracture surface taken close to the outer layer of the tubing.

Fig. 5. Fracture surface within REGION A of Fig. 4.

figurations with 1/2 (Fig. 10a) and 1 in. (Fig. 10b) flange connections, respectively. It is interesting to note that the peak displacement for the transverse coil (in both connection sizes), is nearly 15 times that for axial coil configuration (which acts as a compression spring). This difference is due to the fact that the axial coil is more able to absorb excitation along its axis, thereby reducing the tubing vibration. It is also noted that the peak displacement is doubled between the 1 and 1/2 in. connection sizes (with similar coil configuration).

Fig. 6. Fracture surface away from the outer edges.
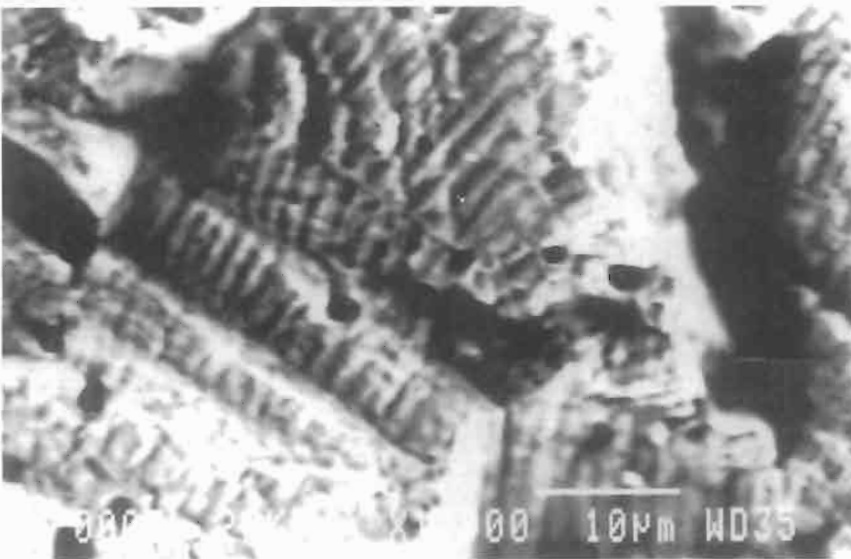
Fig. 7. Close-up view of the highlighted area in Fig. 6.

4. CONCLUSIONS AND RECOMMENDATIONS

The microscopic examination showed that the impulse line failed through high-cycle fatigue. This is confirmed by FE analysis in that peak vibration (in the tubing) occur at low frequencies, with maximum stress points localised at the failure point. The root cause of failure is excessive vibration emanating from the connecting flange at the discharge pipe. It is believed that a significant amount of this vibration is induced by the dynamics of the flow within the discharge manifold. Without decoupling this motion, it is probable that similar failure will occur in the future. The following measures were recommended:

Fig. 8. Schematic of the FE model and parameters.
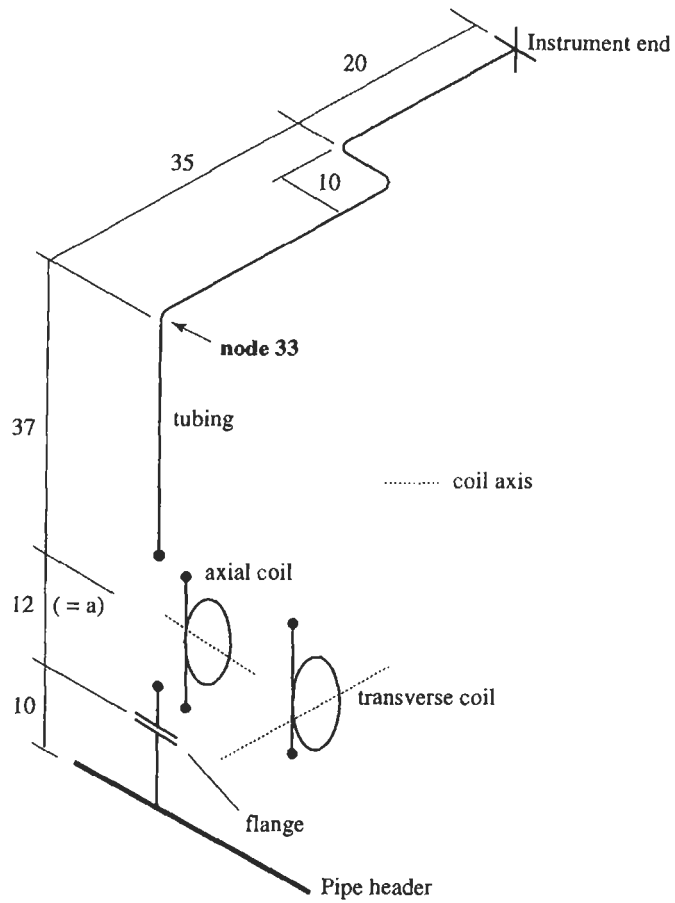
Tubing: Outside diameter, d_o = 9.5 mm
Inside diameter, d_i = 6.3 mm
Stainless steel type 316

Coil: Coil diameter, D = 80 mm
Number of turns, N = 2
Axial Coil Stiffness, $K_a = G(d_o^4 - d_i^4)/(8D^3N)$
Transverse Coil Stiffness, $K_t = EI/(\pi DN_a^2)$

where G = modulus of rigidity; I = 2nd moment of area of the tubing x-section,
E = modulus of elasticity.

Flange: Flange diameter, df = 100 mmm
Connection size = 1/2, 1 inch
Carbon steel

Fig. 9. First four mode shapes of the impulse line with transverse coil configuration and 1/2 in. flange connection.

Table 1. Natural frequencies for 1/2 and 1 in. flange connections with transverse coil configuration

Mode	1/2'	1'
1	11.45	11.45
2	12.26	12.26
3	44.53	44.93
4	44.82	73.72
5	44.99	126.93
6	74.58	129.92
7	95.41	177.17
8	127.16	178.04
9	130.08	247.76
10	247.75	308.50

(1) The over-hung mass on the flange connection and its cantilever effect should be minimised. This can be achieved by using smaller flanges with short connections.

(2) The tubing length should be kept to a minimum to avoid resonance at low frequencies.

(3) The instrument end should be as far as possible decoupled from the pipe end. This can be achieved more effectively by using axial-coil configuration with larger coil diameter and/or increased number of turns. A sensitivity analysis is needed to determine the exact dimensions.

(4) The installation procedures on site be reviewed to ensure that tubing connections are properly aligned, as per manufacturer's recommendations.
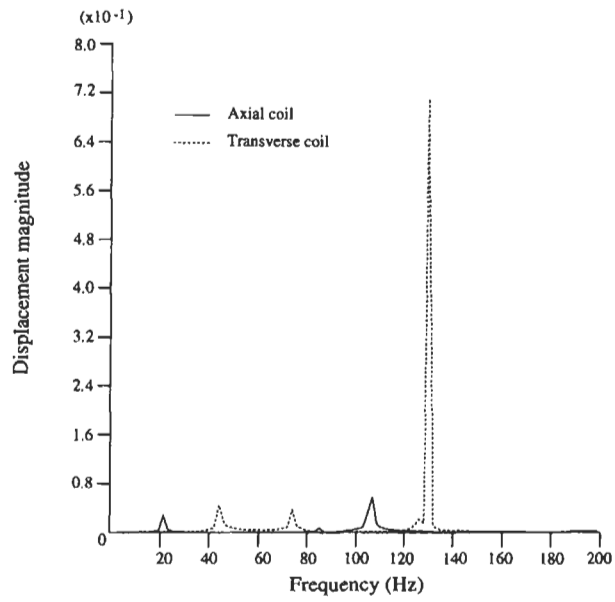
(a) 1/2 inch flange size
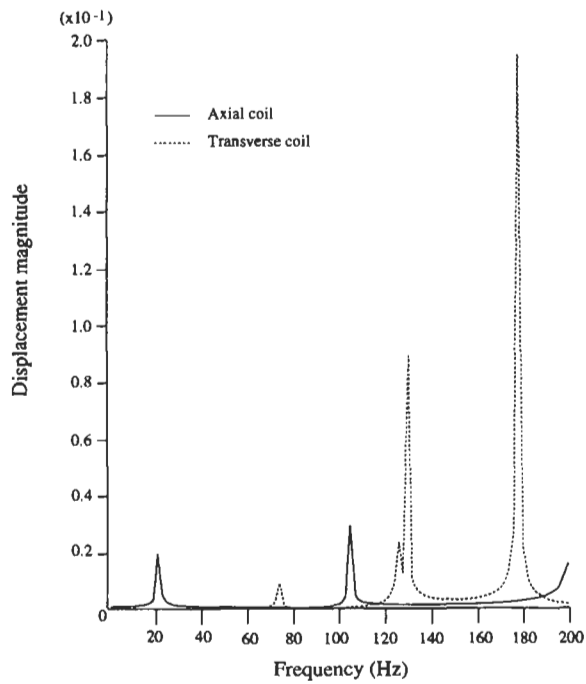
(b) 1 inch flange size

Fig. 10. Frequency response of node 33 showing peak displacement for the transverse and axial coil configurations.

Table 2. Natural frequencies for 1 in. flange connections, with axial coil, showing the effects of reducing tube height and flange size; (A) infield configuration, (B) modified configuration

Mode	A	B
1	11.5	16.5
2	22.5	53.4
3	35.9	100.0
4	45.5	132.3
5	111.6	144.8
6	147.8	246.2
7	299.3	300.2
8	344.1	354.0
9	353.1	356.3
10	356.3	428.4

REFERENCES

1. Al-Asmi, K., Seibi, A., Samanta, B. and Siddiqui, R., *Investigation into the Failure of Pressure Transmitter Impulse Line*. Sahma Booster Station, Internal Report ME/SQU/July, 1995.
2. Callister, Jr, W. D., *Material Science and Engineering—An Introduction*, 3rd ed. John Wiley & Sons, Inc., 1994.
3. Hertzberg, R. W., *Deformation and Fracture Mechanics of Engineering Materials*, 2nd ed. John Wiley & Sons, Inc., 1983.
4. Shigley, J. S. and Mischke, C. R., *Mechanical Engineering Design*, 5th ed. McGraw-Hill, 1989.

MALFUNCTIONS OF A STEAM TURBINE MECHANICAL CONTROL SYSTEM

J. H. BULLOCH* and A. G. CALLAGY

Power Generation, ESB., Lower Fitzwilliam Street, Dublin 2, Ireland

Abstract—This paper is aimed at elucidating the cause of a series of malfunctions involving the bending or breaking of main steam turbine throttle valve spindles which occurred at service times ranging from hundreds to several thousand hours in a number of 270 MW steam raising units. It was clearly established, by two distinct approaches (one engineering, one micromechanistic) that the stresses which produced these malfunctions were bending in nature and were the result of out-of-alignment deflections. In the case of the bent spindles the stresses were very high and approached flow strength levels of around 8000 MPa while the broken spindles were the results of fatigue initiation and subsequent growth from a thread root (stress concentration) location on the spindle. Using relevant fatigue crack propagation data for the valve spindle material at 300°C it was demonstrated that fatigue failures occurred at spindle deflections of between 0.9 and 1.6 mm. Finally, it was demonstrated that the fatigue breakage problem could be significantly reduced, especially at the lower end of the valve spindle deflection range, by a combination of re-profiling the thread root and shot peening. © 1998 Published by Elsevier Science Ltd. All rights reserved.

Keywords: Fatigue, fatigue crack growth, fatigue markings, plastic deformation, power-plant failures.

1. INTRODUCTION

During the past decade or so certain ESB stations that operate 270 MW units have encountered operational problems involving main steam turbine throttle valve spindles. Basically the problems were identified as:

(i) valve sticking as a direct result of spindle undergoing permanent plastic deformation or bending; or

(ii) spindle fracturing during operation near the top of the valve spindle in the threaded section.

The present study considered four separate spindle failures which occurred over a three year period and involved:

(i) a detailed failure analysis or micromechanic assessment; and

(ii) a basic engineering stress analysis approach.

2 MECHANICAL CONSIDERATIONS

A detailed view of the valve spindle arrangement is shown in Fig. 1 and in this instance the valve was in the closed position. All failures occurred at position A at the root of a spindle thread while the spindle bending problem was observed at position B. At these positions the working temperature was assessed at about 300°C. Also, the forces acting on the valve spindle are illustrated in Fig. 1 between piston C and the actuating lever where the vertical force is the result of steam pressure and the angular force was caused by the angle of the actuating or lifting lever. The resultant force is a sideways bending force on the valve spindle and it was calculated that the relationship between the bending stress σ_B, and value of spindle deflection λ, at position A could be expressed as follows:

$$\sigma_B = 342(\lambda), \tag{1}$$

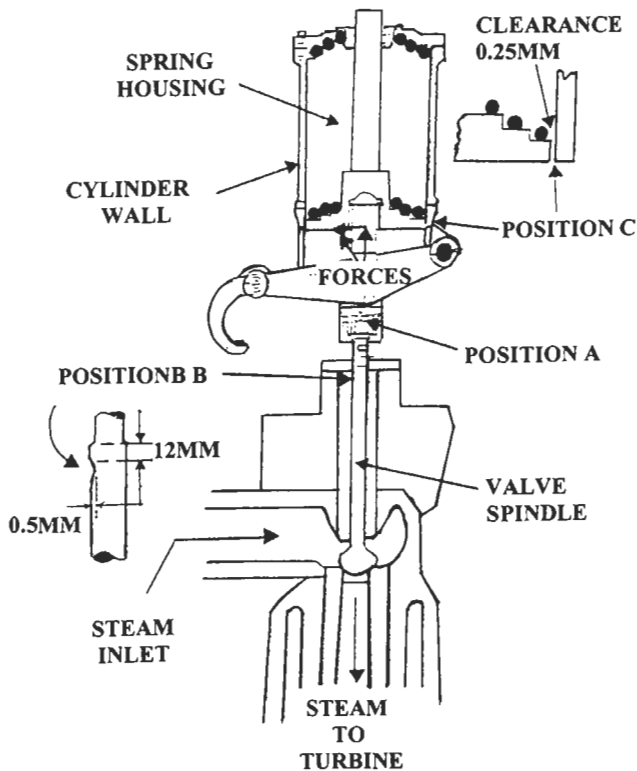* Author to whom correspondence should be addressed.

Fig. 1. Valve spindle system.

where σ_B was in MPa and λ was in mm. At the valve spindle bending location, i.e. position B, the value of σ_B was 1.37 times greater because it was 118 mm further away from the applied force. In the stainless steel valve spindle, bending occurred when the material flow stress was attained, i.e. half the sum of the yield and tensile stress, viz., 830 MPa, and hence the maximum stress at position A (see Fig. 1) was around 600 MPa or a spindle deflection value of 1.75 mm. As this coincided with a machined ISO thread, a local stress concentration factor (SCF) of around 4 was prevalent.

At position B an area of wear, around 0.5 mm deep (see Fig. 1) was observed on one side of the valve spindle surface indicating the presence of a significant bending action or stress. This bending stress could have been the result of:

(i) clearance between the piston and cylinder wall, position C (see Fig. 1) or
(ii) misalignment of the value actuating housing.

However, the facts that (i) clearance related bending stresses are negligible at unit loads approaching 200 MW and (ii) failure occurred at high loads, suggested that the failures observed at position A were the result of spindle deflections or bending stresses caused by misalignment or possible thermal distortion in the valve spindle system.

3. FAILURE CONSIDERATIONS

From a detailed examination of the broken spindle fracture surfaces it was assessed that failure was the result of a ductile fatigue crack extension process which was initiated at the thread root

Fig. 2. Fatigue initiation site at thread root location.
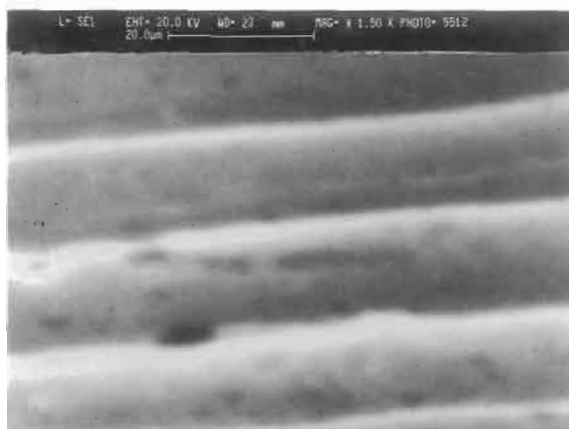
Fig. 3. Coarse fatigue striations. Striation spacing around 15 μm.

location (see Fig. 2) and propagated by ductile striated crack growth (see Fig. 3). In three of the four failures surface crack initiation was helped by the presence of near surface titanium based non-metallic inclusions. The coarse nature of the striation spacing (see Fig. 3) suggested a high stress, low cycle fatigue situation. Indeed the short service lives of the four broken spindles, viz., 33, 136, 167 and 316 days added credence to this suggestion.

4. FATIGUE CRACK GROWTH ASSESSMENT

In this section relevant real material fatigue crack growth data at 300°C was used in an effort to assess the valve spindle deflection values required to cause the real "in field" short service time failures observed over the past few years. Amzallag and Maillard [1] have reported fatigue crack growth results at 300°C for a similar martensitic stainless type bolting steel and the upper bound data was described as:

$$\frac{da}{dn} = 1.05 \times 10^{-6} (\Delta K)^2, \tag{2}$$

where da/dn = fatigue crack growth rate in mm per cycle and ΔK = stress intensity range = $1.12\Delta\sigma$ $\sqrt{\pi a}$ in MPa $\sqrt{m}$.

In an attempt to determine the number of fatigue cycles based on the unit power load a typical load profile is shown in Fig. 4. From this figure it can be seen that over a one day period there was one large unit power change and about four transient power changes which were around half this value.

Using a range of spindle deflection values (bending stresses), ΔK and thus the fatigue crack growth characteristics, over a range of defect sizes, could be assessed. Also, taking the spindle failure criteria as being that fatigue crack length where K approaches the materials fracture toughness of ~ 250 MPa $\sqrt{m}$, the number of fatigue cycles or time to spindle failure was obtained. The relationship between valve spindle deflection and time to failure is illustrated in Fig. 5. From Fig. 5 it can be seen that the four fatigue failures occurred over a valve spindle deflection range of 0.9 to 1.6 mm and resided somewhat below the maximum spindle deflection possible at this location of 1.75 mm.

It is clear that certain facts have emerged which strongly indicate that spindle breakages occurred due to a high stress, low cycle, ductile, fatigue process, viz.:

(i) high bending stress or deflections are needed to bend spindles;
(ii) significant surface indentations of about 0.5 mm were observed;
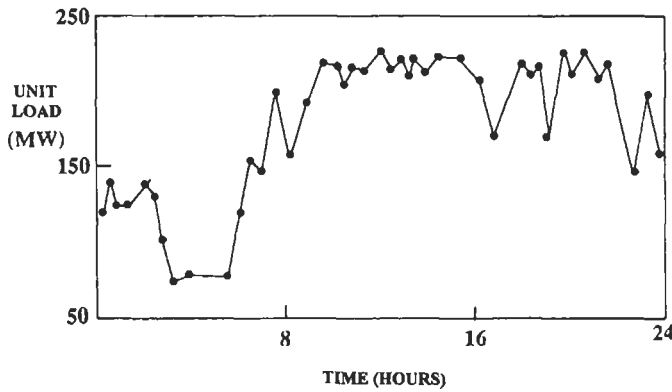
Fig. 4. Typical load profile.
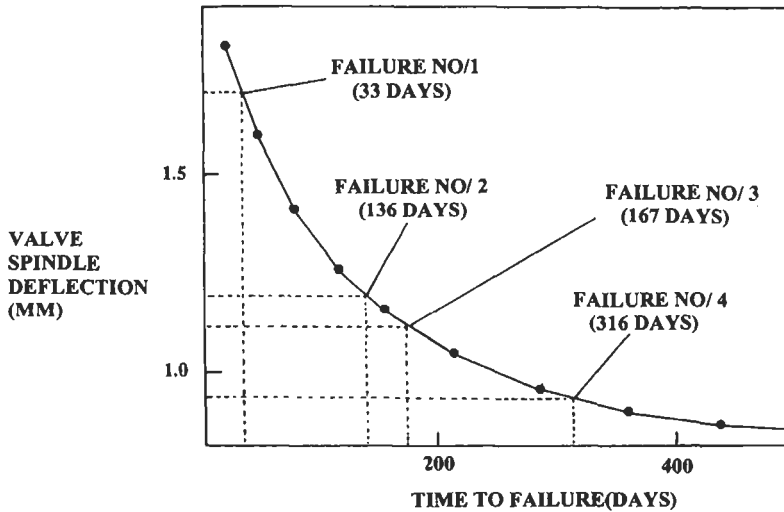
Fig. 5. Time to fatigue failure versus spindle deflection.
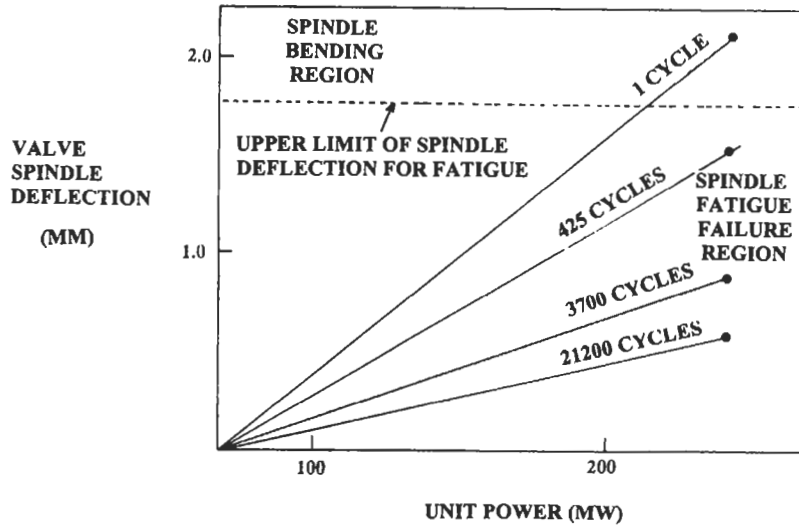
Fig. 6. Schematic of spindle deflection versus unit power and calculated cycles to fatigue failure.

(iii) the failures occurred over very short and unacceptable service durations; and large spindle deflections occurred at high unit loads as failures occurred in this regime and could only have come from out of alignment of the actuating mechanism.

As a result Fig. 6 is semi-schematic in nature and illustrates the spindle bending and spindle fatigue breakage regions together with the notional increase in valve spindle deflection with unit power and the number of fatigue cycles required to cause spindle failure. It is clear that reducing the spindle deflection increased the working life of the spindle; indeed at deflections approaching 0.6 mm it was predicted that the spindle life was 21,200 cycles or almost 12 years.

5. DISCUSSION AND RECOMMENDATIONS

It has been reasonably demonstrated that the series of spindle failures were the result of a high stress, ductile fatigue process that was caused by significant out-of-alignment of the actuating mechanism during service. During an outage, an exercise was conducted to determine the "cold" amount of misalignment of an actuating mechanism where a fatigue failure occurred. The measured amount was 0.38 mm which was more than 40% of the lower end valve spindle deflection level of 0.9 mm required to cause fatigue failure. As such, it is not difficult to envisage that thermal distortions during the hot "on-load" excursion could easily account for spindle deflections attaining the critical range necessary for fatigue failure.

Such a recurring failure in a critical plant component needed to be urgently addressed in an effort to obviate or at least mitigate the problem. In the present instance it was suggested that the high stress situation at the spindle threaded location be reduced by two actions; firstly, changing the thread profile to a rounded thread (e.g. NF000-032 type thread) which had an associated stress concentration factor which was about 25% lower than the present square ISO thread and secondly by introducing significant compressive stresses (which need to be overcome before fatigue can occur) by shot peening. The influence of these actions on the valve spindle deflection–time to fatigue failure relationship is illustrated in Fig. 7. From Fig. 7 it can be seen that both shot peening and re-profiling the thread significantly increased the valve spindle life at spindle deflection levels of around 1 mm. Indeed at 0.9 mm spindle deflection the spindle service life was increased from less than one year to around 8 years. The service temperature in the region of valve spindle failure was estimated to be around 300°C and it is known that thermal relaxation of the compressive stresses can occur at high temperature. However, recently Gauchet et al. [2] have reported encouraging results where significant
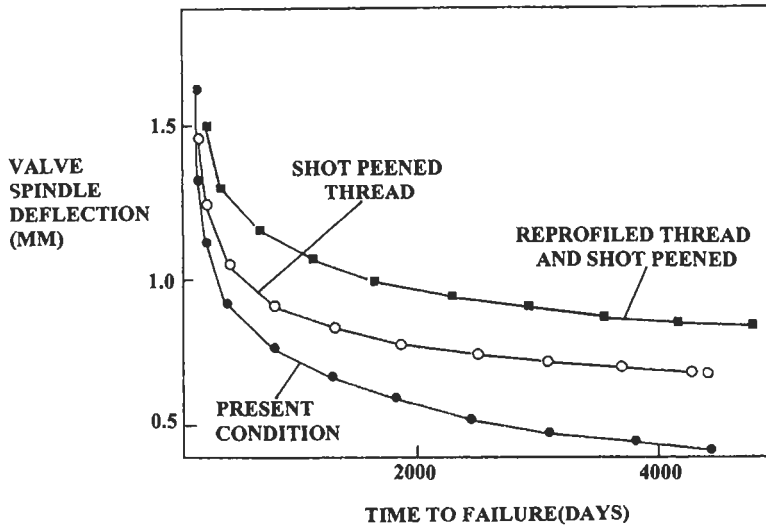
Fig. 7. Time to fatigue failure versus spindle deflection.

compressive stresses (by shot peening) have remained in HP heater water chambers after 5 years at 270°C.

Finally, it has been shown that thread re-profiling and shot peening can mitigate fatigue failure in valve spindles. Also regular checks of actuating system out-of-alignment should be carried out together with good insulation at key locations which should help minimise thermal distortions.

REFERENCES

1. Amzallag, C. and Maillard, J. L., 9th Inter. Conf. Structural Mechanics in Reactor Technology, Smirt, Lausanne, Switzerland, Aug. 1987, Vol. F, pp. 173–180.
2. Gauchet, J. P., Reversat, C., Leguernic, Y., Lebrun, J. L., Castax, L. and Barrallier, L. K., EDF Feedback on French Feedwater Plants Repaired by Shot Peening, EPRI Inter. Conf. Welding & Repair Technology for Fossil Power Plants, March 1994, Williamsburg, Virginia, U.S.A.

241

FATIGUE FAILURE OF HOLD-DOWN BOLTS FOR A HYDRAULIC CYLINDER GLAND

C. TAO,* N. XI, H. YAN and Y. ZHANG

AVIC Failure Analysis Center, PO Box 81-4, Beijing, 100095, P.R. China

Abstract—A hydraulic-cylinder gland system used in aircraft failed by leaking because the hold-down bolts broke in the course of a trial run. The metallographic examination of the fracture surface and the stress calculations for the bolts are described in this article. The investigation showed that the failure was caused by fatigue and the reason for failure was considered in relation to the processing, surface condition and assembly of the bolts. Measures to increase the fatigue strength of the bolts are proposed. © 1998 Elsevier Science Ltd. All rights reserved.

1. INTRODUCTION

A hydraulic-cylinder gland system used in aircraft failed by leaking in the course of a trial run. The gland was fixed with one hold-down and four hold-down bolts. Three of the four bolts broke in service. The bolts were manufactured by turning and threading from 17-4PH steel. The nominal composition of 17-4PH is 0Cr–17Ni–4Cu–4Nb and typical mechanical properties are yield strength $\sigma_{0.2} = 1200$ MPa, tensile strength $\sigma_b = 1300$ MPa after solution heat treatment at 1040°C, then water quenching and tempering for 4 h at 495°C. This paper describes an analysis of the nature and the causes of fracture as well as preventive measures for avoiding fatigue failure of the hold-down bolts.

2. METALLOGRAPHIC EXAMINATION

A schematic drawing of the hold-down and bolts is shown in Fig. 1. The positions of the hold-down bolts are indicated by 1#, 2#, 3# and 4#. Each bolt head was cross drilled with two assembly holes at right angles to one another. The 3# bolt broke away in the middle of the threaded portion. The 1# and 2# bolts broke away in the head between the assembly holes and the shoulder transition radius. General views of the fracture surfaces taken in the scanning electron microscope are shown in Fig. 2.

The fracture surface (Fig. 2(a)) of the 3# bolt was characteristic of a typical fatigue fracture, i.e. there was a crack initiation zone, a fatigue crack propagation zone and a final ductile fracture zone. The fatigue crack initiated at one position in the thread root at a machining mark. The crack propagated towards the far edge of the thread. The origin zone was rough (Fig. 3) and had many radial lines. The propagation zone was smooth and there were distinct fatigue striations (Fig. 4). In comparison with the fatigue surface, the final ductile zone was smaller and was around 20% of the total cross sectional area. According to the above-mentioned features, the fracture surface is characteristic of fatigue. The final ductile fracture zone was typically dimpled. No material defects were found in the fatigue origin zone.

The fracture surfaces of the 1# and 2# bolts initiated at the edges of the assembly holes, as shown in Fig. 2(b) and Fig. 2(c). A schematic of the fatigue fracture sites is shown in Fig. 5. The cracks obviously propagated towards the root of the bolt until the remaining cross section became unable to support the load and failed by fast fracture. In comparison with the macro-fracture surface of 3#

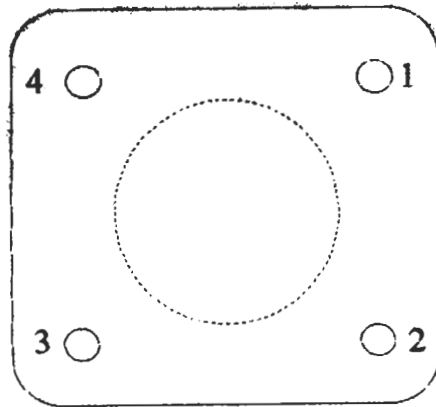* Author to whom correspondence should be addressed.

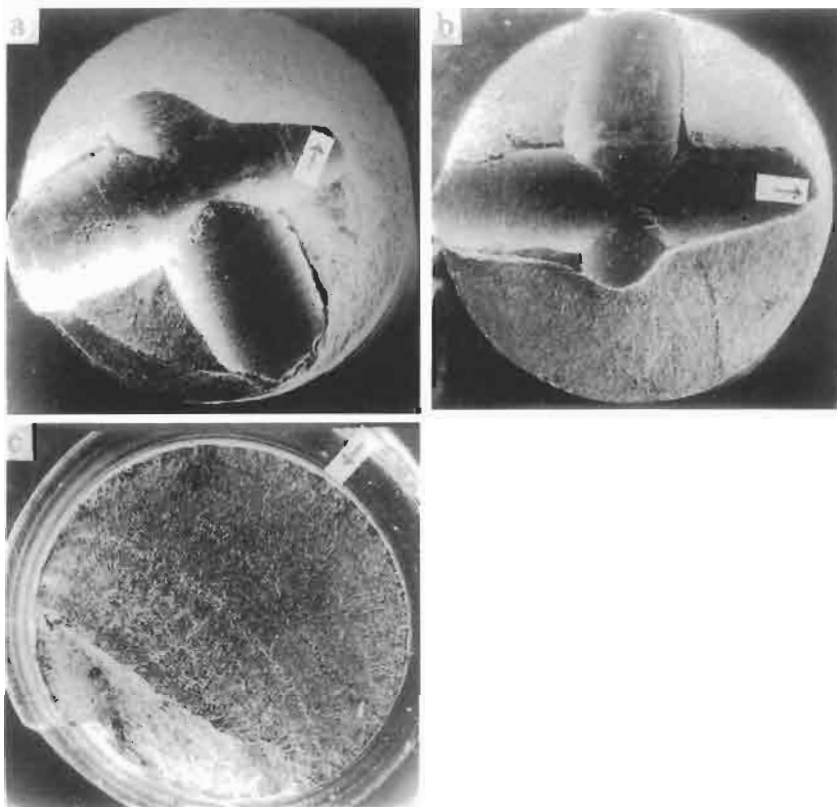Fig. 1. Schematic of hold-down and bolts (numbered 1–4).

Fig. 2. Fracture surfaces of bolts. (a) 1#; (b) 2#; (c) 3#. Fracture origins are marked with an arrow.

bolt, the fracture surfaces of bolts 1# and 2# were rather rough with propagation radial lines, but no fatigue beach marks. However, the photographs of the fracture surfaces taken in the SEM at high magnification showed that there were fatigue striations (Fig. 6). Mixed zones between the dimples and the fatigue striations existed in the fracture surfaces of bolts 1# and 2#.
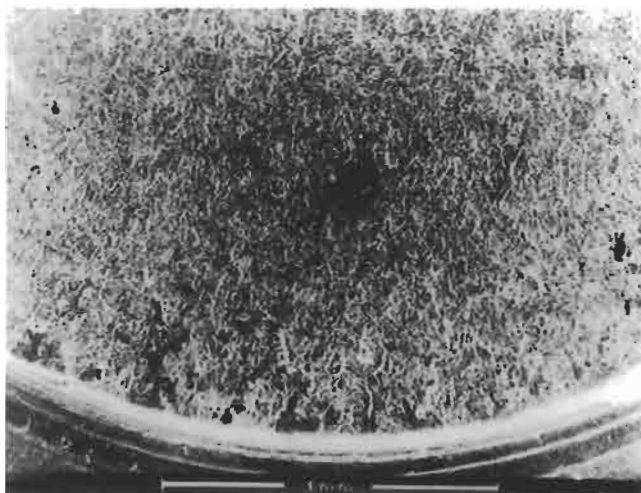
Fig. 3. Fatigue origin zone of 3# bolt.
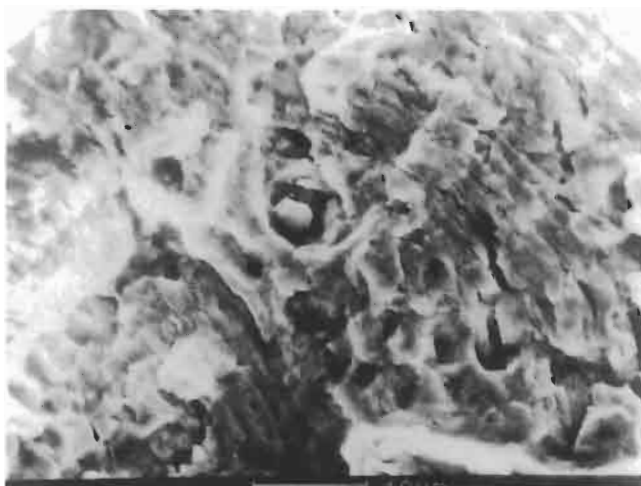
Fig. 4. Fatigue striations in fatigue propagation zone of 3# bolt.
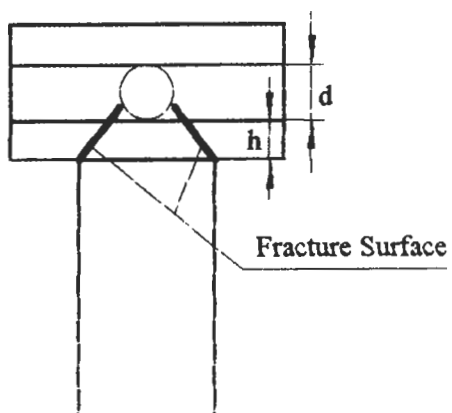
Fig. 5. Schematic of fracture position of 1# and 2# bolts.
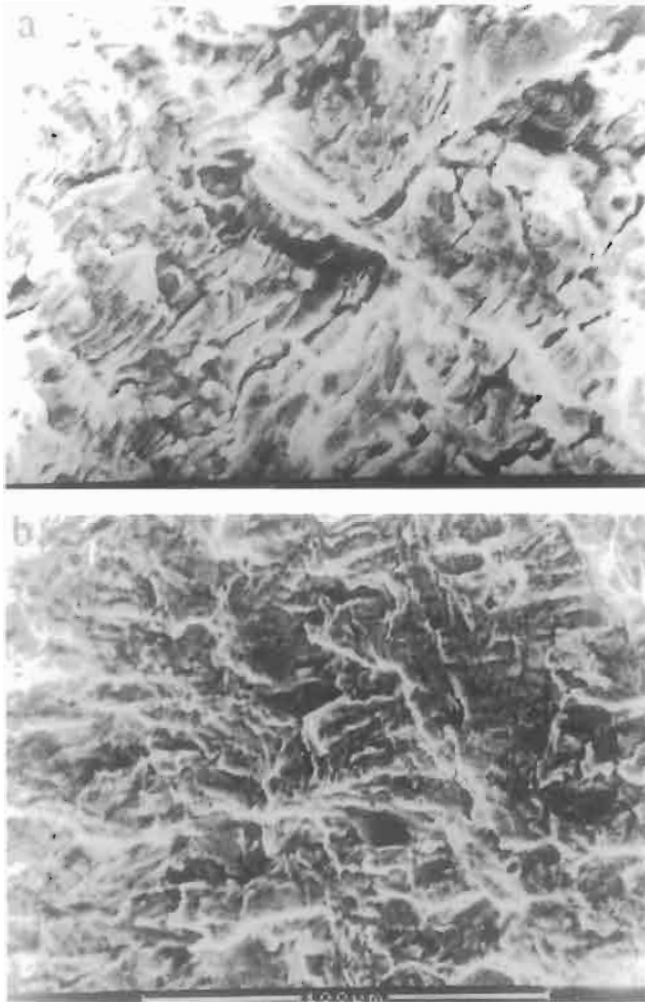
Fig. 6. Photographs of the fracture surfaces taken in the SEM. (a) 1#; (b) 2#.

3. STRESS ACTING ON THE BOLTS

Consider that the platform and the shell of the hydraulic cylinder are rigid because of sufficient thickness. The forces acting on the bolts (Fig. 7). are tensile stresses produced by the changes of oil pressure in the working condition.
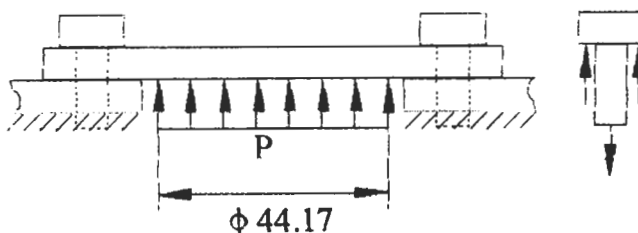
Fig. 7. Forces acting on the bolts.
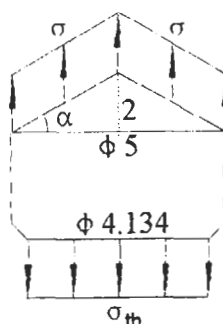
Fig. 8. Stress acting on the fracture surface for 1# and 2# bolts.

3.1. Stress (σ_{th}) acting on the thread root

First, the effect of stress concentration was not considered. The stress acting on the minimum section of the bolt, i.e. the minor diameter, $d_1 = 4.134$ mm, was the maximum. The oil pressure transmitted by the hold-down platform ($d_2 = 44.17$ mm) was borne by four bolts. The maximum oil pressure P_{max} was 3.42 MPa. Take the static estimation as follows:

$$\sigma_{th} = \frac{P\pi\dfrac{d_2^2}{4}}{4\pi\dfrac{d_1^2}{4}} = \frac{P\pi\dfrac{44.17^2}{4}}{\pi 4.134^2} = 28.5P, \tag{1}$$

giving

$$\sigma_{th.max} = 28.5P_{max} = 97.5 \, \text{MPa}. \tag{2}$$

The fatigue strength of the alloy is much greater than $\sigma_{th.max}$ and the bolts should not fail from the thread root if there is a good surface finish, low stress concentration and absence of tensile residual stress.

The result of tensile tests for the same group of bolts showed that σ_b was around 1260 MPa. This showed that the maximum stress was about 1/13 of tensile strength of material even in the minimum section.
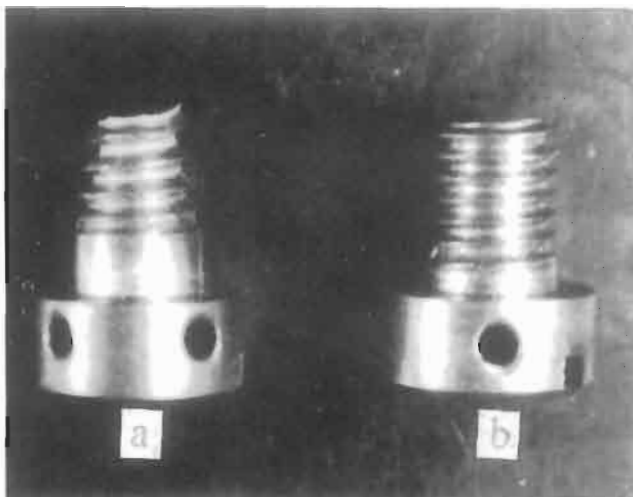

Fig. 9. Comparison of fracture surfaces for (a) tensile fracture, and (b) 3# bolt fatigue fracture.

3.2. *Stress acting between assembly hole and bolt root*

It is known from Fig. 5 that 1# and 2# bolts fractured at the location between the assembly holes and the bolt root. Assume that the fracture surfaces were circular cones and were acted on by a uniform tensile stress σ (Fig. 8).

On this basis, σ_{max} is comparable to the value obtained above for $\sigma_{th.max}$. However, the load-bearing area is reduced by the presence of the assembly holes, and there are appreciable stress concentration factors at the various changes in cross-section. However, a tensile test to fracture of the bolt showed that the threaded portion was still the weakest element with respect to static loading (Fig. 9).

4. REMEDIAL MEASURES

(1) Increase the distance between the shoulder and the assembly holes (dimension h in Fig. 5).
(2) Increase the radius of the filler between the head and shank of the bolt.
(3) Use thread rolling instead of threading for manufacturing the thread form.
(4) Consider the use of forging for producing the basic bolt shape.

ANALYSIS OF A VEHICLE WHEEL SHAFT FAILURE

J. VOGWELL

Department of Mechanical Engineering. University of Bath, Bath BA2 7AY, U.K.

Abstract—This paper describes an investigation which was carried out on a failed wheel/drive shaft component used on an unmanned, remotely operated vehicle for manoeuvring military targets. As many vehicles had been manufactured and delivered to customers it was necessary to establish whether it was thought likely that more failures might occur. A study of the broken shaft shows how vulnerable such a rotating component can be to failure by fatigue, even when operating under steady conditions, if basic preventative design actions are not taken. The analysis considers the effects of both transmission torque and weight (thus bending) upon stress levels and assesses their individual affect on the breakage and upon any subsequent modifications needed to improve the design. The drive shaft arrangement is compared with the feasible alternative of using a driven wheel arrangement rotating on a stationary axle. Findings confirm the importance of recognizing in advance the salient factors leading to fatigue and the necessity in paying adequate attention to detail during design and manufacture if long service life is to be achieved. © 1998 Elsevier Science Ltd. All rights reserved.

Keywords: Fatigue, fatigue design, machinery failures, vehicle failures.

1. INTRODUCTION

Having a wheel shaft which is directly driven from a power source (in this case, a battery operated electric motor) using a timing belt transmission is a common means for driving small, relatively low cost vehicles. The attraction of a rotating wheel shaft is that it can be made very simple because it can accommodate the driven pulley, be used to mount the bearings and also attach a pair of wheels all on a single component. Such a design has undoubted advantages compared to the alternative of using a driven wheel hub arrangement located on an axle; as occurs, for example, with a chain sprocket on a bicycle wheel. However, there is a fundamental difference in the two designs—with a shaft, as it rotates, bending stresses alternate between tension and compression each revolution, whereas with an axle, since it remains stationary, this is not the case. Even when travelling at constant speed and carrying a steady load across level terrain, the alternating stress in a shaft can lead to fatigue damage, especially when wheel diameters are small and consequently the number of rotations becomes very significant. In the case of military target vehicles the problem is compounded by the fact that they carry heavy batteries and must be protected by armour plating which adds considerably to the weight carried and thus the potential for high bending moments along the shaft.

The design requirement is further complicated by additional factors, many of which are of a variable nature. These include the effect of changing torque transmitted during acceleration of the vehicle from start up to full speed and also abrupt breaking (these effects will result in torsion and thus changing shear stresses), travelling over uneven terrains without suspension will contribute shock loading (further adding to fluctuating bending stresses). Consequently, the vulnerability to fatigue damage is clearly very real and so it is essential to realise this and identify weak locations and take preventative steps at the design and manufacturing stages.

2. THE WHEEL SHAFT DESIGN

The wheel shaft has been made from a stainless steel bar (grade 316) and has been turned down to a central diameter of 20 mm with an overall length of 725 mm. A keyway slot is machined near

one end to secure the driven timing belt pulley wheel. The ends of the shaft are reduced in diameter (to nominally 12 mm diameter along a 76 mm length with 3 mm fillet radius at the shoulder) and act as hubs for mounting the 150 mm diameter wheels (which are shrink-fitted onto 76 mm long sleeves) as shown in Fig. 2. A keyway slot runs 73 mm along the length of the 12 mm hub diameter and a M6 screw fits in the sleeve to secure the wheel from moving axially along the shaft as more clearly illustrated in Fig. 3.

3. ASSESSING THE FAILURE

The failed wheel shaft had broken in two, having separated close to the end of the keyway slot on one of the 12 mm diameter hubs—approximately 73 mm from one end, as shown in Fig. 2. A fatigue crack is clearly evident for about half of the broken sectional area (that nearest to the keyway groove) as the characteristic circular lines radiating outwards from the corner of the keyway are clearly visible. The remaining section failed through static fracture—being insufficient to support the loads. From observation of the failed shaft it is not evident whether shaft bending or torsion is the primary cause or whether it is a combination of the two and so analysis is necessary.

4. SHAFT ANALYSIS

Because it is not immediately obvious whether bending or torsion has been the major cause of failure, both effects are considered independently.

4.1. *Bending under static loading*

The trolley weight (with armour plate), $W = 320$ kg (3.2 kN) and is assumed to be evenly shared among the four wheels. The bending moment occurring along the shaft may simply be determined from taking the product of the wheel reaction force and the moment arm (from wheel centre to location of interest).

At end of keyway, bending moment,

$$M = \frac{W}{4} \times (73 \text{ mm} - 30 \text{ mm}) = 34.4 \text{ Nm}.$$
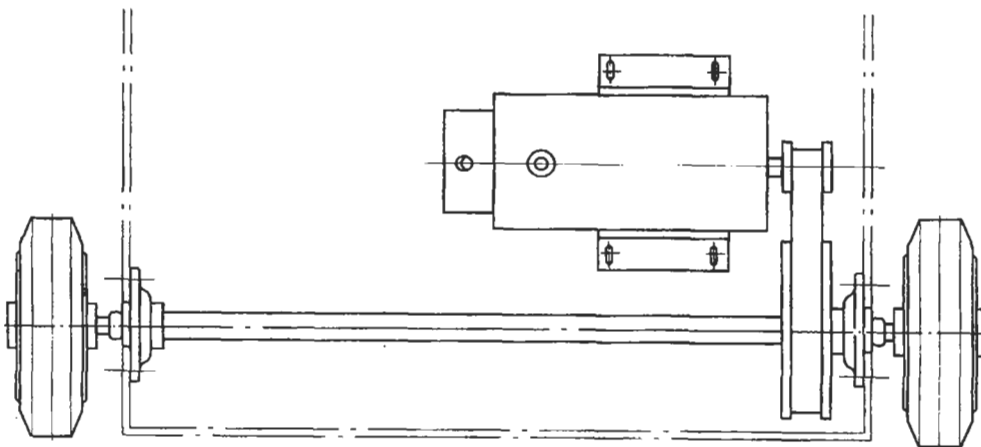

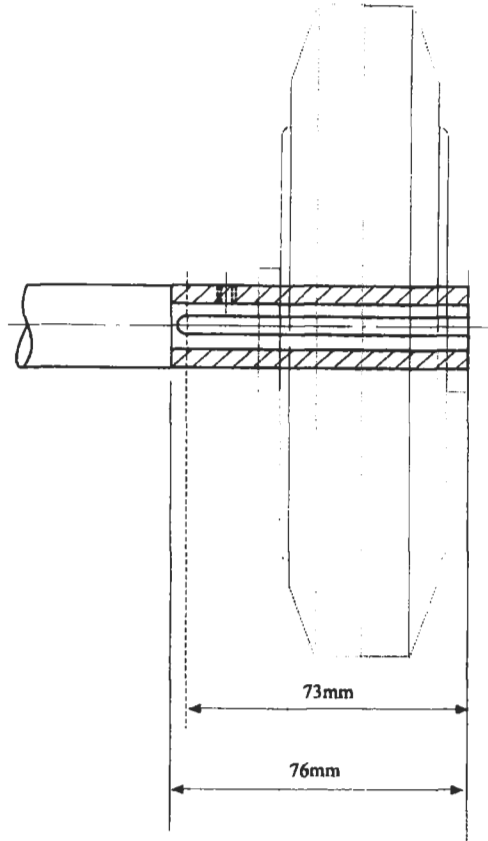Fig. 1. Schematic plan view of vehicle transmission system.

Fig. 2. Drive shaft detail design.

As the shaft wheel hub diameter, $d = 12$ mm, so bending stress,

$$\sigma = \frac{32M}{\pi d^3} = \frac{32 \times 34.4}{\pi \times 0.012^3} = 203 \text{ MN/m}^2.$$

4.2. Torsion due to drive transmission

The electric motor power rating, $P = 0.25$ kW with an output speed, $N = 1500$ rpm.
The maximum shaft driven speed, $N = 1500 \times 16/48$ (pulley teeth ratio) $= 500$ rpm.

The maximum applied torque in drive shaft, $T = \dfrac{250 \times 60}{500 \times 2\pi} = 4.77$ Nm.

Shear stress due to drive, $\tau = \dfrac{16T}{\pi d^3} = \dfrac{16 \times 4.77}{\pi \times 0.012^3} = 14 \text{ MN/m}^2$

Consider effect of sudden braking:

Applied torque, $T = \mu \dfrac{W}{4} \dfrac{D_{\text{wheel}}}{2} = \dfrac{0.5 \times 3200 \times 0.145}{4 \times 2} = 29$ Nm

Shear stress, $\tau = \dfrac{16 \times 29}{\pi \times 0.012^3} = 85.6 \text{ MN/m}^2.$
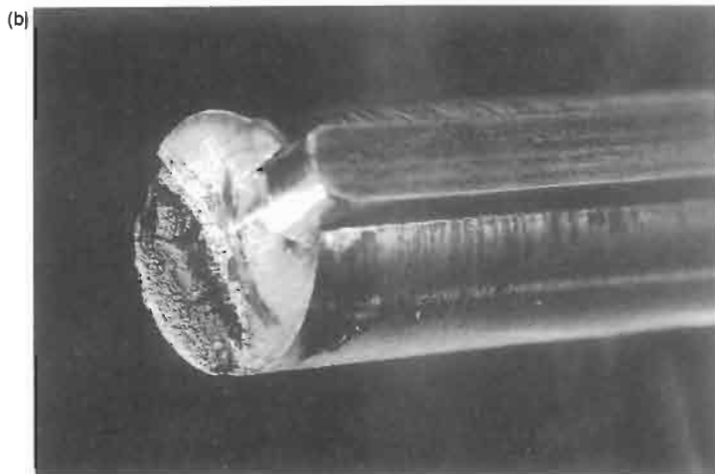
Fig. 3. The failed wheel shaft. (a) and (b) close examination of fracture; (c) failed hub portion and wheel.

4.3. *Material fatigue strength*

Grade 316 stainless steel grade is used for the shaft and the following material data is obtained from Appendix B of Ref. 3 and stress concentration factor data also from Appendix C of Ref. [3]:

Tensile strength, $\sigma_T = 552$ MN/m^2.

Unnotched bending fatigue strength, $\sigma_e = 262$ MN/m^2 (at 10^7 cycles).

Stress concentration factor at end of keyway, $K_T = 1.9$ (shaft with radial hole chart $d/D = 4/12$).
Stress concentration factor at change of dia., $K_T = 1.4$ (stepped diameter with fillet $r/D = 3/12$).

Working endurance limit, $\sigma_e = 262/1.9$ MN/m$^2 = 138$ MN/m^2.

This last value is approximate and is quoted for guidance purposes and will be even lower if surface finish effects are also considered. When the properties are translated on to an *S–N* fatigue strength diagram, it helps show the typical life which would result under a given applied alternating stress as shown in Fig. 4.

As illustrated in Fig. 4, having an applied alternating stress magnitude of 203 MN/m^2 is clearly very significant, especially when combined with a high stress concentration factor, and leads to finite fatigue life. When viewed in terms of distance travelled rather than numbers of revolutions of the wheel a clearer perspective of the duty is gained. A 150 mm diameter wheel rotates more than 2100 times each kilometre the vehicle travels and so the operational life, from nominal bending considerations alone, will be measured in just tens or hundreds of kilometres travelled. The scenario looks even bleaker if secondary factors are also included in the analysis, such as shock loading and material surface finish effects, and confirms that the design leaves no safety margin for misuse; which is very likely as the vehicle may well be used for transporting additional loads.

5. DISCUSSION OF FINDINGS

The wheel shaft failure is a classic fatigue problem—high magnitude bending stresses (which alternate between tension and compression) occur together with shear stresses at a sudden change
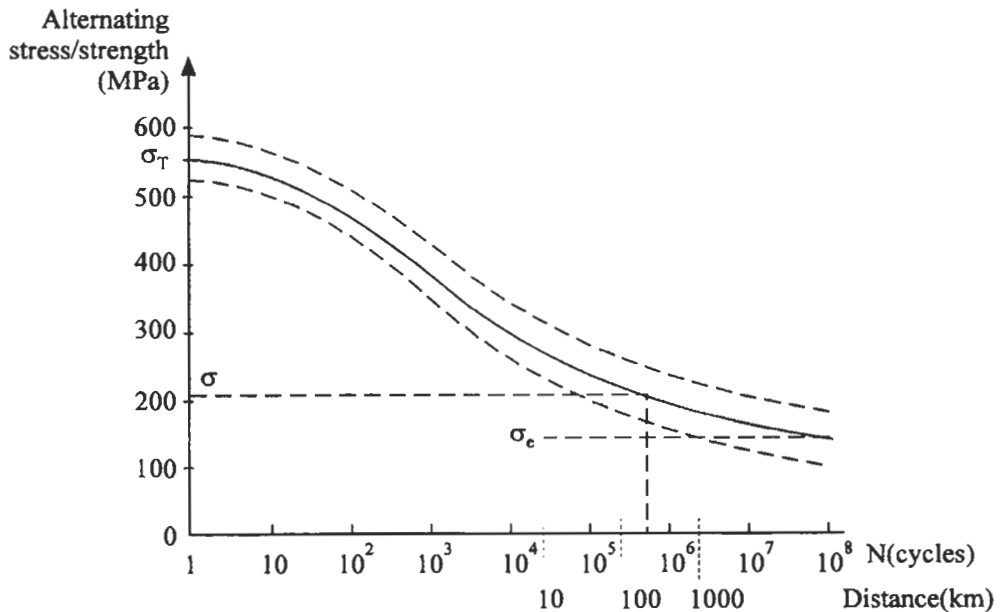

Fig. 4. Predicted *S–N* curve for stainless steel with stress concentration.

252

of section location (causing a stress raiser) and premature failure results. The position of failure, interestingly, is not exactly where the maximum nominal bending stress occurs (which is at the step change of diameters) but nearby at the end of keyway region—where the stress concentration is greater. At the fillet radius at the step change in diameters, though, the shaft is nearly as vulnerable.

Calculations show that the bending stress magnitude is much greater than the shear stress caused by torsion due to accelerating and braking, and this combined with the much lower frequency of occurrence of fluctuation of shear stresses effectively eliminates torsion effects as a significant contribution to fatigue damage. This finding has important implications upon the possible improvement made to the design, as discussed in Section 6.

6. PROPOSED DESIGN MODIFICATIONS

As the current shaft assembly is prone to fatigue failure after a relatively short operational life, modifications to the detail design are essential if long life is to be obtained. A number of relatively simple changes to the detail design would substantially improve the resulting safe life of future drive shafts in service. These can be achieved in a number of ways and some of the most effective and simple alterations are as follows:

(1) Shortening the length of the keyway groove. The current length is far greater than that required to transmit the torque from shaft to the wheel. The length may readily be reduced and located at the outside ends of the shaft as shown in Fig. 5. This will ensure that the end of the keyway groove (hence location of stress raiser) will be kept clear of the more highly stressed inner portion of the shaft.

(2) Increasing the diameter of the inner portion of the shaft hub. This may readily be increased from 12 mm to, say, 16 mm diameter along a 30 mm length and the drive wheel sleeve bore correspondingly increased to accommodate it. There should remain sufficient depth of thread left for the M6 locking screw but a smaller screw may readily be used (an M4 would be adequate).

(3) Increasing the shoulder fillet radius. Although the shaft did not fail at the change of diameter shoulder, an increase from R3 to R5 would nevertheless be desirable in lowering the stress concentration.

(4) Reducing the drive wheel hub/sleeve length. If this were reduced even slightly (and the shaft shoulder increased accordingly) this would be desirable from fatigue considerations and still leave adequate space for the locking screw.

A drawing showing the proposed four modifications incorporated into the design is given in Fig.

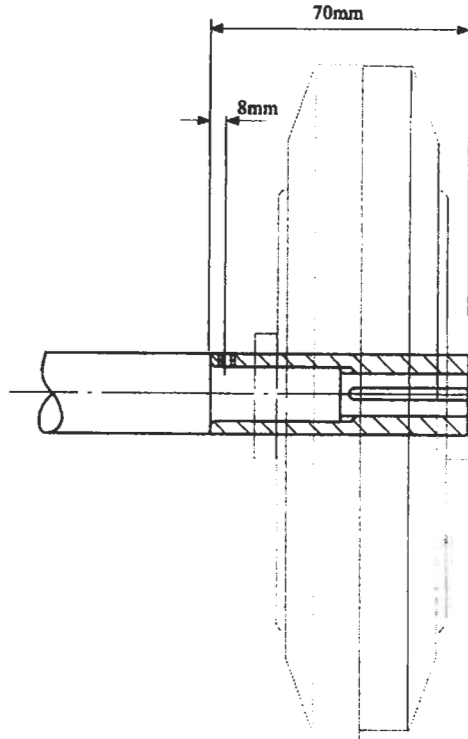Fig. 5. Wheel shaft with reduced length keyway groove.

Fig. 6. Proposed redesign.

6. It is believed that the first two changes would have the greatest effect and if made it would avoid the need for specifying a stronger and inevitably a more expensive material.

It is not thought likely that any of the suggested changes would add significantly to total machining costs.

7. CONCLUSIONS

Clearly, the detail design of the wheel shaft hub assembly is found wanting. Even when operating under ideal circumstances, the predicted life is relatively short and leaves no margin for vehicle misuse, a distinct possibility with such an application. Recognition of the vulnerability to fatigue of a rotating component subjected to bending and torsion loading should lead automatically to taking fatigue preventative measures at the detail design stage. It is essential to avoiding having high stress concentrations at locations of greatest nominal stress if at all possible. Even taking relatively simple measures, such as those described, will greatly improve component reliability without affecting manufacturing costs and prolong the life of components.

REFERENCES

1. Deutschman, A. D., Michels, W. I. and Wilson, C. E., *Machine Design—Theory and Practice*, Collier McMillan, New York, 1975.
2. Juvinall, R. C. and Marshek, K. M., *Fundamentals of Machine Component Design*, J. Wiley, 1991.
3. Shigley, J. E., *Mechanical Engineering Design*, McGraw-Hill, 1986.
4. Ryder, G. H., *Strength of Materials*, Macmillan Press Limited, 1969.

Fatigue failure analysis of a leg press exercise machine

P.J. Vernon, T.J. Mackin*

University of Illinois at Urbana-Champaign, Department of Mechanical and Industrial Engineering, 1206 West Green St., Urbana, IL 61801, U.S.A.

Abstract

The following paper is an engineering failure analysis of an adjustment pin used in a leg press exercise machine. The pin is used to allow adjustment of the machine for people of different heights. It was modeled as a cantilever beam subjected to varying forces depending on the weight stack setting. The fracture occurred at a point of localized stress concentration. The analysis shows an elastic stress concentration of 1.67 which would cause plastic deformation and a fatigue stress concentration of 1.38 that led to the eventual fatigue failure. Based on actual user data, a block loading analysis was used to calculate a pin lifetime of approximately one year. The pin actually failed after $1\frac{1}{2}$ years of use. Design changes are recommended to reduce the size of the stress concentration and subsequently increase the life of the adjustment pin. © 1998 Elsevier Science Ltd. All rights reserved.

Keywords: Fatigue; Fatigue design; Sports equipment failures

1. Background

1.1. Machine description

The following engineering analysis concerns the fatigue failure of an adjustment pin used within a piece of weight training equipment. The particular piece of fitness equipment is called a leg press/squat machine. It is specifically designed to exercise the quadricep muscles of the upper leg, Fig. 1. The machine consists of a moveable sled mounted to a set of linear bearings that travel along a pair of hardened steel shafts. The two steel shafts are mounted to a steel support frame and are inclined at an angle of 10° to horizontal. The user lies on the moveable sled with his/her shoulders squarely positioned against a set of padded shoulder stops and places his/her feet against

---

* Corresponding author.

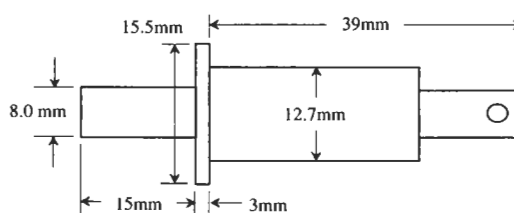Fig. 1. Person performing a leg press.

Fig. 2. Diagram of adjustment pin.

a fixed footpad. To perform the exercise, the user pushes against the footpad and shoulder stops using the upper leg muscles. The sled rolls along the shafts until the person's legs are fully extended. The user then slowly allows the sled to return to the original position. This constitutes one exercise repetition. An adjustable stack of cast iron weights provides the resistance force. The weight stack is connected to the sled by a steel cable. The steel cable travels through a series of pulleys and is connected to the sled by a telescoping box beam. To accommodate people of different heights, the distance between the shoulder stops and the footpad must be adjustable. This is accomplished by the telescoping box beam connected in series between the cable and the bottom of the sled. The inner tube is connected to the cable while the outer tube is firmly welded to the sled. The load is transferred from the inner beam to the outer one through a spring-loaded steel pin, Fig. 2. The pin is firmly attached to the outer box tube and locks into a series of holes drilled in the inner tube. Adjustments are made by disengaging the spring loaded pin from one hole in the inner box tube and engaging it into another. By engaging the pin into different holes, the sled can be moved a
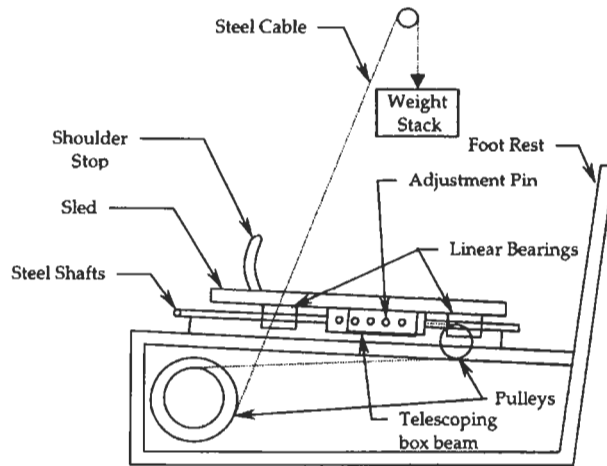
Fig. 3. Diagram of leg press machine.

total of $8\frac{3}{4}$ in. to adjust for different height people. Figure 3 shows a diagram of the major components of the machine. The resistance force from the stack of weights is transferred through the set of cables. These cables run through a series of pulleys that magnify the effective resistance force supplied by the weight stack. One end of a cable is attached to the inner tube of the telescoping box beam. The adjustment pin in question prevents the inner and outer tubes from moving relative to each other. Consequently, the pin transfers the effective force supplied by the weight stack to the sled. The pin experiences a complete loading cycle with each exercise repetition. The pin is loaded in a cantilevered manner from zero load to a maximum load and then back to zero during each lifting repetition. The weight stack is composed of a series of cast iron plates and can be adjusted to provide a resistance force from 15 to 285 lb in 15 lb increments, Fig. 4. From the wear marks along the center of the weight stack, it is evident that the most use was in the range of 45–150 lb.

1.2. Pin failure

The pin was in service for approximately $1\frac{1}{2}$ years before failure occurred. At that time, the machine was disassembled to reveal the fractured adjustment pin, Fig. 5. Upon close inspection of the pin, two distinct regions on the fracture surface were seen. One region is indicative of fatigue crack growth and the other of fast fracture. Once the fatigue crack reached a critical size of approximately 3 mm, the pin failed completely due to fast fracture, Fig. 6. A micrograph of the fracture surface clearly shows the transition line from the fatigue driven crack growth to fast fracture as well as a micrograph of the transition region. It was at this transition line that the crack reached a critical length and the pin failed completely due to fast fracture, Fig. 6. In Fig. 6, the upper portion of the micrograph shows a relatively smooth (smeared) surface consistent with fatigue crack growth. The surface smearing was caused by crack closure and surface contact. The lower portion of the picture in Fig. 6 shows a region of ductile tearing with less smearing evident at the point of crack instability and the region of fast fracture. The transition line from fatigue
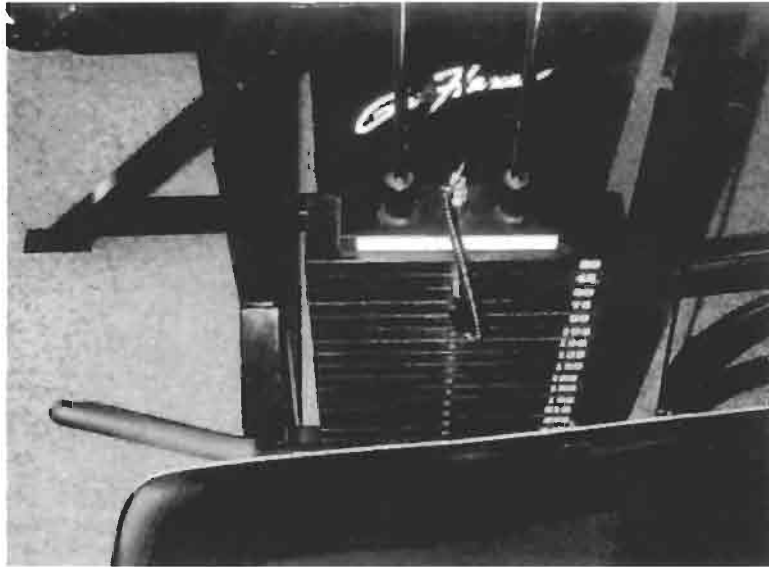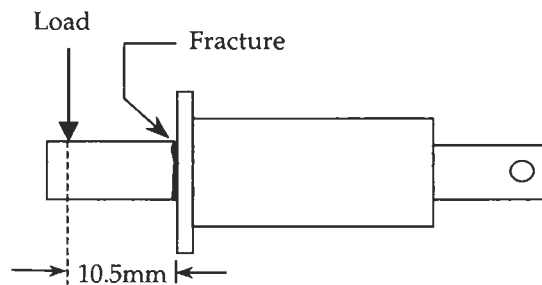
Fig. 4. Picture of weight stack.

Fig. 5. Diagram of pin loading and failure.

crack growth (upper portion) to fast fracture (lower portion) is very distinct and was measured to be about 3 mm from the top surface of the pin.

1.3. Material properties

To calculate the fatigue lifetime of the adjustment pin, an estimate of the ultimate tensile strength is needed. With most common metals, the tensile strength can be directly correlated to the surface hardness. For this particular case, a Rockwell B hardness test was performed on a cylindrical section of the pin. The test measured a surface hardness of 90 HRB. Since the test was performed on a circular cross section 8.0 mm diameter, a corresponding circular correction factor (CF) of 4 HRB was added to the measured hardness, resulting in a surface hardness of 94 HRB [1]. From the hardness, the approximate tensile strength of the steel can be calculated using the following relationship [2]:
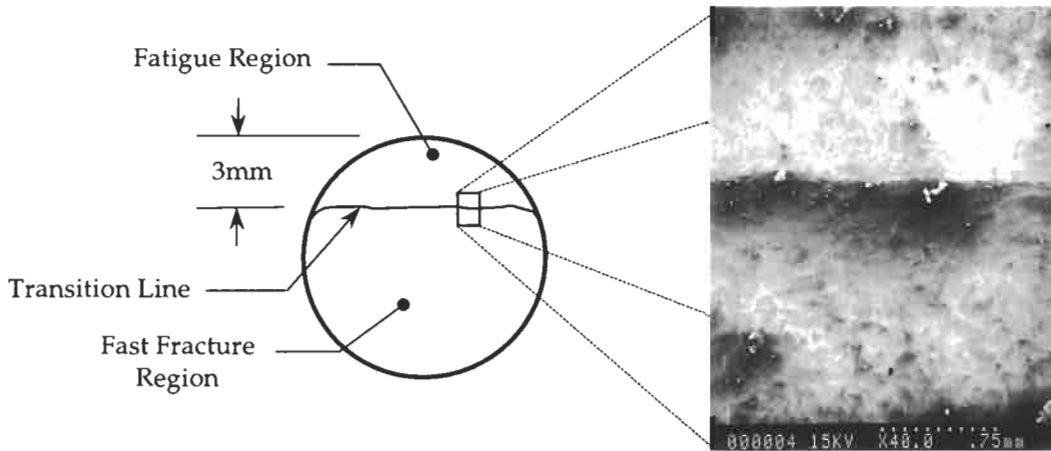
Fig. 6. SEM picture of the transition region from fatigue to fast fracture.

$$\sigma_{ult} = 3.45 \times (HRB + CF). \tag{1}$$

According to this relationship the approximate ultimate tensile strength of the steel was calculated to be 324 MPa. This relatively low tensile strength indicates that the pin was probably made of a low carbon steel such as AISI 1005 or 1010 low carbon steel.

2. Fatigue failure

2.1. Beam stresses

To determine the cyclic stresses experienced by the pin during the exercise repetitions, the pin was modeled as a circular cantilever beam of 8.0 mm diameter and a length of 15 mm. From this model, the maximum bend stresses along the top edge of the pin were calculated using the following standard beam flexure equation,

$$\sigma_{bend} = \frac{My}{I}, \tag{2}$$

where M = moment created by the cantilevered load, y = pin radius and I = first moment of inertia.

From examining the wear patterns of the fractured pin, it was evident that the force from the weight stack was applied about 10.5 mm from the site of failure, Fig. 5. Using a 10.5 mm moment arm and a pin diameter of 8.0 mm, the bend stress can be calculated for any weight stack setting. Since the amount of weight was adjustable to account for people of varying strengths, the bending stresses experienced by the pin depends on the particular machine user. To correctly analyze the entire loading spectrum, a block loading scenario must be employed and a typical distribution of users must be determined.
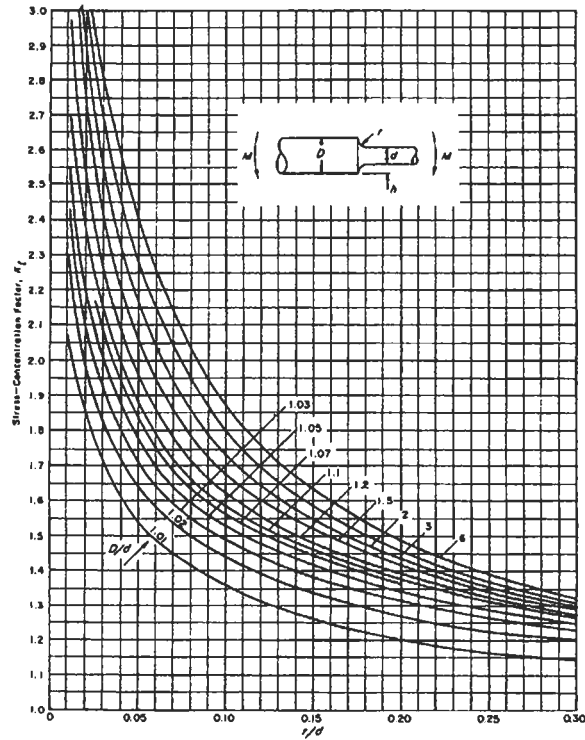
Fig. 7. Elastic stress concentration for a round shaft in bending. (Reprinted with permission from Machine Design, 1951. A Penton publication.)

2.2. Elastic stress concentration

As seen in Fig. 5, the fracture of the pin occurred at a point where the diameter changed abruptly. The abrupt change in part diameter created an elastic stress concentration at the shoulder root radius. The root radius at the shoulder was measured to be 0.8 mm ($\frac{1}{32}$ in.). The elastic stress concentration factor depends on two different ratios of part dimensions. The first ratio is the root radius divided by the smaller part diameter and the second is the ratio of the larger diameter to the smaller diameter. The elastic stress concentration factor (K_t) can be read from standard charts developed from experimental data, Fig. 7 [3]. For this particular application, the ratio of the diameters is $D/d = 1.6$ and the ratio of the root radius to the smaller part diameter (r/d) is 0.1. Using Fig. 7, the corresponding elastic stress concentration factor (K_t) is approximately 1.67.

2.3. Plastic yielding

As an initial check of the system design, it is prudent to determine the maximum static stress on the pin at the maximum selectable load. The maximum setting of the weight stack was 285 lb. This setting produced a force of 1268 N on the pin. Using this value and equation (2) produces a bending stress of 265 MPa. As was stated in the previous section, an elastic stress concentration

factor must be included to account for the stress riser caused by the abrupt change in pin diameters. Multiplying the bend stress by the elastic stress concentration factor ($K_t = 1.67$) produces a maximum bending stress of approximately 443 MPa. This value is greater than the ultimate stress of 324 MPa as calculated from the hardness test and equation (1). Even though the maximum bend stress is greater than the ultimate stress, the pin will not necessarily fail under this loading scenario. As the material along the top surface of the pin is plastically deformed, the stress level remains relatively constant and additional loads are redistributed toward the center of the pin. After the pin has undergone plastic deformation, the elastic beam equation for the bend stress is no longer valid. Once this happens, an inelastic bending analysis must be performed. The important point to note from this analysis is that under the maximum loading scenario, the pin will be plastically deformed. This fact alone indicates that the pin was poorly designed.

2.4. Fatigue stress concentration

Close examination of the fracture surfaces has indicated a fatigue failure. The elastic stress concentration factor previously determined is measured under conditions of elastic stress and cannot be directly applied in fatigue calculations. Experiments have shown that the fatigue stress concentration factor may differ significantly from the elastic stress concentration factor. From the microscopic viewpoint, the steep gradients of an elastic stress field may not be sufficient to shuttle dislocations and nucleate a fatigue crack. Hence, considerable experimental evidence has shown that the fatigue stress concentration (K_f) is less than or equal to the elastic stress concentration (K_t). The elastic concentration factor can be converted to a fatigue stress concentration factor by the following formula [4],

$$q = \frac{K_f - 1}{K_t - 1} \tag{3}$$

where q is the notch sensitivity parameter of the given material. The notch sensitivity is dependent upon the notch root radius and the materials ultimate tensile strength. The notch sensitivity was determined from a plot of notch root radius versus notch sensitivity for steels, Fig. 8 [4]. In this case, the notch root radius was 0.8 mm ($\frac{1}{32}$ in.) and the approximate ultimate tensile strength of the steel was 324 MPa as calculated from equation (1). Using these values and Fig. 8 produces a notch sensitivity value of $q = 0.58$. Using equation (3) and the value for q, the fatigue stress concentration factor (K_f) was calculated to equal 1.38. The fatigue stress concentration factor was incorporated into the analysis by multiplying the bending stress calculated in equation (2) by K_f.

2.5. Machine usage

To make an accurate prediction of the life of the adjustment pin, it is crucial to determine the amount of use the machine typically sees. The repetitions at each weight level were recorded over a period of three weeks. Figure 9 shows a graph of the number of repetitions at each weight level during the three week period. The majority of the use was between 45 and 135 lb with only a small amount of use at the very high weight levels. We will consider the three week time as one period in the block loading scenario.
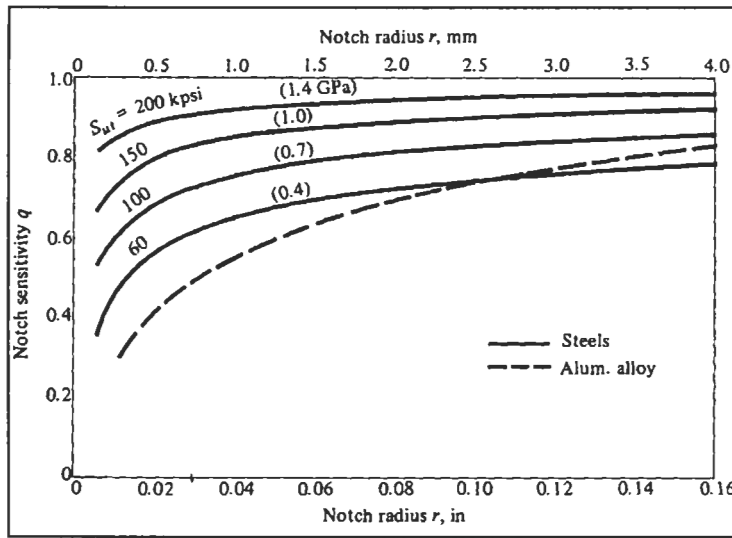
Fig. 8. Notch sensitivity for various materials. (Metal Fatigue, George Sines, editor, © 1959. Reprinted by permission of Prof. George Sines.)
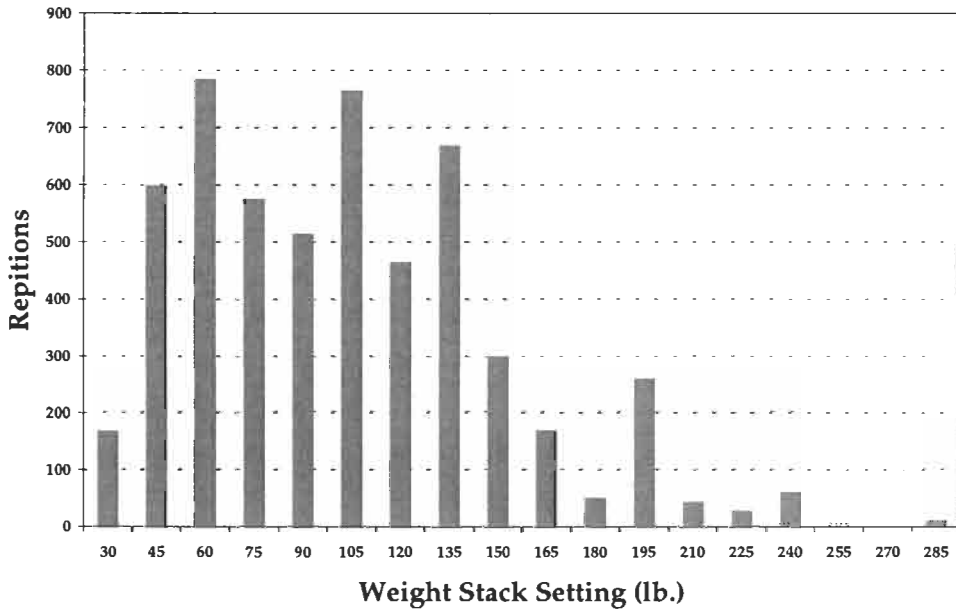
Weight Level Distribution

Fig. 9. Machine usage over a three week period.

Table 1
Bend stress incurred in the adjustment pin at each weight stack setting

Weight stack (lb)	Fatigue bend stress (MPa)
15	19
30	38
45	58
60	77
75	96
90	115
105	135
120	154
135	173
150	192
165	212
180	231
195	250
210	269
225	289
240	308
255	327
270	346
285	366

2.6. Bending stresses

From the previous section, we see that individuals use varying weight stack settings. Each weight stack setting produces a unique bending stress in the adjustment pin. For each weight stack setting, the bend stress was calculated using equation (2) and multiplied by the fatigue stress concentration at the pin shoulder. The corrected bending stresses for each weight stack setting are summarized in Table 1.

2.7. Full reversed loading

The expected number of cycles to failure for each bending stress were estimated using Basquin's law [5], where,

$$\sigma_{ar} = A(N_f)^b. \tag{4}$$

However, Basquin's law is only valid for the case of fully reversed loading. In the case of the adjustment pin, it was being loaded from zero to various values. Therefore, the cyclic bending stresses were converted to equivalent fully reversed stresses. This was done using the Goodman mean stress correction [6],

Table 2
Equivalent reversed stresses and cycles to failure for each weight stack setting

Weight stack setting (lb)	Fully reversed equivalent stress (MPa)	Cycles to failure
15	23	1,337,234,019,763
30	47	6,465,350,374
45	70	285,787,954
60	93	31,259,118
75	116	5,617,138
90	140	1,381,747
105	163	422,137
120	186	151,134
135	210	61,077
150	233	27,158
165	256	13,047
180	279	6681
195	303	3609
210	326	2041
225	349	1200
240	373	731
255	396	458
270	419	295
285	442	195

$$\frac{\sigma_a}{\sigma_{ar}} = \left(1 - \frac{\sigma_m}{\sigma_{ult}}\right), \tag{5}$$

where

$$\sigma_a = \frac{1}{2}(\sigma_{max} - \sigma_{min}), \tag{6}$$

$$\sigma_m = \frac{1}{2}(\sigma_{max} + \sigma_{min}). \tag{7}$$

The ultimate stress of the pin used in Goodman's equation (5) was estimated to be 324 MPa based on a Rockwell hardness test and equation (1). The σ_{min} was zero for all weight levels while σ_{max} was taken from Table 1 for each weight level. The Goodman equation (5) was used to calculate an equivalent fully reversed stress for each weight level. These new equivalent stresses take into account the effect of the mean stress on the fatigue life. Once the equivalent fully reversed stresses were calculated, each was substituted into Basquin's law (5) to determine the number of cycles to failure at each weight level. Using the following constants for AISI 1005 steel [5]: $A \cong 878$ MPa, $b \cong -0.13$ and equation (5), the number of cycles to failure were calculated at each weight level. Table 2 summarizes the equivalent fully reversed stresses using the Goodman equation and the corresponding cycles to failure according to Basquin's law for each weight setting.

As expected, Table 2 shows that the higher weight levels require considerably fewer cycles to failure than the lower weight levels.

2.8. Cumulative damage

The final step in determining the total number of cycles to failure was to combine the various weight levels and the user distribution for the three week period using Miner's rule for block loading. According to Palmgren and Miner, failure occurs when the cumulative damage caused by each loading cycle equals one. The general form of the Palmgren–Miner rule [6] is given by,

$$\sum_{i=1}^{k} \frac{n_i}{N_i} = 1, \tag{8}$$

where k = number of stress levels in the block loading spectrum, n_i = number of cycles at each stress level in the block loading spectrum and N_i = number of cycles to failure at each stress level.

Using equation (8) and the values from Table 2 the cumulative damage incurred by one three week loading block was 0.057. Therefore, a total of 17.7 loading blocks would be required to cause failure of the adjustment pin. This translates into approximately 53 weeks of typical use before failure. According to the purchase records of the machine the actual failure occurred after $1\frac{1}{2}$ years of operation.

It should be remembered that fatigue calculations are only an estimate and the calculated lifetimes are very sensitive to small changes in geometry that affect stress levels. This analysis ignores the presence of plastic deformation that occurs at the higher stress levels. In addition, the standard notch sensitivity formulas are derived from data where the notch depth does not exceed four times the notch radius. So, according to R.E. Peterson, "This means that caution should be exercised in application to cases of deep sharp notches or very small fillets on stepped shafts ...". However, the analysis does show the pin design to be inadequate.

3. Design implications

The analysis confirms that the pin failure was due to a poor design and lack of engineering. The stress calculations indicate that the pin plastically deformed under the maximum load. The fatigue analysis determined that the pin should fail after only approximately one year of typical service. This is clearly unacceptable and the design should be altered to take the maximum load and fatigue loading into account.

One way to improve the design to avoid fatigue failure would be to redesign the machine to add support at the end of the pin. This would reduce the bending stresses by half since the pin could be modeled as a simply supported beam instead of a cantilever beam. Another method of changing the design would be to increase the pin diameter and/or use a stronger grade of steel. However, this would probably increase material and manufacturing costs. It has also been shown that the addition of a relief groove behind the shoulder causes a reduction in the stress concentration, Figure 10.

The addition of relief grooves does require extra machining and may not be possible due to the geometry of the machine. Since the localized stress concentration is dependent on the shoulder root
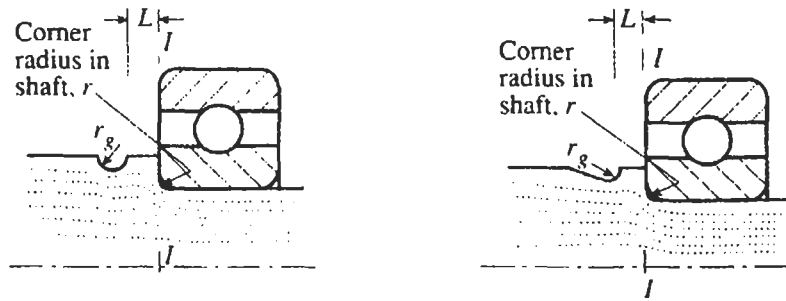
Fig. 10. Examples of relief grooves behind the shoulder to reduce the stress concentration at the radius, r. (Peterson's Stress Concentration Factors, Walter D. Pilkey, © 1997. Reprinted by permission of John Wiley & Sons.)

radius, increasing the radius causes a decrease in both the elastic and fatigue stress concentrations. Reducing the stress concentration decreases the effective stress at the shoulder, avoiding plastic deformation and increasing the fatigue lifetime.

References

[1] Newby JR. ASM handbook, mechanical testing, Vol. 8, 1985. pp. 82.
[2] Callister WD. Materials science and engineering. New York: John Wiley & Sons, 1994. pp. 132.
[3] Peterson RE. Design factors for stress concentration. Machine Design 1951;5(23):159–161.
[4] Shigley JE, Mischke CR. Mechanical engineering design. St. Louis: McGraw-Hill Inc., 1989.
[5] Lampman SR. ASM handbook, fatigue and fracture, Vol. 19, 1996. pp. 233, 969.
[6] Hertzberg RW. Deformation and fracture mechanics of engineering materials. New York: John Wiley & Sons, 1996. pp. 530–32.
[7] Pilkey W. Peterson's stress concentration factors. New York: John Wiley and Sons, 1997. pp. 146–7.
[8] Peterson RE, Sines G. editors. Metal fatigue. New York: McGraw-Hill Book Company, Inc., 1959. pp. 296–7.

Failure analysis of rubber fuel pipes in aero-engines

Guoru Fu

Beijing Aeronautical Technology Research Center, Box 9203-16, Beijing 100076, China

Abstract

This paper describes a series of examinations and the fracture analysis of burst rubber fuel hosepipes on aero-engines. The bursting of the hosepipes was caused by fatigue failure and major reasons are improper design of hosepipe structure, low fatigue bearing capacity and severe deformation in mounting. © 1999 Published by Elsevier Science Ltd. All rights reserved.

Keywords: Aircraft failures; Engine failure; Fatigue; Hosepipes

1. Introduction

The bursting of rubber fuel hosepipes on aero-engines seriously compromises flight safety. Though much research has done, the problem has not been solved. At least 10 incidents were recorded in 1994–1995 alone. The bursting happened in two types of hosepipes which we designate as A and B respectively for convenience. This article describes the characteristics of bursting hosepipes, analyzes the failure and proposes prevention measures.

2. Visual inspection of hosepipes

The characteristics of bursting hosepipes are as follows:

(1) There were, to some extent bending deformations in both ends of the hosepipes, with more deformation taking place near the end of the elbow pipe (see Fig. 1).
(2) For most hosepipes only one opening existed in the exterior of the rubber at the bending position near the end of the metal elbow adapter, but two openings were observed in one A type hosepipe.
(3) The distance from the bursting position to the end of the adapter housing was 0–15 mm.
(4) The bursting shape of the outer rubber was irregular and there with axial, circumferential and branched cracking.

B type hosepipe

Fig. 1. Appearance of bursting hosepipes (arrowheads aim at openings).

3. Dissection of hosepipes

The hosepipes were dissected from the outer to the inner layers in order to study the characteristics of bursting hosepipes. The results showed that:

(1) The steel wire layer was intact.
(2) In all A type hosepipes, there was only one opening in the inner rubber layer. Similar results were obtained for most B type hosepipes except two, where two openings were observed.
(3) The opening in the inner rubber layer was situated in the outside of the bend near the metal elbow adapter. The distance between the opening and the metal core is about 2.0–12.5 mm (see Fig. 2).
(4) The openings in the inner rubber layer are circumferential, as shown in Fig. 2.
(5) No other defects were observed in the inner layers of the hosepipes.

A type hosepipe
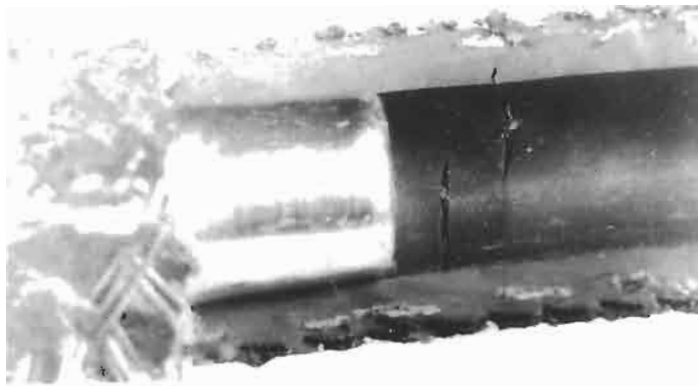
B type hosepipe

Fig. 2. The openings in the inner rubber layer.

(6) There were small openings in the outer surface of the inside middle layer in one B type hosepipe (see Fig. 3).

4. Fracture analysis of layers

4.1. Fracture analysis of inner layer

Opening the fracture and inspecting by SEM, it was found that the fracture surfaces in both A and B type hosepipes have the same characteristics, showing flats and radiating ridges (see Figs 4 and 5). Fatigue markings in the later period of propagation could be clearly observed (Fig. 6). The

Fig. 3. The openings in the outer surface of the inside middle layer.

Fig. 4. The fracture appearance of an A type hospipe.

fatigue cracks were possibly initiated at the interface between the cotton thread and the inner layer. Finally, there were no obvious defects in the fatigue initiation zone (Fig. 5).

Smaller cracks had similar fatigue characteristics (Fig. 7).

4.2. Fracture analysis of outer layer

Opening the outer layer fractures and observing by SEM, it was concluded that cracks initiated from the outer surface and propagated towards the inner surface. Multiple initiation sites and some fatigue striations were observed (Fig. 8).

Fig. 5. The fracture appearance of a B type hosepipe.
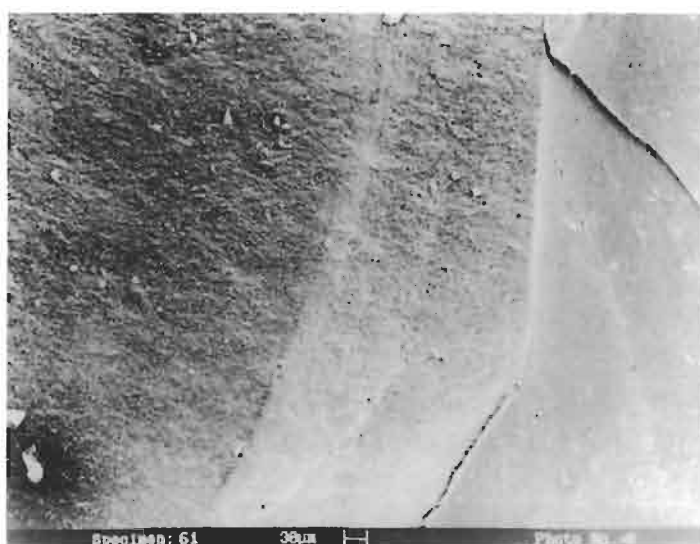
Fig. 6. Fatigue beach marks.

5. Analysis of hosepipe bursting failures

Fracture analysis shows that hosepipe bursting is caused by fatigue failure, but the characteristics of failure are different in the inner and outer layers.

In structure, the hosepipe is composed of seven layers (Fig. 9). Steel wire is the main load-bearing layer. The inside layer was projected from the steel wire by a middle layer and a cotton layer internal to the steel wire layer. The inner layer was in direct contact with kerosene and carried
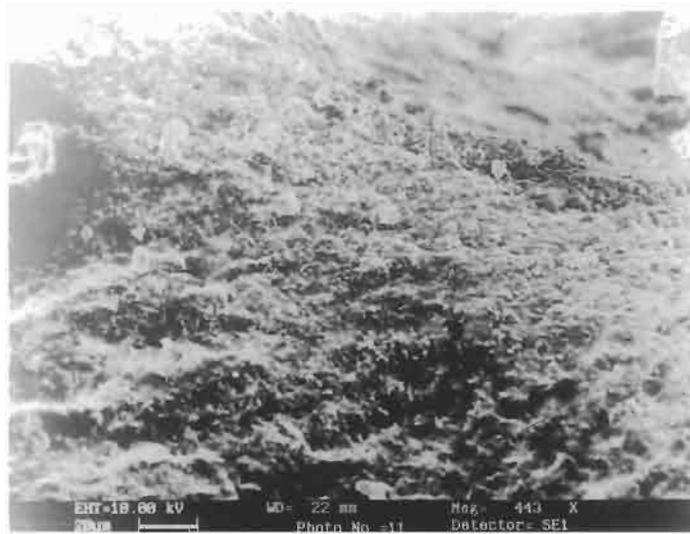
Fig. 7. The fracture appearance of small cracks.
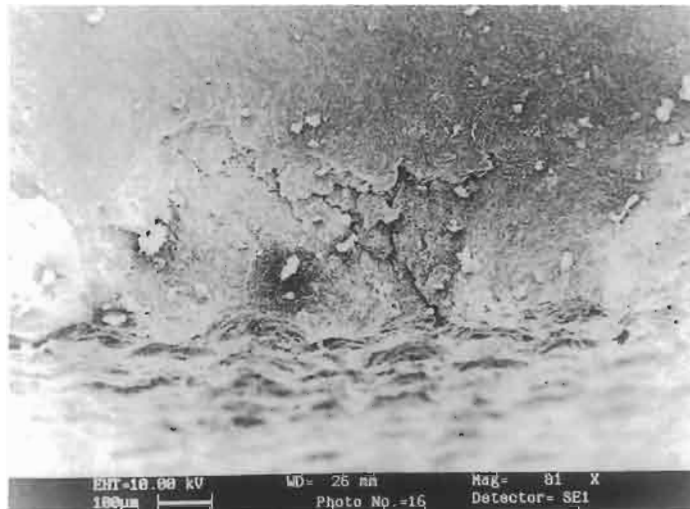
Fig. 8. The fracture appearance of the outer layer.

alternating stress caused by pressure variations. The outer layer bears stress and bursts after the inner layer bursts. When kerosene has penetrated the inner and middle layers as well as the steel wire layer, kerosene gathered between the steel wire and the outer layer. Large fatigue cracks initiated in the most highly bent position of the outer layer and formed the multiple fatigue crack sources.

There were three openings in the inner layer of one B type hosepipe; two of them were fully penetrating and the other was not. Fatigue cracks originated from the interface between the cotton

1--inner layer   2--cotton   3--middle layer   4--steel wire layer
5--middle layer   6--cotton   7--outer layer
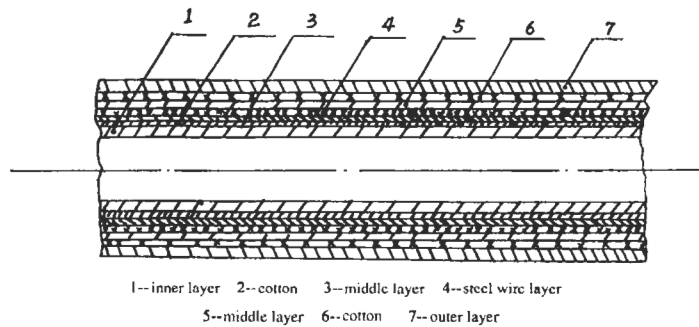
Fig. 9. Sectional diagram of the bursting hosepipe structure.

layer and the inner layer. The two penetrating cracks propagated both inwards and outwards. The non-penetrating crack outwards.

From the above-mentioned, the course of hosepipe bursting failure can be described as follows: fatigue cracks originated first from the interface between the cotton layer and the middle layer, and then propagated into the middle layer. Afterwards, further fatigue cracks initiated at the interface between the cotton layer and the inner layer and propagated into the inner layer. When the crack had penetrated the inner layer under the steel wire layer, the outer layer could not bear the pressure of the kerosene, resulting in a large stress fatigue failure leading to bursting.

Improper design is the main reason for inner layer fatigue failure. The interface between the cotton and the inner layer is a weak position. Under working conditions, pressured pulses cause a radial bulge in the hosepipe. At the same time, there were bending deformations in the hosepipe. Insufficient fatigue resistance of the hosepipe is the most important reason for failure. However, only static pressure requirements were demanded for the hosepipes.

Serious bending deformation in mounting is another important reason for hosepipe bursting. Limited by the space, bending deformation could not have been avoided in mounting the hosepipes. It was reported that the minimum bending radius in a high pressure hosepipe is about 6–7 times the external diameter [1]. The pressure capacity of the hosepipe will drop rapidly if the radius is too small. When the hosepipe works in normal conditions the working life will drop. For example, the service pressure of A style hosepipes is 700 MPa. When the bending radius is 70% of the minimum required in mounting only 58% of the rated working pressure of the hosepipe can be applied in service, i.e., 406 MPa (Fig. 10). If the working pressure is kept at 700 MPa, the working life is shortened to 12% (Fig. 10).

6. Conclusions

(1) The bursting of the hosepipes was caused by fatigue failure. The fatigue cracks originated from the interfaces between the cotton and the inner and middle layers.

(2) Fatigue cracks first propagated into the middle layer. Afterwards, cracks propagated into the inner layer. After the inner layer had been penetrated, a layer fatigue stress was applied to the outer layer.
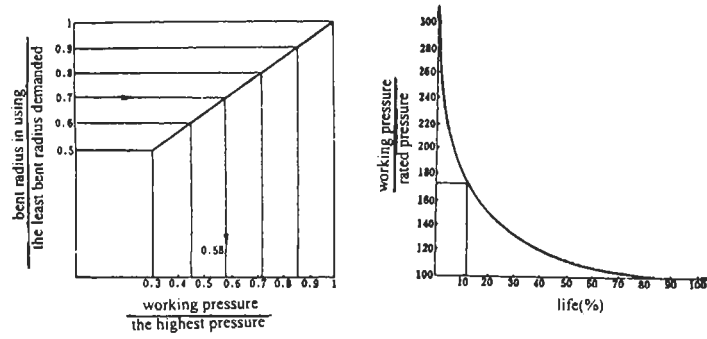
Fig. 10. Relation between bent radius, pressure capacity and working life of hosepipe.

(3) The main reasons for hosepipe failure are as follows:
   (a) inadequate structure;
   (b) low fatigue resistance;
   (c) severe bending deformation in mounting.

Reference

[1] Beijing Institute of Aeronautical Materials, Aeronautical Material Science, Shanghai Science and Technology Press, 1985, p. 6.

Environmental attack

FAILURE OF AUSTENITIC STAINLESS STEEL COMPONENTS USED IN NITROGEN OXIDE PLANT

V. M. J. SHARMA, A. K. JHA, P. RAMESH NARAYANAN,
S. ARUMUGHAM and T. S. LAKSHMANAN*

Material Characterisation Division, Materials and Metallurgy Group, Vikram Sarabhai Space Centre,
Thiruvananthapuram, 695 022, India

Abstract—Austenitic stainless steel components of a nitrogen oxide plant have been found to leak in service. The failed components, namely pipe-to-pipe joints and pipe-to-flange joints, have been studied through standard metallographic techniques to analyse the cause of the failure. In case study I, involving the failure of pipe-to-flange joints, cracking was observed in the pipe wall next to the pipe-to-flange weld. In case study II, involving the failure of a sight port flange, cracking was observed in the flange adjacent to the pipe-to-flange weld. In both cases, cracking was by an intergranular mechanism, and carbon contents were much higher than permitted for "L" grades of austenitic stainless steel. © 1997 Elsevier Science Ltd

Keywords: Metallography, residual stress, fractography.

1. INTRODUCTION

Liquid propellants, with their higher specific impulse than solid propellants, have emerged as efficient fuels for satellite launch vehicles. For combustion during flight, various types of oxidizers have been used. One such oxidizer is dinitrogen tetroxide (N_2O_4). In view of the nonusability of dinitrogen tetroxide with some of the storage materials, mixed oxide of nitrogen (MON) has emerged as a better choice. Its lower freezing point ($-14\,°C$) makes this one of the best oxidizers. MON mainly consists of a mixture of N_2O_4, NO and NO_2. Further classification of MON has been done as MON-3 (3% NO) and MON-10 (10% NO), depending on the content of NO. The plant, which produces mixed oxides of nitrogen (MON-3), consists of reactors, absorption columns, collection tanks, storage tanks, interconnecting piping, flanges and valves. One such plant, commissioned 7 years back, is in operation. However, for the last 2 years, leaks were observed in some of the components, mainly in pipe-to-pipe joints and pipe-to-flange joints. While attempting to rectify such a leak by tightening the flange, the flange broke into pieces. Various components, which have cracked and leaked at different locations of the process plant, have been grouped into two categories. In the first, the failure is in the pipe portion, and, in the second, the failure is in flange portion. As such, two failed components, (i) a pipe-to-flange joint and (ii) a sight port flange, were selected for detailed studies.

2. CASE STUDY I: FAILURE OF PIPE-TO-FLANGE JOINT

The joint consists of a tube (25 mm ID and 32 mm OD) made of AISI 304 L grade stainless steel welded to a flange made of the same steel (Fig. 1) The joint is used to transfer HNO_3 from a storage tank to an NO reactor. A leak was noticed in the pipe portion of the joint.
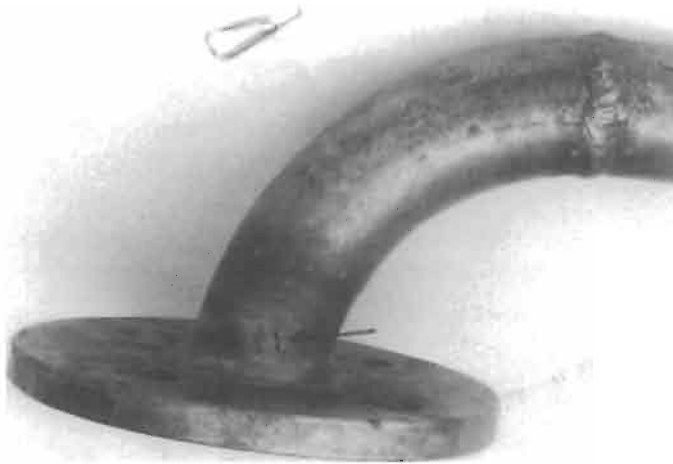
---

*Author to whom correspondence should be addressed.

Fig. 1. Photograph of the pipe-to-flange joint (arrow shows the leaking portion).

2.1. *Observations*

The leaking joint, removed from the assembly line, was found to have a crack in the pipe portion adjacent to the pipe-to-flange weld. Figure 2 shows a stereomicroscopic view of the crack. Table 1 shows the chemical analysis of the material of the components.

The chemical analysis of the material from the flange portion conforms to AISI 304L grade, whereas that from the pipe portion conforms to AISI 304 grade only. The whole component is exposed to 90% HNO_3 at room temperature. The component had a crack 5 mm long in the pipe portion, about 4 mm away from the weld between the flange and the pipe. The component was cut open to reveal the inside portion of the pipe. It was noticed that the inside surface of the pipe had a corroded band about 7 mm in width throughout the inner circumference of the pipe, and the crack
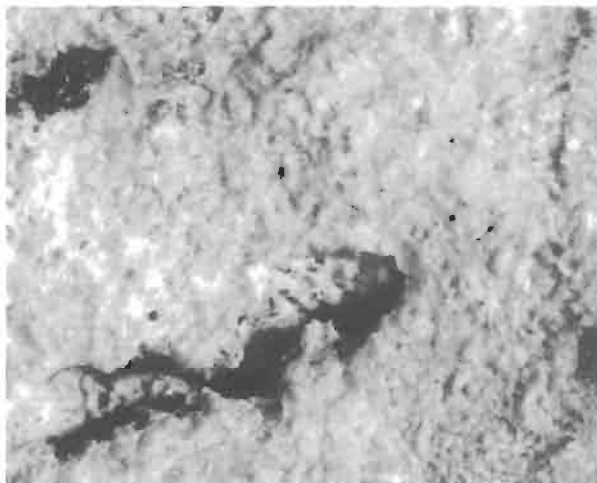

Fig. 2. Stereomicrograph of the crack on a pipe-to-flange joint. × 16

Table 1. Chemical analysis (wt%) of the failed pipe-to-flange joint

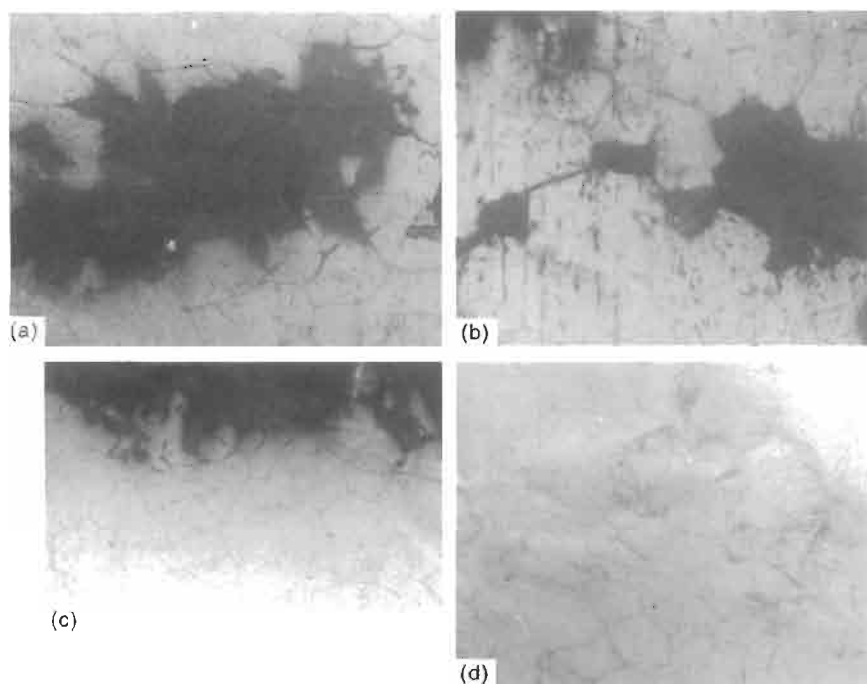| Component	C	S	Cr	Ni	Mn	Mo	Fe
Flange	0.034	0.010	19.3	9.8	1.3	0.3	Balance
Pipe	0.093	0.011	19.7	9.4	1.2	0.2	Balance

Fig. 3. Optical micrographs of the failed pipe-to-flange joint. (a) Microstructure near the crack, showing equiaxed austenite grains with slip bands, and the absence of annealing twins (circumferential side). (b) and (c) Microstructure of through-thickness section, showing intergranular fracture. (d) Microstructure away from the cracked region, showing equiaxed austenite grains with slip bands (note the absence of twins). All × 200.

was seen to be located in the middle of this corroded band. However the longitudinal weld in the pipe (produced during pipe manufacture) did not reveal any such corroded band. The cracked portion of the piece was cut open. The outer circumferential portion, as well as the through-thickness section, was polished to metallographic finish, and electrolytically etched using 10% oxalic acid solution for observation under an optical microscope. Figure 3(a)–(c) shows the microstructure in the cracked portion in both the circumferential portion and the through-thickness section. The microstructure showed equiaxed austenite grains with slip bands, and the absence of annealing twins. The microstructure slightly away from but adjacent to the crack also revealed the presence of slip bands in the austenite grains [Fig. 3(d)]. The fracture surface of the sectioned other piece was observed under the scanning electron microscope (SEM) for fractographic features which revealed the intergranular nature of the cracks.

2.2. Discussion

Welding of dissimilar materials (with respect to chemical composition) will result in a difference in electrode potential, and, hence, preferential attack may take place near the weld joint. Welded tubing of austenitic stainless steel is recommended for use only after full-finishing, wherein the δ-ferrite networks within the weld metal structure are altered by cold work followed by a recrystallization anneal or solution anneal at 1065 °C to dissolve most of the ferrite, and to change the cold worked structure to equiaxed recrystallized grains [1]. The microstructure revealed the absence of annealing twins, and, at the same time, the presence of slip bands, indicating that cold rolled sheets were used for tube making. Subsequently welding the pipe to the flange might have introduced thermal stresses in the component near the weld. However, at and near the longitudinal weld, there was no dissolution of metal (corroded band). It is observed that severely deformed areas will be chemically more active, and will rust before areas on the same part that have been subjected to little or no deformation. Residual stresses due to cold bending of a pipe, together with additional thermal stresses due to welding, have apparently accelerated the corrosion attack, with the subsequent

formation of a corroded band and crack initiation within the band during 7 years of service. Intergranular cracks, typical of stress corrosion attack, as noticed on the fracture surface, are the evidence for such stress-induced preferential attack along the grain boundaries. This type of intergranular fracture is typical of the HNO_3 stainless steel system [2]. The pipe-to-flange weld has a longer thermal mass than the pipe weld, so presumably required a comparatively large input. Because of the high carbon content of the pipe, sensitization may have occurred in the pipe-to-flange weld as a result of the weld thermal cycle.

2.3. Conclusions

Cold working and welding processes used for component fabrication introduced stresses. Welding of dissimilar metal compositions introduced electrode potential differences. This combination created conditions conducive to preferential corrosion attack. Sensitization may also have been a factor owing to the high carbon content of the pipe, and the high heat input which may have been required to make the pipe-to-flange weld.

2.4. Recommendations

(1) Components should be given an annealing treatment after fabrication processes like bending, welding etc.
(2) Joining by welding of dissimilar materials should be avoided.
(3) Possible sensitization can be avoided by using the L grade of stainless steel.

3. CASE STUDY II: FAILURE OF SIGHT PORT FLANGE

The second case study refers to the failure of the sight port flange, which was located between flanges in the NO absorption column. Austenitic stainless steel AISI 304L pipe of 80 mm OD and 75 mm ID was welded to a flange which was also said to be made of similar steel. A Teflon gasket was used between the flanges to provide a leak-proof system.

3.1. Observations

Figure 4 shows a photograph of the failed component. The failure was in the flange portion 7 mm away from the pipe-to-flange weld zone. During the operation of the plant, there was a leak in one portion of the flange, and, while tightening, it crumbled. The material in this component is exposed

Fig. 4. Photograph of failed sight port flange.

Table 2. Chemical analysis (wt%) of the failed sight port flange

Component	C	S	Cr	Ni	Mn	Mo	Fe
Flange	0.34	0.01	18.9	11.4	1.30	0.50	Balance
Pipe	0.02	0.01	18.5	9.5	1.50	0.40	Balance

to 70% HNO_3 (average) at temperatures between 10 and 35 °C. The chemical compositions (Table 2) show high carbon (0.34%) in the flange, but conformity with AISI 304L in the pipe.

Figure 5 shows a stereomicrograph of the cracked region of the component. Figure 6(a) and (b) shows the microstructure of the component in the flange and pipe portion, respectively. The microstructure of the flange portion does not correspond to AISI 304 L type steel, whereas the microstructure of the pipe portion is typical of AISI 304 L type steel, which agrees with the chemical analysis results. Figure 7(a) shows the microstructure in the interface region of the pipe and flange, revealing the corrosion attack on the interface, and its propagation intergranularly into the flange portion with grain dissolution [Fig. 7(b)]. However, the pipe portion and the weld region do not show any such corrosion attack [Fig. 7(c)]. The microstructure in the flange portion shows grain boundary thickening at and near the interface and intergranular cracking. Figure 8(a)–(d) is SEM fractographs of the failed flange, which show the completely intergranular nature of cracking and grain dissolution. The preferential attack of the corrosive medium along slip bands is shown in Fig. 8(b) and (c). Figure 8(d) shows the corrosion product (tar-colored powder) observed on the fracture surface, and found to be Fe_2O_3 by XRD analysis (Fig. 9).
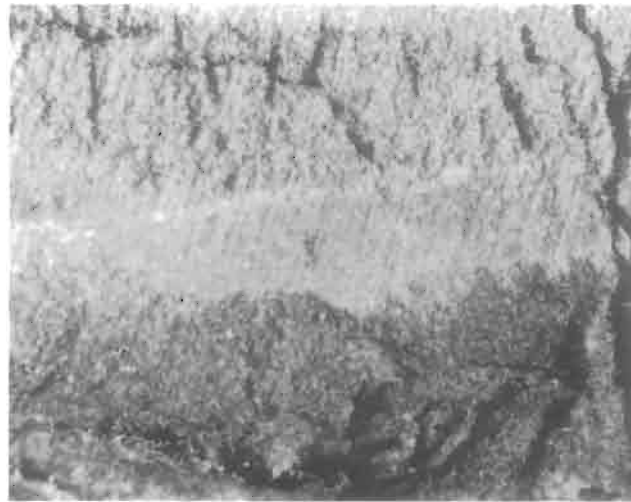

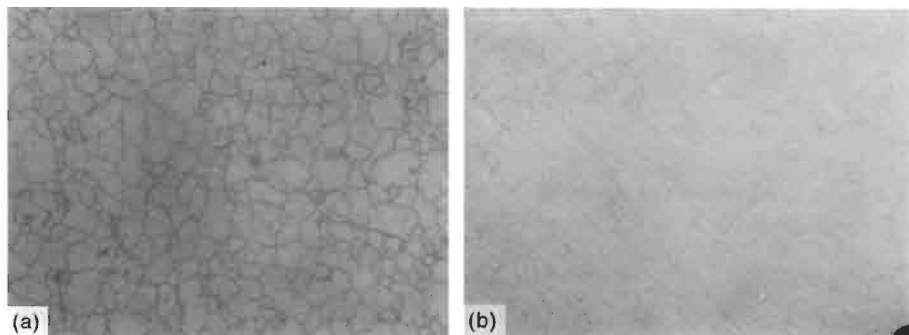Fig. 5. Stereomicrogaph of the cracked portion of the sight port flange. × 16

Fig. 6. Optical micrographs of sight port flange. (a) Flange portion (does not correspond to AISI 304 type). (b) Pipe portion (typical of AISI 304 microstructure). Both × 80.
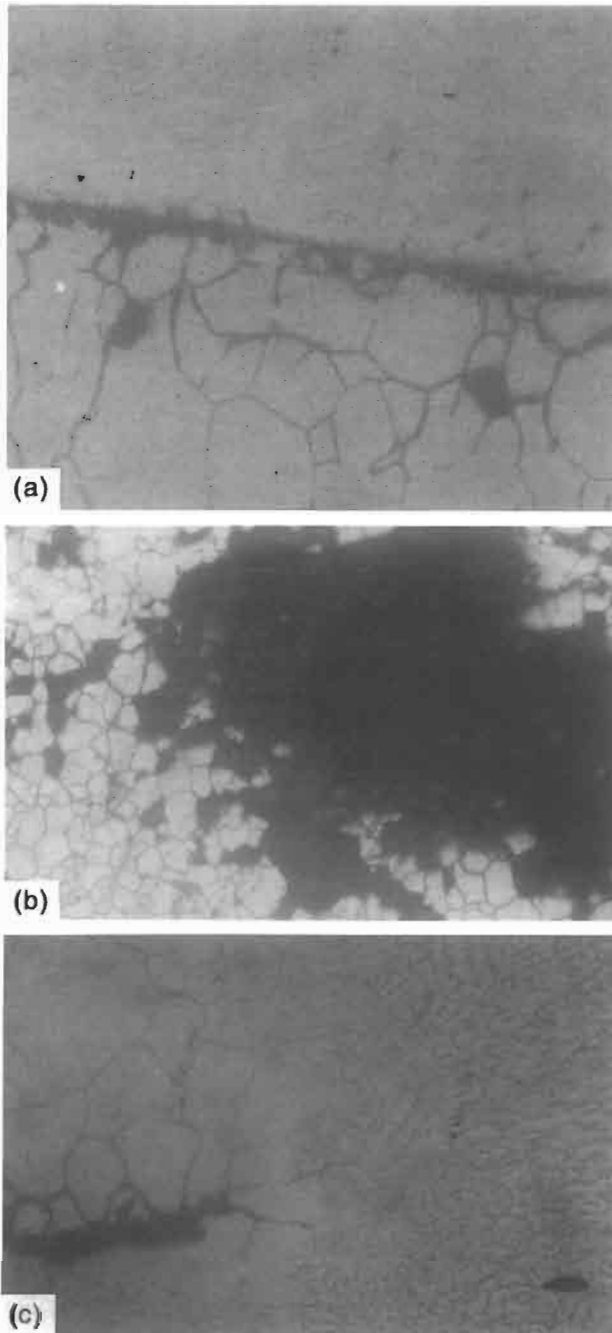
282

Fig. 7. Optical micrographs of sight port flange. (a) Interface between flange and pipe portion, showing corrosion attack on the interface and propagation intergranularly. ×120. (b) Cracked area in the flange portion, showing individual grain dissolution. ×80. (c) Weld region (dendritic type), flange (left top) and pipe (left bottom), showing corrosion attack in flange only. ×120.

3.2. *Discussion*

Chemical analysis of the material from the flange and pipe revealed significant differences in carbon content (Table 2). Welding of such dissimilar metals can introduce differences in electrode potential, and assist corrosion attack near the weld joint. Observations revealed that the cracks
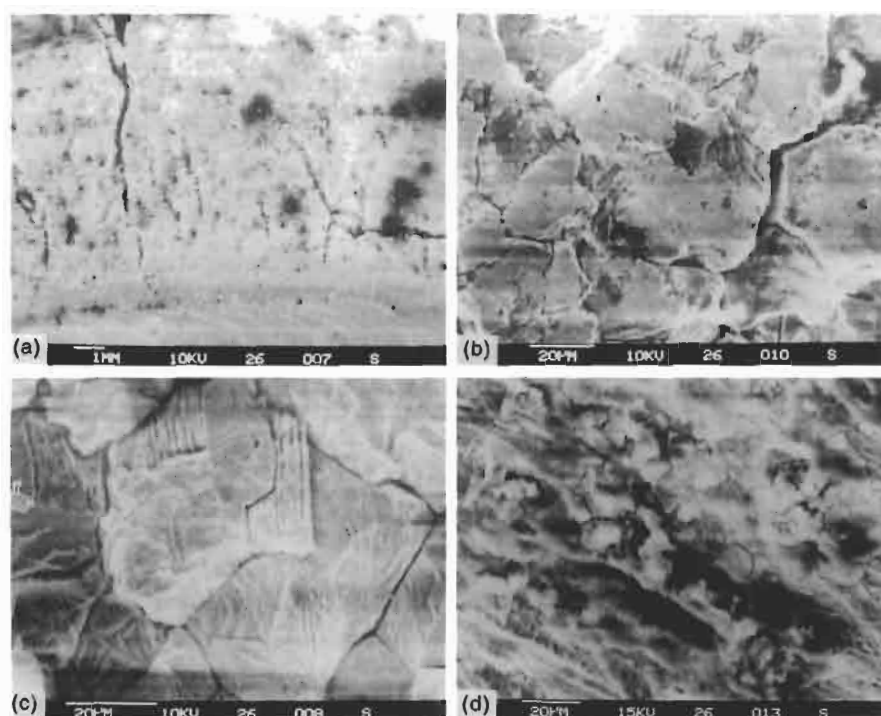
Fig. 8. SEM fractographs of failed sight port flange. (a) Radial cracks starting from the pipe-to-flange interface. (b) Intergranular cracks with grain dissolution. (c) Intergranular cracks with preferential attack along slip bands. (d) Corrosion product (Fe_2O_3).

have started at the flange–pipe interface, and propagated along the radial direction in the flange. The pipe portion, however, did not reveal any cracks. The grain boundary thickening in the flange portion is due to sensitization of the microstructure during welding of the flange to the pipe. The sensitized microstructure contains $Cr_{23}C_6$-type carbides precipitated along the grain boundaries in a fine network. The area adjacent to the grain boundaries becomes depleted of chromium, and the corrosion resistance in this area deteriorates. Two dissimilar metal compositions are in contact, and a large unfavorable area ratio is present. The net effect is rapid attack in the impoverished areas, resulting in intergranular fracture [3]. The use of Teflon as gasket material can also enhance the corrosion attack. It is reported [4] that, in the system consisting of austenitic stainless steel, N_2O_4 and Teflon, the latter can enhance the corrosion rate if any moisture is present in the system.

3.3. Conclusion

Usage of incompatible materials for different components has resulted in the failure of the component.

3.4. Recommendations

(1) Joining by welding of dissimilar materials should be avoided.
(2) Chrome plating of components enhances the resistance to corrosion attack.
(3) In oxidizing atmospheres like HNO_3, care should be exercised to avoid moisture while using Teflon as the gasket material in combination with austenitic stainless steels.
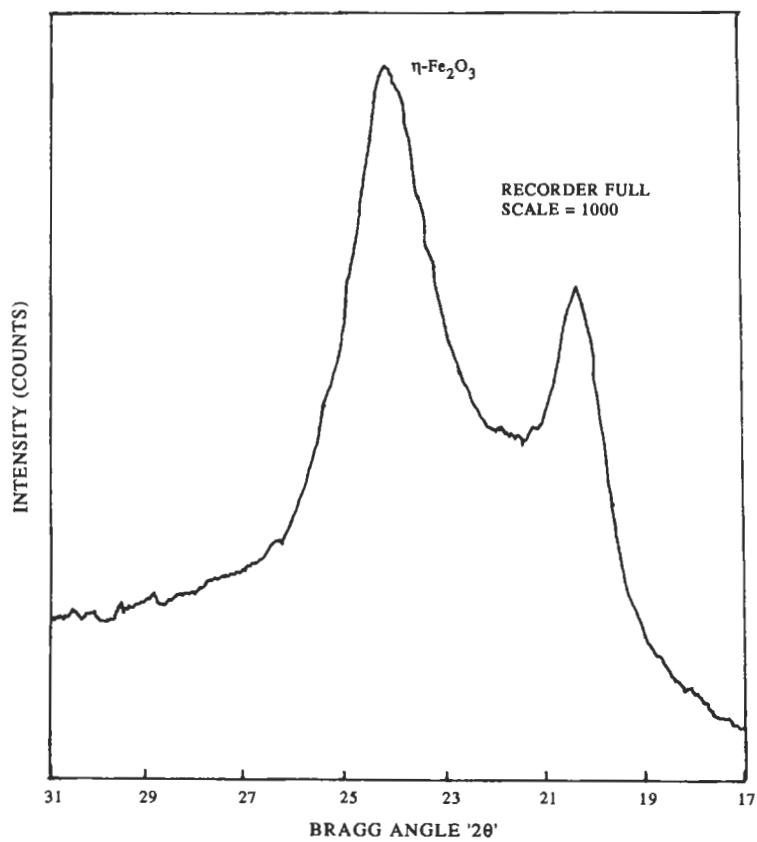
Fig. 9. XRD pattern of corrosion product (Fe₂O₃) on sight port flange.

REFERENCES

1. *Metals Handbook*, Vol. 13: *Corrosion*, 9th edn. ASM, Metals Park, OH, 1987, p. 348.
2. *Metals Handbook*, Vol. 7: *Atlas of Microstructures*, 8th edn. ASM, Metals Park, OH, 1972, p. 133.
3. Fontana, M. G. and Greene, N. D., *Corrosion Engineering*. McGraw-Hill, New York, 1967, p. 59.
4. Liberto, R. R., *Titan II Storable Propellant Hand Book*, Revision A, AFBSD-TR-62-2. Airforce Ballistic Systems Division CA, 1962, p. 5-2.

CORROSION OF CENTRAL HEATING SYSTEMS

D. R. H. JONES

Department of Engineering, University of Cambridge, Trumpington Street, Cambridge CB2 1PZ, U.K.

Abstract—This paper begins by summarizing the main mechanisms by which components in central heating systems can corrode, and indicating the factors which can increase or decrease the rates of corrosion. The basic principles are then applied to the analysis of three case studies of corrosion failure in heating systems: rusting through of mild steel radiators after only 2 years in service; premature pitting corrosion of aluminium heat-exchanger tubes; and external corrosion of mild steel water pipes. © 1997 Elsevier Science Ltd

1. BACKGROUND

Figure 1 is a schematic diagram of a typical closed recirculating heating system. The heat-exchange medium (water) is circulated between the heat source (boiler) and the heat sink (radiators). The maximum water temperature at the exit from the boiler is typically 80 °C. A typical radiator is made from two separate sheets of mild steel 1–2 mm thick, which are press-formed to produce the shapes of the waterways, and joined by electrical-resistance welding (Fig. 2). The water pipes are generally made from thin-walled copper tube. The heating modules in the boiler are made from steel, copper or aluminium alloy. Fittings such as valves are usually made from brass.

2. OXYGEN REDUCTION—BASIC MECHANISMS

Mild steel has a strong tendency to rust when exposed to water and oxygen. Because the mains water which is used to fill the system is saturated with air, one might think that mild steel was an unwise choice of material for radiators and heat exchangers. As shown in Appendix A, the conditions under which a metal corrodes in water can be summarized using the electrochemical equilbrium (or Pourbaix) diagram [1]. Figure 3 shows the Pourbaix diagram for iron at 25 °C. Mains water usually
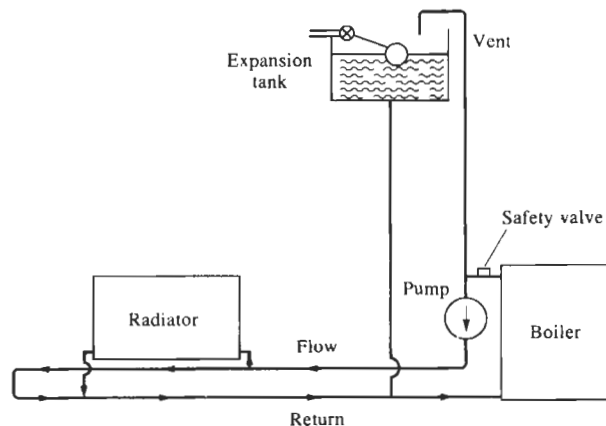

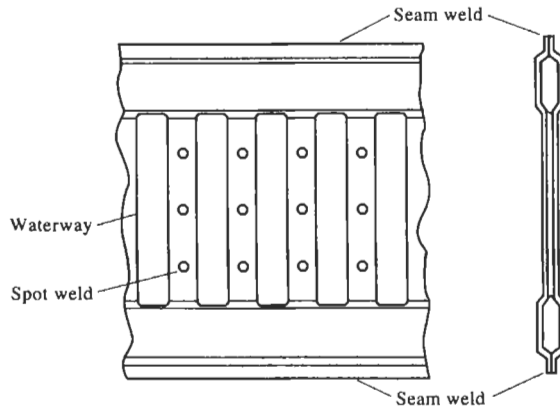Fig. 1. Schematic diagram of a closed recirculating heating system.

Fig. 2. Construction of a typical mild-steel radiator.

has a pH of 6.5–8 [2], so as long as the potential of the iron is kept below −0.6 V (standard hydrogen-electrode scale) the iron will be immune from corrosion. The Pourbaix diagram also shows the line for the oxygen-reduction reaction. The open-circuit potential for this reaction in mains water is ≈0.8 V. This means that if iron is immersed in mains water saturated with oxygen the voltage difference available to drive the corrosion process will be $0.8 − (−0.6) = 1.4$ V.

In practice, the oxygen content of the water in the heating system rapidly falls towards zero. The water is only saturated with air when the system is first filled. The solubility of oxygen in water decreases as the temperature increases: it is 8 mg l^{-1} at 25 °C [2], but only 3 mg l^{-1} at 80 °C [3]. When the water is heated to the operating temperature, air is driven out of solution: it escapes through the vent and is bled off through the valve at the top of each radiator. The steel only has to corrode to a small extent to consume the remaining oxygen, and the water becomes de-aerated. It takes typically 75 days for this to happen; at steady state the oxygen concentration is only 0.3 mg l^{-1} [4]. The oxygen-reduction reaction effectively stops, and further corrosion is negligible. Under these conditions, mild steel radiators and heat exchangers can last for well over 30 years without rusting through. However, if fresh oxygen gets into the system in any quantity it is possible for radiators to perforate after only 2 years in service.
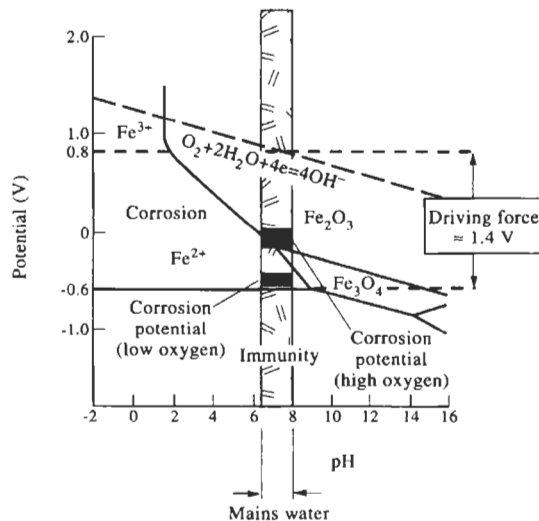

Fig. 3. The Pourbaix diagram for iron at 25 °C, showing the oxygen-reduction reaction.
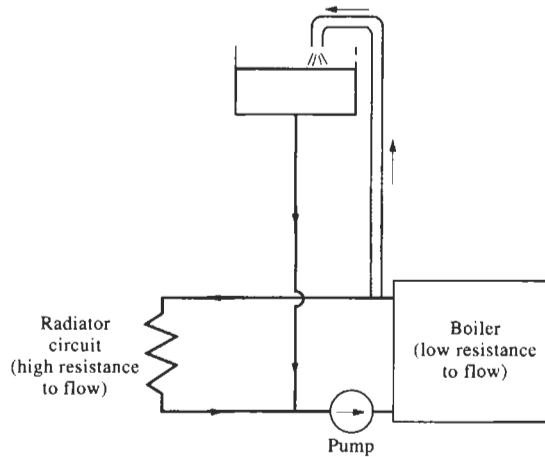
Fig. 4. Design fault 1—pumping water through the expansion tank.

2.1. *Oxygen pick-up*

There are a number of ways in which the water can pick up oxygen. Obviously, some air will get in when the circuit is drained down (e.g. for repairs, or when there is a risk of freezing) and then refilled. A limited amount of fresh water is taken into the system to compensate for evaporation from the expansion tank or losses due to leaks, and this, too, is a source of oxygen. But a major intake of oxygen is usually caused by design faults in the pipework.

A typical fault is shown in Fig. 4 [4]. If the flow resistance of the radiator circuit is large compared to that of the boiler, then, depending on the location of the pump, water can be forced up the vent and discharged into the expansion tank. A particularly bad location for the pump is shown in Fig. 4—in the return line between the cold feed and the boiler. It is easy to see that, when a large pressure drop is needed to get the water to flow around the radiator circuit, then the water will tend to take the easier route, and there will be a circulation loop between the boiler and the expansion tank. Naturally, as the water pours out of the vent it continually picks up air. This "pumping over" would not have happened if the pump had been positioned to the *left* of the cold feed instead of to the right. Figure 1 shows the standard position for the pump in a modern installation—in the flow line after the vent. When the pump is put in this position pumping over cannot occur.

Figure 5 shows another fault—when air is drawn in down the vent pipe [4]. In order to pull water through the boiler the pump must generate a low pressure in the flow line from the boiler. This low pressure depresses the head of water in the vent pipe. If the expansion tank is not high enough, the surface of the water in the vent pipe will be pulled down to the level of the flow line, and bubbles of air will be swept into the circuit. Oxygen concentrations of ≈ 5 ppm have been found in systems
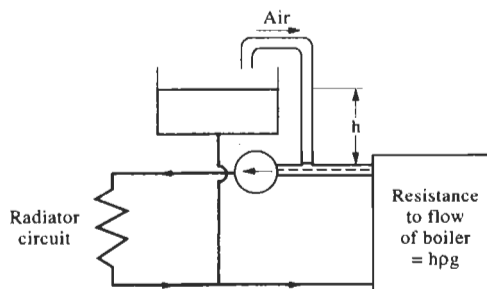

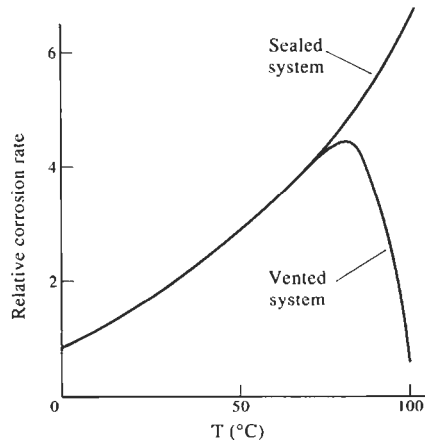Fig. 5. Design fault 2—drawing air in through the vent.

Fig. 6. Rate of corrosion of mild steel in aerated mains water as a function of temperature.

suffering from this defect [4]. To avoid air intake, the static head h must be greater than the flow resistance of the boiler by a suitable safety margin; a typical value for h is 1.5 m.

In order to guarantee that oxygen is excluded from the system, the trend in most modern installations has been to replace the traditional open expansion tank with a sealed air cushion expansion tank. The system water expands into a polymeric bag which is contained in an outer tank of pressurized air.

2.2. *Corrosion rates*

When the water is saturated with oxygen, the steel will corrode rapidly. The rate of corrosion is controlled by the oxygen-reduction reaction, which is in turn controlled by the rate at which oxygen diffuses through the water to the surface of the steel. Because diffusion is a thermally-activated process, the rate of diffusion will increase exponentially with temperature. So also will the corrosion rate, as shown by the rising curve in Fig. 6. As one approaches 80 °C, the curve divides into two branches [3, 5]. If the system is pressurized (so none of the dissolved oxygen can escape), the curve carries on upwards. But if the system is vented (as most central heating systems are), the oxygen can come out of solution as the water warms up. As the oxygen concentration falls below 3 mg l^{-1}, the oxygen-reduction reaction slows considerably, and at 100 °C the steel is corroding no faster than it would have done in aerated water at 25 °C.

2.3. *Diagnosis*

It is relatively easy to find out whether excessive oxygen has been getting into a heating system. When oxygen is plentiful, the iron corrodes rapidly at a relatively high potential. The reaction takes place in the Fe_2O_3 field of the Pourbaix diagram (see Fig. 3), and a red sludge of hydrated ferric oxide collects at the bottom of the radiators. When oxygen is scarce, the iron corrodes slowly at a relatively low potential. The reaction generates ferrous ions, and a thin black coating of hydrated magnetite (magnetic iron oxide) forms instead. Both oxides are 5 times as dense as water: although oxide particles can be carried around with the circulating water, most of the sludge remains in the radiators. Contrary to the view commonly held by many heating engineers, oxide sludge cannot be removed by flushing water through the radiators (although it can be removed by circulating a warm solution of inhibited phosphoric acid through the system).

3. OXYGEN REDUCTION—SOME COMPLICATIONS

There are several things which can make steel corrode faster in the presence of oxygen. These are summarized as follows.

3.1. *Galvanic corrosion*

The mixture of copper pipes and steel radiators makes up a galvanic couple. The Pourbaix diagram for copper is shown in Appendix A. Copper will be immune from corrosion in mains water as long as its potential is kept below 0 V. This is 0.6 V higher than the corrosion potential of iron. The copper is in excellent electrical contact with the steel through soldered joints or compression fittings. Because of this, the iron corrodes in preference to the copper, and acts as a sacrificial anode. The copper is protected by cathodic protection and provides an inert surface at which the cathodic oxygen-reduction reaction takes place. In practice, the extent of galvanic corrosion is limited by the ionic conductivity of the water. If the conductivity is low, the electrical resistance of the galvanic cell is high, and the steel will only corrode galvanically near to a copper surface. On the other hand, if the conductivity is high galvanic attack will occur some distance away from the copper. The solution conductivity can be decreased considerably if insoluble corrosion products form.

There is another way in which the copper pipes can lead to galvanic corrosion. The bore of the tubes corrodes slowly, and releases copper ions into the circulating water. At steady state, it is quite common to find concentrations of Cu^{2+} of 0.1–0.2 mg l^{-1} [4]. Because steel is more reactive than copper, the following reaction takes place where the water passes over the steel surfaces:

$$Cu^{2+} + Fe = Fe^{2+} + Cu. \tag{1}$$

The copper metal produced by the reaction deposits on the surface of the steel as an extremely thin layer. Galvanic cells are then set up between the islands of deposited copper and the steel in between [3, 6]. However, opinions vary as to how important this mechanism really is.

3.2. *Dissolved ions*

Mains water typically contains approximately 50 ppm Cl^- and SO_4^{2-} in association with Na^+, Ca^{2+} and Mg^{2+}. The ions increase the conductivity of the water, and help the corrosion processes. The metal ions migrate to the cathodic surfaces where they neutralize the OH^- ions produced by the oxygen-reduction reaction. The Cl^- ions are small and highly mobile: they migrate rapidly to the anodic areas, and neutralize the Fe^{2+} ions produced when the iron dissolves. When mains water enters the system to make up for evaporation, it brings dissolved ions with it, and over time the concentration of the ions in the circulating water will increase. Both Cl^- and SO_4^{2-} are aggressive ions: they help to stop passive oxide films forming on the surface of steel, and this encourages corrosion even more.

3.3. *Pitting*

The surface of the steel tends to divide itself into anodic areas (where the iron corrodes) and cathodic areas (where the oxygen-reduction reaction takes place). This separation is encouraged by anything which makes the environment of the steel non-uniform. In most places, the metal is exposed to the flowing water (and the oxygen it contains), and behaves cathodically. However, steel in crevices has almost no exposure to oxygen, and behaves anodically. Crevices are present in many places: under deposits of sludge, next to welds, and in screwed connections. Obviously, the current of electrons produced by the anodic areas must balance the current of electrons delivered to the cathodic area. Since the anodes are small compared to the cathodes, the current density at the anodes will be large compared to the current density at the cathodes. The steel will corrode rapidly over a small area, and localized pits will form.

4. REDUCTION OF HYDROGEN

Figure 7 shows the line for the hydrogen-reduction reaction superposed on the Pourbaix diagram for iron. The open-circuit potential for the hydrogen-reduction reaction in mains water is -0.4 V. The voltage difference available to drive the corrosion process is $-0.4 - (-0.6) = 0.2$ V. The hydrogen-reduction reaction *polarizes* rapidly: an "overvoltage" is needed to make the reaction go at a reasonable rate. The extent of the polarization depends strongly on the metal or alloy concerned,
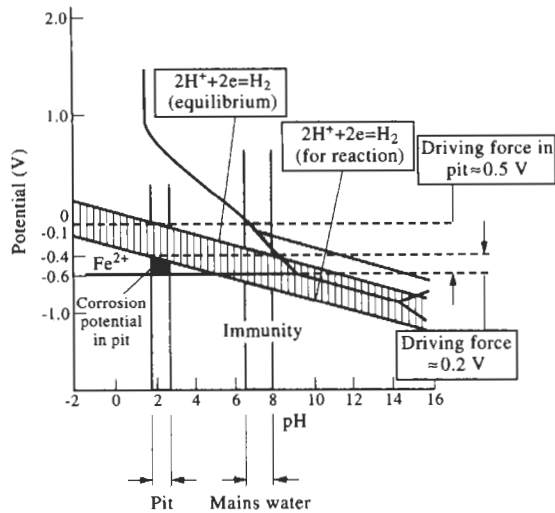
Fig. 7. The Pourbaix diagram for iron at 25 °C, showing the hydrogen-reduction reaction.

the condition of the surface, and the nature of the environment. Polarizations of ≈ 0.2–0.3 V are common when hydrogen is reduced on the surface of iron. As shown in Fig. 7, the practical line for the hydrogen-reduction reaction probably lies below the corrosion potential of iron in mains water. In theory, therefore, steel radiators should not corrode by the hydrogen-reduction reaction.

In spite of this, hydrogen is often given off in central heating systems. The usual symptom is that one or more of the radiators suddenly goes cold for no apparent reason. This is because hydrogen gas has collected at the top of the radiator, and has blanketed the top ends of the vertical waterways. Heating engineers often claim that this is caused by dissolved air coming out of solution. In fact, when the gas is vented off it can usually be lit with a match! Provided there is no risk of explosion, having to vent radiators in this way is just a nuisance. However, the corrosion process produces magnetite, which can deposit in the waterways and clog the pumps.

Why does this hydrogen reduction occur? If the temperature is high enough, a reaction called the Schikorr reaction can take place [4, 7]. This has two steps as follows.

$$Fe + 2H_2O = Fe(OH)_2 + H_2, \tag{2}$$

$$3Fe(OH)_2 = Fe_3O_4 + 2H_2O + H_2. \tag{3}$$
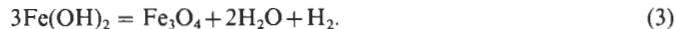
The Schikorr reaction is catalysed by copper ions: when these are present, it can take place above 60 °C. In systems where the water is aggressive to copper, the concentration of Cu^{2+} which is released into the circulating water can be large enough to provide the required catalyst. A survey carried out on one central heating system gave the results shown in Fig. 8. Below 63 °C, there was no detectable evolution of hydrogen. However, at 70 °C, the radiators had to be vented every week; and at 80 °C they had to be vented every day. An obvious way of suppressing the reaction, therefore, is to keep the temperature in the system below 60 °C.

4.1. Hydrogen and bacterial corrosion

Heating systems can become contaminated by bacteria [3, 8]. The most common are the anaerobic sulphate-reducing bacteria (SRB) such as *Desulfovibrio* which live in oxygen-starved conditions. As part of the metabolic cycle, the organisms convert sulphate ions into sulphide ions. Sulphide greatly speeds up the hydrogen-reduction reaction, and this allows steel to corrode even in neutral oxygen-free solutions. *Desulfovibrio* grows in the pH range 5–10, and the temperature range 5–50 °C. Some SRB can survive to even higher temperatures. If aerobic bacteria are present, these can colonize deposits and produce anaerobic conditions under the deposit where SRB can thrive under nominally aerobic conditions. The bacteria require nutrients, which are usually present in the form of hydro-
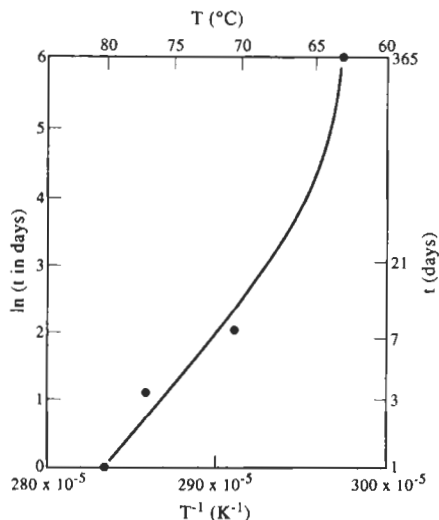
Fig. 8. Rate of hydrogen evolution as a function of temperature. Radiators have to be vented after a time interval t. Typical data only [4].

carbons. The usual way of preventing bacterial corrosion in heating systems is to add a biocide to the water.

4.2. *Hydrogen and pitting corrosion*

Once pitting has started, it is unlikely to stop. In order to maintain electrical neutrality in the pit, the Fe^{2+} ions attract Cl^- ions from the water outside. The pit becomes concentrated with $FeCl_2$, and this hydrolyses according to the reaction [2]

$$FeCl_2 + 2H_2O = Fe(OH)_2 + 2HCl. \tag{4}$$

The corrosion product forms a crust which covers the mouth of the pit, and isolates it from the water outside. The HCl which is trapped inside the pit lowers the pH to ≈ 2 [5]. At this low value of pH, the hydrogen-reduction reaction gives a voltage differential of $\approx 0.5\,V$ (see Fig. 7), and this is enough to make the iron corrode quite rapidly. Hydrogen gas is given off inside the pit, and the crust bursts to let it escape. Of course, the new Fe^{2+} produced by this attack will suck in fresh Cl^- ions, and the cycle of events will repeat itself. The pitting process is therefore said to be *autocatalytic*. Because the corrosion is intense and localized, it can perforate the radiator wall after only a short time. Hydrogen evolved at low temperatures (where the Schikorr reaction is suppressed) is almost certainly a sign of rapid pitting corrosion.

5. USING INHIBITORS

These problems can be avoided by using *inhibitors* [3, 9]. A common inhibitor for steel is sodium nitrite, which is dissolved in the water to give a concentration of $\approx 800\,mg\,l^{-1}$ of NO_2^- ions. The nitrite functions as an *oxidizing agent* [10]. It increases the potential at the surface of the steel, and if the concentration is high enough the steel is moved up into the Fe_2O_3 field on the Pourbaix diagram (see Fig. 3). A thin stable film of γ-Fe_2O_3 forms, and this acts as a very effective barrier to further corrosion. The pH is kept above about 9 in order: (a) to avoid the corrosion field on the diagram, and (b) to reduce the potential at which the Fe_2O_3 field starts. Because sodium nitrite interferes with the anodic reaction (the oxidation of Fe to Fe^{2+}), it is called an *anodic inhibitor*.

It is very important to have a large enough concentration of nitrite in the water. Figure 9 shows how the rate of corrosion is affected by the nitrite concentration [9]. Above a critical concentration, there is no corrosion at all. However, as the concentration is decreased the corrosion rate increases
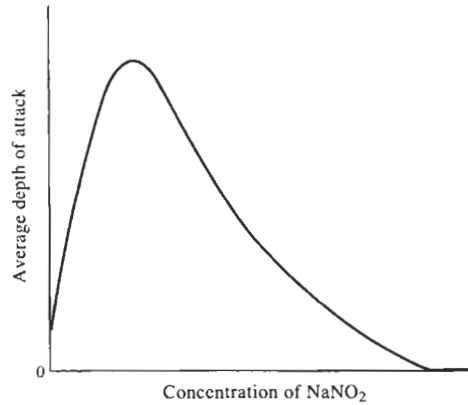
Fig. 9. Schematic effect of sodium nitrite concentration on the rate of corrosion of mild steel in mains water.

enormously; the maximum corrosion rate is much greater than it is when there is no inhibitor present at all. When the concentration is below the critical level, the surface of the steel is not fully passivated. The electron current taken by the cathodic reaction is concentrated at the weak points in the film, and these are subjected to rapid localized attack. The nitrite also increases the ionic conductivity of the water, and this increases the corrosion rate even more. Sodium nitrite is therefore classified as a *dangerous* inhibitor.

The actual value of the critical concentration depends on several factors. It is difficult for the nitrite to get at the steel when it is covered by deposits or shielded inside crevices: the concentration of inhibitor in the bulk of the water has to be increased considerably to stop the shielded areas corroding. Cl^- and SO_4^{2-} ions attack the passive film, so the concentration of the inhibitor must be increased to compensate. The minimum amount of extra sodium nitrite is given by [3]

$$(\text{weight } NaNO_2)/(\text{weight } NaCl + \text{weight } Na_2SO_4) \approx 1. \tag{5}$$

Because it is so important to keep the concentration safely above the critical level, the water in the system must be analysed at regular intervals, and topped up with extra inhibitor as required. Inhibitor will obviously be lost if the system leaks or if it is drained down. What is less obvious is that sodium nitrite can also be removed by the action of bacteria such as *Nitrobacter* which are very efficient at oxidizing nitrite to nitrate [3, 8]. Because of this, it is particularly important to use a biocide in any system which relies on sodium nitrite for its protection.

The best inhibitors for copper are specific organic chemicals such as benzotriazole [3, 7]. These react with the copper at the surface of the metal to produce a uniform adherent film. Benzotriazole is classed as a *cathodic* inhibitor because it interferes with the cathodic oxygen-reduction reaction. Around $5 \, mg \, l^{-1}$ is usually required to stop the copper corroding. Benzotriazole can also deactivate (chelate) copper ions which have already dissolved in the water. The Schikorr reaction cannot occur (because there are no active copper ions to catalyse it), and galvanic attack is inhibited (because copper ions are not reduced at steel surfaces). Finally, benzotriazole is a *safe* inhibitor. Because it is an organic compound, it cannot increase the ionic conductivity of the water. In addition, because it inhibits the *cathodic* reaction it does not cause pitting.

6. CASE STUDY 1—RAPID RUSTING OF STEEL RADIATORS

6.1. *Background*

The subject of this case study is a large central heating system in an office block. When the system was about 20 years old, the radiators started to leak and had to be replaced. However, because of the age of the system it was decided not to clean the existing pipework with a chemical descaling agent. The new radiators had a wall thickness of only 1.25 mm, and it was decided to protect them against rusting by adding a corrosion inhibitor to the water. The inhibitor was supplied as a concentrated solution of sodium nitrite and sodium borate. The solution was added to the system
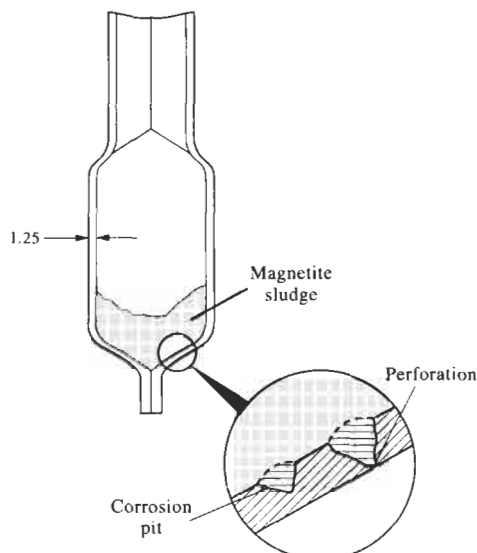
Fig. 10. A layer of magnetite sludge had formed in the water space at the bottom of the radiator. Pitting corrosion had occurred where the sludge covered the steel. Dimensions in mm.

until the concentration of sodium nitrite in the water was 1300 ppm (parts per million, or $mg\,l^{-1}$). The sodium nitrite was the active ingredient in the inhibitor package; the sodium borate was added as a buffer to keep the pH of the water at about 9. However, after only 2 years the new radiators started leaking. The offending radiators were removed, and one was cut open. As shown in Fig. 10, a layer of black sludge had formed in the water space at the bottom of the radiator. The corrosion had originated beneath this deposit, and had developed into deep pits. One of these had penetrated right through to the outside surface. However, there was no evidence of any pitting above the sludge.

The water had been analysed every 2 months to make sure that the inhibitor concentration was up to the recommended level. In most cases, it was found that the concentration had fallen significantly since the previous service, and extra inhibitor had to be put in to make up the shortfall. The average concentration reading was ≈ 500 ppm. However, on several occasions the nitrite level was as low as 100 ppm. An analysis of the mains water gave: $pH \approx 8$; $Cl^- \approx 500$ ppm; $SO_4^{2-} \approx 100$ ppm; high hardness. However, samples of water taken from the system itself gave: $pH \approx 10$; $Cl^- \approx 250$ ppm (max); $SO_4^{2-} \approx 300$ ppm (max); strong indications of nitrite-oxidizing bacteria.

6.2. *Failure analysis*

The first thing that one notices about the system is the high concentration of Cl^- and SO_4^{2-}. The minimum concentration of sodium nitrite which must be added to compensate for these aggressive ions can be estimated from Eqn (5). The ionic mass of Cl^- is 35, and the molar mass of NaCl is 58. The 250 ppm of Cl^- is therefore equivalent to $(58/35) \times 250 = 414$ ppm of NaCl. The ionic mass of SO_4^{2-} is 96, and the molar mass of Na_2SO_4 is 142. The 300 ppm of SO_4^{2-} is therefore equivalent to $(142/96) \times 300 = 444$ ppm of Na_2SO_4. The combined mass of NaCl and Na_2SO_4 is 858 ppm. Equation (5) shows that this must be balanced by at least 858 ppm of $NaNO_2$. As seen earlier, the average concentration of inhibitor was ≈ 500 ppm, and the minimum concentration was ≈ 100 ppm. These levels are far below the minimum requirement, so it is hardly surprising that the radiators corroded rapidly. The situation was still worse in practice because the sludge would have screened the metal from the inhibitor. The routine analyses show that the inhibitor level regularly fell from the recommended dose of 1300 ppm to as little as 100 ppm after only 2 months. Presumably nitrite was consumed by the nitrite-oxidizing bacteria. This would have been avoided if a biocide had been added to the water when the system was first filled.

7. CASE STUDY 2—HOLES IN ALUMINIUM HEAT-EXCHANGER TUBES

7.1. *Background*

Figure 11 is a simplified drawing of a heat exchanger from a large gas-fired central heating boiler. It consists of a number of externally finned aluminium tubes arranged concentrically around a tubular gas burner. The tubes are enclosed by a perforated sleeve of stainless steel; this is meant to spread the hot gases out uniformly as they flow away from the burner. Figure 12 shows a cross-section through one of the heat-exchanger tubes. The ends of the tubes are expanded into headers cast from eutectic aluminium–silicon alloy LM6. The cover plate on the return header is also cast in LM6. The cover plate on the inlet/outlet header is cast in grey cast iron, and so too are the pair of curved elbows. The boiler contains between two and six of these units depending on the heat output required. Technical data for a single heat exchanger are as follows.

Maximum heat output $= 100\,\text{kW}$.
Heat flux at bore of tube $\approx 230\,\text{kW m}^{-2}$.
Flow rate $\approx 2\,\text{l min}^{-1}$.
Flow velocity inside tube $\approx 0.5\,\text{m s}^{-1}$.
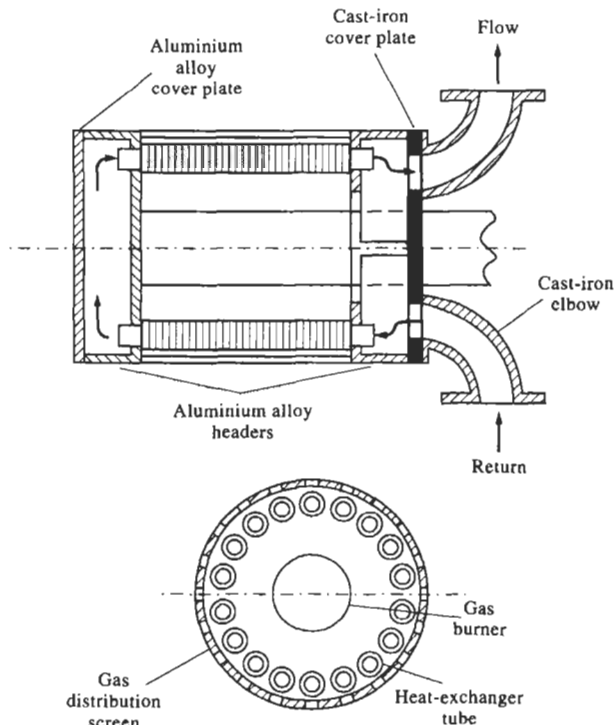Maximum temperature at return elbow $\approx 80\,°\text{C}$.

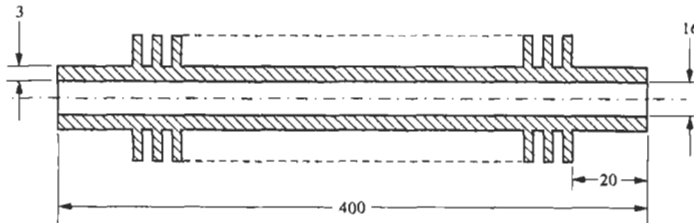Fig. 11. Simplified drawing of the heat exchanger. Not to scale.

Fig. 12. Cross-section through the heat-exchanger tube. Dimensions in mm. Not to scale.

Maximum temperature at flow elbow $\approx 90\,°C$.

Maximum temperature drop across tube wall $\approx 10\,°C$.

Reynolds number at $80\,°C \approx 20,000$ (fully turbulent).

The tubes were made from wrought aluminium–magnesium–silicon alloy 6063. The specified composition is shown in Table 1.

A number of failures were reported where the heat-exchanger tubes had perforated from the inside. The water had been treated with a liquid inhibitor package containing sodium nitrite, sodium borate, sodium silicate, sodium hydroxide, and "organic scale and corrosion inhibitors". When the water contained less than $50\,mg\,l^{-1}$ of chloride, the recommended dose of sodium nitrite was $1250\,mg\,l^{-1}$. This was achieved by adding 5 parts by volume of the inhibitor liquid to 1000 parts by volume of water. The organic corrosion inhibitor was presumably added to protect any copper in the system; it could well have been benzotriazole. The neat inhibitor had a pH of 11.5, so the pH of the diluted solution was probably around 9.

7.2. *Failure analysis*

7.2.1. Corrosion resistance of aluminium. The Pourbaix diagram for aluminium is given in Appendix A. It shows that a protective film of aluminium oxide can form on the surface of the metal as long as the pH of the water is between 4 and 8.5. The diagram does not give any information about the effectiveness of this barrier layer. When aluminium is exposed to oxygen in the atmosphere, it immediately forms a thin invisible film of aluminium oxide [11–13]. The film is bonded firmly to the surface, and is an excellent electrical insulator. Because of this, aluminium (a very reactive metal which would otherwise oxidize very rapidly) is widely used as a corrosion-resistant material. Even when the surface is damaged by mechanical abrasion, the oxide film reforms immediately. Although this repaired film is very thin to begin with, it is still a good barrier to corrosion. On further exposure to the air, the film thickens, typically by 100 times, and the barrier becomes more effective. Because of this film, aluminium does not corrode in water where the pH is in the range 4–8.5.

Outside this pH range, the oxide film is unstable, and the aluminium corrodes: the rate of uniform corrosion increases by roughly 10 times for every unit increase in pH above 8.5 [1]. The film can, however, be stabilized by adding chemicals to the water. At low pH, aluminium is hardly affected by dilute or concentrated nitric acid or dilute sulphuric acid because the oxidizing action of these chemicals provides a strong film-forming tendency [14]. At high pH, the film is stabilized by *silicates* [6, 15, 16]—compounds having the variable composition $n Na_2O.m SiO_2$. These are most effective on aluminium when the *module* of the silicate (the ratio m/n) is high (typically $\approx 3–3.5$) [9]. But even sodium disilicate ($Na_2Si_2O_5$; module $= 2$) can stop uniform corrosion at a pH of ≈ 11.5 [12].

7.2.2. Aluminium alloy 6063. 6063 alloy is one of a series of wrought aluminium alloys containing silicon and magnesium. They have good corrosion resistance, especially in alkaline solutions [11]. Alloying elements, mainly iron and copper, can lead to local weaknesses in the oxide film, and can cause pitting [10, 17]. 6063 resists corrosion well because the concentration of the alloying elements (silicon and magnesium) is small, and the harmful elements (iron and copper) are present only as low-level impurities. In contrast, the corrosion resistance of the 2000 series alloys (which contain 2–7% copper as an alloying element) is relatively poor. Minute particles or films of copper can deposit on these alloys as a product of corrosion, and the galvanic cells which are created attack the film [12]. 6063 alloy was therefore a good choice for the heat-exchanger tubes. High-purity aluminium would have been better still, although it might not have had the neccessary mechanical properties.

Table 1. Composition of aluminium alloy 6063

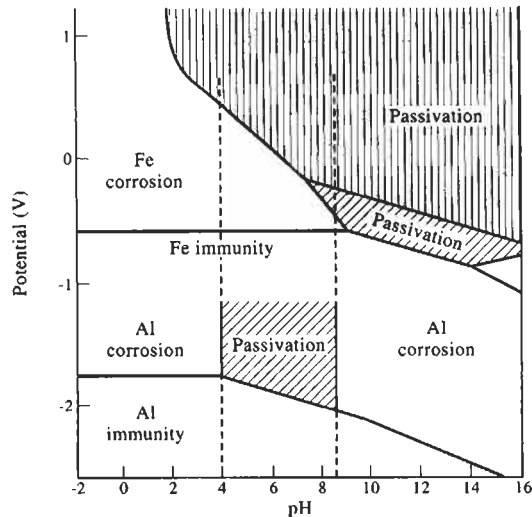| Element	Weight %	Element	Weight %	Element	Weight %
Silicon	0.20–0.6	Magnesium	0.45–0.9	Tin	0.05 maximum
Iron	0.35 maximum	Zinc	0.10 maximum	Lead	0.05 maximum
Copper	0.10 maximum	Chromium	0.10 maximum	Aluminium	Balance
Manganese	0.10 maximum	Titanium	0.10 maximum		

Fig. 13. Superposition of the Pourbaix diagrams for iron and aluminium at 25 °C.

7.2.3. *Function of inhibitor package.* It is not easy to get the optimum protection of both steel and aluminium in the same system. The situation is summarized in Fig. 13. To protect the steel best, the pH needs to be buffered to at least 9, so that it misses the corrosion field on the Pourbaix diagram. However, this is above the pH at which the oxide film on aluminium breaks down. The approach which was adopted here was presumably to protect the steel in the usual way with sodium nitrite and an alkaline solution, but to add sodium silicate to stop the film of aluminium oxide breaking down. An alkaline pH is also compatible with any copper in the system: the Pourbaix diagram for copper (see Appendix A) shows that a protective oxide film can form in the pH range 7–12.5. The protection of the copper can be completed by adding benzotriazole.

The Pourbaix diagrams show that iron is a more reactive metal than copper. Because of this, copper ions can be reduced to copper metal by a steel surface [see Eqn (1)]. Aluminium is more reactive than both copper and iron. When water containing dissolved copper flows over an aluminium surface, there is a tendency for copper metal to precipitate out [12, 15]. If the water contains dissolved iron, there is a tendency for metallic iron to precipitate out as well [12]. It has already been seen that metallic copper and iron are likely to damage the aluminium oxide film. It is therefore necessary to keep the concentration of copper and iron in the water as low as possible when there is aluminium about. This is another (and very important) function of the inhibitors.

7.2.4. *Conclusions.* The most straightforward explanation of the failures is an inadequate concentration of inhibitor. The situation is made critical by the special environment of the heat-exchanger tubes. As was seen earlier, the bore of the tube is subjected to conditions of high heat flux and temperature ($230\,\mathrm{kW\,m^{-2}}$ and 90 °C). For comparison, conditions at the surface of the heating element in an electric kettle are $\approx 130\,\mathrm{kW\,m^{-2}}$ and 100 °C. The chemical environment at the aluminium surface (pH, concentration of ionic species) may be significantly different from that in the bulk of the water. The oxide film can also be worn away by suspended particles of corrosion product circulating with the water. When the rate of mechanical damage becomes greater than the rate of chemical healing, rapid corrosion will result.

8. CASE STUDY 3—EXTERNAL CORROSION OF STEEL WATER PIPES

8.1. *Background*

In the final case study, we look at a central heating system which failed from corrosion on the *outside*. The system was installed in 1970 in a large new student residence. The building was made from columns and slabs of reinforced concrete. The water pipes were made from mild steel, and
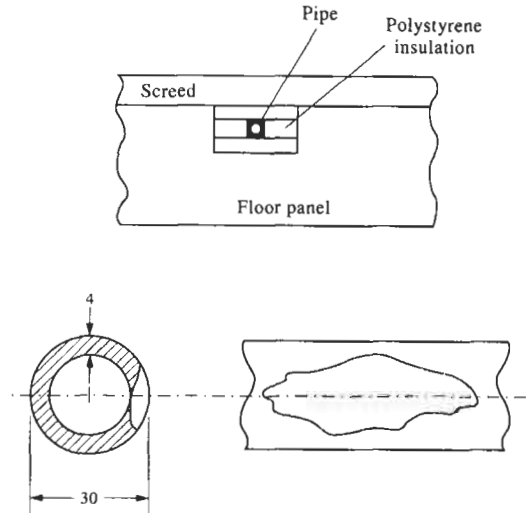
Fig. 14. The corroded steel pipe. Dimensions in mm.

were laid in the concrete during the construction. By 1985, the pipes had started to leak. A typical failure is shown in Fig. 14. The pipe had an outside diameter of ≈ 30 mm, and a wall thickness of ≈ 4 mm. It had been cast into the floor panel of one of the student rooms, and was insulated with slabs of expanded polystyrene. When the floor was dug up, it was found that the pipe had rusted from the outside. The wall of the pipe had perforated, and the water inside the heating system had started to leak out. The corrosion deposits were reddish-brown in colour.

8.2. *Failure analysis*

The roof of the building consisted of a series of horizontal pre-cast concrete slabs. These had started to take in rain-water at the joints. The structure of the building was complex, and the rain-water travelled large distances before leaking into the rooms or the public areas. It was concluded that the most likely explanation for the corrosion was that the pipes had come into contact with the leaking rain-water. The horizontal runs of piping on each floor were connected by vertical runs laid in open ducts, and it was thought that these could have channelled the rain-water from one floor to another.

Since air was able to get to the surface of the pipe, the cathodic oxygen-reduction reaction would have taken place easily. In addition, the incoming rain-water would have been saturated with oxygen. The corrosion product was presumably red rust (hydrated Fe_2O_3). The Pourbaix diagram for iron (see Appendix A) shows that this oxide is produced when the oxygen content is high. Rain-water is also saturated with carbon dioxide: it contains ≈ 1300 mg l^{-1} of the gas [3]. The carbon dioxide converts to carbonic acid, and the pH falls to ≈ 4.5 as a result [2]. As can be seen from the Pourbaix diagram, rain-water is aggressive to mild steel: iron cannot start to produce an oxide film at a pH of 4.5 unless the potential is taken up to $+0.4$ V. A strong oxidizing agent would be needed to get the potential this high.

Mild steel typically corrodes at the rate of 0.05–0.15 mm/year in slowly moving soft water saturated with air at 15 °C [16]. However, the pipes were not always at 15 °C: when the heating system was operating they were closer to 70 °C. Figure 6 shows that the corrosion rate should go up by ≈ 2.7 times over this temperature interval. The heating system was generally used only for 6 months out of each year; on average the corrosion rate was probably ≈ 1.8 times greater than it would have been at 20 °C. This would give a corrosion rate of ≈ 0.09-0.27 mm/year. If it is assumed that rain-water had been leaking into the building for ≈ 7 years, the depth of attack would be ≈ 0.6–1.9 mm. If the steel develops pitting corrosion, the rate of attack in the pit can be up to 10 times the rate of general corrosion [16]. In this case, the pits would easily be capable of perforating the wall

of the pipe after 7 years. Localized attack of this sort would have been encouraged by the wet crevices which probably formed between the polystyrene and the outside of the pipe.

9. DESIGN IMPLICATIONS

Many central heating installations function perfectly well without corrosion inhibitors. But what must be done to avoid corrosion when inhibitors are not used? The first requirement is to make sure that a uniform, stable film of oxide forms on the metal to act as a barrier to corrosion. The pH of the water must be in the range where a passive layer is thermodynamically possible. pH ranges can be estimated from the Pourbaix diagrams (see Appendix A): they are 7–12.5 and 9–14 for copper and iron, respectively. Hard water ($pH \approx 8$) is less aggressive to copper and steel than soft water ($pH \approx 6.5$). The initial condition of the system has an important influence on the state of the protective films. It is bad to test a system with water and then leave it drained down. Corrosion will occur in the aerated pool of water at the bottom of each radiator, and the film may be penetrated by corrosion pits. It is best to put the system into working order straight away, and to keep it filled with water. Because chloride and sulphate ions attack the oxide films, the water should be as free from them as possible. Copper pipes are sometimes attacked by residues of soldering flux or graphite, and these, too, should be avoided.

Once a stable film has formed, the rate of corrosion depends on the cathodic reaction. The oxygen-reduction reaction can be prevented by keeping the oxygen content of the water as low as possible. Pumps should be placed so they do not pump water through an open expansion tank or draw air into the system. The water in an open expansion tank should be kept cold to minimize evaporation. It is preferable to use a sealed air cushion expansion tank instead of an open expansion tank. Obviously, the system should not be drained if this can be avoided. The hydrogen-reduction reaction can be minimized by keeping the pH high, and the temperature low.

Because many systems depart from these ideals, it is common to add inhibitors. But these must be used and specified correctly. They are generally recommended for systems which contain aluminium because its oxide film breaks down under mildly alkaline conditions. To get the best results, the internal surfaces should first be cleaned by circulating a chemical descaling agent through the system. The system is then rinsed, and the inhibitor is added immediately afterwards. The inhibitor will react strongly with the bright metal surfaces, and will penetrate well into the crevices formed at the welds.

Inhibitors are often supplied as a multicomponent "package". Sodium nitrite can attack the lead–tin solder in soldered joints; nitrite-based inhibitors often contain sodium *nitrate* to prevent this. Sodium benzoate is often added because it resists pitting better than sodium nitrite. When the water contains more than one inhibitor, the overall effect is usually better than the sum of the effects of the individual inhibitors (there is usually a *synergistic* effect). The pH of the water is controlled by adding a buffer such as sodium borate. Many packages contain specific copper inhibitors such as benzotriazole; this is especially important when the system contains aluminium. In hard-water areas, a scale inhibitor is also added to stop hardness deposits building up in the boiler. Finally, a biocide is needed to stop bacterial corrosion. The design of inhibitors is a complex business which draws on long experience of laboratory tests and field performance.

REFERENCES

1. Pourbaix, M., *Atlas of Electrochemical Equilibria in Aqueous Solutions*. Pergamon Press, Oxford, 1966.
2. Shreir, L. L., ed., *Corrosion*, Vol. 1: *Metal/Environment Reactions*, 2nd edn. Newnes–Butterworths, Oxford, 1976.
3. Boffardi, B. P., in *Metals Handbook*, Vol. 13, 9th edn: *Corrosion*. American Society for Metals, Metals Park, OH, 1987, p. 487.
4. von Fraunhofer, J. A., *British Corrosion Journal*, 1971, **6**, 23.
5. Butler, G., Ison, H. C. K. and Mercer, A. D., *British Corrosion Journal*, 1971, **6**, 32.
6. Fontana, M. G., *Corrosion Engineering*, 3rd edn. McGraw-Hill, New York, 1986.
7. Cotton, J. B. and Jacob, W. R., *British Corrosion Journal*, 1971, **6**, 42.
8. Stott, J. F. D., *Metals and Materials*, 1988, **4**, 224.
9. Rozenfeld, I. L., *Corrosion Inhibitors*. McGraw-Hill, New York, 1981.
10. Scully, J. C., *The Fundamentals of Corrosion*, 2nd edn. Pergamon Press, Oxford, 1975.

11. Polmear, I. J., *Light Alloys*. Arnold, London, 1981.
12. Hollingsworth, E. H. and Hunsicker, H. Y., in *Metals Handbook*, Vol. 13, 9th edn: *Corrosion*. American Society for Metals, Metals Park, OH, 1987, p. 583.
13. Evans, U. R., *An Introduction to Metallic Corrosion*, 2nd edn. Arnold, London, 1975.
14. Durrant, P. J., *General and Inorganic Chemistry*, 2nd edn. Longmans, London, 1952.
15. LaQue, F. L. and Copson, H. R., *Corrosion Resistance of Metals and Alloys*, 2nd edn. Reinhold, New York, 1963.
16. Uhlig, H., *The Corrosion Handbook*. Wiley, New York, 1948.
17. Evans, U. R., *The Corrosion and Oxidation of Metals*, 2nd supplement. Arnold, London, 1976.

APPENDIX A: POURBAIX DIAGRAMS

Pourbaix diagrams for the metals commonly used in central heating systems are shown in Figs A1–A4 [1]. The vertical axis of the diagram is the electrochemical potential of the metal in volts measured relative to the standard hydrogen electrode. The horizontal axis is the pH of the water-based solution in which the metal is immersed. The diagram is divided into a number of fields as follows. A field of *immunity* shows the range of potential and pH where corrosion of the metal is thermodynamically impossible. A field of *corrosion* shows the range of conditions where there is a thermodynamic driving force trying to make the metal dissolve as ions in the solution. A field of *passivation* shows where there is a thermodynamic driving force trying to make a stable film (such as an oxide or hydroxide) form on the surface of the metal. It is important to note that the film may or may not be an effective barrier to corrosion. If it is, then the passivation field is also a field of no corrosion. If it is not, the passivation field will be a field in which corrosion takes place.

The edges of the corrosion fields are defined by a concentration of metal ion in solution of $10^{-6}\,\text{mol}\,\text{l}^{-1}$. This is an arbitrary value which is taken to represent such a low tendency of the solid to dissolve that the rate of attack is essentially zero.

It should be noted that diagrams for alloys will be different from those of the parent metals mainly because of the effect of the alloying elements on the nature of the surface film. The stability of the film will also be affected by the presence in the solution of ions which have a chemical interaction with the film.

Fig. A1.

Fig. A2.

Fig. A3.

Fig. A4.
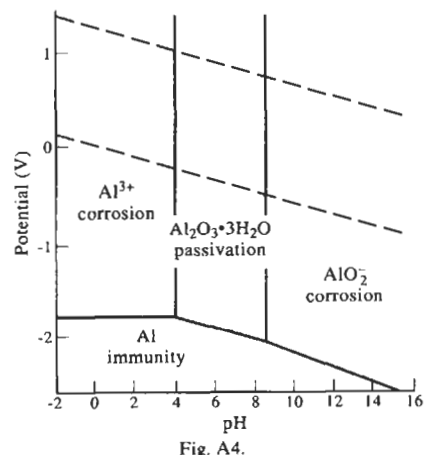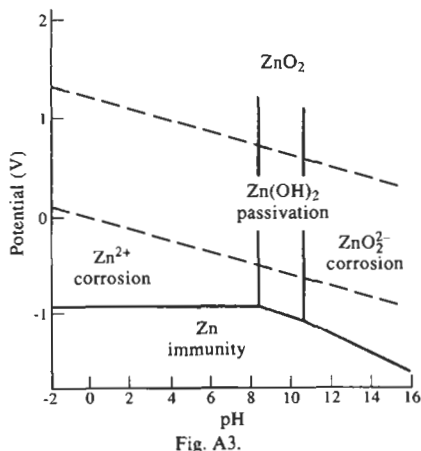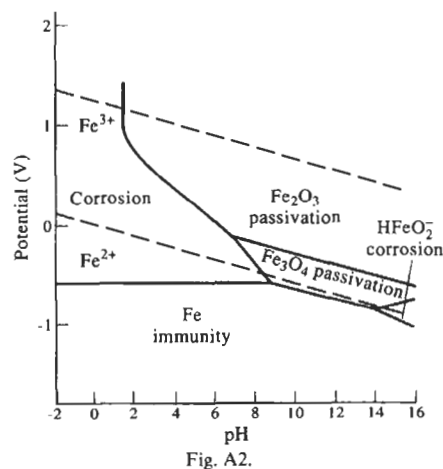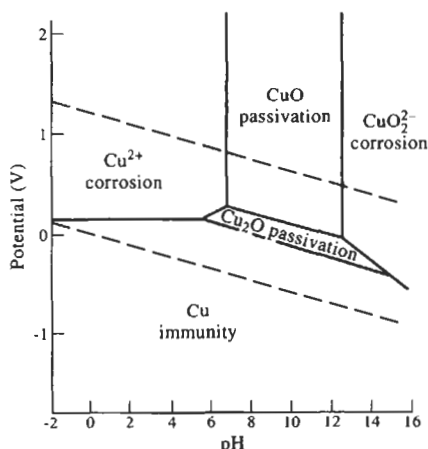
The diagrams give no indication of the rates of corrosion: these can only be found by doing suitable experiments. The diagrams show: (a) where corrosion cannot occur, and (b) where a surface film should form which might prevent or slow down corrosion.

Corrosion cannot occur in practice unless an electron-accepting (cathodic) reaction also takes place. The two most important cathodic reactions (which involve hydrogen and oxygen, respectively) are marked on the diagrams as dashed lines. They are detailed in Fig. A5 [1].
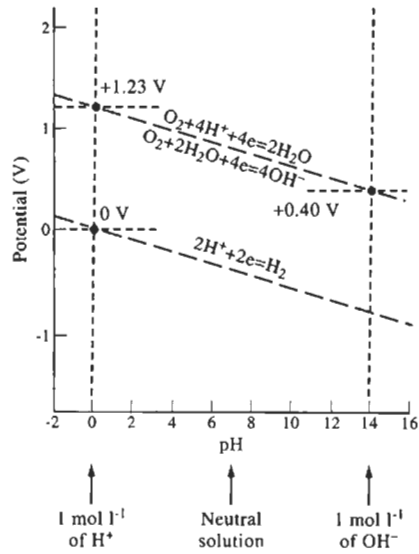

Fig. A5.

CREVICE CORROSION OF 316L CAUSED BY CHLORIDE PARTITION IN WATER–BUTANONE MIXTURES

J. H. CLELAND

Cambcor Ltd, 30 Windsor Road, Cambridge CB4 3JW, U.K.

Abstract—Chloride-induced crevice corrosion of a 316L pump was found to have occurred in what was nominally a very dilute solution of sodium chloride in a single-phase solution of water in butanone at 25 °C. The hypothesis formed was that water had entered the system in a sufficient amount to form an immiscible mixture of a water-rich phase and a butanone-rich phase. This separation into two liquids was followed by preferential partition into the water-rich phase of the sodium chloride to give a brine. A simple test demonstrated that the hypothesis was tenable. © 1997 Elsevier Science Ltd.

1. BACKGROUND

Product contamination first alerted the operators of a production unit that they had a corrosion problem. The unit was a mixing unit used for batch processing at 25 °C a single-phase mixture which contained, among other components, a high proportion of butanone in which small amounts of water and chloride ions were dissolved. The only metallic components in the unit, which was built of Pyrex glass, and had given trouble-free service for some time, were four identical 316L stainless steel pumps.

The production unit was dismantled, and the problem was traced to crevice corrosion in one of the stainless steel pumps. No corrosion was found in the other three pumps. The pump which had suffered the crevice corrosion was located at almost the lowest point in the unit (the lowest point was a drainage tap). It was reported that the liquid collected when the system was drained was an emulsion. It therefore appeared that the liquid in the pump may have been a mixture of two immiscible liquids: an aqueous solution of butanone as well as the expected solution of water in butanone. Unfortunately, no samples were retained for analysis.

2. THE MATERIALS

2.1. *The pump body*

The stainless steel used for the pump body was UNS S31603 (316L) and chemical analysis (Table 1) showed that the metal conformed to the requirements of this specification.

2.2. *The solution*

The solution pumped was basically an 8 wt% solution of distilled water in analytical grade butanone (methyl ethyl ketone). The phase diagram for the water–butanone system is shown in Fig.

Table 1. Chemical analysis of a section from the corroded pump: composition in wt%

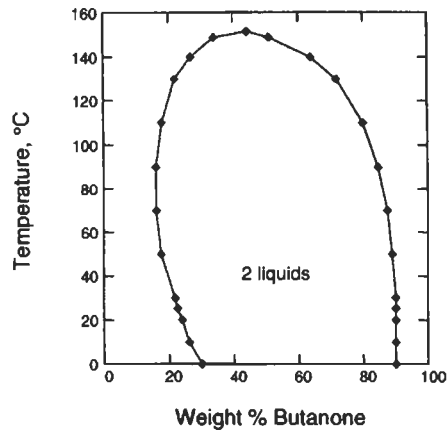|	C	Mn	Si	P	S	Cr	Ni	Mo
Pump body	0.019	1.73	0.59	0.028	0.004	16.5	10.2	2.14
UNS S31603	0.03 maximum	2.00 maximum	1.00 maximum	0.045 maximum	0.030 maximum	16.0–18.0	10.0–14.0	2.00–3.00

Fig. 1. Water–butanone phase diagram showing single-liquid phases for water- and butanone-rich solutions separated by a two-phase region of liquid immiscibility.

1, and an 8% solution of water in butanone lies in the single-phase region at the butanone end of the system [1, 2]. The phase diagram shows that water–butanone mixtures separate into two liquids for water contents between 9.9 and 77.4 wt% at 25 °C. The major dissolved species in this solution was analytical-grade sodium chloride at a concentration of 0.05 wt%. No information on either the nature or the amounts of the other components in the mixture was made available on the grounds of commercial sensitivity.

3. THE CORROSION

An example of the crevice corrosion is shown in Fig. 2. Small crystals can be seen on the corroded face of this section of pump body, especially in the two recessed central holes and the groove which connects them. EDX analysis showed that these crystals contained sodium and chloride.

4. DISCUSSION

The association of the chloride-containing crystals on the corroded faces of the pump body with the presence of the aqueous solution of butanone reportedly found when the system was dismantled led to the conclusion that the corrosion is chloride-induced crevice corrosion. However, this conclusion was resisted on the grounds that a 0.05 wt% solution of sodium chloride could not cause crevice corrosion of 316L stainless steel at 25 °C.

The hypothesis formed was that water had somehow entered the system in a sufficient amount to form a two-liquid mixture (see Fig. 1), when it mixed with the 8% solution of water in butanone. Given that the density of a 10 wt% solution of water in butanone is just under $0.84 \, \text{kg} \, \text{l}^{-1}$, any water-rich phase so formed would have separated to the bottom of the unit, and the butanone-rich phase would have floated on it. This separation into two liquids was followed by preferential partition into the water-rich phase of the sodium chloride present in the process liquor to give a much more concentrated chloride solution. Such a hypothesis would explain not only how the conditions conducive to crevice corrosion had developed, but also why only the lowest pump in the production unit had suffered crevice corrosion.

The water–butanone phase diagram given in Fig. 1 shows that at 25 °C a two-liquid phase field is formed for water contents between 9.9 and 77.4 wt%. Given that each charge of the 8 wt% solution of distilled water in butanone used in the batch process was 200 l (~ 168 kg), an additional 3.7 l of water would have been just slightly more than sufficient to have caused the formation of a mixture of two liquids. The Lever rule predicts that in such a mixture the weight of the butanone-rich phase would be 171.44 kg, and the weight of the water-rich mixture would be 0.26 kg. The

Fig. 2. Crevice corrosion suffered by the 316L stainless steel pump. Small crystals of sodium chloride can be seen on and around the corroded area.

corresponding volumes would be 204.1 and 0.23 l, respectively. There is a slight (~ 0.3%) increase in volume on mixing.

Data for the solubility of sodium chloride in water–butanone mixtures could not be found. However, there are data for the solubility of sodium chloride in water–acetone mixtures at 20 °C [3]. These are given in Table 2.

The 'lower' and 'upper' layers in Table 2 refer to the water- and acetone-rich solutions, respectively. Comparison of the data in Table 2 and the water–butanone phase diagram shown in Fig. 1 shows that the solubility of acetone in water is roughly comparable to that of butanone in water, and that water is more soluble in acetone than in butanone. Thus, the solubility of sodium chloride in water–acetone mixtures should only be considered as a guide to what might happen in water–butanone mixtures. Although the lower and upper layers in the immiscible water–acetone mixtures are in equilibrium, and the activity of the sodium chloride in each layer is therefore equal, inspection of Table 2 shows that in acetone–water mixtures the partition coefficient for sodium chloride between the water-rich lower layer and acetone-rich upper layer is 40:1.

If in the present case of a two-liquid water–butanone mixture, the partition of sodium chloride between the water-rich phase and the butanone-rich phase is of a similar magnitude, calculations indicate that the concentration of sodium chloride in the water-rich phase will be higher than in both the butanone-rich phase and the original 8 wt% solution of distilled water in butanone.

Table 2. Solubility of sodium chloride in aqueous solutions of acetone at 20 °C

Weight % acetone	8.0	16.5	25.3 Lower layer	27.1 Upper layer	84.1	85.3	87.7
g NaCl per 100 cm³ of solution	27.18	23.10	19.32	18.05	0.45	0.43	0.25

The weight of sodium chloride in the 168 kg of the liquor used in the batch process is 0.084 kg. With a partition coefficient of 40:1, this amount of sodium chloride would be partitioned thus: the water-rich layer would contain 0.082 kg, and the butanone-rich layer would contain 0.002 kg. The calculations given previously show that addition of the minimum volume of water required to cause separation of the 8% water-in-butanone solution used in the batch process into two immiscible liquids results in the formation of 0.23 l of the water-rich phase. Using the data shown in Table 2 as a guide, the greatest amount of sodium chloride which could dissolve in 0.23 l of water-rich solution is 0.045 kg. Thus, if only 0.23 l of the water-rich phase had been formed, it is probable that sodium chloride would have precipitated from the water-rich phase.

Since no solids had been observed when the system was dismantled, it appears that at least 0.5 kg of water-rich phase must have been formed. This led to a reappraisal of the amount of water which had been introduced to the system. Calculations based on the Lever rule indicated that this would have required the addition of just under 4 kg of water to the feed liquor.

Although the strict applicability of these calculations to the present case may be questioned, since data for the solubility of sodium chloride in water–acetone mixtures have been used, they do suggest that the hypothesis is tenable. The result would have been that the pump which had suffered the crevice corrosion was not exposed to a very dilute solution of chloride but to a brine, and crevice corrosion of 316L would inevitably have occurred.

5. A DEMONSTRATION

Since there were doubts about the applicability of these calculations to the present case, a demonstration was carried out in which 5 mm nominal diameter 316L stainless steel rods were exposed to: (i) an 8 wt% solution of water in butanone which contained 0.05 wt% sodium chloride, and (ii) the same solution after the addition of just sufficient water to cause the formation of two liquids. Artificial crevices were formed by slipping Viton o-rings up the rod. In the second case, the o-rings were positioned so that there was one in the water-rich phase and one in the butanone-rich phase. The composition of the stainless steel used in this demonstration is given in Table 3.

After 12 days of exposure at 25 °C, a pale yellow discolouration of the originally clear water-rich phase was observed, and a light ring of rust began to appear at the edge of the o-ring immersed in this phase (Fig. 3). Neither discolouration of the solutions nor rings of rust at the o-rings were
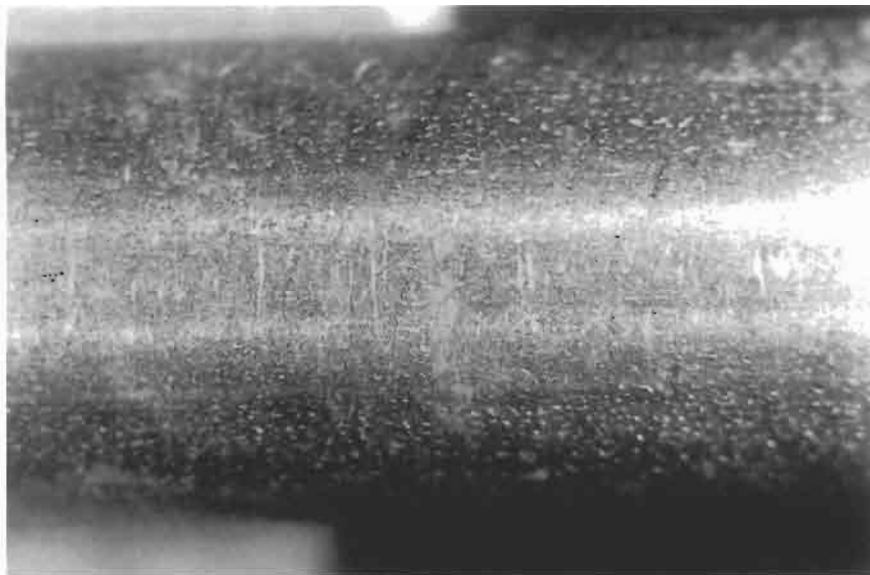

Fig. 3. Light ring of rust which appeared at the o-ring immersed in the water-rich phase after 12 days of exposure at 25 °C (× 16)

Table 3. Chemical analysis of the stainless steel rod used in the demonstration: composition in wt%

	C	Mn	Si	P	S	Cr	Ni	Mo
Rods	0.024	1.55	0.59	0.030	0.023	16.3	11.1	2.02
UNS S31603	0.03 maximum	2.00 maximum	1.00 maximum	0.045 maximum	0.030 maximum	16.0–18.0	10.0–14.0	2.00–3.00

observed in either the butanone-rich phase or the original 8 wt% water-in-butanone mixture. These observations show that crevice corrosion had just begun to initiate in the water-rich phase, but had not initiated in either the 8wt% solution of water in butanone, or in the butanone-rich phase formed after the addition of water.

6. CONCLUSION

The hypothesis presented in the discussion is tenable, and can explain how crevice corrosion of 316L occurred in what was supposed to be a very dilute solution of sodium chloride in an 8 wt% solution of water in butanone.

The unresolved question was how the additional water required to cause separation of this solution into two immiscible liquids was introduced into the system.

REFERENCES

1. Francis, A. W., *Liquid–Liquid Equilibriums*. Interscience, New York, 1963.
2. Seidell, A., *Solubilities of Organic Compounds*, 3rd edn. Van Nostrand, Princeton, NJ, 1941.
3. Seidell, A., *Solubilities of Inorganic Compounds*, 3rd edn. Van Nostrand, Princeton, NJ, 1941.

TYPE I PITTING OF COPPER TUBES FROM A WATER DISTRIBUTION SYSTEM

PAULO J. L. FERNANDES

Advanced Engineering and Testing Services, MATTEK, CSIR, Private Bag X28, Auckland Park, 2006, South Africa

Abstract—Samples of copper tubes from a cold water distribution system which had failed due to pitting whilst in service were subjected to a detailed failure investigation. Analysis of the tubes showed that failure was a result of Type I pitting attack. While the exact cause of pitting was unknown, it was hypothesised that it could have been due to changes in the water quality and/or content. The tubes were found to be made from phosphorus de-oxidised copper and no anomalies were evident in either the chemical composition or the microstructure which could have caused the pitting observed. It was recommended that the tubes be replaced and that due attention be given to ensure that the new tubes are free of internal carbonaceous deposits or other foreign matter. © 1998 Elsevier Science Ltd. All rights reserved.

Keywords: Corrosion, pitting corrosion.

1. INTRODUCTION

Copper tubes are used extensively in water distribution systems due to their corrosion resistance and ease of installation. In Europe and North America they account for more than 80% of all tubes installed in water service [1], amounting to over 100 million metres of tubing. In spite of these large quantities, tube failures are relatively rare. Of the failures that do occur, pitting corrosion accounts for approximately 60%.

This study presents an investigation of the failure of copper tubes from a cold water distribution system carrying potable water in a shopping centre. The tubes, which were built into the brick walls, sprang leaks in several premises in the shopping centre after approximately 12 years' service, causing severe staining of the walls. Examination of the tubes revealed the presence of pin holes perforating the tube walls.

2.. EXPERIMENTAL PROCEDURE

2.1. *Visual examination*

Several tubes sections were received for analysis. These were sectioned to reveal the internal surfaces, which were found to be covered with a greenish-white scale (Fig. 1). Furthermore, localized deposits of green corrosion product in the form of tubercules were also evident (see arrow in Fig. 1). Some tubercules were carefully removed by light scrubbing to reveal the underlying metal. A shiny, black layer of an unidentified compound was found to exist beneath the greenish-white scale. Beneath this black layer, in turn, pits penetrating into the tube wall were found. An example of the various layers and the underlying corrosion pit is shown in Fig. 2. Some of the pits observed were relatively large and deep, as shown in Fig. 3.

2.2. *Chemical analysis of internal scale and corrosion products*

Samples of the tubes were examined in a scanning electron microscope (SEM) equipped with an energy dispersive spectroscopy of X-rays (EDS) facility. The results of the EDS analysis of the greenish-white scale found on the internal surfaces of the tubes are shown in Fig. 4. The large copper

Fig. 1. The internal surface of a tube (×2). The arrow indicates the presence of a tubercule of corrosion product.

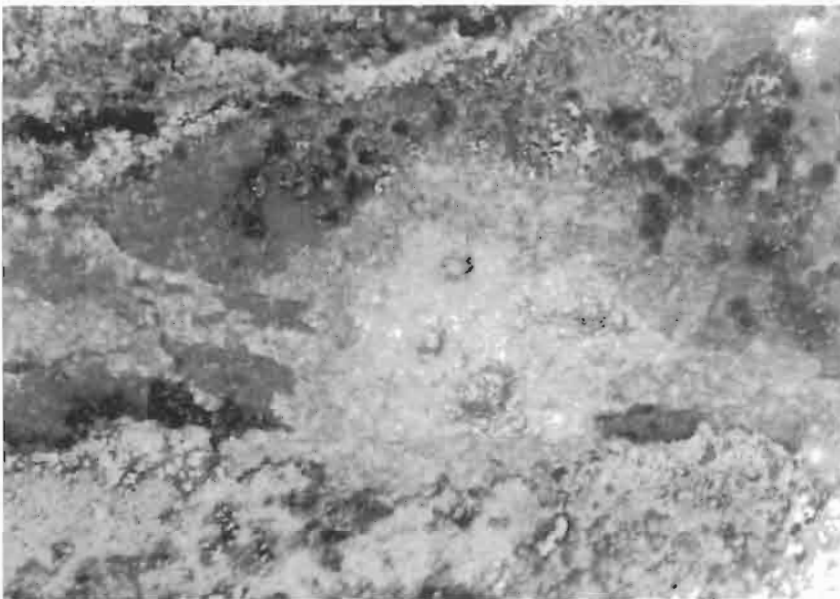Fig. 2. A high magnification photograph of the region beneath a corrosion tubercule (≈ ×50). Note the presence of the greenish-white scale, the underlying black layer and the corrosion pit.

peak originates from the base metal. The large silicon and calcium peaks, and the smaller aluminium peak are due to the presence of these elements in the scale. These elements are readily oxidised and are therefore frequently detected in scale deposits. A minor chloride peak was also detected. This ion is usually associated with pitting attack but the quantity of chloride in this case does not appear to be large.

Fig. 3. The internal surface of a tube showing extensive pitting (× 3).

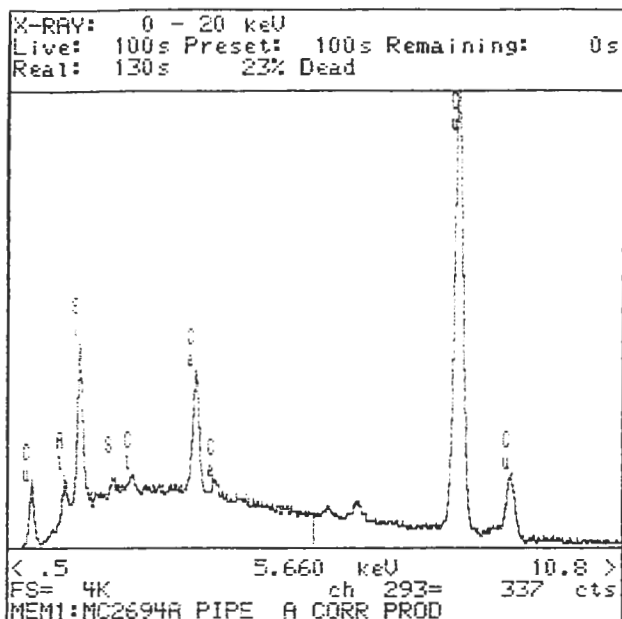

Fig. 4. The EDS results of the greenish-white deposits found on the internal surfaces of the tubes.

3. METALLOGRAPHY

Samples from the tubes examined were prepared for metallographic analysis using standard grinding and polishing techniques. Etching was carried out in acidified ferric chloride. The typical microstructure observed in all cases consisted of large equi-axed grains, indicating that the tubes were in the annealed condition.

310

3.1. *Chemical analysis*

An analysis of the chemical composition of the tubes was carried out using a wet chemical analysis method. From the high phosphorus content it was evident that the tubes were made from phosphorus de-oxidised copper.

4. TYPE I PITTING

Pitting corrosion is the most common failure mechanism for copper tubes in water distribution systems. Essentially two different types of pitting attack have been identified, and these are referred to in the literature as Type I and Type II pitting*. The former is known as cold water pitting and occurs more frequently than the latter.

Type I pitting is usually encountered in cold water systems carrying borehole or well waters free from organic matter [1]. It occurs sporadically and can result in tube wall penetration within a few months. In some cases, however, penetration occurs only after 15 years or more. The internal surfaces of tubes undergoing Type I pitting are usually covered with a greenish scale of a copper compound called malachite. Beneath this scale, the tube surface is covered with a smooth, shiny layer of dark cuprite which is very friable and easily spalled off. Pits are usually associated with the presence of tubercules which form over pin hole defects in the cuprite layer.

The characteristics of Type I pitting attack are such that many pits at all stages of development can usually be found [1]. Larger pits are generally linearly arranged along the bottom half of horizontal water lines. When pits are very close together, tubercules can extend over a number of pits to form one long tubercule. Although pitting has been observed in annealed, half-hard and hard-drawn tube, susceptibility is generally greatest in the annealed condition. The pits formed are usually saucer-shaped and relatively wide.

A number of causes of Type I pitting have been identified [1]. Firstly, the incidence of pitting has been associated with the presence of carbonaceous films on the internal surface of the tube. These films are residues of the lubricant used for the drawing operation and which are carbonized during annealing. The quantity and distribution of these films on the internal surface appears to affect the severity of pitting. The problems arising from the presence of these carbonaceous films can be overcome in practice by scouring the tubes with a water–sand or a water–air blast.

Secondly, pitting has been associated with the presence of foreign matter deposits on the bottom half of horizontal tubes [1]. This is in agreement with observations on the preferential location of pits discussed above. The foreign matter deposits can be introduced into the water lines in a number of ways. Metal chips and filings and dirt can be allowed to contaminate the system during installation. If these are not properly removed before service, they may deposit along sections of the water lines where the water velocity is low. Foreign matter deposits may also be introduced into the system in the water or may be due to corrosion products formed during surface corrosion of the tubes during service. The concentration of these deposits, and hence their deleterious effects, can be reduced by the installation of filters in the water line.

Thirdly, another factor said to cause pitting attack is the presence of soldering pastes on the insides of the tubes. This generally results from bad workmanship and can be avoided by ensuring that adequate quality standards are maintained during installation. The soldering pastes may act as deposits in the same way as foreign matter. Alternatively, during soldering or brazing these pastes may be converted to oxides which form as a thin film on the copper surface. These oxides are generally cathodic to copper and can therefore give rise to pitting corrosion.

The effect of water quality on the incidence of Type I pitting is the subject of some controversy and no consensus has been reached in this regard. Some general observations have been made, however, on the effects of various constituents and characteristics of water on the extent of pitting,

---

*Some researchers have also reported the existence of Type III and Type IV pitting, but these appear to be variations of Type I pitting [1].

Table 1. The effect of various water constituents and characteristics on Type I pitting

Chemical species	Effect
Sulphate (SO_4^{2-})	Assists pit initiation and growth, but its effect depends on the concentration of other chemical species.
Chloride (Cl^-)	Essential for pitting attack. Assists the breakdown of protective surface films and results in the formation of wide, shallow pits
Nitrate (NO_3^-)	Inhibits pitting
pH	Increases in pH generally decreasing the probability of pitting.
Dissolved oxygen (O_2)	Increased O_2 content increases the probability of pitting.
Carbon dioxide (CO_2)	Increased CO_2 content increases the probability of pitting due to a decrease in pH.

and these are summarised in Table 1. An empirical screening process has also been developed to assess the risk of Type I pitting in various waters [2] (Fig. 5). This process has been used extensively with reasonable success.

A number of characteristics of Type I pitting discussed above were evident in the failed copper tubes from the shopping centre. The presence of tubercules of corrosion product and the greenish scale on the internal surface of the tubes were clearly evident (Fig. 1). The friable underlying layer of shiny, dark cuprite was also observed (Fig. 2). The wide, saucer-shaped pits and their approximately linear distribution were also evident and are shown in Fig. 3. It is also evident that pits at various stages of development were observed.

5. CONCLUSIONS

It was concluded that the failure of the copper tubes was due to Type I pitting attack. It is not clear at this stage what the exact cause of pitting failure was, particularly given the fact that pitting only became evident after 12 years' service. It is highly unlikely that it may be due to the presence of foreign matter deposits introduced during installation of the system. The introduction of foreign matter in the water is, however, a possibility, particularly if the water is not filtered. A change in water quality or content (e.g. resulting from mixing of the water with borehole or well waters) could also be responsible for pitting.

Once initiated, pitting attack can in some cases be halted through the application of appropriate treatments of the water and the metal. The extent of pitting observed in the present case, however,
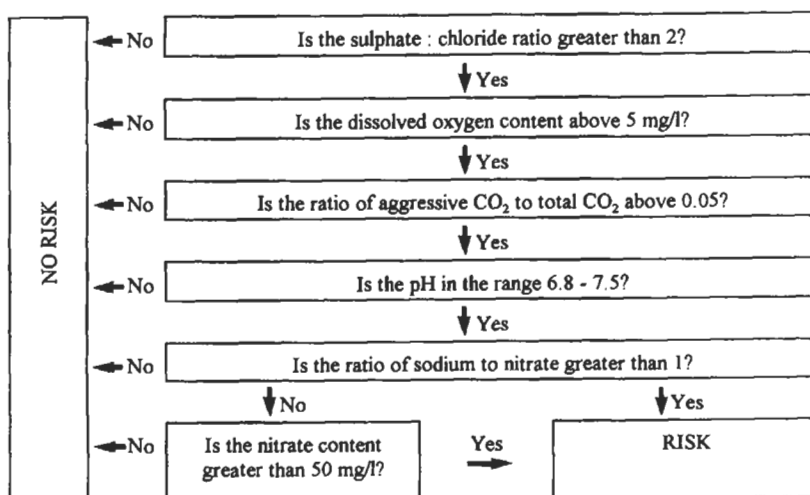

Fig. 5. Evaluation of waters for Type I pitting [2].

suggested that such treatment would be both unsuccessful and unfeasible. It was therefore recommended that the copper tubes be replaced. Careful attention should be given to the usual causes of Type I pitting. In particular, it should be ensured that all tubes be thoroughly cleaned and freed of any carbonaceous deposits prior to installation. The tubes should also be cleaned to ensure complete removal of any foreign matter deposits and solder pastes after installation. The use of water filters could also be considered to prevent the introduction of foreign matter in the water. Furthermore, the quality and content of the water should be determined and its potential to cause pitting assessed. The extent of replacement or modifications to the water distribution system would, to some degree, depend on the results of such water analyses.

REFERENCES

1. *Internal Corrosion of Water Distribution System.* Report of Cooperation Research, AWWA Research Foundation, USA, 1985.
2. Billiau, M., Drapier, C., *Materiaux et Techniques,* Nos 1 and 2.

CORROSION OF FLEXIBLE WAVEGUIDES

D. PAPATHEODOROU, M. SMITH and O. S. ES-SAID*

Mechanical Engineering Department, Loyola Marymount University, 7900 Loyola Blvd, Los Angeles,
CA 90045-8145, U.S.A.

Abstract—Waveguides are commonly used in spacecraft subsystems to convey signals. After noticing a transponder ouput power drop, borescope inspection of a flexible waveguide revealed a green contaminating residue on silver plated brass and copper sections. Analysis revealed that the residue, primarily copper hydroxy nitrate, $Cu(OH)_2NO_3$, was created by exposure of the plating to nitric acid. Possible sources of nitric acid include inadequate cleanliness after parts were exposed to a nitric acid containing silver bright dip, or high temperature electrical arcing in the presence of air and moisture. Whatever its source, it is suggested that the waveguide be plated with a more corrosion resistant metal such as rhodium. © 1998 Elsevier Science Ltd. All rights reserved.

Keywords: Corrosion, electronic-device failures, surface coatings.

1. INVESTIGATION

Flexible waveguides, common in spacecraft payload sub-systems, transport signals between various units (e.g., filters, transponders, and converters). During preliminary testing at ambient temperature and pressure, an output power drop was detected within a signal generating unit of a waveguide system. Green contamination residue was found in the waveguides. An investigation commenced to characterize the corrosion and determine its cause.

The flexible waveguide, Fig. 1, has a rectangular thin wall cross section having corrugations which allow it to be formed. The green residue was found on brass and copper surfaces, primarily in the bottom of those corrugations (dark bands in Fig. 2). In some areas, the waveguide wall had corroded through.

To determine the material damage severity, as well as the composition of the residue, an analysis of samples taken from the waveguide was conducted using visual inspection, optical microscopy, scanning electron microscopy and X-ray methods. Samples were prepared by cutting and spreading open the waveguide to expose its internal surfaces containing many voids and much debris (Fig. 3).
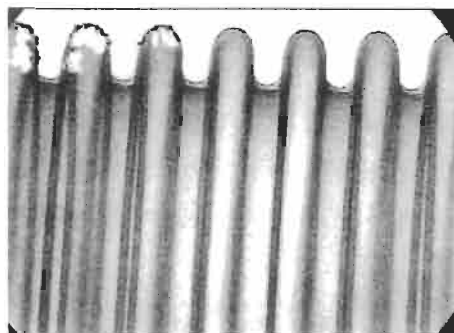

Fig. 1. Profile of waveguide. Dark bands are low points in waveguide or corrugations.

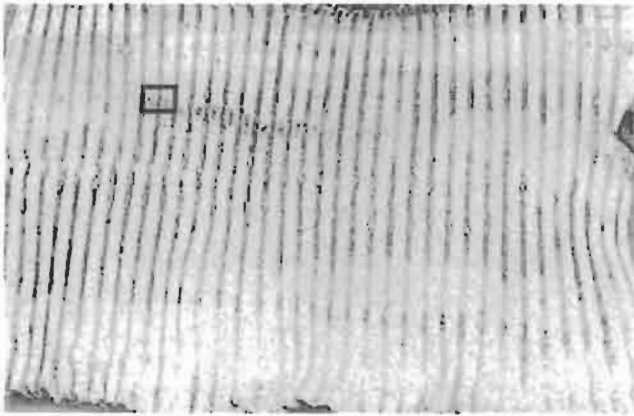* Author to whom correspondence should be addressed.
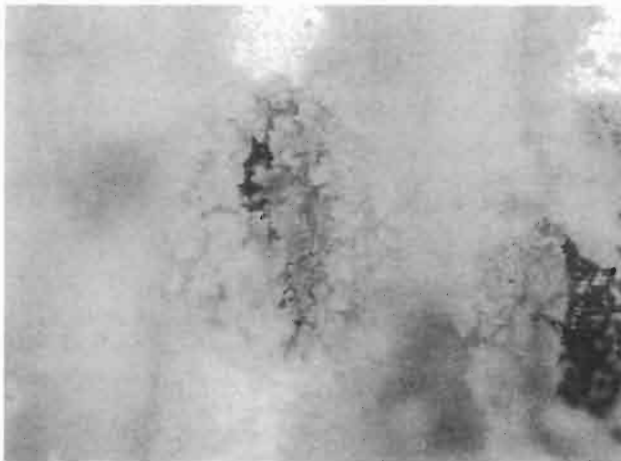
Fig. 2. Inner surface of waveguide.

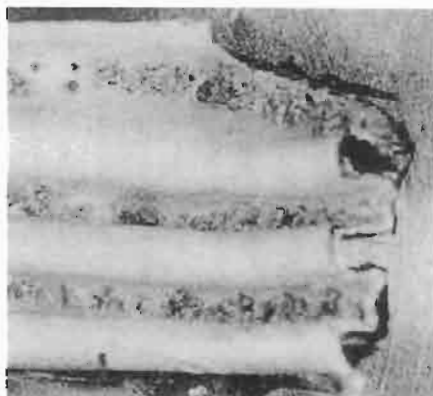Fig. 3. Debris on waveguide surface. Copper hydroxy nitrate corrosion along corrugations in waveguide.

Fig. 4. Corrosion product along corrugations in the waveguide.

In addition to pitting of the silver plating, there were burnt areas where it appeared as if silver plating had been melted by electrical arcing.

Closer investigation of the pitted areas seemed to show that corrosion on the waveguide internal passages probably started on the exposed silver plated surface. It is theorized that these pits, however formed, allowed attack of the underlying copper bearing base material.

A chemical analysis using X-ray diffraction analysis, subsequently verified by Fourier transform infrared spectroscopy and energy dispersive X-ray spectroscopy, revealed that the debris is primarily copper hydroxy nitrate $Cu(OH)_2NO_3$. To determine how it got there, a laboratory test was performed to try to create the same debris on clean waveguide samples by placing on them a small amount of nitric acid. Two hours later, a blue color was observed in the acid. After about 12 h, blue crystals began forming at the silver plated interface. After 5 days, most of the solution had been replaced by green corrosion analyzed as a copper hydroxy nitrate. Nitric acid clearly caused the corrosion. Its source could be either faulty fabrication processes or arcing induced chemical reactions.

2. FABRICATION PROCESS

The silver plating on the brass waveguide is applied after the brass has undergone a multi step surface preparation process. First, the brass surface is cleaned and etched in a caustic cleaning solution for 5–60 s. After subsequent rinsing under running tap water, the brass is immersed in a bright dip solution for 5–20 s. This removes scratches and oxide, making the brass look shiny. The bright dip solution is composed of 5–10% tap water, 60–75% sulfuric acid, 20–35% nitric acid. To remove the bright dip, parts are washed in running tap water. The use of pumice and a brush is required for assemblies. The bright dip vendor specifies that this cleaning technique is sufficient.

Once bright dipping is complete, parts should be first immersed in clean running water, then boiling hot water, and then dried. To avoid contamination between one dip operation and another, parts should be rinsed in running water, hot water and then dried at each step [1].

Both silver and copper bright dips exist to make either copper or silver shiny. Once silver plating was complete, a bright dip step may have been inadvertently included despite its lack in vendor process specifications. For instance, a silver bright dip may have been performed to relieve the effects of poor silver plating, inadvertently leaving behind an acidic residue.

3. ARCING INDUCED CHEMICAL REACTIONS

If nitric acid was indeed produced by arcing, nitric oxide (NO) would need to be present. Colorless and noncombustible, nitric oxide can be produced from atmospheric oxygen and nitrogen in the presence of an electric arc. In this instance, such production is possible—there was evidence of arcing on the waveguide surface. In addition, arcing could have initiated pits in the silver plating, exposing the underlying copper bearing base material to chemical attack.

A similar incident of corrosion in an aircraft waveguide system occurred about 20 years ago. In that case, arcs were created in a clean noncorroded waveguide while gas samples were taken for an analysis by mass spectrometry. An analysis of two samples is shown in Table 1.

Table 1.

	Mole percent	
	Sample #1	Sample #2
Hydrogen	0.001	0.003
Water	0.003	0.002
Nitrogen	79.816	79.819
NO, as nitric oxide	39 ppm	28 pm
Oxygen	18.731	18.708
Argon	1.015	1.022
Carbon dioxide	0.430	0.443

This confirms that nitric oxide could be formed by electrical arcing. Despite the small concentration, it still exceeds that normally found in air by several orders of magnitude. Nevertheless, even if such nitric oxide is present, it must react with moisture for nitric acid to form. With humidity controlled between 30 and 60%, available evidence suggests that the current waveguide system was not exposed to excessively moist conditions.

4. RECOMMENDATIONS

Silver is attacked by nitric acid and will be corroded by reducing acids in the presence of oxidizing agents [2]. Nitric acid is a strong oxidizing agent. It oxidizes all metals except gold, platinum, rhodium and iridium [3]. In strong acid solutions, the hydrogen is continuously evolving as bubbles from the corroding metal and this process continues until either all the metal or acid is consumed.

If the waveguide system is operated in conditions in which moist air is not absorbed during operation and if the system is purged of any nitric oxide after operation, the corrosion can be eliminated. It would also be best to pass the air through a dryer prior to introducing it into the waveguide to guarantee moisture levels are minimized.

For improved protection against nitric acid formation, if arcing does occur, it is best to electroplate with noble metals other than silver, since it is attacked by nitric acid. The noble metals have extremely high corrosion stability and do not rely on the formation of an oxide coating. Their high cost and low strength limits their use to thin films and liners on other structural materials [4]. They are economical for numerous corrosion applications. Platinum is resistant to nitric acid at all temperatures and concentrations [5].

Electrodeposited platinum is reasonably dense and generally adheres well. Mechanical and physical properties depend greatly on plating conditions and thin coatings are used for corrosion and wear resistant electrical contacts [5]. Gold is very good in dilute nitric acid and strong sulfuric acid.

Rhodium electroplates well and is used for critical valve parts and other applications where total resistance to an aggressive environment is necessary [2]. A 37% rhodium 63% nickel alloy has better resistance to general corrosion than 14 carat yellow gold [5]. Rhodium finds most of its applications as an element in platinum to which it imparts added corrosion resistance to many acids. In general, electrodeposition has been employed for thin rhodium coatings. A rhodium thickness of 5×10^{-6}–20×10^{-6} inch over silver minimizes tarnishing [5]. In this case, these metals can be used for protection against nitric acid if formed due to arcing.

Quality control during waveguide manufacturing must guarantee that no nitrate ions are on the waveguide. In bright dipping, a small amount of metal is corroded but the part has a shiny finish as opposed to a dull oxide coating. Speed of operation and uniformity are the essentials of bright dipping. The acid acts very quickly and long exposure time will result in more corrosion. After dipping the parts should be very quickly rinsed in cold water and then hot water and dried [1].

Pure, clean water, e.g. distilled water, is undoubtedly the best for making solutions. It is very difficult for small amounts of silver nitrate to dissolve in water that has impurities in it. However, in distilled water the silver nitrate will perfectly dissolve to a clear solution [1]. Water taken from wells is sometimes found unfit for the best results in plating, if it contains lime or is strongly mineralized with iron, sulfur or magnesium.

REFERENCES

1. Hawkins, H. J., *The Polishing and Plating of Metals*, Lindsay Publication, Bradley, IL, 1987, pp. 98–100.
2. National Association of Corrosion Engineers, (N.A.C.E.) *Corrosion Basics, An Introduction*. N.A.C.E. Publication, Texas, 1984, pp. 590.
3. Waser, J., Trueblood, K. N. and Knobler. C. M., *Chem One*, McGraw Hill, New York, 1976, pp. 80.
4. Butler, G. and Ison, H. C. K., *Corrosion and its Prevention in Waters*, Reinhold Publishing Corp., New York, 1966, pp. 101.
5. Metals Handbook Committee. *Metals Handbook*, Vol. 1, 8th edn, American Society For Metals, Metals Park, OH, 1961. pp. 805, 1178, 1179

Failure of automobile seat belts caused by polymer degradation

J.M. Henshaw[a],*, V. Wood[a], A.C. Hall[b]

[a] *The University of Tulsa, Department of Mechanical Engineering, 600 South College Avenue, Tulsa, OK 74104, U.S.A.*
[b] *The University of Illinois, Materials Science and Engineering, Urbana, IL 61801, U.S.A.*

Abstract

This paper analyzes the failure of a particular brand of automobile seat belts. The failures described were part of what nearly became the most expensive and widespread automobile recall in U.S. history, affecting about 8.8×10^6 vehicles and with a potential total cost of U.S. 10^9. The failures were caused by the degradation and fracture of the seat belts' polymeric release buttons. When fragments break away from the buttons, they can become lodged within the seat belt mechanism in a variety of locations, such that any one of three distinct failure mechanisms can result: (1) the belt fails to latch, (2) the belt will latch but will not unlatch, and (3) the belt appears to be latched but is not. The seat belt mechanism, and the ways in which the degraded button can cause it to fail, are described in detail. The buttons themselves were found to have been injection molded of ABS and to have undergone photo-oxidative degradation. This degradation process is documented and described. Conclusions from the analysis and lessons learned from the failures are described, along with the auto industry's short- and long-term solutions to the problem. © 1998 Elsevier Science Ltd. All rights reserved.

Keywords: Photo-oxidative degradation; Polymer degradation; ABS; Seat belts

1. Background

In the spring of 1995, a major news story in the United States recounted what was potentially the largest formal automobile recall in the history of the industry. While news reports in the popular press were lacking in technical detail [1, 2] it was noted that 'Apparently part of a plastic release button deteriorates...' [1] sometimes causing seat belts to malfunction. It was further noted that about 8.8×10^6 vehicles were affected from the model years 1986–1991, including models from Honda, Nissan, Mazda, Ford, GM, and Chrysler, among others. (About 75% of the affected vehicles were from Honda and Nissan. Toyota alone among the U.S. and Japanese carmakers was

---

* Corresponding author.

not affected.) The cost to carmakers should a mandatory recall become a reality was estimated at U.S. 10^9.

Ultimately, this incident did not result in a formal mandatory recall by the U.S. National Highway Traffic Safety Administration. The manufacturer of these seat belts, the Takata Corporation, and the affected automakers agreed to a voluntary recall of these vehicles. The following excerpt is from a recall letter from Honda to owners of the affected vehicles:

> The Reason for This Notice: Honda has determined that front seat belt buckle release buttons have broken, and others may break in the future, in some (1986–91) Honda cars equipped with seatbelts made by the Takata Corporation. These seat belt buckle release buttons are made of red plastic, and are marked PRESS. If a button breaks, pieces may fall into the buckle assembly. If this occurs, the buckle may not operate properly, thereby creating a safety risk. To prevent this problem from occuring, Honda will replace all broken front seat belt buckles, free of charge. In addition Honda will modify all unbroken buckles manufactured by Takata to prevent future button breakage.

Under the terms of the voluntary recall, owners of affected vehicles were asked to take their cars to their dealer who would perform an inspection and then either replace or modify the seat belts. The details of the inspection and modification procedure are described later in this report.

2. The seat belt mechanism and its failure

2.1 The seat belt mechanism

While there are some variations in design among the various models of Takata-manufactured seat belts affected, the basic mechanisms are quite similar. All include a release button, which is part of the seat belt receptacle mechanism, that is adjacent to the slot into which the seat belt clasp fits when the belt is engaged. A typical Takata seat belt receptacle of the affected design is shown in Fig. 1.

In order to understand the function of the release button, and how it contributes to the various system failures, it is necessary to first understand how the seat belt receptacle mechanism works. A schematic of the seat belt latching mechanism is shown in Fig. 2. In the top part of the figure, four key parts of the mechanism are shown and named. (Other parts are omitted for simplicity.) In the middle part of the figure, the steel 'clasp', at left, is inserted towards the right into the mechanism where it encounters a polymeric 'slider'. The clasp forces the slider to compress a spring. In the bottom part of the figure, the 'latch' and 'locking slider' rotate counterclockwise into the locked position when the opening in the clasp becomes aligned with the male portion of the latch. As the latch rotates into the locked position, the locking slider slides to the left into a position where it is constrained along with the latch (by the unshown housing) from rotating back to the unlatched position. To release the belt, the release button is pushed against the locking slider, sliding it back out of the way of the housing, and allowing both the locking slider and latch to rotate clockwise until the male portion of the latch no longer engages the opening in the clasp. Finally, the compressed spring behind the slider can extend itself, ejecting the clasp from the mechanism.
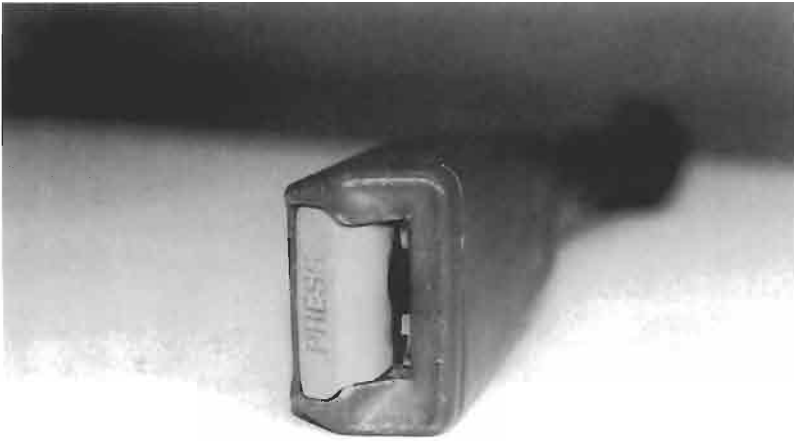
Fig. 1. Typical Takata seat belt receptacle of one of the affected designs. This receptacle was removed from a 1989 Honda Accord. Note impact damage especially to the plastic housing.
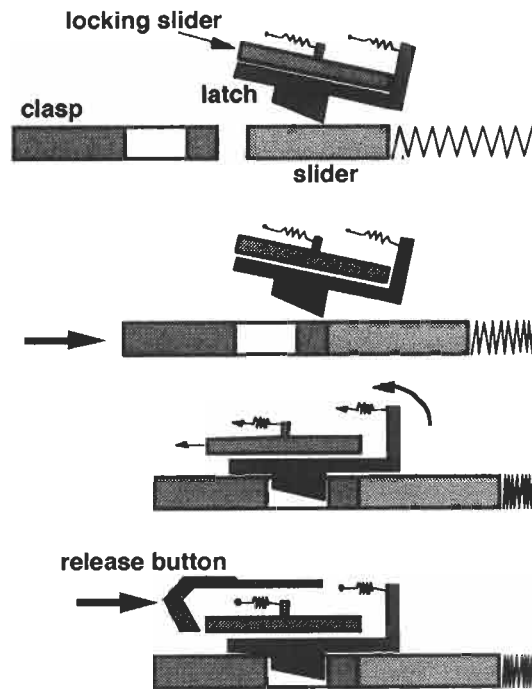

Fig. 2. Schematic side view of the seat belt latching mechanism showing the interactions among the main components, including the release button (bottom).
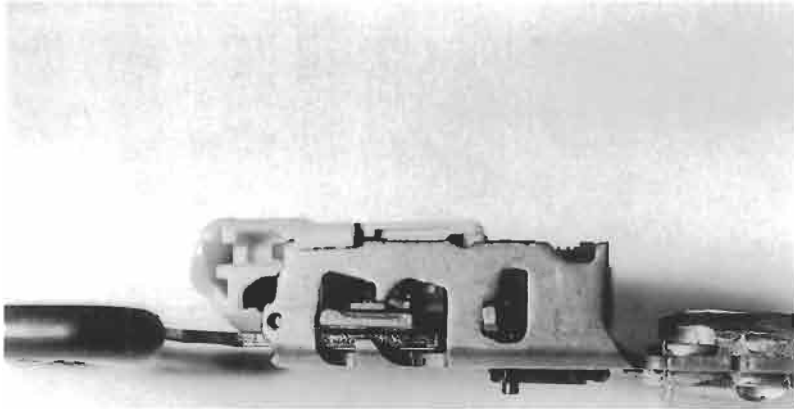
Fig. 3. Seat belt receptacle, with housing removed to show mechanism components. The clasp, at left, is latched in place.
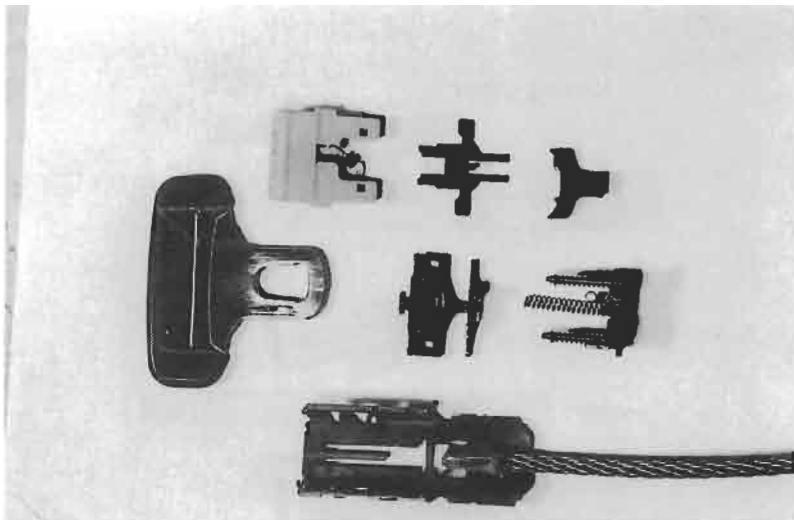

Fig. 4. Disassembled components of seat belt. Top row: release button, locking slider, and slider. Middle row: clasp, latch, spring subassembly. Bottom row: housing and cable.

A photograph of the actual receptacle is shown in Fig. 3. The receptacle's plastic housing has been removed in this Figure. Figure 4 is a photograph of the disassembled components in the belt receptacle along with the clasp.
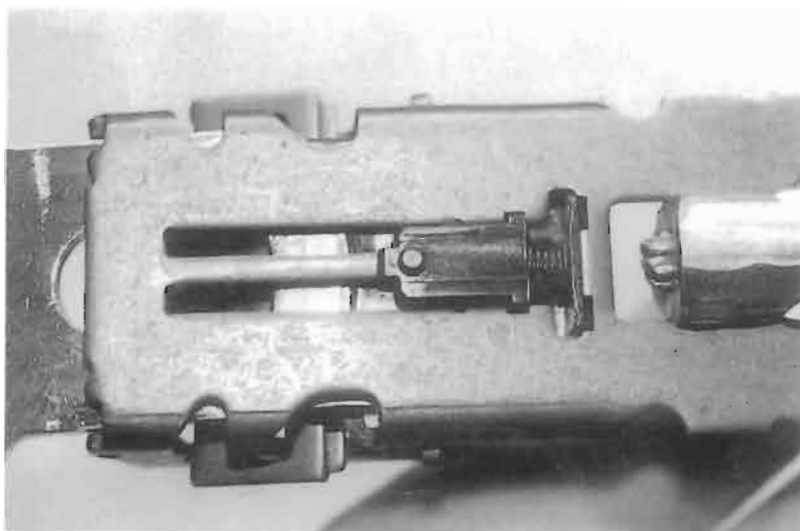
Fig. 5. 'Mode one' failure, showing a bottom view of the receptacle housing. The clasp, at left, is attempting to completely enter the receptacle, but it cannot, because of the button fragment lodged behind the slider.

2.2. Failure of the belt receptacle mechanism

Various used seat belt receptacles were purchased from an automobile salvage yard. All were from Honda Accords from the affected range of model years (1986–91). One of the receptacles was in a failed condition when it was removed from the used Accord at the salvage yard. That is, this receptacle was exhibiting what the authors later termed a 'mode 1' failure: the clasp could be inserted into the receptacle, but it refused to lock in place. Disassembly of the receptacle revealed why, as shown in Fig. 5. A small fragment from the release button had fractured away from the button and fallen into the receptacle, whereupon it became lodged in the slot along which the slider must travel when the clasp is inserted. Since the slider is thus prevented from sliding to its latched position, the buckle is likewise prevented from latching.

Further examination of the receptacle mechanism revealed two other potential failure mechanisms. A 'mode 2' failure, wherein a small piece of plastic from the release button gets wedged in behind the locking slider (Fig. 6), preventing it from sliding to its unlatched position when the release button is pressed. This is perhaps the most frightening failure mechanism, since it means that the belt wearer is unable to unlatch the belt, no matter how hard he or she presses on the release button.

The third failure mechanism results when a small piece of plastic from the release button becomes lodged in such a way the locking slider cannot quite slide to its fully locked position (Fig. 7). Thus, while the clasp can be inserted into the receptacle, seemingly latching the belt, in reality the clasp can be removed by pulling on the belt with relatively little force.

Of course, the one element that each of these three failure modes has in common is the presence of fractured pieces of the release button. It is ironic that the breaking away of these small pieces does not impede the function of the release button itself. It is only when fate allows these fragments to become lodged in just the wrong place that the seat belt mechanism fails.
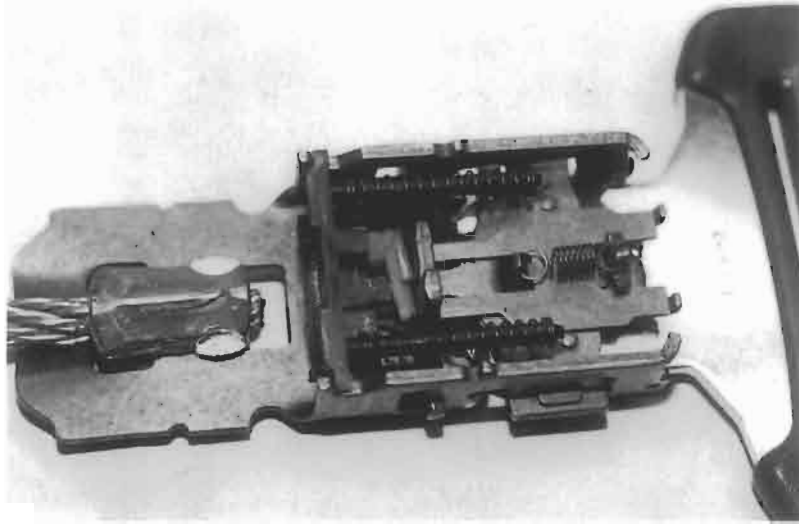
Fig. 6. 'Mode two' failure, showing a fragment of the release button lodged just to the left of the locking slider. In this case, the fragment keeps the locking slider from sliding to the unlocked position when the release button (not shown) is pressed.

3. Degradation and failure of the release button

3.1. Characterization of the button material

Once the three failure modes described above had been discovered, attention was focused on the degradation and eventual fracture of the release button. SEM studies of a fractured surface of the seatbelt, solubility tests, and a flame test of the seatbelt button revealed that the release button in question is injection molded from ABS (acrylonitrile–butadiene–styrene) copolymer. While there are numerous different grades of ABS, all consist of a continuous styrene–acrylonitrile (SAN) copolymer phase throughout which a discontinuous butadiene phase is dispersed. The rubbery butadiene phase serves to toughen the relatively brittle SAN phase. The SAN phase is chemically bonded to the butadiene phase by a graft copolymerization mechanism. The greater the amount of butadiene phase, the tougher the ABS material will be. The tradeoffs for this increased toughness are decreased strength and modulus of elasticity, and a potential reduction in environmental resistance.

Figure 8 shows a release button along with several fragments. This figure also shows (at left) a release button that is still intact. Both buttons came from Honda Accords, although from different model years, which accounts for small differences in the designs. A closeup of the fracture surface of the button from Fig. 8 is shown in Fig. 9.

A scanning electron micrograph of a fracture surface of a degraded release button reveals a two phase material, as shown in Fig. 10. The small round holes on the fracture surface are typical of a rubber-modified polymer such as ABS. The material was further characterized as ABS through solubility and flame tests, using techniques described in [3]. Release button shavings placed in four different solvents (ethanol, acetone, dichloromethane, and benzene) behaved very similarly to

Fig. 7. 'Mode three' failure. In this case the button fragment (not shown) does not allow the locking slider to slide all the way to the latched position (compare to Fig. 3) giving the appearance that the buckle is latched when it is not.
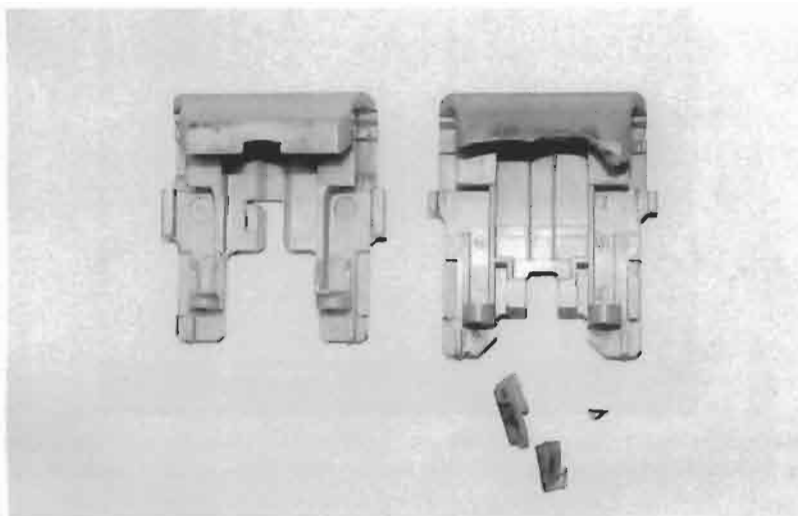

Fig. 8. Two release buttons from Honda Accords. The button at right has degraded and fractured, while the one at left is in better condition.

shavings of known ABS placed in the same solvents. Similarly, when chips taken from release buttons and from known samples of ABS were burned, they both showed similar flame characteristics (sustained ignition, orange-yellow flames, black sooty smoke). As with the solubility tests, these characteristics also match with those tabulated for ABS in [3]. The flame and solubility tests,
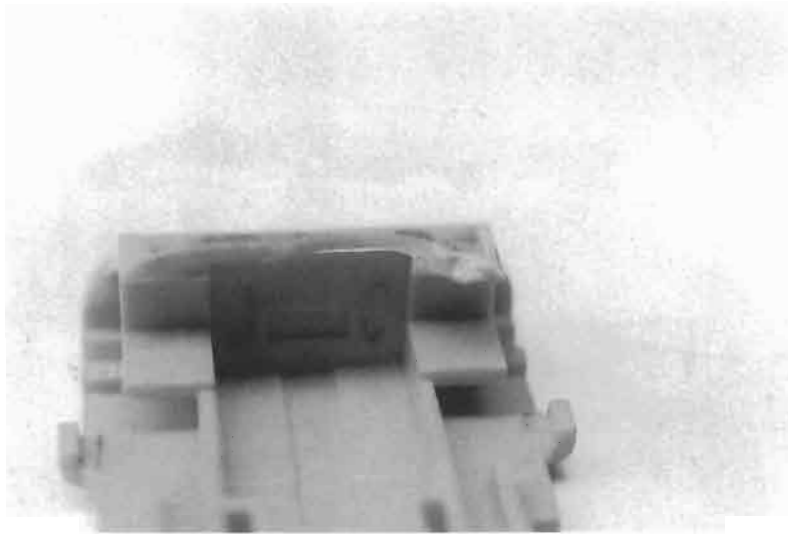
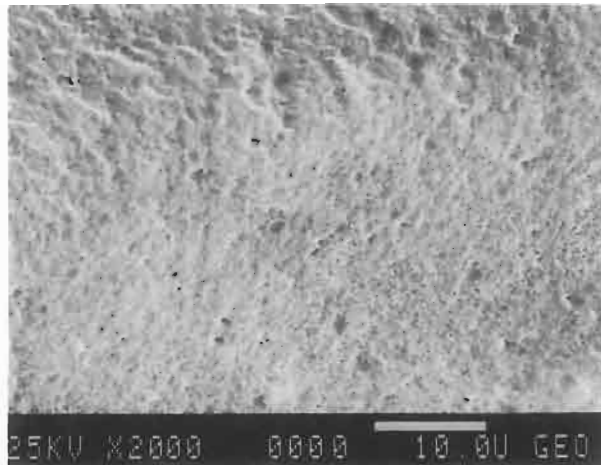Fig. 9. Close up of the fracture surface of the button on the right in Fig. 8.

Fig. 10. Scanning electron micrograph of a fracture surface of a degraded release button. The presence of a discontinuous phase (typical of a rubber-modified polymer) is indicated by the round holes on the fracture surface.

combined with the SEM appearance of the fracture surface, led to the conclusion that the release buttons are molded from ABS.

3.2. Environmental degradation of the ABS release buttons

Figure 11 shows a closeup of the 'Press' surface of a release button. The surface of the button has faded (become discolored) and is criss-crossed with crazing. Further magnification, as shown in Figs 12 and 13, confirms the presence of a network of crazing cracks extending into the button.

Fig. 11. 'Press' surface of release button showing discoloration and crazing.

Fig. 12. Light microscope closeup of the button in Fig. 11 showing crazing.

As noted earlier, the presence of the discontinuous rubber phase in ABS is necessary in order to improve the impact resistance of the otherwise brittle SAN matrix. However, the polybutadiene phase in ABS also reduces its environmental resistance for two reasons. First, the backbone of the butadiene chain contains unsaturated C=C bonds, which have the effect of destabilizing adjacent bonds. This makes those bonds more susceptible to attack by, for example, dissolved oxygen. Second, the polybutadiene phase has a very low glass transition temperature (the T_g for polybutadiene is $-90°C$). This is why this phase improves the toughness of the glassy SAN phase,
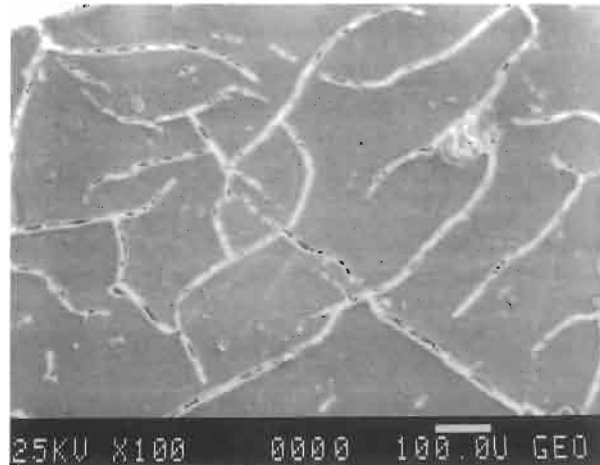
Fig. 13. Scanning electron micrograph of the button in Fig. 12. The crazing cracks are seen to extend through the surface of the material.

since the butadiene phase is rubbery throughout the range of usage temperatures for an automobile interior (approximately $-40°C$ to $+75°C$). However, polymers are much more susceptible to environmental degradation above T_g since the diffusion of, for example, dissolved oxygen is so much more rapid above T_g.

The operating conditions inside an automobile are relatively harsh for many polymers, including ABS. Because of solar loads, the temperature inside a parked car with its windows closed can reach 75°C. Visible and ultraviolet radiation from the sun can also degrade most of the plastic components inside a car, including the seat belt release buttons. Oxygen and moisture are of course present as well.

The failure of the release buttons involved a combination of (1) repeated, low-level impact damage and (2) degradation of the material due to the combined effects of radiation and oxidation (photo-oxidative degradation). Because of the design of the seat belt receptacle in question, it is relatively easy for the release button to be subjected to impact loads from the clasp since there is no barrier between the button and the entrance for the clasp. These impacts result when the seat belt wearer is slightly off with his or her aim when attempting to insert the clasp in the receptacle, thus striking a blow to the receptacle housing and/or the release button. Evidence of impact damage to the release button and receptacle housing is visible in Fig. 1.

3.3. Photo-oxidative degradation of ABS

'Weathering' of polymers refers to all the possible effects that may occur when polymers are exposed to the outdoor environment (which is taken here to include the interior of an automobile). The effects of weathering on polymers can include discoloration, loss of surface gloss, surface chalking, and reductions in mechanical properties such as tensile and impact strength.

The molecular mechanism for photo-oxidation of ABS has been studied and is described by Grassie and Scott [4]. Their description details how the combined effects of radiation and oxygen

can sever the covalent bond between a polybutadiene molecule (rubber phase) and the styrene–acrylonitrile copolymer matrix. The various chemical reactions involve the creation of free radicals and the incorporation of oxygen into the polymer molecules. The reactions also tend to be autocatalytic—once they start, they feed on themselves and tend to accelerate. In addition, high temperatures tend to increase the rates of the various degradation reactions.

When the loss of the chemical bond between the rubber phase and the matrix phase becomes widespread, the rubber phase loses its ability to absorb impact energy for the material as a whole. That is, once the rubber phase becomes disbonded from the matrix, the impact properties of ABS are, for all practical purposes, reduced to those of the brittle SAN matrix.

Most polymers are treated to prevent or slow the effects of photo-oxidation and other forms of degradation—both in service and during fabrication. Chemicals known as anti-oxidants and stabilizers are blended into polymers in order to slow the creation of free radicals and the incorporation of oxygen into polymer molecules and/or to absorb damaging radiation. Some of the rather complex mechanisms by which these additives work are described by Grassie and Scott [5].

Like most polymers, ABS can and usually does contain antioxidants and stabilizers designed to retard the effects of photo-oxidation. However, the presence of the rubbery phase (for the reasons noted earlier), still tends to make ABS more susceptible to environmental degradation than most non-rubber-modified polymers. It is possible that the subject series of failures were exacerbated by improper stabilization of random batches of ABS release buttons installed on the subject cars. This possibility was not investigated as a part of this report.

4. Short- and long-term industry solutions

4.1. Short-term solution

As noted earlier, no formal automobile recalls resulted in the U.S. from this series of failures. Instead, automakers (such as Honda in the letter quoted earlier), instituted a voluntary recall in which car owners could take their vehicles to authorized dealers for inspection and repair (free of charge). One of the authors owned an affected vehicle (a 1989 Honda Accord). When this vehicle was returned to the dealer as part of the voluntary recall, a Honda mechanic made a very brief visual inspection of the front seat belt receptacles. Noting no breakage of the release buttons, the mechanic quickly installed a small plastic impact guard (Fig. 14) on each seat belt receptacle. The mechanic noted that, had he seen evidence of severe degradation of the release buttons, he would have replaced the seat belt receptacles from the floorboards up with new assemblies. Having the discretion to simply add the impact guard instead of replacing the entire assembly saves Honda roughly $100 per vehicle in parts and labor. As can be seen in Fig. 14, the impact guard is unlikely to be completely effective in eliminating impact damage to the seat belt release buttons.

4.2. Long-term solution

The basic design of many Takata seat belt receptacles remains very similar to those that are the subject of this report. However, it appears that ABS has been phased out and replaced by more environmentally resistant polymers such as various acetal copolymers [6].

Fig. 14. Short-term solution to the seat belt failure problem. The plastic guard installed on the seat belt receptacle is intended to reduce impact damage to the release button.

These acetal copolymers are somewhat more expensive than the ABS materials they replace. The manufacturing cost of the ABS release buttons might conservatively be estimated at U.S. $0.05, about 50% of which would be material costs [7]. By using the less expensive ABS material on the affected vehicles, automakers may have saved a few pennies per car, but it very nearly cost them a billion dollars in the long run.

5. Conclusions

1. The subject failures resulted from a classic 'failure chain' of events and conditions. These included a polymer susceptible to environmental degradation (ABS), the presence of repeated, low energy impacts over a period, perhaps, of years, a hostile environment that included temperatures up to 75°C, ultraviolet radiation, oxygen, and a design that allowed fragments of the release button to interfere with the function of the release mechanism. Had any one of the elements in this failure chain been absent, it is likely that the widespread failures of the subject seat belts would never have taken place.
2. Each of the three reported modes of failure can be explained in terms of a specific location within the seat belt mechanism in which a fragment of the release button becomes lodged.
3. The short-term solution to the problem agreed upon by industry and government (that is, the installation of the plastic guard) was economical, if less than satisfying from a safety standpoint.
4. The longer-term solution arrived at (the specification of a more environmentally resistant material) breaks the failure chain and appears to be satisfactory.
5. This seat belt release button, with a manufacturing cost of approximately $0.05, nearly resulted in the most expensive automobile recall in industry history. Thus, the failure of even the humblest of parts can have grave consequences.

References

[1] Business Week, June 5, 1995. p. 37.

[2] Consumer Reports 1995;60(7):447.

[3] Braun D. Simple methods for identification of plastics. 3rd ed. Hanser Publisher, 1996. pp. 35–54.

[4] Grassie N, Scott G. Polymer degradation and stabilisation. Cambridge University Press, 1985. p. 94.

[5] Ibid, p. 119.

[6] Advanced Materials and Processes 1997;151(6):19.

[7] Busch JV. Technical cost modeling of plastic fabrication processes. Ph.D. dissertation, Massachusetts Institute of Technology, 1987. p. 17.

Oxidation failure of radiant heater tubes

K.B. Yoon[a],* D.G. Jeong[b]

[a] *Department of Mechanical Engineering, Chung-Ang University, 221 Huksuk, Dongjak, Seoul 156-756, Korea*
[b] *Samsung Heavy Industries Co., 40-1 Woongnam, Changwon, Kyungnam 641-290, Korea*

Abstract

A radiant heater tube with a burner installed inside designed to transfer the heat generated by the burner from the outside of the tube by radiation. Accordingly, the tube metal must endure a high temperature of approximately 900–1000°C. The radiant tube was manufactured by centrifugal casting with high Ni–Cr alloy steel.

In this study, a failure analysis of a radiant heater tube was performed by careful visual inspection of the tube cracks, metallographic observation of the near crack region and chemical analysis of tube metal and oxide scales. It is argued that the principal cause of the cracking is progressive oxidation of the tube metal beneath cracked thick oxide scales attached to the inside of the tube. The oxide scales are generated by abnormally high operating temperatures which can be verified by the aged microstructure and internal void formation. © 1999 Elsevier Science Ltd. All rights reserved.

*Keywords:* Cracks; Overheating; Oxidation; Process-plant failures.

1. Introduction

For heat treatment of moving steel plates in a hot rolling process of an iron foundry, the plates are usually allowed to pass between two radiant heater tube rows that are located above and below the pathway. The plates are heated by radiation from the radiant heater tubes with inside burners. Since the burner is located inside the tube and hot flue gas pass through the tube, the radiant tubes are continuously operated at high temperature which causes materials degradation due to thermal aging and corrosion/erosion problems due to the combustion gas. As a result, thinning of the tube and crack initiation occur frequently [1] and leaking of the gas through the crack may cause serious surface finish problems to the rolled plate product as well as operating problems. Since the operating temperature of the heater tubes is expected to be well above 900°C, they are generally fabricated by centrifugal casting with HK or HP steels having high contents of Ni and Cr.

In this study, a failure analysis of locally fabricated radiant heater tubes was performed. A

---

* Corresponding author.
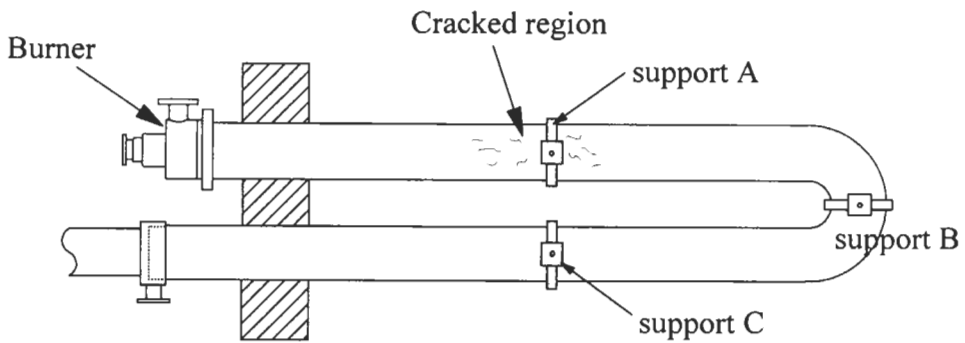
a) Top View
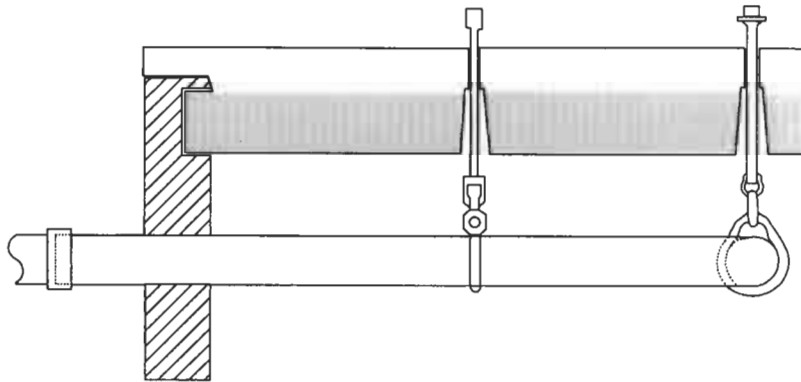
b) Side View

Fig. 1. Schematic illustration of the U-type radiant heater tube structure.

metallographic observation near the crack region of a failed tube was made. Also, a chemical composition analysis of the oxide scales and the base tube metal in the vicinity of the crack was carried out. Using these results, the cracking mechanism was found. Methods of preventing the tube cracking problem are also discussed.

2. Tests and results

2.1. Material and specimens

The arrangement of the U-type radiant heater tube is schematically shown in Fig. 1. At one end of the tube, a burner is installed inside the tube. Flue gas passes through the tube and is exhausted
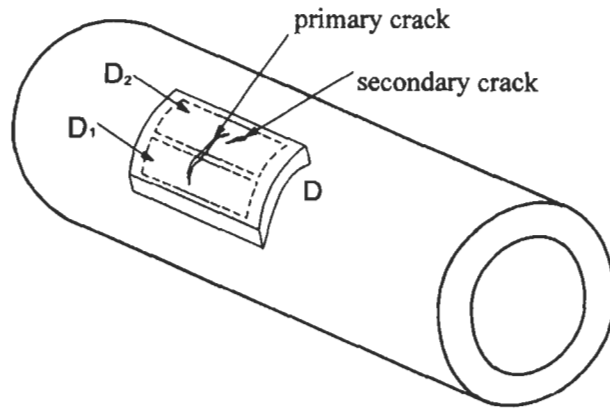
Fig. 2. Samples of a cracked radiant tube for failure analysis.

through the other end of the tube. The tubes are hung from the ceiling of the furnace and laid at the bottom of the furnace. Steel plates moving between the tube rows are heat-treated by radiated heat from the tubes. As shown in the figure, the U-type tube is supported by three hangers. Cracking problems have been frequently reported near the locations where supporting hanger A, which is close to the burner, is in contact with the tube. Cracks initiated at the inside of the tube and propagated to the outside inducing internal combustion gas to leak and cause problems to the heat-treated rolled plates. The cracking direction was random and not related to the principal stress direction. From this observation it can be argued that stresses generated in the tube due to internal pressure or due to thermal gradients are not the major cause of cracking. Hence, for the analysis of the cause of failure of this case, a metallographic investigation of the failed component seems more appropriate than stress analysis.

Cracked specimen D was sampled from the cracked area around the supporting guide A as shown in Fig. 2 for metallographic analysis. Specimen D contained a big primary crack and several secondary cracks which were smaller than the primary crack. Considerable wall thinning was observed at the inside of the cracked tube. Since it is known that a failure analysis with a secondary crack (which usually shows the initial stage of cracking) is preferred to that with a primary crack (which shows almost the final stage of the failure), a failure analysis on the secondary crack which is 8–9 mm long was conducted. The failed radiant tube was fabricated locally by centrifugal casting with 25 Cr–20 Ni steel. The chemical composition of the tested sample is shown in Table 1 with the standard composition.

Table 1
Chemical composition of the 25 Cr–20 Ni radiant tube steel (in wt%)

Elements	C	Si	Mn	P	S	Ni	Cr	Mo	Fe
Test sample	0.43	1.83	—	0.025	0.008	22.28	22.65	0.068	bal.
Manufacturing standard	0.20–0.60	<2.00	<2.00	<0.04	<0.04	18.00–22.00	24.00–28.00	<0.50	bal.

2.2. Visual inspection

To make a detailed observation of the cracked specimen, specimen D was cut in a direction perpendicular to the primary crack as depicted in Fig. 2, generating two small sub-specimens, D_1 and D_2. With the specimen D_1 the primary crack was opened to fracture with intention of observing the crack surface. The crack tip region of the specimen D_2 which was not opened was observed by a microscope. Figure 3(a) and (b) show the inner and outer surfaces of the other specimen D_2.

All other failed tube samples as well as specimen D showed many locally thinned areas at the inside of the tubes. As observed from Fig. 3(b), which shows the inner surface of the specimen D_2, thinning was fairly localized and occurred irregularly. It should be noted that thinning did not occur gradually with distance from the burner. From this observation, we can rule out the possibility of erosion damage by solid particles included in the burner combustion gas as the main cause of tube thinning. Hence, it may be predicted that local oxidation or local corrosion is the main causes of thinning.

A thick oxide scale indicated by an arrow in Fig. 3(b) was attached at the locally thinned area. Similar oxide scales were also observed in a number of local oxidation pits. Most of the oxide scales contain several cracks formed in random directions. The oxide scale in Fig. 3(b) is enlarged in Fig. 4. Cracking of the scale must be mainly due to the difference in thermal expansion coefficient between the oxide scale and the tube metal on which the scale is attached.

Generally at the initial stage of oxidation, an oxide film forms on the metal to prevent further oxidation. Therefore, when a stabilized oxide film is formed on the surface, the resistance to oxidation under high temperature conditions is increased. As for the radiant tube of this failure analysis, the high content (25%) of Cr enables the formation of a Cr_2O_3 film that increases resistance to high temperature oxidation. If this oxide film is removed, the base metal of the tube will undergo repeated oxidation which results in continuous thickness reduction [2]. When cracking occurs in the oxide scale, as illustrated in Fig. 4, the crack tip area loses the protective effect of the oxide film and the base metal beneath the crack tip will be repeatedly oxidised. As a result, a sharp oxide spike will be gradually formed in the base metal under the oxidation layer where oxide cracking occurred. Observation of the opened fracture surface of specimen D_1 showed an oxide layer extending to the crack tip.

2.3. Metallographic observation

To confirm the forementioned crack initiation mechanism, a small metallographic sample was taken from the location of a local oxidation pit of specimen D_2 where the oxide scale is attached, as shown in Fig. 4. It was mounted and the scale was ground out until the tube metal right beneath the cracked oxide scale appeared. An observation was made to see if any tube metal cracking occurred at the location beneath the oxide scale crack. The specimen preparation procedure is shown in Fig. 5. From this observation, a small crack of 4-mm length was found in the base metal right beneath the oxide scale and this crack was oriented in the same direction as the crack in the oxide scale. Each crack tip area of the tube metal was observed by a scanning electron microscope and is shown in Fig. 6(a) and (b). The crack tip was not sharp but looked like a blunt notch. Also, Fig. 6(b) shows that the matching crack surfaces are separated from one another. These two observations confirm that the crack was not initiated by mechanical loading such as fatigue load
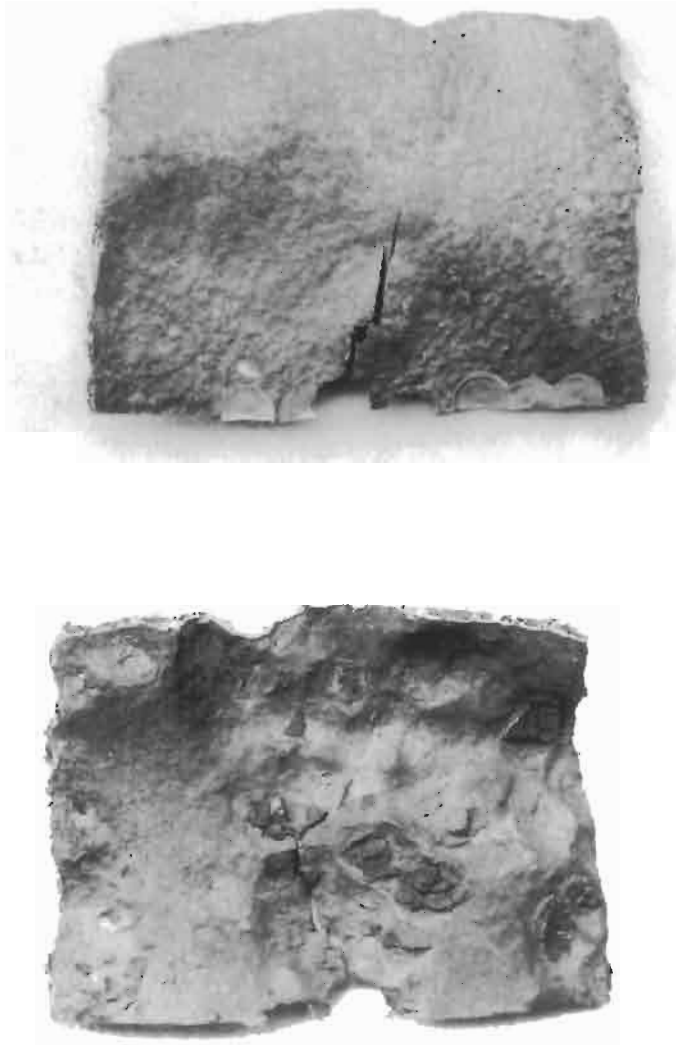
Fig. 3. Appearance of internal and external surfaces of the cracked tube specimen D_2.

but rather by repeated oxidation. Hence, the crack initiation mechanism assumed in the previous section is confirmed.

The primary crack in the specimen D_1 which was opened to fracture is illustrated in Fig. 7. The top line of the specimen represents a fracture surface of the primary crack where a deep oxide layer is present. Beneath the primary crack, the formation of a secondary crack with a shallow oxide layer is observed. It is evident that the characteristics of the crack are similar to the crack shown
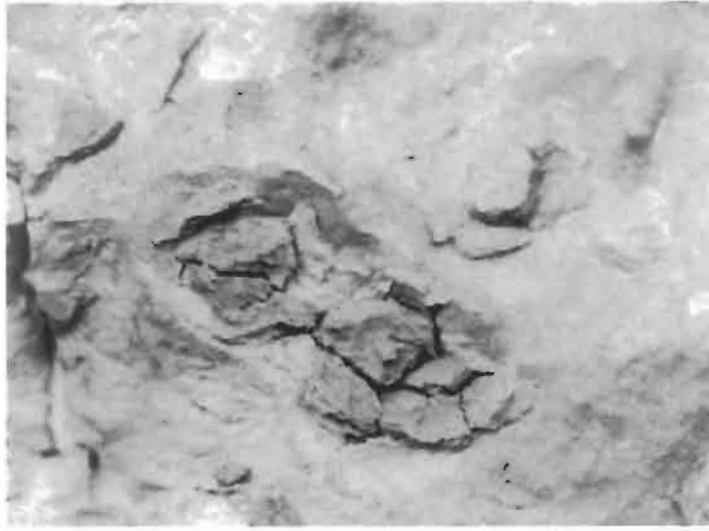
Fig. 4. Enlarged view of a cracked oxide scale located in thinned area.
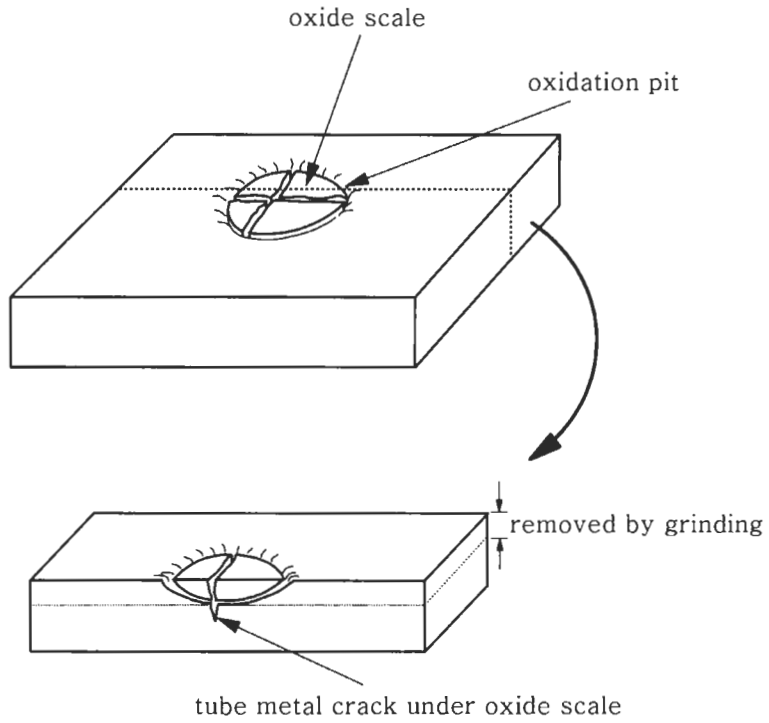
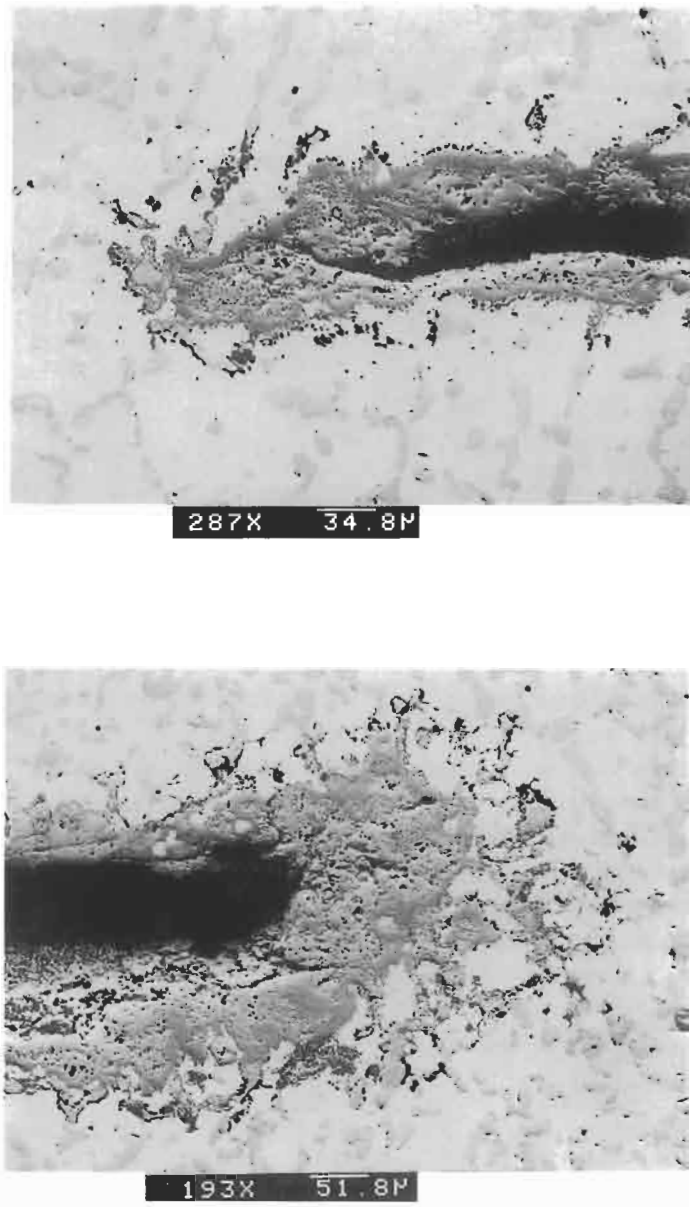Fig. 5. Preparation of metallographic sample for studying crack initiation mechanism.

Fig. 6. Crack tip morphology.

in Fig. 6. Thus, it can be argued that the main cause for the formation of cracks in the tube is oxidation.

2.4. Chemical analysis

To investigate the cause of the severe oxidation, a chemical analysis was performed on tube metal and oxide scale. Composition analysis was carried out both on the sound part of the tube
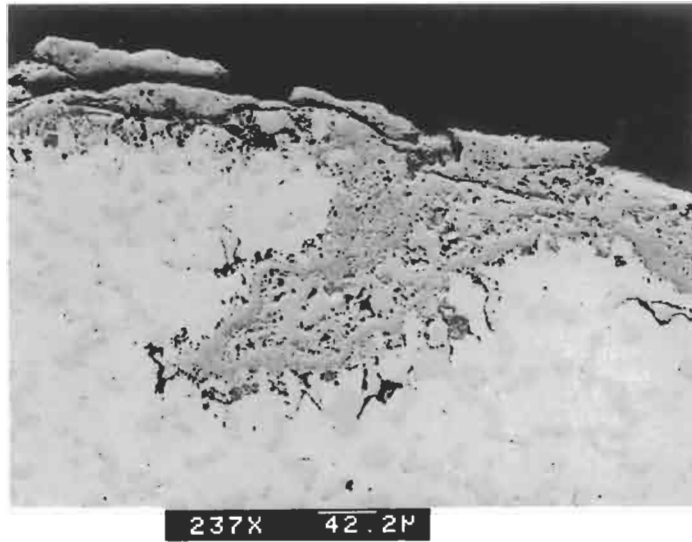
Fig. 7. Oxide spike under the fractured surface of primary crack.

which was located far from the oxide layer and on the tube metal in the vicinity of a primary crack whose composition may be affected by oxide scale formation. These two analysis results were compared, to predict the cause of oxidation. Also, a piece of oxide scale was detached from the tube's interior surface and analyzed. Compositional analysis of the oxide layer at the crack tip was also conducted. EDAX analysis in the electron microscope was used for composition analysis and the results are summarized in Table 2. It is shown that the Cr content of the metal right beneath the primary crack decreased compared to the sound part of the tube. This is due to the formation of Cr_2O_3 at the crack surface resulting in a decrease of the Cr content in the neighboring base metal. Analysis results of three oxide scales (two pieces detached from different locations and one attached at the crack tip) showed that the Ni content did not vary while the Cr content increased and the Fe content decreased considerably. Thus, it can be predicted that Cr_2O_3 is the main

Table 2
EDAX analysis results of the radiant tube at several locations (in wt%)

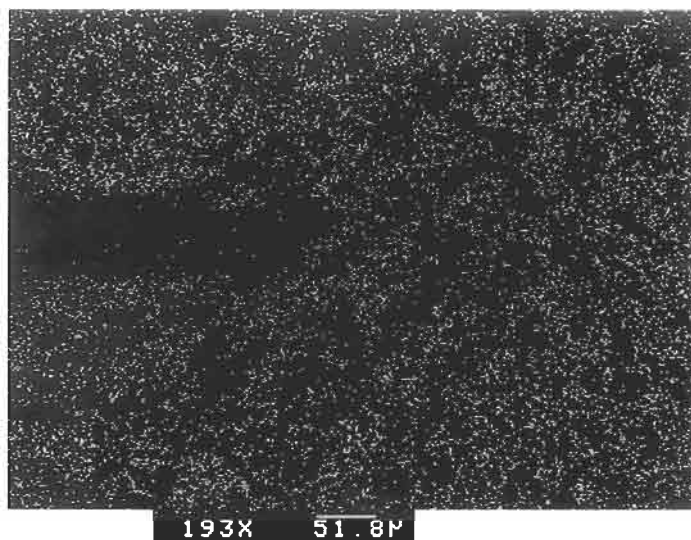| Locations	Composition						
	Ni	Cr	Fe	Si	Mo	S	V
Sound tube metal far from the cracked region	18.67	30.16	49.74	1.43	---	—	—
Tube metal near to the cracked region	19.56	27.34	51.57	1.53	---	—	—
Crack tip oxide scale	17.19	33.52	44.86	2.44	1.21	0.47	0.30
Detached oxide scale 1	20.22	31.24	44.84	1.41	1.53	0.54	0.22
Detached oxide scale 2	18.05	41.24	35.48	3.06	1.33	0.61	0.22

Fig. 8. Ni distribution map of crack tip region (same location as shown in Fig. 6(b))

oxidation product in the oxide scale. Other minor elements appeared in the scales such as 0.4–0.6% of S and 0.2–0.3% of V apparently produced by contact with combustion gas. A high content of S may generate a corrosion problem; vanadium usually forms V_2O_5, which, together with high velocity combustion gas, may cause erosion problems. In this tube failure, however, S and V seemed not to contribute to the failure.

Figure 8 is a composition map obtained by EDAX that shows the Ni distribution at the crack tip region of Fig. 6(b). This picture shows that the oxidation layer is not correlated with Ni. Figure 9 shows the Cr distribution at the same location. Focusing on the Cr concentration of the oxide scale in Fig. 9, it is evident that the oxide layer at the crack tip is of Cr oxide product.

3. Discussion

Abnormal oxidation problems of high temperature steels are generally caused by improper operating temperature exceeding the recommended temperature range. The manufacturing process of the radiant tube of this study is similar to a well-known centrifugally-cast HK steel, but the chemical composition of the tube is different from that of the HK steel since Si was added to the tube metal. If we consider the composition only, which is Cr = 23–26%, Ni = 19–22%, C = 0.25%, Si = 1.5–3.0%, and Fe = balance, it is a typical composition of 314 stainless steel (UNS31400 steel). This material is known to have excellent high temperature oxidation resistance by forming Cr_2O_3 protective oxide film. However, if the service temperature exceeds 1000°C, the stabilized Cr_2O_3 film becomes unstable and transforms into volatile CrO_3 losing its protective effect. Therefore, the current radiant tube material should be used in a temperature range which does not exceed 1000°C, to prevent abnormal oxidation. Also, it was reported that for high Cr–Ni
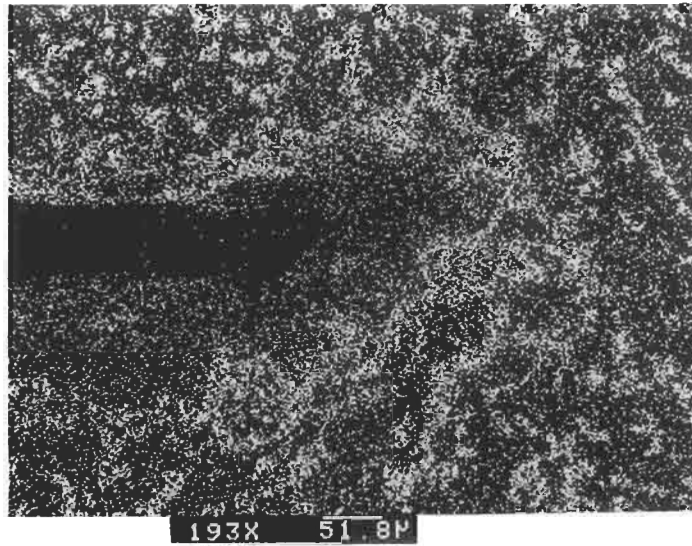
Fig. 9. Cr distribution map of crack tip region (same location as shown in Fig. 6(b))

steel, excessive oxidation can occur in a short period if the operation temperature is higher than 1090°C [4].

In order to know whether the failed radiant tubes had been in service below or above 1000 C, the degradation level of the microstructure due to thermal aging was assessed. In most of the cases, the service temperature of the tube can be predicted by comparing the microstructure with that under known service conditions. Figure 10 shows a typical microstructure of the failed tube.
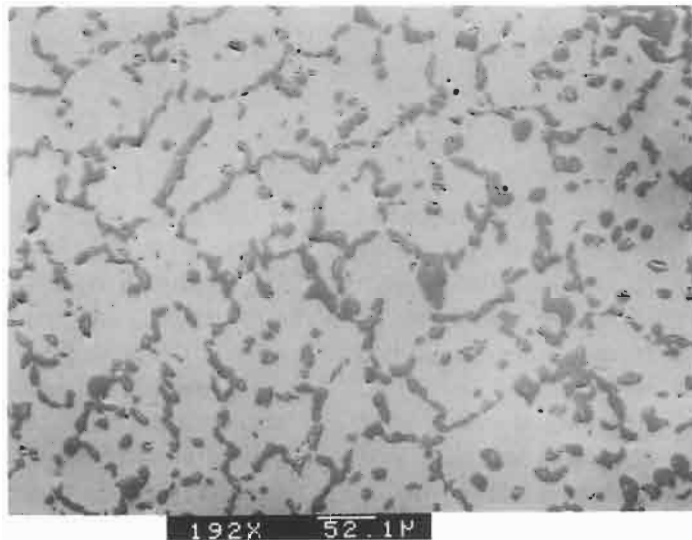

Fig. 10. Microstructure of uncracked region of the tested radiant tube.
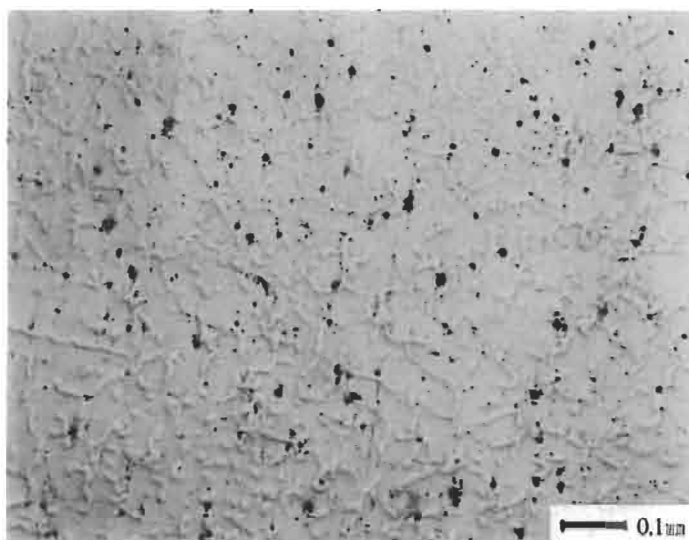
Fig. 11. Microstructure of cracked region of the tested radiant tube showing void formation

Referring to the known reference microstructures of HK tubes degraded at high temperature [3], the microstructure shown in Fig. 10 corresponds to the microstructure similar to one aged at 950–1000°C for 60,000 h. Since the service period of the failed tube was only 15,000 h which is much less than the 60,000 h of the corresponding microstructure, it can be predicted that the service temperature of the tube was above 1000°C. Figure 11 shows a microstructure near the cracked area which shows internal void formation. Voids of this kind were reported to be formed when the service temperature reaches 1090–1230°C in the case of Ni–Cr steel [4]. Hence, it can be argued that the local metal temperature during the service must go up to this high temperature. This overheating can be induced by touching of the flame to the tubes near the supporting guide A in Fig. 1. Therefore, to prevent radiant tube failures methods should be sought to lower the tube metal temperature below 1000°C, particularly in the vicinity of supporting guide A. Modification of burner tips or improving combustion systems can be considered.

4. Conclusions

By conducting a failure analysis on the cracked radiant heater tubes used in a high temperature furnace, the following conclusions are derived.

The radiant heater tube which was centrifugally-cast with the same chemical composition as a typical HK steel except additional Si could be used without problems if it is operated at a temperature less than 1000°C so a protective Cr_2O_3 oxidation film forms. However, as the operating temperature exceeded 1000–1100°C, the stabilized Cr_2O_3 transformed into volatile CrO_3 and abnormal oxidation or rapid oxidation occurred. The failed tube of the current study must have been used at or above the recommended temperature range and as a result, locally thinned areas were formed by excessive oxidation. Some of the oxidation pits were filled with oxide scales formed

342

by rapid oxidation. This thick oxide scale was usually cracked because the heat expansion coefficient of the oxide was different from that of the tube metal on which the scale is attached. Through the opening of the oxide crack, fresh tube metal which was located beneath the oxide crack tip suffered repeated oxidation resulting in small cracks initiating in the tube metal. Tube failure finally occurred as a result of propagation of these small cracks to the outer surface of the tube. The failure could be prevented by maintaining the temperature of the tube at the flame side of the burner, that is, in the vicinity of supporting guide A in Fig. 1, below 1000°C by improving the existing combustion system or by modifying the burner tips.

Acknowledgements

References

[1] Williamson J, Shipley M. Life assessment and monitoring of furnace heaters, improving reliability in petroleum refineries and chemical and natural gas plants. Houston, TX, USA, November 9–12, 1992.
[2] Walter M, Schutze M, Rahmel A. Oxidation of Metals, 1993;40:37.
[3] Life prediction of tubes for steam reformer and cracker. Document for Information Document No. 85, KHK, 1983.
[4] Lai GY. High temperature corrosion of engineering alloy, ASM International, 1990.

Environmentally assisted cracking

SUSTAINED LOAD CRACK GROWTH LEADING TO FAILURE IN ALUMINIUM GAS CYLINDERS IN TRAFFIC

J. W. H. PRICE*, R. N. IBRAHIM and D. ISCHENKO

Mechanical Engineering Department, Monash University, 900 Dandenong Road, East Caulfield,
Victoria 3145, Australia

Abstract—Some common portable aluminium gas cylinders have shown a liability to develop cracking. This cracking has in some cases led to leaks and on occasions to violent and sometimes fatal failures. There are a number of features of this cracking which have not been properly explained. Previous modelling of the growth of these cracks under sustained load has been developed from specimen testing. As is shown in this paper these data produce results which appear to produce values of crack growth which are too slow by a factor of the order of 10^8 to explain the observed phenomenon. It also appears that crack growth can be rapid even in cylinders with low levels of lead. This paper presents a numerical simulation of the growth of these defects based on the local stresses in the vicinity of the crack edge. This information is related to cracks actually found in cylinders which have leaked or failed in service. From this procedure an equation for the crack growth rate is developed. This also leads to an explanation as to why "leak before break" is not always observed in these cylinders. © 1997 Elsevier Science Ltd.

1. INTRODUCTION

Portable aluminium cylinders are in common use in the world for purposes such as self-contained underwater breathing apparatus (SCUBA), respirators for fire and medical use and other uses. In Australia about 1,700,000 of these cylinders are in circulation, and large numbers exist in all developed countries. There has been a history of cracking developing in some of these cylinders in the position shown in Fig. 1.

1.1. *The nature of the cracking*

The cracking tends to grow from notches created during the forming process for the top end of the cylinders and is driven by stress not only from the pressure contained in the cylinder, but also residual stresses from their manufacture. Understanding the cracking and estimating the rate of cracking growth is an objective which has interested a number of researchers in order to achieve a basis for assessing acceptable defect sizes [1, 2].

The crack growth has in many quarters been stated to involve a phenomenon called solid metal induced embrittlement (SMIE) where crack growth is aided by surface diffusion of certain elements, the most important of which is lead. The cracks grow under constant load, so it is also described as "sustained load cracking". Since diffusion of elements is involved, there are some similarities to creep crack growth and this terminology has also been used. The fundamentals of this process are described elsewhere [2, 3].
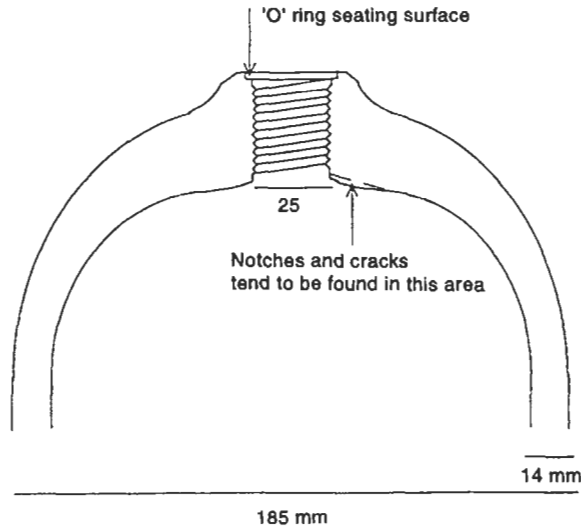
---

*Author to whom correspondence should be addressed.

Fig. 1. The top of an aluminium gas cylinder with the area of crack initiation and growth indicated.

1.2. *Failure experience*

In 1983, two fatal ruptures of hoop-wrapped aluminium cylinders occurred in the United States. A significant report made of those incidents at the time was prepared by Failure Analysis Associates [4]. This report considered and compared three categories of cylinders which were provided by the manufacturers. This and other work led to the identification of risk factors associated with the aluminium cylinders in traffic in the U.S. These were:

- cracking originating at the neck shoulder region as shown on Fig. 1;
- folds in the neck region; and
- lead levels of 100 ppm or higher in the aluminium alloy.

There have been recent incidents in the U.S., namely the death of a fire fighter filling a cylinder in 1993 [5] and an injury in a Miami dive shop in June 1994 [6].

In Australia, most cylinders in circulation are made locally. These cylinders do not have high lead contents and are not made with recycled scrap, which were two of the factors featured in the early U.S. studies. Nevertheless, there has been some failure experience with Australian cylinders, though no serious injuries. Poole [7] describes a cylinder made to Australian standards which failed catastrophically in 1994 in New Guinea during hydrotest in a shop.

One key area of protection of the public is a requirement that all cylinders be inspected regularly. For scuba tanks the frequency in Australia is annual; for other aluminium cylinders, the required frequency is four-yearly. This inspection is visual and carried out with lights and dental mirrors.

A number of testing stations in Australia have reported that a significant number of locally made cylinders experience cracking from the neck. The authors have themselves investigated a number of cracked cylinders. For some years of cylinder manufacture in the mid-1980s, the frequency of detection of cracking at the necks in 1995 was as high as 10% at some test stations. Because of the method of inspection, it is not clear how serious these detections are, and the cracking can often be shallow. Since 1995, all cylinders with visible cracking must be condemned.

The alloy in use in Australia and other countries was changed from 6351 in T6 temper to 6061 T6 during the last few years. The 6061 alloy is believed by the industry to have less susceptibility to cracking, though the authors have one cylinder in this alloy which has a crack in the neck area. Stark and Ibrahim [8] present data comparing the two grades that do not indicate a significant difference in either K_{1c} or crack growth rates.

2. EXAMINATION OF TWO SEVERELY CRACKED CYLINDERS

Among several defected cylinders and samples the authors have investigated two Australian made SCUBA cylinders which have large defects in them. Cylinder A leaked during filling and cylinder B failed catastrophically during hydrotest.

These cylinders do not conform to the model of failure as described by Failure Analysis Associates [4]. Although the origin of the cracking was in the same location on the neck as the U.S. experience, neither cylinder has significant neck folds and lead levels are below the limit of measurability using the standard spectral analysis test, that is, below 10 ppm.

2.1. *Cylinder A*

Cylinder A was made in 1983 and leaked during filling in 1994. In 1994 the Health and Safety Organisation (HSO) in Victoria withdrew an aluminium cylinder from traffic and provided it to the authors for investigation. This cylinder exhibited cracking so large as to cause a leak, making it impossible to fill. There is a second defect of almost the same size almost opposite the leaking crack (see Fig. 2). The cylinder is of 8.65 kg water capacity with a test pressure of 32.4 MPa, manufactured in August 1983. The leaking defect penetrated through to the upper surface of the cylinder outside the O-ring contact surface and thus caused the leak.

The fracture surfaces have been examined under scanning electron microscope as reported in Price *et al.* [9]. Most of the defect surface exhibits the features observed before (for example by Lewandowski *et al.*) and thus probably has the SMIE growth mechanism. However there is evidence of a defect about 3 mm deep by 15 mm long at the neck shoulder which has a different appearance and is probably a pre-existing defect from which the whole defect grew.

2.2. *Cylinder B*

The other specimen is part of the cylinder which failed in New Guinea. Discussed by Poole [7], this was made in August 1987 but otherwise has similar specifications to cylinder A. This cylinder failed catastrophically during hydrotest in New Guinea on 13 February 1994 and was inside a water-filled concrete tank which also burst. The failure occurred in four places around the neck and the
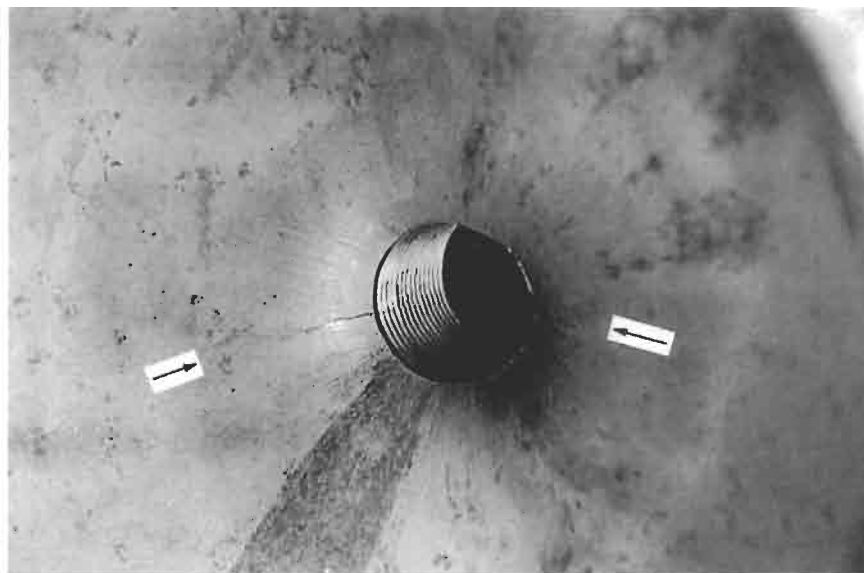

Fig. 2. Inside the top of cylinder A. Two large cracks almost opposite each other are marked. This specimen has been broken open and crack growth was found to proceed under the surface further than detectable using dye penetrant on the surface. The defect appearance conforms to the intergranular growth mechanism.
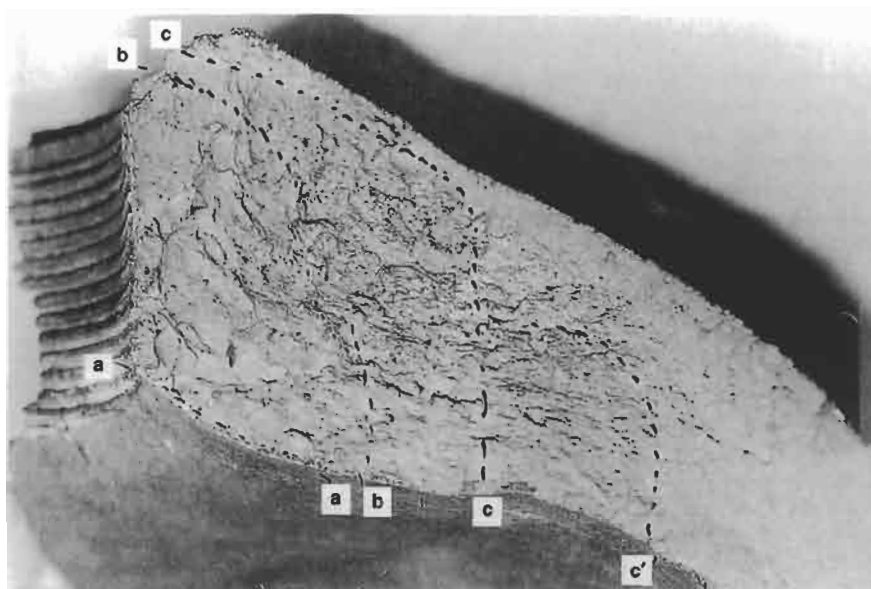
Fig. 3. The fracture surface of one of the four fractures of cylinder B. The photograph has been marked to highlight beachmarks caused either by damage during hydrotests of the cylinder or indicating changes to the crack growth mechanism. Some growth stages might leave no clear beachmark.

a   Area of different morphology indicating initial defect.
a–b   Area of growth which is mainly intergranular which is consistent with SMIE. Note that in this
                region some grains are very large because of recrystallisation during the heat treatment cycle
b–c, c–c'   Faster area of growth, plastic areas mixed with SMIE.
After c, c'   Plastic rupture, surface approaches 45° to other fracture plane.

bottle broke into two. Figure 3 shows one of the cracks in the neck region. It appears that there is a region of quite different crack growth prior to the final failure which is indicated by regions of 45° shear. There are at least two visible beach marks, indicating crack growth stopped for a time, on this specimen.

The characteristics of the growth observed by examining beachmarks in both the specimens indicate fairly stable growth for a time moving mainly up the threaded portion but then there is a tendency to move more quickly without penetrating the outer surface with some growth totally interior to the cylinder.

3. MODELS OF CRACK GROWTH

3.1. *Existing means of calculation of crack growth rate*

Crack propagation due to SMIE in small specimens under different imposed K_1 values has been studied previously by Ibrahim [1]. One set of specimens was cut from aluminium ingots with an assay of 100 ppm Pb. The lowest value of K_1 used for this series of tests was 13 MPa $\sqrt{m}$. The following equation was determined for crack growth rate in mm/h:

$$\log_{10}(da/dt) = 0.234K_1 - 7.719. \tag{1}$$

Ibrahim and Stark [10] present additional studies on some specimens cut from Australian pressure vessels and tested at room temperature. The alloys used in these gas cylinders had very low levels of lead present, probably less than 10 ppm. The growth was much slower and the equation derived for crack growth rate in mm/h was

$$\log_{10}(da/dt) = 0.20164K_1 - 8.889. \tag{2}$$

The prediction is of limited validity for K_I less than $18\,\mathrm{MPa}\sqrt{m}$, since no failures had occurred to specimens loaded to this level after 4 years.

Lewandowski et al. [2] give experimental data for alloy 6351 at tested at three temperatures in specially prepared ingots doped with controlled Pb additions. Some of the data from Lewandowski et al. is shown in Fig. 4. The data has been replotted by the authors on linear axes. The original papers give the data on log–log axes, a fact which may conceal what is an important piece of information; namely, that there appears to be a threshold to the growth curve. If this is assumed to be the case then the Lewandowski data is closely described by the linear Eqns (3) and (4).

Upper bound growth rate 100 ppm at 30°C (mm/year):

$$v = \mathrm{d}a/\mathrm{d}t = 13.4 \times (K_I - 11.5). \tag{3}$$

Upper bound growth rate 30 ppm at 30°C (mm/year):

$$v = \mathrm{d}a/\mathrm{d}t = 7.73 \times (K_I - 12.7). \tag{4}$$

3.2. Threshold K_I below which no growth occurs

One feature of these equations when written in this form is that they clearly imply that there is threshold value of K_I below which no growth occurs. This is $K_I = 11.5\,\mathrm{MPa}\sqrt{m}$ for Eqn (3) and $K_I = 12.7\,\mathrm{MPa}\sqrt{m}$ for Eqn (4). This is consistent with the fact that in experiments no growth on any test specimen has ever been recorded at K_I below $10\,\mathrm{MPa}\sqrt{m}$. This is a key issue in determining a realistic model for the growth in cylinders. It is a fact that, in traffic, many cylinders show no evidence of crack growth even after being in use for many years and containing folds at the neck.

3.3. Growth rates predicted from previous work

Equations (1) and (2) relate to room temperature whereas Eqns (3) and (4) relate to 30 °C. Price et al. [9] have reinterpreted the Lewandowski et al. data on the basis of temperature sensitivity data given in that paper to determine that the growth rates would be reduced by a factor of about 4 for temperatures of 18–20 °C. This means that at room temperature the first factors in the equations should be $7.73 \div 4 = 1.93$ and $13.4 \div 4 = 3.4$.

To determine the crack driving stress intensity, the stresses presented for an aluminium cylinder in Price et al. [11] were used. K_I was estimated made using British Standards PD 6493: 1990 Level 2 for a crack of 4 mm depth by 20 mm long in the position shown on Fig. 1. If there is no residual stress, K_I is $5.54\,\mathrm{MPa}\sqrt{m}$.
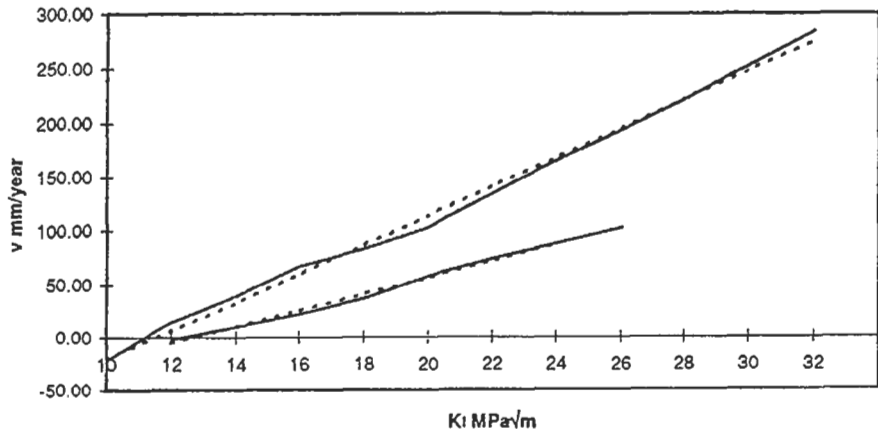

Fig. 4. Data from Lewandowski et al. [2] for crack growth at 30 °C (solid lines). The upper data is for 100 ppm Pb and the lower data is for 30 ppm. The data appear to obey a linear relationship (dashed lines). A linear relationship implies there is a threshold below which no growth occurs.

Residual stress is an important when remaining life is to be calculated. The maximum residual stress is estimated from the tempering regime. Temper T6 involves solution heat treating at 530 °C and quenching in water. The effect of this is to produce tension residual stress at the inside surface (Schröder [12]). The value of this stress could be as high as the yield stress of the material at room temperature in an unaged condition (called temper T4) and this is listed as 155 MPa in the material specification. In the case of temper T6, these residual stresses will be reduced, but not completely removed, by an artificial aging treatment for 18 h at 160 °C. Thus 155 MPa is an upper bound estimate of residual stress.

If a residual stress of 155 MPa is included (such as is proposed in Price *et al.* [1]) then $K_1 = 22.3$ MPa $\sqrt{m}$. The calculated growth rates predicted by Eqns (1) to (4) above are as shown in Table 1.

From Table 1 it is seen that Eqns (1) to (4) predict that with no residual stress there would be either no growth or virtually no growth.

If maximum residual stress is included, three of the predictions suggest growth could be rapid, though the prediction which relates specifically to specimens removed from Australian cylinders is still too slow. While residual stresses can produce a reasonable growth it must be remembered that residual stress can only effect growth for the first one or two millimetres. After that stage the residual stresses will quickly drop to the value predicted by the models with low residual stress.

Given the fact that in some cases in traffic the crack grows through the walls of the gas cylinder in a few years, the growth rates predicted by these equations are unsatisfactory. This is discussed below.

3.4. *Leak before break*

The argument to substantiate the case of leak before burst requires K_1 at the time of leak to be less than the material critical stress intensity factor, K_{Ic}. K_{Ic} was found during our testing to be 32 MPa $\sqrt{m}$ for Al 6351. The data presented in Table 2 indicates there is a margin between leak and burst for all the most extreme situations.

Given the above analysis it is not clear why some cylinders, such as cylinder B fail catastrophically without leaking, while some cylinders such as cylinder A leak prior to failure.

The principal explanation of this probably lies in the fact that the growth of the defect as observed does not occur in the regular fashion assumed in classical crack growth analysis. If crack growth can occur in a shape which does not lead to leak, but is nevertheless eventually large enough to produce rapid failure, then leak before break could occur. This possibility is suggested in both the cylinders which were examined and is discussed below.

Table 1. Growth rates predicted by various equations for various cracks and stresses

	Type of specimen used in tests to develop equations	Growth rate with zero residual stress	Growth rate with zero residual stress	Growth rate with 155 MPa residual stress
Defect size		4 mm deep 20 mm long	20 mm deep 45 mm long	4 mm deep 20 mm long
K_1		5.54 MPa $\sqrt{m}$	9.95 MPa $\sqrt{m}$	22.3 MPa $\sqrt{m}$
Equation		mm/year	mm/year	mm/year
(1)	Specimens with 100 ppm Pb	0.0033	0.036	28
(2)	From Australian cylinders (< 10 ppm Pb)	0.00015	0.0011	0.36
(3)	100 ppm Pb (adjusted to 20 °C)	(below threshold)	(below threshold)	36
(4)	30 ppm Pb (adjusted to 20 °C)	(below threshold)	(below threshold)	18.5

Table 2. Some estimates of K_I and the possible related growth rates

Description of defect and stresses	Upper bound K_I (MPa $\sqrt{m}$)
Notch without residual stress*	3.4
Notch with 72 MPa residual stress†	11.1
Notch with 155 MPa residual stress‡	22.3
Through thickness defect, no residual stress*	17.4

*Stresses due to internal pressure of 22.4 MPa are derived from our finite element analysis.
†Residual stress derived from experimental data from Ibrahim [1].
‡Residual stress derived from upper bound estimate described above.

4. LOCAL STRESS MODEL FOR CALCULATING CRACK GROWTH RATE

4.1. *Loading and growth model*

In the current work the crack shape was found at different stages of propagation under sustained load. The load used is that due to the maximum fill pressure in the cylinder. The cylinder was loaded with a pressure which was applied to the whole internal surface of the cylinder including the thread (see Fig. 1). Residual stresses were not considered, because after initiation and a small growth the sustained load derived from pressure is the most important load. An initiating notch was included. The growth was iterated through steps as the crack grew until it reached the outer surface or otherwise indicated instability.

From observations (including those discussed in [3] below) it was known that growth does not proceed consistently along the whole crack front. The normal formulation of K_I is given by:

$$K_I = \sigma\sqrt{(2\pi a)}, \tag{5}$$

where σ = average membrane stress in the region of the crack acting normal to the plane of the crack, and a = depth of the defect.

However, this formulation cannot distinguish between several separate points along a crack front. In preceding work (Ibrahim [1]) another formulation of K_I was tested and found to work for the specimens considered in that work. It was proposed to test a modification of this formula for the present case to give a localised value of K_I which is a function of r, termed $K_I(r)$ as follows:

$$K_I(r) = \sigma_\theta\sqrt{(2\pi r)}, \tag{6}$$

where σ_θ = circumferential local stress in the crack tip region acting normal to the plane of the crack as determined by stress analysis, and r = a fixed distance from the crack edge within the crack tip region.

Ibrahim found that the appropriate value for r is more than 0.2 mm in order to obtain convergence. In this trial the value of 0.3 mm was chosen, that is $K_I(r) = 0.0434\sigma\theta$.

To carry out the crack growth the process was started with a calculation of stress distribution along the initial notch. Stress intensity factor, $K_I(r)$, was calculated for a set of points at the crack edge using Eqn (6).

The increment in crack size Δa after fixed period of time Δt was calculated using crack growth Eqn (1) replacing K_I with $K_I(r)$. Thus, for a set of points approximately 5 mm apart at the crack edge the new position of the crack was determined after the time increment Δt. The crack was presumed to move normal to its previous front.

This new position of the crack was then plotted on a drawing of the cylinder section. For the next step of analysis a new mesh was constructed with the crack front moved to a new position. The remeshing of the model is a key feature of the process used in this paper.

4.2. *Finite element analysis*

Stress analysis was carried out using the finite element package MSC/NASTRAN at each step of crack growth. The problem is not necessarily symmetrical, since only one crack may be growing in

the cylinder, but often there is more than one crack observed spaced around the neck. In this study, two opposed cracks were effectively modelled since a mesh covering one-quarter of the cylinder was used, which is rather like the situation in Fig. 2. The model contains 800 three-dimensional elements with mid-nodes and 4098 degrees of freedom. In order to converge the stresses given the singularity of $1/\sqrt{r}$ at $r=0$ at the crack front, singularity pentahedron elements were employed. This type of element is obtained by moving the side nodes near the crack tip to the one-quarter position.

After the stress distribution in the crack-tip region had been calculated, Eqn (1) was used to determine the location of the crack and the finite element model was rebuilt for the next step calculations. This involves generating a new finite element mesh, applying boundary conditions and pressure, including those at the crack plane as extended after crack propagation. The finite element mesh for the neck region to calculate the stress around initial and subsequent notches is shown in Fig. 5.
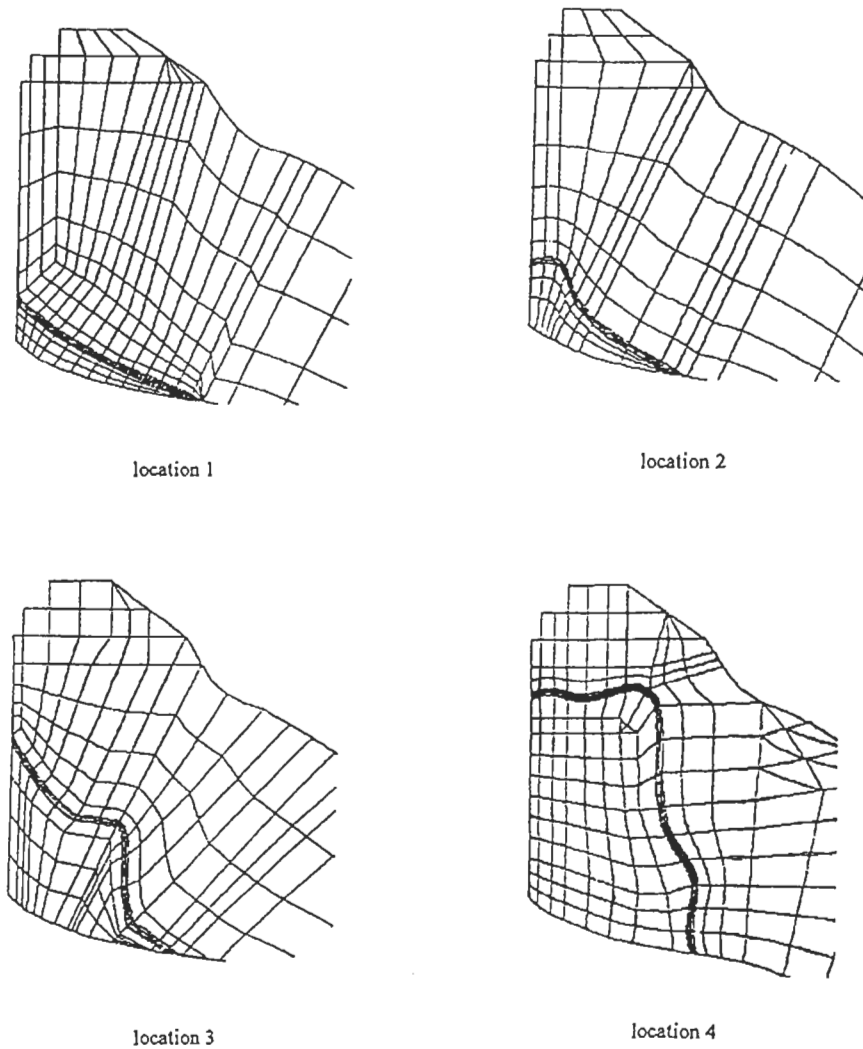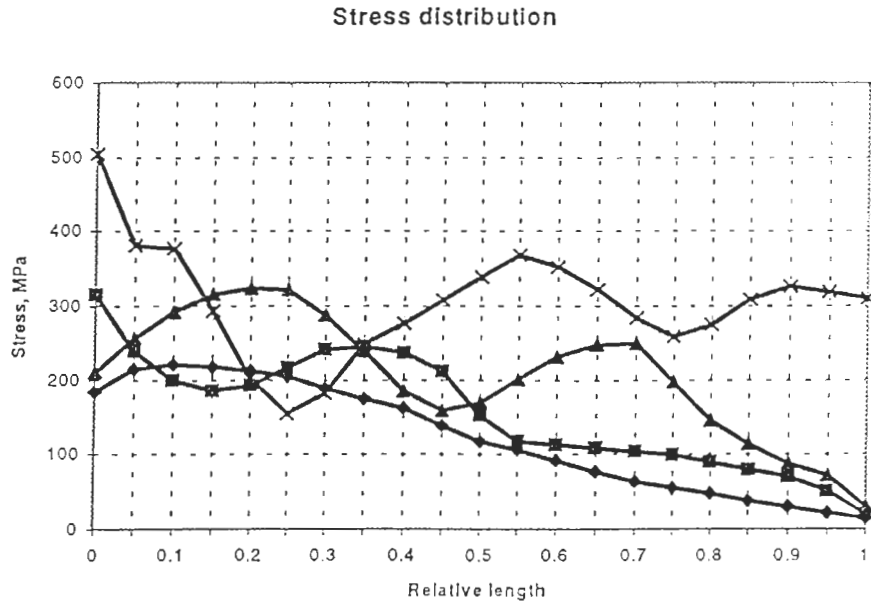

location 1

location 2

location 3

location 4

Fig. 5. The finite element mesh for the neck region used to calculate stress around initial and subsequent notches.

Stress distribution

Key: ◆ Defect Location 1, × Location 2, ▲ Location 3, ■ Location 4

Fig. 6. The local hoop stress distribution at 0.3 mm from the crack front for the four locations calculated. (Multiply stress by 0.0434 to obtain $K_1(r)$ in MPa $\sqrt{m}$.)

5. RESULTS

The reason why the crack does not grow at exactly the same rate over its entire front is suggested by Fig. 6. This figure shows the stress distribution at 0.3 mm from the crack front for the four locations calculated.

From this figure it is seen that the level of stress at the points marked along the crack edge is sensitive to the shape of crack. For situations where the crack is concave in direction of crack propagation (the centre of the radius of the curvature is in front of the crack) the value of stress near the crack tip is higher than that for sections where the curvature of the crack is convex (the centre of the curve is behind the crack growth).

This characteristic of the stress distribution along the crack tip explains why the phenomenon of crack growth tends not to be uniform along the crack. During the growth the crack can advance at times more quickly on the interior edge because that area tends to be concave. Meanwhile, where the features tend to be convex, there can be a resistance to the defects propagating. This can occur near the visible surface inside the cylinder. Thus in some cases the crack grows more readily inside the material of the cylinder rather than along free surfaces.

Figure 7 shows theoretically calculated crack fronts in a cross-section of the neck region of the cylinder. This presentation shows the following.

- The shape of crack predicted is consistent with the observations on cracked cylinders which have been examined (for example see Figs 2 and 3).
- The crack growth accelerates as the crack grows larger.
- By the time a leak is detected at the O-ring mating surface at the top of the opening the crack may be growing very fast under the surface.
- Crack growth sometimes appears to be retarded at the exterior surface of the cylinder and the crack can grow faster on the interior. The most noticeable example of this is the fourth location.

The uneven growth predicted for the crack is in conformance with the speculation in Section 3.4 above that the growth of the defect does not conform with the classical "leak before break"
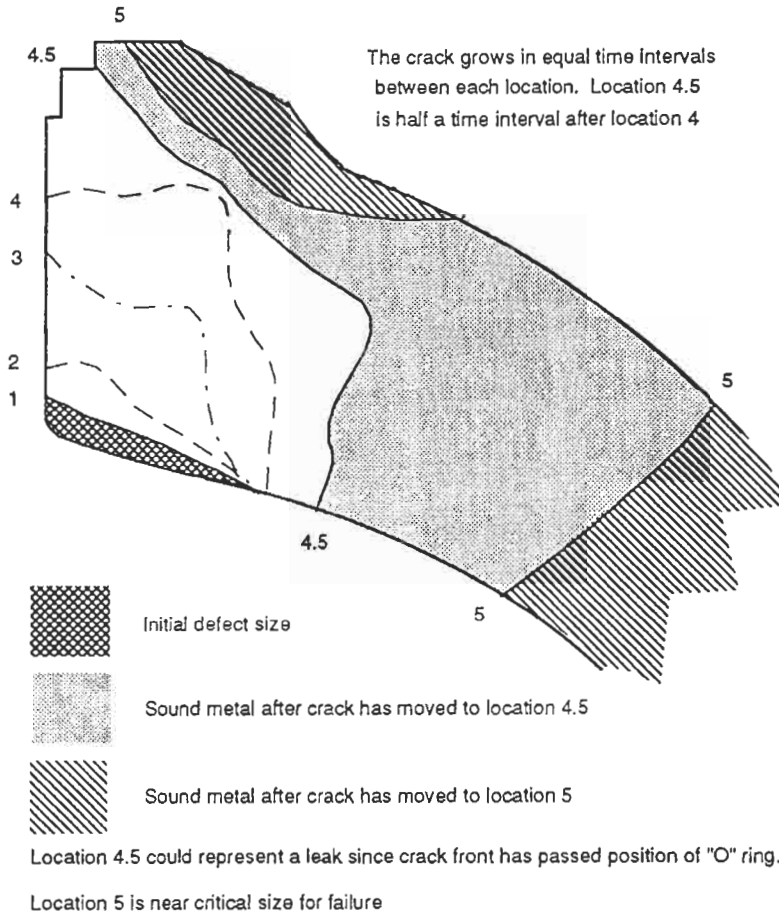
Fig. 7. Theoretically calculated crack positions for the pressurised cylinder over a period of time. These positions are similar to beachmarks such as those seen on Fig. 3. The theoretically determined positions approximate both the shape and the acceleration of the crack growth rate which has occurred in practice. The constants in the growth model were adjusted until the time of growth plausibly fitted the time available for growth in observed cylinders.

argument. The inclination of the defect to grow more on the interior than on the surface could mean that growth can occur to critical size before leak occurs.

There is, however, an important problem with the model presented in Fig. 7. Using the crack growth models derived from specimen testing [Eqn (1)] the time interval between the various crack fronts used was 150 years and thus the growth position 4.5 would take 750 years. This is clearly not representing the time scales observed in the cylinders examined.

5.1. Modification of the model

Despite the very long time intervals involved, the shapes predicted by the model are sufficiently similar to the crack shapes seen in practice to permit revision of the model. If the model is used to match the crack growth in a cylinder for which the loading conditions are reasonably well known, an estimate can be made of the parameters in Eqn (1) to suit that actual cylinder.

The most accurate procedure for doing this would be to examine cylinders which had been pressurised under laboratory conditions. However, there are significant difficulties with this concept

because there are long time intervals involved. In addition the test cylinders may have to be given deliberately cut notches which may not accurately represent the real case.

The alternative procedure is to estimate growth parameters from cylinders removed from traffic which have large defects in them such as those reported above. The problem with cylinders removed from traffic is that there is only approximate knowledge about their service life, in particular temperature and pressure history. For example in the two cylinders used in this paper, cylinder A was 10.5 years old at failure and operated in the South of Australia, and cylinder B was 5.5 years old at failure and operated in the tropics. It is not known how much of the time the cylinders were at full pressure.

To obtain an estimate for the growth model it was assumed that cylinder A grew to the point of leakage in 4.5 time intervals and that cylinder B took 5 time intervals to reach the critical size from whence it failed during test. The time interval was set to one year which presumes that neither cylinder was continuously filled during its service period.

Crack growth phenomena was assumed to be the same in both cylinders and that the operating temperature was not a feature (a difference of 10°C in operating temperature makes for a difference of a factor of about 4 from the Lewandowski data). While these assumptions may seem to involve significant approximations, these approximations would have an effect of less than a factor of 10. To put this in context, the existing estimates of crack growth rate are several orders of magnitude incorrect for these two cylinders.

The equation predicted by this method has the following form:

$$\log_{10}(da/dt) = 0.346K_I - 0.027, \tag{7}$$

where da/dt is in mm/h. The ratio of this result to the model given in Eqn (1) is $10^{(0.112K_I + 7.6)}$, that is, a value exceeding 10^8.

6. DISCUSSION

The above model cannot apply to the vast majority of cylinders in traffic or there would be far more failures than have actually been experienced. The situation is that many cylinders have small visually observable defects at the neck (for some manufacturing periods up to 10% of cylinders have been questioned by inspectors). If the growth rate described above applied to all these cylinders then leak and violent failure would be more prevalent. It is thus necessary to identify what is unusual about the cylinders which fail or are detected with very large defects. This, in the view of the authors, still has not been done.

The main proposal in the literature is that the lead level in the aluminium will explain the situation, but this is not confirmed by the Australian cylinders which have always had low levels of lead (below 10 ppm where measured in this work) and where recycled scrap has never been used. Fatigue cycling is one issue which has been briefly studied. Stark and Ibrahim [8] show that 100 short cycles increased crack growth rate by two orders of magnitude. Since all cylinders in traffic are subjected to pressure cycling, it would be necessary to identify what type of cycle puts a cylinder at special risk. It also has been identified that a very large grain size has an effect on crack growth [1], but this is a characteristic of most aluminium cylinders. Incorrect filling, or filling with corrosive species, is another possibility, but none of the cases studied have shown any indications that this may have occurred.

7. CONCLUSIONS

In this paper a new approach was used for modelling sustained load cracking in aluminium gas cylinders. The earlier models of crack growth were based on specimen testing which predicts extremely low or zero crack growth rates when applied to actual cylinders. These models cannot predict the failure of the cylinders which have actually occurred.

This paper presents a method of estimating constants in the crack growth equation by examining actual failed cylinders and matching the theoretical model to the observations. The new equation which is derived gives a crack growth velocity up to 10^8 faster than earlier models.

356

While the model developed in this paper describes cylinders which have a rapid mode of crack growth, the model apparently does not apply to the vast majority of cylinders which do not fail in traffic. There must be additional effects which have not yet been identified which will make some cylinders follow a faster mode of crack growth.

The paper also shows that the classical fracture mechanics approach suggests that there will be "leak before break" for the cylinders. However, there have been cases were there have been no precursor leaks before a violent failure. The paper shows that the growth of the defects is not necessarily uniform along the crack front and this leads to the possibility of burst before leak.

REFERENCES

1. Ibrahim, R. N., Ph.D. Thesis, University of New South Wales, School of Mechanical and Industrial Engineering, 1990.
2. Lewandowski, J. J., Kim, Y. S. and Holroyd, N. J. H., *Metallurgical Transactions A*, 1992, **23A**, 1679–1689.
3. Lynch, S. P., *Materials Science and Engineering*, 1989, **A108**, 203–210.
4. Failure Analysis Associates, *Examination of Scott Air-Pak cylinders*. Los Angeles, 31 May 1984.
5. NIOSH, U.S. Department of Health and Human Services (DHHS), *Respirator Users Warning*, National Institute for Occupational Safety and Health (NIOSH), Division of Safety Research, Morgantown, WV, 21 July 1983. See also Safety advisories: Federal Register, Research and Special Programs Administration Notice 93-22, Vol. 58, No. 221, 18 November 1993, and Notice 94-7, Vol. 59, No. 142, 26 July 1994.
6. *Diver News*, United States commercial publication, September 1994.
7. Poole, R., *Professional Diver Journal*, 1995, **1**(1), Sydney, Australia, Winter.
8. Stark, H. L. and Ibrahim, R. N., *Engineering Fracture Mechanics*, 1992, **48**, 569–574.
9. Price, J. W. H., Ibrahim, R. N. and Ischenko, D., *Int. Conf. on Pipes and Vessels*, Singapore, February 1996.
10. Stark, H. L. and Ibrahim, R. N., *Engineering Fracture Mechanics*, 1988, **30**(3), 409.
11. Price, J. W. H., Ibrahim, R. N. and Ischenko, D., *Pressure Vessel Technology Conference*. ASME, Montreal, July 1996.
12. Schröder, R., *Materials Science and Technology*, 1985, **1**(Oct), 754.

357

HYDROGEN-ASSISTED STRESS-CORROSION OF PRESTRESSING WIRES IN A MOTORWAY VIADUCT

L. VEHOVAR*

Institute of Metals and Technology, Lepi pot 11, 1000 Ljubljana, Slovenia

V. KUHAR

National Building and Civil Enginering Institute, Dimičeva 12, 1000 Ljubljana, Slovenia

and

A. VEHOVAR

University of Ljubljana, FNT-Department of Metallurgy and Material Science, 1000 Ljubljana, Slovenia

Abstract—This paper deals with the stress corrosion cracking of cold-drawn stress relieved prestressing wire in a prestressed reinforced-concrete structure due to the influence of atmospheric water and especially the chlorides which were present during the winter salting of the road pavements of a motorway viaduct in Slovenia. Twenty-two years after the bridge was first opened for traffic, numerous wires in the prestressing cables had become brittle, and had broken and many others were damaged, to a greater or lesser degree, by corrosion and the effect of stress corrosion supported by the additional operation of hydrogen at the crack tips. Investigations showed that as the degree of corrosion increased the mechanical properties of the steel, particularly its toughness, were reduced drastically. As a result, such material is unable to prevent the initiation or spreading of cracks in the case of the static and dynamic loadings occurring on the bridge. Systematic SEM investigations of the morphology of the fracture surfaces of the wires confirmed the authors' assumption that stress corrosion and hydrogen embrittlement had made possible the occurrence of brittle areas with cleavage fracture surfaces, the proportion of which increased with an increase in the degree of corrosion. © 1998 Elsevier Science Ltd. All rights reserved.

Keywords: Bridge failures, brittle fracture, hydrogen-assisted cracking, stress-corrosion cracking.

1. INTRODUCTION

During the visual inspection of the main load-bearing longitudinal and transverse beams of a viaduct measuring 500 m in length (Fig. 1), a large number of cracks were observed in the surface layer of the concrete. The cracks, up to 2 m long, extended the length of the external stirrup reinforcement, and brown-coloured corrosion products of steel were observed leaking out of these cracks. Through an analysis of the concrete and of the corrosion products, it was determined that aggressive corrosion-causing chlorides were present, which had reached the concrete with the atmospheric water filtering down from the inadequately protected pavement slabs. However, since the chloride ions are fairly mobile and capable of diffusing deeper into the internal part of the beams up to the prestressing wire of the main load-bearing cables (Fig. 2), these locations, too, were included in the diagnostic investigations of the damaged beams. It was found that at certain locations the cables had undergone heavy corrosion damage (Fig. 3). Samples of the prestressing wires were taken from the prestressing cables at locations where the degree of the corrosion threat varied from lesser to greater. Samples of concrete and the grouting mixture were also taken.

---

*Author to whom correspondence should be addressed.

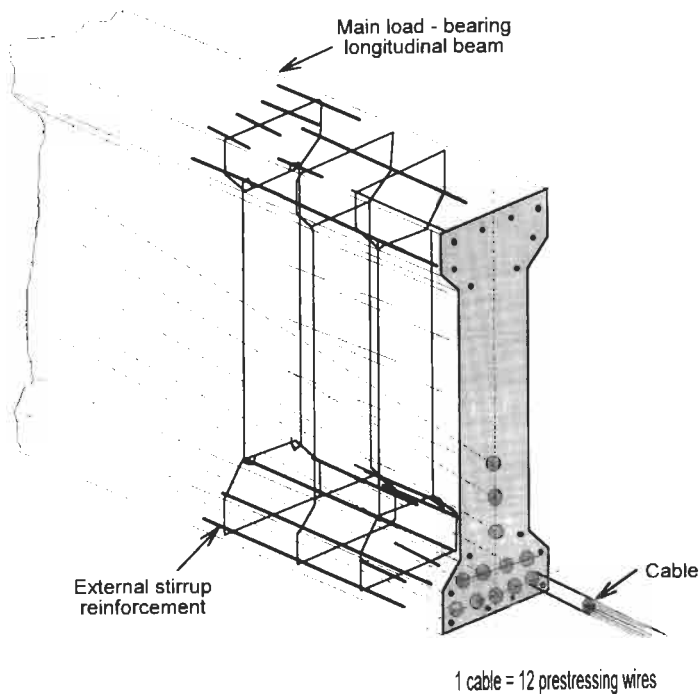Fig. 1. Prestressed concrete construction of the viaduct.

Fig. 2. The arrangement of cables in the longitudinal beam.

2. EXPERIMENTAL INVESTIGATIONS AND DISCUSSION

Out of all the samples of prestressing wire of 7 mm diameter and strength class 1800 N/mm^2 which had been removed from the beams of the viaduct, a selection of samples was made showing different degrees of corrosion, from samples that appeared to be intact with a zero degree of corrosion, up to samples which showed heavy corrosion defined by a corrosion degree of "5". The corrosion degree ("Corr. d.") was expressed by means of the actual cross-section, which represents the change from the initial, uncorroded condition. These specimens were tested to failure in a tension testing-machine in order to determine their mechanical characteristics, including the elongation,

Fig. 3. Corrosion damage of cables.

reduction of area and, particularly, the number of bend/rebends; also, indirectly, the brittleness of the material. The fractured surfaces were analysed in detail by fractographic examination. The average values of the parameters obtained from the mechanical tests are shown in Table 1.

From the results given in Table 1 it can be concluded that only the uncorroded wire (Corr. d. = 0) satisfied the requirements of the original tender. $R_{p0.2}$ and R_m are still within the permitted limits. The elongation is greater than the minimum prescribed value of 4%, reduction of area exceeds the minimum prescribed value of 25%, and the number of bends/rebends is near the minimum required limit, i.e. 4. However, in the case of all the other test specimens the mechanical properties worsen as the degree of corrosion increases, and there is an important increase in the brittleness of the material.

The (SEM) fractographic analyses of the fractured surfaces of the test specimens, after the mechanical testing, agree well with the results shown in Table 1. The material defined by Corr. d. = 0 is tough (Fig. 4). In the middle a so-called fibrous zone can be seen, where the crack is only progressing slowly. This means that for the crack to progress during the tension test in a stable manner, a relatively large amount of energy is needed. In the shear-lip zone (the ring area surrounding the fibrous zone) a change in the rate of progress of the crack can be observed. In this area its spreading is unstable and quicker. In the fibrous zone the fracture surface with typical relatively large dimples (Fig. 5) appears tough. A tough fracture can also be observed in the shear zone, but, as the material in the tension test slips at an angle of 45°, characteristic shears occur which make the characteristic dimples more or less invisible.

It is quite clear that stress corrosion and hydrogen embrittlement reduce the size of the fibrous and shear-lip zones (Figs 6 and 7), and the proportions in both of brittle locations increases. It is a fact that the nucleation and propagation of microcracks, their coalescence into larger cracks together

Table 1. The mechanical characteristics of typical test specimens

Corr. d.	Actual cross-section (mm²)	$R_{p0.2}$ (N/mm²)	R_m (mm²)	Elongation A_{70} (%)	Reduction of area (%)	No. of bends rebends over 45 mm dia.
0	38.5	1546	1793	6.3	40	3.5
1	38.0	1418	1616	5.7	36	3.0
2	35.0	1221	1408	5.6	ca. 20	2.5
3	35.0	1325	1546	2.9	ca. 20	2.0
4	25.0	—	857	2.0	0	0.5
5	22.0	—	878	2.0	0	Breaks at an angle of 25

Note: $R_{p0.2}$ and R_m have been calculated taking into account a nominal diameter of 7 mm, i.e. a cross-section of 38.5 mm².
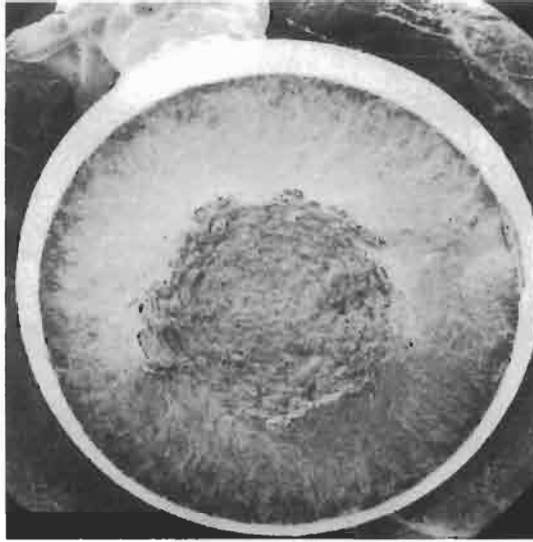
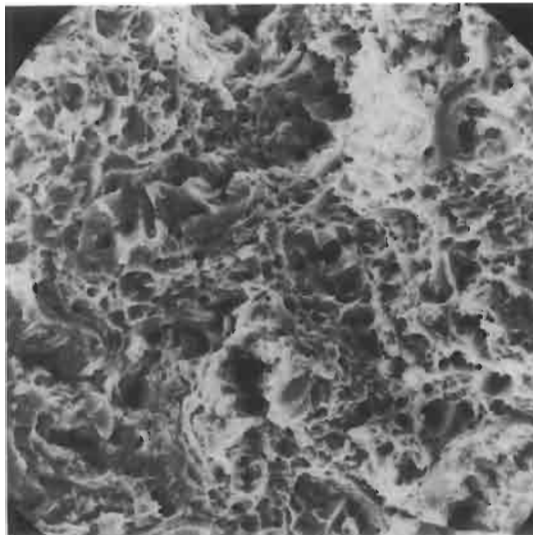Fig. 4. SEM photograph of the fracture surface of a specimen with Corr. d. = 0. × 13.

Fig. 5. SEM photograph of a specimen with Corr. d. = 0, showing the tough fibrous zone. × 2000.

with the smaller and shallower dimples (those with a low fracture energy), is more rapid in the brittle regions of the material. These brittle areas were formed due to the effects of stress corrosion which is now increasingly more attributable to hydrogen embrittlement. Examples of significant shallow dimples are shown in Fig. 8, whereas Fig. 9 shows a cleavage fracture surface. Such fractographic analyses clearly show that in the investigated viaduct there exist very brittle wires.

Stress corrosion cracking is connected with the free chlorides, the proportion of which in the grouting mixture in the direct vicinity of the cables is up to 1.01 %. This is a very high concentration so that the grouting mixture, with a pH which was found to be within the limits of 11.3 to 11.6, is unable to provide the necessary passivation of the steel [1, 2]. The local depassivation of the prestressing wire made possible the start of the corrosion process. On the basis of the results of the

Fig. 6. SEM photograph of a specimen with Corr. d. = 2, with a reduced fibrous zone, and increased brittleness of the shear-lip zone. × 13.
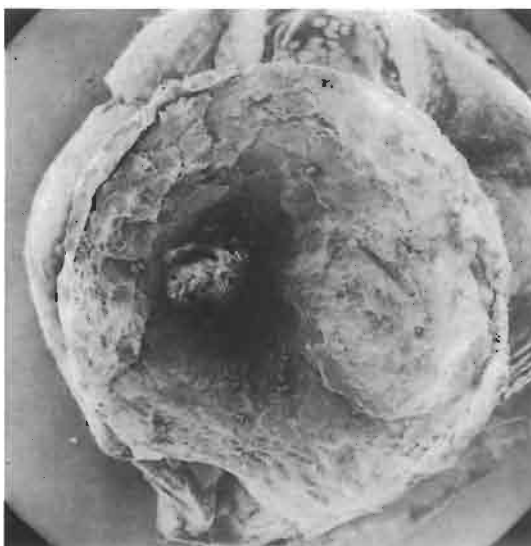
Fig. 7. SEM photograph of a specimen with Corr. d. = 5, showing the very brittle nature of the fracture surface. × 10.

fractographic tests, it has been assumed that what is involved is stress corrosion in the presence of Cl^- ions and supported by hydrogen [3].

The occurrence of hydrogen in the presence of Cl^- ions is made possible as, in the initial stage, the chlorides break down passivity and at damaged locations corrosion pits occur [4, 5]. In the pits the metal (M) dissolves anodically with the release of valence electrons and the formation of M^{n+} ions which, together with the chlorides, form soluble corrosion products M^+Cl^-. With the hydrolysis of these products:

$$M^+Cl^- + H_2O = MOH + H^+Cl^- \tag{1}$$
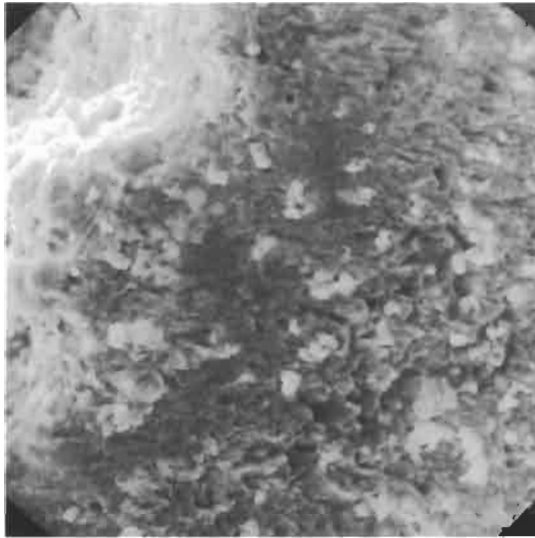
Fig. 8. SEM photograph of a specimen with Corr. d. = 2, showing the shallow dimples. × 1000.
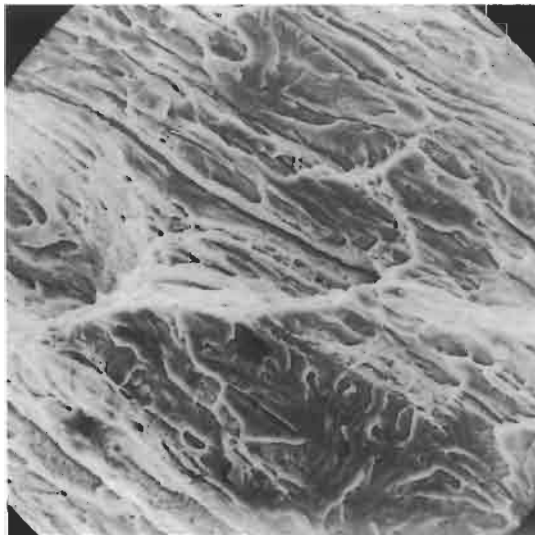
Fig. 9. SEM photograph of a specimen with Corr. d. = 5, showing the brittle nature of the fracture surface. × 1000.

the H^+ and Cl^- ions regenerate. The H^+ ions increase the acidity in the pit (the pH value reached is 3.5) [6]. Due to the lack of oxygen as a depolarizer at the cathode, H^+ ions act as depolarizers in the pit:

$$H^+ + e \rightarrow H_{ad} \tag{2}$$

$$H_{ad} + H_{ad} \rightarrow H_2 \tag{3}$$

However, the reaction [eqn. (3)] does not take place in its entirety. At favourable locations the adsorbed atomic hydrogen migrates into the crystal lattice where, due to various mechanisms [7, 8, 9], it causes hydrogen embrittlement. This results in uncorroded regions which are the forerunners
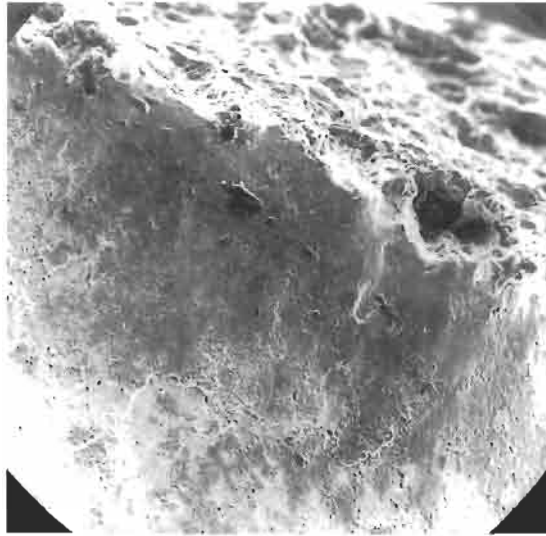
Fig. 10. SEM photograph of a specimen with Corr. d. = 5, with corroded (black) and uncorroded (white) regions. × 100.

of corroded areas in the stress corrosion crack (Fig. 10). Such uncorroded areas only occur due to transcrystalline slips at those locations where the hydrogen has reduced the cohesive force between the atoms of the metal at the crack tip or, for example, by the pressure mechanism in which molecular hydrogen occurs with the recombination of atomic hydrogen. As the molecules of hydrogen occur, high pressures of up to 10^6 bar are released, resulting in the occurrence of local microcracks which join together into macrocracks thereby leading to failure of the wire. The final result of all these mechanisms of cracking is the occurrence of the already mentioned brittle regions, with the cleavage appearance of the fracture surfaces.

3. CONCLUSION

The fractographic analyses of the fracture surfaces of the corroded prestressing wires have shown that the brittle regions with a cleavage appearance can only be the result of the operation of hydrogen at the crack tip. The occurrence of hydrogen is made possible by the presence of the free chlorides and the corrosion reaction, which provides the electrons needed for the transformation of H^+ ions into atomic hydrogen, which then migrates into the crystal lattice of the metal.

REFERENCES

1. Burdekin, F. M. and Rothwell, G. P., Survey of corrosion and stress corrosion in prestressing components used in concrete structures with particular reference to offshore applications, pp. 8–33. Cement and Concrete Association, Wexham Springs, Slough, U.K., 1981.
2. Brachet, M., Report on prestressing steel: 5. Stress corrosion cracking restistance test for prestressing tendons. FIP-Technical Report, 1980.
3. FIP Commission on Prestressing Steels and Systems. Report on prestressing steel. FIP 5 3 1976.
4. Bergsma, F., Boon, J. W. and Etienne, C. F., *Heron*, 1977, **22**, 46–70.
5. Vehovar, L., Corrosion of high-strength steel in prestressed concrete containing calcium sulphide. United Nations—Steel Committee, Seminar Geneva, 1984.
6. ASM International, *Metals Handbook*, Vol. 13, *Corrosion*, pp. 108–113, ASM International, Metals Park, Ohio, U.S.A., 1987.
7. Foroulis, Z. A., Environment-sensitive fracture of engineering materials, Conference Proceedings, Metallurgical Society of AIME, Chicago, 1977, pp. 379–406.
8. Troiano, A. R., *Trans. ASM*, 1960, **52**, 54 1960.
9. Beachem, C. D., *Metall. Trans.*, 1972, **3**, 437.

365

FAILURE ANALYSIS OF CARRIER CHAIN PINS

G. A. SLABBERT,* J. J. McEWAN and R. PATON

Physical Metallurgy Division, Mintek, Private Bag X3015, Randburg 2194, Republic of South Africa

Abstract—A sugar plant is designed to operate with the minimum disruption during the sugar cane harvesting season, and equipment must be maintained in a high standard of repair. When failure of equipment does take place, it is important to identify the cause to minimize the likelihood of any future problems. This paper details the analysis of a failure of conveyor chain pins that had operated for only six weeks. The pins had been heat treated so that they had become susceptible to hydrogen embrittlement, and had cracked. The source of hydrogen was attributed to corrosion of other steel components in the system. In order to minimize the likelihood of future failures, it was recommended that the source of the corroded components be identified. In addition, it was recommended that the authors should liaise with the plant personnel in order to recommend a suitable heat treatment schedule for future pins. © 1998 Elsevier Science Ltd. All rights reserved.

Keywords: Sugar plant, hydrogen embrittlement, stress corrosion cracking, corrosion.

1. INTRODUCTION

A sugar mill operates continuously during the sugar cane cropping season which, in South Africa, runs for more than six months. It is important that the plant down-time is maintained at an absolute minimum during this period. Unforeseen failure of critical components does occur, however, and repair and maintenance is done rapidly in order to get the plant back into full production. In many instances, it is imperative that the cause of failure be ascertained to avoid future problems and minimize costly breakdowns. This paper details the failure of carrier chain pins from a conveyor used to transport moist sugar cane pulp.

1.1. *Background*

The sugar mill was commissioned in 1994 and the original chain conveyor operated for three years before it had to be replaced due to excessive wear. The new carrier chain had only been operating for about six weeks when the chain pins started failing.

Sugar cane pulp is conveyed at a temperature of about 80°C. This temperature is maintained by means of steam, which has a temperature of approximately 90°C. The material specification for the chain was either AISI 431 or BS 970 grade 431S29 ('En 57') stainless steel. The hardness was specified as HRC 43 to 45 (Rockwell 'C') although the material specification did not give any details on the heat treatment required to obtain this range. AISI 431 and BS 970 grade 431S29 are related specifications, but there are differences, as shown in Tables 1 and 2.

2. INVESTIGATION

2.1. *Visual examination*

Twelve pins were examined, three of which had fractured. All the pins examined had been in operation in the conveyor for about six weeks. The three failed pins had fractured at an angle of approximately 45° (Fig. 1). Although pin C failed close to the bottom of the pin, plant personnel reported that the majority of fractures were in the middle portion of the pin.

---

* Author to whom correspondence should be addressed.

Table 1. Specifications for AISI 431 and 'En 57' stainless steel, and the chemical analysis of the chain pins

	%C	%Cr	%Ni	%Mn	%Si	%S	%P
Specification for AISI 431	0.2 max	15–17	1.25–2.5	1 max	1 max	0.03 max	0.04 max
Specification for 'En 57'	0.12–0.2	15–18	2.0–3.0	1 max	1 max	0.03 max	0.04 max
Pin A (fractured)	0.16	15.2	2.54	0.42	0.36	0.021	0.019
Pin B (fractured)	0.15	15.2	2.54	0.42	0.37	0.019	0.018
Pin C (fractured)	0.16	17.2	2.88	0.52	0.54	0.020	0.022
Pin N1 (not fractured)	0.15	15.2	2.55	0.42	0.37	0.002	0.019

Table 2. Vickers hardness measurements (HV_{30})

Pin	Average	Standard deviation	Rockwell 'C' equivalent
A (fractured)	470	4.1	46
B (fractured)	476	8.0	47
C (fractured)	464	1.5	46
N1 (not fractured)	467	6.5	46

Fig. 1. Three fractured pins showing the position and angle of the fractures.

The major portion of the outside surface of the pins was covered in a dark brown corrosion product, except at the position of wear. This product was also present on all three fracture surfaces. X-ray diffraction analysis of a sample of this brown product confirmed that it was a corrosion product that consisted mainly of iron oxide (Fe_2O_3). No chromium was present in this corrosion product, indicating that it originated from a source other than the stainless steel pins. This was confirmed by examining the pins after cleaning them in an ASTM-recommended cleaning solution.

2.2. *Chemical analysis*

Four pins were analyzed. They all complied with the chemical composition for 'En 57', as shown in Table 1. Except for the fractured pin, C, all the pins had the same chemical composition. Pin C had a slightly higher nickel and silicon content, and, as a result, contained some ferrite in the
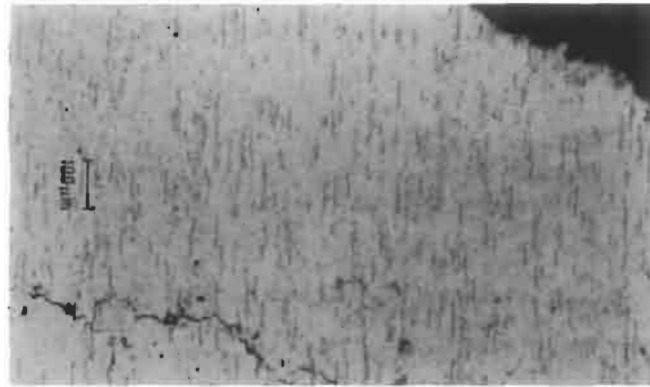
Fig. 2. Fractured pin C. Note the intergranular nature of the fracture surface on the bottom left, and the crack running parallel to the main fracture. The ferrite stringers can also be seen.
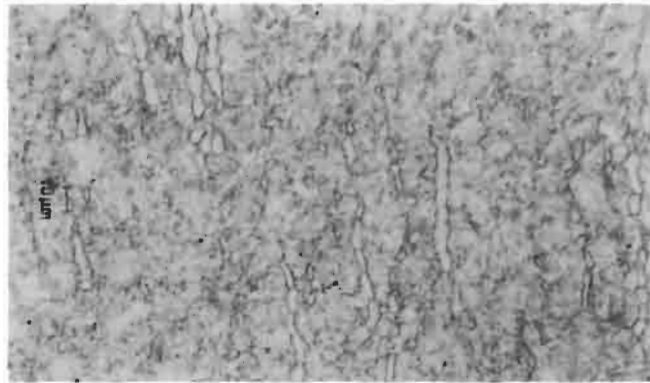

Fig. 3. A high magnification of the structure shown in Fig. 2, showing the tempered martensite and ferrite stringers of pin C.

microstructure (Figs 2 and 3). Pin C also had higher levels of chromium and manganese. This is considered beneficial to the alloy since it leads to grain refinement, which increases toughness, strength, and resistance to quench cracking [1].

2.3. *Metallographic analysis*

The metallurgical structure of all the samples, except for pin C, was tempered martensite and pin C contained ferrite stringers in a tempered martensite matrix, as shown in Figs 2 and 3. Since all the pins failed in a similar manner, the presence of ferrite stringers in pin C did not influence its failure.

All of the fractures, of which the example in Fig. 4 is typical, are intergranular. They exhibit features, including yawning grain boundaries, micropores and no grain boundary corrosion, which indicate that they were caused by hydrogen embrittlement (HE) (Fig. 5) [2]. A small section of a fracture surface can be seen at the bottom of both Figs 2 and 4. In Fig. 2, the intergranular nature of the fracture, as well as the crack running parallel to the main fracture surface, confirms that the ferrite stringers did not contribute to the propagation of the crack, and thus the failure of the pins.

The surface on the right-hand side of the pin in Fig. 4 shows the original machining marks on the outside of the pin. This confirms that little corrosion had placc on the pin.
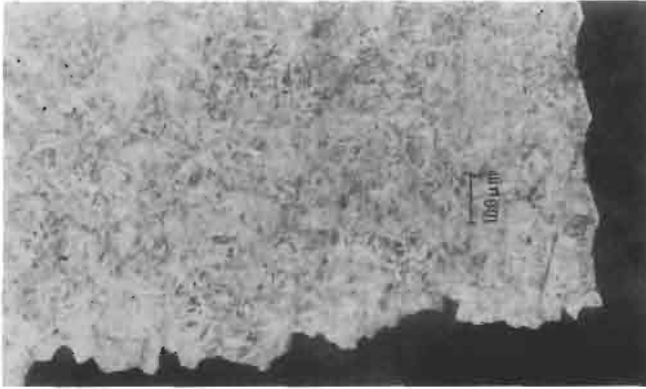
Fig. 4. The tempered martensite matrix as found in all the pins, except pin C, whose structure is shown in Figs 2 and 3. Note the intergranular nature of the fracture surface on the bottom as well as the machining marks on the right.
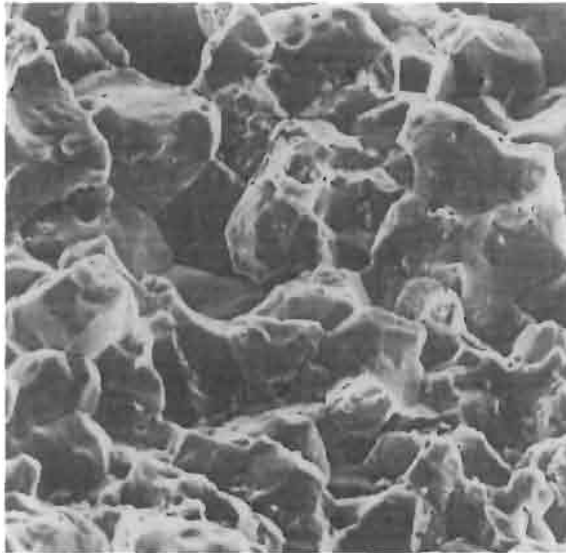

Fig. 5. An SEM picture of the fracture surface of a pin showing the intergranular nature of the fracture. Micropores, yawning grains, and the absence of grain boundary corrosion, characteristic features of HE, are shown.

2.4. *Mechanical properties*

The Vickers hardness of the pins ranged between 464 and 476 Vickers, as shown in Table 2. These results are equivalent to HRC 46–47. The British standard specification specifies a hardness for En 57 of HRC 24–33. No specified hardness is available for AISI 431, although values of up to HRC 47 are reported in the literature [3].

The eight remaining pins were used to measure the mechanical properties of the steel. The ultimate tensile strength (UTS) varied between 1439 and 1579 MPa, as Table 3 shows. These values correlate well with the hardness values obtained. The 0.2% yield strength of the material varied between 1162 and 1182 MPa. It is generally considered that high strength steels with a yield strength above 700 MPa are susceptible to HE. The pins thus fall well within the susceptibility range. The British standard specification specifies a UTS of 850–1000 MPa and a 0.2% yield strength of 635 MPa for

Table 3. Mechanical properties of the pins

Pin	0.2% yield strength (MPa)	Ultimate tensile strength (MPa)	Elongation (%)	Impact energy at room temperature (J)
N2	1182	1439	23.2	—
N3	1182	1458	21.6	—
N4	1162	1579	24.8	—
N5	—	—	—	22
N6	—	—	—	57
N7	—	—	—	23
N8	—	—	—	24
N9	—	—	—	45
Average	1175	1492	23.2	34
Standard deviation	11.5	76	1.6	16
'En 57'[1]	635	850–1000	—	—
AISI 431[2]	—	1210–1515	—	—
AISI 431[3]	1030	1370	16	—
AISI 431[4]	1080	1360	23	—

[1] British standard specification BS 970 (950–1020°C, oil quenched and tempered at 550–650°C).
[2] 980–1065°C, oil quenched and tempered at 230–370°C [3].
[3] Quenched and tempered at 260°C (Alloy Digest).
[4] Quenched and tempered at 427°C (Alloy Digest).

En 57. UTS values up to 1515 MPa have been reported for AISI 431. The percentage elongation varied between 22 and 25%, which complies well with that required for AISI 431.

The Charpy impact strengths are acceptable for this material, although the scatter is fairly high but not atypical. Figure 6 shows the Charpy impact toughness for a stainless steel complying with the specification for both En 57 and AISI 431, as a function of tempering temperature at various
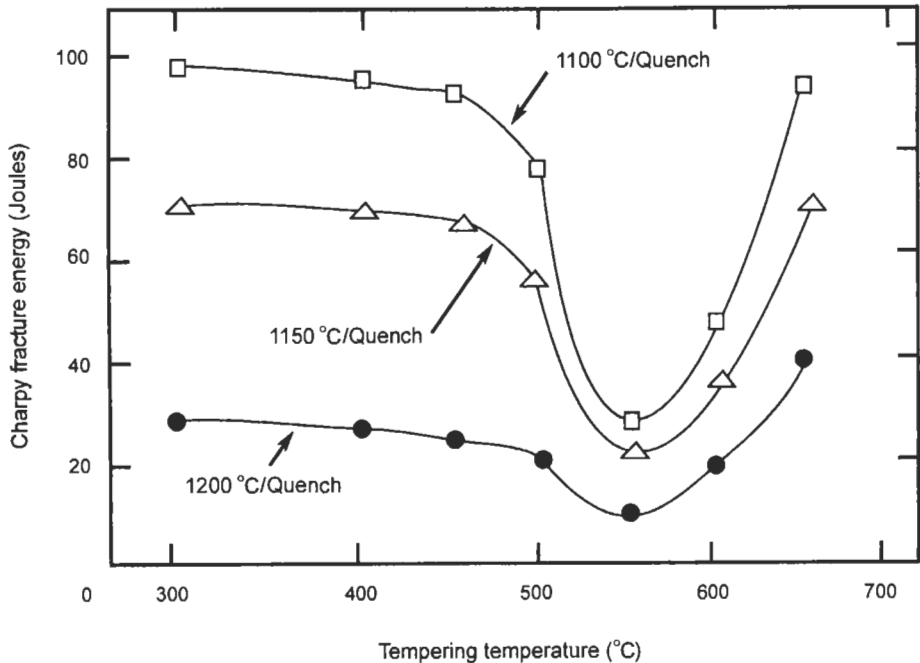
Fig. 6. Charpy impact toughness of either AISI 431 or En 57 as a function of tempering temperature, austenitized at various temperatures and oil quenched.

370

austenitizing temperatures [4]. The steel is susceptible to temper embrittlement at temperatures near 550°C.

3. DISCUSSION

The pins failed due to hydrogen embrittlement (HE). They had been heat treated into the susceptible range for HE. HE is a mechanical/environmental failure process that results from the absorption of hydrogen into the metal, usually in combination with stress (residual or applied) [5]. HE is one of four types of environmental cracking [6] and is mainly a problem in high strength steels. The susceptibility of a material increases with:

(i) The strength (e.g. hardness).
(ii) Increasing amounts of cold work.
(iii) Increasing residual and applied stress.

An example to illustrate the effect of tempering on the yield strength and cracking resistance of a martensitic stainless steel in a marine atmosphere is presented in Fig. 7 [7]. Accordingly, it has become accepted practice to define resistance to cracking due to HE in terms of yield strength, hardness, or heat treatment conditions.

HE is cracking that is induced when atomic hydrogen is supplied to the steel. The hydrogen can be supplied by many sources. One common source of hydrogen is as a by-product of a corrosion reaction.

It is believed that there is not only one mechanism that causes cracking, and the mechanism differs from material to material and it can even differ for the same material in different environments. There are three theories that explain the mechanism of HE [3]:
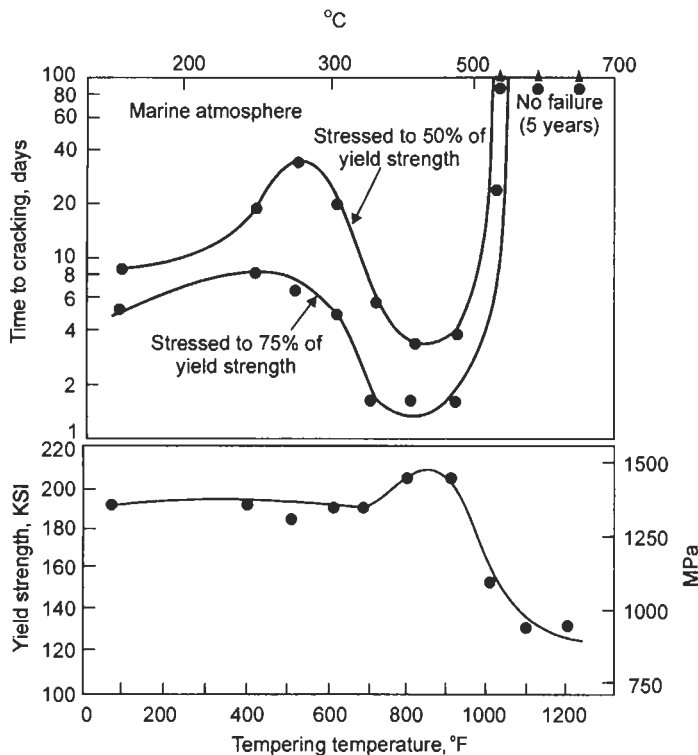
Fig. 7. Effect of tempering temperature on the cracking resistance and yield strength of martensitic stainless steel in a marine atmosphere.
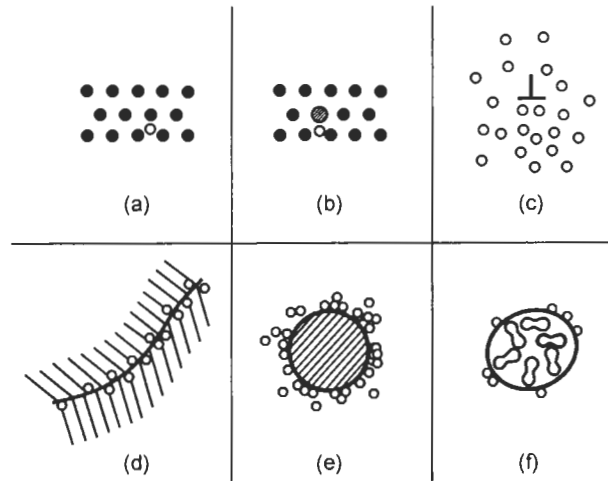
Fig. 8. Schematic view of destinations for hydrogen in a metal microstructure, discussed in the text: (a) solid solution; (b) solute hydrogen pair; (c) dislocation atmosphere; (d) grain boundary accumulation; (e) particle matrix interface accumulation; (f) void containing recombined H_2.

(i) Reduction in bonding energy between atoms.
(ii) Reduction in surface energy required for cracking.
(iii) Increase in pressure as atomic hydrogen forms molecular hydrogen.

Only atomic hydrogen can enter and diffuse through metal since hydrogen molecules are too large to do this. However, molecular hydrogen can form within structural defects such as voids, microcracks, etc., where it can remain. The behaviour of hydrogen within a steel is a function of its solubility and diffusivity. The effect that hydrogen has on a steel is controlled by:

(i) The form of the hydrogen in the steel (molecular or atomic).
(ii) The position of hydrogen accumulation (solid solution, solute hydrogen pair, dislocations, grain boundaries, particle matrix interface, or void), as shown in Fig. 8 [8].
(iii) The strength and stress state of the steel. Annealed steel will tend to blister; hardened, cold-rolled or highly stressed steel will tend to be embrittled and crack.

Molecular hydrogen in voids and defects does not cause embrittlement. Atomic hydrogen does not affect the elastic properties of a steel, only the plastic properties are impaired. The greatest affect on the plastic properties is found at temperatures between $-20°C$ and $40°C$, particularly at slow strain rates. As little as 2–2.5 ppm atomic hydrogen can lower the mechanical properties of a steel while 5–6 ppm atomic hydrogen can be detrimental [9].

The source of hydrogen in this instance has been a corrosion reaction that has taken place on some other steel component in the system. The pins had been heat treated into a susceptible region and even most conditions would provide sufficient hydrogen to cause HE.

In order to prevent HE in the future, it is thus important to identify the source of hydrogen.

The hardened alloy used in these pins is less corrosion resistant than an alloy in a softer condition (HRC 35 for example) would be. The important point, however, is that the previous chain lasted for three years without cracking and the environment in that case was the same as that during the failure. Therefore, the stainless steel used in the previous chain pins was not susceptible to HE. Before recommendations for a suitable heat treatment and associated hardness can be made, more details of the stresses involved during operation need to be furnished. In this way the optimum life of the conveyor chain pins can be obtained.

4. CONCLUSIONS

The conveyor chain pins failed due to hydrogen embrittlement. The hydrogen came from the corrosion of steel components in the system and not the actual pins themselves. The actual corroded

component(s) have not been identified, but should be found so as to minimize the likelihood of any future fractures.

The pins had been heat treated to give a hardness in the range HRC 46–47. Although this was only slightly higher than the hardness specified, it brought the steel to within the HE susceptibility range.

Hydrogen embrittlement can be avoided by:

 (i) Removing the source of hydrogen.
 (ii) Reducing the strength of the steel.
(iii) Using a steel that is more resistant to HE.

Before any recommendations can be made for a suitable hardness, and thus heat treatment schedule for future pins, more details of the operating stresses are required.

REFERENCES

1. Kemp, M. S. and van Bennekom, A., *Stainless Steel*, 1995, **16**.
2. Engel, L. and Klingele, H., *An Atlas at Metal Damage*. Wolfe Publication Ltd, London, 1981.
3. *ASM Handbook*, **4**, ASM International, 1991.
4. Ning, L., Zhonggang, D. and Mengen, H., *Materials Science and Technology*, 1991, **7**, 1058.
5. *Metals Handbook*, Vol. 10, 8th edn. ASM International, Ohio, 1975.
6. McIntyre, D. R., in *Process Industries Corrosion*, ed. B. J. Muniz, W. I. Pollock. NACE, Houston, 1986.
7. Sedriks, A. J., *Corrosion of Stainless Steels*. Wiley-Interscience, New York, 1979.
8. Thompson, A. W. and Bernstein, I. M., in *Advances in Corrosion Science and Technology*, Vol. 7, ed. M. G. Fontana and R. W. Staehle. Plenum Press, New York, 1980.
9. Warren, D., in *Process Industries Corrosion*, ed. B. J. Muniz, W. I. Pollock. NACE, Houston, 1986.

UNUSUAL CASES OF WELD-ASSOCIATED CRACKING EXPERIENCED IN A HIGH TEMPERATURE CATALYST REDUCTION REACTOR

M. L. HOLLAND

Metallurgical & Inspection Services, Mossgas, Private Bag X14, Mossel Bay 6500,
Republic of South Africa

Abstract—Two case studies are described which concern instances of weld-associated cracking discovered in a high temperature Cr–Mo catalyst reduction reactor soon after commissioning. One of the defects was diagnosed as re-heat cracking at a heavy section nozzle-to-shell weld, which was attributed largely to the high stress concentration at the toe of the weld in conjunction with tri-axial stress, resulting from the thick section geometry. Cracking was believed to have initiated during post-weld heat treatment which was only carried out 2 months after completion of welding.

The other defect described is a classic case of HAZ cracking at the external support legs of the reactor, again attributed largely to the delay in conducting post-weld heat treatment after fabrication.

In situ replication metallography was instrumental in establishing the failure modes in both instances, and was also able to demonstrate that the HAZ cracks were present before PWHT was carried out. © 1998 Elsevier Science Ltd. All rights reserved.

Keywords: Hydrogen-assisted cracking, metallurgical examination, process-plant failures, reheat cracking, welded fabrications.

1. INTRODUCTION

The following case histories relate to two instances of weld-associated cracking encountered in a catalyst reduction reactor soon after commissioning. The locations of the cracks and the mechanism of cracking is different in each case, although there is a common linkage in terms of original fabrication error.

The failure investigation undertaken is an interesting illustration of the value of *in situ* metallographic replication techniques as a non-destructive means of establishing vital microstructural data needed to confirm the failure mode.

The catalyst reduction reactor operates in a hydrogen-rich environment at a temperature of 385°C and a pressure of 1770 kPa and is therefore fabricated in 1Cr–1/2Mo steel. During routine inspection of the internals of the reactor after approximately one month's operation, a crack was detected in the hydrogen inlet nozzle C1. A more comprehensive inspection of all weld seams was therefore undertaken and revealed the existence of numerous cracks in the external support ring of the vessel.

The failure investigations undertaken into the causes of these cracks are summarised in the following sections.

2. CASE 1—EXAMINATION OF CRACKED NOZZLE C1

2.1. *Visual examination*

The nozzle was a heavy wall set-in forging to SA182 gr F12, having a maximum section thickness of 133 mm at the shell/nozzle weld where it was welded to SA 387 gr 12 cl 2 plate (see Fig. 1). Magnetic particle testing revealed that the major crack was on the top of the nozzle and extended for a distance of 240 mm along the toe of the weld, in the heat affected zone of the forging. The defect was initially assumed to be a fatigue crack. It was noted that there was a relatively sharp transition at the toe of the weld joining the nozzle to the shell wall.
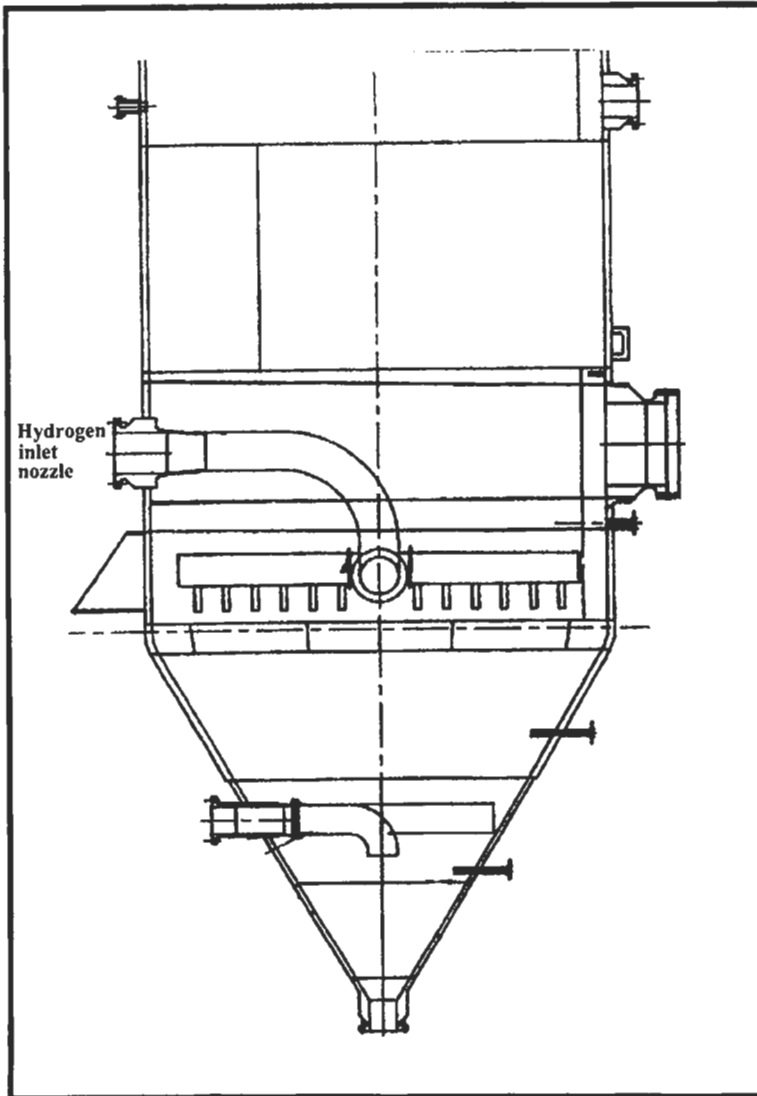
Fig. 1. Schematic view of catalyst reduction reactor (bottom section).

2.2. Metallographic examination

The two extremities of the crack were prepared for microstructural replication, polished to a 1 μm diamond finish and etched with 2% nital. Examination of the replicated micrograph in the laboratory showed the microstructure of the HAZ to consist of tempered martensite/bainite. The crack path was inter-granular in form, following the prior austenite grain boundaries (see Figs 2 and 3). The nature and location of the crack was typical of re-heat cracking of a low-alloy Cr–Mo steel, rather than a fatigue crack.

2.3. Hardness

Hardness measurements were taken across the cracked zone on one of the polished replicated areas using a "Microdur" portable hardness tester. The results showed generally acceptable hardness
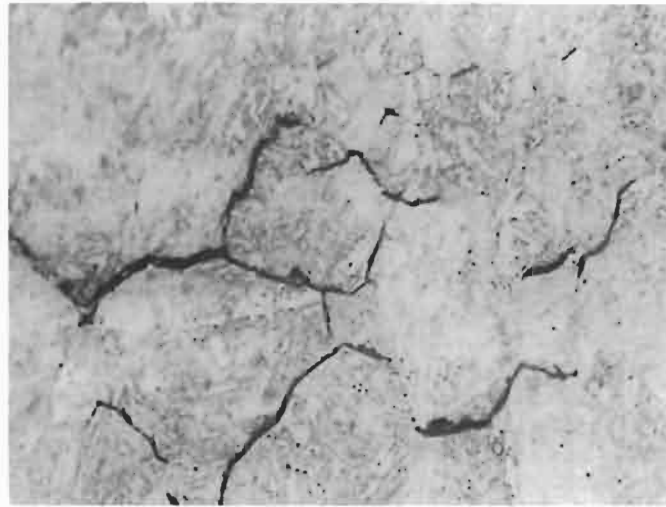
Fig. 2. Replicated micrograph of reheat crack showing bainitic microstructure and crack path following prior austenite grain boundaries (magnification × 100).
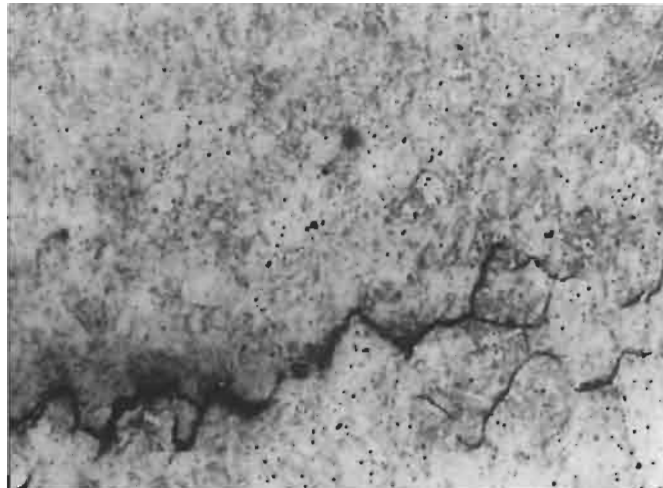
Fig. 3. Replicated micrograph of reheat crack showing bainitic microstructure and crack path following weld heat affected zone (magnification × 50).

values consistent with the original weld procedure qualification record (PQR), of between 181 and 204 HB.

2.4. *Discussion*

A literature survey [1] reveals that reheat or stress relaxation cracking may occur in the HAZ of welds in low-alloy steel during post-weld heat treatment or during service at elevated temperature. The factors that contribute to reheat cracking are:

(a) a susceptible alloy composition;
(b) a susceptible HAZ microstructure;
(c) a high level of residual strain combined with some degree of triaxiality;
(d) temperature in the strain relaxation (creep) range.

Most alloy steels suffer some degree of embrittlement in the coarse-grained region of the HAZ when heated at 600°C. Elements that promote such embrittlement are Cr, Cu, Mo, B, V, Nb and Ti, while S, and possible P and Sn, influence the brittle intergranular mode of reheat cracking. Molybdenum--vanadium and molybdenum–boron steels are particularly susceptible, especially if the vanadium is over 0.1%. The relative effect of the various elements has been expressed quantitatively in formulae, due to Nakamura (1) and Ito (2):

$$P = Cr + 3.3Mo + 8.1V - 2 \tag{1}$$

$$P = Cr + Cu + 2Mo + 10V + 7Nb + 5Ti - 2 \tag{2}$$

When the value of the parameter P is equal to or greater than zero, the steel may be susceptible to reheat cracking. The cracks are intergranular relative to prior austenitic grains and occur preferentially in the coarse-grained HAZ of the weld, usually in the parent metal but also sometimes in the weld metal. There are two distinct fracture morphologies: low-ductility intergranular fracture (as shown in Figs 2 and 3) and intergranular microvoid coalescence. The former is characterised by relatively smooth intergranular facets with some associated particles, and occurs during heating between 450 and 600°C. The brittle intergranular mode is initiated by stress concentrators such as pre-existing cracks or unfavourable surface geometry.

Compositions that have suffered reheat cracking in practice are Mo or Cr–Mo steels with more than 0.18% V, all of which have parameter values greater than zero. ASTM steels that are known to be subject to reheat cracking in thick sections are A508 Class 2, A517 Grades E and F, A533B, A542 and A387 Grade B. Time constraints precluded a detailed chemical analysis of the nozzle forging, and the material certificate does not quote residual values of V, Cu, Nb or Ti. According to eqn (1) above, however, the value of parameter P is 0.571 which would indicate susceptibility to reheat cracking.

The cracks generally occur during the PWHT heating cycle before reaching soaking temperature, probably in the 450–700°C range. The heating and cooling rates do not appear to have any significant effect on the result. Reheat cracks may also form or extend in service if the welded component is operating at elevated temperature and if joints are exposed to tensile stress, due to either inadequate PWHT or service loads.

The literature indicates that reheat cracking may be avoided by the following means:

(a) Material selection: for heavy sections, alloy content should be limited as indicated by the Japanese formulae and vanadium should be limited to 0.10% maximum.
(b) Design to minimise restraint: where restraint is unavoidable, consideration should be given to intermediate PWHT after the vessel is part welded.
(c) Use of a higher preheat temperature: dressing the toes of fillet and nozzle attachment welds; use of a lower-strength weld metal.

2.4.1. *Fabrication considerations.*. Consideration of the foregoing discussion in relation to the cracking experienced in the nozzle C1 of the catalyst reduction reactor indicates that many of the factors contributing to reheat cracking were present during fabrication. The following factors are believed to be particularly pertinent:

(a) Very heavy section thickness (133 mm) of forged nozzle in susceptible material.
(b) High stress concentration at toe of shell-to-nozzle attachment weld.
(c) Over-matched high yield strength filler metal E8015-B2 (UTS 567 MPa/±83,000 p.s.i.) compared with parent metal specification requirements of A182 gr F12 (min UTS 485 MPa/70,000 p.s.i.) and A387 gr 12 cl 2 (min UTS 450 MPa/65,000 p.s.i.).
(d) Significant delay between completion of welding and subsequent PWHT. The vessel code data book indicates that the completed weld was subjected to NDE examination by MT and UT on 15 November 1990 but the vessel was eventually only post weld heat treated some 2 months later on 11 January 1991.

2.5. *Conclusions and recommendations*

Metallographic evidence, supported by a review of the circumstantial evidence leads to the conclusion that the crack in the hydrogen inlet nozzle C1 was a reheat crack which probably initiated

during the PWHT of the very heavy section nozzle forging. Contributory factors would have been the high stress concentration at the toe of the weld, a degree of tri-axial stress resulting from the thick section geometry in this area, and an over-matching of mechanical properties of the filler metal. It is possible that the re-heat cracking may have occurred during service, but it is considered to be unlikely as the normal operating temperature of 385°C is believed to be too low to initiate the mechanism.

The possibility of some delayed cold-cracking in the HAZ cannot be ruled out in view of the protracted delay between welding and PWHT, and if present, would also have assisted in the nucleation of the reheat cracking.

Unfortunately it was impractical to weld these materials with a lower-strength filler metal since the lowest strength Cr–Mo filler specified under ASME II SFA 5.5 has a minimum UTS of 80,000 p.s.i. The following measures were included in the repair procedure for the nozzle:

(a) Pre-heat temperature was increased from 150°C as used in the original fabrication, to 200–250°C.
(b) Pre-heat was maintained until PWHT was carried out.
(c) The weld toe was dressed to a generous transition radius.

3. CASE 2—EXAMINATION OF CRACKS IN EXTERNAL SUPPORT RING

3.1. *Visual examination*

Cracking in the 1Cr–1/2Mo external supports fabricated from SA387 GR 12 cl 2 was detected by magnetic particle testing. All eight of the support legs contained cracks which were associated with the gusset-to-ring weld or the gusset-to-shell weld. Some were relatively short, transverse cracks, typically 30–40 mm in length, and some were relatively long 300–400 mm cracks running longitudinally along the toe of the weld. Figures 4–6 are typical of many of the cracks observed.

It was noted that much of the welding contour and weld surface finish was rather rough, as evidenced in the photographs. Particularly noteworthy, however, was the complete absence of any "rat holes" at the tri-axial joints between gussets, shell and horizontal ring (Fig. 7 shows typical detail of this area). The presence of "rat holes" at such intersections is considered to be normal, good fabrication practice in order to reduce or eliminate the complex tri-axial stresses that are otherwise imposed on these members. It was ascertained that this detail had indeed been clearly specified on the relevant fabrication drawings.

Fig. 4. Typical cracks found at external support welds.

378

Fig. 5. Typical cracks found at external support welds.

Fig. 6. Typical cracks found at external support welds.

3.2. *Metallurgical examination*

Three of the more easily accessible cracks were chosen for microstructural replication, polished to a 1 μm diamond finish and etched with 2% nital.

Examination of the replicated micrographs in the laboratory showed that in each case the cracks followed the martensitic region of the heat affected zone. Figures 8 and 9 are "panorama" micrographs across the HAZ from parent metal to weld metal in order to illustrate more clearly the location of the cracks in relation to the microstructure.

A significant feature is that all three of the cracks were filled with an oxide phase, which is shown particularly clearly in Fig. 10. This is indicative that the cracks were exposed to an elevated temperature oxidizing environment *after* initiation [2, 3].

3.3. *Discussion*

All three of the cracks examined above are typical of heat-affected-zone cracking which is also referred to as "hydrogen-induced cracking", "weld cracking", "delayed cracking" or "underbead cracking".

Fig. 7. Typical detail of gusset welds showing complete absence of "rat hole" at the junction of the three members.

Cracks in the HAZ are usually sited either at the weld toe, the weld root, or in an underbead position. The interaction between the factors responsible for cracking and the ways in which control over them may be achieved are discussed below [4].

3.3.1. *Hydrogen level*. During welding, hydrogen is absorbed by the weld pool from the arc atmosphere. During cooling, much of this hydrogen escapes from the solidified bead by diffusion but some also diffuses into the HAZ and the parent metal. The amount which does so depends on several factors such as the original amount absorbed, the size of the weld, the decreasing solubility, and the time–temperature conditions of cooling.

In general the more hydrogen present in the metal the greater the risk of cracking. Control over this hydrogen level may be achieved either by minimising the amount initially absorbed or by ensuring that sufficient is allowed to escape by diffusion before the weld cools. Frequently a combination of both measures provides the best practical solution.

3.3.2. *Stress level*. Stresses are developed by thermal contraction of the cooling weld and these stresses must be accommodated by strain in the weld metal. The presence of the hydrogen appears to lower the stress level at which cracking will occur. In rigid structures the natural contraction stresses are intensified because of the restraint imposed on them by the different parts of the joint. These stresses will be concentrated at the toe and root of the weld and also at notches constituted by inclusions and other defects. The higher degrees of strain which result produce higher risks of cracking for a given microstructural hardness.

The stress acting upon a weld is a function of weld size, joint geometry, fitup, external restraint, and the yield strengths of the plate and weld metal.

3.3.3. *Microstructure*. The heat affected zone (HAZ) of the parent metal adjacent to the weld is raised to a high temperature during welding and subsequent rapid cooling (quenching) by the surrounding parent metal causes hardening by transformation to martensite. Close to the fusion boundary the HAZ is raised to a sufficiently high temperature to produce a coarse grain size. This high temperature region, because of its coarse grain size is not only more hardenable but also less ductile than regions further from the fusion boundary. It is thus the region in which the greatest risk of cracking exists. As a general rule, for both carbon–manganese and low alloy steels, the harder the microstructure the greater is the risk of cracking. Soft microstructures can tolerate more hydrogen than hard before cracking occurs.

3.3.4. *Temperature*. Hydrogen embrittlement of ferritic steels occurs only at low temperatures,

Fig. 8. "Panoramic" section of crack location in support F1 (magnification ×100).

Fig. 9. "Panoramic" seection of crack location in support G1 (magnification ×100).

Fig. 10. Detail of oxide filled crack in martensite area of HAZ, support G1 (magnification × 100).

close to ambient. It is therefore possible to avoid cracking in a hard, i.e. susceptible, microstructure by maintaining it at a sufficiently high temperature, either until hydrogen has diffused away or until the microstructure is softened by tempering, to render it less susceptible. This principle is employed in multipass welding and in post-weld heat treatments.

An increase in temperature increases the rate of diffusion of hydrogen and thus accelerates its removal from the weld. Any measure which slows down the weld cooling rate is therefore helpful in reducing the hydrogen level. Preheat, for example, by slowing the cooling rate, not only softens the microstructure but also helps hydrogen to escape. As a result, higher hardness levels can be tolerated without cracking than if preheat had not been used.

For welds in those steels with hardenability so high that soft microstructures cannot be produced at all, and where preheat cannot remove sufficient hydrogen, (such as the Cr–Mo steels) a weld interpass temperature, or a post-weld heating temperature, high enough to avoid cracking must be held for a sufficiently long time to allow hydrogen to diffuse away before the weld cools.

3.4. *Fabrication considerations*

During fabrication of the supports of the catalyst reduction reactor, details of possible hydrogen sources and measures taken to effectively diffuse out the hydrogen are not known. Factors which would exacerbate the tendency to heat affected zone cracking, however would be the complex tri-axial stresses acting on the gusset/shell supporting welds due to the absence of the specified "rat holes", and the suspected delay between welding and subsequent post-weld heat treatment as reported in Section 2.4.1(d). If this delay was also applicable to the fabrication of the support ring it would have been essential to carry out an intermediate heat treatment to diffuse out hydrogen, as discussed above.

The oxidation of the cracks as shown in Fig. 10 can only have occurred in the Cr–Mo steel by exposure to an oxidising environment at a temperature of at least 550°C [2, 3]. This is well above the vessel operating temperature of 385°C and therefore indicates that oxidation of the cracks most probably occurred during post-weld heat treatment, or possibly during some subsequent undocumented welding operation.

3.5. *Conclusions*

It is concluded that the cracking found in the catalyst reduction reactor supports is due to heat affected zone cracking, otherwise known as "hydrogen-induced cracking". Significant contributory factors are believed to be the complex tri-axial stresses imposed due to the absence of the specified

"rat holes", and a suspected delay between the completion of welding and subsequent post-weld heat treatment. Oxidation of the cracks leads to the conclusion that they were most probably present before post-weld heat treatment was carried out [2, 3].

4. POSTSCRIPT

In both of the above cases it is evident that there was considerable debate over whether the defects were original fabrication defects, or whether they occurred in service. These are real, practical issues which often have contractual as well as technical implications, and for the failure investigator it is sometimes difficult to be dogmatic either way, as he is rarely in possession of all the facts at the time the investigation is carried out. If the above cases had been entirely fabrication related then the question arises as to why they were not detected during the final release inspection or during the pre-commissioning inspection?

The metallographic evidence which was presented builds a strong case for the defects having originated at the fabrication stage. The absolute truth of the matter, however, probably lies somewhere between the two extremes, in that the initial defects may not have been easily detectable during routine inspection but probably propagated during service to a size that only subsequently became readily detectable.

An interesting corollary to the saga of the external support leg cracking became apparent shortly after the above investigation was undertaken. A design review of the reactor installation revealed that radial thermal expansion of the support brackets had been restricted by grouting in the hold-down bolts in the slotted holes, which would probably have exerted considerable stress on the existing HAZ cracks, and caused crack propagation. The problem was rectified by removing the grouting, and installing a stainless steel foot plate under the bracket, resting on a bronze support plate to reduce friction.

In the final analysis, it must be recorded that weld repair of all of the defects was carried out meticulously under close supervision during August/September 1992, and that numerous subsequent inspections carried out on the vessel have failed to reveal any re-occurrence of the cracking.

REFERENCES

1. Lancaster, J. F., *Metallurgy of Welding*, 1987, Allen & Unwin, pp. 206–209.
2. *ASM Metals Handbook*, Vol. 1, 10th edn, "Properties & Selection: Irons, Steels & High-Performance Alloys", 1990, p. 617.
3. Smithells, *Metals Reference Book*, Butterworth, 1983, p. 31-13.
4. Coe, F. R., *Welding Steels Without Hydrogen Cracking*, The Welding Institute, 1973.

HYDROGEN CRACKING OF FERRITIC STAINLESS STEEL THERMAL STORAGE TANKS

SHINJI KONOSU* and TSUYOSHI NAKANIWA

Department of Mechanical Engineering, Ibaraki University, 4-12-1 Nakanarusawa, Hitachi 316, Japan

Abstract—A ferritic stainless steel (SUS436L), which was subjected to various kinds of reduction ratio was precharged with hydrogen at 40°C in 15% HCl solution by employing galvanic reaction with zinc. Tensile tests were performed in air at room temperature on both uncharged and charge specimens. Finite element method (FEM) analyses were carried out to obtain strain at panel corners under various different internal radii in a thermal storage tank when it was subjected to internal pressure. As a result, it was found that the value of internal corner radius/thickness of the panel (R/t) should be more than about 2 in order to prevent hydrogen embrittlement cracking. © 1998 Published by Elsevier Science Ltd. All rights reserved.

Keywords: Cleavage fracture, embrittlement, heat-exchanger failures, hydrogen-assisted cracking, tanks (failures).

1. INTRODUCTION

Ferritic stainless steel is frequently used in the manufacture of waterheating appliances due to its excellent formability and its extremely high resistance to such shortcomings as pitting and stress corrosion cracking associated with austenitic stainless steel. However, because ferritic stainless steel possesses high hydrogen embrittlement susceptibility, investigations are being conducted [1] on the effect of hydrogen on the mechanical properties of the material. Meanwhile, numerous accidents thought to be due to hydrogen embrittlement are occurring at the corner portions of cold-bent ferritic stainless steel (SUS436L) panels used in thermal storage tanks. It is believed that fracture elongation in hydrogen-charged ferritic stainless steel is largely due to the influence of cold working and, further, that the strain occurring on the inside of bent portions during water proof tests is attributable to the influence of the inner radius of the bent portion.

Hence, using ferritic stainless steel in the current series of investigations, the influence of cold working on fracture elongation in hydrogen-charged specimens was determined experimentally and the limits of hydrogen embrittlement cracking on the inside of cold-bent portions were studied and clarified by analyses employing the finite element method.

2. FAILURE OF THERMAL STORAGE TANK

Figure 1 shows a portion of a thermal storage tank assembly measuring 4 m in height, 3 m in width and 10 m in length. It consists of 4 banks of tanks stacked vertically, with three rows arranged in the longitudinal direction. The tank panel is made from ferritic stainless steel (SUS436L), with the corner portions being bent by cold forming, as shown in Fig. 2. Hot-dip zinc-coated steel tubes are laid inside the tank. Coolant is passed through these tubes to freeze the water in the tank during the night and the heat of melting is utilized during the day by means of air conditioners.

After water proof tests were conducted at the respective pressures concerned (Case 1: hydraulic pressure 3.52×10^{-2} MPa, Case 2: 6.36×10^{-2} MPa), cracks were found in the corner portions (inner radius $R = 1.62$ mm). The appearance of the cracked portion in Case 2 is shown in Fig. 3. It can be seen that the crack has propagated from the inside of the panel toward the outside.

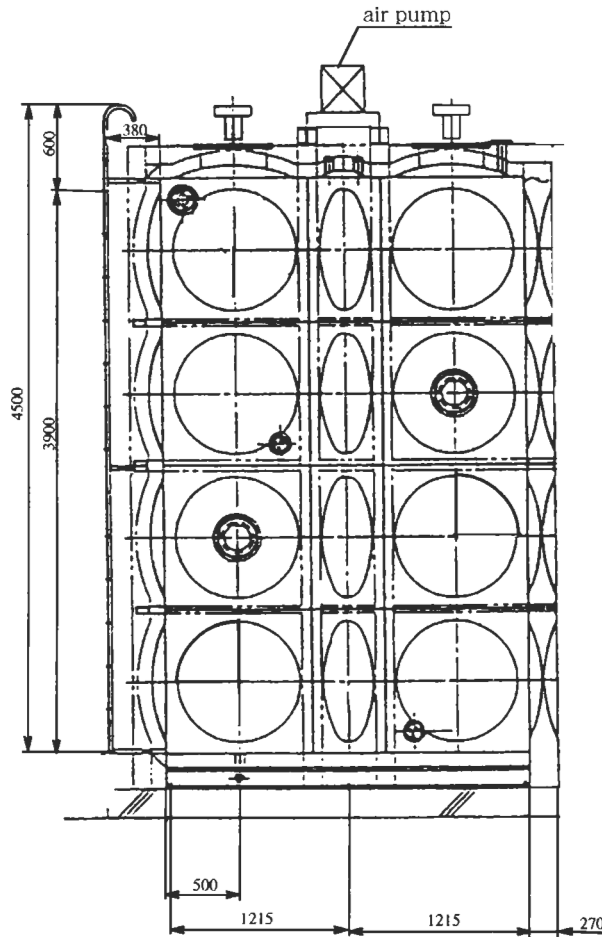* Author to whom correspondence should be addressed.

Fig. 1. Schematic diagram of thermal storage tank.

Figure 4 shows the microscopic structure of the crack and the results of observation thereof. Plastic deformation (hardness of inside surface of bent portion Hv = 250–300) attributable to cold working is evident in the corner section where the hydrogen charge of the steel was 3.5 ppm. The crack, which had propagated transgranularly in a brittle manner, was a cleavage fracture exhibiting features typical of hydrogen embrittlement cracking. Accordingly, it is considered that the following reactions (galvanic corrosion [2]) between zinc and ferritic stainless steel occurred in the tank during acid washing at the fabrication stage, causing the stainless steel to become hydrogen-charged.

$$\text{anode reaction: } M \rightarrow M^{n+} + ne^-$$

$$\text{cathode reaction: } nH^+ + ne^- \rightarrow nH$$

The cracking is believed to have occurred in the subsequent water proof testing when the material was subjected to tensile strain.

Cold working becomes more pronounced as the inner radius of the corner portion shown in Fig. 2 becomes smaller and, consequently, hydrogen embrittlement susceptibility is thought to increase. Further, it is conceivable that the amount of tensile strain occurring on the inside surface during water proof testing also increases with smaller inner radii.
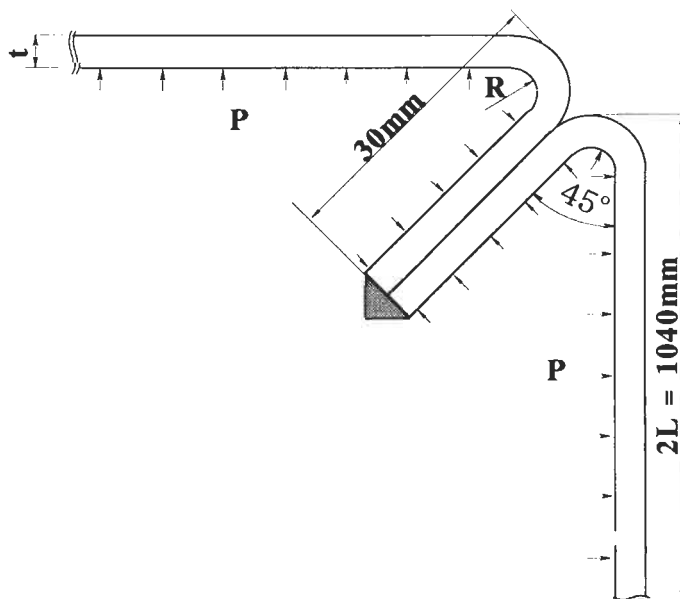
Fig. 2. Enlarged sketch of corner of thermal storage tank panel.

5mm
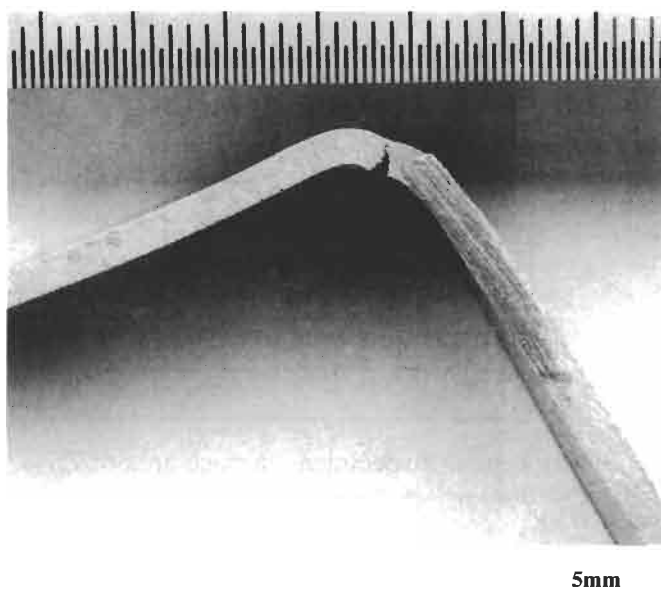
Fig. 3. Cracking in corner.

3. EXPERIMENTAL METHODS

The chemical composition of the ferritic stainless steel (SUS436L) used as the test material is given in Table 1. Using a rolling mill, plate of 3.16 mm thickness was rolled to reduction ratios

(a)   (b)
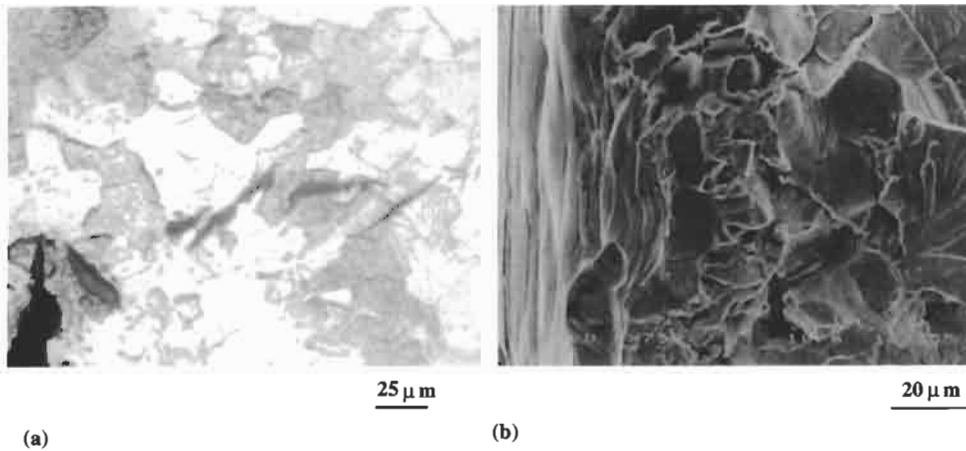
Fig. 4. Microstructure of cracks and SEM micrographs of fracture surface in panel corner.

40°C,15%HCl

specimen

heater

Zn
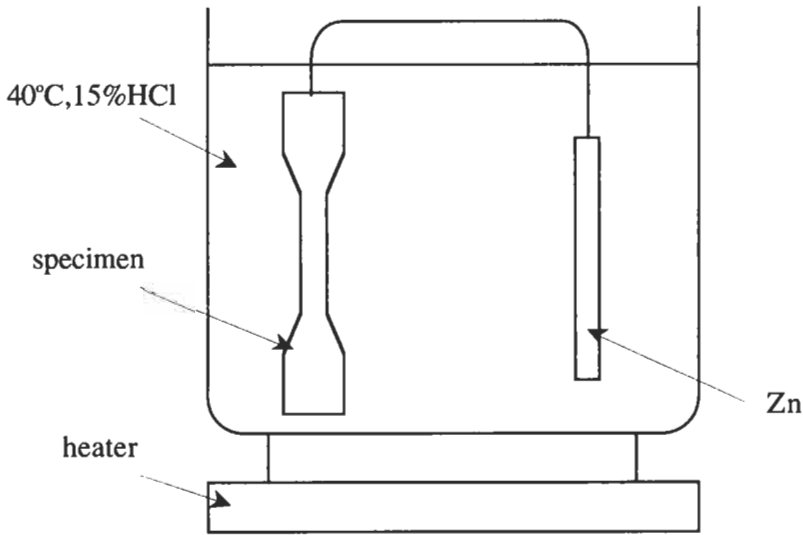
surface area of specimen : surface area of Zn = 2 : 1

Fig. 5. Hydrogen absorption method using galvanic reaction.

Table 1. Chemical compositions

	C	Si	Mn	P	S	Cr	Ni	Mo	N	Ti
Test material	0.006	0.21	0.20	0.028	0.001	17.91	0.11	0.96	0.007	0.31
JIS G 4305 SUS 436L	⩽0.025	⩽1.00	⩽1.00	⩽0.040	⩽0.030	16.00–19.00	—	0.75–1.25	⩽0.025	—

ranging from 10% to 40%. Then JIS 14 flat test pieces (JIS Z2201) with a parallel portion of 35 mm were prepared and used in the tests.

The test pieces were precharged with hydrogen by immersing the test pieces, together with zinc (2 : 1 surface area ratio), in a 15% HCl aqueous solution for 24 h at 40°C, thereby forming a galvanic coupling between the test piece and the zinc. As a result of this procedure, the charged hydrogen content of the steel of the 30% reduction ratio test piece was 2.3 ppm, which is virtually the same as that of the bent portion of the actual equipment. The test pieces were subjected to tensile tests at ambient temperature at constant cross-head speed (a strain rate of 4.8×10^{-4} sec^{-1}, which is a sufficiently low speed to evaluate hydrogen embrittlement [1]) immediately after being hydrogen-charged and the surfaces and fractures of the test pieces were then examined.

4. EXPERIMENTAL RESULTS AND DISCUSSIONS

4.1. *Strain at bent portion*

Strain ε_i on the inner side of a panel which has been subjected to bending was approximated by applying the following formula [3]:

$$\varepsilon_i \cong -\frac{\lambda_1 t}{R + \lambda_1 t}, \lambda_1 = 0.386\left(\frac{R}{t}\right)^{0.157}, \tag{1}$$

where R = inner radius of bent portion, t = plate thickness and λ_1 = distance from inner surface to neutral axis.

Then, by substituting the values applicable to the bent portion of the actual equipment ($R = 1.62$ mm, $t = 2$ mm) in the above formula, it is estimated that the compressive strain occurring at the inner surface of the bent portion was about 31%. The results of hardness tests carried out on specimens possessing the various reduction ratios due to rolling are given in Fig. 6. Here, the hardnesses of specimens whose reduction ratio is of the same magnitude as the compressive strain (about 31%) on the inside surface resulting from the bending process are Hv = 240–280. This is about the same as the hardness (Hv = 250–300) of the inner surface attributable to the bending process.

4.2. *Tensile properties*

Using material that had been cold-rolled at various reduction ratios, tensile tests were conducted on hydrogen-charged test specimens to study the effect of reduction ratio on rupture elongation.
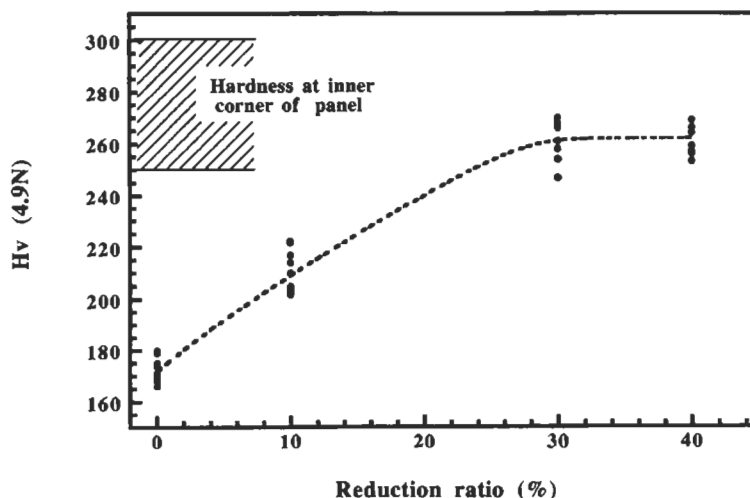
Fig. 6. Relationship between reduction ratio and hardness.
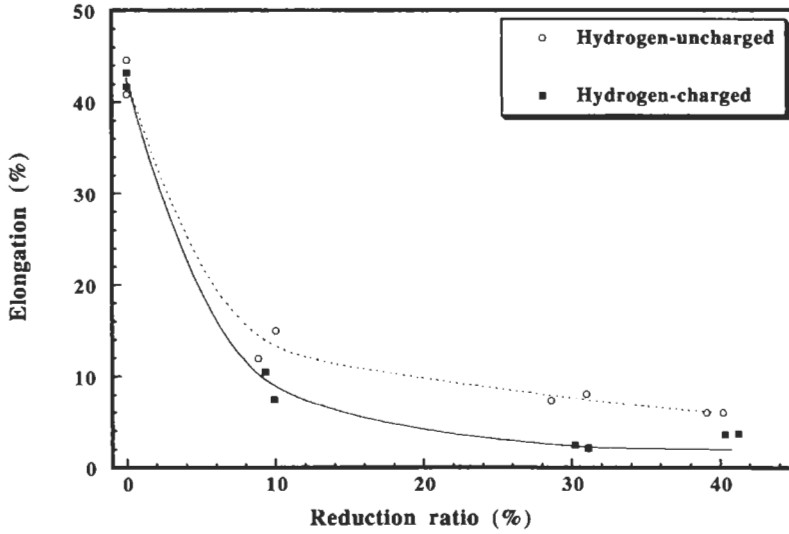
Fig. 7. Influence of reduction ratio on rupture elongation of specimens.

The results are given in Fig. 7. With both the hydrogen-charged and hydrogen-uncharged specimens, it was found that rupture ductility decreased with increased reduction ratios (increased magnitude of cold working). Furthermore, rupture elongation decreased still further in the hydrogen-charged specimens, as compared with the hydrogen-uncharged specimens.

A chart showing the stress–strain relationship in the case of a reduction ratio of 30% is given in Fig. 8. From this, it can be seen that the rupture elongation of hydrogen-charged specimens is very markedly reduced. The results of observations of the cross sectional microscopic structure in the vicinity of ruptures in a 30% reduction ratio specimen and related scanning electron micrographs are shown in Fig. 9. The hydrogen-uncharged specimen had ruptured in a ductile manner and the entire surface of the fracture is dimpled (Fig. 9(a)). On the other hand, cleavage fractures had occurred in the hydrogen-charged specimen (Fig. 9(b)), indicating the large influence of hydrogen.
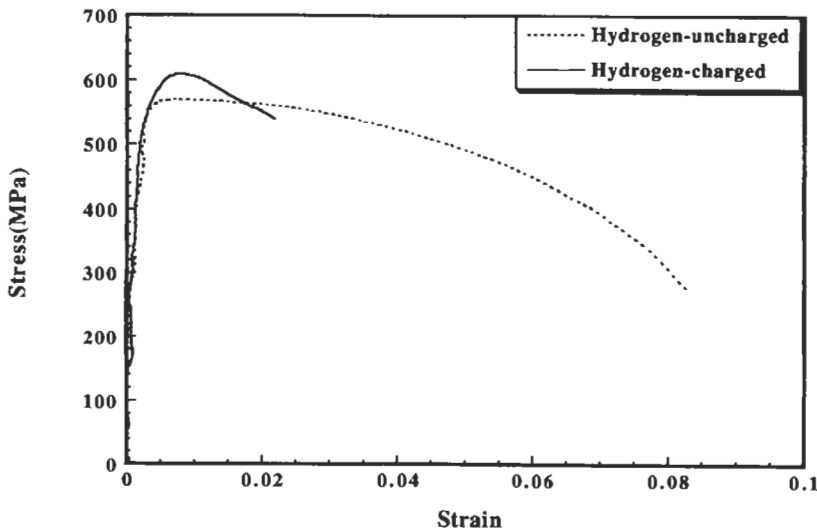
Fig. 8. Stress–strain relation of a tensile test specimen for the case where reduction ratio = 30%.
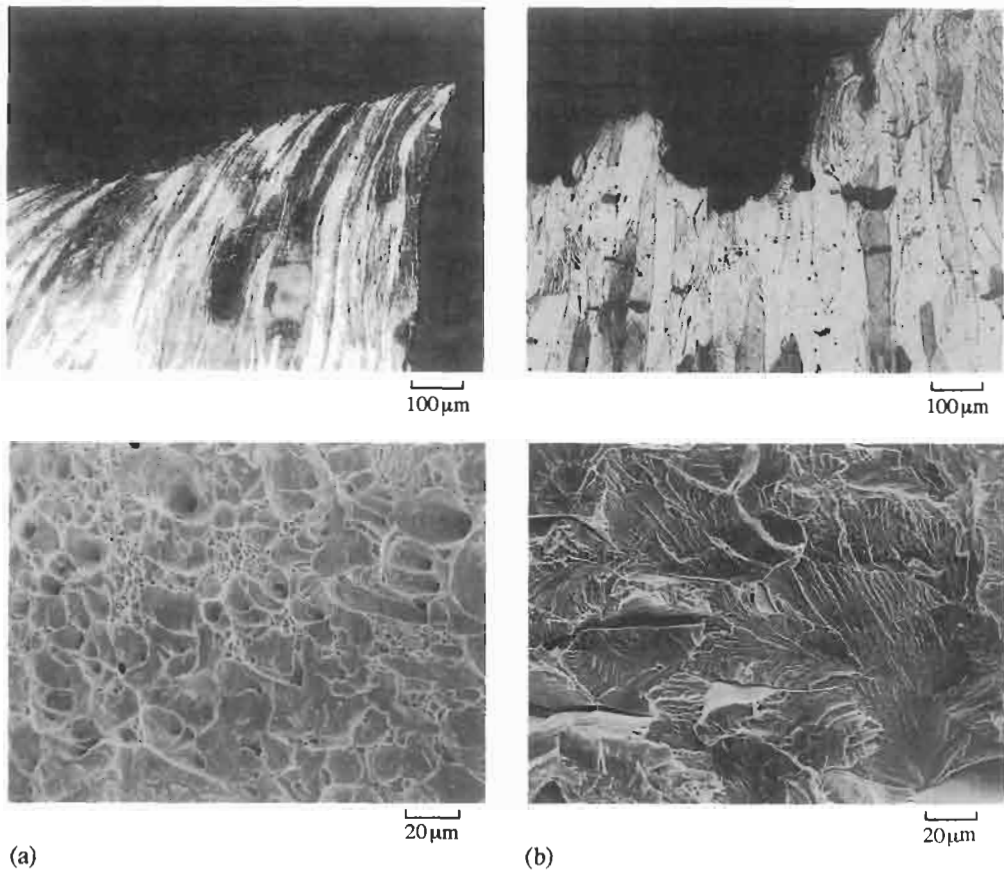
Fig. 9. Microscopic structures and SEM micrographs of fracture surfaces of tensile test specimens for 30% reduction ratio. (a) Hydrogen-uncharged; (b) hydrogen-charged.

4.3. *Analysis of strain occurring in bent portion*

Tensile strain is imposed on the inner surface of the bent portion during water proof testing. While rupturing will occur when the strain at this time exceeds the rupture elongation concerned, which has been degraded as a result of hydrogen charging, the magnitude of the strain differs according to the inner radius of the bent portion.

So, taking the case of a bent portion, as shown in Fig. 2, which is subject to internal pressure, a finite element method (FEM) model was devised in which the inner radius was varied. A two-dimensional eight-node quadrangle (approx 8000 nodes, 2000 elements) was employed and elastic analyses (Young's modulus 2.1×10^5 MPa, Poisson's ratio 0.3) were carried out under plane strain conditions to obtain the strain ε_{max} occurring on the inner surface of the bent portion when it is subjected to internal pressure. ε_{max} was divided by the strain ε^*, which is the strain at the end of a beam simply supported at both ends and having a uniformly distributed load. The ratio is plotted against R/t as shown in Fig. 10. The relation was approximated by using the following formula:

$$\frac{\varepsilon_{max}}{\varepsilon^*} = 1 + 0.371\left(\frac{R}{t}\right)^{-0.745},$$

$$\varepsilon^* = \frac{M}{E'Z},$$

$$M = \frac{p(2L)^2}{12}, Z = \frac{bt^2}{6}, E' = \frac{E}{(1-v^2)}, \tag{2}$$
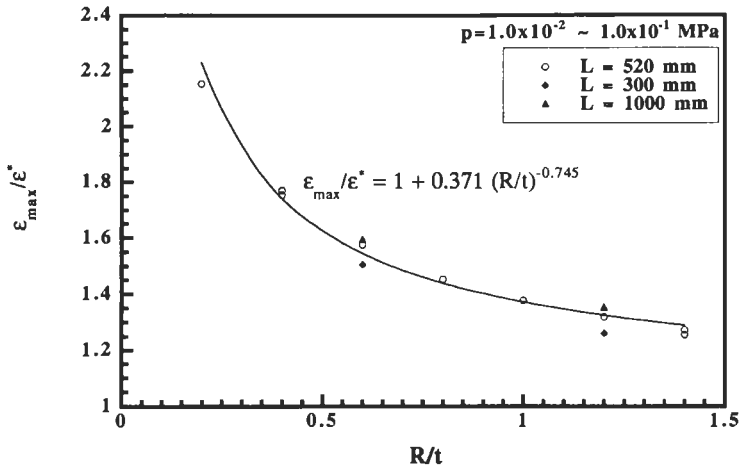
Fig. 10. Influence of internal corner radius on pressure-induced strain at inner side of a corner (data ◯ are derived from FEM analysis. Solid line indicates approximate eqn (2)).

where b = width, E = Young's modulus, v = Poisson's ratio, p = internal pressure, L = half length of span.

Clearly, ε_{max} increases as R/t decreases.

4.4. Evaluation of hydrogen embrittlement cracking

Because the tensile strain on the inner surface of a bent portion during water proof testing can be estimated by the analyses mentioned in Section 4.3, in addition to the fracture elongation which was sought experimentally in Section 4.2 for the material subjected to various magnitudes of cold working, criteria for the development of hydrogen embrittlement cracking can be found on condition that the tensile strain on the inner surface exceeds the fracture elongation of the material.

Figure 11 shows the relationship between R/t and the calculated strain which develops on the
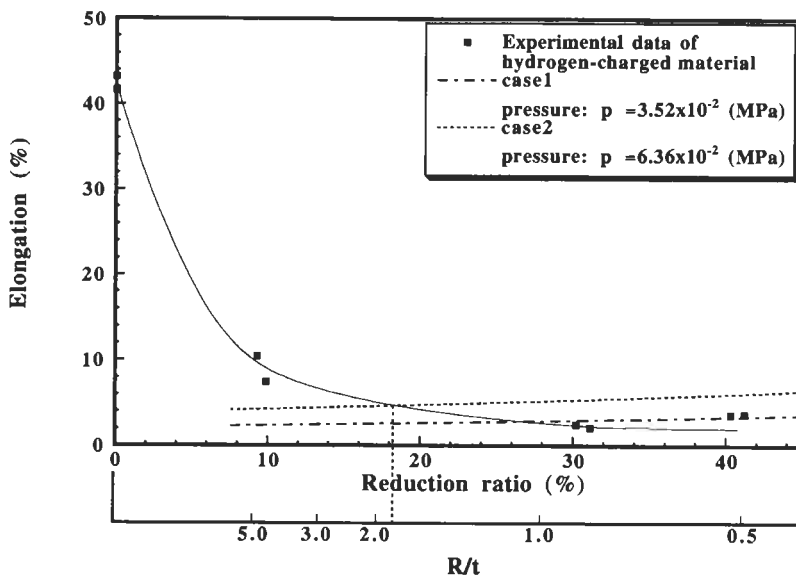
Fig. 11. Conditions for occurrence of hydrogen embrittlement cracking (condition whereby pressure-induced strain at the corner exceeds the rupture elongation of the hydrogen-charged material).

inside of the bent portion when it is subjected to internal pressure and also the relation between reduction ratio and fracture elongation. Because reduction ratio (namely, the compressive strain occurring at the inner surface) can be determined from R/t through eqn (1), both reduction ratio and R/t (corresponding to the magnitude of cold working) are plotted on the horizontal axis. The figure shows that a dangerous situation develops when R/t is less than about 2 because the strain on the inside of the bent portion due to the load imposed at water proof testing exceeds the rupture elongation. Hence, when carrying out bending work, it is important, from the mechanical standpoint, to perform the work so that R/t exceeds approximately 2 in order to prevent hydrogen embrittlement cracking for similar applications.

5. CONCLUSION

The damage occurring at the cold-bent corner portions of thermal storage tanks made of ferritic stainless steel (SUS436L) is believed to be due to hydrogen embrittlement cracking brought on by tensile strain which developed during water proof tests performed after the stainless steel had been charged with hydrogen by galvanic corrosion during acid washing at the fabrication stage. The corner portions were analyzed by the finite element method and the dependency, on bending radius, of the strain developing at the corner portion during water proof tests was clarified. Additionally, the dependency of magnitudes of cold working on fracture elongation of tensile test specimens hydrogen-precharged was ascertained. Based on these results, it was clarified that, from the mechanical standpoint, inner radius/thickness (R/t) must exceed approximately 2.

REFERENCES

1. Grubb, J. F., in *New Developments in Stainless Steel Technology*, ed. R. A. Lula, ASM, Metals Park, OH. 1985, p. 175.
2. *Metals Handbook*, "Failure Analysis and Prevention", Vol. 10, 8th edn, ASM, Metals Park, OH, p. 182.
3. Saito, K., Japan Soc. Mech. Engrs. (in Japanese), 1972, 16(53), 133.

Hydrogen embrittlement failure of hot dip galvanised high tensile wires

N.K. Mukhopadhyay, G. Sridhar, N. Parida, S. Tarafder, V.R. Ranganath*

National Metallurgical Laboratory, Jamshedpur 831 0017, India

Abstract

A case of failure of high carbon eutectoid steel wires is investigated. During the production stage, i.e. cold drawing and subsequent coiling/stranding operations, the wires of ~ 4.0 mm diameter failed by central splitting along longitudinal planes. Microscopic examination, fractography and mechanical tests along with acoustic emission monitoring were carried out on the wire samples. The experimental results confirm that the failure is related to hydrogen embrittlement which has been characterised by fractography, strain rate sensitivity and susceptibility to delayed fracture as indicated by acoustic activity. It has been argued that the cohesive energy model for hydrogen embrittlement, where hydrogen reduces the bond strength and cohesive strength ahead of pre-existing cracks, can explain the failures observed in the present case. It appears that improper pickling and subsequent baking processes, during the final stages of drawing operations, are responsible for the hydrogen related failures.

Keywords: Hydrogen embrittlement; Galvanised wire; High tensile wire; Acoustic emission

1. Introduction

Several types of wire rod failures are reported in the literature, mostly due to inclusions, strain ageing, hydrogen embrittlement, liquid metal embrittlement, improper control of microstructure etc. resulting in bulging, flaking and splitting. Splitting failures may occur spontaneously when the material is embrittled along a longitudinal plane and the residual stresses generated during the drawing and handling operations are relieved. Cold drawn high carbon steel wires are amenable to being more weak along the longitudinal plane as compared to the transverse planes due to the fibre-like deformation of pearlitic phases in the longitudinal direction [1]. It has been observed that metallurgical embrittlement may also take place due to interfacial segregation of hydrogen (H) in high strength steels, which leads to delamination/decohesion type failures [2]. A short discussion

---

* Corresponding author. Tel.: +91 657 426091; fax: +91 657 426527; e-mail: vrr@csnml.ren.nic.in

follows on hydrogen embrittlement theories and acoustic emission techniques used to detect hydrogen activity in metals under stress.

1.1. Hydrogen embrittlement

The effect of H has been the subject of extensive studies to understand the mechanisms of degradation in mechanical properties of metals and alloys because industries often encounter failure of products due to hydrogen embrittlement (HE) [3–6]. Generally atomic H, which is absorbed initially by the metal surface, transforms to molecular H when the concentration of H is high. Molecular H resides in voids, pores and interfaces among many other defect sites. If these defects are not present in the vicinity of a high H area, then blisters or hair line cracks are formed to release the high pressure. In the equilibrium situation, both atomic and molecular H will be present inside the material at a high concentration of H. Highly tensile stressed regions will be the most suitable sites for atomic H. During welding the H picked up, from residual H_2O or damp electrodes, diffuses to the base plate when the weld is hot and subsequently causes cold cracking. During electroplating and pickling H can enter the lattice, but is diffused-out by a subsequent baking treatment at 200–250°C.

Some of the important models of HE are discussed below. One of the models, the planar pressure mechanism, predicts that the high pressure developed due to molecular H within gas pores inside the material causes cracking [7, 8]. Although this model explains the embrittlement of H charged metal, it is not accepted as a universal mechanism for HE as it cannot explain the delayed cracking phenomenon. A model proposed by Troiano et al. [9], suggested that the cohesive strength is reduced due to the presence of H atoms. Hydrogen atoms diffuse easily to regions of triaxial tensile stress, as at the tip of a crack, and assist crack propagation by reducing the cohesive strength of the material ahead of it. Thus the crack propagates discontinuously, controlled by a critical concentration of atomic H built up near the tip of the crack. One model based on the reduction of surface energy, explains easy crack growth in the presence of H [10, 11]. The model proposed by Beachem [12, 13] is based on enhancement of dislocation mobility which induces highly localised plastic flow at very low stress levels. HE is also explained by metal hydride formation in materials such as titanium, vanadium and zirconium (group IVa and Vb) [14]. It has also been suggested that hydride-induced embrittlement may occur in steels containing these metals. A completely different type of HE in the presence of H and C in plain carbon steel at high temperature and pressure occurs due to formation of methane inside the material. The formation of methane and the development of high pressure causes blistering which gives rise to typical failures observed in the petroleum industry [15]. This process produced decarburisation and is somewhat different from low temperature HE.

The process of H cracking is the result of one or more of the micro-mechanisms such as: (i) cleavage, (ii) intergranular decohesion, or (iii) microvoid coalescence. All the three mechanisms in the same steel alloy, when tested at different strength levels, have been reported in the literature [6]. Therefore, depending on materials and operational parameters various characteristic fracture surfaces of HE will be generated.

1.2. HE and acoustic emission

Acoustic emission (AE) is the name given to the elastic waves that are generated within a material as a consequence of deformation and fracture processes. Acquisition and analysis of these signals

can be used to detect, with high sensitivity, deformation and fracture in a material [16]. As HE is characterised by the tendency to crack leading to failure at reduced ductility, acoustic emission techniques (AET) can be applied to detect hydrogen embrittlement failure. It has been shown that AE as a result of HE and stress corrosion cracking (SCC) provides information on the crack growth process in greater detail than is otherwise possible [17–19]. Hartbower et al [18] monitored crack initiation and propagation during SCC of maraging steel, and their results could be excellently correlated with the cumulative counts of the AE signals. Dunegan and Tetelman [19] have also used this technique to monitor the onset of unstable fracture in hydrogen charged 4340 steel test specimens and bolts under constant load. They proposed a power law relationship between count rate and stress intensity factor and suggested a critical AE rate at onset of rapid fracture. Similar studies by Parida and Bhattacharya [20], on bend specimens of the same steel, have shown that the incubation time to nucleate microcracks can be monitored in terms of some directly observable AE parameters.

2. Investigation

High strength steel wire rods which are used for manufacturing steel ropes, in a local industry, have been found to be failing at the final stage of production [21]. Stelmor cooled billets of 120×120 mm^2 having a nominal composition of C—0.82, Mn—0.7, Si—0.2, S—0.02 max. and P—0.02 max., are hot-rolled in stages to 12 mm diameter wire rods, which are first pickled and baked at 150°C for 15 min, followed by flux coating. The wires are then pre-drawn to 10 mm diameter before patenting. A gap of 10 h is allowed between coating and pre-drawing and patenting. Subsequent to the patenting process, the wires are again pickled and dipped in hot water and drawn through a flux to 6 mm diameter. This is followed by galvanising and final drawing to 4.15 mm diameter followed by stranding/spooling.

The wire rods, which have failed at various stages during spooling and stranding, typically show a split along the drawing direction (Fig. 1). The longitudinal splitting into layers during the rolling
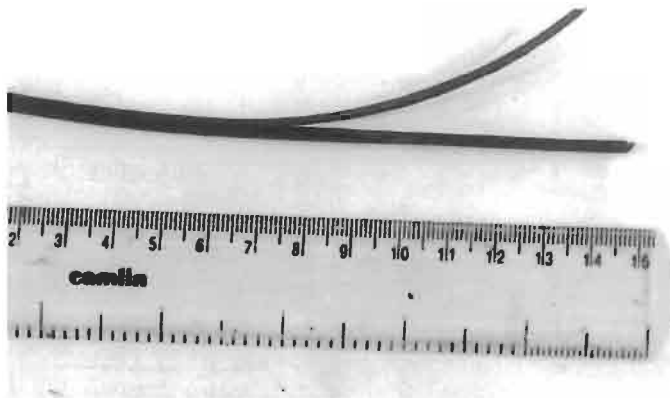
Fig. 1. Wire rod showing a typical split failure.

operation, termed delamination, is one of the qualitative indication of the decrease in ductility. The fresh fracture surfaces were observed to be shiny, indicating the possibility of HE. No other distinctive features were observed on the surfaces of failed wire rods.

The present investigation was carried out to confirm embrittlement either due to metallurgical reasons or due to the presence of H. An attempt has also been made in this investigation to identify HE by means of AE monitoring during delayed cracking experiment.

3. Experimental details

Metallographic examinations, after polishing with diamond paste in the final stage, in the unetched and etched condition, were carried out on the longitudinal and transverse cross sections of the wire. The failed surfaces were examined with the help of a scanning electron microscope (S.E.M.) equipped with EDX facility.

Delayed cracking tests were conducted on partially split wire samples, by hanging a dead weight (800 g), resulting in approximately 70% of the yield stress of the material, to one of the split ends. During these tests, the AE signals were monitored on partially split wire samples using a 150 kHz resonant piezoelectric sensor placed on the wire surface. The AE signals were amplified by a 40 dB per-amplifier and fed to a computerised AE system to record and analyse the signals. A schematic of the experimental set-up is shown in Fig. 2.

Since there is no single theory to prove H attack conclusively, recourse may be had to confirm or eliminate the presence of H in the steel wire rod samples by conducting mechanical tests [1, 22]. For the tensile tests, the samples were cut such that the parallel length between the grip ends was maintained at 100 mm. The tests were conducted on a servohydraulic test system equipped with digital controls. For obtaining comparative estimates of the toughness of the wire rod material, samples of 55 mm length were employed and tested on an impact test machine.

Since it is believed that the deleterious effects of H would diminish if the suspected components are baked, all the tests as described above were conducted both on the as-received as well as the baked specimens. The baking treatment given to the specimens, after removing the galvanised layer by polishing, was 30 min at a temperature of 250°C, to eliminate any atomic hydrogen.
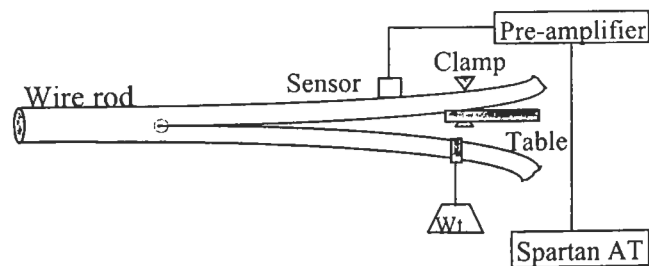
Fig. 2. Schematic view of the experimental set up to study delayed cracking using AE.

4. Results

4.1. Microscopy

Microscopic examination was conducted to observe both the inclusions and the microstructural features. Typical features are shown in Fig. 3(a and b). In addition to the few inclusions that are observed, a number of pores approximating to 1–2% volume fraction were present in most of the areas that were examined. It may be noted that the inclusions and the pores could be distinguished from each other by varying the focusing plane, as their planes of foci are different, and this has been demonstrated in Fig. 3(a and b). It is also observed that some of the pores have coalesced to form crack like defects. Figure 4(a and b) presents the typical features that are expected in a cold drawn steel wire rod, viz., a fibrous appearance comprising elongated ferrite and cementite lamella (pearlite). A crack along the drawing direction has been marked in Fig. 4(a).

4.2. Fractography

The longitudinal fracture surfaces of the failed surfaces, examined under the SEM, showed a fibrous appearance with secondary cracks (marked by arrows in Fig. 5). The presence of secondary cracks suggests H attack of some form or other. A detailed look at a crack embedded in the material supports the classification of this failure as delamination. The presence of some non-inclusion hard particles (marked by an arrow head) segregated randomly on the fracture surface is observed. EDX survey carried out on these particles indicated them to be cementite. The formation of globular cementite during drawing operations occurs by the densification of cementite through wrinkling or buckling, aided by accelerated diffusion of C during deformation [2, 23].

4.3. Tensile and impact tests

It is believed that a material affected with atomic H would show similar toughness values as that of the same material without any H in it, when tested under high strain rate (such as in the impact
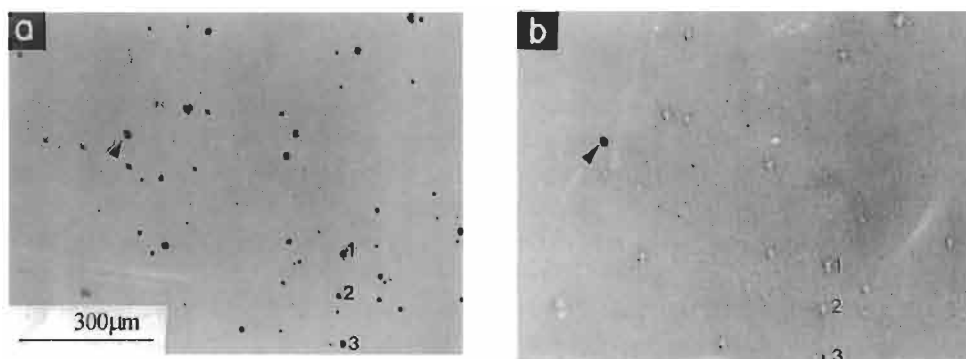
Fig. 3. Optical micrographs of unetched wire drawn sample. (a) Transverse section shows abundance of pores in focused condition. (b) Over-focused condition showing pores as illuminated spots and inclusions as dark spots. The correspondence between (a) and (b) can be noted.
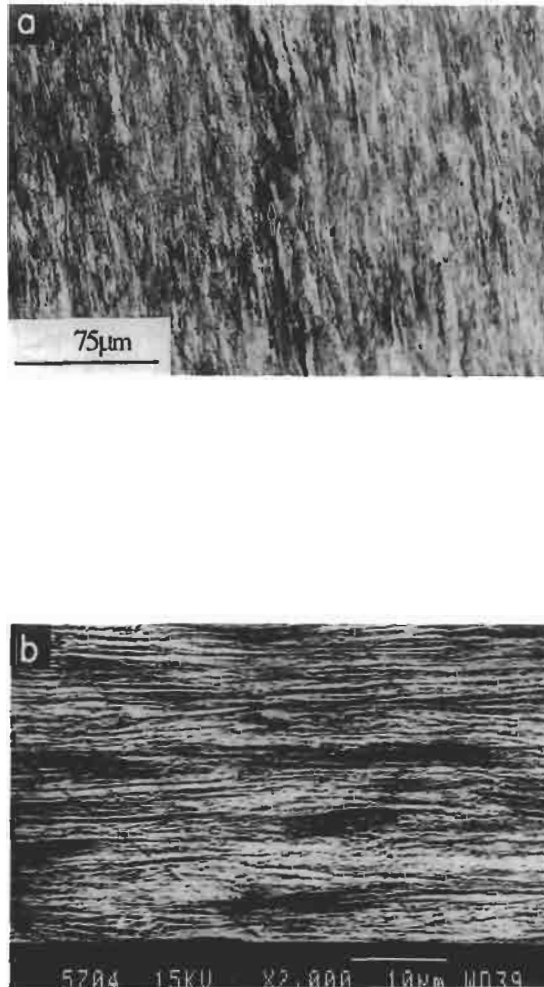
Fig. 4. (a) Optical micrograph and (b) SEM photograph showing microstructures featuring typical fibrous nature comprising elongated ferrite and cementite lamella. The cracks along the drawing direction can be observed in (a).

test), and that under a slow strain rate test (such as in a standard tensile test) would show a significant difference in toughness. The impact toughness results from both as-received and baked specimens are shown in Table 1. It may be noted that although the specimen geometry was non-standard for CVN toughness tests, the impact toughness values from identical specimens would be useful for making comparisons. It was observed that both the lots showed an average value of 33 J under identical test conditions.

The nature of the stress-strain plots does not show any evidence of strain ageing. Figure 6, and also Table 1, show the tensile properties of the baked as well as the as-received samples. A noticeable increase may be observed in the % elongation and yield stress of the baked specimens, suggesting hydrogen embrittlement to be operative in the as-received wire. A quantitative estimate of the residual hydrogen in the wires could not be attempted because atomic hydrogen would
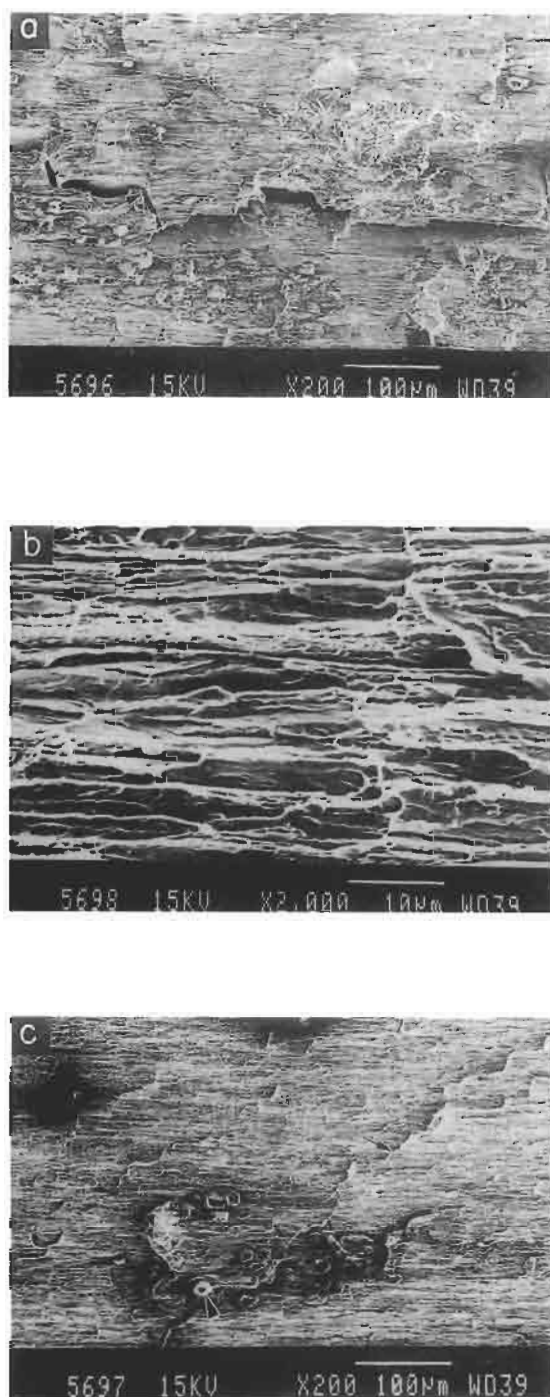
Fig. 5. SEM fractographs of the failed wire samples. (a) Subsurface secondary cracks indicative of hydrogen damage; (b) the fracture features at high magnification appear to correlate well with interlamellar spacing; (c) globule shaped cementite particles segregated in a colony.

Table 1
Tensile and impact test results

Specimen	% Elongation	0.2% YS (MPa)	UTS (MPa)	Impact toughness (J)
As-received*	3.02	1433	2204	33.7
Baked (250°C)[a]	5.32	1543	2178	33.3

[a] Values reported are the average of three specimens.
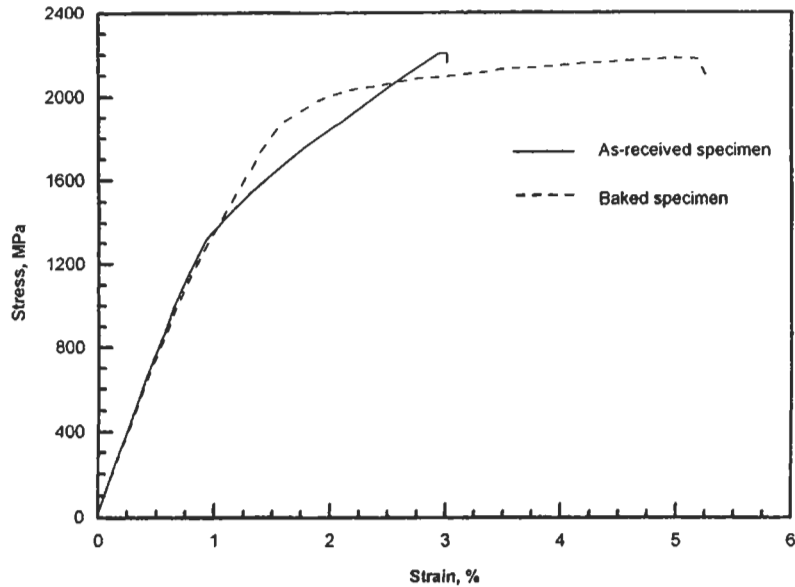
Fig. 6. Tensile behaviour of high tensile wires in as-received and baked condition. Significant improvement in elongation of the baked specimen can be noted.

diffuse during the specimen preparation stage itself. The fracture surfaces of the tensile test specimens were also observed under the SEM and are reported in Fig. 7(a, b and c). Figure 7(c) shows the dimple network in the centre of the fracture surface of the as-received sample. Similar features were observed on the fracture surfaces of the baked samples.

4.4. Delayed cracking test with AE monitoring

The AE signals collected from a wire rod sample that was kept under constant load for a period of 5.5 h are presented as cumulative AE events vs time in Fig. 8 and as amplitude of the AE events vs time in Fig. 9. It is seen from these figures that even though the wire rod was under constant load, a number of AE signals (39 AE events) were generated during the test and it may also be
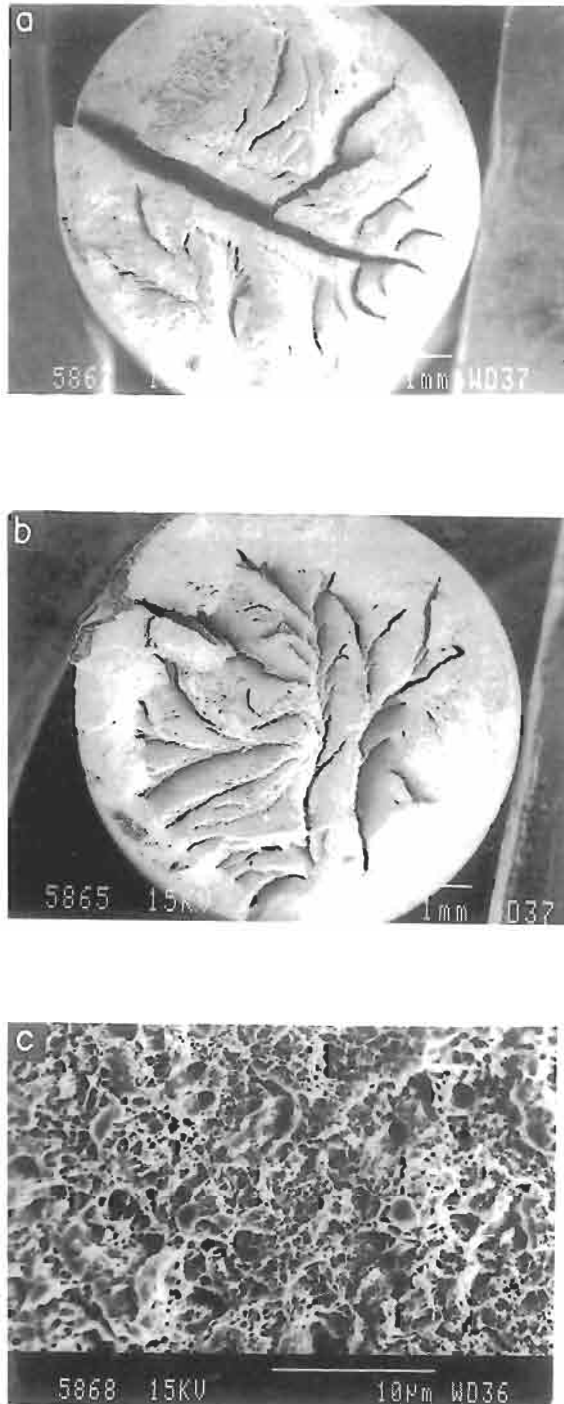
Fig. 7. SEM fractographs of (a) as-received specimen; (b) baked specimen; (c) dimple fracture observed at higher magnification, location as at (a).
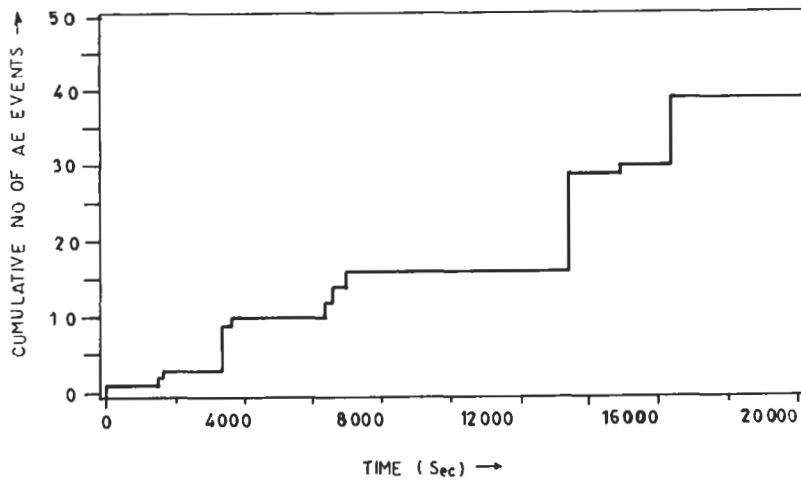
Fig. 8. Cumulative number of AE events generated during delayed cracking test of the wire.
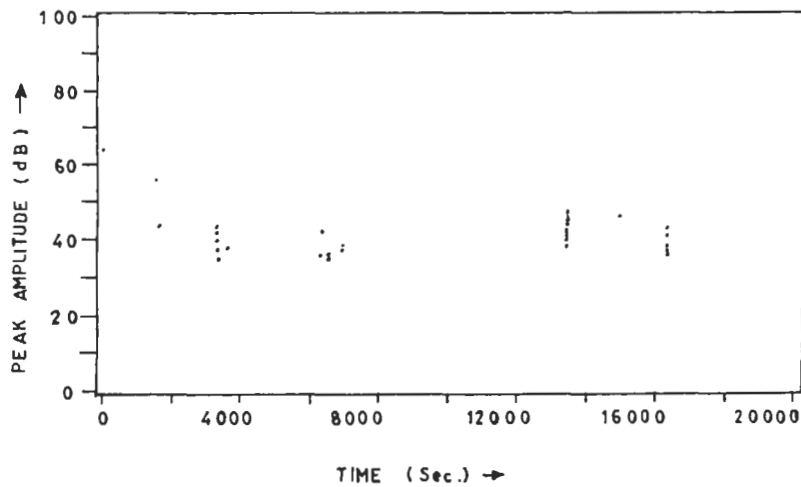
Fig. 9. Peak amplitude of AE events generated during delayed cracking test of the wire showing intermittent nature of the events.

noted that these signals were generated at intervals and not continuously. This indicates that some dynamic substructural phenomenon is taking place in the material during the test, and the process is time dependent and therefore is diffusion controlled. Moreover, as can be seen from Fig. 9, the peak amplitude of these signals is between 35-60 dB. Signals having an amplitude of this nature are attributed to H evolution or due to H induced microcrack formation by diffusion of H to the most stressed region (encircled area in Fig. 2) [14]. All these observations indicate that the atomic hydrogen present in the material diffused to the highly stressed region and formed microcracks which resulted in the generation of intermittent AE signals.

5. Discussion

The present material has undergone nearly 80% cold working resulting in a fine and elongated pearlitic microstructure. The strength level is more than 2000 MPa. Therefore this material has a tendency to absorb H and retain the same at the interfaces of the pearlitic microstructures. The cold working by way of the drawing operation also leads to a residual stress pattern where high tensile stress exists in the central region. It is well known that H has a tendency to stay in a high tensile stress region. Hydrogen evolved during pickling operations ($Fe + HCl \rightarrow FeCl_2 + [H]$) is adsorbed by the wire rod. In industrial practice the ingress of H is retarded by employing a proper inhibitor in the pickling solution. In spite of the inhibitor, any trace of hydrogen that may have remained in the products would then be removed by a suitable baking operation. If any one of the above processes is ineffective, retention of H even of the order of 1 ppm would render the product prone to hydrogen related failure [24].

An attempt is made to explain, by decohesion model, as to how even a low level of H can cause brittle fracture, by invoking Griffith's theory [22].

$$\sigma_f = \sqrt{\frac{2E\gamma_s}{\pi c}} \tag{1}$$

where σ_f is the fracture stress necessary to cause the propagation of an elliptical crack of length $2c$; E is the Young's modulus; γ_s is the surface energy. When H is absorbed, it decreases the bond strength and the surface energy [11]. From eqn (1) it can be seen that the fracture strength is reduced appreciably due to the reduction of surface energy. This reduction in fracture strength can also be expressed as a function of H concentration at the root of a pre-existing crack [25]:

$$\sigma_f - \sigma_H = \beta c^\lambda \tag{2}$$

where σ_H is the fracture strength of material containing H; c is the concentration of H; β and λ are appropriate constants which can be determined by experiments.

As this material is heavily cold worked, a number of defects, primarily dislocations, interfaces, globular shaped cementite, pores, microcracks etc. are generated and these defects are the most potential sites for H entrapment. In the presence of any external stress, the microcrack tips act as stress raisers and would further attract H from the surrounding region. When this H concentration reaches a critical limit, the fracture stress is reduced drastically and the crack extends to the limit of accumulated H before it stops. Again, H diffuses more readily to the fresh crack tip and assists in further propagation of the crack. The data obtained from the AET during delayed cracking tests confirms the general understanding, as explained above, of the way the cracks propagate under stress, below the yield stress, in presence of H.

It is interesting to note that baking for half an hour has improved the ductility and yield strength of the material and reduced the cracking tendency as evidenced in the fractograph (Fig. 7). The early yielding in the as-received sample, as compared to the baked sample, can be explained by H assisted plasticity. As H reduces the cohesive strength, there will be a corresponding reduction in resistance to localised dislocation mobility in the as-received sample as compared to the H free sample (baked sample). It has been reported that hydrogen can diffuse out even at room temperature if the materials are left in fresh air for a lengthy period. However, H trapped in the lattice

can not be removed completely once the galvanising treatment has been carried out [24]. The baking operation may not have removed all the H, particularly the molecular H which caused the pores in the microstructure. Therefore, the baking operation has to be carried out immediately after pickling, before galvanising, in order to avoid entrapment of H by defects present in the material. The profusion of pores observed during microstructural examination (Fig. 3) indicates that molecular H has evolved in the material. The fracture surfaces showing dimples in tensile tests should not be taken as a signature of ductile fracture. The pores are in fact responsible for the presence of dimples on the fracture surface and reduction in the ductility of the material. It is reported in the literature that H assisted cracking can also occur by microvoid coalescence alone and H affects the rate of nucleation of voids and reduces plasticity at later stages of fracture [25]. The split wire surface, however, does not show dimples but shows major features of delamination/decohesion type of fracture with interspersed hard particles (cementite) and longitudinal cracks. These defects are effective during bending and twisting, but not during tensile testing, and lead to a delamination or decohesion type of cracking. From the microstructural features (Fig. 4(b)), it appears that the delamination has taken place either along the prior austenite grain boundaries, i.e., along the interface of the pearlite colonies or along ferrite/cementite interfaces, which have been weakened by the presence of H. In the case of tensile tests these defects do not play a role as they are parallel to the tensile axis of the test sample.

The reason for failures of the wire rods has thus been attributed to hydrogen induced cracking. After the H has been trapped inside the material due to improper pickling and baking operations, it has initiated the cracking in the presence of a high tensile residual stress at the axis of the wire and led to a delamination type failure. During coiling or twisting, plastic bending is induced in a plane which, along with residual stress, causes the wires to fail by splitting along the weakest plane i.e., the direction of drawing.

6. Concluding remarks

Based on the investigations carried out, and the observations thereon, it appears that the cohesive strength of the boundaries/interfaces was reduced by the presence of atomic H. This ultimately led to abrupt splitting during subsequent twisting and bending because the symmetric residual stress pattern developed during the drawing operation is relieved. It appears that a proper inhibitor during the pickling process can prevent ingress of H into the wire rods. Further, the baking operation after pickling can be optimised to avoid interaction of H with the materials leading to H assisted cracking.

References

[1] Colangelo J, Heiser FA. Analysis of metallurgical failures. NY: John Wiley & Sons. 1974, p. 134.

[2] Base CM, Nam WJ, Lee CS. Scripta Materialia 1996;35:641.

[3] Hirth JP, Ashby MF. Perspective in hydrogen in metals. Oxford: Pergamon Press, 1984.

[4] Gibala R, Hebemann RF. Hydrogen embrittlement and stress corrosion cracking. Metals Park, OH: ASM, 1984.

[5] Thompson AW, Bernstein IM. Advances in corrosion science and technology 1980;7:145.

[6] Hertzberg RW. Deformation and fracture mechanics of engineering materials. John Wiley & Sons, 1976, p. 425.

[7] Zapfree C, Sims C. Trans. AIME 1941;145:225.

[8] Tetlman AS, Robertson WD. Trans. AIME 1962;224:775.

[9] Troiano AR. Trans ASM 1960;52:54.

[10] Oriani RA, Josephic PH. Acta Met 1977;52:979.

[11] Petch NJ, Stables P. Nature 1952;169:842.

[12] Beachem C. Stress corrosion cracking and hydrogen embrittlement of iron base alloys. Houston: NACE, 1977, p. 376.

[13] Lynch SP. Metals Forum 1979;2:189.

[14] Gahr S, Grossbeck ML, Birnbaum HK. Acta Met 1977;25:125.

[15] Viswanathan R. Damage mechanisms and life assessment of high temperature components. ASM International, 1989, p. 352.

[16] Wadley HNG, Scruby CB, Speak JH. Int Met Rev 1980;2:41.

[17] Chaskelis HH, Cullen WH, Kraft JM. ASTM-STP 559. Philadelphia: American Society for Testing and Materials. 1973, p. 31.

[18] Hartbower CE, Renter WG, Morris CF, Crimmins PP. ASTM-STP 505. Philadelphia: American Society for Testing and Materials. 1971, p. 187.

[19] Dunegan HL, Tetelman AS. Eng Fract Mech 1971;2:387.

[20] Parida N, Bhattacharya AK. Advances in structural testing analysis and design. New Delhi: Tata McGraw-Hill, 1990, 1331.

[21] Ranganath VR, Mukhopadhyay NK, Sridhar G, Tarafder S., Parida N. Internal report on failure analysis of high tensile galvanised wires, component integrity evaluation programme (CIEP). NML, Jamshedpur, December, 1996.

[22] Deiter GE. Mechanical metallurgy. NY: McGraw-Hill, 1988, p. 490.

[23] Nam WJ, Base CM. Material Science & Engg 1995;203:278.

[24] Dopler T, Nistelberger M, Jeglistsch F, Hampejs G. Wire 1996;46:15.

[25] Lancaster JF. Metallurgy of welding. London: Chapman & Hall, 1994, p. 206–207.

Bearing failures

409

CONTACT FATIGUE IN ROLLING-ELEMENT BEARINGS

P. J. L. FERNANDES

Advanced Engineering and Testing Services, CSIR, Private Bag X28 Auckland Park 2006, South Africa

1. INTRODUCTION

In the paper entitled "Surface contact fatigue failures in gears", Fernandes and McDuling [1] discuss the mechanism of contact fatigue damage frequently encountered on the active flanks of gear teeth. This mode of failure operates not only on counterformal surfaces in contact, as in matching gear teeth, but also on conformal surfaces (Fig. 1). The latter are found in ball bearings in contact with the inner and outer raceways, in roller or needle bearings in contact with the outer raceway, and in shafts in contact with sliding bearings [2]. In the case of gears, three types of contact fatigue damage were identified, depending on the relative movement of the contacting bodies, and the resulting stress distribution in the surface and near-surface material [1]. The characteristics of each type of failure were discussed in detail in [1].

Rolling-element bearings consist of balls or rollers positioned between raceways which conform to the shape of the rolling element. Depending on the bearing design, the loads acting on the bearing may be radial, angular or axial [3]. These loads lead to elastic deformation at the points of contact between the rolling elements and the raceways. The stress distribution in the surface and near-surface material under these conditions depends on the loads and the curvature and relative movement between the contacting bodies.

2. ROLLING AND ROLLING–SLIDING CONTACT FATIGUE

When bearing operation leads to pure rolling contact between the rolling elements and the raceway, the maximum shear stress occurs at some distance below the surface. This situation is similar to that encountered along the pitch-line of gear teeth [1]. In the early stages of damage, pure rolling forms a highly polished surface, as shown in the case of a bearing cup from a large thrust

| (a) | (b) |
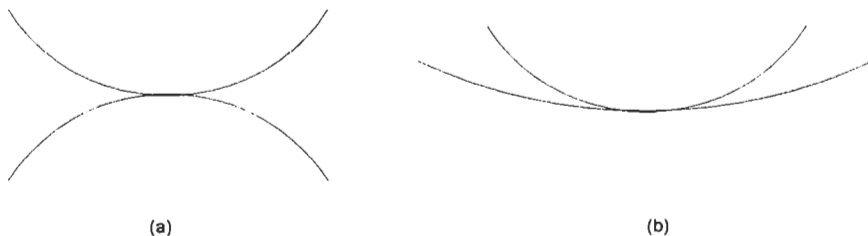
Fig. 1. Schematic illustration of counterformal (a) and conformal (b) surfaces in contact.

bearing (Fig. 2) [4] Under repeated loading, cracks ultimately initiate at the point of maximum stress, and propagate parallel to the surface. At some stage, these cracks deviate and grow towards the contact surface, resulting in the formation of steep-sided pits. These pits are usually microscopic, but may, with continued bearing operation, act as stress concentration sites for further damage.

Under normal bearing operation, it is more common that contact between the rolling elements and the raceway includes both rolling and sliding. The resulting stress distribution in the near-surface material under these conditions changes, and the maximum stress point moves closer to the surface. Again, this situation is similar to that encountered in the addenda and dedenda of gear teeth [1]. Cracks initiate at the contact surface, and propagate to form small, irregular-shaped pits. In some cases, the pits may form in the shape of an arrow-head pointing in the direction of load approach [3]. This is similar to the "cyclone pitting effect" also observed in gear teeth [1].

The initiation of surface cracks under rolling–sliding contact can be significantly accelerated by the presence of stress concentration sites on the contact surfaces [3]. These include corrosion pits, handling damage, surface inclusions, and dents formed by solid particles entrapped in the lubrication fluid. These geometric inhomogeneities lead to high localized stresses, rapid crack initiation, and the formation of contact fatigue pits. In some cases, the cracks initiated in this way may propagate through the bearing rings to cause complete fracture. An example of this is given in Fig. 3, which shows the inner ring of a thrust bearing [5]. Extensive surface damage, probably resulting from the action of solid particles entrapped in the lubricating fluid, is clearly noticeable, as is the through-crack emanating from this damage. Figure 4 shows the crack face in the vicinity of the region marked with an arrow in Fig. 3, and clearly indicates that crack growth was by fatigue.

3. FLAKING AND SPALLING

Under continued operation, the pits formed by rolling and rolling–sliding contact fatigue may progress to form a more severe form of damage known as flaking [3]. This results in the formation of large, irregular pits which cause rapid deterioration and failure of the bearings. Flaking is usually first observed on the stationary ring of a bearing, since the surface of this ring is subjected to the maximum stress every time a rolling element passes over it. In the case of the rotating ring, the
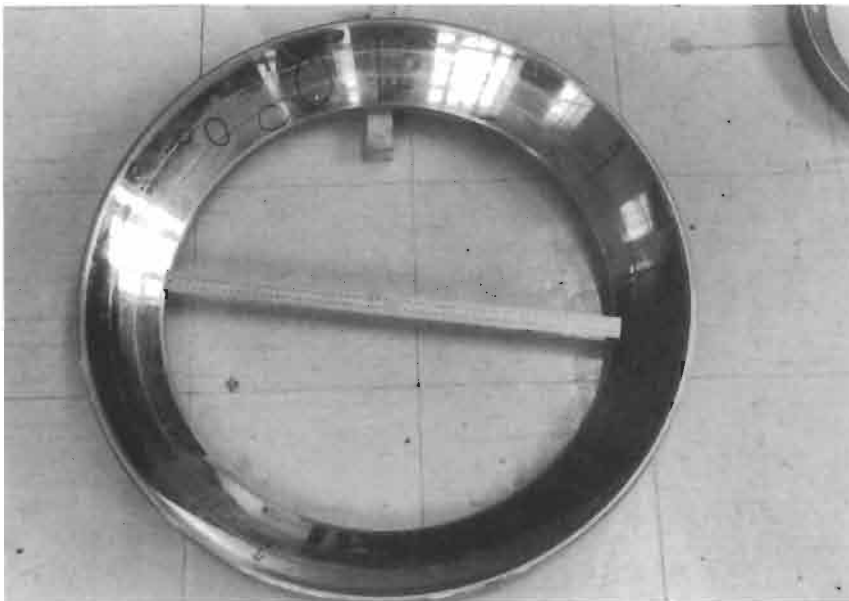

Fig. 2. Thrust bearing cup showing highly polished surfaces typical of the initial stages of rolling contact fatigue.
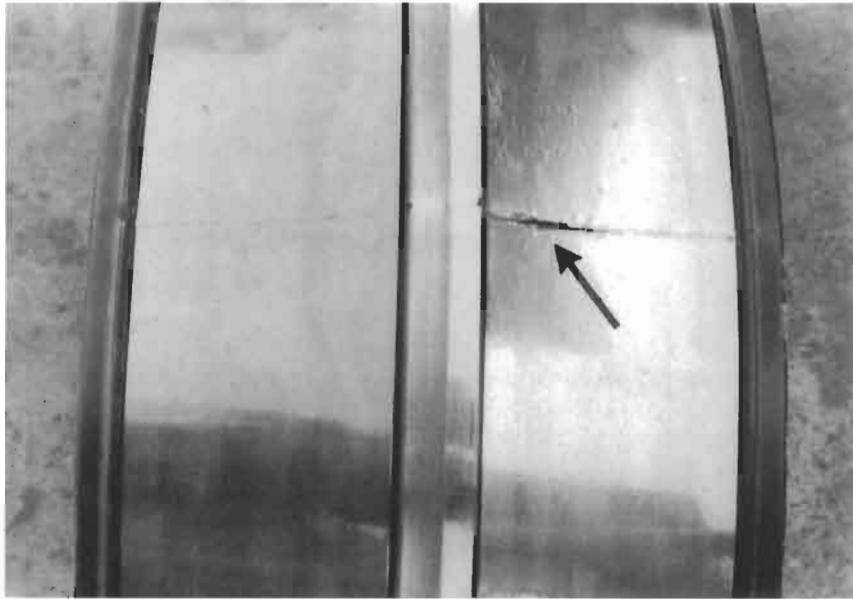
Fig. 3. Inner ring of a thrust bearing showing extensive surface damage on one raceway, and through-cracking of the bearing ring.

Fig. 4. Crack face in the vicinity of the region marked with an arrow in Fig. 3.

position of maximum stress changes continuously, so that any one point on the surface effectively undergoes fewer load cycles. Figure 5 shows an example of extensive flaking damage on the outer raceway of a roller bearing [6].

The location and distribution of flaking damage provides an indication of the cause of failure. Under marginal lubrication conditions, flaking is widespread and distributed over the entire raceway. If the damage is localized, as is the case on the inner ring of a thrust bearing in Fig. 6 [5], flaking is

Fig. 5. Flaking damage on the outer raceway of a roller bearing.
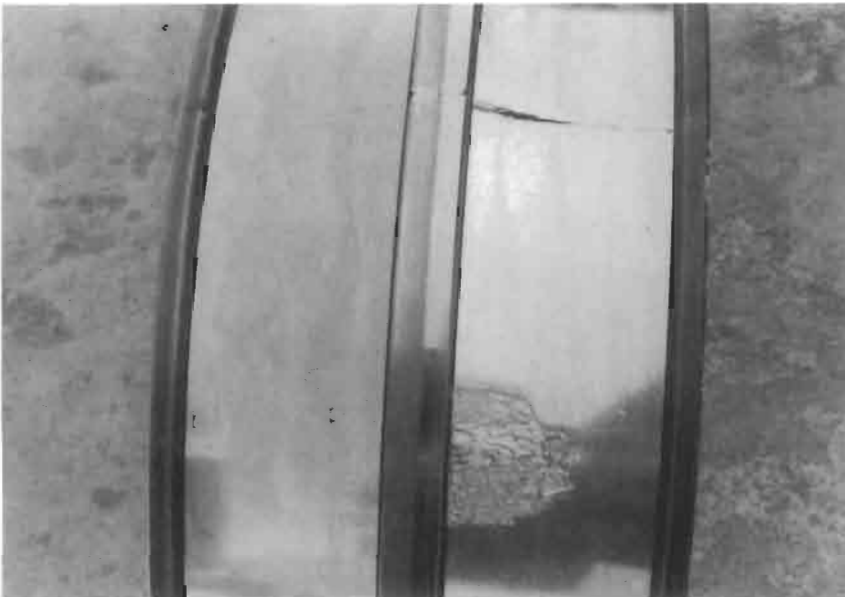
Fig. 6. Localized flaking damage on the inner ring of a thrust bearing.

generally found to be associated with pitting originating from surface stress concentration sites. In roller bearings, flaking sometimes occurs along a ring on a plane corresponding to the end of the rollers. This indicates that the bearing is misaligned, and the loads unevenly distributed. Finally, flaking damage is occasionally found at regular intervals corresponding to the rolling element spacing. In these cases, damage is associated with indentations produced when the stationary bearing is loaded, these indentations being referred to as *true brinnelling*.

Another form of severe contact fatigue damage is known as *spalling*. As in the case of gear teeth [1], spalling occurs as a progression of the pits formed by rolling and rolling–sliding contact fatigue,
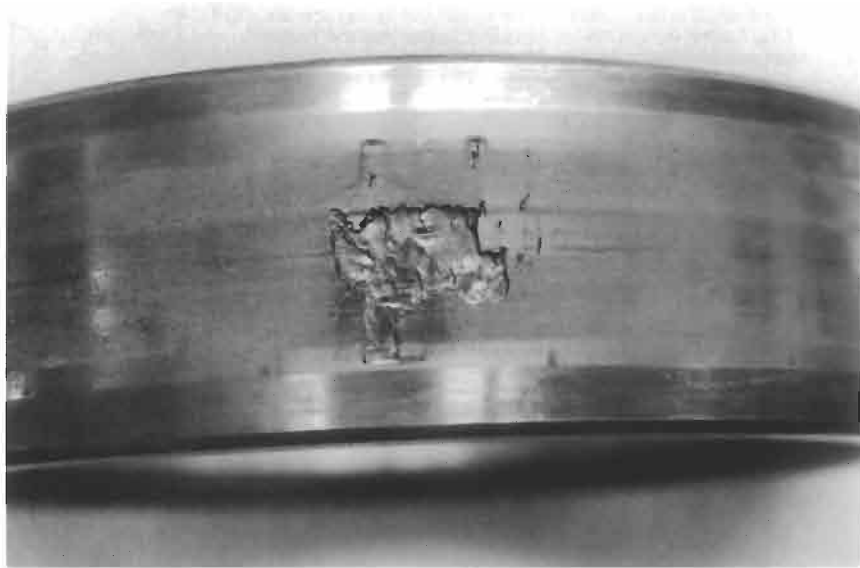
Fig. 7. Severe spalling on the inner ring of a thrust bearing.

or as a result of cracking at the case–core interface in case-hardened components. The damage in this case results in the formation of large, deep pits with sharp edges, steep sides, and flat bases. A good example of this is given in Fig. 7, which shows the inner raceway of the failed thrust bearing [6].

4. SUMMARY

Surface contact fatigue is a common cause of failure in rolling-element bearings. The extent of damage observed depends on the contact loads, the curvature of the rolling elements, and the relative motion between the contacting surfaces. The characteristics of the various types of contact fatigue are as follows:

(a) Microscopic pits form under pure rolling contact. These may act as stress concentration sites for further damage.
(b) Under rolling–sliding contact, irregular-shaped pits are formed. This type of damage is accelerated by the presence of geometric inhomogeneities such as corrosion pits, handling damage, and dents.
(c) Flaking occurs as a progression of the pits formed under rolling and rolling–sliding contact fatigue, and leads to the formation of large, irregular-shaped pits.
(d) Spalling refers to the formation of large, deep pits with sharp edges, steep sides, and flat bases, or to cracking at the case–core interface in case-hardened surfaces.

A number of practical examples of bearing failure have been used to illustrate the various types of contact fatigue damage.

REFERENCES

1. Fernandes, P. J. L. and McDuling, C., *Engineeering Failure Analysis*, 1997, **4**(2), 99–107.
2. Wulpi, D. J., *Understanding How Components Fair*. American Society for Metals, Metals Park, OH, 1985, pp. 183 204.

3. ASM Metals Handbook, *Failure of Rolling-element Bearings*, Vol. 11, *Failure Analysis and Prevention*, 9th edn. American Society for Metals, Metals Park, OH, 1986, pp. 490–513.
4. James, A., *Failure Analysis Report*. Advanced Engineering and Testing Services, CSIR, 1996.
5. Fernandes, P. J. L., *Failure Analysis Report*. Advanced Engineering and Testing Services, CSIR, 1995.
6. James, A., *Failure Analysis Report*. Advanced Engineering and Testing Services, CSIR, 1994.

AN AIR CRASH DUE TO FATIGUE FAILURE OF A BALL BEARING

I. SALAM, A. TAUQIR*, A. UL HAQ and A. Q. KHAN

Metallurgy Division, Dr. A. Q. Khan Research Laboratories, GPO Box 502, Rawalpindi, Pakistan

Abstract—The failure analysis of an air crash conclusively shows that the cage of the central main bearing of the compressor region failed due to fatigue. The broken piece of the cage got struck between the bearing balls and the races and impaired the function of the bearing resulting in the crash. © 1998 Elsevier Science Ltd. All rights reserved.

1. INTRODUCTION

A fighter plane crashed in 1996; Fig. 1a. The plane had two engines. The on site investigations pointed out that the fault was probably in the compressor region of one of the engines and the problem was suspected to be in a bearing of the compressor region. In this region there are three main bearings. Those at the front and back are roller bearings while the central one (CMB) is the ball bearing type. The bearings are lubricated by way of a closed loop lubrication system and metallic filters are inserted to clean the debris. The life of the CMB, which is suspected to have caused the accident, is 600 h. The bearing of the engine which failed had completed a total of 467 h and 5 h had elapsed since it was last inspected. The inspection report shows that the parameters measured were within the specified limits. The CMB of the other engine had completed about 130 h and was found undamaged. There are some previous cases in which an aircraft landed safely after an indication of a problem in the engine; in all these cases failures in the cages of the CMB were detected. The cage of the CMB from the plane under consideration in this study was retrieved in a broken condition (Fig. 1b).

To isolate the cause of failure, the bearing components were subjected to detailed analysis. The main components of the bearing included the steel balls, inner and outer races and the cage. The material of these components was investigated and the details are summarized in Table 1. The cage material was subjected to detailed metallurgical investigations.

The retrieved balls exhibited significant wear/erosion. They were studied for smearing of foreign material. Similarly the surfaces of the races were extensively deformed and these were analyzed to investigate the deformation details and the material smeared on them.

2. CMB ASSEMBLY

The bearing is mounted on the compressor shaft and is located in a housing [1]. The main components of the CMB are inner and outer races on which the bearing ball roll and a soft cage to keep the balls at a distance from each other. The arrangement of these components is shown in Fig. 2.

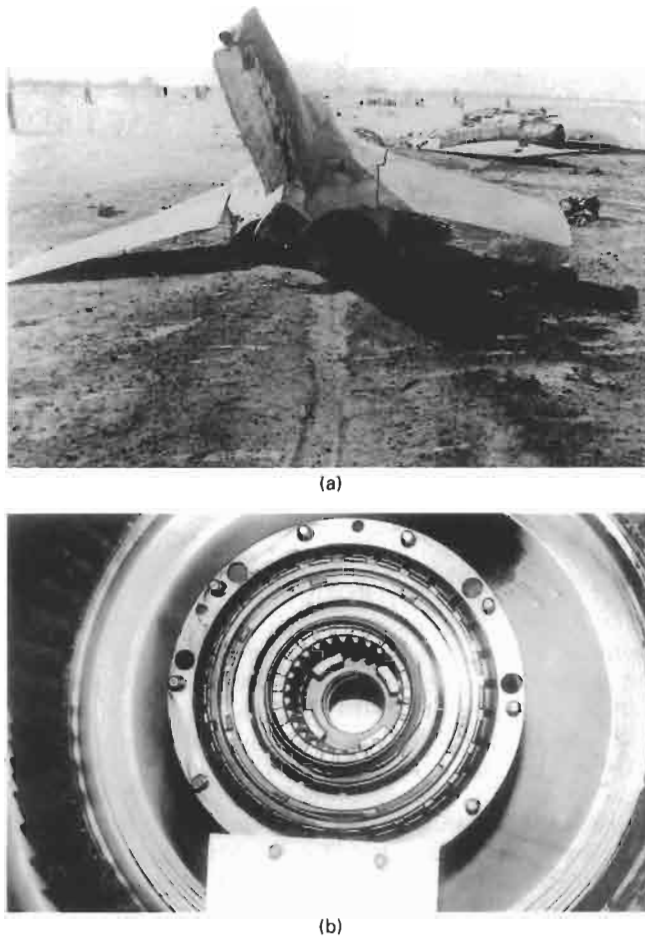* Author to whom correspondence should be addressed.

(a)

(b)

Fig. 1. (a) The plane after the accident. (b) Bearing components on the compressor shaft after the accident.

Table 1. Chemical composition of the different parts of the CMB

| Element | Composition wt.% of components | | | | |
	Cage	Balls	Inner race	Outer race	Bearing lock
Cr	—	1.67 ± 0.12	1.76 ± 0.11	1.63 ± 0.02	1.06 ± 0.16
Mn	1.33 ± 0.12	0.40 ± 0.10	0.37 ± 0.07	0.25 ± 0.05	0.60 ± 0.07
Si	—	0.25 ± 0.04	0.30 ± 0.09	0.35 ± 0.15	0.28 ± 0.06
C	—	0.92 ± 0.01	1.02 ± 0.01	0.98 ± 0.01	0.37 ± 0.01
S	—	0.001	0.003	0.001	0.002
Al	7.82 ± 0.12	—	—	—	0.44 ± 0.06
Cu	Bal.	—	—	—	—
Fe	1.62 ± 0.07	Bal.	Bal.	Bal.	Bal.
Material	QAl10-3-1.5†	AISI 52100	AISI 52100	AISI 52100	38 Cr Al†

† Closest standard.

2.1. *After the accident*

Examination of the compressor region revealed that the cage was broken and significantly deformed. The inner and outer races were put together with the cage and the probable configuration
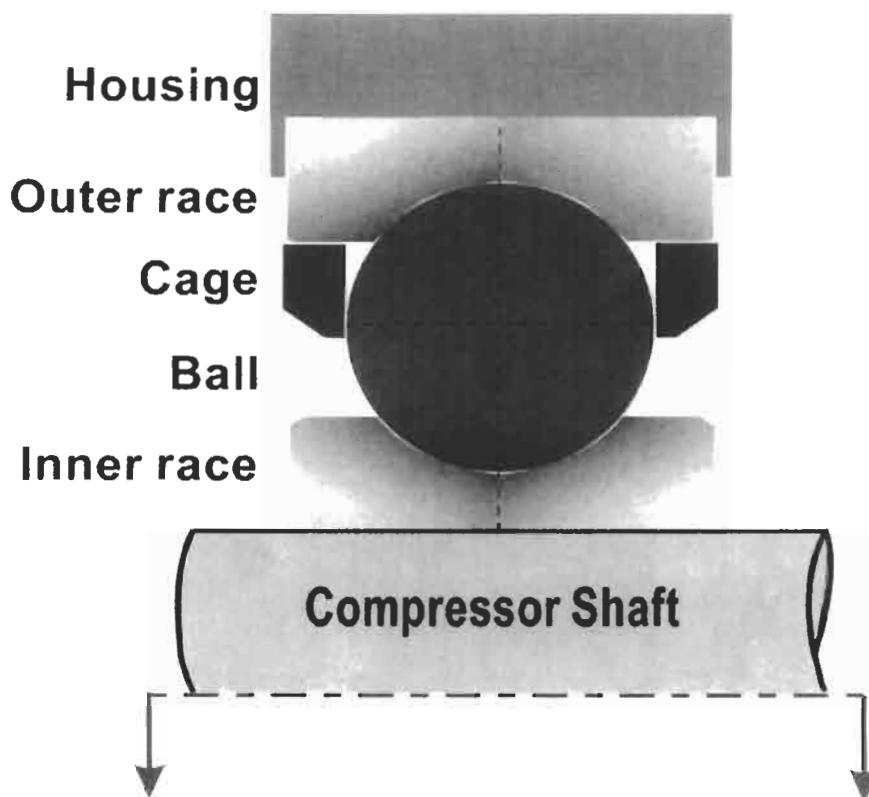
Fig. 2. Sketch of the bearing assembly.

of bearing components after mishap is shown in Fig. 3a. The compressor and then the CMB components were disassembled; the latter were retrieved in a severely distressed condition. The condition of the retrieved components was compared with ones which were in normal use in another engine. The retrieved cage compared with a new one is shown in Fig. 3b. A detailed study of the retrieved components was conducted using stereo, optical and electron microscopes to establish the mechanism of damage. Detailed views of the sections of interest of each component are discussed in the following with the help of the micrographs in Fig. 4.

The worst condition was that of the cage; Fig. 4a-i. Its outer surface is compared with that of another used cage. During the accident the cage was fractured and the results of fractography are discussed in Section 3. The inner surface of the cage, as evident from the crushed hole peripheries in Fig. 4a-ii, had been severely deformed by the hard Cr-steel bearing balls.

In Fig. 4b-i the inner surfaces of the retrieved outer races are shown where significant deformation and smearing is visible. The sections of the edges of a used and of a retrieved outer race are compared in Fig. 4b-ii and b-iii. The cross sections of the edges clearly show extensive deshaping indicating high stresses acting on them; this is quite significant on the left-hand side (LHS) edge shown in Fig. 4b-iv.

The photograph in Fig. 4c-i shows delamination of surface layers of the steel inner race. It can be seen, at a higher magnification in Figs 4c-ii and c-iii, that a layer of the cage material was smeared on the surface and the subsequent deformation was so severe that inner race material covered it up, sandwiching the cage material completely.

The view of the left and right edges in Fig. 4c-iv was obtained following necessary sectioning of the component. The degree of deformation is compared with the edges of another used inner race in Fig. 4c-v. A closer look at the edges in Fig. 4c-vi shows serious deshaping of the edges. It is noted that LHS edges of the inner and the outer races were much more deformed than the respective RHS edges.
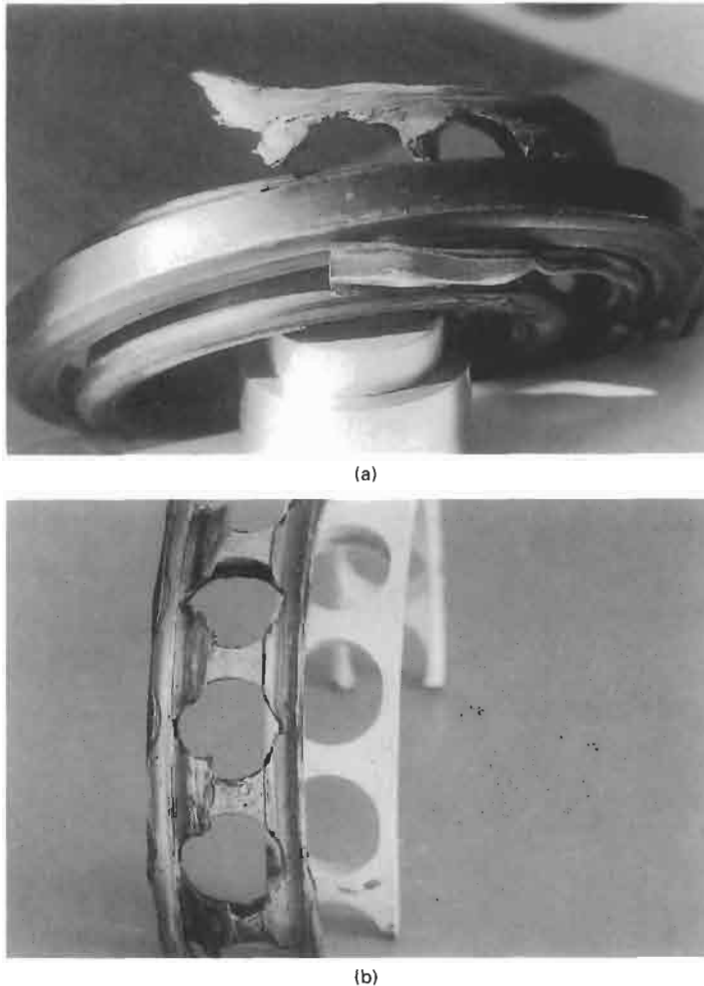
(a)

(b)

Fig. 3. (a) Probable configuration of bearing components after mishap. (b) Retrieved cage compared with the new one.

The rolling elements, Cr-steel balls, also experienced severe deformation and wear; see Fig. 4d-i. One of these balls, which was stressed to a relatively small extent was sectioned to study the locations where stresses were overbearing. The etched sample in Fig. 4d-ii shows a band of the stressed region which is ∼4 mm wide and generated while the ball was rolling.

To summarize the above observations, the inner and one of the outer races of the retrieved bearing were heavily deformed from one side. The off-center extensive deformation indicates high stresses operating in these areas prior to the failure. The inner and outer races put together with the cage in Fig. 3a show the probably configuration in which the cage broke and was trapped between the balls and the races. The balls shifted towards one side and severely deformed the races. The function of the bearing was impaired resulting in the air crash. The observations concerning the deformation and smearing of the components are sketched in Fig. 4e to show the possible position and condition of the bearing components just before the accident.

2.2. *Material of CMB components*

The chemical analysis of different parts of the bearing was carried out using energy dispersive X-ray analysis (EDX), atomic absorption spectroscopy (AAS) and carbon/sulphur (C/S) analyzer.

The cage is fabricated from a Cu–Al alloy; its chemical composition is summarized in Table 1.
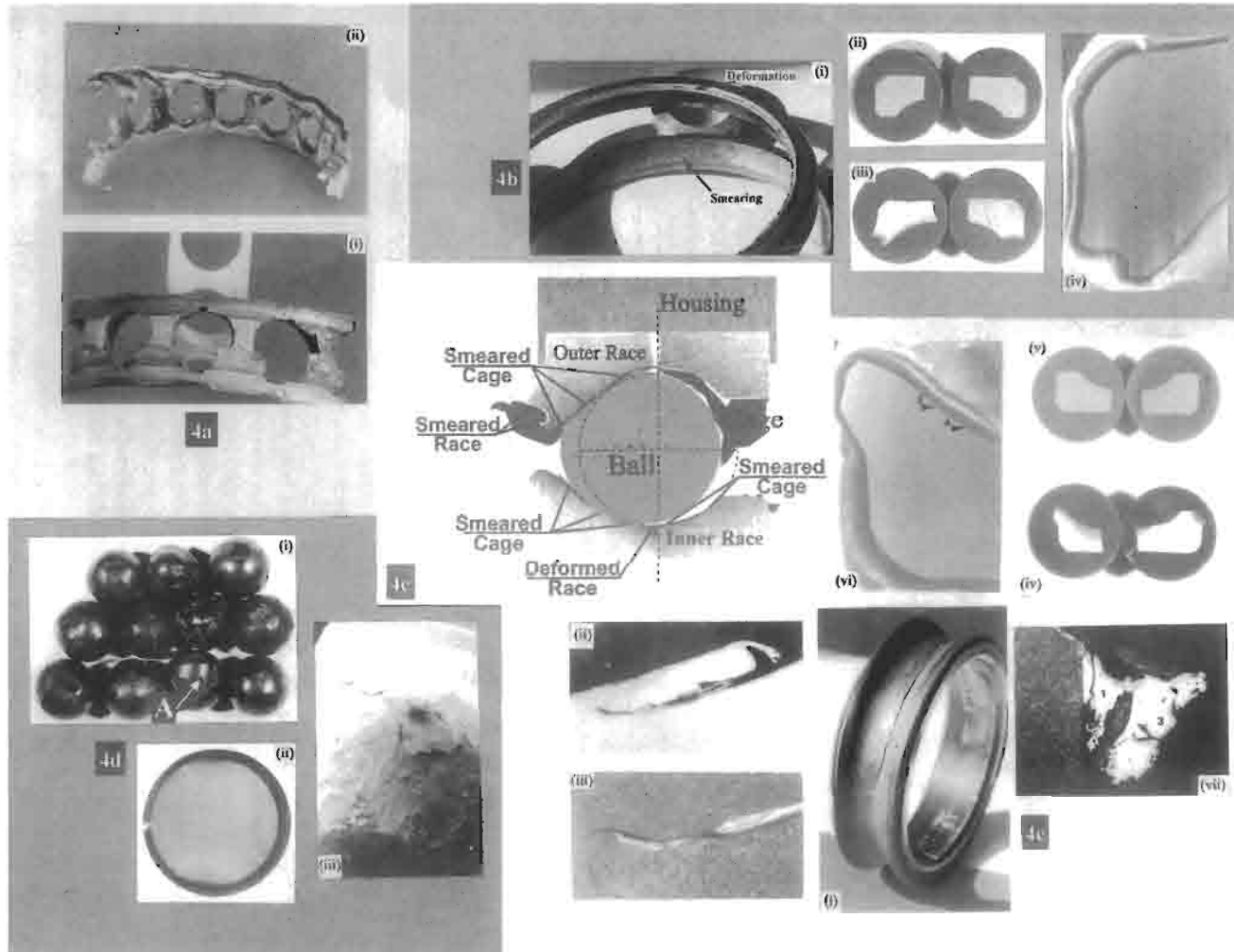
Fig. 4. (a–d) Deformation in the components just before the accident. (e) Hypothetical sketch based on observations in Figs 4a -d.
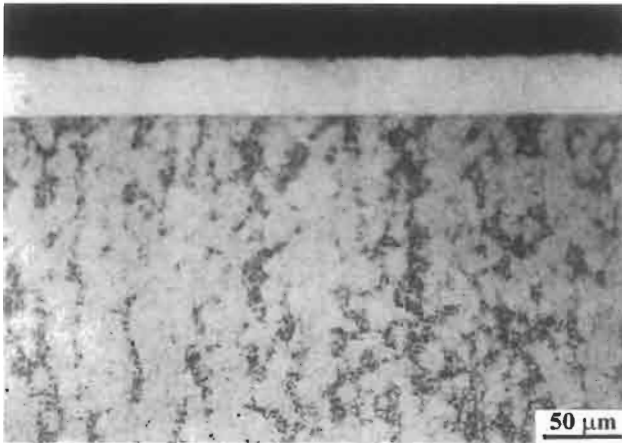
Fig. 5. Optical micrograph of the cage and the silver coating.

Optical microscopy of the cage shows a dual phase structure of the material (Fig. 5). The cage is most probably cast and has a ~38 μm thick silver coating. Silver coating provides good resistance to fretting and improves the bedding-in and running properties of harder bearing materials [2]. Microscopic study revealed that there were darkly etched spherical inclusions in the cage material; the inclusions are up to ~8 μm in diameter and are Al-rich.

The bearing balls, outer and inner races were manufactured from a Cr-steel in the hardened and tempered condition, having a fine distribution of Cr-carbides; the composition is summarized in Table 1. From the point of wear similar material to the components which are in mutual contact have a tendency to "smear" during the wear process [3].

Material of the bearing lock was found to be 38 Cr Al; Table 1. A section of the lock material observed under the optical microscope revealed ~18 μm thick copper coating on the surface.

2.3. Material smeared on components

The material smeared on the surfaces of the components was analyzed following preparation of smaller cross-sectional specimens of the component. These were analyzed in the scanning electron microscope equipped with energy dispersive spectroscopy. The results are summarized in Tables 2 and 3.

The higher magnification view of the bearing ball specimen in Fig. 4d-iii shows the presence of deposited material; this is especially true in the regions where the material close to the surface shows heavy deformation bands. The smearing, confirmed from EDX analysis, was found rich in Fe, Cu, Si, Al and Cr while Ag and Mn were detected at isolated locations. Si is probably from the lubricant or debris. At a location on the surface of the ball (location A in Fig. 4d-i) where it seemed that material was removed due to impact, a high concentration of Fe, Cr, Si, Al and Cu was detected. It seems that the material of the cage was smeared probably at the inner race first and then extensive compressive/shear stresses between the ball and the outer race resulted in chipping or shearing of the ball material.

Smearing on the outer race is accompanied by deformation, as is evident from the deformation bands near the surface in Fig. 6. Three different regions were analyzed and the results are summarized in Table 2a; the first two regions were big enough to permit analysis at a couple of locations. In all the locations cage material was smeared. Region I contained a significant amount of Ag showing that the cage got smeared when the coating was intact. Analysis at Region III, on the other hand, did not show the presence of an Ag coating, indicating that the cage had already been distressed to the level that its coating was completely stripped off before smearing at Region III.

Micrographs in Fig. 4c show the condition of smearing on the inner race. The LHS was quite deformed and damaged. Figure 4c-i shows the seat of the race where extensive smearing and deformation is clearly visible. Four different locations, marked in Figs 4c-vi and c-vii, were analyzed

Table 2. Smeared material on the outer race

	Region I				Region II			Region III
Fe	35.3	27.0	24.6	36.0	80.7	75.8	92.6	96.3
Cu	56.6	63.7	65.1	55.4	14.6	18.5	4.4	1.0
Al	4.6	5.6	5.5	4.9	1.2	1.8	0.2	0.4
Mn	1.0	1.1	1.2	1.0	0.5	0.8	0.3	0.4
Cr	0.7	0.4	0.2	0.3	1.6	1.0	1.7	1.8
Ag	1.5	2.0	3.3	2.1	1.2	1.7	0.3	—
Si	0.4	0.2	0.2	0.3	0.3	0.4	0.4	0.2

Table 3. Smeared material on the inner race

	Region I				Region II		Region III			Region IV			
Fe	92.3	92.2	97.0	96.9	90.0	83.8	77.7	71.3	72.0	97.5	97.0	81.8	84.9
Cr	6.6	7.2	1.0	0.9	1.7	1.3	5.0	5.7	5.8	1.6	1.9	1.6	1.7
Mn	0.4	0.2	1.2	1.2	0.2	0.5	0.7	0.8	0.7	0.4	0.4	0.5	0.5
Si	0.8	0.5	0.9	1.0	0.3	0.4	9.6	11.8	10.9	0.3	0.3	0.1	0.3
Cu	—	—	—	—	6.5	11.3	—	0.3	0.3	—	—	14.6	11.3
Al	—	—	—	—	1.2	1.5	2.4	3.6	5.1	—	—	1.4	1.3
Ag	—	—	—	—	0.5	1.2	—	—	—	—	—	—	—
Mg	—	—	—	—	0.1	—	4.6	6.5	—	5.4	—	—	—
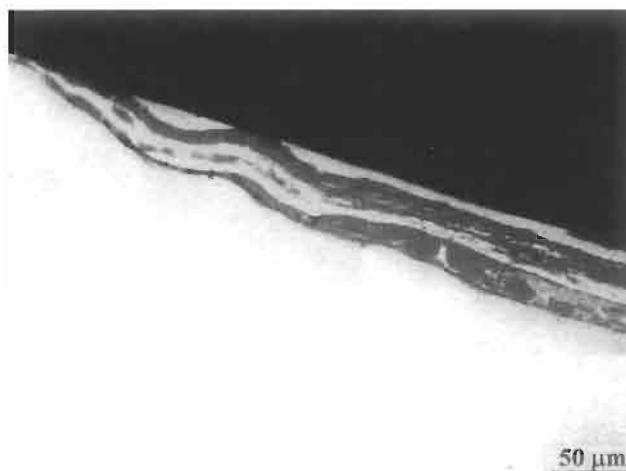
Fig. 6. Deformation bands near the surface of the retrieved outer race.

and they indicate the presence of smeared cage material at Regions II and IV; see Table 2b for the analysis report. At Region II, Ag is also present indicating that when the cage got smeared here the coating was at least partially intact. No bearing component was found to contain Cr, Si, Al and Mg in the amounts detected in Region III of the inner race. Particles rich in Si and Al and containing Mg were retrieved from the lubricating oil and could be transported to the inner race from some other source through the lubricant.

The material protruding from the RHS of the race (Fig. 4c-vii) contained more than 7% Cr which was not found in any of the bearing components. It seems that a component of high chromium content was severely damaged and hit the inner bearing race. No obvious damage was seen on the inner race at the location of impact.

Different portions of the retrieved cage, including the inside surface of the holes, showed smears of steel; an iron content of up to 71% was found near the surface regions. The retrieved balls showed

Cr depletion of up to 1.40% near the surface region; this shows that the balls were running hot for quite some time.

## 3. FRACTOGRAPHY OF THE CAGE FRACTURE STRUCTURE

The fractured surface of the retrieved cage was examined in the SEM (Figs 7a and b). The general features of the surface at low magnification are shown in Fig. 7a. The typical fatigue striations (Fig. 7b) in the central portion of the sample were clearly visible. The crack propagating lines lead to the corner marked 'O'; from where the crack probably initiated. The features disappeared near the exposed surface but bending marks could be observed. Bending could be due to some foreign body impact, quite possibly during the accident after the failure. It is quite clear from the observations that the failure was due to fatigue which was confirmed in the simulated laboratory experiments. The latter were necessary to confirm that the striations were not slip bands which are sometimes observed in these materials [4].

4. POSSIBLE SEQUENCE OF FAILURE

Before the accident excessive wear of the bearing components took place in a short time of approximately 5 h. Cage material was stuck between the ball and the race producing severe
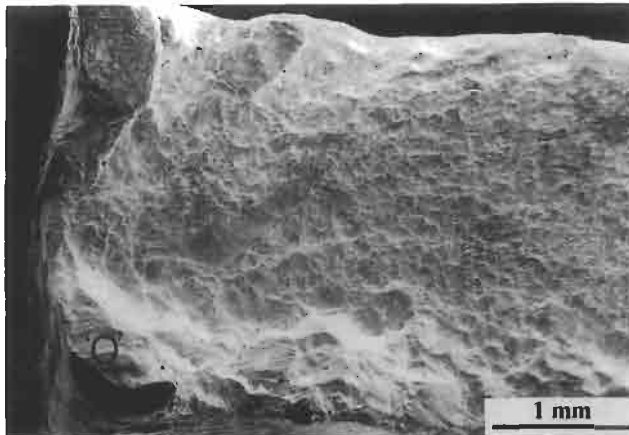
(a)
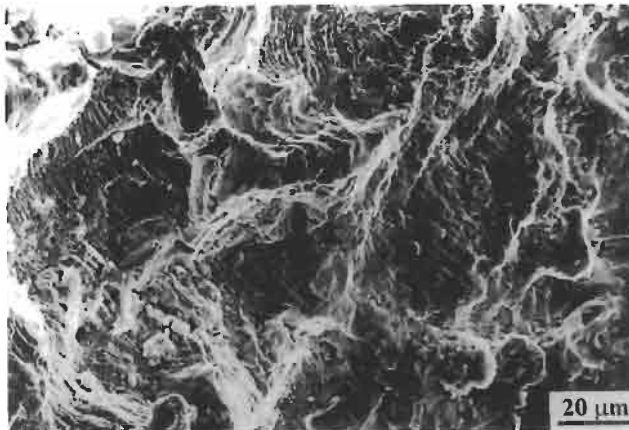
(b)

Fig. 7. SEM photographs of the fractured surface of the retrieved cage: (a) general view; (b) fatigue striations.

misalignment of the outer race with respect to the compressor shaft. The offcentering of the balls exerted overbearing stresses on one side (displaced from the middle) of the inner and outer races inducing heavy deformation on their surfaces. The rotation of the bearing and the main compressor shaft became difficult and led to the accident. To get in between the balls and the races, the cage had to break. The fatigue failure features on the fracture surface of the cage confirmed the above hypothesis [5].

5. CONCLUSION

It has been conclusively shown that the cause of the accident was the failure of the CMB cage. The cage failed due to fatigue. No material defect could be traced at the site of crack initiation.

REFERENCES

1. Widner, R. L., *Metals Handbook*, vol. 11, 9th edn., American Society for Metals, Metals Park, OH 44073, 1986, pp. 490–513.
2. Neal, M. J., ed., *Bearings—A Tribology Handbook*, 2nd edn., Butterworth–Heinemann Ltd., Oxford, 1993, pp. 97–116, 130–134.
3. Kossowskii, R., Emerging Technologies Inc., USA, private communication.
4. Walker, C. R. and Starr, K. K., *Failure Analysis Handbook*, Pratt & Whitney Report August 1989, Materials Laboratory, Wright Research and Development Center, OH 45433-6533, pp. 206, 267, 272, 354, 358.
5. Widner, R. L. and Wolfe, J. O., *Metal Progress*, April 1968, pp. 52–59.

Failure analysis of a condensate pump shaft

A.M. Lancha*, M. Serrano, D. Gómez Briceño

Materials Programme, DFN, CIEMAT, Avda. Complutense 22, 28040 Madrid, Spain

Received 19 October 1998; accepted 6 November 1998

Abstract

This paper presents the failure analysis of a condensate pump from a nuclear power plant. The failed components were the martensitic stainless steel shaft and a chromium-plated sleeve in the first stage sealed area. The failure occurred during normal operation of the plant after a service of 8 years. The cause of the fracture was found to be quench cracking due to overheating. Taking into account the results obtained in the destructive examination of the shaft and the sleeve, and the low operation temperature of the pump ($\sim 100°F$), it was deduced that the heat source was the friction between the shaft (or the associated components) and the casing. © 1999 Elsevier Science Ltd. All rights reserved.

Keywords: Pump failures; Metallurgical failure analysis; Overheating; Quench cracks

1. Introduction

This paper describes the failure analysis of a condensate pump shaft from a nuclear power plant (NPP). The catastrophic failure of the pump shaft occurred during normal operation of the plant, after a service for 8 years.

In a secondary cooling system of a NPP (which includes the main steam system and the condensate–feedwater systems), cooler water is pumped from the condenser, by the condensate pumps, through the feedwater system to the steam generator tubes where it is heated by the primary water from the reactor pressure vessel and converted to steam. The steam then passes through the main steam line to the turbine, which is connected to the electric generator. The steam from the turbine condenses in a condenser to close the cycle.

The failed condensate pump is a vertical six stage enclosed impeller unit with double suction in the first stage. The liquid pumped is condensate at 100°F and the nominal flow is 1180 m³/h. The shaft failure is located in the sealed area of the first stage. The shaft was made of martensitic stainless steel AISI 410 and has a diameter of 4.5 in.

In the original design, the first stage sealing was performed by a bronze bearing. It is well known

---

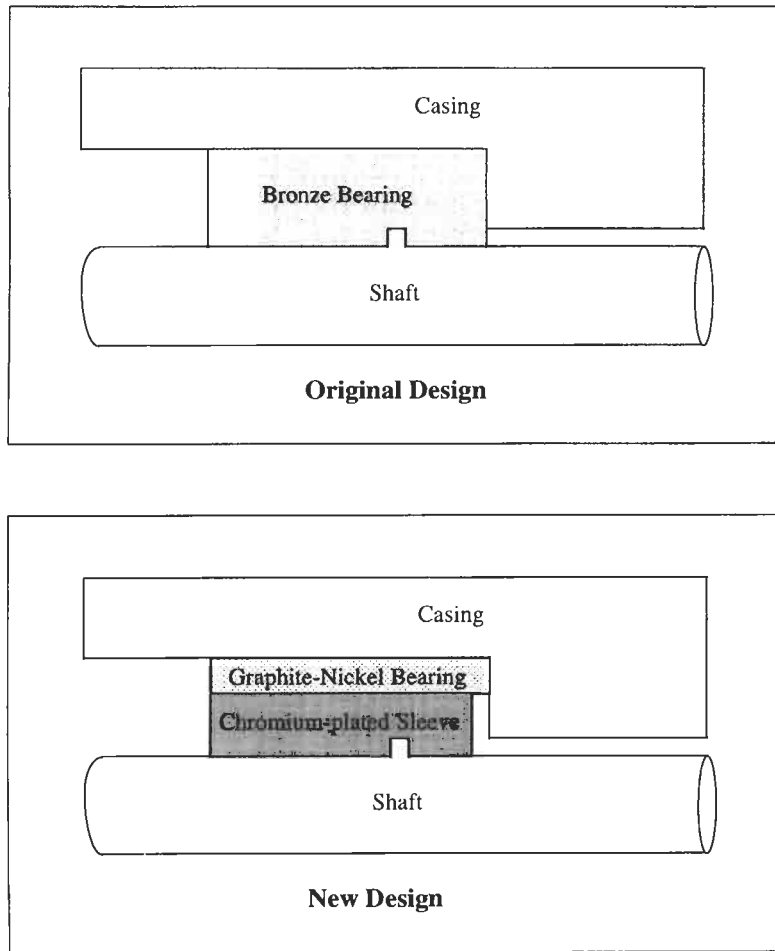* Corresponding author. Tel.: +34-91-346-6000; fax: +34-91-346-6005; e-mail: martasg@ciemat.es

Fig. 1. Original and new design of the first stage sealed area.

that the presence of copper components in the secondary cooling system of a NPP could affect the integrity of the steam generator tubes [1]. Due to this possible contamination, the bronze bearing was replaced by a sleeve and a bearing (Fig. 1). The sleeve was made of chromium-plated martensitic stainless steel AISI 416 and the bearing was made of graphite–nickel. The failure occurred with this new design.

2. Visual inspection after the failure

Figure 2 shows the appearance of the shaft and the chromium-plated sleeve after the failure. The marks existing in the sleeve indicate that both the upper part and the lower part of the sleeve have been displaced from their initial position in the shaft. In the case of the upper part of the sleeve this fact is clearly confirmed by the displacement existing in the screw footprint. The upper

Fig. 2. Photograph of the failed shaft and chromium-plated sleeve.

part shows a bright and flat band on the top, typical of the chromium plating, while the rest of its surface is matte with many heterogeneous grooves. This last appearance, matte, with grooves and mechanical damage signs, is the appearance of the external surface of the lower part of the sleeve. However, in this case the grooves are positioned almost exclusively close to the fracture area.

Also seen in Fig. 2 is the irregular shape of the fracture surface in the lower sleeve part, this fracture surface being located in some areas below the fracture surface of the shaft. In contrast, in the upper sleeve part, the fracture surface of the shaft is totally obscured by the sleeve. In addition, in this part, the sleeve does not show the typical and irregular appearance of a fracture surface. Its edge is completely regular and homogeneous, as if machined. These facts may indicate that after the failure the fracture surface of the upper part of the sleeve was rubbing against the casing while
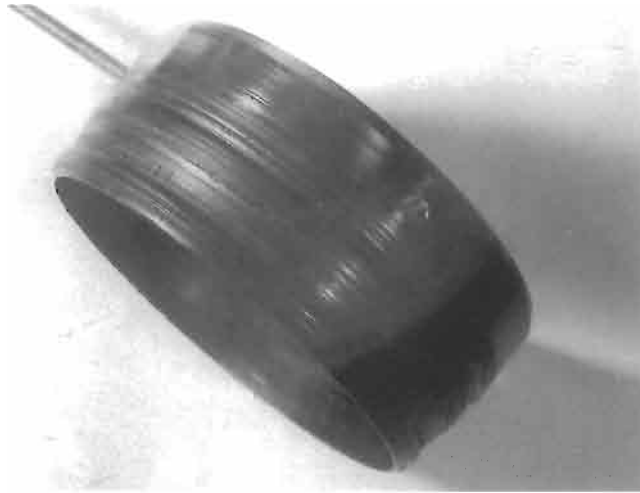
(a)

(b)

Fig. 3. Photographs of the failed chromium-plated sleeve after separation from the shaft.

the shaft was rotating, and consequently it was essentially machined. All these characteristics can be seen with more detail in Fig. 3, taken after separation from the shaft.

Figure 4 shows the fracture surface of the shaft. The appearance and topography is different in the outer part and in the inner part. In the outer part, the fracture is rough and bright, and it becomes smoother and more matte towards the center of the shaft. It is possible to differentiate

(a)

(b)

Fig. 4. Photographs of the failed shaft.

two zones: one external zone, rough and bright, as a symmetrical ring up to approximately half of the radius, and one internal zone, flat and matte, wherein can also be seen some ligaments. The shape and appearance of these ligaments suggest that they have been originated by torsion in the final fracture of the shaft.
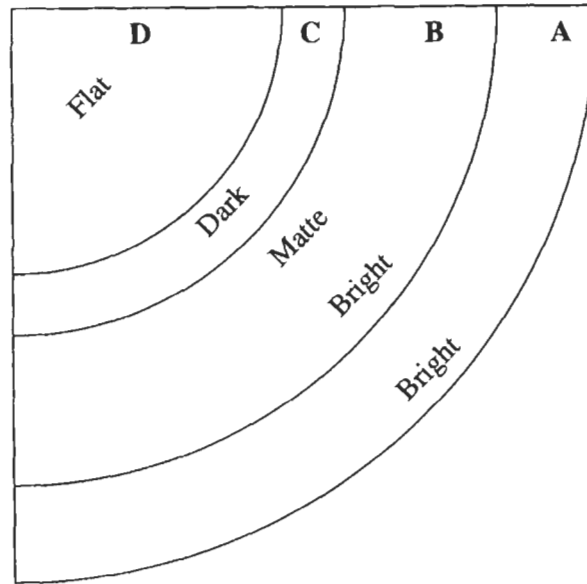
Fig. 5. Schematic illustration of the shaft fracture surface.

3. Destructive examination of the shaft

3.1. Fractography

Figures 5 and 6 show the results obtained in the fractographic examination performed by SEM. The schematic illustration of Fig. 5 represents the different zones with different fractographic characteristics.

In the outer part, zone A (Fig. 6a), which is approximately 10 mm wide, the fracture morphology is mainly intergranular, with grains up to 600 μm in diameter, but showing also some small areas with transgranular fracture. This morphology is constant in all the zone A, but the grain size decreases considerably from the external diameter towards zone B. In zone B (Fig. 6b), approximately 15 mm wide, progressively from zones A to C, the grain size decreases and the proportion of transgranular fracture increases. Close to zone C the fracture is almost transgranular, although some grain boundaries are still visible. Zone C (Fig. 6c), of ~ 5 mm width, shows a dark coloration due to the presence of deposits. Under the deposits there are mainly transgranular areas but also some intergranular facets. Grains ~ 20 μm in diameter can be measured in this zone. Finally, the morphology of zone D (Fig. 6d) is typical of fatigue and torsion processes.

3.2. Metallography of the fractured area

Several axial metallographic sections cut from zones close to the fracture surface were prepared with two aims: to know if the material was damaged in these areas, and to study their microstructural characteristics, mainly grain size.

Two different metallographic sections can be seen in Figs 7 and 8. Figure 7 shows a macro-
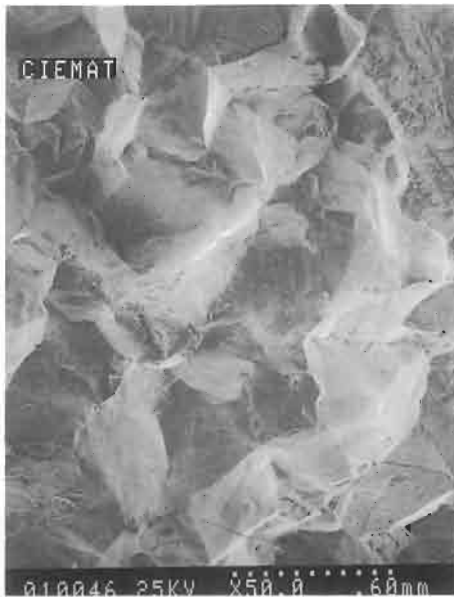
(a)
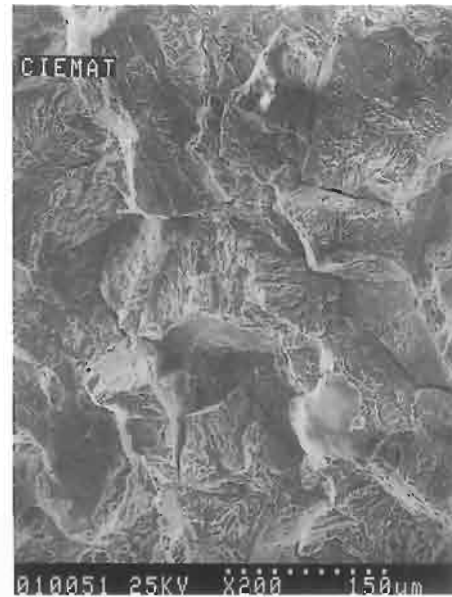
(b)

(c)
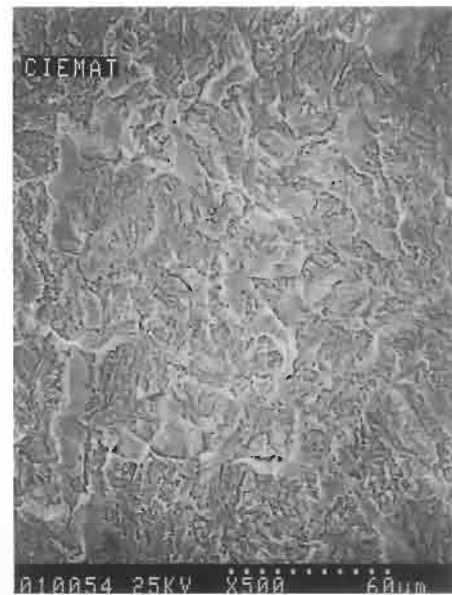
(d)

Fig. 6. Fractography of the shaft fracture surface: (a) zone A (OD) of Fig. 5; (b) zone B of Fig. 5; (c) zone C of Fig. 5; (d) zone D of Fig. 5.

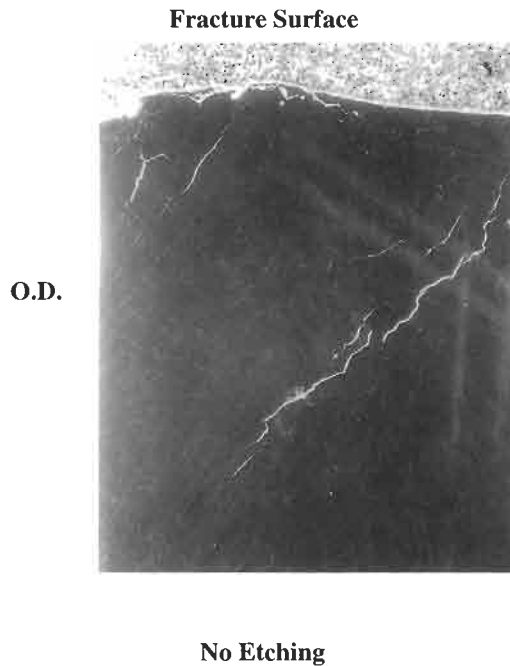**Fracture Surface**

O.D.

No Etching

Fig. 7. Metallographic section close to shaft fracture surface.

photograph taken without etching the metallographic sample, while Fig. 8 consists of a micrographic montage performed after etching the sample. In both cases it can be observed that there are many subsurface cracks under the fracture surface. The cracks are parallel within them, and they have a defined orientation. As regards the grain size, this gets large close to the external diameter and close to the fracture surface, in accordance with the fractographic observations.

No decarburized zone at the outer diameter, close to the fracture surface or at the cracks, has been detected.

3.3. Microstructure and microhardness

The microstructure and the microhardness, with a load of 200 g, were studied in axial metallographic sections from zones far from the fracture surface (~ 30 mm away) and from zones close to the fracture.

In the sections far from the fracture surface, no variation either in the microstructure or in the grain size, between the external diameter and the center of the shaft was observed. The microstructure is the typical one of tempered martensite, in accordance with the thermal treatments of quenching and tempering suffered by this material. As regards the microhardness in these zones, no changes were detected in the values from the edge of the external diameter to the center of the shaft. The average value obtained is 250 HV, typical of this type of material.

In contrast, the microstructure and hardness results obtained close to the fracture surface were
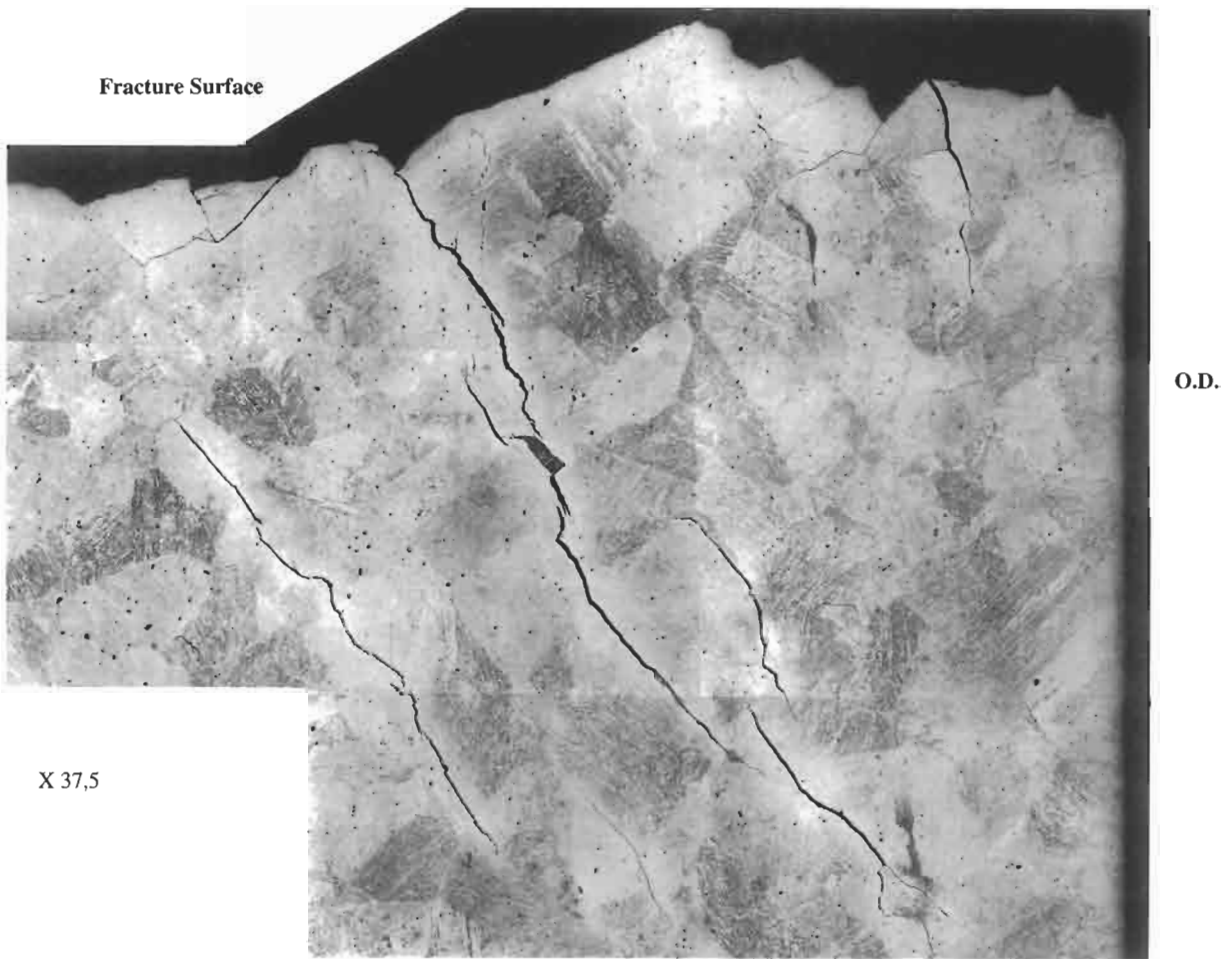
Fracture Surface

O.D.

X 37,5

Fig. 8. Detailed metallographic section close to shaft fracture surface.

different. As mentioned before, the grain size gets large close to the fracture surface and close to the external surface. The microhardness shows higher values in the external diameter than in the center of the shaft. Close to the external surface the microhardness is approximately 500 HV, decreasing to an average value of 410 HV at 1 mm from the edge and 375 HV at the center of the shaft. This last value is even higher than the value measured far away from the fracture.

4. Destructive examination of the chromium-plated sleeve

4.1. Fractography

Fractographic examination by SEM was performed on the fracture surface of the lower part of the sleeve. Close to the outer diameter (OD) different morphologies were detected: intergranular

with big grains (up to ~400 μm in diameter); intergranular but with small grains (~20 μm in diameter); and mixed modes of fracture, transgranular and intergranular with large grains (see Fig. 9).

In the center of the sleeve thickness, the fracture morphology was brittle cleavage (Fig. 10), and at the inner diameter (ID) the fracture was ductile by nucleation and coalescence of microvoids, indicating that the final fracture of the sleeve was produced in this zone.

4.2. Metallography

In the lower part of the sleeve a metallographic study was carried out on axial sections cut from the fracture surface up to 70 mm below it. In all these sections no damage at the ID was found. At the OD, the sections including up to 30 mm below the fracture, corresponding to the external area of grooves, showed damaged material. This damage consisted of crack initiations, and loss and dissolution of material (Fig. 12). EDS analysis were performed in some of these zones (see Section 4.3). On the other hand, no chromium-plated areas were visible in these sections. After etching the sections, different microstructural characteristics were observed (Fig. 13), indicating that these areas have suffered heterogeneous heating at different temperatures and, even, at very high temperatures as demonstrated by the large grain size existing in some zones. These changes in the microstructure explain the different morphologies detected in the fracture surface.

In the metallographic samples containing the material from 30 to 70 mm under the fracture, where externally no grooves were observed, the chromium plated layer was clearly detected although with variable thickness (from 90 to 550 μm) and with some small cracks. In these sections no changes in the microstructure were observed through the thickness of the sleeve.

Some metallographic sections were prepared from the upper part of the sleeve. The characteristics observed were similar to the ones described above.

4.3. EDS analysis

EDS analyses were carried out in some of the damaged zones existing at the O.D. As an example of the results obtained, Fig. 14 shows that generally the main element detected is chromium.

Taking into account the amount of this element in the base material, ~13%, it can be assumed that these high concentrations are related to the original chromium-plated layer. There are also significant amounts of copper in all the analyses and lead in almost all the analyses. These elements may come from the initial bronze bearing. In addition, nickel is detected in some of the analyses, an element that can be related to the graphite–nickel bearing placed after the bronze bearing.

4.4. Microhardness

Vickers microhardness with a load of 200 g were measured in zones close to the fracture surface and in zones 30 mm from the fracture. In the last case the average value obtained was 325 HV, in accordance with the hardness of this material. However in areas close to the fracture, the average value at the center of the sleeve thickness was 420 HV while at the O.D., where different microstructural characteristics were observed, microhardness values from 250 to 375 HV were measured.

(a)
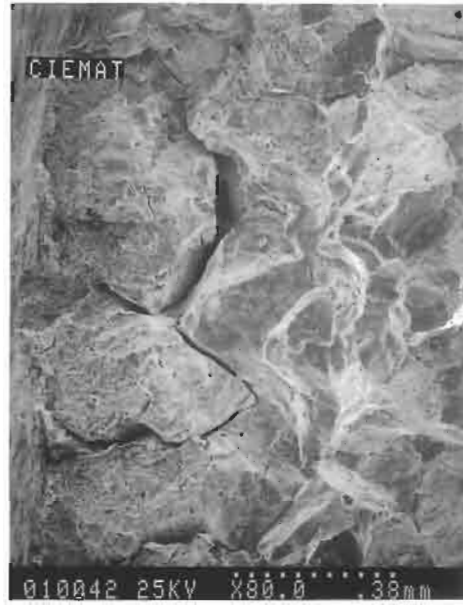
(b)
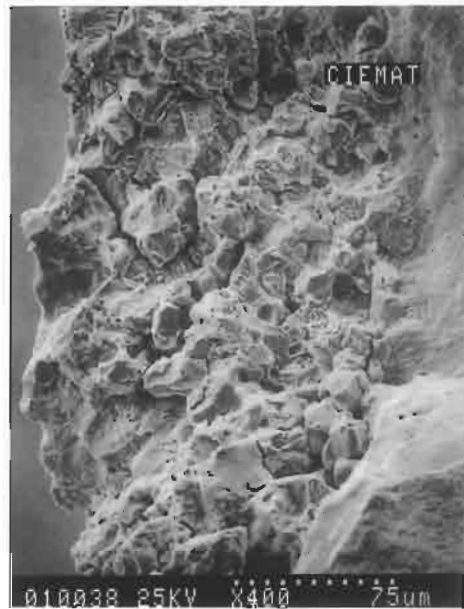
(c)

Fig. 9. Fracture surface of the failed chromium-plated sleeve (OD).
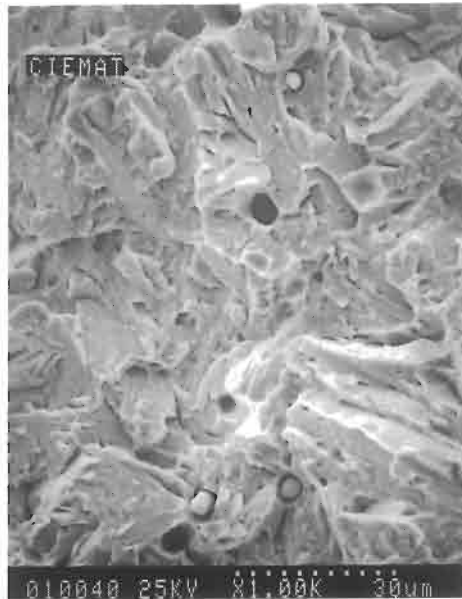
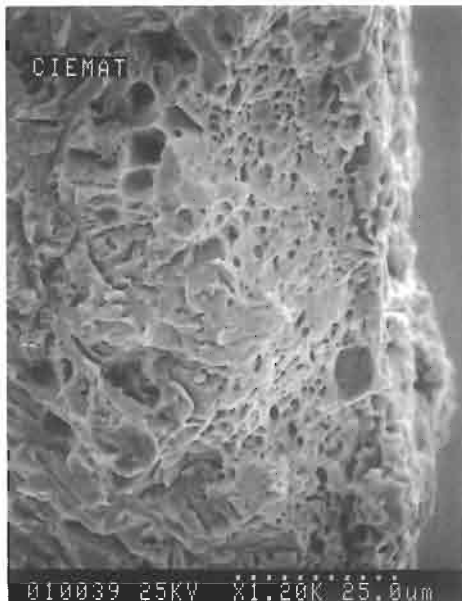Fig. 10. Fracture surface of the failed chromium-plated sleeve (center).

Fig. 11. Fracture surface of the failed chromium-plated sleeve (I.D.).

5. Discussion

The destructive examination of the shaft has shown that the failure initiated at the external surface (where the fracture is intergranular with big grains, up to $\sim 600\ \mu$m in diameter), progressing
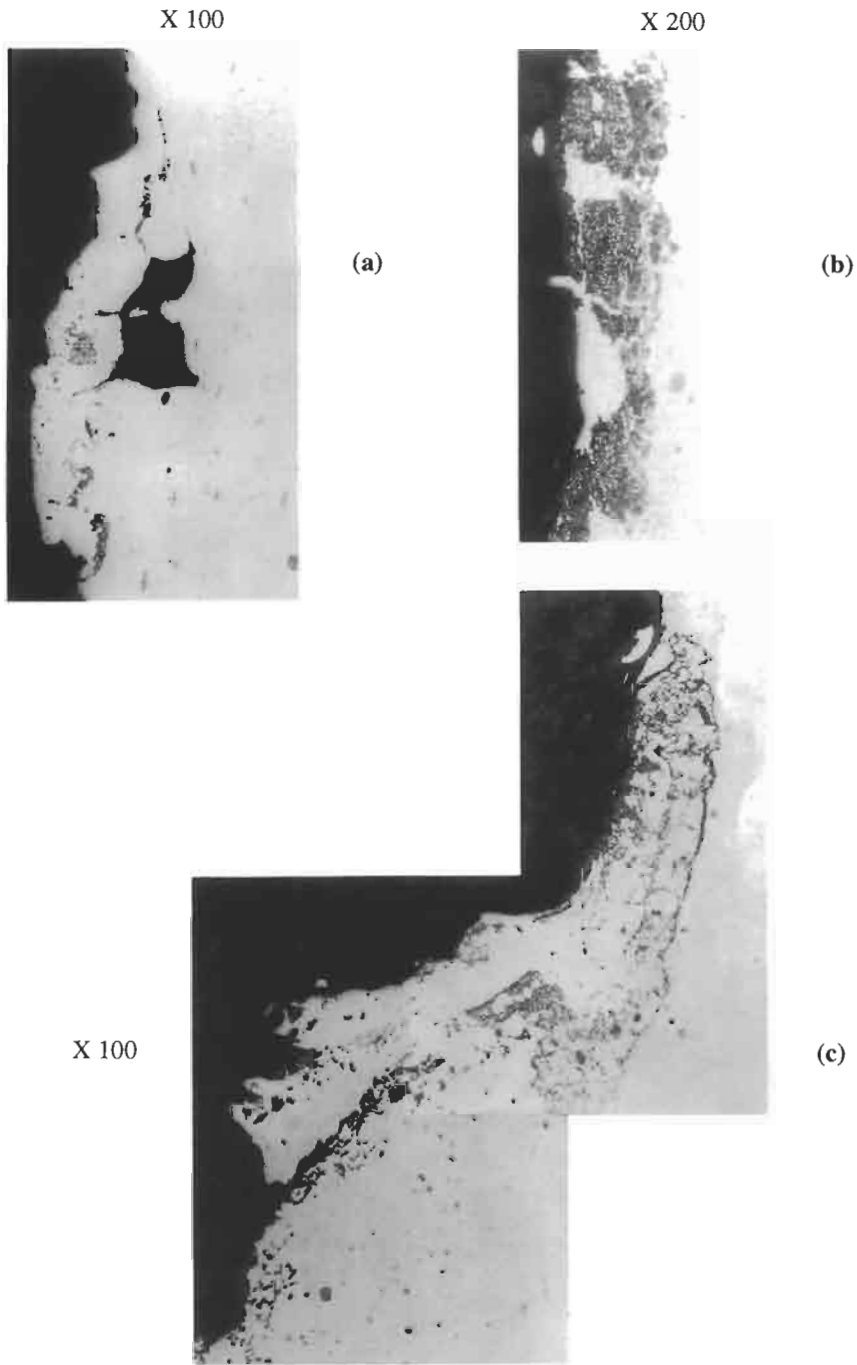
X 100

X 200

(a)

(b)

X 100

(c)

Fig. 12. Metallographic sections, not etched, close to the fracture surface of the chromium-plated sleeve (OD).

438

O.D.

O.D.

X 100

(b)

x 75
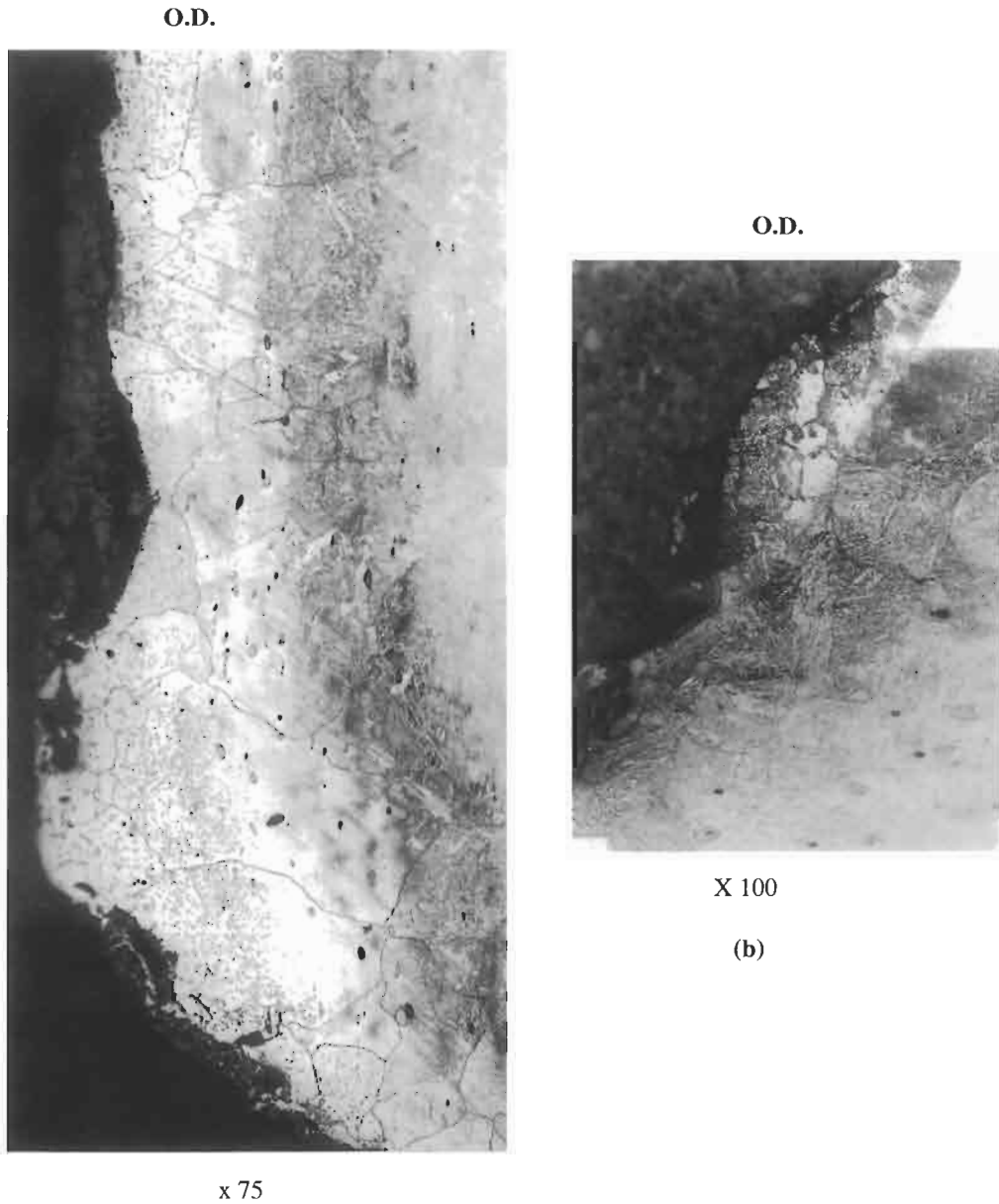
Fig. 13. Metallographic sections, after etching, close to the fracture surface of the chromium-plated sleeve (OD).

towards the shaft center and changing gradually from intergranular to transgranular (with decreasing grain size, up to ~ 20 μm in diameter). The final failure of the shaft was produced at the center by fatigue and torsion due to the operation stresses. Metallographically, important variations of the grain size have also been observed: the grains get large close to the outer diameter and close to the fracture. On the contrary, no changes in the grain size from the surface to the center were
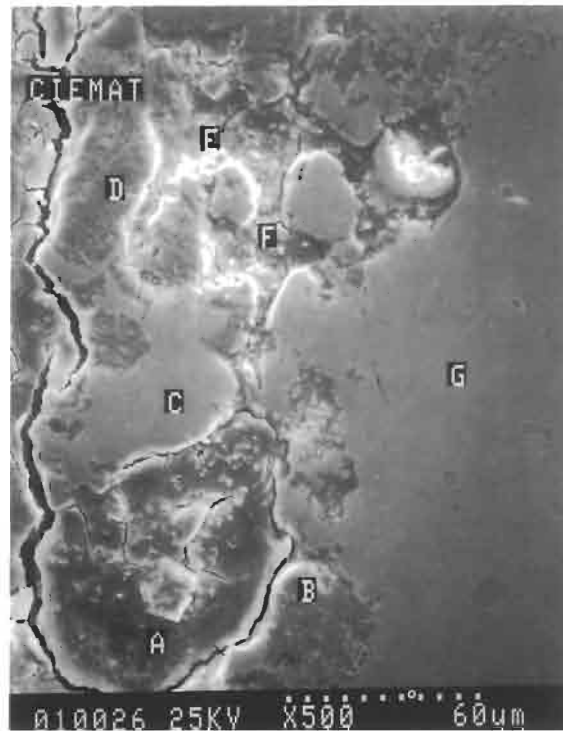
	Al	Si	Ca	Cr	Mn	Fe	Ni	Cu	Pb	
A	2.44	2.01	3.80	17.90	---	50.22	16.27	5.84	1.52	% wt
	1.16	1.00	2.70	16.47	---	49.63	16.91	6.57	5.56	% ato.
B	---	2.47	---	74.19	7.24	2.76	---	9.94	3.40	% wt
	---	1.19	---	66.35	6.84	2.65	---	10.86	12.11	% ato.
C	13.13	1.85	---	53.36	18.18	9.91	---	0.15	3.41	% wt
	6.50	0.96	---	50.92	18.33	10.16	---	0.17	12.97	% ato.
D	---	6.33	---	79.77	4.63	1.98	---	4.85	2.44	% wt
	---	3.23	---	75.37	4.62	2.01	---	5.60	9.17	% ato.
E	0.75	4.68	---	76.76	4.92	5.92	---	6.11	0.86	% wt
	0.38	2.48	---	75.16	5.09	6.22	---	7.31	3.36	% ato.
F	---	12.74	1.86	36.42	---	35.69	7.20	5.33	0.85	% wt
	---	6.76	1.42	36.04	---	37.93	8.04	6.44	3.37	% ato.
G	---	---	---	9.74	---	88.75	---	1.51	---	% wt
	---	---	---	9.11	---	89.17	---	1.73	---	% ato.

Fig. 14. EDS analysis close to the fracture surface of the chromium-plated sleeve (OD).

detected in zones far from the fracture surface. In addition, other cracks were detected under the fracture surface with a defined orientation, that seems to support the existence of internal stresses in these areas. Moreover, the microhardness of the material close to the fracture is very high, reaching values up to 500 HV close to the outer diameter.

As regards the chromium-plated sleeve, this shows macroscopically at the OD close to the fracture many grooves of different widths and depths. Microscopically these correspond to damaged zones without the chromium-plated layer, with different microstructural characteristics and with significant grain growth. These microstructural changes were also reflected in the fractographic examination. In addition, the fractography indicated that the final fracture of the sleeve was produced at the ID.

All these observations, related to the changes in the microstructure and in the microhardness, in the shaft and in the sleeve close to the fracture, point to both having been subjected to very high temperatures, above the recrystallization temperature. It is well known that one of the more clear indications that a metal has been overheated is the coarse grain fracture surface that results [2].

The characteristics detected in the shaft cracking, macroscopically and microscopically, suggest that the cracking originated in quench cracks due to localized overheating. This process results from stresses produced as a consequence of the volume increase accompanying the austenite to martensite transformation. When a steel is quenched, untempered (hard and brittle) martensite is formed at the outer surface first. As cooling continues, the austenite transformation progresses towards the center of the piece, accompanied by a volumetric expansion. This results in internal stresses that place the surface in tension and cracking occurs. Moreover, the resultant martensite is very hard and brittle, making the material very susceptible to cracking [2]. On the other hand, in the shaft failure the appearance of internal cracks (another type of thermal crack), may have contributed to the failure. Internal cracks occur when the overheating is too fast as a result of unequal temperatures of the surface relative to the center of the mass [2].

Taking into account that the operating temperature conditions cannot produce the overheating, it may be deduced that the heat source has been friction between the shaft, or its associated components, and the casing. This implies that, firstly, the failure of the graphite–nickel bearing was produced. Then the chromium-plated sleeve started to rub with the pump casing as demonstrated by the presence of copper and lead, coming from the original bronze bearing in contact with the casing. This fact is also supported by the grooves observed in the outer surface of the sleeve. The friction with the casing originated an overheating that was transferred through the sleeve to the shaft, producing finally a microstructural change in the shaft material and its consequent embrittlement.

6. Conclusions

The failure sequence has been as follows:

(1) The graphite–nickel bearing fails.
(2) The chromium-plated sleeve rubs against the casing and the heat generated by this friction is transferred through the sleeve to the shaft.

(3) This high temperature embrittles the shaft, initiating the fracture.

(4) The fracture of the shaft leads to the fracture of the chromium-plated sleeve.

References

[1] Steam generator reference book. EPRI-TR-103824, vol. 1. 1994.

[2] Failure analysis and prevention. ASM Metals Handbook, vol. 11. 9th ed.

AUTHOR INDEX